Greenhouse Gas Reduction via Co-optimization of Alternative Diesel Fuels with Compression Ignition Engines

by

Taemin Kim

A dissertation submitted in partial fulfillment
of the requirements for the degree of
Doctor of Philosophy
(Mechanical Engineering)
in the University of Michigan
2021

Doctoral Committee:

Professor André L. Boehman, Chair
Professor Herek L. Clack
Professor Angela Violi
Professor Margaret S. Wooldridge

Taemin Kim
askytm@umich.edu
ORCID iD: 0000-0002-5298-5724

사랑하는 엄마, 아빠, 그리고 내 동생 윤진이에게…

And also to "7.8 billion -1" different versions of me who are struggling to find the better ways for their lives. ☺

Acknowledgments

First of all, I sincerely appreciate Prof. André Boehman being my academic advisor for about seven years of my graduate study. Not to mention that he has supported my research technically and financially, it was also such a great pleasure to work with a researcher like him who tries to contribute to societies and environment using the power of science. Sometimes I had difficult times with solving technical issues regarding my research projects, but his support and openness led me to come up with creative solutions, which, in turn, led to the successful completion of my doctoral study.

Next, I would like to thank all the people that provided invaluable technical and financial support for the "Biodiesel CO_2" project. Eric Kurtz and Waheed Alashe at Ford Motor Company provided excellent technical support during the entire project duration which improved my understanding on the project and guided me toward the right direction. Steve Howell at NBB and Robert McCormick at National Renewable Energy Laboratory also provided me precious advices and inputs during the project. Thank you all and I wish all of our efforts to increase the adoption of biodiesel for better environment will soon see the great results.

I would also like to thank Eric Sattler at Tank Automotive Research, Development, and Engineering Center (TARDEC) who gave precious technical and financial support for the bulk modulus study on jet fuels. I also appreciate those people who accepted my industry interview

when I was conducting DME-glycerol blend research: Ron Sills, Rebecca Boudreaux, Emmanuel Varenne, and Myles Bohon. Thank you all, and way to go for DME!

Next, I would like to thank my thesis committee members, Prof. Herek Clack, Prof. Angela Violi, and Prof. Margaret Wooldridge, who shared their precious time and did not hesitate providing precious advices.

I have been financially supported via being GSI for ME433 for two semesters, and I actually learned a lot from conducting the GSI role for this coursework. This coursework is wonderful in that it enlightens a number of students with different majors at University of Michigan about the importance of tackling climate change issues. So, I would like to express special thanks to Prof. David Kwabi, Prof. Wooldridge and Prof. Donald Siegel who have contributed a lot to improve this coursework.

I would also like to thank research associates in the Lay Autolab, especially to Stani Bohac, Robert Middleton and John Hoard for being always helpful for my research and giving practical guidance and inputs for different engine research.

I would like to thank our technical and administrative staffs in Lay Autolab and ME department who have been always helpful for my research. This includes William Kirkpatrick, Kent Pruss, James Elkins, Charles Solbrig, Karen Brown, Matthew Jastrzembowski and all the other staffs who have been doing their crucial jobs to help students do better research.

I cannot thank more to my senior and fellow graduate students who have struggled and shared interesting ideas together to resolve the research problems. Vickey Kalaskar, Dongil Kang, Chenxi Sun, Kwanghee Yoo, Jonathan Martin, Shuqi Cheng, Taehoon Han, Yan Chang, Jeongyong Choi, Vassilis Triantopoulos, Justin Koczak, Minato Tomuro, Fawaz Ali, Rinav Pillai, Erick Garcia, Kaustav Bhadra, Andrew Di Mauro, Muhammad Abdullah, Jordan Easter, Michael Mayo, Yoshihiko Hagiyama, Mitchell Bieniek, Saravanan Duraiarasan, Ripudaman Singh, Puneet Valecha, Benjamin Samuel, Cansu Doganay, Courtney Videchak and all the other students interacted with me during my graduate study, thank you all!

For the last, I would like to thank my parents and my sister who have been supportive throughout my graduate study. I love you so much and I would have not been able to come all the way here if it were not for your support.

Table of Contents

List of Figures

List of Tables

List of Appendices

List of Abbreviations

2.5A	2.5 degrees advanced injection timing
2.5R	2.5 degrees retarded injection timing
5A	5 degrees advanced injection timing
5R	5 degrees retarded injection timing
ADM	Archer Daniels Midland
AFRL	Air Force Research Laboratory
AGP	Agricultural Processing Inc.
ANL	Argonne National Laboratory
ASTM	American Society for Testing and Materials
ATJ	Alcohol-to-Jet
B100	100% Biodiesel (neat biodiesel)
B20	20 vol. % Biodiesel
BD	Biodiesel
BFE	Brake Fuel Conversion Efficiency
BG12	1,2-Butanediol
BG13	1,3-Butanediol
BG14	1,4-Butanediol
BMEP	Brake Mean Effective Pressure

BP	Boost Pressure
BSCO	Brake Specific Carbon Monoxide
BSCO2	Brake Specific Carbon Dioxide
BSNOx	Brake Specific Nitrogen Oxides
BSPM	Brake Specific Particulate Matter
BSTHC	Brake Specific Total Hydrocarbon
bTDC	before Top Dead Center
BUOH	Butanol
CA	Crank Angle
CAC	Charge Air Cooler
CAS	Chemical Abstracts Service
CGP	Crude Glycerol Product
CI	Compression Ignition
CID	Cetane Ignition Delay
CN	Cetane Number
CNL	Combustion Noise Level
CNS	Central Nervous System
DCN	Derived Cetane Number
DEG	Diethylene glycol
DF	Default injection timing
DIPPR	Design Institute for Physical Properties
DME	Dimethyl Ether
DOC	Diesel Oxidation Catalyst
DOE	Design of Experiment
DOT	Department of Transportation
DP	Default boost pressure
DPF	Diesel Particulate Filter
DPG	Dipropylene glycol
DRP	Default rail pressure
DSH	Direct Sugar-to-Hydrocarbon diesel
DSL	Diesel

ECU	Engine Control Unit
EG	Ethylene Glycol
EGR	Exhaust Gas Recirculation
EIA	Energy Information Administration
EOC	End of Combustion
EPA	Environmental Protection Agency
ETOH	Ethanol
EV	Electric Vehicle
FAME	Fatty Acid Methyl Ester
FFA	Free Fatty Acids
FID	Flame Ionization Detector
FSN	Filter Smoke Number
FT	Fischer-Tropsch
FTIR	Fourier-Transform Infrared Spectroscopy
FTP75	Federal Test Protocol 75
GDA	Glycerol Diacetate
GHG	Greenhouse Gas
GHS	Globally Harmonized System of Classification and Labelling of Chemicals
GMA	Glycerol Monoacetate
GMST	Global Mean Surface Temperature
GREET	Greenhouse Gases, Regulated Emissions, and Energy Use in Transportation
GVWR	Gross Vehicle Weight Rating
HD	Heavy Duty
HP	High boost pressure
HRJ	Hydrotreated Renewable Jet
HRJC	Hydrotreated Renewable Jet fuel derived from Camelina
HRP	High rail pressure
HSP	Hansen Solubility Parameter
HVO	Hydrotreated Vegetable Oils
ID	Ignition Delay
IEA	International Energy Agency

IFE	Indicated Fuel Conversion Efficiency
IMEP	Indicated Mean Effective Pressure
IPCC	Intergovernmental Panel for Climate Change
ISO	International Organization for Standardization
ITEC	Isobaric Thermal Expansion Coefficient
LCA	Life-Cycle Assessment
LFE	Laminar Flow Element
LHV	Lower Heating Value
LOO	Leave-One Out
LP	Low boost pressure
LRP	Low rail pressure
MBSP	Minimum Bio-propylene Selling Price
MCR	Minimum Co-solvent to Glycerol Ratio
MDME	Michigan Dimethyl Ether
MEOH	Methanol
MFB10	10% Mass Fraction Burn Angle
MFB50	50% Mass Fraction Burn Angle
MFB90	90% Mass Fraction Burn Angle
MHP	Mid-high boost pressure
MIQ	Main Injection Quantity
MIT	Main Injection Timing
MM	Mini-Map
MMP	Mole Multiplier
MONG	Material Organic Non-Glycerol
MY	Model Year
NBB	National Biodiesel Board
NBG	Neutralized Bio-Glycerine
NFIS	Novel Fuel Injection System
NG	Natural Gas
NH	Not Hazardous
NIST	National Institute of Standards and Technology

NOx	Nitrogen Oxides
NREL	National Renewable Energy Laboratory
PG	Propylene Glycol
PIQ	Pilot Injection Quantity
PIT	Pilot Injection Timing
PLN	Pump-Line-Nozzle
PM	Particulate Matter
PMD	Para-Magnetic Detector
PMEP	Pump Mean Effective Pressure
PROH1	1-Propanol
PROH2	2-Propanol
PTOH	n-Pentanol
PTW	Pump-to-Wheels
RD	Readily Degradable
RED	Relative Energy Difference
RME	Rapeseed Methyl Ester
RMSE	Root-Mean Square Error
RP	Rail Pressure
RPIT	Relative Distance between Main Injection Timing and Pilot Injection Timing
SB32	Senate Bill 32
SCORE	Sandia Compression-Ignition Optical Research Engine
SCR	Selective Catalytic Reducer
SOC	Start of Combustion
SOI	Start of Injection
SOP	Start of Pumping
SSR	Sum of Squared Residuals for Model
SST	Sum of Squared Residuals for Test
STOT	Specific Target Organ Toxicity
TARDEC	Tank Automotive Research, Development, and Engineering Center
TDC	Top Dead Center
TEA	Techno-Economic Assessment

TGP	Technical Grade Glycerol Product
THC	Total Hydrocarbon
TLP	Throttled Low Boost Pressure
TRL	Technology Readiness Level
UB	Upper Bound
ULSD	Ultra-low Sulfur Diesel
USP	United States Pharmaceutical
VFVM	Volatile Fuel Viscometer
VGT	Variable Geometry Turbocharger
WF	Weight Factor
WPAFB	Wright-Patterson Air Force Base
WTP	Well-to-Pump
WTW	Well-to-Wheels

Abstract

Global warming is real and fast. According to the Intergovernmental Panel for Climate Change (IPCC), the global mean surface temperature will likely reach at 1.5ºC above the pre-industrial level in 2040 even if we successfully achieve net-zero CO_2 emissions by 2040. We need to utilize all of the available technologies at this moment to immediately reduce greenhouse gases, and the application of biofuels in compression ignition engines is one of the key technologies. Thus, in this thesis, the co-optimization of three different alternative diesel fuels (i.e., biodiesel, dimethyl ether, alternative jet fuels) with conventional diesel engines is investigated as means to reduce greenhouse gas emissions from transportation sector.

For the application of biodiesel in diesel engines, this thesis focuses on the impact of B20 and engine control unit (ECU) setting on the greenhouse gas and criteria pollutant emissions, and also focuses on the optimization of the ECU of a medium-duty diesel engine for B20 to minimize the greenhouse gas emissions. When compared at the default ECU setting, B20 did not show statistically meaningful difference in the brake fuel conversion efficiency from the baseline diesel while emitting up to 25% more NOx and up to 10% less particulate matter at certain engine operating conditions. This clearly implied the opportunity for improving the brake fuel conversion efficiency for B20 via ECU optimization. With the optimized ECU setting, B20 achieved about relative 1% improvement in its brake fuel conversion efficiency at certain operating conditions, which, at the end, was translated to the relative 0.5% improvement in its

tank-to-wheels (TTW) GHG emissions during the Environmental Protection Agency (EPA) Federal Test Protocol 75 (FTP75) certification test cycle. In addition to the slight improvement in its TTW GHG emissions, B20 with the optimized ECU setting also achieved 25.5% decrease in BSNOx and 16.7% decrease in BSPM emissions during the same certification cycle. The range of optimized ECU parameters and the engine operating conditions investigated in the current study were more comprehensive than any of the previously reported studies, and were comprehensive enough to estimate the engine-out emissions results during the FTP75 certification cycle.

For the application of dimethyl ether (DME) in compression-ignition engines, this thesis focuses on the optimization of the physico-chemical properties of the dimethyl ether (e.g., viscosity) to the existing diesel fuel injection system via glycerol blending. To prevent the phase separation between DME and glycerol, effective co-solvents are found using various selection criteria including co-solvent effectiveness based on Hansen Solubility Parameter theory, viscosity, oxygen content, health and environmental risks, and renewable production availability. Propylene glycol and di-propylene glycol are selected as the two final co-solvents, and are used to develop two different DME-glycerol blends. Those blends are named as Michigan DME I (i.e., mixture of DME, glycerol, and dipropylene glycol) and Michigan DME II (i.e., mixture of DME, glycerol, and propylene glycol). Both Michigan DME blends achieved No.2 diesel level viscosity (i.e., ~1.9cSt at 40ºC) with around 45 wt. % of DME without phase separation at ambient temperature (~20ºC). Both of the novel DME blends are expected to burn soot-free and are assessed to have about 50% reduction in well-to-wheels GHG emissions compared to the petroleum-derived diesel.

For the application of jet fuels in diesel engines, this thesis focuses on the characterization of bulk modulus and speed of sound of the conventional and alternative jet fuels applicable to the U. S. Army ground vehicles equipped with pump-line-nozzle fuel injection system. The un-optimal operations of the fuel injection system due to the difference between the bulk modulus and speed of sound of jet fuels and petroleum-based diesel fuel were the motivation for this research. The bulk modulus and speed of sound of 3 different petroleum-based jet fuels and 3 different alternative jet fuels are measured and compared with each other. The rank order of bulk modulus and speed of sound were same: petroleum-based diesel > 3 petroleum-based jet fuels ≈ Farnesane > Hydrotreated Renewable Jet fuel derived from Camelina (HRJC) > Alcohol-to-jet (ATJ) fuel. Quantitatively speaking, the isothermal bulk modulus of the three petroleum-based jet fuels was 20-25% lower than that of the petroleum-based diesel due to the combined effect of lower aromatic content and lower carbon number of the major components of the petroleum-based jet fuels. Farnesane had similar isothermal bulk modulus to the three petroleum-based jet fuels while the HRJC had about 4% lower isothermal bulk modulus than Farnesane due to its lower carbon number. Alcohol-to-jet (ATJ) fuel had the lowest isothermal bulk modulus out of all measured fuels: 14% lower isothermal bulk modulus than Farnesane. The difference in the isentropic and isothermal bulk modulus is found to be significant for these liquid fuels, and the origin and principles regarding the difference is also investigated and presented in this thesis.

Chapter 1

Introduction

1.1 Motivation

Climate change is already happening throughout the planet at this moment due to the global warming caused by the excessive increase in atmospheric greenhouse gases (GHG) from anthropogenic activity. The intensity of climate change will only become more severe if we do not reduce GHG emissions and significantly change the current "business-as-usual" approach in almost every area of our economy. Figure 1.1 presents the observed global mean surface temperature (GMST) up to 2017 and the projected GMST after 2017 based on three different carbon emissions reduction scenario suggested by Intergovernmental Panel for Climate Change (IPCC).[1] The observed GMST change until 2017 is in grey line and the range of GMST change with over 66% statistical confidence is shaded in orange. The red line denotes the average of the estimated range of the GMST change, and it shows that the GMST has already increased about 1ºC from the pre-industrial era (i.e., 1850-1900 A. D.) as of 2017, which is the culprit for the currently observed climate change.[1] The projection for GMST after 2017 is provided in three different scenarios suggested by the IPCC. The best case scenario in blue lines and shades assumes that net-zero CO_2 emission is achieved in 2040 with the reduction in "non-CO_2 radiative forcing" effect (i.e., greenhouse effect from potent GHGs such as methane (CH_4) and nitrous oxide (N_2O)) after 2030. Even in this best case scenario, the "1.5ºC increase in GMST" will *likely"* (i.e., over 66% statistical confidence) happen around 2040. The IPCC report warns that the impact of 1.5ºC rise in GMST can possibly cause a more aggressive self-reinforcing mechanism in global warming than before, thus making it an important target for GMST that we

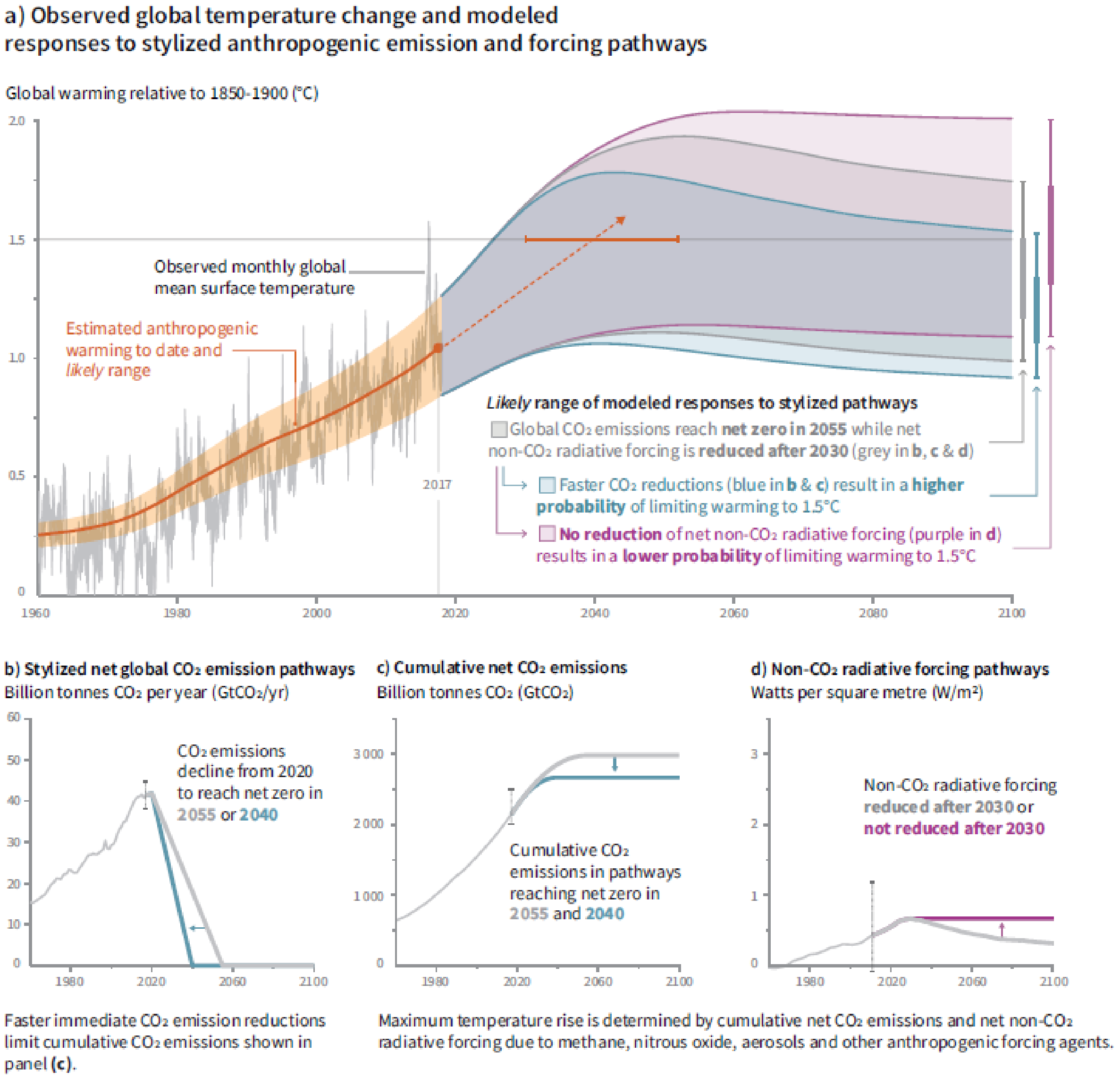

Figure 1.1 a) Observed (before 2017) and projected (after 2017) global mean surface temperature based on three different scenarios (best: blue, neutral: grey, worst: magenta) suggested by Intergovernmental Panel for Climate Change. b) Net global CO_2 emissions trajectory assumed for the best (blue) and neutral (grey) scenarios. c) Cumulative net CO_2 emissions trajectory assumed for the best (blue) and neural (grey) scenarios. d) Non-CO_2 radiative forcing trajectory assumed for the best and neutral cases (grey) and the worst case (magenta).

want to avoid if possible, or that we want to move away from as soon as possible if we cannot help reaching it in 2040.[1]

The problem is that achieving the best case scenario shown in Figure 1.1 is actually a very ambitious goal. Figure 1.1b shows the required trajectory of CO_2 emissions to achieve the best case scenario. From 2020 to 2040, we are required to reduce 42 billion metric tonnes of CO_2 globally, which requires 2.1 billion tonnes of CO_2 reduction each year while also achieving the reduction in other potent GHG emissions (see Figure 1.1d). As a mid-term goal, we need to achieve 50% CO_2 emissions reduction from 2020 to 2030 which is even more intense reduction than the "considered-to-be" ambitious goal set by California Senate Bill 32 (SB32) requiring 40% reduction between 2020 and 2030.[2] Thus, GHG emissions reduction is one of the most difficult, yet impending goals that needs to be met in every aspect of our life and economy.

From a sector-based viewpoint, "transportation" is responsible for a large fraction of carbon emissions we emit these days. Figure 1.2 shows the portion of GHG emissions from each economic sector in the U. S. as of 2017 based on the GHG inventory conducted by the U. S. Environmental Protection Agency (EPA).[3] Transportation sector emits the largest fraction (29%) of GHGs than any other sectors in the U. S., thus providing a strong rationale to pay attention to GHG emissions reduction in the transportation sector.

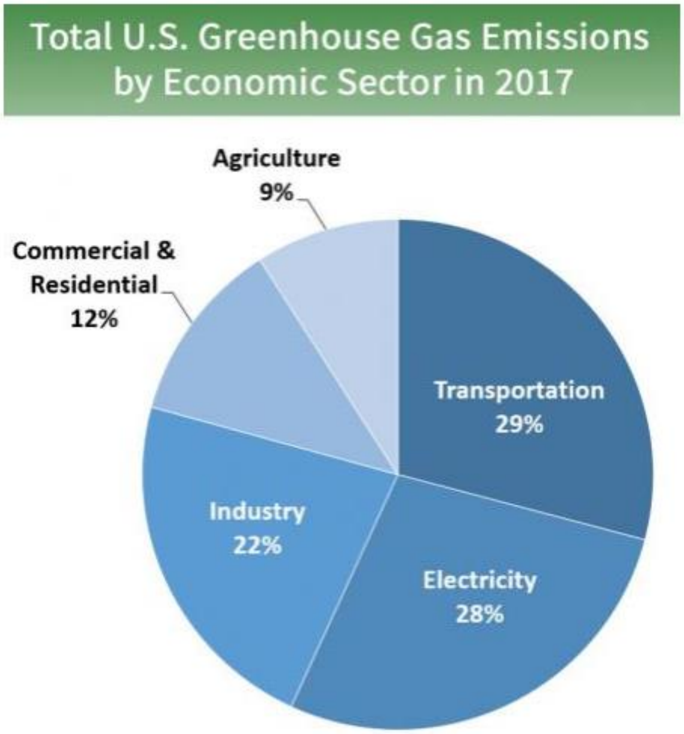

Figure 1.2. Total U. S. GHG emissions by economic sector as of 2017

Wider adoption of electric vehicles (EVs) can be one of the solutions to reduce GHG emissions from the transportation sector. Since the energy required for unit travelling distance (i.e., MJ/mile) for a typical modern electric passenger car is about two or three times lower than the gasoline-engine counterpart, significant GHG emissions reduction can be achieved if the carbon intensity of electricity (i.e., gCO_{2e}/MJ) can be reduced to a level similar to gasoline fuel. The State of California is one of the successful examples that has achieved a better statewide carbon intensity of its electricity (i.e., ~$75gCO_{2e}/MJ$)[4] than that of gasoline (i.e., ~$93gCO_{2e}/MJ$)[5], and we can expect significant carbon emissions reduction in this case from using more EVs.

However, GHG emissions reduction via more EVs still has limitations. First, in case the electricity is carbon intensive (i.e., high gCO_{2e}/MJ associated with electricity production), the

GHG emissions reduction impact from more EV adoption can be either insignificant or even negative. In these cases, the reduction in the carbon intensity of electricity must precede the implementation of EVs to get a GHG benefit from using more electric cars. Moreover, the time required for the transition in electricity generation from high carbon intensity sources such as coal to low carbon intensity sources such as solar and wind might be longer than what the IPCC suggests is left for us. For example, even with aggressive subsidies and regulation to reduce GHG emissions, the State of California took 13 years to reduce the carbon intensity of its electricity by 50% between 2004 and 2017.[6] The average carbon intensity of electricity in the U. S. is about 150gCO_{2e}/MJ these days[4,5] which is about twice the carbon intensity of electricity in the State of California, and we might not have enough time to wait for the rest of the U. S. to reduce its carbon intensity of electricity to the level of the State of California.

Furthermore, regardless of the carbon intensity of electricity, the adoption of more EVs also takes its own time. Many energy research organizations such as U. S. Energy Information Administration (EIA)[7] and International Energy Agency (IEA)[8,9] generally project that 25-30% of the "passenger" cars (not including the vehicles such as long-haul trucks and buses responsible for commercial transportation) will likely be powered by electric batteries either fully (i.e., all-electric) or in part (i.e., plug-in hybrid electric) by 2030. Given that remaining 75% of passenger cars and an even higher percentage of the commercial ground vehicles will still be powered by combustion engines, there must be some means to reduce GHG emissions from these existing engines in parallel with the adoption of more EVs.

Application of low-carbon biofuels in combustion engines is one of the promising solutions for this issue because their application does not have such difficulties that EV adoption has: limited travel range per fueling due to low energy storage density of the battery, and intermittency of solar or wind farm-based electricity supply, etc.

Biofuels in combustion engines can reduce GHG emissions in two different ways. The first is via the reduction in carbon intensity of fuel per unit energy (i.e., gCO_{2e}/MJ) due to the biogenic carbon content in biofuels. The second is via the reduction in required energy per unit travelling distance (i.e., MJ/mile) with optimized fuel and engine calibration. For example, bio-ethanol produced from U. S. corn can be blended with a gasoline blendstock to reduce the carbon intensity of the gasoline fuel. Previous studies report that ethanol from corn reduces well-to-wheel (WTW) GHG emissions by about 30% (“induced” land use impact not included) on a gCO_{2e}/MJ basis.[10] Employing lignocellulosic feedstocks such as corn stover can potentially reduce gCO_{2e}/MJ further. In addition, since the adoption of ethanol can increase the heat of vaporization and octane number of the fuel, the compression ratio of the engine can be increased, which, in turn, will result in the improved thermal efficiency, or eventually the “MJ/mile”.

Since compression-ignition engines (or diesel engines) generally exhibit greater thermal efficiency than the spark-ignition engines (or gasoline engines), and their alternative fuels (i.e., biodiesel, dimethyl ether (DME)) also exhibit greater reduction in gCO_{2e}/MJ than bioethanol[5,11], the application of diesel alternative biofuels in compression-ignition engines can significantly reduce GHG emissions from the transportation sector in parallel with the adoption of more EVs.

1.2 Objectives

Therefore, in this study, the GHG emissions reduction via application of different low-carbon diesel alternative fuels in compression ignition engines is investigated. Also, the relevant engine-fuel compatibility issues and calibration issues are addressed in parallel with the GHG emissions reduction impact. Since the application of different alternative fuels in combustion engines to reduce GHG emissions often accompanies unintended changes in other criteria pollutants such as particulate matter (PM), nitric oxides (NOx), carbon monoxide (CO), and unburned total hydrocarbons (THCs), the impact of fuels on these criteria pollutant emissions are also addressed in this study.

1.3 Chapters Overview

Chapter 1 presents the overall motivation and objectives of the current study, and also provides the overview for each chapter.

Chapter 2 presents some of the selected background theories required to better understand the main results and discussion presented in this thesis which are presented from Chapters 3 – 5. Since this thesis combines three fairly different topics under an overall umbrella of GHG emissions reduction, it was better to include the background theories relevant to each topic in the "Introduction" or "Experimental" sections of each chapter. Thus, Chapter 2 does not provide a comprehensive literature review for all of the studies conducted in this thesis.

Chapter 3 presents the well-to-wheels (WTW) and pump-to-wheels (PTW) GHG emissions reduction potentials of B20 applications in a medium-duty compression ignition engine. The chapter presents the PTW GHG emissions benefit from optimized ECU calibration between B20 and a medium-duty compression-ignition engine, and its overall implication on WTW GHG emissions.

Chapter 4 presents a novel dimethyl ether (DME) blend exhibiting viscosity on a level of petroleum-based diesel oil via addition of glycerol and two different co-solvents, which is expected to enable wider adoption of DME in existing compression-ignition engines without intensive modification. The chapter also provides the WTW GHG emissions reduction potentials of the application of the invented DME blends (i.e., Michigan DME blends) in compression ignition engines.

Chapter 5 presents the experimentally measured values of the important physical properties (i.e., bulk modulus and speed of sound) of different conventional and alternative jet fuels. These values are measured to establish a correlation between the unintended injection timing shifts in pump-line-nozzle type fuel injection system in conventional compression-ignition engines often used by the U. S. military. The chapter provides a fundamental foundation for the co-optimization of different jet fuels with the U. S. military ground vehicles and equipment, which will, in turn, can reduce the GHG emissions from the U. S. military operations.

Chapter 6 provides the overall summary and conclusions for this thesis. It also provides relevant recommendations for future work.

1.4 References

[1] IPCC, 2018: Summary for Policymakers. In: Global Warming of 1.5°C. An IPCC Special Report on the impacts of global warming of 1.5°C above pre-industrial levels and related global greenhouse gas emission pathways, in the context of strengthening the global response to the threat of climate change, sustainable development, and efforts to eradicate poverty.

[2] *California's 2017 Climate Change Scoping Plan: Executive Summary*; California Air Resources Board: Sacramento, CA. November, 2017.

[3] *Inventory of U.S. GHG emissions and sinks: 1990-2018;* EPA 430-R-20-002*;* U. S. Environmental Protection Agency (U. S. EPA): Washington, D. C., April 13th 2020.

[4] Cai, H.; Wang, M.; Elgowainy, A.; Han, J. *Updated Greenhouse gas and Criteria Air Pollutant Emission Factors and Their Probability Distribution Functions for Electric Generating Units*; ANL/ESD/12-2; Argonne National Laboratory: Lemont, IL, May 2012.

[5] Lee, U.; Han, J.; Wang, M.; Ward, J.; Hicks, E.; Goodwin, D.; Boudreaux, R.; Hanarp, P.; Salsing, H.; Desai, P.; Varenne, E.; Klintbom, P.; Willems, W.; Winkler, S.; Maas, H.; De Kleine, R.; Hansen, J.; Shim, T.; Furusjo, E. Well-to-Wheels Emissions of Greenhouse Gases and Air Pollutants of Dimethyl Ether from Natural Gas and Renewable Feedstocks in Comparison with Petroleum Gasoline and Diesel in the United States and Europe, SAE Technical Paper (2016), 2016-01-2209.

[6] *California Greenhouse Gas Emission Inventory: 2000-2017;* 2019 Edition; California Air Resources Board: Sacramento, CA. 2019.

[7] *Annual Energy Outlook 2020 with projections to 2050*; AEO2020; U. S. Energy Information Administration, U. S. Department of Energy: Washington, D. C., January 2020.

[8] *2018 Shell Energy Transition Report;* Royal Dutch Shell: The Hague, Netherlands, 2018.

[9] *Global EV Outlook 2020: Entering the decade of electric drive?*; International Energy Agency (IEA): Paris, France, 2020.

[10] Wang, M.; Han, J.; Dunn, J.; Cai, H.; Elgowainy, A. Well-to-wheels energy use and greenhouse gas emissions of ethanol from corn, sugarcane and cellulosic biomass for US use, *Environmental Research Letters*, **2012**, 7, 045905.

[11] Chen, R.; Qin, Z.; Han, J.; Wang, M.; Taheripour, F.; Tyner, W.; O'Connor, D.; Duffield, J. Life cycle energy and greenhouse gas emission effects of biodiesel in the United States with induced land use change impacts, *Bioresource Technology*, **2018**, 251, 249-258.

Chapter 2

Background

Due to the variety of research topics covered in the main chapters (i.e., Chapters 3 – 5) of this dissertation, most of the background knowledge relevant to each main chapter is covered in either the “Introduction” or the “Experimental” section in each main chapter. This chapter does not cover all of the background knowledge for the current work. Instead, the background knowledge that was difficult to include in the main chapters for the sake of brevity and coherence will be covered here in detail.

2.1 Fundamentals of Solubility Parameter Theory

The solubility parameter (δ) was first defined by Hildebrand et al.[1] as shown in Equation 2.1. It is the square root of “cohesive energy density ($C.\ E.\ D.$)”, which, in turn, is the energy of vaporization (ΔE_{vap}) required for a unit molar volume (V_m) of a molecular species to vaporize.[2] In other words, the solubility parameter is a measure of the energy required to remove a unit volume of molecular species from its surrounding molecules, which depends on the size and structure of the molecular species. Thus, molecular species with similar molecular size and structure have similar solubility parameter as well. When the solubility parameters of two different molecular species are similar to each other, each of the unit volumes of the two species can be swapped with each other with less amount of energy of mixing (ΔE_{mix}).[2] Simply put, the solubility parameter is the theoretical foundation for the "Like dissolves like" rule. Equation 2.2 shows the mathematical relationship between the solubility parameters of two different species and the required energy of mixing for mixing the two species.[2] Here, ϕ is the volume fraction of each species in the mixture, and subscript "*1*" and "*2*" denotes the two different molecular species, respectively.

$$\delta = [C.E.D.]^{1/2} = [\frac{\Delta E_{vap}}{V_m}]^{\frac{1}{2}} \quad \text{(Eq. 2.1)}$$

$$\Delta E_{mix} = \phi_1 \phi_2 \cdot V_m (\delta_1 - \delta_2)^2 \quad \text{(Eq. 2.2)}$$

Although Hildebrand's solubility parameter method could predict the solubility of non-polar species well, it had limitation that the theory does not work as well for polar species.[2] Many researchers have attempted to extend the solubility parameter theory to polar species by dividing the formerly one-dimensional solubility parameter into multiple sub-types of solubility parameters. Blanks et al.[3] and Weimer et al.[4] divided the solubility parameter (δ) into two different sub-types. Each sub-type was dedicated to each of the contributions from two different intermolecular interactions: the contribution from i) non-polar molecular interaction (i.e., dispersion, or "induced dipole-induced dipole" interaction); and ii) polar molecular interaction. This approach was progressed further by Hansen[5]. He divided the polar contribution into two different groups of contributions: the contribution from i) dipole-dipole interaction; and ii) hydrogen bonding. Thus, Hansen's approach divides the solubility parameter into 3 different sub-types in total (i.e., dispersion, polar, and hydrogen). Equation 2.3 shows the relationship between the original solubility parameter (δ) and each of the sub-types of the solubility parameter (δ_d: solubility parameter for dispersion, δ_p: solubility parameter for polar interaction, and δ_h: solubility parameter for hydrogen bonding) defined by Hansen.

$$\delta^2 = \delta_d^2 + \delta_p^2 + \delta_h^2 \quad \text{(Eq. 2.3)}$$

Hansen's three dimensional approach on solubility parameter has worked very well for predicting the solubility of a comprehensive range of molecular species including hydrocarbons, polymers, and elastomers. Thus, it has been used by many researchers to predict unknown solubility between different molecular species.[6-9] Examples of the application includes, but not limited to, the prediction of the solubility between unconventional candidate fuels and water[10,11], and the solubility (or interaction) between candidate fuels and elastomers or plasticizers commonly used in internal combustion engines[12-14].

Thus, in this work, Hansen's three dimensional solubility parameter approach is used in Chapter 4 to predict the effectiveness of the co-solvent preventing the phase-separation between DME and glycerol. More fundamental discussion of the principles underlying the Hansen Solubility Parameter (HSP) theory is presented in the following section.

2.2 Hansen Solubility Parameter (HSP) theory

Hansen Solubility Parameter (HSP) theory defines the "solubility distance (R_a)" between two different molecular species as shown in Equation 2.4. In HSP, the solubility distance is divided by the "solubility radius (R_o)" (or interaction radius) of a particular species to result in "relative energy difference (*RED*)", which is used as the measure to tell how easily other species will mix with that particular molecular species of interest. Equation 2.5 shows the definition of *RED*.

$$R_a = \sqrt{4 \cdot \left(\delta_{d,1} - \delta_{d,2}\right)^2 + \left(\delta_{p,1} - \delta_{p,2}\right)^2 + \left(\delta_{h,1} - \delta_{h,2}\right)^2} \quad \text{(Eq. 2.4)}$$

$$RED = \frac{R_a}{R_o} \quad \text{(Eq. 2.5)}$$

Figure 2.1 shows the concept of the solubility distance (R_a), interaction radius (R_o), and the relative energy difference (*RED*). Figure 2.1a shows the case where the relative energy difference is less than 1 (i.e., solubility distance between the two species is shorter than the interaction radius of species 1). In this case, species 2 is predicted to be readily soluble in species 1. Figure 2.1b shows the opposite case where the relative energy difference is greater than 1 (i.e., solubility distance between the two species is longer than the interaction radius of species 1). In this case, species 2 is not likely to be mixed with species 1. In case *RED* values are close to 1, the prediction of solubility between the two species based on HSP theory can be different from the experimental measurement results. Thus, the best way to check the solubility in this case is via experimental measurements.

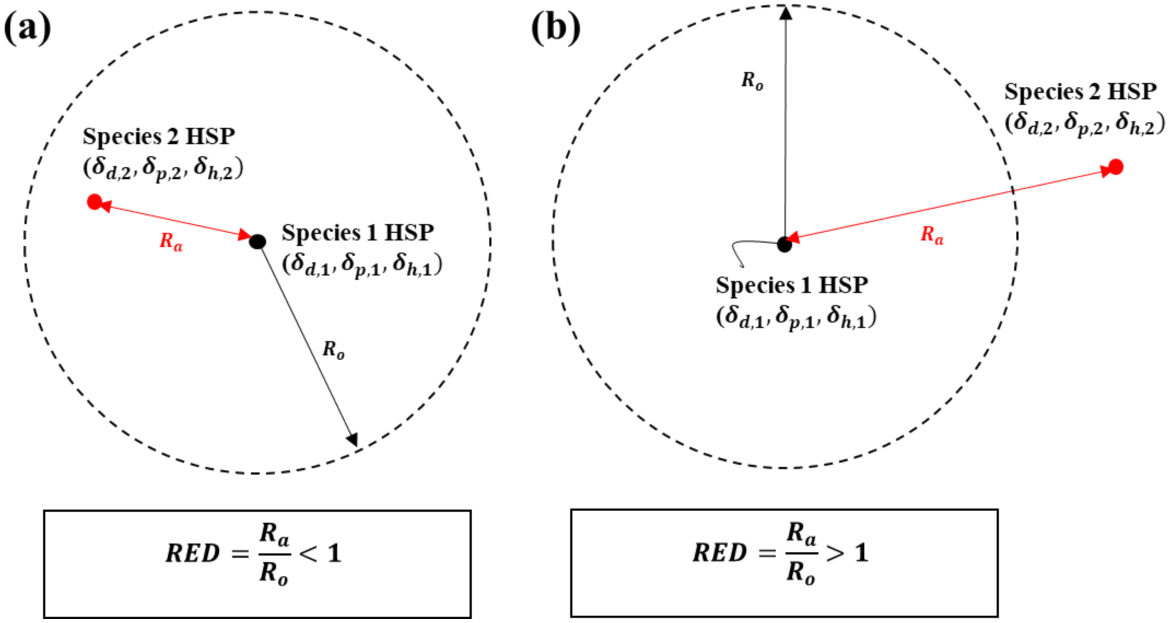

Figure 2.1 Concepts of the solubility distance (R_a), interaction radius (R_o), and relative energy difference (RED) in Hansen Solubility Parameter (HSP) theory. Case (a): RED less than 1, Case (b): RED greater than 1.

2.3 References

[1] Hildebrand, J.H.; Scott, R.L. *The Solubility of Non-Electrolyte: Monograph Series, American Chemical Society (no. 17)*; 3rd ed.; Dover Publications: New York, 1949.

[2] Koenhen, D.M.; Smolders, C.A. The determination of solubility parameters of solvents and polymers by means of correlations with other physical quantities, *Journal of Applied Polymer Science*, **1975**, 19, 1163-1179.

[3] Blanks, R.F.; Prausnitz, J.M. Thermodynamics of Polymer Solubility in Polar and Nonpolar Systems, *Ind. Eng. Chem. Fundamen.*, **1964**, 3, 1-8.

[4] Weimer, R.F.; Prausnitz, Screen Extraction Solvents This Way, *Hydrocarbon Processing*, **1965**, 44, 237-242.

[5] Hansen, C. M. *Hansen Solubility Parameters: A User's Handbook,* 2nd Ed.; CRC Press: Boca Raton, FL. June 2007.

[6] Srinivas, K.; Potts, T.M.; King, J.W. Characterization of solvent properties of methyl soyate by inverse gas chromatography and solubility parameters, *Green Chemistry*, **2009**, 11, 1581-1588.

[7] Vincent, J.D.; Srinivas, K.; King, J.W. Characterization of the Solvent Properties of Glycerol Using Inverse Gas Chromatography and Solubility Parameters, *Journal of American Oil Chemists' Society*, **2012**, 89, 1585-1597.

[8] Cascant, M.M.; Breil, C.; Garrigues, S.; Guardia, M.; Fabiano-Tixier, A.S.; Chemat, F. A green analytical chemistry approach for lipid extraction: computation methods in the selection of green solvents as alternative to hexane, *Analytical and Bioanalytical Chemistry,* **2017,** 409, 3527-3539.

[9] Yara-Varon, E.; Fabiano-Tixier, A.S.; Balcells, M.; Canela-Garayoa, R.; Billy, A.; Chemat, F. Is it possible to substitute hexane with green solvents for extraction of carotenoids? A theoretical versus experimental solubility study, *RSC Advances,* **2016**, 6, 27750.

[10] Fiorini, G.; Fouts, L.; Luecke, J.; Vardon, D.; Huq, N.; Christensen, E.; Huo, X.; Alleman, T.; McCormick, R.; Kass, M.; Polikarpov, E.; Kukkadapu, G.; Whitesides, R.A. Screening of Potential Biomass-Derived Streams as Fuel Blendstocks for Mixing Controlled Compression Ignition Combustion, SAE Technical Paper (2019), 2019-01-0570.

[11] McCormick, R.L.; Fioroni, G.; Fouts, L.; Christensen, E.; Yanowitz, J.; Polikarpov, E.; Albrecht, K.; Gaspar, D.J.; Gladden, J.; George, A. Selection Criteria and Screening of Potential

Biomass-Derived Streams as Fuel Blendstocks for Advanced Spark-Ignition Engines, SAE Technical Paper (2017), 2017-01-0868.

[12] Kass, M.D.; Daw, C. Compatibility of Dimethyl Ether (DME) and Diesel Blends with Fuel System Polymers: A Hansen Solubility Analysis Approach, SAE Technical Paper (2016), 2016-01-0835.

[13] Kass, M.D.; West, B.H. Compatibility of Fuel System Elastomers with Bio-Blendstock Fuel Candidates Using Hansen Solubility Analysis, SAE Technical Paper (2017), 2017-01-0802.

[14] Kass, M.; Janke, C.; Connatser, R.; West, B.; Szybist, J.; Sluder, S. Influence of biodiesel decomposition chemistry on elastomer compatibility, *Fuel*, **2018**, 233, 714-723.

Chapter 3

Greenhouse Gas Reduction in Medium-Duty Compression Ignition Engines with B20 Applications

3.1 Introduction

Biodiesel is a low carbon fuel produced from a number of renewable feedstock options. It can be produced from 1st generation feedstocks such as plant-based oils (e.g., soy oil, canola oil, rapeseed oil, etc.) and animal fats (e.g., tallow), or from 2nd generation feedstocks such as algae or lignocellulosic biomass.[1-3] Currently, biodiesel production in the U. S. is predominantly from the transesterification reaction of soybean oil[4], meanwhile much research is being conducted to reduce the cost and life-cycle impact by exploring better feedstocks and production pathways.[5-7]

Soy-based biodiesel can reduce well-to-wheels (WTW) greenhouse gas (GHG) emissions per unit energy (i.e., gCO_2e/MJ) by 66-72% with currently adopted agricultural and industrial practices as compared to the petroleum-based diesel fuel.[8] Employing less carbon intensive farming processes and more efficient utilization of its co-product (i.e., soymeal and glycerol) are expected to further improve the life-cycle performance of biodiesel.[8] Furthermore, the adoption of the higher energy density feedstocks such as algae is expected to reduce the GHG emissions significantly by reducing the land use impact of biodiesel production.[1]

In addition to the low carbon emissions, application of biodiesel in compression ignition (CI) engines has other benefits. Biodiesel can reduce particulate matter and carbon monoxide emissions with a manageable degree of increase in NOx emissions.[9,10] It also improves the oxidation reactivity of the soot inside the diesel particulate filter (DPF), which, in turn, improves the efficiency of the operation of DPF regeneration.[11] Its energy density (33.0 MJ/L) is about 9% lower than that of the petroleum-based diesel (36.2MJ/L). Although this moderate decrease in lower heating value (LHV) will require either an increase in fuel tank size or an increase in refueling frequency for the drivers, the degree of the decrease in LHV with biodiesel from the petroleum-based diesel is much better than the degree of decrease in LHV with bio-ethanol from its petroleum based counterpart (i.e., gasoline fuel), thus providing a rationale for widespread adoption of biodiesel in CI engines.

However, neat biodiesel (B100) has operational problems with conventional CI engines.[12] It can degrade the performance of the after-treatment system by metal oxide ash accumulation, and can degrade the engine oil quality due to its high boiling point.[13,14] It can also clog the fuel injection system due to the poor cold flow properties or due to the peroxidation with air or water.[12,15]

Thus, B20 (i.e., 20 vol. % of biodiesel in petroleum-based diesel) is currently the highest accepted blend level of biodiesel in the U. S. for production CI engine applications. Unlike B100, B20 does not impose operational problems listed above when applied to lightly modified diesel engines (i.e., B20-compatible engines) while partially achieving the benefits of neat biodiesel.

However, even for B20, it is still not a good idea to apply it to CI engines without any changes in Engine Control Unit (ECU) settings. From the perspective of GHG emissions reduction per unit travelling distance (i.e., gCO_2e/mile), the application of B20 in CI engines without the adjustment in ECU settings will not extract the best carbon emissions reduction that B20 could achieve.[16-21] This is because the difference in fuel properties causes an unintended shift in the ECU settings to increase the fuel energy required per unit mileage (i.e., MJ/mile). Following are examples of the result of the B20 application in CI engines with un-optimized ECU settings.

First, due to the lower energy content of B20, the driver will increase the acceleration pedal angle to meet certain brake torque, which will, in turn, change different input parameter settings in the ECU (e.g., Exhaust Gas Recirculation (EGR) rate, boost pressure (BP), rail pressure (RP), main injection timing (MIT), pilot injection quantity (PIQ), relative distance between MIT and PIT (RPIT)).[22] The unintended shifts in ECU input parameter settings can result in un-optimized brake fuel conversion efficiency (BFE) for B20. Secondly, even for the fixed ECU settings, higher fuel oxygen content in B20 can result in higher exhaust oxygen concentration, which will result in higher intake oxygen concentration via EGR. This will make intake charge condition favorable for NOx generation, thus failing to meet criteria pollutant emissions certification standards.[9]

Thus, to extract the best GHG reduction per unit mileage from B20 while satisfying the criteria pollutant standards, the ECU setting must be re-calibrated to achieve the maximum BFE based on the impact of “fuel” and “ECU calibration” on BFE and criteria pollutant emissions.

There has been a number of studies focused on the biodiesel “fuel” impact on BFE and emissions in diesel engines. Table 3.1 shows the summary of the test engine, operating conditions (i.e., engine load and speed), input variables (e.g., rail pressure, main injection timing), and fuel types investigated in the selected previous studies on the biodiesel fuel impact in CI engine. Yehliu et al.[23] investigated the impact of neat biodiesel on BFE and criteria pollutant emissions in a light-duty diesel engine at four different modes (i.e., 2 different engine speeds at 2 different brake mean effective pressure (BMEP)) with and without pilot injection. The study provided great understanding on the impact of B100 at different operating conditions (i.e., more intense particulate matter (PM) reduction at higher loads) and with pilot injection event (i.e., decrease in particle concentration and NOx emission than single injection strategy). However, the study did not cover the impact of biodiesel with a more comprehensive range of the ECU settings (i.e., impact of biodiesel at different rail pressure, boost pressure, main injection timing, and EGR rate from the default ECU settings). Ye et al.[24] investigated the impact of B40 (i.e., 40 vol. % biodiesel with petro-diesel) on BFE and criteria pollutant emissions in a medium-duty diesel engine at three different loads with varying main injection timing and rail pressure. The study narrowed the gap left from Yehliu et al.'s previous work in that it provided biodiesel fuel's impact at varying input parameters such as main injection timing (i.e., biodiesel NOx and PM effect is more intense at extremely advanced injection timings) and rail pressure (i.e., biodiesel PM reduction is more intense at lower rail pressure). However, the work still did not provide the impact of biodiesel at different charge gas conditions via varying EGR rate or boost pressure. Thus, it could not provide a fully optimized new ECU calibration for biodiesel application. Mueller et al.[25] investigated the impact of neat biodiesel in a single-cylinder research engine (i.e., Sandia Compression-ignition Optical Research Engine, or SCORE) designed to simulate a Caterpillar Heavy-duty diesel engine. The study provided great fundamental understanding on different origins of the biodiesel NOx increase (i.e., difference in ignition delay, bulk cylinder temperature, lift-off length, and oxygen ratio at the lift-off length between neat biodiesel and petroleum-based diesel) at different indicated mean effective pressures

(IMEP) with and without oxygen dilution. Since the study was focused on the investigation of the fundamental origin of biodiesel NOx increase, the impact of biodiesel in a wide range of ECU settings and the impact of unintended shifts in ECU settings were not covered in the study.

	Yehliu et al., 2010[23]		Ye et al., 2012[24]		
Engine type	DDC Light duty 2.5L, common-rail, turbocharged, direct-injection engine		Ford Powerstroke, Medium duty, 6.4L, common-rail, turbocharged, direct-injection engine		
Compression ratio	17.5		17.2		
Fuel type	Soy-derived B100		Soy-derived B40		
BMEP [bar]	3	5.5	4.3	9.2	12.5
Engine speed [rpm]	1850	2400	Fixed at 1500		
EGR rate [%]	Fixed at 0		Fixed at 10		
Boost Pressure	Default boost pressure setting only		Fixed around 2bar		
Rail Pressure	Default injection pressure setting only		80 - 120% of the default injection pressure.		
Main injection timing	Default injection timing setting only		12CAs range (9bTDC – 3aTDC)		
Pilot application	1 pilot event		No pilot application		

	Mueller et al., 2009[25]				Current study
Engine type	SCORE, Single-cylinder version of Caterpillar Heavy-duty engine, common-rail, turbocharged, direct-injection engine				Ford Powerstroke, Medium duty, 6.7L, common-rail, turbocharged, direct-injection engine
Compression ratio	16.0				16.2
Fuel type	Soy-derived B100				Soy-derived B20
BMEP [bar]*	4	8	12	15	6 different operating conditions (Table 3.5)
Engine speed [rpm]	Fixed at 800				
EGR rate [%]	No EGR (O_2: 20.9%)		Moderate EGR (O_2 16.5%)		Varied between 0 to max.
Boost Pressure	Default boost pressure setting only				Varied between min. and max.
Rail Pressure	Default injection pressure setting only				80 – 120% of the default injection pressure
Main injection timing	Default injection timing setting only				10CAs range around the default injection timing
Pilot application	No pilot application				1 or 2 pilot application

Table 3.1 Summary of the selected previous studies on the impact of biodiesel on CI engine performance and emissions (*: IMEP is used instead of BMEP for Mueller et al., 2009).

There has also been some research to investigate the impact of “ECU calibration” with biofuel application in CI engines to improve the unintended worsening in BFE due to the unintended shift in the ECU settings. Larsson et al.[21] adjusted the EGR and main injection timing settings for different types of Fischer-Tropsch (FT) oils and Rapeseed-derived biodiesel to maximize BFE. However, the range of engine operating conditions and ECU input parameters adjusted in the study was not comprehensive enough to suggest a full new set of ECU settings dedicated for biodiesel. Hermitte et al.[16] invented a calibration system based on a “Fuel Quality Sensor” which can adjust the ECU settings on-board based on different fuel properties diagnosed by the sensor. However, despite the comprehensive range of the engine operating conditions and fuel variability that the sensor could cover, some of the important ECU input parameters such as rail pressure, boost pressure, and pilot injection quantity were still not accounted for in the study, thus leaving the room for further research on the more comprehensive ECU optimization for biodiesel. Murr et al.[18] presents a report on how the ECU optimization for each different type of biofuel should generally, or qualitatively, be conducted based on their observation on ECU shifts with those biofuels. However, it does not provide a quantitative, or specific optimized ECU settings for each fuel. Omari et al.[19] presents the optimization of ECU settings for hydrotreated vegetable oils (HVO) in a light-duty diesel engine. The study covers 8 different ECU input parameters to cover a comprehensive range of engine operating conditions. It also compares the BFE and emissions characteristics of the diesel and HVO in different “drop-in” scenarios to quantitatively account for the unintended shifts in ECU settings caused by different fuel types. However, because the fuel properties of HVO and biodiesel are still significantly different in that biodiesel contains oxygen atoms while HVO does not, the research for the ECU optimization focused on biodiesel is still required.

Therefore, in this study, the optimization of ECU settings with 6-8 different input parameters is conducted in a comprehensive range of engine operating conditions to maximize the GHG emissions reduction with the B20 application based on the comprehensive understanding on both the fuel's and calibration's impact on engine performance and emissions. The study can be distinguished into three stages. First, the impact of B20 "fuel" on GHG and criteria pollutant emissions (i.e., NOx, PM, CO, THC) is investigated by comparing the experimental measurements of B20 to petroleum-based diesel at fixed, default ECU calibration. Second, the ECU calibration is optimized for B20 to maximize the GHG emissions reduction while satisfying the criteria pollutant emissions standard. Lastly, the maximum GHG emissions reduction with B20 application is experimentally measured with the optimized ECU calibration, thus providing the understanding of the combined impact of biodiesel fuel and calibrations on engine performance and emissions. The experiment is conducted in a 6.7L Ford Powerstroke medium-duty turbodiesel engine.

3.2 Experimental

3.2.1 Test Fuels

Certified ultra-low sulfur diesel (cert-ULSD) obtained from Corrigan Oil Company is used as the baseline fuel. Cert-diesel is chosen against the regular pump-grade diesel to avoid the seasonal differences in fuel properties. During the study, total 4 different batches of the cert-diesel are used while the fuel properties of the different batches were maintained consistent as shown in Table 3.2.

	1st batch	2nd batch	3rd batch	4th batch
Density [kg/m^3]	846.7	848.1	847.2	846.4
Cetane Number	47.2	47.5	47.9	46.0
LHV [MJ/kg]	42.77	42.64	42.76	42.76
Carbon wt. %	87.25	87.38	87.06	87.24
Hydrogen wt. %	12.75	12.62	12.94	12.76

Table 3.2. Fuel properties of the different batches of the cert-ULSD used for the current study.

Soybean-derived biodiesel obtained from Agricultural Process Inc. (AGP) is used as the neat biodiesel blendstock for the B20 used in the current study. The B100 from AGP is sent to Corrigan Oil Company, then it is mixed with the cert-ULSD with 20% volume fraction to form B20. Properties of the B100 is presented in Table 3.3. Cetane number (CN) and viscosity were moderately higher than the cert-diesel. Lower heating value (LHV) was about 12% lower than that of the cert-diesel. In terms of the molecular composition, the neat soy-biodiesel contained high fractions of polyunsaturated esters (i.e., C 18:2 methyl linoleate and C 18:3 methyl linolenate), and contained about 11% fuel oxygen mass content.

Properties [Unit]	Test method	Results
Flash point [ºC]	ASTM D93	117
Sulfur content [ppm]	ASTM D5453	<1
Cloud point [ºC]	ASTM D2500	-2
Oxidative stability [hrs]	EN15751	9.17
Specific gravity [kg/m^3] @15ºC	ASTM D1298	883.13
Kinematic viscosity [cSt] @40ºC	ASTM D445	4.010
Cetane number	ASTM D613	51.7
Copper Strip Corrosion	ASTM D130	1a
Nace Corrosion	TM-0172	B+
LHV [MJ/kg]	[-]	37.4
C 14:0 mole fraction [%]	FAME analysis	Trace
C 16:0 mole fraction [%]	FAME analysis	11
C 18:0 mole fraction [%]	FAME analysis	5
C 18:1 mole fraction [%]	FAME analysis	23
C 18:2 mole fraction [%]	FAME analysis	53
C 18:3 mole fraction [%]	FAME analysis	8
C/H/O mass ratio [%]	Based on FAME analysis	77.22/12.82/10.96

Table 3.3. Properties and molecular composition of the neat soy biodiesel (B100).

The properties of the B20 used for the current work are presented in Table 3.4. Density, LHV, and Carbon-Hydrogen-Oxygen mass ratio of the B20 are estimated from the linear interpolation of the properties of the cert-diesel and B100. For the estimation of the ignition quality of the B20, linear interpolation of the cetane numbers of B100 and ULSD could also be used. However, to ensure more reliability on the ignition quality of the test fuels, the derived cetane number (DCN) of B20 and ULSD are directly measured in the Cetane Ignition Delay (CID) equipment based on the ASTM D7668 standard method.[26] The DCN for B20 was 43.88 while the DCN for cert-diesel was 43.76 showing negligible difference.

Density [kg/m^3]	854.39
LHV [MJ/kg]	41.65
Derived Cetane Number (DCN)	43.88
C/H/O mass ratio [%]	85.03/12.71/2.27

Table 3.4. Properties of the B20

3.2.2 Test Equipment and Definitions

Table 3.5 presents the selected features of the test engine. An 8-cylinder 2015 Model Year (MY) Ford 6.7L Powerstroke turbodiesel engine is used for the current work. The engine is turbocharged with a single variable geometry turbocharger (VGT). A high pressure common rail fuel injection system with the maximum rail pressure of around 2000bar controlled the fuel injection via the Engine Control Unit (ECU). Compression ratio is 16.2. For emissions treatment, Exhaust Gas Recirculation (EGR) with high-pressure EGR loop, and the after-treatment system composed of diesel oxidation catalyst (DOC), selective catalytic reducer (SCR) and diesel particulate filter (DPF) is used. For the current study, the DPF is replaced with an empty steel can to set the back pressure at ambient. The commercial vehicle application of the test engine is

Ford F-250 or 350 medium-duty pickup truck of which gross vehicle weight rating (GVWR) is class 2b (8,501-10,000 lbs) or class 3 (10,001-14,000 lbs).

Engine name	Ford 6.7L Powerstroke diesel V-8
Model year (MY)	2015
Chassis Type	Pickup
Compression ratio	16.2
Bore [mm]	99
Stroke [mm]	108
Aspiration	Garrett GT37, Single Variable Geometric Turbocharger (single-VGT)
Injection	Direct injection with high pressure common-rail (~2000bar)
Peak power [hP]	440 at 2800rpm
Peak torque [lb-ft]	860 at 1600rpm
Emissions treatment	Exhaust gas recirculation (EGR), Diesel oxidation catalyst (DOC), Selective catalytic reduction (SCR), Diesel particulate filter (DPF).

Table 3.5. Test engine specification

Figure 3.1 is the schematic describing the air flow, EGR flow, and fuel flow inside the test engine. The fresh air first passes through the compressor part of the turbocharger, and it is cooled through the charge air cooler (CAC), then, it mixes with the EGR gas after a throttle valve. The throttle valve is set to 100%, wide-open, throughout the current study except for one operating condition which will be mentioned in section 3.2.5.1. Mass flow rate of the intake gas ($\dot{m}_{int}$) is the sum of the mass flow rate of the fresh air ($\dot{m}_{air}$) and the mass flow rate of the EGR ($\dot{m}_{egr}$). The intake gas enters the combustion chamber when the intake valve is open. Fuel is injected through the injector nozzle, the combustion event happens, and the combustion products are expelled during the exhaust stroke. The engine exhaust exits the exhaust valve, then, is divided into two streams. One goes through the EGR valve and is recirculated back into the engine intake while the other passes through the turbocharger and the after-treatment system. In the current study, the exhaust gas stream passing through the turbine is defined as the “Exhaust flow”. Thus, Equations 3.1 and 3.2 apply for the relationship of the mass flow rate of the different streams inside the test engine.

$$\dot{m}_{air} + \dot{m}_{egr} = \dot{m}_{int} \qquad \text{(Eq. 3.1)}$$

$$\dot{m}_{air} + \dot{m}_{f} = \dot{m}_{exh} \qquad \text{(Eq. 3.2)}$$

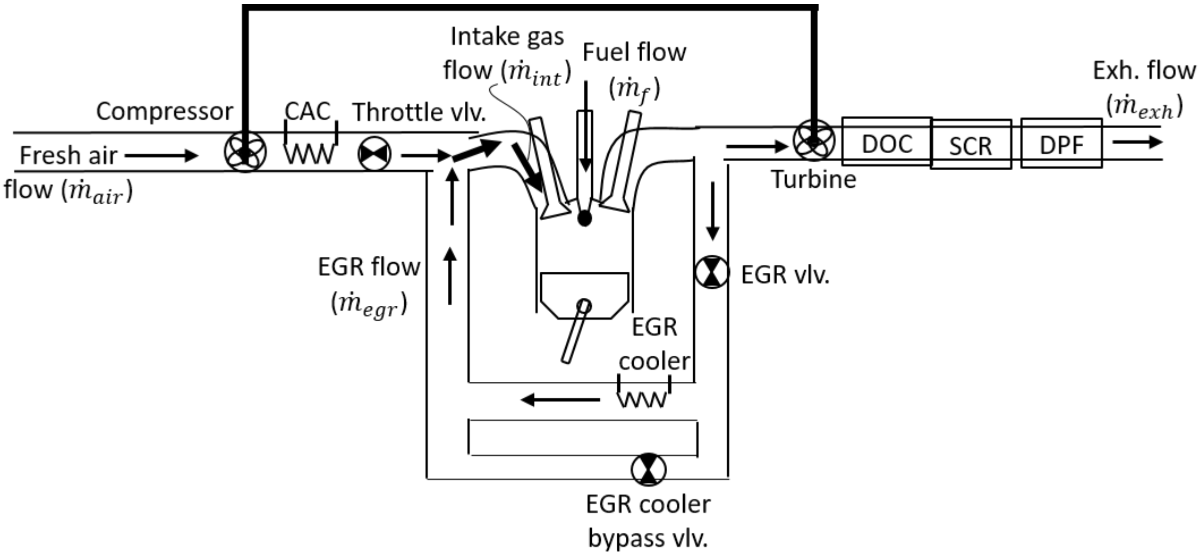

Figure 3.1. Schematic of the flows of the fresh air, EGR, and fuel inside the test engine

Figure 3.2 shows the schematic describing the important locations of the measurements taken in the current study. Intake air temperature and relative humidity is controlled by a combustion air unit (36±2ºC, 25±5% relative humidity). The fresh air from the combustion air unit passes through a laminar flow element (LFE) where the differential pressure over the element is measured and used for the estimation of the mass flow rate of the intake air ($\dot{m}_{air}$). The net fuel flow into the combustion chamber is measured by a MicroMotion Coriolis Flow and Density Sensor. The air-fuel mass ratio is calculated by dividing the mass flow rate of the fresh air by the mass flow rate of the fuel (Equation 3.3).

$$AF_m = {}^{\dot{m}_{air}}\!/_{\dot{m}_f} \qquad \text{(Eq. 3.3)}$$

The brake fuel conversion efficiency (BFE) is calculated by dividing the brake power ($\dot{W}_b$) by the net fuel energy flow ($\dot{Q}_f = \dot{m}_f \cdot LHV$) into the engine. (Equation 3.4).

$$\text{BFE} = {}^{\dot{W}_b}\!/_{\dot{Q}_f} \qquad \text{(Eq. 3.4)}$$

The charge air cooler (CAC) exit temperature is held constant for each operating condition regardless of the fuel type. The exhaust gas is sampled between the turbine exit and the DOC inlet to measure the engine-out emissions. A fraction of the exhaust gas is sampled by the AVL415S smoke meter for Filter Smoke Number (FSN) measurement while another fraction of the exhaust gas is sampled by an emissions sampling cart, which, then, is analyzed by the AVL SESAM i60FT S2 emissions bench. The measured FSN is converted into the soot concentration by using the AVL MIRA empirical correlation (Equation 3.5) proposed by the smoke meter manufacturer.

$$\text{SC}\left[{}^{mg}\!/_{m^3}\right] = \frac{1}{0.405} \cdot \alpha \cdot FSN \cdot e^{\beta \cdot FSN} \qquad \text{(Eq. 3.5)}$$

(SC: “soot concentration” at standard thermodynamic condition (i.e., 25ºC, 1bar), α: 4.95, β: 0.38 based on the empirical correlation provided by AVL).

Then, the mass flow rate of the soot is calculated by the multiplication of the soot concentration at the standard condition and the volume flow rate of the exhaust gas (Equation 3.6) while the volume flow rate of the exhaust gas was simply calculated by dividing the mass flow rate of the exhaust gas by the density of the gas at the standard condition (i.e., 1.1846kg/m^3, Equation 3.7).

$$\dot{m}_{soot} = SC \cdot \dot{V}_{exh} \quad \text{(Eq. 3.6)}$$

$$\dot{V}_{exh} = {}^{\dot{m}_{exh}}\!/_{1.1846} \quad \text{(Eq. 3.7)}$$

Then, brake specific particulate matter (BSPM) emission is calculated by dividing the mass flow rate of the soot by the brake power (Equation 3.8).

$$\text{BSPM}\left[{}^{g}\!/_{kWh}\right] = {}^{\dot{m}_{soot}}\!/_{\dot{W}_b} \quad \text{(Eq. 3.8)}$$

The gaseous emissions measured from the exhaust gas sample include total hydrocarbons (THC) using Flame Ionization Detector (FID), CO and NOx using Fourier Transform Infrared Spectroscopy (FTIR), and exhaust O_2 using Paramagnetic Detector (O_2 PMD). The mole fractions of the above species in the exhaust gas were measured in the unit of parts per million (ppm). The averaged molecular weight of the exhaust gas could be calculated from the mole-based composition of the exhaust gas. (Equation 3.9).

$$M_{avg} = \sum X_i M_i \quad \text{(Eq. 3.9)}$$

(*M*: molecular weight, *X:* mole fraction, *i*: species “*i*”).

Then, this averaged molecular weight is used to calculate mass fraction (*Y*) of each exhaust gas species to finally calculate the mass flow rate of each species (Equations 3.10-3.11).

$$Y_i = X_i \cdot \left({}^{M_i}\!/_{M_{avg}} \right) \quad \text{(Eq. 3.10)}$$

$$\dot{m}_i = Y_i \cdot \dot{m}_{exh} \quad \text{(Eq.3.11)}$$

Then, the brake specific (BS) emissions of the gaseous species such as CO_2, CO, NOx, and THCs are calculated by dividing the mass flow rate of the species by the brake power (Equation 3.12).

$$\text{BS gaseous emissions} \left[{}^{g}\!/_{kWh} \right] = {}^{\dot{m}_i}\!/_{\dot{W}_b} \quad \text{(Eq. 3.12)}$$

Wet concentration is measured in FID and FTIR while dry concentration was available from O_2 PMD. Thus, the dry exhaust O_2 concentration measured from O_2 PMD was converted into the wet exhaust O_2 concentration using the exhaust water concentration measured from FTIR (Equation 3.13).

$$X_{o2,wet} = X_{o2,dry} \cdot (1 - X_{water}) \quad \text{(Eq. 3.13)}$$

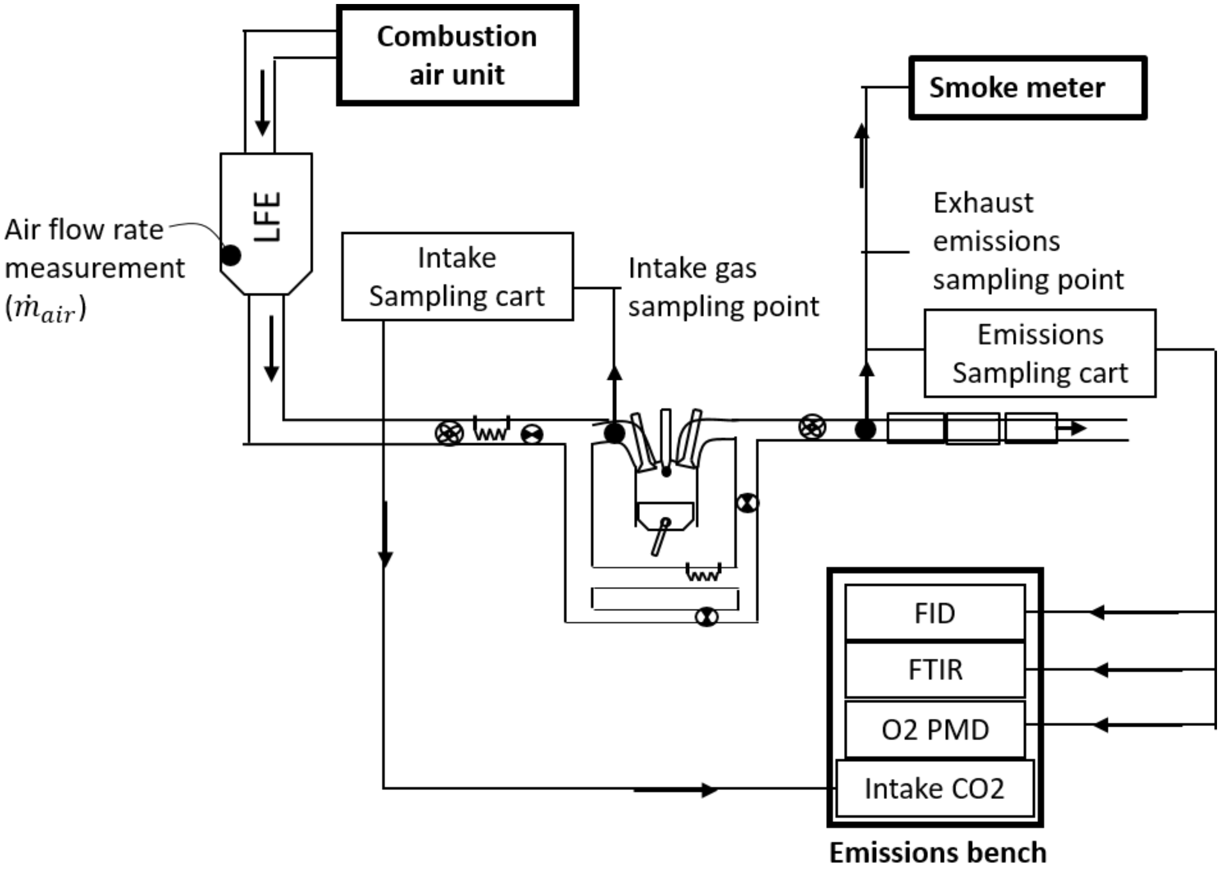

Figure 3.2. Experimental setup of the measurement devices for the test engine.

To measure EGR rate, intake gas manifold is sampled downstream of the EGR mixing point. The sampled intake gas passes through the intake sampling cart, then, to the intake CO_2 analyzer in the emissions bench. Intake CO_2 mole fraction is measured on a dry-mole basis. Thus, to calculate EGR rate on a dry-mole basis, the exhaust CO_2 mole fraction measured in a wet-mole basis is also converted into the dry-mole basis, using Equation 3.13.

Equation 3.14 shows the definition of the EGR rate used for the current study.[22]

$$EGR\ rate\ [\%] = \frac{X_{CO2,int}\ [ppm] - X_{CO2,amb}[ppm]}{X_{CO2,exh}\ [ppm] - X_{CO2,amb}[ppm]} \cdot 100 \qquad \text{(Eq. 3.14)}$$

Here, X stands for the dry-mole fraction of the species. The subscript “*int*” stands for intake gas, “*amb*” stands for the ambient air, and “*exh*” stands for the exhaust gas. The mole fraction of the CO_2 in the ambient air is assumed to be 400ppm in the current work. The above definition of EGR rate is mathematically equal to the ratio of the total mole flow rate of the EGR gas to the total mole flow rate of the intake gas (Equation 3.15).

$$EGR\ rate\ [\%] = \frac{\dot{n}_{egr}}{\dot{n}_{int}} \qquad \text{(Eq. 3.15)}$$

The intake O_2 mole fraction is calculated as follows. First, the dry O_2 mole fraction of the fresh air (20.9%) is converted into the wet O_2 mole fraction by using the measured relative humidity and temperature of the fresh air. Then, the wet O_2 mole fraction of the EGR gas is assumed to be the same as the measured wet O_2 mole fraction in the exhaust gas. Then, the intake O_2 mole fraction could be calculated from the combination of the O_2 mole fractions of the fresh air and EGR gas. Then, by using the measured intake manifold temperature and pressure, intake O_2 mole "concentration" (i.e., dimension of "mole/volume") could also be calculated based on the ideal gas law.

In-cylinder pressure traces of all 8 cylinders are measured by piezoelectric pressure sensors in each of the 8 cylinders. Apparent heat release rate and burn fraction angles (e.g., MFB10, MFB50) are calculated from the in-cylinder pressure trace based on the first law analysis.[27] The method of heat release analysis conducted in the study will be covered in more detail in section 3.2.6. Gross indicated mean effective pressure (IMEPg) and pump mean effective pressure (PMEP) are calculated by using the calculated gross indicated work ($W_{i,g}$) and pumping work (W_p) from Indicom software. Also, the gross indicated fuel conversion efficiency (IFEg) is calculated using Equation 3.16.

$$\mathrm{IFEg} = {\dot{W}_{i,g}}\big/{\dot{Q}_f} \qquad \text{(Eq. 3.16)}$$

Engine combustion noise level (CNL) is also calculated from the in-cylinder pressure trace using the previously published MATLAB code.[28] The source code was provided by Ford Motor Company.

For data measurement and control interfaces, ETAS INCA software is used to control the ECU input parameters such as EGR rate, engine boost pressure, rail pressure, injection quantity and timing. AVL Indicom software is used to measure the in-cylinder pressure and the parameters relevant to the in-cylinder pressure (e.g., heat release rate, burn fraction angles, mean effective pressures). Other parameters such as compressor inlet temperature and intake manifold temperature are measured and controlled by AVL PUMA interface. The engine coolant temperature was maintained constant at around 90ºC (±2ºC) and this helped setting the oil temperature constant for each operating condition.

3.2.3 Mini-Map Point Operating Conditions

As mentioned earlier, the test engine is subject to either class 2b (8,501-10,000 lbs.) or class 3 (10,001-14,000 lbs.) pickup trucks. These gross vehicle weight ratings (GVWRs) are subject to the 2010 Heavy Duty (HD) chassis certification standard for the criteria pollutants emissions control and to the Phase 1 HD GHG emissions standard for the GHG emissions control. The relevant certification test cycle for both standards is the Environmental Protection Agency (EPA) Federal Test Protocol 75 (FTP75).

To make a valid comparison of the engine-out emissions between the conventional petroleum-based diesel and B20 at warmed-up, steady-state conditions, the FTP75 cycle is converted into the six representative steady-state operating conditions. Table 3.6 presents the engine speed, brake torque, BMEP, and the default ECU settings for those six points. These six points are defined as the "Mini-map" (MM) points in the current study. The emissions, engine CNL, and BFE of the petroleum-based diesel fuel and B20 will be compared at these 6 MM points.

These MM points are obtained by using the engine cycle analyzer in ETAS ASCMO software. It converts the "speed (mph) – time (s)" trace of the FTP75 cycle to the "brake torque (N·m) – engine speed (rpm)" trace using the experimental data input given by the user. Ford Motor Company conducted the conversion of the FTP75 certification cycle corresponding to the test engine to the 6 MM points for the current study.

	MM1	MM2	MM3	MM4	MM5	MM6
Engine Speed [rpm]	600	1000	1200	1200	1300	1600
Brake Torque [N·m]	66	80	159	371	265	397
BMEP [bar]	1.25	1.5	3.0	7.0	5.0	7.5
EGR rate [%]	42	41	34	21	27	20
Boost pressure [hPa]	977	1030	1070	1210	1164	1317
Rail pressure [bar]	281	446	711	1335	1021	1612
Main injection timing [aTDC]	-0.8	1.6	2.9	-1	0	-0.4
Pilot 1 injection timing [aTDC]	-9.1	-10.7	-11.5	-15.0	-14.9	-14.8
Pilot 1 injection quantity [mg/stroke]	3.3	3.1	3.9	2.15	2.9	1.8
Pilot 2 injection timing [aTDC]	-17.1	[-]	[-]	[-]	[-]	[-]
Pilot 2 injection quantity [mg/stroke]	1.85	[-]	[-]	[-]	[-]	[-]

Table 3.6. Test engine operating conditions and the default ECU setting for 6 MM points

3.2.4 Definitions of the Input and Output Parameters for ECU Optimization

A set of output parameters are chosen to evaluate the degree of the pump-to-wheels (PTW) GHG emissions reduction from B20 while satisfying other bound criteria such as brake specific (BS) emissions and combustion noise level (CNL). These output parameters include brake fuel conversion efficiency (BFE), brake specific carbon dioxide ($BSCO_2$) emission, brake specific NOx (BSNOx) emission, brake specific particulate matter (BSPM) emission, brake specific carbon monoxide (BSCO) emission, brake specific total hydrocarbons (BSTHC) emission, and combustion noise level (CNL). Table 3.7 presents the list of the chosen output parameters, and the way each of the parameters is used to recalibrate the ECU setting.

	BFE	$BSCO_2$	BSNOx	BSPM	BSTHC	BSCO	CNL
MM1	Maximizing	Minimizing	Upper bound (UB)	UB	UB	UB	UB
MM2	Max.	Min.	UB	UB	UB	UB	UB
MM3	Max.	Min.	UB	UB	UB	UB	UB
MM4	Max.	Min.	UB	UB	-	UB	UB
MM5	Max.	Min.	UB	UB	-	UB	UB
MM6	Max.	Min.	UB	UB	-	UB	UB

Table 3.7. List of the optimization output parameters used for each operating condition.

Brake fuel conversion efficiency (BFE) is used as a proxy to determine the level of PTW GHG emissions reduction per mile. To prove that BFE is the right parameter for this purpose, how the PTW GHG emissions per mile is determined must be discussed here. Grams CO_2 equivalent per mile (i.e., gCO_2e/mile) emissions can be thought as the multiplication of the grams CO_2 equivalent per MJ (i.e., gCO_2e/MJ) by the mega-joules per mile (i.e., MJ/mile). The former term (i.e., gCO_2e/MJ) can vary by two different ways. The first is by the fuel type. The second is by the amount of the potent GHG emissions resulting from different PTW combustion processes even with the same fuel. Thus, unless the potent GHG emissions such as methane (CH_4) and nitrous oxide (N_2O) differ in appreciable degrees for different engine operating conditions, “gCO_2e/MJ” for a given fuel cannot be changed depending on the PTW combustion processes. For the current study, the methane and nitrous oxide emissions were minimal (<10ppm) with no measurable variations between the two fuels and among the different operating conditions. Thus, when applying B20, “MJ/mile” is the only term that we can reduce to eventually reduce the PTW GHG emissions per mile (i.e., gCO_2e/mile).

Now, energy use per mile (i.e., MJ/mile) of a vehicle can be calculated by multiplying different energy conversion efficiencies at different levels. First, there is the efficiency of converting the chemical energy of the fuel into the mechanical energy of the engine crank shaft. This efficiency is defined as the BFE, and it can depend on the fuel type and ECU calibration. Then, there is the efficiency of converting the mechanical energy of the crank shaft to the mechanical energy of wheel shaft, and then, finally to the kinetic energy of the vehicle. However, these energy conversion efficiencies between the crankshaft energy and the kinetic energy of the vehicle must be consistent regardless of the fuel type and ECU calibration because the factors (i.e., transmissions, aerodynamic drag and surface friction drag of the vehicle) determining these efficiencies are identical for the baseline and B20 at any ECU calibrations. Thus, the difference in BFE is the only factor causing the difference in MJ/mile. And since MJ/mile is the only variable determining gCO_2e/mile emissions for a given fuel, BFE can be determined as the parameter representing the PTW GHG emissions reduction on a gCO_{2e}/mile basis.

Since the fuel mass flow meter measurement inaccuracy is increased at lower loads, brake specific CO_2 ($BSCO_2$) from the direct CO_2 measurement using the emissions bench is also used to confirm the reliability of the BFE measurement. In other words, $BSCO_2$ emission is used as a secondary output parameter to judge the PTW GHG emissions reduction per mile. In case the BFE measurement has statistically meaningful discrepancy from the $BSCO_2$ measurement, both BFE and $BSCO_2$ are used as the final parameters to determine whether the PTW GHG emissions have been reduced or increased with B20 application.

Four brake specific emissions of the criteria pollutants defined by U. S. EPA (i.e., NOx, PM, CO, THC) are used as the output parameters to maintain the criteria pollutant emissions under the certification standard.[29] The brake specific (BS) emissions of the baseline diesel were used as the upper bounds for the recalibrated ECU settings. Out of the four criteria pollutants BS emissions, BSNOx and BSPM were of the primary interest. Thus, they are set to be the bound criteria for all 6 MM points. BSTHC and BSCO were of the secondary interest. Thus, BSTHC is set to be the bound criteria only for lower loads (i.e., MMs 1-3) where THC emissions are at appreciable level. BSCO emission is set to be the “weak” bound criteria for all 6 MM points, thus allowing BSCO at the re-calibrated ECU to exceed up to moderate and acceptable degree.

Since engine noise level is one of the critical factors affecting the commercial value of the engine, the baseline CNL is also used as a bound criteria. It is set to be the bound criteria for all 6 mini-map points with 0.5-1dB allowance.

A set of input parameters are chosen to vary the PTW combustion process as shown in Table 3.6. The chosen input parameters are EGR rate, intake boost pressure (BP), fuel injection rail pressure (RP), main injection timing (MIT), pilot injection quantities (PIQ), and relative distance between main injection timing and pilot injection timings (RPIT). For MM1, two pilot injection events are applied, and the far pilot from the main injection event is defined as the pilot2 injection while the close pilot event is defined as the pilot 1 injection. For MMs 2-6, only one pilot injection event is applied. Thus, the total number of the input parameters were 8 for MM1 (i.e., EGR rate, BP, RP, MIT, RPIT1, PIQ1, RPIT2, PIQ2) and 6 for MMs 2-6 (i.e., EGR rate, BP, RP, MIT, RPIT1, PIQ1). For clarification, the equation used to calculate RPIT1 and RPIT2 are presented in Equations 3.17 and 3.18.

$$RPIT1[CA] = MIT[aTDC] - PIT1[aTDC] \qquad \text{(Eq. 3.17)}$$

$$RPIT2[CA] = PIT1[aTDC] - PIT2[aTDC] \qquad \text{(Eq. 3.18)}$$

3.2.5 Test Methods and Conditions

3.2.5.1 Diesel Baseline Test

The baseline test is conducted with the cert-diesel fuel. The “single-parameter sweep” test is conducted for four different input parameters: EGR rate, boost pressure (BP), rail pressure (RP) and main injection timing (MIT). During each of the sweep test, all the other input parameters are fixed the same as the default ECU settings shown in Table 3.6. For example, when EGR sweep test is conducted at MM3, the boost pressure is fixed at 1070hPa and the rail pressure is fixed at 711bar while the EGR rate was varied from the highest achievable EGR rate at MM3 (i.e., 47%) to 0%. During a boost pressure sweep, the lowest and highest boost pressure achievable at each MM point are measured while throttle valve is fully open. Then, the lowest achievable BP with wide open throttle is defined as the low boost pressure (LP) and the highest is defined as the high boost pressure (HP), respectively. Then, the boost pressure in the middle of the default boost pressure (DP) and the HP is defined as the mid-high boost pressure (MHP). Depending on the MM point, either all of these 4 regular boost pressure conditions (i.e., LP, DP, MHP, and HP) or 3 selected boost pressure conditions are measured. For MM1 (idling), boost pressure conditions of LP, DP and MHP are tested for the baseline and B20. Due to the inherently noisy characteristics of the idling condition, the variation of the boost pressure at fixed turbo-vane position was relatively high at MM1. For MM2, boost pressure conditions of LP, DP and MHP are tested for both the baseline diesel and B20. At MM2, engine operation at HP was hard to be kept stable, thus making us to not take data at HP. Thus, the boost pressure 10% lower than HP was labelled as the MHP at MM2. Furthermore, for the baseline diesel test at MM2, lowest boost pressure achievable by partial throttling is defined as the “throttled low boost pressure (TLP)”, and the data was also taken at this boost pressure condition. Additional measurement at TLP provided better understanding of the trend of fuel conversion efficiency and emissions by boost pressure at MM2. For MM points from 3 to 6, all four regular boost pressure conditions (i.e., LP, DP, MHP, HP) are tested for both the baseline diesel and B20. During the rail pressure sweep, the rail pressure 20% higher than the default rail pressure (DRP) is defined as the high rail pressure (HRP) and the rail pressure 20% lower than the DRP is defined as the low rail pressure (LRP), and the measurement is taken at those 3 points. During the main injection timing sweep, not only the main injection timing, but also the other injection timings (i.e., pilot 1 injection timing for MM1-6 and pilot 2 injection timing for MM1) are shifted together with the same degrees: the whole injection block was shifted altogether. This was to fix the relative distance between the different injection events. The main injection timing sweep is conducted for five different injection timings: 5 degrees advanced (5A), 2.5 degrees advanced (2.5A), default timing (DF), 2.5 degrees retarded (2.5R), 5 degrees retarded (5R).

Table 3.8 shows the ranges and values of the ECU input parameters imposed during the 4 single parameter sweeps of each MM point.

	MM1		MM2		MM3		MM4		MM5		MM6	
EGR swp. range [%]	0-58		0-56		0-47		0-27		0-39		0-28	
Boost pressure (BP) swp. range [hPa]	TLP	-	TLP	945	TLP	-	TLP	-	TLP	-	TLP	-
	LP	955-970	LP	997	LP	1020	LP	1100	LP	1060	LP	1245
	DP	960-980	DP	1030	DP	1070	DP	1210	DP	1164	DP	1317
	MHP	985-990	MHP	1050	MHP	1145	MHP	1380	MHP	1300	MHP	1515
	HP	[-]	HP	[-]	HP	1225	HP	1460	HP	1395	HP	1750
Rail pressure swp. range [bar]	LRP	226	LRP	357	LRP	569	LRP	1068	LRP	817	LRP	1290
	DRP	281	DRP	446	DRP	711	DRP	1335	DRP	1021	DRP	1612
	HRP	338	HRP	535	HRP	853	HRP	1602	HRP	1225	HRP	1934
MIT during MIT swp. Range [aTDC]	5A	-5.8	5A	-3.4	5A	-2.1	5A	-6.0	5A	-5.0	5A	-5.4
	2.5A	-3.3	2.5A	-0.9	2.5A	0.4	2.5A	-3.5	2.5A	-2.5	2.5A	-2.9
	DF	-0.8	DF	1.6	DF	2.9	DF	-1.0	DF	0	DF	-0.4
	2.5R	1.7	2.5R	4.1	2.5R	5.4	2.5R	1.5	2.5R	2.5	2.5R	2.1
	5R	4.2	5R	6.6	5R	7.9	5R	4.0	5R	5.0	5R	4.6
PIT1 during MIT swp. Range [aTDC]	5A	-14.1	5A	-15.7	5A	-16.5	5A	-20.0	5A	-19.9	5A	-19.8
	2.5A	-11.6	2.5A	-13.2	2.5A	-14.0	2.5A	-17.5	2.5A	-17.4	2.5A	-17.3
	DF	-9.1	DF	-10.7	DF	-11.5	DF	-15.0	DF	-14.9	DF	-14.8
	2.5R	-6.6	2.5R	-8.2	2.5R	-9.0	2.5R	-12.5	2.5R	-12.4	2.5R	-12.3
	5R	-4.1	5R	-5.7	5R	-6.5	5R	-10.0	5R	-9.9	5R	-9.8
PIT2 during MIT swp. Range [aTDC]	5A	-22.1										
	2.5A	-19.6										
	DF	-17.1										
	2.5R	-14.6										
	5R	-12.1										

Table 3.8. ECU input parameter settings for the four single parameter sweep tests (EGR sweep, boost pressure sweep, rail pressure sweep, main injection timing sweep) for the baseline diesel.

3.2.5.2 Measurement of the Unintended Shifts in ECU Setting with B20

When B20 is applied to the test engine without the re-calibration of the ECU or the imposing of certain values to ECU input settings, the ECU settings can unintendedly shift due to the increase in pedal angle demand to compensate for the lower LHV of B20. This trend of the unintended shift in ECU settings when B20 is applied is measured as follows.

The test engine is brought up to the target brake torque and engine speed defined at each MM point without fixing any ECU variables. Then, the ECU input variables of interest (i.e., EGR rate, boost pressure (BP), rail pressure (RP), main injection timing (MIT), relative distance between pilot1 injection timing and main injection timing (RPIT1), pilot1 injection quantity (PIQ1) for MM1-6, and relative distance between pilot1 injection timing and pilot 2 injection timing (RPIT2), pilot2 injection quantity (PIQ2) additionally for MM1) are monitored if they converge to the certain values after the stabilization of the test conditions. The converged values of the ECU input variables are defined as the unintendedly shifted ECU settings, and these are recorded.

3.2.5.3 B20 Test with Default ECU Calibration

To describe how the B20 testing with the default ECU setting is conducted, the basic algorithm of the engine ECU needs to be discussed here. To determine the values of the ECU input parameters for different operating conditions, the ECU first takes in the “pedal angle” and engine speed demands. Pedal angle is simply the angle of the accelerator that the driver demands. In the current test setup, the pedal angle is controlled by the engine dyno. Then, the ECU estimates the gross indicated torque based on the pedal angle and engine speed. The estimated gross indicated torque is often called “ECU Inner torque” and this property is the basis for all of the ECU input parameters of the interest in the current study. Six (for MMs 2-6) to eight (for MM1) input parameters presented in Table 3.6 are determined based on the map of the engine speed and the ECU Inner torque. Also, the main injection quantity (MIQ), which cannot be imposed by the user through the ECU, is determined the same way. For example, at MM3, the engine runs at 1200rpm with the pedal angle of 15%, which corresponds to the ECU Inner torque of about 196 N·m. Then, the ECU commands the fuel injection system to inject the corresponding main injection quantity (i.e., 16.7 mg/stroke) at the corresponding main injection timing (i.e., 2.9aTDC).

Thus, there are two ways that the ECU settings can be unintentionally shifted. First, unless all of the ECU input parameters shown in Table 3.6 are fixed at the default ECU calibrations while the pedal angle is increased to compensate for the lower LHV of B20, the unintended shift in ECU settings will happen. Second, even if the input parameters shown in Table 3.6 are all fixed at the default settings with increased pedal angle, the main injection quantity (MIQ) will increase alone and make the ratio of the MIQ to PIQs different. A valid comparison between B20 and baseline fuel is not possible in these cases. Thus, MIQ and PIQs should be increased with the same proportion while all the other ECU input parameters are fixed. This can be achieved by increasing the injection duration for B20 while the pedal angle is fixed the same as for the baseline fuel.

In the ECU algorithm used for the current study, the injection duration is determined based on the value of rail pressure and "generic" fuel injection quantity that applies generally to any injection events. Thus, when the injection duration is controlled for a certain rail pressure and nominal fuel injection quantity, the actual main and pilot injection quantities are increased with the same proportion while the "nominal" MIQ and PIQs in ECU do not change.

Therefore, instead of increasing pedal angle to meet the target brake torque, the injection duration of B20 is increased until the target brake torque is met while the pedal angle and all of the ECU input parameters are fixed the same as the baseline condition. To check if the ratio of the MIQ and PIQ demand from ECU are kept constant for baseline and B20, the ratio of the MIQ to the total injection quantity (i.e., sum of MIQ and PIQs) is measured and presented in Figure 3.3.

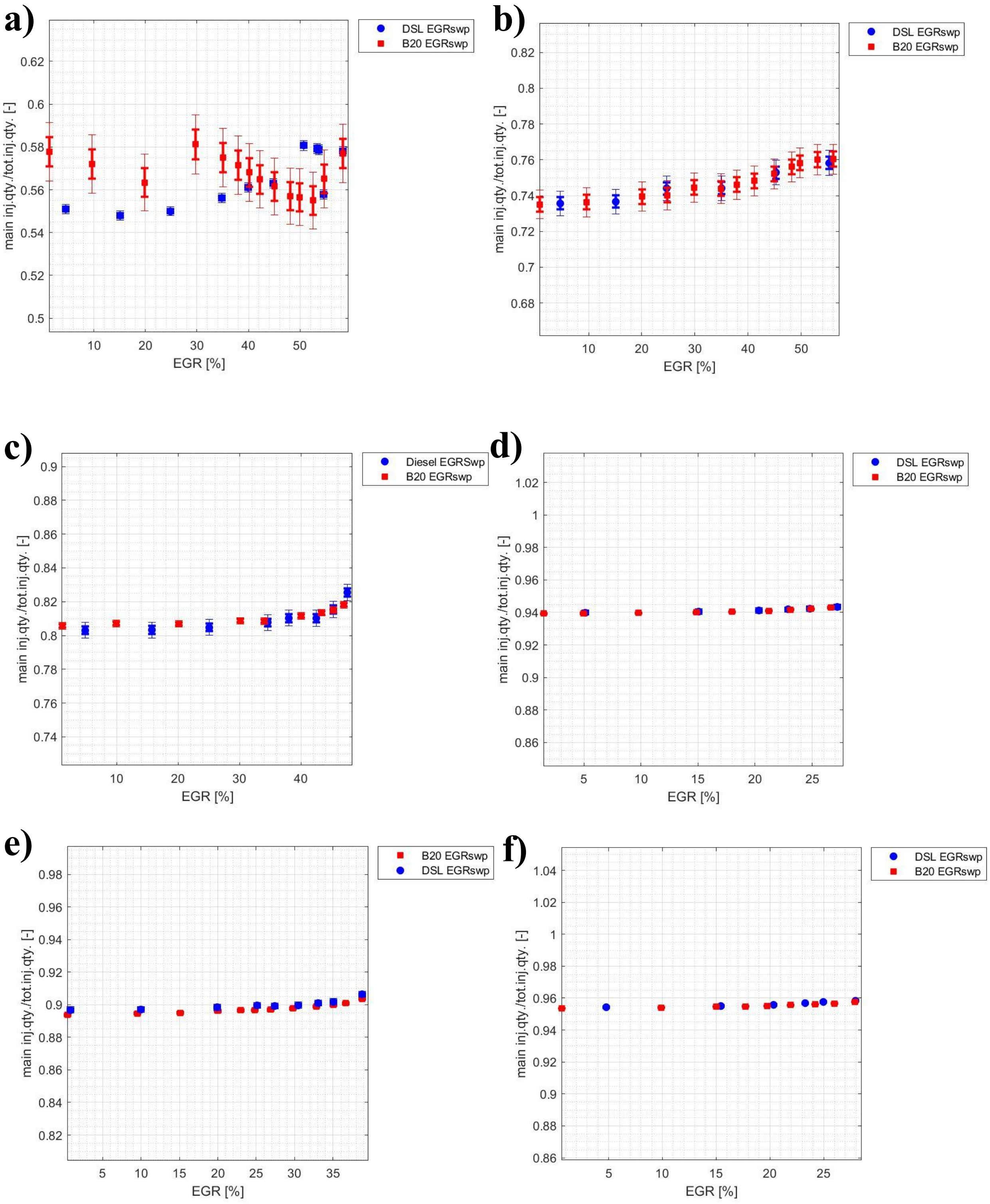

Figure 3.3. Comparison of the ratio of the main injection quantity to the total injection quantity during the baseline diesel and B20 EGR sweep test at a) MM1, b) MM2, c) MM3, d) MM4, e) MM5, and f) MM6

As shown in Figure 3.3, the ratio of main injection quantity demand from ECU to the total injection quantity demand from ECU was maintained consistent for baseline and B20, guaranteeing the increase in the actual MIQ and PIQs in the same proportion during the test. This means that all of the ECU settings are set the same for baseline fuel and B20.

3.2.5.4 B20 Test with Adjusted ECU Calibration

After the BFE and emissions from B20 are modeled using the ASCMO software as covered in section 3.2.8, an EGR sweep test is conducted at the "first" adjusted ECU settings at each MM point. The first adjusted ECU settings mean the "originally" recommended ECU settings based on the ASCMO modeling and optimization which is expected to perform the best BFE while meeting other bound criteria.

During this EGR sweep, the parameters other than EGR rate (i.e., boost pressure, rail pressure, main injection timing, relative distance between main injection timing and relative injection timings, pilot injection quantities) are fixed at the first adjusted values from the ASCMO model while the EGR rate was only varied around the suggested EGR rate. The BFE, BS emissions, and CNL are measured and compared to the baseline, and the improvement from the baseline is verified.

In case some of the bound criteria (i.e., BS emissions and CNL) exceed the baseline value, a different EGR rate setting is considered as one of the alternative calibration settings to use. However, if the BFE decreased appreciably (>absolute 1%) by changing EGR rate from the original suggestion from the ASCMO model to meet the bound criteria, different input parameter sweep tests are conducted to see if there are other options to meet the bound criteria without sacrificing BFE. For example, at MM2, the CNL was unacceptably higher than the baseline value with the “first” adjusted ECU calibration. At the same time, the change in EGR rate from the first adjusted ECU settings to meet the CNL criteria decreased BFE more than absolute 1%. Thus, instead of changing EGR rate from the “first” adjusted calibrations, the pilot 1 injection quantity (PIQ1) is reduced by 0.25mg/stroke from the “first” adjusted ECU calibrations. At MM4, the CNL was again unacceptably higher than the baseline value with the “first” adjusted ECU calibration, thus requiring the reduction in rail pressure (RP) by 46bars from the “first” adjusted ECU calibrations. At MM3, the CNL was higher than the baseline at unacceptable degree. However, the increase in EGR rate was the only solution to meet the CNL criteria at MM3. The change in other input parameter settings did not reduce the CNL enough. Thus, EGR rate was increased by absolute 4% from the “first” adjusted ECU calibration to meet the CNL bound criteria. At all other MM points (i.e., MM1, MM5 and MM6), no further change in ECU settings was required from the “first” adjusted ECU calibration.

3.2.6 Heat Release Rate Analysis

The engine in-cylinder pressure traces for all 8 cylinders are used for the net (or apparent) heat release rate analysis in AVL Indicom software. The principle used for the heat release analysis in the Indicom software is as follows. First, it calculates the “net” heat release rate from the change of in-cylinder pressure and cylinder volume per crank angle degree based on the 1st law of thermodynamics (Equation 3.19). This calculation is conducted between -30aTDC and +90aTDC for all of the testing conditions in the current study.

$$Q_i[{}^{kJ}/_{deg}] = \frac{1}{\kappa-1} \cdot [\kappa P_i(V_i - V_{i-1}) + V_i(P_i - P_{i-1})] \quad \text{(Eq. 3.19)}$$

(Q: net (or apparent) heat release rate, κ: polytropic coefficient, i: at crank angle “i”).

Second, the Indicom software sums the net heat release rates from the initial CA degree (i.e., -30aTDC) to certain CA degree "i" to calculate the "cumulative" net heat release from -30aTDC to certain CA degree "i". (Equation 3.20).

$$I_i[kJ] = \sum_{j=-30aTDC}^{j=i\ aTDC} Q_j \qquad \text{(Eq. 3.20)}$$

(I_i: Cumulative heat release from -30aTDC to certain CA degree "i").

Then, by using the Q curve and I curve calculated from the Indicom software, the combustion phasing and burn fraction angles of the pilot and main events are calculated separately based on the lab-made MATLAB code. The combustion phasing is defined as the crank angle at which the net heat release rate curve (Q) hits its closest local minimum value to its peak value. The burn fraction angle is defined as follows. First, the cumulative heat release from pilot and main combustion events are calculated separately from the cumulative heat release (I) curve. Then, the crank angle at which x% of the pilot/main cumulative heat release is achieved is defined as the pilot/main "x% burn fraction angle". These definitions of the combustion phasing and burn fraction angles used in the current work are consistent with the general practice used in the field of internal combustion engines research.[27] Figure 3.4 is presented to give a practical example of the algorithm for determining the combustion phasing and burn fraction angles.

Figure 3.4a shows an example of the net heat release rate from two selected test conditions (MM3 at EGR45% and EGR47% with the baseline fuel at default ECU calibration). We can see the net heat release rate curve has the main combustion event peak at around 14aTDC for EGR45% and 17aTDC for EGR47%. Thus, the main start of combustion (SOC) is defined to be 8aTDC for EGR45% and 9aTDC for EGR47%, which are the closest local minimum to the main combustion peak. In case there is appreciable fluctuation (or noise) in the value of the net heat release rate near the closest local minimum to the main combustion peak, the second closest and third closest local minimums are also taken into account to estimate the reasonable SOC value. Then, as we follow the net heat release rate curve from the main SOC to the earlier crank angles, we can see that the pilot combustion peak is located at around 1aTDC for EGR45% and 2.5aTDC for EGR47%. Now, the pilot SOC could be said to be at around -2aTDC for both EGR rate conditions.

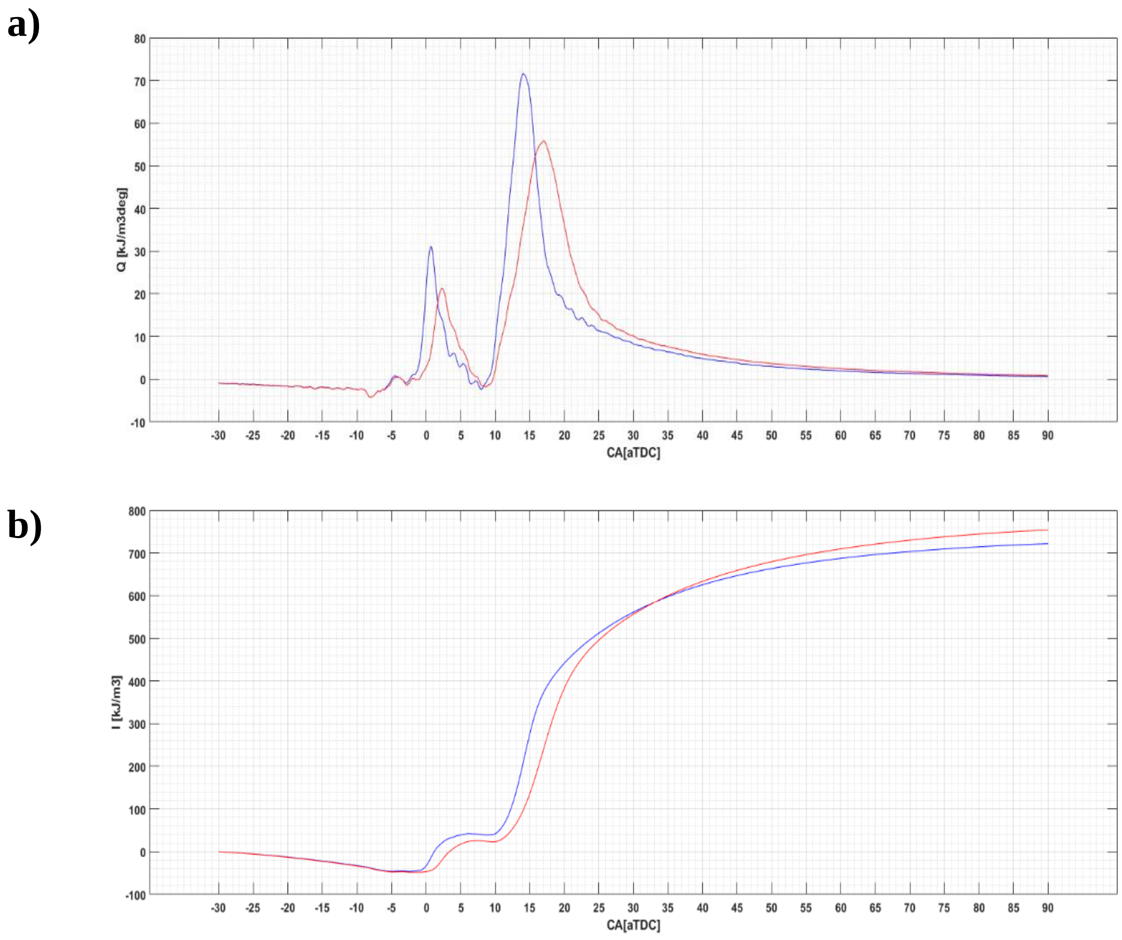

Figure 3.4. An example of a) net heat release rate ($\dot{Q}_{net}$) and b) cumulative heat release (I_{net}) curve. Data obtained at MM3 with the baseline diesel and the default ECU calibration at EGR45% (blue) and 47% (red).

Figure 3.4b shows an example of the cumulative heat release curve from the same test condition as Figure 3.4a, and we can see how the burn fraction angles are determined from the curve. The value of cumulative heat release decreases from -30aTDC to -5aTDC, then, it stays constant between -5aTDC and TDC. This constant value is defined to be the minimum value of the cumulative heat release. Then, after TDC, the cumulative heat release ramps up to a certain value (i.e., 40kJ/m^3 for EGR45% and 20kJ/m for EGR47%) due to the pilot combustion event, and stays constant before the main combustion event begins. The difference between this maximum cumulative heat release before the main combustion event and the minimum cumulative heat release is defined as the “pilot” cumulative heat release (i.e., cumulative heat release from the pilot combustion event only). Then, pilot 5%, 10%, 50%, and 90% burn fraction angles (i.e., pilot MFB5, pilot MFB10, pilot MFB50, pilot MFB90) are determined by locating the crank angle at which 5%, 10%, 50%, and 90% of the pilot cumulative heat release is achieved. The same algorithm is used to determine the main burn fraction angles.

The difference between the start of injection (SOI) timing measured from the ETAS INCA and the start of combustion (SOC) obtained from the heat release rate curve is defined to be the ignition delay (ID). Since SOI and SOC for pilot and main event could be obtained separately, ID for pilot and main event are also calculated separately.

More detailed understanding of the combustion process can be extracted from Figure 3.4 if we fully understand what exactly the calculated net heat release rate (Q) means. For the detailed explanation on the net heat release rate, refer to Appendix A.

Figure 3.5 describes the different terms of the energy flow rate with different levels of the conversion from the original fuel energy flow.[30] The energy flow term at the highest or the most upstream level is the fuel chemical energy flow ($\dot{Q}_f$). This is simply the total chemical energy flow contained in the injected fuel, which is the multiplication of the fuel mass flow rate by LHV (Equation 3.4). Then, there is the gross heat release rate ($\dot{Q}_{gross}$): the thermal energy flow resulting from the combustion of the fuel. The energy conversion efficiency between $\dot{Q}_f$ and $\dot{Q}_{gross}$ is defined as the combustion efficiency (Equation 3.21). The next term is the net heat release rate ($\dot{Q}_{net}$): the energy flow successfully used for the increase in the internal energy and volume expansion work of the working fluid. The difference between the gross and net heat release rate is defined as the heat loss flow ($\dot{Q}_l$). There is heat loss from the working fluid to the chamber wall or other surrounding object such as valves. There is also other types of heat losses due to the evaporation of the liquid fuel droplets, crank-case blow-by, and crevice volume effect. In this study, all these different heat losses are lumped into one heat loss term ($\dot{Q}_l$) as shown in Equation 3.22. The ratio of the $\dot{Q}_{net}$ to $\dot{Q}_f$ is calculated for different test conditions and presented in the results and discussion section.

$$\dot{Q}_{gross} = \dot{Q}_f \cdot \eta_c \qquad \text{(Eq. 3.21)}$$

(η_c: combustion efficiency)

$$\dot{Q}_{net} = \dot{Q}_{gross} - \dot{Q}_l \qquad \text{(Eq. 3.22)}$$

($\dot{Q}_l$: all sources of heat losses during the heat release rate calculation crank angle durations (i.e., from -30aTDC to +90aTDC)).

Then, there is the gross indicated power ($\dot{W}_{i,g}$). The only major difference between the net heat release rate and the gross indicated power is the loss of enthalpy associated with the exhaust gas (Equation 3.23).

$$\dot{W}_{i,g} = \dot{Q}_{net} - \dot{H}_{exh} \qquad \text{(Eq. 3.23)}$$

Then, the net indicated power ($\dot{W}_{i,n}$) is the net power between the gross indicated power and the pumping loss (Equation 3.24). Lastly, the brake power ($\dot{W}_b$) is the actual power transmitted to the engine crankshaft. The difference between the brake power and the net indicated power is the friction loss (Equation 3.25). In this study, the friction loss accounts for the mechanical friction of reciprocating parts of the engine, parasitic loads such as fuel pump loads and coolant pump loads.

$$\dot{W}_{i,n} = \dot{W}_{i,g} - \dot{W}_p \qquad \text{(Eq. 3.24)}$$

($\dot{W}_{i,n}$: net indicated power, $\dot{W}_p$: pumping loss).

$$\dot{W}_b = \dot{W}_{i,n} - \dot{W}_f \qquad \text{(Eq. 3.25)}$$

($\dot{W}_f$: friction loss).

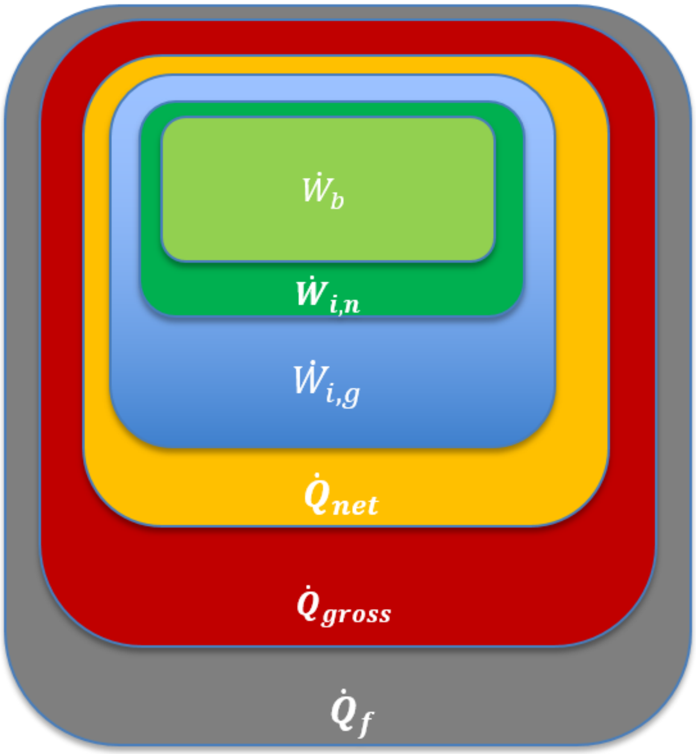

Figure 3.5. Hierarchy of the different terms of the energy based on the different stages of the conversion from the original fuel energy

3.2.7 Calculation of Lift-off Length and Oxygen Ratio

Lift-off length (i.e., the distance between the injector nozzle tip and the upstream end of the stabilized diffusion flame, clarified in Figure 3.6[25]) and oxygen ratio provide fundamental understanding on the NOx and soot generation from the fuel-rich premixed auto-ignition zone in a mixing-controlled compression ignition engine. In general, higher oxygen ratio at the lift-off length caused by the increase in lift-off length causes potential increase in NOx emissions by allowing more oxygen in the auto-ignition zone.[25] This mechanism also affects PM emission oppositely, and is well-known as a main factor causing PM-NOx trade-off for oxygenated fuel application. Thus, information on lift-off length and oxygen ratio at different test conditions often provides a more in-depth understanding on the trends of NOx and PM emissions that are not fully explained by charge gas "bulk" properties such as overall oxygen concentration or overall equivalence ratio.

Therefore, the lift-off length and oxygen ratio at the lift-off length are estimated for each different testing condition in the current study to provide better understanding of the impact of fuels and ECU input parameters on the BFE, BSNOx, and BSPM.

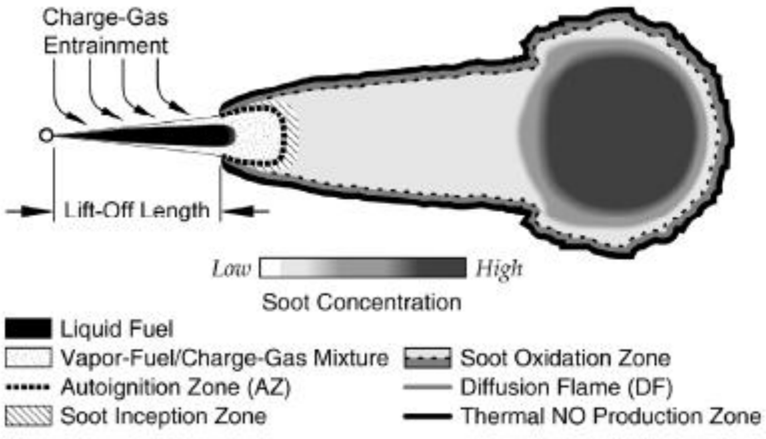

Figure 3.6. Schematic of different combustion zones and emissions generation mechanisms in mixing-controlled compression ignition engines (from Muller et al., 2009)

To estimate the lift-off length and oxygen ratio at the lift-off length, the lift-off length correlation model proposed in a serious of publications from Sandia National Laboratory is used.[31-34] First, for the estimation of the oxygen ratio along the axial coordinate, "x", the radially averaged equivalence ratio at x is first calculated from Equation 3.26.

$$\langle \phi(x) \rangle = \frac{2AF_{st}}{\sqrt{1+16(\frac{x}{x^{+}})^{2}-1}} \qquad \text{(Eq. 3.26)}$$

Here, $\langle \phi(x) \rangle$ is the radially averaged equivalence ratio at axial coordinate x, AF_{st} is the stoichiometric "charge gas to fuel" mass ratio, and x^{+} is the characteristic length scale for the jet. The stoichiometric charge gas to fuel mass ratio is different from the air-fuel mass ratio in that it is relevant to the charge gas than fresh air only. Thus, depending on the oxygen mole fraction of the charge gas, the AF_{st} can change even for the same type of fuel: the AF_{st} increases with decreasing O_2 mole fraction in charge gas. The characteristic length scale, x^{+}, reflects the characteristics of the fuel jet such as density ratio of the fuel and charge gas and fuel injection behavior, and is calculated using Equation 3.27.

$$x^{+} = \sqrt{\frac{\rho_f}{\rho_a}} \cdot \frac{d\sqrt{C_a}}{a \cdot \tan\frac{\theta}{2}} \quad \text{(Eq. 3.27)}$$

In Equation 3.27, ρ_f is the density of the fuel injected, ρ_a is the density of the charge gas, *d* is the injector nozzle diameter, C_a is the area contraction coefficient, *a* is the proportional constant "0.75", and θ is the fuel jet spreading angle. In this study, the fuel density is assumed to be the corresponding fuel density at fuel pump inlet temperature and ambient pressure. The air density is assumed to be the corresponding charge density at the cylinder temperature and pressure at start of injection (SOI). For in-cylinder temperature calculation, the ideal gas law is used (Equation 3.28).[25]

$$T_i = \frac{P_i V_i}{n_i \bar{R}} \quad \text{(Eq. 3.28)}$$

In Equation 3.28, subscript "i" means the properties at crank angle "i". The cylinder pressure and volume could be measured from the in-cylinder pressure sensor and crank angle encoder. The total charge gas mole count at each crank angle (n_i) had to be estimated using the following method. The initial charge gas mole count is first calculated from the "intake" gas mole flow rate ($\dot{n}_{int}$) using Equation 3.29.

$$n_{int} = {}^{\dot{n}_{int}}\!\Big/\!\left(\frac{rpm}{120}\right) \quad \text{(Eq. 3.29)}$$

In Equation 3.29, n_{int} is the intake charge gas mole count per cycle, and this is set as the initial value for the charge gas mole count. The "rpm" is the engine speed. Then, there are four events that change the charge gas mole count from its initial value: i) pilot injection; ii) pilot combustion; iii) main injection; and iv) main combustion. For fuel injection events, constant fuel injection rate during the injection duration is assumed. For pilot fuel combustion events, constant fuel burn rate is assumed for 3 different segments of the pilot combustion duration: i) between pilot SOC and pilot MFB10; ii) between pilot MFB10 and pilot MFB50; and iii) between pilot MFB50 and pilot end of combustion (EOC). For main combustion event, constant fuel burn rate is assumed for 4 different segments of the main combustion duration: i) between main SOC and main MFB10; ii) between main MFB10 and main MFB50; iii) between main MFB50 and main MFB90; and iv) between main MFB90 and main EOC. Mole multipliers (MMP), "the ratio of the moles of product gas to the moles of reactant gas", for the baseline and B20 are calculated using Equation 3.30. Then, the mole multiplier is used to update the charge gas mole count for the next crank angle during the combustion events.[25,35]

$$C_xH_yO_z + a\cdot(O_2 + 3.76N_2) \rightarrow x\cdot CO_2 + \frac{y}{2}\cdot H_2O + a\cdot(3.76N_2)$$

$$\mathrm{a} = \mathrm{x} + \frac{y}{4} - \frac{z}{2}$$

$$\mathrm{MMP} = {(4.76x + 1.44y - 1.88z)}\Big/{\left\{1 + 4.76\left(x + \frac{y}{4} - \frac{z}{2}\right)\right\}} \qquad \text{(Eq. 3.30)}$$

The resulting cylinder temperature is plotted against the crank angle. Figure 3.7 shows an example of the calculated bulk cylinder temperature curve. From this curve, peak cylinder temperature timing is obtained for each testing condition. The charge gas temperature during the ignition delay is also obtained from this curve by averaging the charge gas temperature at SOI and SOC: Equation 3.31 for the pilot event and Equation 3.32 for the main event.

$$T_{IDp} = \frac{T_{SOIp}+T_{SOCp}}{2} \qquad \text{(Eq. 3.31)}$$

$$T_{IDm} = \frac{T_{SOIm}+T_{SOCm}}{2} \qquad \text{(Eq. 3.32)}$$

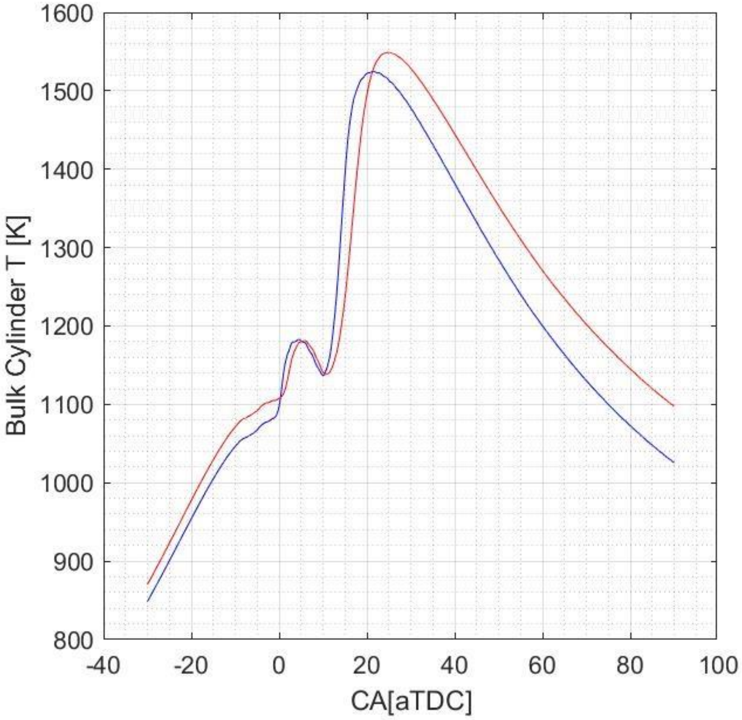

Figure 3.7. An example of the calculated bulk cylinder temperature curve. Test condition: MM3 EGR47% (blue) and 45% (red) with the baseline diesel fuel at default ECU calibration.

Injector nozzle dimeter is assumed to be 139μm as provided by Ford Motor Company. The area contraction coefficient is interpolated from the values provided in Pickett et al.[36] as follows. Table 3.9 presents the values of the area contraction coefficient depending on the rail pressure and the fuel injector nozzle diameter from Pickett et al. in its first two rows (i.e., *d*=100μm and *d*=180μm). For the current study (i.e., *d*=139μm), the area contraction coefficients at the two given injector nozzle diameters are linearly interpolated at different rail pressures (Third row). Then, the linearly interpolated value of C_a between 0.88 and 0.84 is used for different rail pressure conditions.

Value of C_a	Rail Pressure = 720bar	Rail Pressure = 1380bar
d=100µm	0.91	0.86
d=180µm	0.85	0.82
d=139µm	0.88	0.84

Table 3.9. Area contraction coefficient depending on the injector nozzle diameter and rail pressure. The values for 100 and 180µm nozzle diameters are referenced from Pickett et al.[36], and the values for 139µm is linearly interpolated from the two values.

For the tangent of the half spreading angle, Equation 3.33 is used.

$$\tan\frac{\theta}{2} = c \cdot \left[\left(\frac{\rho_a}{\rho_f}\right)^{0.19} - 0.0043\sqrt{\frac{\rho_f}{\rho_a}}\right] \qquad \text{(Eq. 3.33)}$$

In Equation 3.33, the value of constant "*c*" is obtained as follows. The values of "*c*" for injector nozzle diameter 100µm (*c*=0.255) and 180µm (*c*=0.271) are referenced from Picket et al.[37] Then, the value of "*c*" for the currently used injector nozzle diameter (139µm) is linearly interpolated to result in 0.263.

Since the definition of the conventional equivalence ratio has limitations when comparing between the regular hydrocarbon fuels and the oxygenated fuels such as biodiesel, the radially averaged equivalence ratio,"$\langle\phi(x)\rangle$", is converted to the radially averaged "oxygen" equivalence ratio using Equation 3.34.

$$\phi_{\Omega} = \frac{\phi}{1-\frac{(1-\phi)}{\phi_{\Omega,f}}} \quad \text{(Eq. 3.34)}$$

Equation 3.34 converts the regular equivalence ratio (ϕ) to the oxygen equivalence ratio (ϕ_{Ω}) by accounting for the fuel oxygen equivalence ratio ($\phi_{\Omega,f}$), which is calculated based on the definition of the oxygen equivalence ratio (Equation 3.35).

$$\phi_{\Omega,\mathrm{f}} = \frac{2n_C+0.5n_H}{n_O} \qquad \text{(Eq. 3.35)}$$

In Equation 3.35, each "*n*" denotes the number of each atom in a fuel molecule. The fuel oxygen equivalence ratio value for the baseline diesel was infinity while it was 144.78 for B20. Then, finally, the oxygen ratio (Ω), "the reciprocal of the oxygen equivalence ratio in % unit", is calculated using Equation 3.36. The oxygen ratio is literally the percentage of oxygen available at the axial coordinate to burn the total mass of injected fuel in stoichiometry. Thus, higher oxygen ratio in the fuel-rich premixed auto-ignition zone often implies the reduction in soot generation and the increase in NOx generation. And the oxygen ratio at the lift-off length is often used as a representative indicator to judge the level of oxygen ratio in the auto-ignition zone.[9]

$$\Omega(x)\ [\%] = \frac{100}{\phi_{\Omega}(x)} \quad \text{(Eq. 3.36)}$$

The lift-off length (*H*) is estimated using Equation 3.37.

$$H = C \cdot {T_a}^{-3.74} \cdot {\rho_a}^{-0.85} \cdot d^{0.34} \cdot U \cdot {Z_{st}}^{-1} \quad \text{(Eq. 3.37)}$$

In Equation 3.37, proportionality constant "*C*" is referenced to be $7.04 \cdot 10^8$ from Picket et al.[36] The T_a is the charge gas temperature at SOI, and ρ_a is the charge gas density at SOI. U is the fuel jet velocity, and is calculated based on the Bernoulli's law as suggested in Picket et al.[36] (Equation 3.38).

In Equation 3.38, " $\frac{C_d}{C_a}$ " accounts for the non-ideality from the Bernoulli's law, and C_d is the discharge coefficient. The values of the discharge coefficient of the injector nozzle diameters of 100μm (C_d=0.80) and 180μm (C_d=0.77) are referenced from Picket et al.[36] Then, the value of the discharge coefficient for the current injector nozzle diameter (139μm) is linearly interpolated from the two values resulting in 0.785. "ΔP_{inj}" is the pressure gradient between the fuel injector and the charge gas. In this work, the difference between the rail pressure and the charge gas pressure is assumed to be the same as "ΔP_{inj}".

$$U = \frac{C_d}{C_a} \cdot \sqrt{\frac{2 \cdot \Delta P_{inj}}{\rho_f}} \qquad \text{(Eq. 3.38)}$$

Lastly, Z_{st} is the stoichiometric mixture fraction, the ratio of the mass of fuel to the total mass of fuel "and" the charge gas required for stoichiometric combustion of the fuel.

3.2.8 Design of Experiment (DOE), Modeling, and ECU Optimization

3.2.8.1 Design of Experiment (DOE)

Design of Experiment (DOE) is a method to efficiently plan the testing conditions of which measurement results will be used for the modeling of the impact of multiple input parameters on the measured results. In a conventional "sweep" test planning, if we want to investigate the impact of "*n*" different input variables on an output variable, and need "*m*" test conditions per each input variable, the total number of data points required becomes "m^n", which can be a huge number depending on the scale of "*m*" and/or "*n*". However, instead of the sweep test planning, the current study used a "space-filling" DOE method that fills up the n-dimensional input variable space with the least number of combinations of the input variables. In this study, ETAS ASCMO DOE software (i.e., ETAS ASCMO Static Test Plannning) is used for the DOE. The software set 72 data acquisition points to model the impact of 6 input parameters at the MMs 2-6, and required 120 data points to model the impact of 8 input parameters at MM1. Table 3.10 presents the list of the input parameters and their ranges of the settings for the DOE. At MM1, the 8 input parameters were EGR, boost pressure (BP), rail pressure (RP), main injection timing (MIT), relative distance between MIT and PIT1 (RPIT1), relative distance between PIT1 and PIT2 (RPIT2), pilot 1 injection quantity (PIQ1), and pilot 2 injection quantity (PIQ2). At MMs 2-6, the 6 input parameters were EGR, BP, RP, MIT, PIQ1, and RPIT1.

The ranges of the input parameters used in DOE are set as follows. First, regarding the range of EGR rate, the lowest and highest achievable EGR rate at each MM point for the baseline diesel are used. Second, for boost pressure, the turbo-vane position corresponding to the LP and HP at default EGR rate are used as the lower and upper limit of the boost pressure range in DOE. The use of turbo-vane position instead of the direct use of the boost pressure was to avoid inoperable combinations of the EGR and boost pressure. Third, the LRP (80% of the DRP) and HRP (120% of the DRP) are used as the lower and upper limits of the range of rail pressure used in DOE. Fourth, 5 degrees advanced injection timing (5A) and 5 degrees retarded injection timing (5R) are used as the lower and upper limits of the range of main injection timing used in DOE. Fifth, 1.5-4.0mg/stroke is used as the range of PIQ1 for all six MM points. Then, the same range is applied for PIQ2 at MM1. Lastly, 8-17 CAs is used as the range of the relative distance between MIT and PIT1 in MMs 2-6 while 5-10 CAs is used as the range of the relative distance between MIT and PIT1 and relative distance between PIT1 and PIT2 at MM1.

DOE settings	MM1	MM2	MM3	MM4	MM5	MM6
EGR rate [%]	0-58	0-57	0-47	0-27	0-39	0-28
Turbovane closing [%]	55-95	65-85	50-95	48-95	35-93	40-70
RP[% to the def. settings]	80-120					
MIT [relative CA to def. settings]	-5-5					
PIQ1 [mg/stroke]	1.5-4					
RPIT1 [CA]	5-10	8-17				
PIQ2 [mg/stroke]	1.5-4					
RPIT2 [CA]	5-10	[-]	[-]	[-]	[-]	[-]

Table 3.10. The list of input parameters and their range of the settings used for the DOE

The concept of “block” assignment is also used in the current study. A “block” assignment is the division of the total DOE data points into multiple data blocks each of which space-fills the entire input variable space. For example, at MM1, the total 120 DOE data points are divided into the 5 data blocks, and each of these blocks covered the entire range of the input variables. This enabled the testing of some fractions of the total DOE data points first to establish a tentative model to see the necessity of the additional data acquisition. And for each data block, a repeat point test is conducted at the default ECU calibration. For MM1, 5 repeat point tests are conducted in total for the 5 data blocks. For MMs 2-6, 3 repeat point tests are conducted in total for the 3 data blocks. Thus, for MM1, 5 data blocks are obtained and each data block consisted of 24 data points and 1 repeat point. For MMs 2-6, 3 data blocks are obtained and each data block consisted of 24 data points and 1 repeat point. The repeat points obtained are used for the repeat point analysis that checked the repeatability of the test based on the root-mean-squared-error (RMSE) of the primary output parameters such as BFE, BSNOx, and BSPM.

3.2.8.2 Modeling and ECU Optimization

After the test is conducted at all DOE data points, the test result is used to model the impact of the ECU input parameters by using the ETAS ASCMO Static Modeling and Optimization software. The software takes the measurement results in, and uses a "Gaussian Process" to model the correlation between the input parameters and the output parameters. The Gaussian Process is different from conventional "parametric methods" that have a fixed number of correlation coefficients to fit the data points. It is a non-parametric method that predicts the output result at each input condition with a Gaussian distribution. Thus, it can flexibly determine the number of correlation coefficients and the type of correlation functions depending on the size of the data set and can also put different weights on different training data points.

Once a model is established, "cross-validation" can be conducted in the software to determine the statistical quality of the established model. "Cross-validation" is a preliminary validation of the model by using a fraction of the previously obtained data points instead of using a full new validation data set. One of the most common cross-validation method is the "Leave-One-Out" (LOO) validation where the model is established with N-1 data points (where N is the number of the total training data points) and a data point is left out for the cross validation. Then, the software conducts N times of the LOO validation for each left-out data point, and calculates the averaged measures to determine the statistical quality of the model. Based on this LOO validation method, there were several parameters provided from the software regarding the statistical quality of the model.

First, the root-mean-square-error (RMSE) of the model is provided. RMSE is the root mean of the squared discrepancy between the predicted value and measured value at each input condition. (Equation 3.39).

$$RMSE(\sigma) = \sqrt{\sum_{i=1}^{N} \frac{\left(x_{pred,i} - x_{meas,i}\right)^2}{N}} = \sqrt{SSR} \qquad \text{(Eq. 3.39)}$$

It is a measure for the accuracy of the predicted values from the model compared to the actual measurement. Thus, the sum of squared residuals (SSR) is simply the square of RMSE.

Second, the R-squared (R^2) value is provided. The R-squared value is calculated using Equation 3.40 in the software. Here, SST is different from SSR in that it indicates the discrepancy in the measured data points and the mean value of the measurement. By accounting for the SST and SSR together, the R-squared value is often used as an ultimate measure of the statistical accuracy of the model. If the R-squared value is lower than 60%, it means the model is not reliable. Between 60-80%, the model can be useful for qualitative explanation with low reliability. Between 80-90%, the model can be useful for qualitative explanation with high reliability. For the model with over 90% R-squared value, it is useful for quantitative description of the phenomena.

$$R^2 = 1 - \frac{SSR}{SST} \quad \text{(Where } SST = \sum_{i=1}^{N} \frac{\left(x_{meas,i} - \overline{x_{meas,i}}\right)^2}{N}\text{)} \qquad \text{(Eq. 3.40)}$$

Although the R-squared value addresses the accuracy of the model well, there is a limitation. In case SST is high due to high inaccuracy of the experimental measurement, high R-squared value alone does not guarantee a low value of SSR. Thus, the RMSE obtained from the repeat point analysis is used as a proxy to check the level of measurement inaccuracy during the test.

Table 3.11 shows the acceptable range of the R-squared values for different output parameters. In this study, the model is improved until the R-squared values for each output parameter are around or over the values presented in Table 3.11. The improvement of the model is achieved by removing the outlying data points. Usually, the outlying data points occurred at extreme input variable settings (e.g., upper end of EGR rate, lower end of boost pressure), thus providing the rationale for the exclusion. However, if a data point with moderate input condition is excluded from the final model, the validity range of the model had to be sacrificed. Thus, the number of outliers excluded from the final model was minimized as much as possible.

Table 3.11 also shows the acceptable range of the normalized RMSE (n-RMSE) of the output parameters from the repeat point analysis. The nRMSE is calculated using Equation 3.41 in this study.

	R-squared values	nRMSE from repeat point analysis
BFE	90%	1%
$BSCO_2$	90%	1%
$BSNO_x$	99%	2%
BSPM	90%	10%
BSCO	90%	5%
BSTHC	80%	10%
CNL	90%	1%

Table 3.11. The accepted ranges of the model R-squared values of the output parameters and nRMSE of the repeat point analysis.

$$nRMSE = \frac{RMSE}{y_{mean}} \qquad \text{(Eq. 3.41)}$$

(y_{mean}: mean value of the output parameters from repeat point test)

After the model is established for the impact of the ECU input variables at each MM point, the ECU optimization is conducted based on the established model. The details of the method used for ECU re-calibrations is presented in the previous section 3.2.4.

3.3 Results and Discussion

3.3.1 Diesel Baseline Test Results

The experimental results of the baseline diesel test with four different single parameter sweeps are presented here. The trend of BFE, $BSCO_2$, BSNOx, BSPM, BSCO, CNL for all 6 MM points and BSTHC for MMs 1-3 by each single parameter sweep test is presented for each MM point. The detailed trend varies by different MM points, but, there are some general trends that represent most of the operating conditions with some exceptions.

During the boost pressure (BP) sweep, the BFE generally decreased with increasing boost pressure. This is due to the increase in pumping loss with increasing boost pressure. The increase in turbine inlet (exhaust valve exit) pressure must be greater than the increment in the intake charge pressure (BP) because of the 2nd law of thermodynamics. This results in the increase in the difference in cylinder intake and exhaust pressure, which generates more pumping loss.[38]

The BSNOx trend during the boost pressure (BP) sweep at different MM points could not be generalized. The NOx emissions must be compared for the baseline fuel and B20 at each MM point. This is because the change in boost pressure causes the change in multiple factors affecting NOx generation, some of which compete with the others. The increase in boost pressure shortens the fuel ignition delay to advance the combustion phasing that potentially increases NOx emission.[39,40] However, the increase in boost pressure can, at the same time, either decrease or increase air-fuel ratio depending on different operating conditions. In case the air-fuel ratio is decreased at certain MM point, the overall equivalence ratio of the charge gas can increase, and this can potentially decrease NOx.[39] In addition, since NOx emission is also dependent on the local equivalence ratio inside the fuel-rich premixed auto-ignition zone[25], the trend of NOx by boost pressure (BP) can be different for each different MM point.

The variation in the trend of BSNOx at different MM point applies the same for the other criteria pollutant emissions (i.e., BSPM, BSTHC and BSCO) and CNL. There are multiple factors that affect the generation of these pollutants and engine noise level in different directions, and each factor can affect the criteria pollutants with different importance depending on the engine operating conditions.

During the main injection timing (MIT) sweep, the BFE generally increased with the advance in main injection timing, which was consistent with the results reported in the previous research.[24,35] This is because the main combustion phasing occurs after Top Dead Center (TDC) with the default main injection timing setting. Thus, the advance in main injection timing causes the main combustion phasing to be closer to TDC, which, in turn, makes the main combustion event more like a constant-volume process. Furthermore, with main start of combustion (SOC) being closer to TDC, the actual compression ratio also increases. These two factors both contribute to the increase in the gross indicated thermal efficiency, thus resulting in the increase in BFE.[41]

The BSNOx generally increased with the advance in main injection timing (MIT), which was consistent with the results reported in the previous research.[42] Although different main injection timings can change the initial charge gas temperature at the start of combustion (SOC) and affect the NOx generation “rate”, the change in the “duration” of NOx generation is the dominant factor in BSNOx change during the main injection timing sweep.[42] Since the advanced main injection timing subsequently advances the SOC, this allows more duration for the charge gas to be at high temperature resulting in higher BSNOx emissions.

The BSTHC and BSCO generally decreased with the advance in main injection timing (MIT) due to the same reason that caused the increase in BSNOx. More time is allowed for the complete combustion of the fuel injected when injection timing is advanced, thus resulting in decreased BSTHC and BSCO.

The BSPM generally peaked around the default injection timing and decreased for both advanced and retarded injection timings. This trend occurs because the oxygen ratio (i.e., the inverse of the local oxygen equivalence ratio, or the ratio of local oxygen presence to the required total oxygen to burn all the injected fuel by stoichiometric combustion) at the lift-off length became minimum around the default injection timing, while it increased for both advanced and retarded injection timings. The charge gas temperature during the ignition delay peaked around the default injection timing, while the other factors affecting the lift-off length (i.e., charge gas density, stoichiometric mixture fraction, fuel jet velocity, injector nozzle hole diameter) remained similar. The high charge gas temperature shortens the lift-off length, and results in the lowest oxygen ratio around the default injection timing.[36] Then, the low oxygen ratio results in higher PM generation at default injection timing.[25] For more detailed explanation on the fundamentals of lift-off length and oxygen ratio in compression ignition engines and their impact on NOx and PM emission, refer to the previous section 3.2.7.

During EGR sweep, the BFE generally decreased with increasing EGR rate, which was consistent with the previously reported results.[43,44] This is because the 2nd law efficiency of the turbine decreases at higher EGR rate due to the lower mass flow rate of the exhaust gas through the turbine. It results in higher increment of the turbine inlet pressure to achieve certain increment in the intake boost pressure, which simply means higher pumping loss.

The BSNOx generally decreased with increased EGR rate, which was consistent with the results reported in previous study.[44] There are two main reasons for the trend. First, increased EGR rate decreases the intake O_2 concentration, and the diluted O_2 concentration decreases NOx generation rate. Second, since the heat capacity of the tri-atomic molecules (i.e., CO_2, H_2O) contained in EGR gas is higher than that of the di-atomics (i.e., O_2, N_2) in the fresh air, the charge gas is thermally diluted with the increase in EGR, thus resulting in lower charge gas temperature suppressing the thermal NOx generation rate.[45] Furthermore, since diluted oxygen and thermal effect both delay the combustion phasing, less time is allowed for the charge gas to be at high temperature to generate NOx, thus resulting in the decrease in NOx emission.

Oppositely, the BSPM generally increased with increasing EGR rate because the overall charge intake O_2 concentration decreases with EGR rate increase.[44] Also, the oxygen equivalence ratio at the liftoff length usually increased with the increase in EGR[25], thus resulting in the PM increase in fuel-rich premixed auto-ignition zone. In general, BSCO and BSTHC also increased with the increase in EGR rate.[44]

During the rail pressure (RP) sweep, the BFE trend depended on different MM points. Increase in rail pressure can increase the friction loss due to the higher work required for fuel pump, but it can, at the same time, advance the combustion phasing by shortening the ignition delay[24], which, in turn, can increase the gross indicated thermal efficiency. Those competing factors result in the different trends of BFE depending on different MM points.

The BSNOx generally increased with the increase in rail pressure (RP), which was consistent with the previously reported results.[24] This is mainly because of the shortened ignition delay leading to the advance in SOC that allows longer duration of charge gas temperature being at the high temperature producing NOx. It is also because of the increase in fuel jet velocity causing the longer lift-off length[25], which, in turn, increases the oxygen ratio at the lift-off length.

Because the lift-off length gets longer with the increase in rail pressure (RP) causing the increase in the oxygen ratio at the lift-off length, BSPM generally decreases with the increase in RP.[25] Better atomization of the fuel molecule is another reason why the increase in RP results in the decrease in BSPM.

The proceeding sections will present the measurement results at each MM point for 4 different single parameter sweep tests.

3.3.1.1 MM1

MM1 represents an idling operating condition. Due to the inherent characteristics of engine idling (i.e., low fuel and air mass flow rate, low brake torque, etc.), the measurement inaccuracy at MM1 was relatively higher than the other mini-map points, which sometimes made it hard to extract a clear impact of each input parameter on the output parameters of interest. Despite the difficulty, the impact of boost pressure (BP), main injection timing (MIT), EGR rate, and rail pressure (RP) on the output parameters of interest (i.e., BFE, BSNOx, BSPM, CNL, BSTHC, and BSCO) is presented here with the best explanation possible. The impact of 4 input parameters on the output parameters of the “primary” interest (i.e., BFE, BSNOx, and BSPM) at MM1 was generally the same as at MM3 about which more details and fundamentals of the observed phenomena are presented. The three only difference between MM1 and MM3 were as follows: i) impact of main injection timing (MIT) on BFE; ii) impact of MIT on BSPM; and iii) impact of EGR on BFE. Since other trends at MM1 are the same as MM3, the underlying physics relevant to those trends at MM1 could be assumed to be similar to those at MM3.

Figure 3.8a presents the impact of boost pressure (BP) on BFE (top-left), BSNOx (middle-left), BSPM (bottom-left), CNL (top-right), BSTHC (middle-right), BSCO (bottom-right) at MM1 for the baseline diesel. Figure 3.8b presents the trend of the BFE (top-left), BSPM (middle-left), $BSCO_2$ (bottom-left), BSTHC (top-right), BSCO (middle-right) and CNL (bottom-right) by BSNOx during the BP sweep at MM1 with the baseline fuel.

Thick error bars indicate the plus and minus one standard deviation interval (68% confidence interval) while the thin error bars indicate the plus and minus two standard deviations interval (95% confidence interval). In case the difference between two data points is smaller than plus and minus one standard deviation, the difference is not considered to be statistically meaningful. If the difference between two data points is larger than plus and minus one standard deviation, but smaller than plus and minus two standard deviations, the difference is considered to be statistically meaningful with low statistical confidence (less than 95%). If the difference between two data points is greater than plus and minus two standard deviations, the difference is considered to be statistically meaningful with high statistical confidence (more than 95%).

First, BFE from the baseline boost pressure (BP) sweep at MM1 decreases from 25.9% at low boost pressure (LP) to 25.6% at default boost pressure (DP), then to 24.6% at mid-high boost pressure (MHP). The main contributor for BFE decrease by the increase in BP is the increase in PMEP as shown in Figure 3.9. PMEP increases from 0.055bar at LP to 0.185bar at MHP (0.13bar increase), which is about 10% of the BMEP at MM1 (1.25bar).

Second, BSNOx decreases from 2.52g/kWh at LP to 2.11g/kWh at DP, then to 2.01g/kWh at MHP. At MM1, the decrease in boost pressure also decreased air-fuel mass ratio, which resulted in the subsequent decrease in intake charge O_2 mole fraction as shown in Figure 3.10. Intake charge O_2 mole fraction decreases from 0.175 at LP to 0.173 at DP, then to 0.172 at MHP. This decrease in intake charge O_2 mole fraction is the main contributor for the decrease in BSNOx with the increase in boost pressure at MM1.

Third, BSPM bottoms at the DP (0.06g/kWh), and increases for both LP (0.123g/kWh) and MHP (0.081g/kWh). The increase in BSPM from DP to MHP can be explained by the decrease in intake O_2 mole fraction in the same range of the boost pressure (Figure 3.10). However, there is significant decrease in BSPM from LP to DP which is not explained well by the trend of the intake O_2 mole fraction in that boost pressure range since intake O_2 mole fraction actually decreases from LP to DP. Thus, there must be other factor that has more importantly contributed to the trend of BSPM during the boost pressure sweep at MM1. According to previous studies, local oxygen availability in the fuel-rich premixed auto-ignition zone is an important factor determining the soot generation at lower load points.[25] It is likely that the oxygen ratio at the lift-off length might have had more dominant and opposite impact on BSPM against the impact of the overall intake O_2 concentration in the charge gas, thus resulting in the convex trend of BSPM during the boost pressure (BP) sweep. Although oxygen ratio at the lift-off length is not estimated at MM1 due to the limited capability of heat release analysis at the mini-map point, it is estimated at all the other mini-map points during the boost pressure (BP) sweep. It is shown that, at other low-to-medium load points (e.g., MM3), the oxygen ratio at the lift-off length is the more important factor determining BSPM trend than the overall intake O_2 concentration in the charge gas.

Lastly, other brake specific (BS) emissions and combustion noise level (CNL) from the baseline fuel during the boost pressure (BP) sweep at MM1 will be briefly addressed here.

Combustion noise level increased from 74.48dB at LP to 74.64dB at DP, then to 74.88dB at MHP. BSTHC decreased from 2.20g/kWh at LP to 2.08g/kWh at DP, then to 2.01g/kWh at MHP. BSCO was maintained the similar around 4.7g/kWh throughout the entire range of boost pressure during the sweep test.

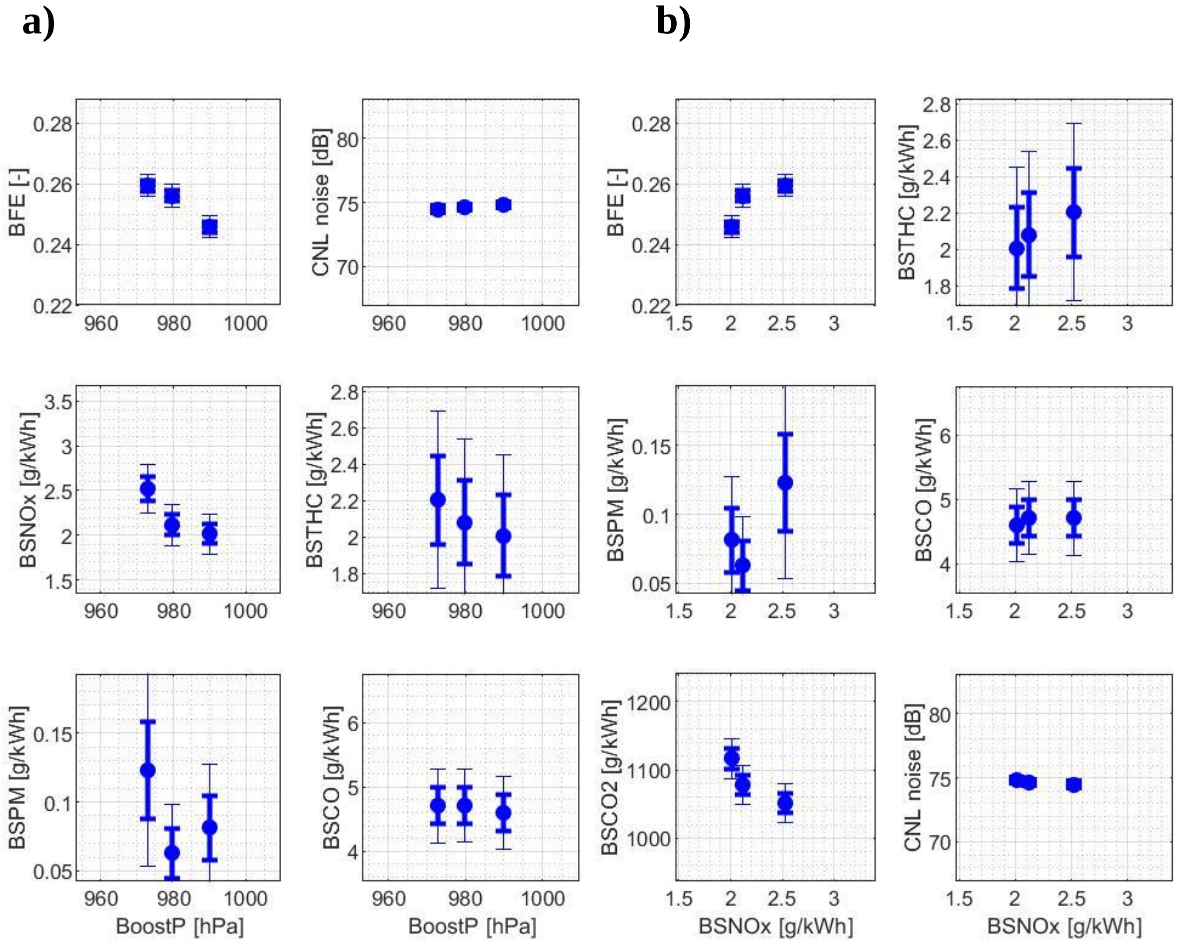

Figure 3.8. BFE, BS emissions, and CNL during the boost pressure (BP) sweep of the baseline diesel at MM1 as a function of a) BP, b) BSNOx

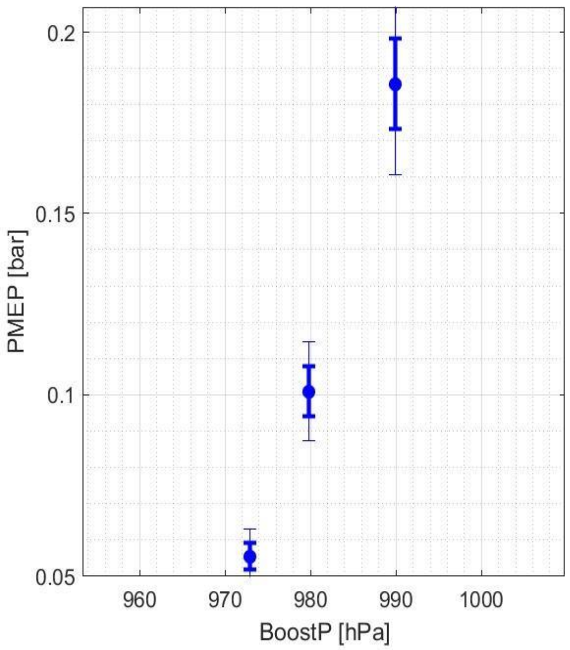

Figure 3.9 PMEP during the boost pressure (BP) sweep of the baseline diesel at MM1.

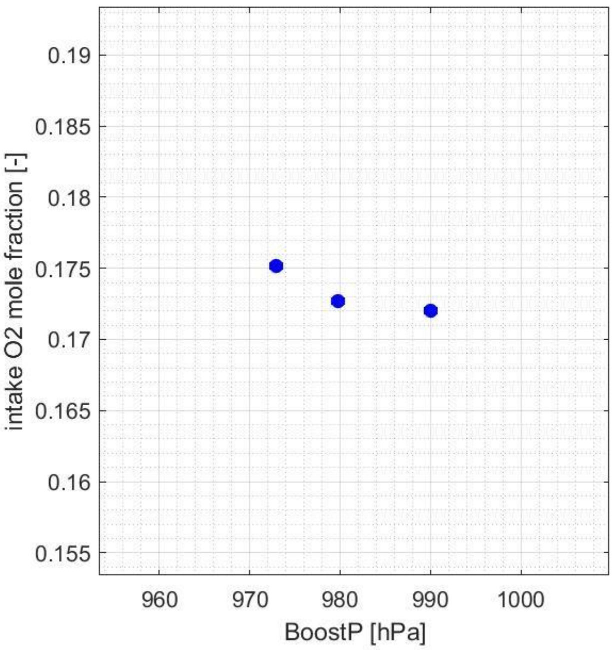

Figure 3.10 Intake charge O_2 mole fraction during the boost pressure (BP) sweep at MM1 for baseline diesel.

Figure 3.11a presents the impact of main injection timing (MIT) on BFE (top-left), BSNOx (middle-left), BSPM (bottom-left), CNL (top-right), BSTHC (middle-right), BSCO (bottom-right) at MM1 for the baseline diesel. Figure 3.11b presents the trend of the BFE (top-left), BSPM (middle-left), $BSCO_2$ (bottom-left), BSTHC (top-right), BSCO (middle-right) and CNL (bottom-right) by BSNOx during the MIT sweep at MM1 with the baseline fuel.

First, BFE of the baseline increases from 25.3% at 5 degrees advanced injection timing (5A), to 25.9% at the default injection timing (DF), then to 26.1% at 5 degrees retarded injection timing (5R). The increase in BFE with the retarding of main injection timing (MIT) at MM1 was one of the unique trends that is not observed at the other mini-map points. This peculiar trend at MM1 is because, unlike other mini-map points, two pilot injections are applied and their injection quantity represents large portion of the total injection quantity at MM1. The underlying principle of how the higher fraction of pilot injection quantity at MM1 could cause the change in the trend of BFE by main injection timing shift is presented below.

When injection timings are retarded, the combustion phasing of main injection event gets further from TDC while the combustion phasing of pilot injection event gets closer to TDC. When either main or pilot injection timings get closer to TDC, the “actual” compression ratio increases, thus increasing the thermal efficiency of the cycle.[41] Also, injection timing closer to TDC makes combustion process thermally more efficient by bringing the process closer to a constant-volume process than a constant-pressure process.[41] Thus, when both of the main and pilot injection timings are retarded at the same time, the impact of the main timing change would be to decrease the thermal efficiency while that of the pilot timing change would be to increase the thermal efficiency.

Since, at other mini-map points, the share of main injection quantity out of the total injection quantity is over 80% for low-to-medium loads (MM2-3), and even over 95% for higher loads (MM4 and 6), the decrease in thermal efficiency of the main combustion event dominates the increase in thermal efficiency of the pilot event. However, at MM1, since there are two pilot events, the share of main injection quantity out of the total injection quantity is only about 60%. Thus, when the injection timing is retarded, the impact of the increase in thermal efficiency of the pilot combustion processes is not negligible, but rather outruns the decrease in thermal efficiency of the main combustion process, thus resulting in the increase in BFE. This argument can be supported by Figures 3.12 and 3.13, where PMEP and IFEg during the MIT sweep at MM1 are presented. As shown in Figure 3.12, PMEP during the MIT sweep remains the same for all injection timings. Thus, PMEP is not a contributor for BFE change during the MIT sweep at MM1. However, as shown in Figure 3.13, IFEg during MIT increases with the retarding of MIT, implying the more efficient overall combustion process with the retarding in injection timings at MM1, which proves the argument above.

Second, BSNOx decreases from 3.57g/kWh at 5 degrees advanced injection timing (5A) to 2.35g/kWh at the default injection timing (DF), then to 1.95g/kWh at 5 degrees retarded injection timing (5R). The decrease in BSNOx by the retarding in main injection timing (MIT) is a well-known trend of BSNOx reported in other studies. Ye et al.[24] reported a decrease in BSNOx emission from both diesel and B40 when MIT is retarded at different rail pressure settings. The decrease in BSNOx with the retarding in MIT is due to the subsequent retarding in peak cylinder temperature timing (i.e., the timing at which the cylinder temperature peaks during the combustion event). Retarding in peak cylinder temperature timing, in turn, allows shorter duration of the high cylinder temperature favorable for NOx generation, thus, resulting in the decrease in BSNOx.[46]

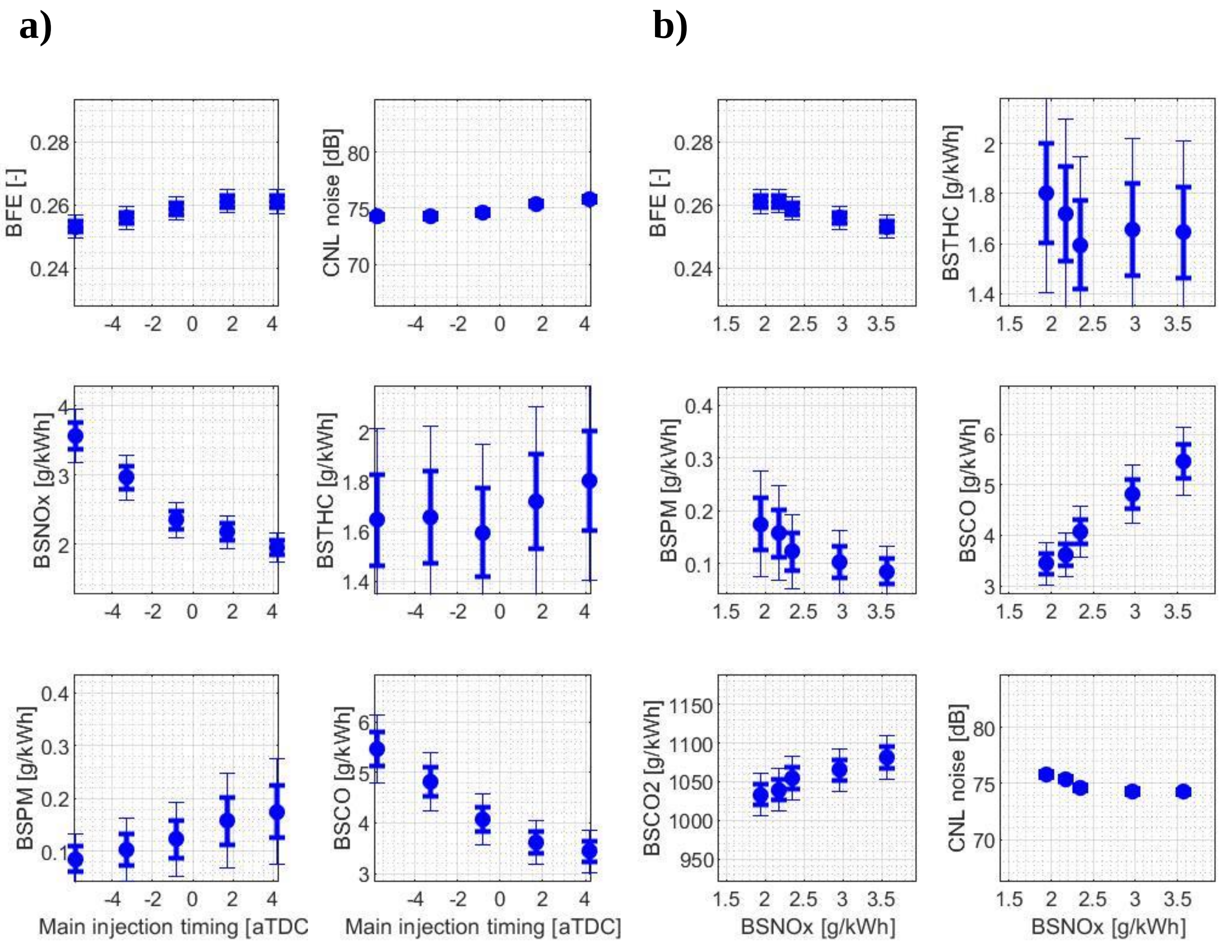

Figure 3.11. BFE, BS emissions, and CNL during the main injection timing (MIT) sweep of the baseline diesel at MM1 as a function of a) MIT, b) BSNOx

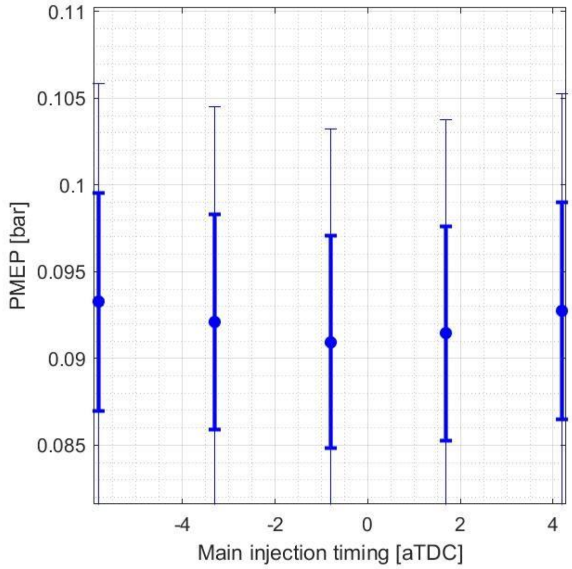

Figure 3.12 PMEP during the main injection timing (MIT) sweep of the baseline diesel at MM1.

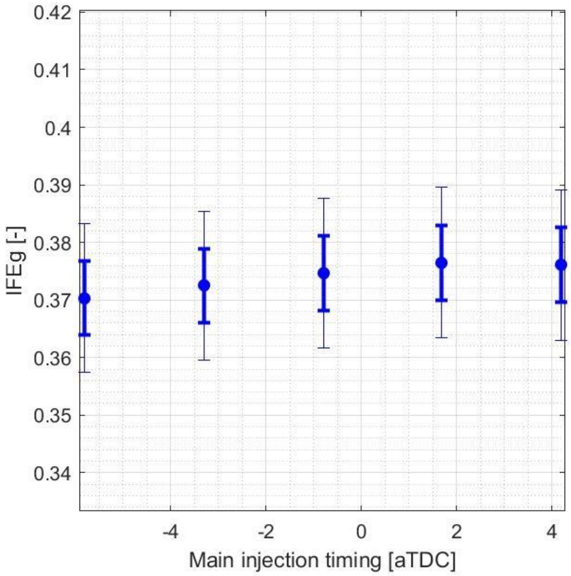

Figure 3.13 IFEg during the main injection timing (MIT) sweep of the baseline diesel at MM1.

Third, BSPM increases from 0.085g/kWh at 5 degrees advanced injection timing (5A) to 0.123g/kWh at the default injection timing (DF), then to 0.175g/kWh at 5 degrees retarded injection timing (5R). As confirmed from the other mini-map points of which results are shown in the following sections, the change in BSPM emission during the main injection timing (MIT) sweep largely depends on the change in oxygen ratio at the lift-off length. Given that intake O_2 concentration is consistent over different injection timings as shown in Figure 3.14, it is likely that oxygen ratio at the lift-off length at MM1 monotonically decreased with the retarding in MIT, thus resulting in the increase in BSPM.

Lastly, the other BS emissions and CNL during the baseline main injection timing (MIT) sweep at MM1 is briefly presented here. Combustion noise level increases from 74.24dB at 5 degrees advanced injection timing (5A) to 74.62dB at the default injection timing (DF), then to 75.78dB at 5 degrees retarded injection timing (5R). BSTHC generally increases for the retarded injection timings than advanced or default injection timing. However, the degree of increase in BSTHC due to the change in MIT is smaller than one standard deviation of the repeated measurement, which means that the difference is not statistically meaningful. BSCO decreases from 5.46g/kWh at 5A to 4.07g/kWh at DF, then to 3.44g/kWh at 5R.

Figure 3.15a presents the impact of EGR on BFE (top-left), BSNOx (middle-left), BSPM (bottom-left), CNL (top-right), BSTHC (middle-right), BSCO (bottom-right) at MM1 for the baseline diesel. Figure 3.15b presents the trend of the BFE (top-left), BSPM (middle-left), $BSCO_2$ (bottom-left), BSTHC (top-right), BSCO (middle-right) and CNL (bottom-right) by BSNOx during the EGR sweep at MM1 with the baseline fuel.

First, BFE from the baseline fuel during the EGR sweep at MM1 is presented in Figure 3.15a (top-left). Due to the large variation in the brake torque settings during the EGR sweep of this idling condition, it was hard to extract meaningful trend in BFE by the EGR rate. BFE during the baseline EGR sweep at MM1 ranged between 24.9% and 26.5%.

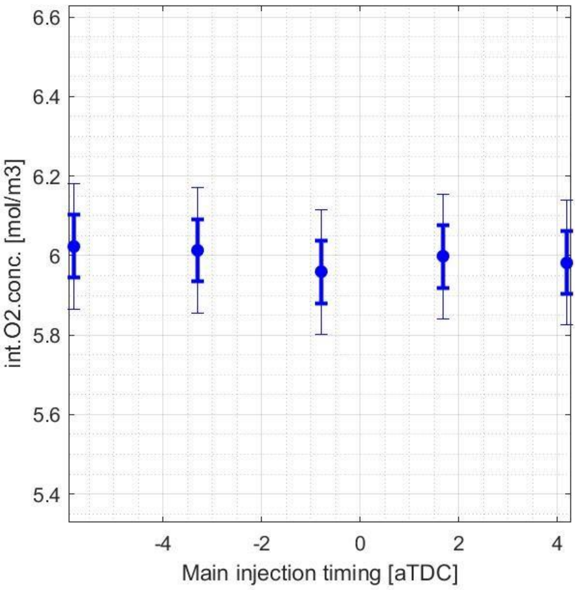

Figure 3.14 Intake charge O_2 concentration during the main injection timing (MIT) sweep of the baseline diesel at MM1.

Second, BSNOx decreases from 10.3g/kWh at EGR5% to 2.5g/kWh around EGR42% (default EGR settings), then to 0.32g/kWh at EGR58%. One of the main contributors for BSNOx decrease with the increase in EGR is the decrease in intake O_2 concentration (i.e., O_2 dilution). Figure 3.16 shows the decrease in O_2 concentration in charge gas during the EGR sweep from 7.9mol/m^3 at EGR5% to 4.75mol/m^3 at EGR58%. The other factor affecting the decrease in BSNOx is the decrease in intake charge gas temperature (i.e., thermal dilution). The thermal dilution impact of EGR is well-reported in other studies.[47] To briefly introduce the physics of the thermal dilution impact of EGR, the increase in EGR increases the share of triatomic molecules (i.e., CO_2 and H_2O) in the intake charge gas and the higher heat capacity of the triatomic molecules results in higher average heat capacity of the charge gas. This increased heat capacity of the intake charge results in lower charge gas temperature, which eventually makes BSNOx decrease.

Third, BSPM increases from 0.071g/kWh at EGR5% to 0.14g/kWh around the default EGR settings (i.e., EGR42%), then to 0.603g/kWh at EGR58%. The increase in BSPM with the increase in EGR rate is mainly attributed to the decrease in intake O_2 concentration shown in Figure 3.16.

Lastly, the other BS emissions and combustion noise level (CNL) during the baseline EGR sweep at MM1 will be briefly addressed here. Combustion noise level remains the same around 74.5dB from the lowest EGR rate imposed to EGR 50%, but then decreases about 1dB at higher EGR range. BSTHC decreases from 2.22g/kWh at EGR5% to 1.72g/kWh at the default EGR settings (EGR42%), then to 1.54g/kWh at EGR58%. BSCO increases from 3.59g/kWh at EGR5% to 4.0g/kWh at the default EGR settings (EGR42%), then to 7.26g/kWh at EGR58%.

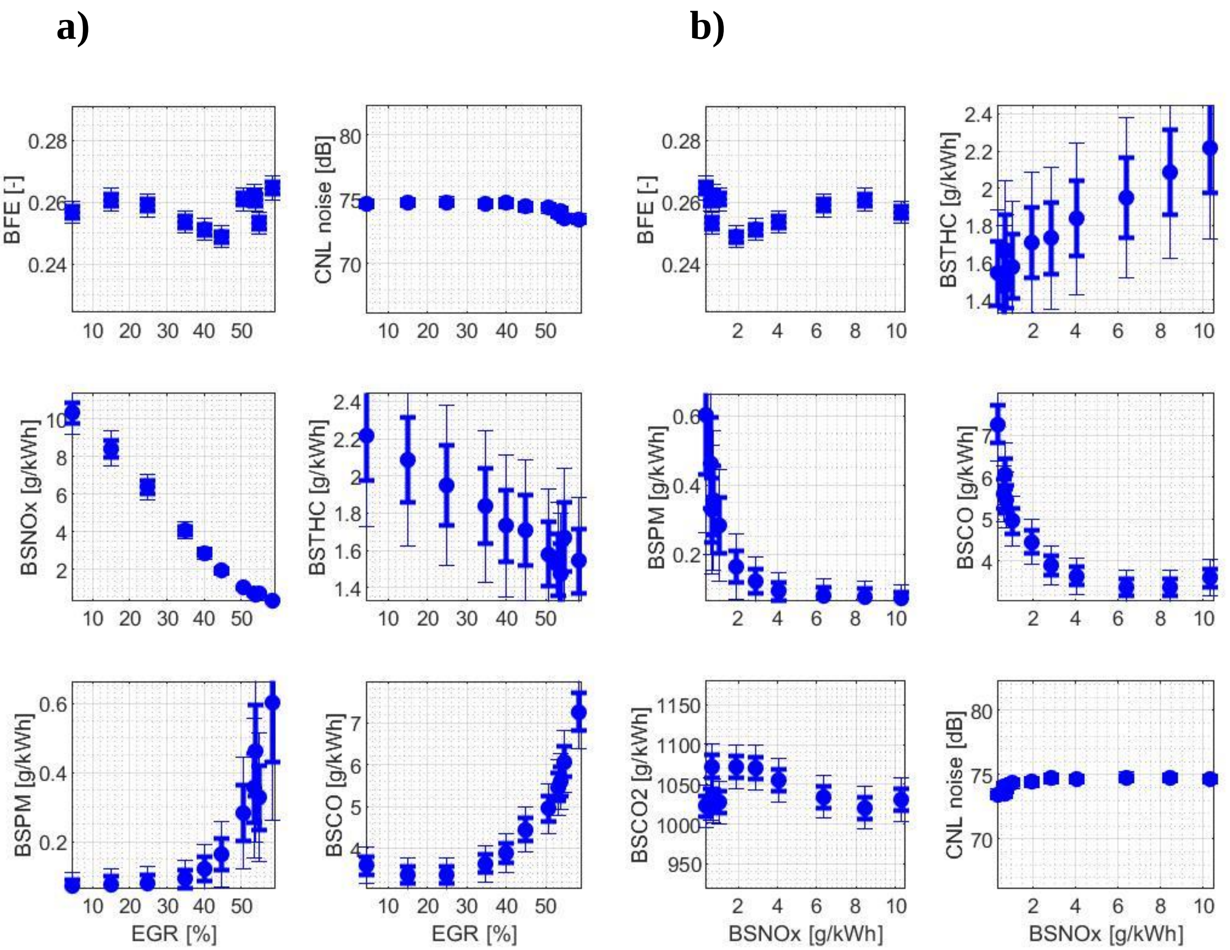

Figure 3.15. BFE, BS emissions, and CNL during EGR sweep of the baseline diesel at MM1 as a function of a) EGR rate b) BSNOx

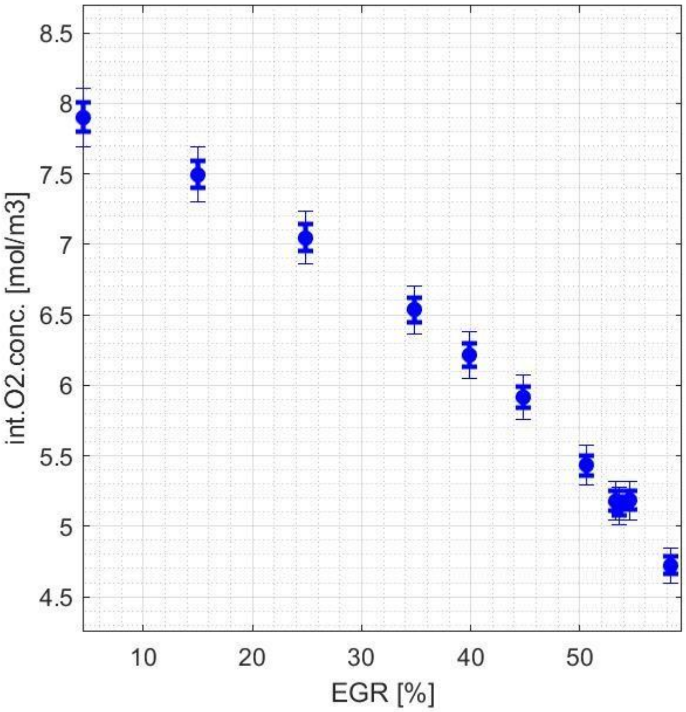

Figure 3.16 The intake O_2 concentration during the EGR sweep of the baseline diesel at MM1.

Figure 3.17a presents the impact of rail pressure (RP) on BFE (top-left), BSNOx (middle-left), BSPM (bottom-left), CNL (top-right), BSTHC (middle-right), BSCO (bottom-right) at MM1 for the baseline diesel. Figure 3.17b presents the trend of the BFE (top-left), BSPM (middle-left), $BSCO_2$ (bottom-left), BSTHC (top-right), BSCO (middle-right) and CNL (bottom-right) by BSNOx during the RP sweep at MM1 with the baseline fuel.

First, BFE increases from 25.6% at low rail pressure (LRP) to 25.9% at the default rail pressure (DRP), then to 26.7% at high rail pressure (HRP). The increase in BFE with the increase in rail pressure was mainly due to the increase in gross indicated fuel conversion efficiency (IFEg) rather than the decrease in PMEP.

Second, BSNOx increases from 1.98g/kWh at low rail pressure (LRP) to 2.35g/kWh at the default rail pressure (DRP), then to 2.74g/kWh at high rail pressure (HRP). The main contributor for the increase in BSNOx with the increase in rail pressure is the better mixing between air and fuel in the premixed auto-ignition zone. The better mixing results in higher oxygen ratio in the auto-ignition zone allowing more NOx generation.[24]

Third, BSPM decreases from 0.279g/kWh at low rail pressure (LRP) to 0.123g/kWh at the default rail pressure (DRP), then to 0.063g/kWh at high rail pressure (HRP). The improvement in air fuel mixing thanks to the better atomization allowed more oxygen available in the premixed auto-ignition zone, thus resulting in the decrease in BSPM with the increase in the rail pressure. In other words, there was a clear BSPM-BSNOx trade-off during the rail pressure sweep of the baseline as shown in the middle-left plot in Figure 3.17b.

Combustion noise level (CNL), BSTHC, and BSCO from the diesel during the rail pressure (RP) sweep at MM1 are presented in top, middle, and bottom-right plot in Figure 3.17a. CNL increased from 73.60dB at LRP to 74.62dB at DRP, then to 75.83dB at HRP. BSTHC decreased from 1.93g/kWh at LRP to 1.60g/kWh at DRP, then to 1.53g/kWh at HRP. BSCO decreased from 5.17g/kWh at LRP to 4.07g/kWh at DRP, then to 3.47g/kWh at HRP.

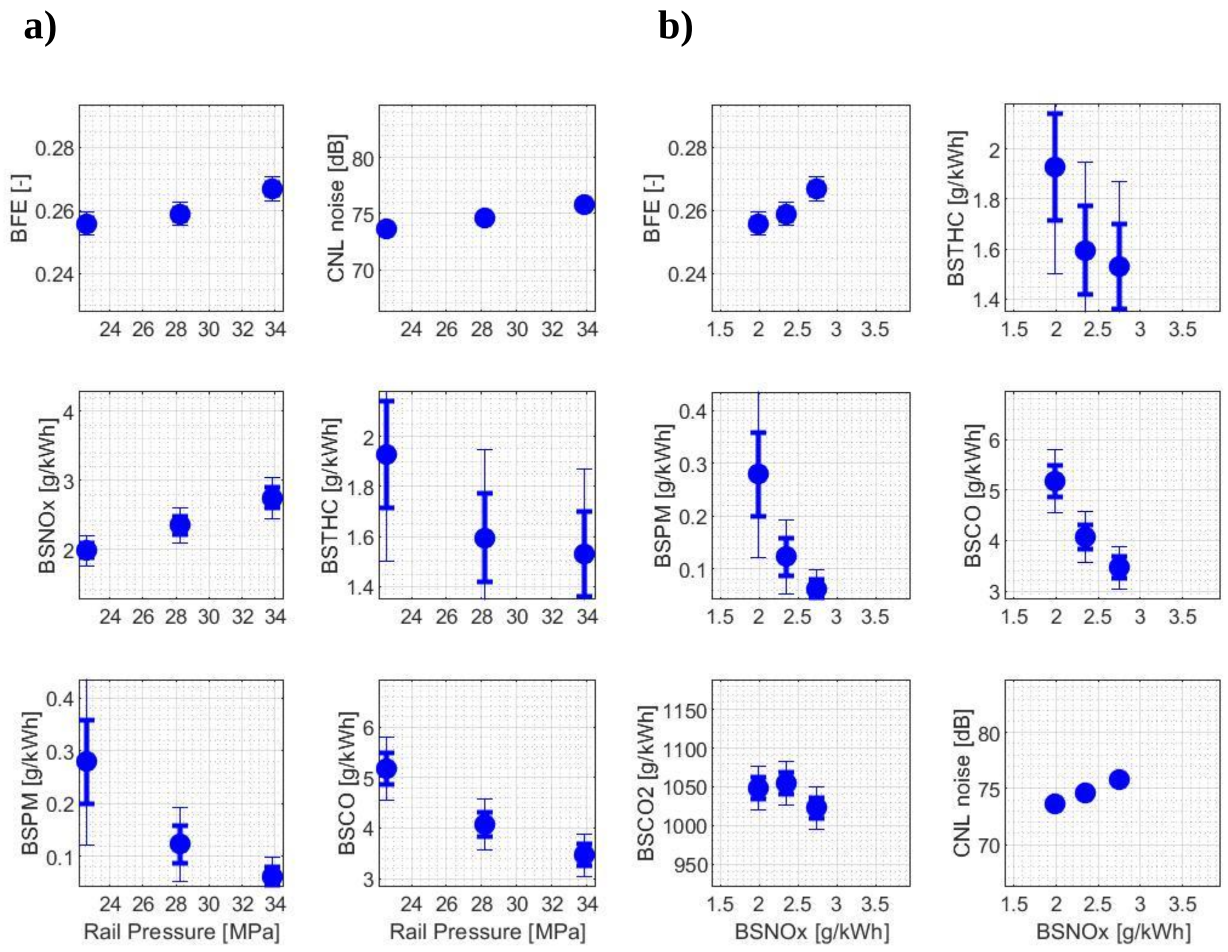

Figure 3.17. BFE, BS emissions, and CNL during the rail pressure (RP) sweep for the baseline diesel at MM1 as a function of a) RP, b) BSNOx

3.3.1.2 MM2

MM2 is a low speed-low load operating conditions out of the 6 MM points. Despite being a low load point, the impact of 4 input parameters (i.e., boost pressure (BP), main injection timing (MIT), Exhaust Gas Recirculation (EGR) rate, rail pressure (RP)) on the output parameters (i.e., BFE, BS emissions, and CNL) at MM2 is similarly observed at other medium-load points such as MM3. Indeed, not only the general trends of the output parameters by the input parameters are the same, but also the underlying physics causing the trends is the same. The trends of output parameters at MM2 by boost pressure (BP) are first presented in this section, followed by the trends by main injection timing (MIT), EGR rate, then finally by rail pressure (RP).

Figure 3.18a presents the impact of boost pressure (BP) on BFE (top-left), BSNOx (middle-left), BSPM (bottom-left), CNL (top-right), BSTHC (middle-right), BSCO (bottom-right) at MM2 for the baseline diesel. Figure 3.18b presents the trend of the BFE (top-left), BSPM (middle-left), $BSCO_2$ (bottom-left), BSTHC (top-right), BSCO (middle-right) and CNL (bottom-right) by BSNOx during the BP sweep at MM2 with the baseline fuel.

Thick error bars indicate the plus and minus one standard deviation interval (68% confidence interval) while the thin error bars indicate the plus and minus two standard deviations interval (95% confidence interval). In case the difference between two data points is smaller than plus and minus one standard deviation, the difference is not considered to be statistically meaningful. If the difference between two data points is larger than plus and minus one standard deviation, but, smaller than plus and minus two standard deviations, the difference is considered to be statistically meaningful with low statistical confidence (less than 95%). If the difference between two data points is greater than plus and minus two standard deviations, the difference is considered to be statistically meaningful with high statistical confidence (more than 95%).

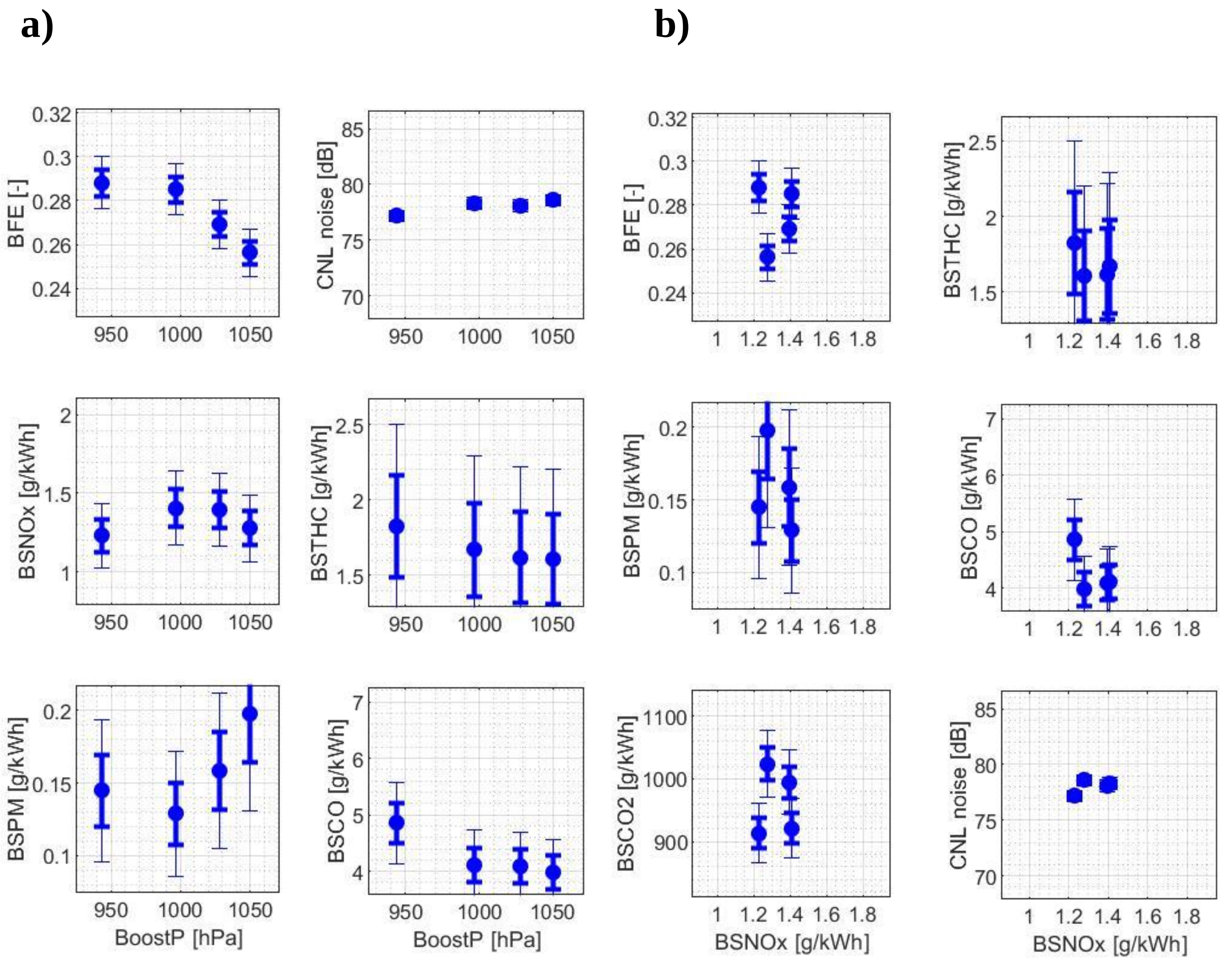

Figure 3.18. BFE, BS emissions, and CNL during boost pressure (BP) sweep of the baseline diesel at MM2 as a function of a) BP, b) BSNOx

First, BFE from the baseline fuel decreases from 28.8% at throttled low boost pressure (TLP) to 26.9% at the default boost pressure (DP), then to 25.6% at mid-high boost pressure (MHP). The decrease in BFE with increasing boost pressure (BP) is mainly due to the increase in pump mean effective pressure (PMEP). Figure 3.19a shows the parameters relevant to the change in BFE during the BP sweep of the baseline at MM2. PMEP (Figure 3.19a, third-to-the-top) increases from 0.092bar at TLP to 0.25bar at DP, then to 0.37bar at MHP. From TLP to MHP, the increase in PMEP was 0.278bar, which is about 5.4% of the BMEP at MM2 (1.5bar). Given that gross indicated fuel conversion efficiency (IFEg) (Figure 3.19a, second-to-the-top) change was not statistically meaningful during the BP sweep, the increase in PMEP can be the main cause of BFE decrease with increasing BP at MM2.

Second, BSNOx from the baseline diesel increases from 1.23g/kWh at throttled low boost pressure (TLP) to 1.41g/kWh at low boost pressure (LP), and plateaus between the LP and default boost pressure (DP). Between DP and mid-high boost pressure (MHP), BSNOx drops from 1.39g/kWh at DP to 1.28g/kWh at MHP. The concave curve of BSNOx with increasing boost pressure (BP) is due to the competition of the oxygen ratio at the lift-off length and other factors affecting NOx. Figures 3.19b and 3.19c present the parameters relevant for the NOx change during the BP sweep at MM2. Due to the minute advance in main SOC (Figure 3.19c, top) with increasing BP, peak cylinder temperature timing (Figure 3.19b, second-to-the-top) also has only minute advance with increasing BP. Intake O_2 concentration (Figure 3.19b, top) increases from 5.69mol/m^3 at TLP to 6.16mol/m^3 between DP and MHP, which is about 8.3% increase during the BP sweep. Compared to the change in intake O_2 concentration during the BP sweep at other mini-map points, 8.3% increase is not a significant increase. (cf. MM3 has 20% increase, MM6 has 45% increase). However, the charge gas temperature during the main ignition delay (Figure 3.19b, third-to-the-top) does have significant increase with increasing BP. It increases from 1180K at TLP to 1250K at MHP. In conclusion, while the charge gas temperature increase from TLP to MHP can play a primary role in NOx increase, the increase in intake O_2 concentration and advance in peak cylinder temperature timing can also secondarily contribute to the increase in NOx. However, there is a competing factor for this potential increase in NOx.

Figure 3.20a shows the lift-off length (top), oxygen ratio at the lift-off length (middle), and BSNOx (bottom) during the baseline boost pressure (BP) sweep at MM2. Due to the increase in charge gas temperature and density, the lift-off length decreases from 6.4mm at TLP to 4.94mm at MHP. The oxygen ratio at the lift-off length also decreases with the increase in BP. It decreases from 3.7% at TLP to 2.64% at MHP. The decrease in oxygen ratio means less oxygen availability in the fuel-rich premixed auto-ignition zone, which results in less NOx generation in that region. Mueller et al.[25] states that the impact of oxygen ratio in the fuel-rich premixed ignition zone on NOx generation becomes more apparent at lower loads due to the higher fraction of energy obtained from "ignition" than "mixing-controlled combustion". MM2 runs at such low-load condition. Although the absolute 1.1% decrease in oxygen ratio with increasing BP might not seem significant, it does have enough impact to change the final BSNOx emissions result. Therefore, at MM2, the decrease in oxygen ratio at the lift-off length competes with the previously mentioned factors that potentially increase NOx emissions. Then, eventually, the competition between these factors results in the concave curve of BSNOx shown in Figure 3.18a.

Third, BSPM from the baseline increases from the lower range of boost pressure (BP) to the higher range of BP. BSPM increases from about 0.13g/kWh in the lower BP range (i.e., between TLP and LP) to 0.198g/kWh at MHP. Although the mean value of BSPM at TLP looks higher than at LP, the difference of BSPM between TLP and LP is not statistically meaningful due to the high standard deviation of the repeated measurement. Thus, it is reasonable to say that BSPM generally increases from lower BP to higher BP than making a convex curve during the BP sweep. As mentioned earlier, the impact of oxygen ratio in the fuel-rich auto-ignition zone at low load conditions like MM2 is significant. Thus, despite the moderate increase in intake O_2

concentration, BSPM generally increases with increasing BP due to the decrease in oxygen ratio at the lift-off length.

Indeed, this competition between the increase in intake O_2 concentration and the decrease in oxygen ratio at the lift-off length is repeatedly observed at other mini-map points. A valuable observation from the comparison of different mini-map points is that, as the engine load gets higher, the relative importance of the oxygen ratio compared to the intake O_2 concentration decreases. For example, at high load points such as MM4 and MM6, although there is still significant decrease in oxygen ratio at the lift-off length with increasing boost pressure, BSPM decreases due to the more dominant impact of increasing intake O_2 concentration. Oppositely, at MM3, of which load is just moderately higher (i.e., BMEP at MM3: 3bar) than MM2, BSPM increases with increasing boost pressure due to the dominance of the decrease in oxygen ratio over the increase in intake O_2 concentration. This different trend of BSPM during the boost pressure sweep at different MM points re-confirms the statement from Mueller et al.: the importance of local oxygen availability in the fuel-rich premixed auto-ignition zone on NOx and PM emissions is greater at lower loads.[25]

Lastly, the other brake specific (BS) emissions and combustion noise level (CNL) values from the baseline boost pressure (BP) sweep at MM2 will be reported briefly here. BSTHC decreases from 1.83g/kWh at TLP to 1.61g/kWh at MHP. BSCO also decreases from 4.86g/kWh at TLP to 3.98g/kWh at MHP. The decreases in BSTHC and BSCO with increasing BP are mainly due to the increase in overall charge O_2 concentration. Combustion noise level (CNL) increases from 77.2dB at TLP to 78.6dB at MHP.

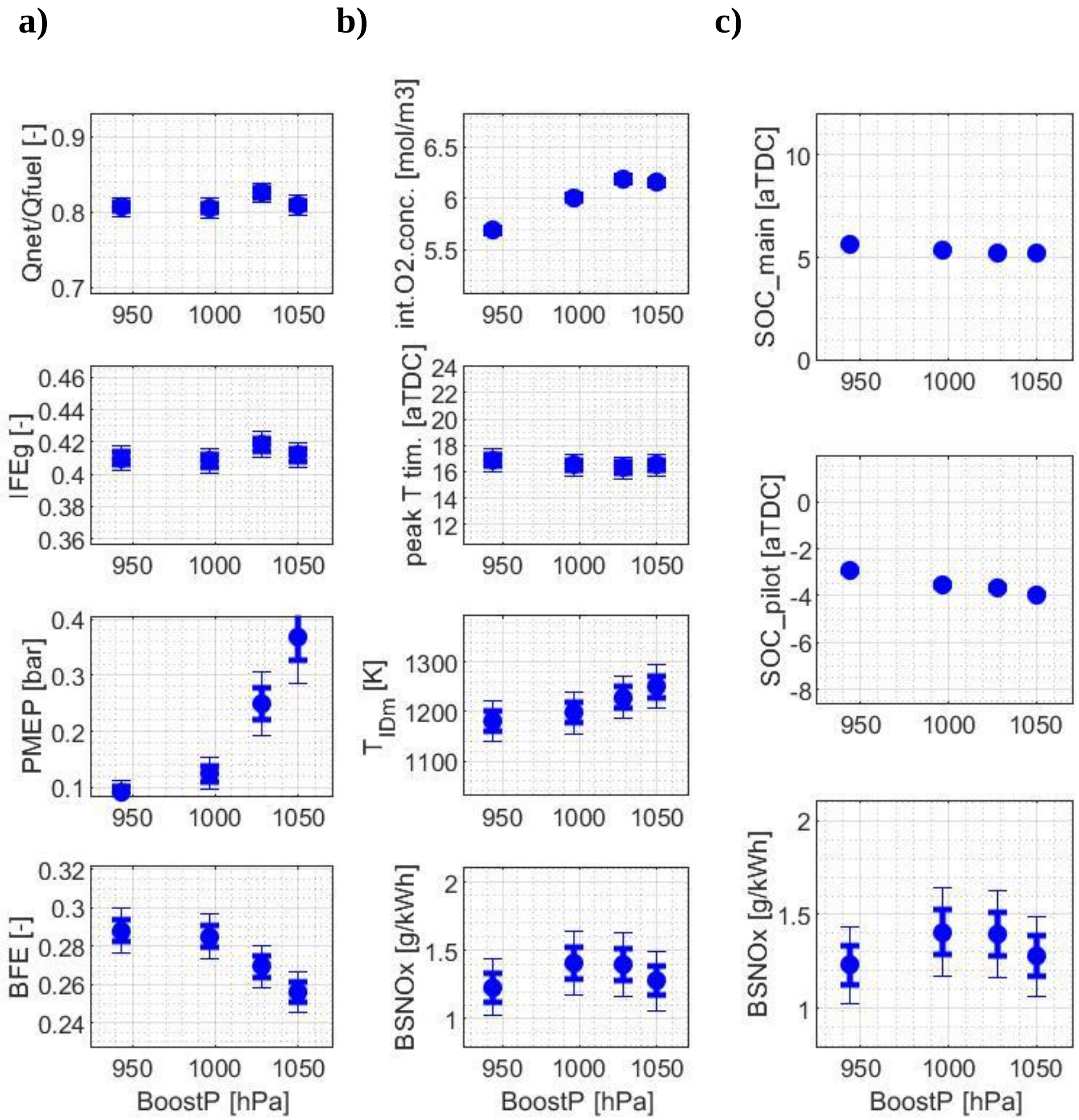

Figure 3.19. The parameters affecting a) BFE, b) and c) BSNOx during boost pressure (BP) sweep of the baseline diesel at MM2

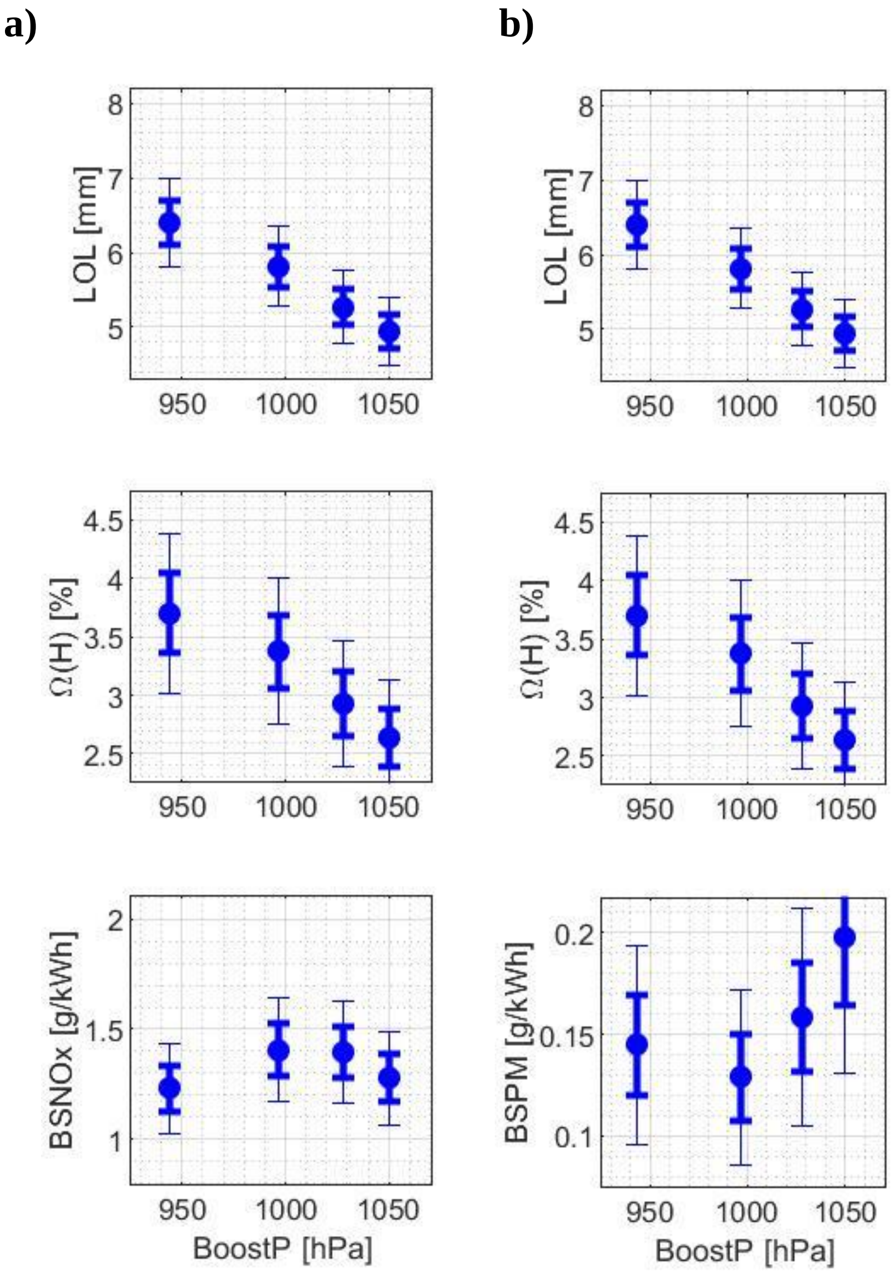

Figure 3.20. Lift-off length and the oxygen ratio at the lift-off length with the trend of a) BSNOx, and b) BSPM during boost pressure (BP) sweep of the baseline diesel at MM2

Figure 3.21a presents the impact of main injection timing (MIT) on BFE (top-left), BSNOx (middle-left), BSPM (bottom-left), CNL (top-right), BSTHC (middle-right), BSCO (bottom-right) at MM2 for the baseline diesel. Figure 3.21b presents the trend of the BFE (top-left), BSPM (middle-left), $BSCO_2$ (bottom-left), BSTHC (top-right), BSCO (middle-right) and CNL (bottom-right) by BSNOx during the MIT sweep at MM2 with the baseline fuel.

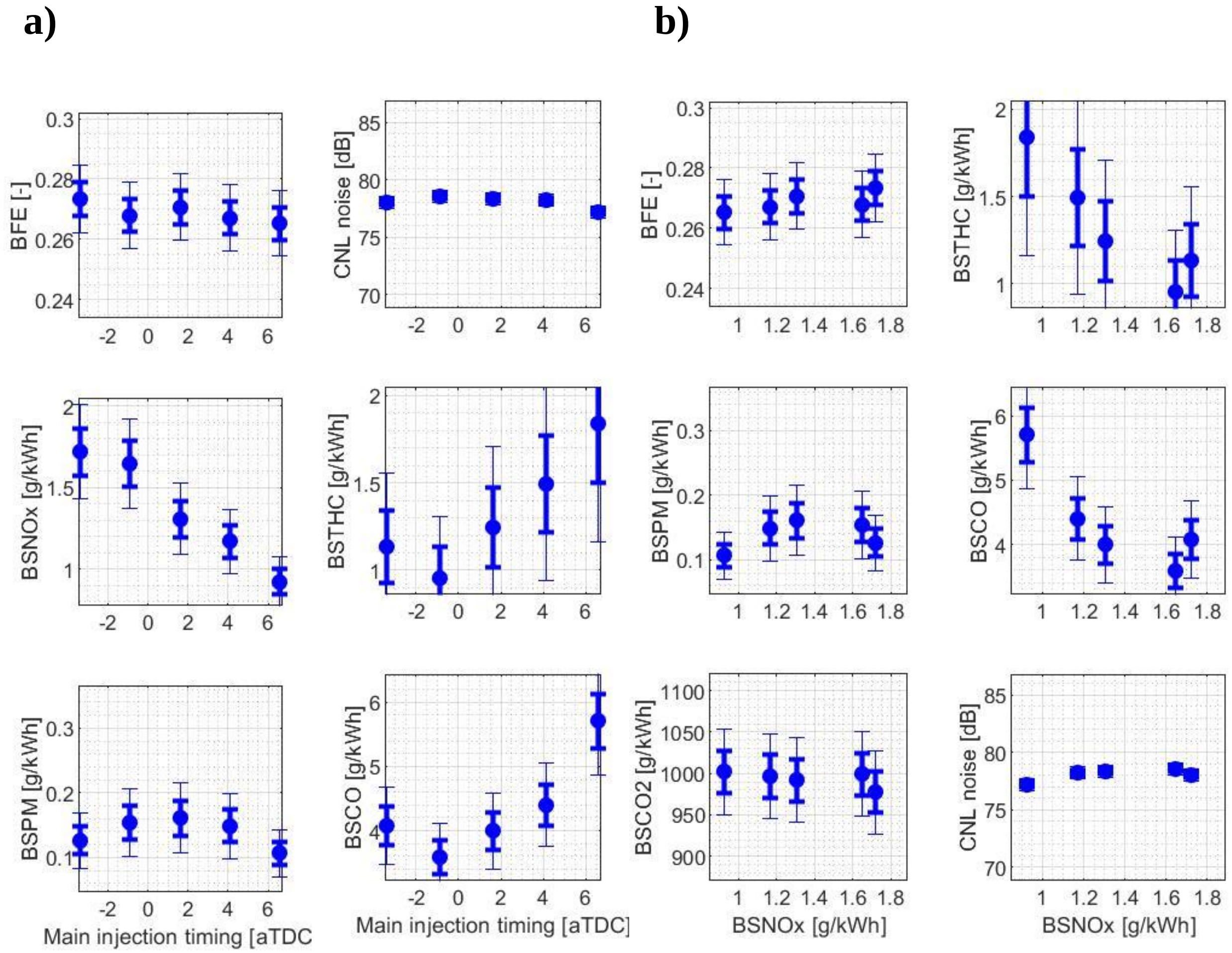

Figure 3.21. BFE, BS emissions, and CNL during main injection timing (MIT) sweep of the baseline diesel at MM2 as a function of a) MIT, b) BSNOx

First, BFE from the baseline decreases from 27.3% at 5 degrees advanced injection timing (5A) to 26.5% at 5 degrees retarded injection timing (5R). The decrease in BFE with retarded main injection timing (MIT) is mainly due to the decrease in gross indicated fuel conversion efficiency (IFEg) caused by the retarded main combustion phasing. Figure 3.22 shows the parameters affecting BFE during the baseline MIT sweep at MM2. The main combustion phasing (Figure 3.22c, top) retards with retarded MIT, and moves further from TDC. When combustion phasing is moved further from TDC, the volume change of the working fluid during the combustion process gets greater, thus making the process more like a constant-pressure process than a constant-volume process.[41] Thus, the combustion process becomes less thermally efficient with retarded MIT. At the same time, with SOC further from TDC, the "actual" compression ratio becomes smaller.[41] This also reduces thermal efficiency. As a result, IFEg (Figure 3.22a, second-to-the-top) decreases with retarding in MIT. While PMEP (Figure 3.22a, third-to-the-top) is maintained the constant during the boost pressure sweep, IFEg decreases from 42.0% at 5 degrees advanced injection timing to 40.4% at 5 degrees retarded injection timing, thus resulting in the decrease in BFE.

Second, BSNOx from the baseline monotonically decreases with retarding in main injection timing (MIT). It decreases from 1.72g/kWh at 5 degrees advanced injection timing to 0.92g/kWh at 5 degrees retarded injection timing. The main contributor for the decrease in BSNOx is the retarding in peak cylinder temperature timing.

Figures 3.22b and 3.22c show the parameters affecting BSNOx during main injection timing (MIT) sweep at MM2. While the intake charge O_2 concentration (Figure 3.22b, top) remains constant within the standard deviation of the repeat tests through the MIT sweep, charge gas temperature during the main ignition delay (i.e., T_{IDm}) generally decreases with the retarding in MIT. This decrease in charge gas temperature partially contributes to the decrease in BSNOx with retarded injection timing. However, the more dominant factor affecting BSNOx trend by MIT at MM2 is the peak cylinder temperature timing shown in Figure 3.22b (second-to-the-top). Peak cylinder temperature timing retards from 12.5aTDC at 5 degrees advanced injection timing to 21.5aTDC at 5 degrees retarded injection timing. This 9 crank angle degrees (CAs) retarding in peak cylinder temperature timing significantly limits the duration of NOx generation, thus resulting in the decrease in BSNOx.

Third, BSPM from the baseline test peaks around the default injection timing (DF) and decreases for both advanced and retarded injection timings. It is 0.127g/kWh at 5 degrees advanced injection timing (5A), 0.161g/kWh at the default injection timing (DF), and 0.107g/kWh at 5 degrees retarded injection timing (5R). This is primarily due to the change in charge gas temperature. Charge gas temperature (Figure 3.22b, third-to-the-top) peaks at 2.5 degrees advanced injection timing (2.5A), and decreases for the more advanced injection timing (5A) and retarded injection timings (i.e., DF, 2.5R, and 5R). The change in charge gas temperature affects the lift-off length (Figure 3.23a, top). Since lift-off length is inversely proportional to the temperature, the lift-off length bottoms at 2.5 degrees advanced injection timing (5.13mm), and increases at other injection timings.[36] Oxygen ratio at the lift-off length (Figure 3.23a, middle) follows the trend of lift-off length, as a consequence, it also bottoms around the 2.5 degrees advanced injection timing. Thus, BSPM peaks between the 2.5 degrees advanced injection timing (2.5A) and the default injection timing (DF). However, although the shape of BSPM generally follows the inversed characteristics of the oxygen ratio at the lift-off length, there is a moderate switch in the curve peak point: while oxygen ratio bottoms at 2.5A, BSPM peaks closer at default injection timing. This is likely due to the impact of pilot injection event.

Unlike main injection event, the pilot injection event has monotonic increase in charge gas temperature during its ignition delay when injection timing is retarded. This makes lift-off length counterpart for the pilot event shorter with retarded injection timing, which, in turn, decreases the oxygen ratio during the pilot auto-ignition. Thus, BSPM from “pilot” event will actually monotonically increase with retarding in injection timing. This small impact from pilot event can be combined with the primary impact from main event, thus resulting in BSPM peak at the default injection timing.

Lastly, the trends of other brake specific (BS) emissions and combustion noise level (CNL) during the main injection timing (MIT) sweep at MM2 will be briefly addressed here. BSTHC generally increases from 1.0g/kWh at advanced injection timings to 1.85g/kWh at 5 degrees retarded injection timing. BSCO also generally increases from 3.5g/kWh at advanced injection timings to 5.5g/kWh at retarded injection timings. Combustion noise level remains consistent during the MIT sweep at MM2 (~77.5dB).

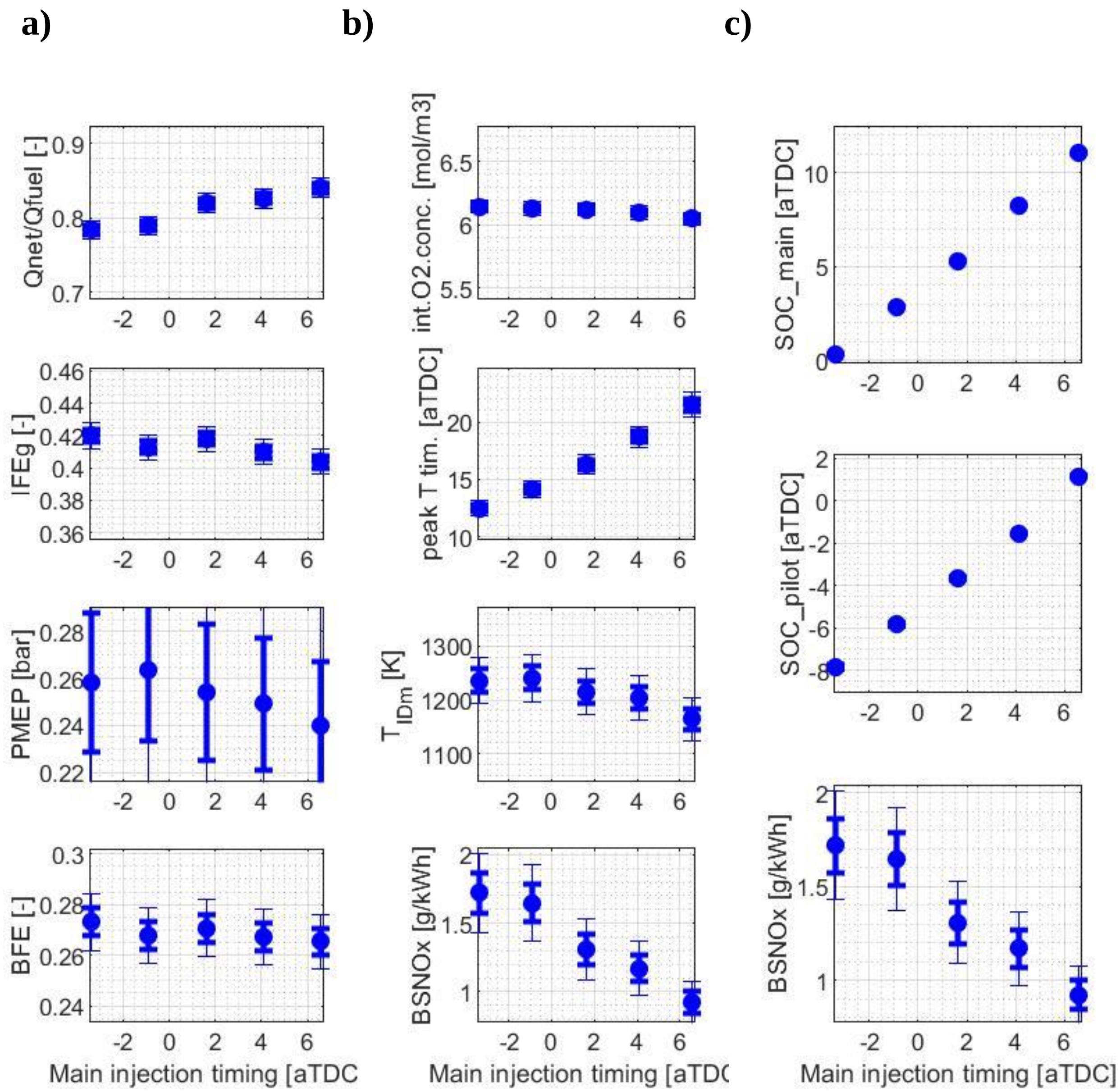

Figure 3.22. The parameters affecting a) BFE, b) and c) BSNOx during main injection timing (MIT) sweep of the baseline diesel at MM2

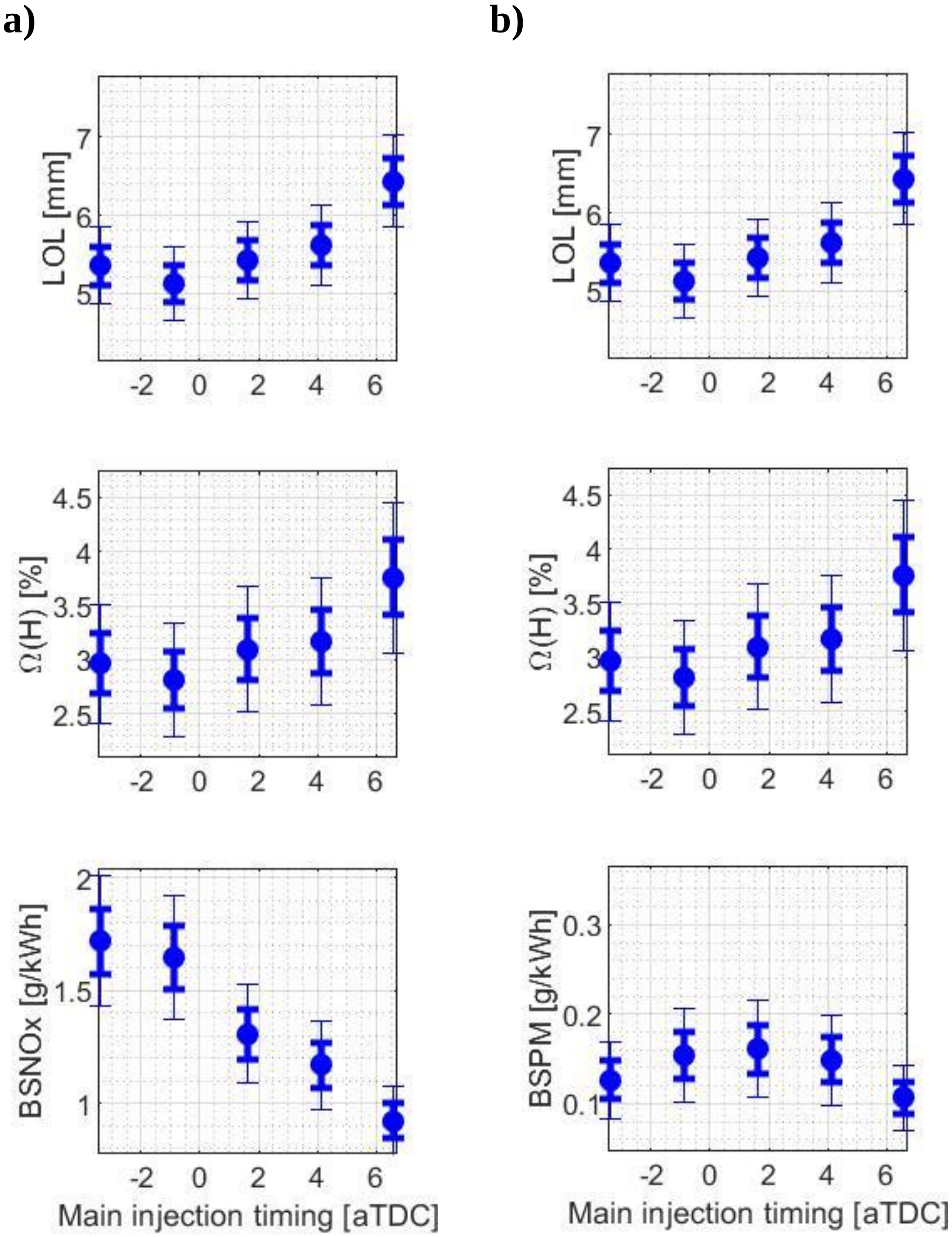

Figure 3.23. Lift-off length and oxygen ratio at the lift-off length with the trend of a) BSNOx and b) BSPM during the main injection timing (MIT) sweep of the baseline diesel at MM2

Figure 3.24a presents the impact of EGR on BFE (top-left), BSNOx (middle-left), BSPM (bottom-left), CNL (top-right), BSTHC (middle-right), BSCO (bottom-right) at MM2 for the baseline diesel. Figure 3.24b presents the trend of the BFE (top-left), BSPM (middle-left), $BSCO_2$ (bottom-left), BSTHC (top-right), BSCO (middle-right) and CNL (bottom-right) by BSNOx during the EGR sweep at MM2 with the baseline fuel.

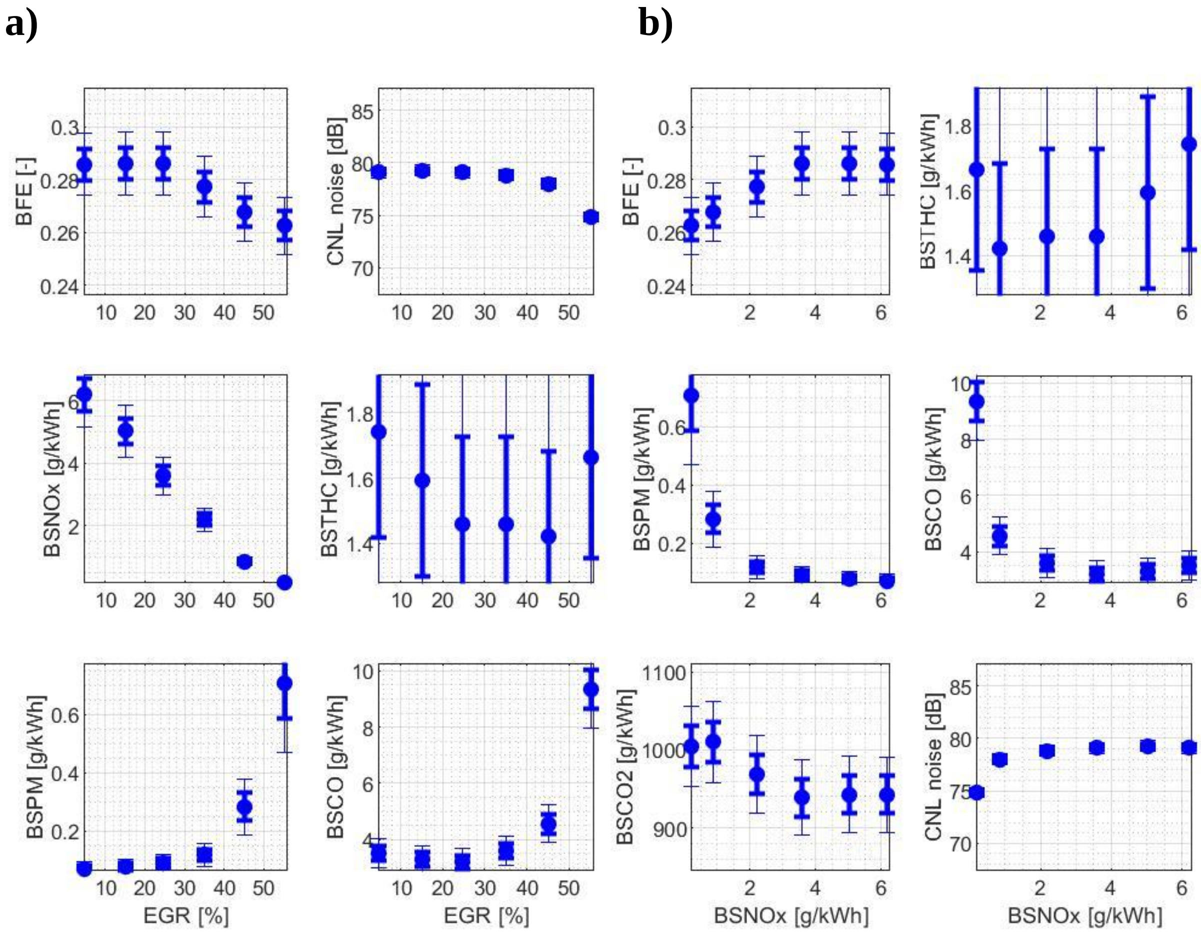

Figure 3.24. BFE, BS emissions, and CNL during EGR sweep of the baseline diesel at MM2 as a function of a) EGR rate b) BSNOx

First, BFE from the baseline decreases from 28.6% at 5% EGR to 26.3% at 55% EGR. Since IFEg (Figure 3.25a, second-to-the-top) stays consistent during most of the EGR range (except the anomaly seen at the 55% EGR condition), the decrease in BFE can be attributed to the increase in PMEP. PMEP (Figure 3.25a, third-to-the-top) increases from 0.15bar at EGR 5% to 0.33bar at EGR 55%. The 0.18bar increase in PMEP corresponds to the 12% of the BMEP (i.e., 1.5bar) at MM2. This results in the absolute 2.3% decrease in BFE, which is about relative 8% decrease in BFE from the lowest EGR rate to the highest EGR rate.

Second, BSNOx from the baseline fuel decreases from 6.19g/kWh at 5% EGR to 0.19g/kWh at 55% EGR. There are several factors contributing to this significant decrease in BSNOx emission with the increase in EGR. First, the intake O_2 concentration (Figure 3.25b, top) decreases from 8.29mol/m^3 at 5% EGR to 4.62mol/m^3 at 55% EGR. Second, the peak cylinder temperature timing (Figure 3.25b, second-to-the-top) is retarded from 15.3aTDC at 5% EGR to 17.3aTDC at 55% EGR. The retarding in the peak cylinder temperature timing is due to the longer ignition delay with the increase in EGR as shown in the top and middle plots in Figure 3.25c. The decrease in overall oxygen availability in charge gas contributes to the decrease in NOx generation “rate” while the retarding in peak cylinder temperature timing decreases the “duration” for NOx generation. Combined together, those two factors primarily decrease the BSNOx emission with the increase in EGR rate.

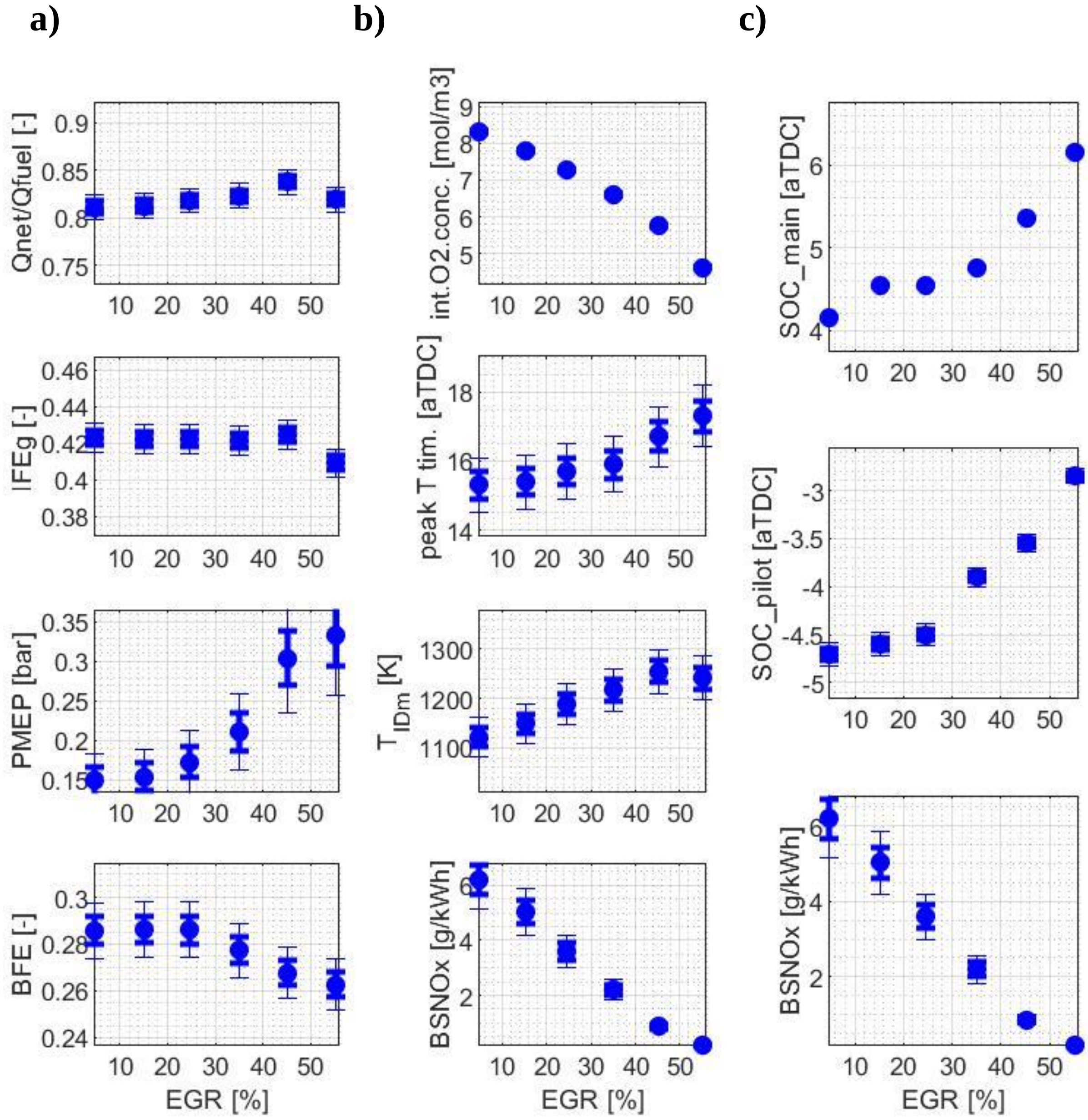

Figure 3.25. The parameters affecting a) BFE, b) and c) BSNOx during the EGR sweep of the baseline diesel at MM2

Figure 3.26 shows the lift-off length (top) and oxygen ratio at the lift-off length (middle) during the EGR sweep at MM2 with the trend of BSNOx (Figure 3.26a, bottom) and BSPM (Figure 3.26b, bottom). From Figure 3.26a, we can find the secondary cause for the BSNOx decrease with the increase in EGR rate. The lift-off length decrease in most of the range of the EGR sweep (from 5% EGR to 45% EGR) leads to the decrease in oxygen ratio at the lift-off length for the same range of EGR rate. The lack of oxygen available in the fuel-rich premixed auto-ignition zone can also contribute to the decrease in BSNOx, thus corroborating the trend of BSNOx mentioned above.

In Figure 3.26b, the lift-off length and oxygen ratio at the lift-off length are presented with the trend of BSPM. BSPM emission monotonically increases with the increase in EGR. Between 5% EGR rate to 45% EGR rate, oxygen ratio at the lift-off length decreases from 4.7% to 2.6%. This decrease in oxygen ratio was the primary cause for the decrease in BSPM. However, the increase in oxygen ratio from 45% EGR rate to 55% EGR rate does not explain the increase in BSPM emission in the same range of EGR. The increase in BSPM within this range of EGR rate can be explained by the overall charge gas O_2 concentration shown in the top plot in Figure 3.25b. It decreases from 5.75mol/m^3 to 4.62mol/m^3, and this decrease in charge gas O_2 concentration could have dominated the impact of oxygen ratio at that high EGR rate range, eventually resulting in the increase in BSPM emission for the particular EGR rate.

Lastly, the trend of other brake specific (BS) emissions and combustion noise level (CNL) during the baseline EGR sweep at MM2 will be briefly addressed here. While BSTHC emission has high measurement inaccuracy noted by the large degree of standard deviation, generally it remains within plus and minus one standard deviation ($\pm\sigma$) range at 1.6g/kWh.

BSCO increases with the increase in EGR. Combustion noise level decreases from 79.2dB at 5% EGR to 74.9dB at 55% EGR.

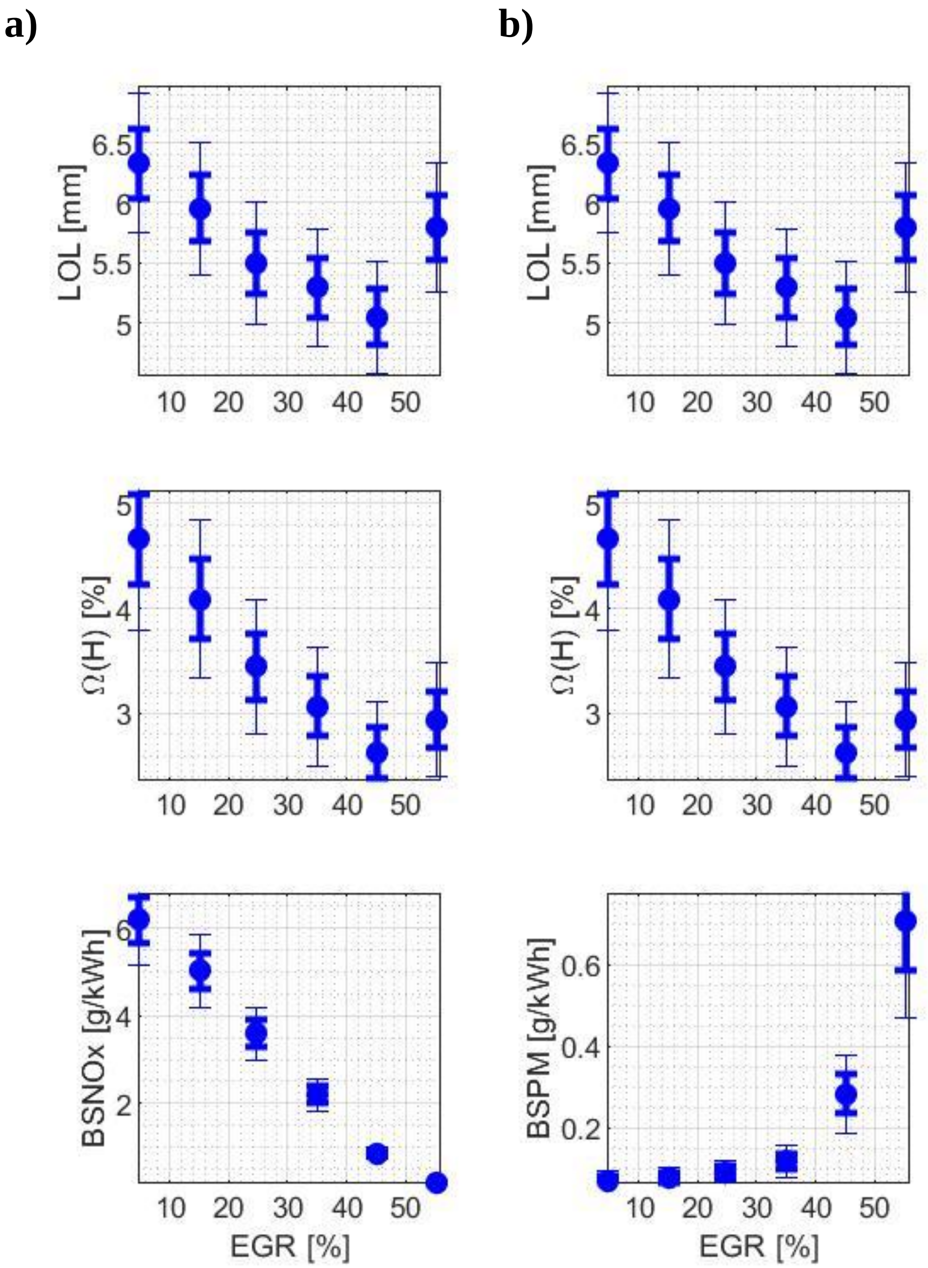

Figure 3.26. Lift-off length and oxygen ratio at the lift-off length during the EGR sweep of the baseline diesel at MM2 with the trend of a) BSNOx, b) BSPM

Figure 3.27a presents the impact of rail pressure (RP) on BFE (top-left), BSNOx (middle-left), BSPM (bottom-left), CNL (top-right), BSTHC (middle-right), BSCO (bottom-right) at MM2 for the baseline diesel. Figure 3.27b presents the trend of the BFE (top-left), BSPM (middle-left), $BSCO_2$ (bottom-left), BSTHC (top-right), BSCO (middle-right) and CNL (bottom-right) by BSNOx during the RP sweep at MM2 with the baseline fuel.

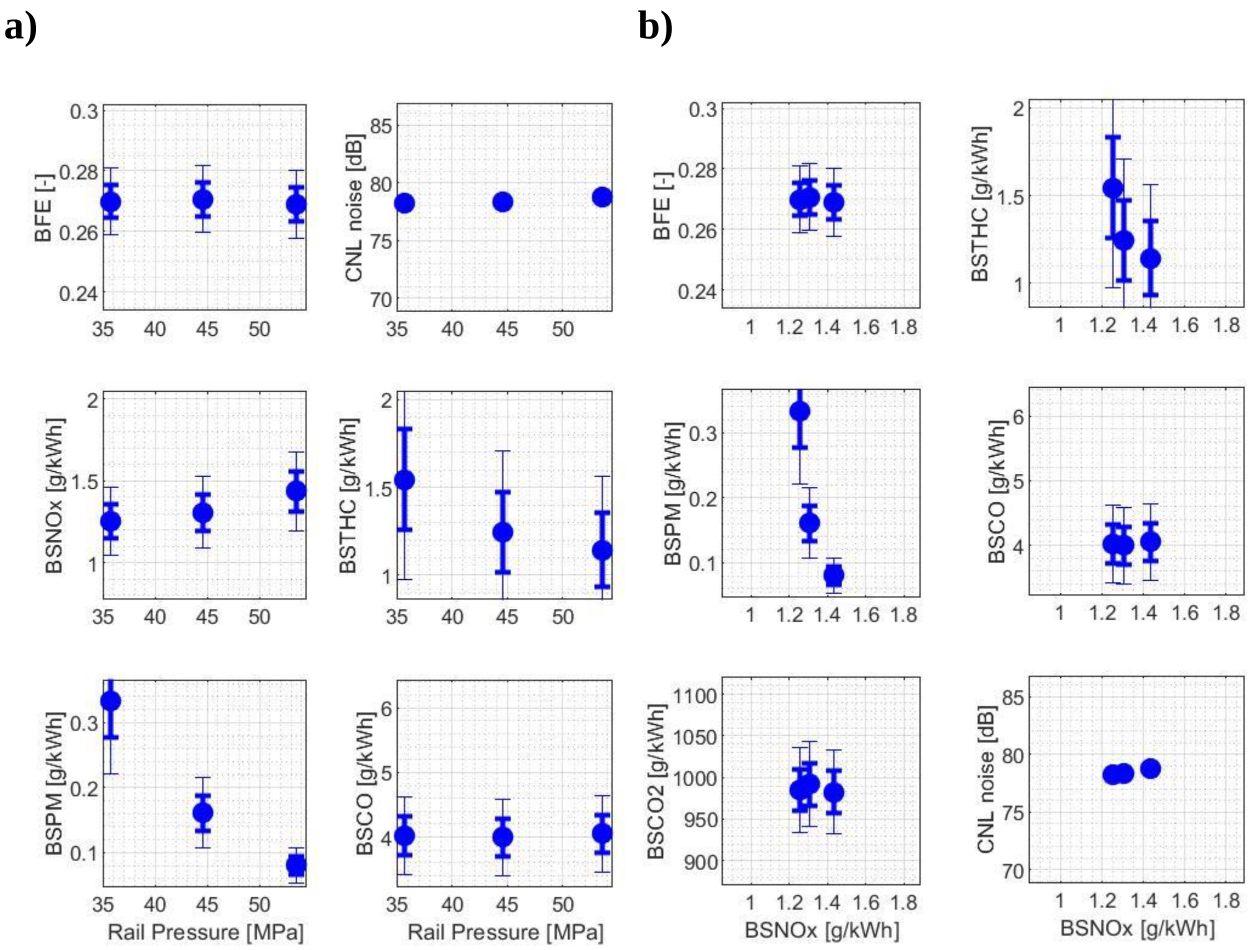

Figure 3.27. BFE, BS emissions, and CNL during the rail pressure (RP) sweep of the baseline diesel at MM2 as a function of a) RP, b) BSNOx

First, BFE remains consistent at around 27% during the rail pressure (RP) sweep at MM2. Pump mean effective pressure (PMEP) (Figure 3.28a, third-to-the-top) and gross indicated fuel conversion efficiency (IFEg) (Figure 3.28a, second-to-the-top) both remain consistent during the RP sweep.

Second, BSNOx increases from 1.25g/kWh at low rail pressure (LRP) to 1.44g/kWh at high rail pressure (HRP). This 15% increase in BSNOx from LRP to HRP is due to the advancing in combustion phasing. As shown in Figure 3.28c, both of the main and pilot start of combustion advance about 1-1.5 degrees from LRP to HRP. The advance in combustion phasing causes advance in peak cylinder temperature timing (i.e., “peak T. tim.”). The peak cylinder temperature timing (Figure 3.28b, second-to-the-top) advances from 17.9aTDC at LRP to 15.5aTDC at HRP. Eventually, this advance in peak cylinder temperature timing results in the increase in BSNOx emission with the increase in rail pressure.

Figure 3.29 shows the lift-off length (top) and oxygen ratio at the lift-off length (middle) during the rail pressure (RP) sweep at MM2 with the trend of BSNOx (Figure 3.29a, bottom) and BSPM (Figure 3.29b, bottom). Due to the increase in fuel jet velocity, the lift-off length monotonically increases with the increase in RP. The increase in lift-off length results in the increase in oxygen ratio at the lift-off length from 5.4% at LRP to 7.5% at HRP. Since the overall charge O_2 concentration (Figure 3.28b, top) is fixed during the RP sweep, the BSPM emission is greatly dominated by the trend of oxygen ratio. Therefore, the increasing oxygen ratio decreases the BSPM emission with the increase in RP.

Lastly, the trend of other brake specific (BS) emissions and combustion noise level (CNL) during the baseline rail pressure (RP) sweep at MM2 will be briefly addressed here.

BSTHC monotonically decreases from 1.55g/kWh at LRP to 1.14g/kWh at HRP. BSCO remains consistent during the RP sweep. Combustion noise level also remains the same at around 78dB.

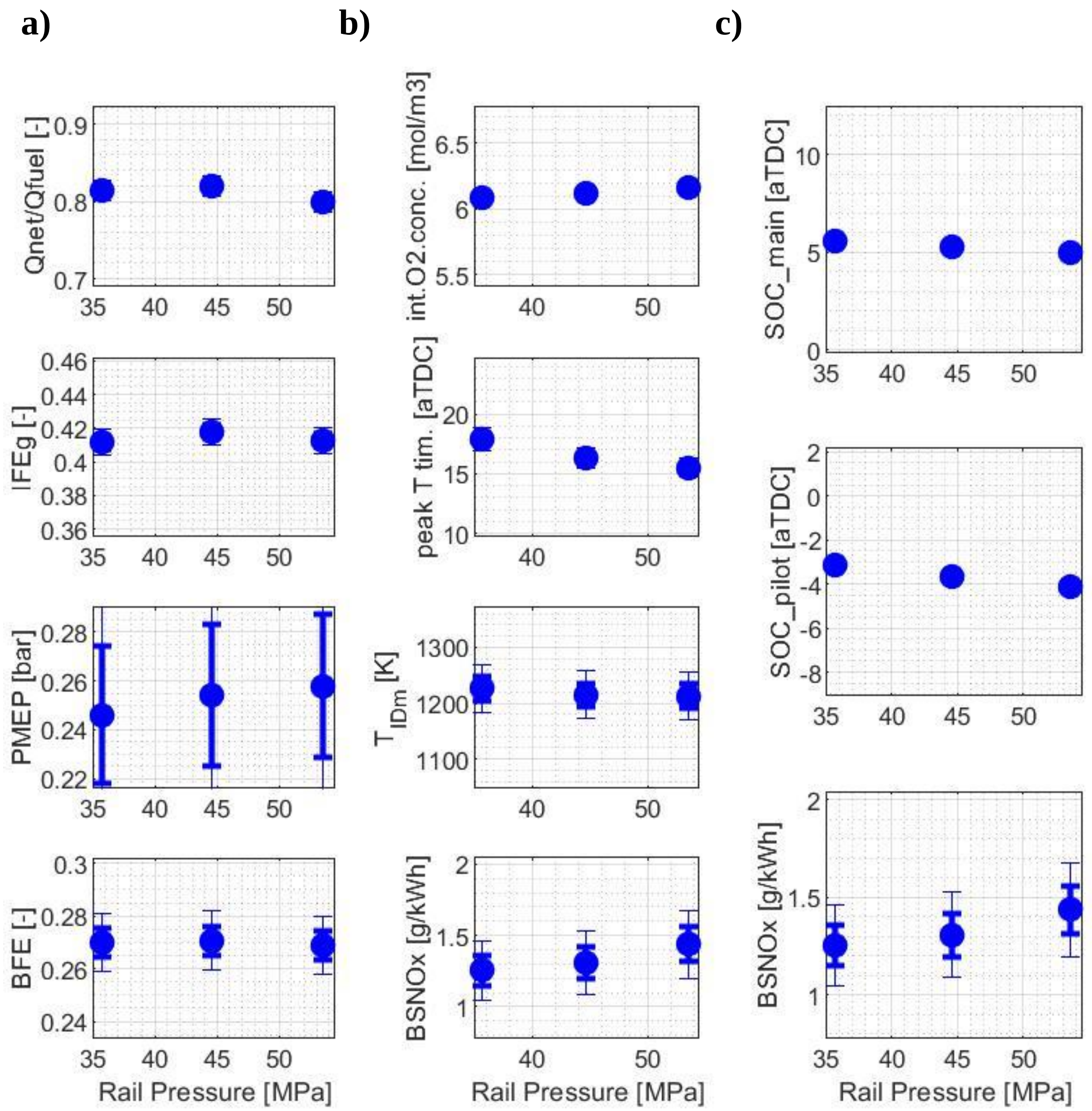

Figure 3.28. The parameters affecting a) BFE, b) and c) BSNOx during the rail pressure (RP) sweep of the baseline diesel at MM2

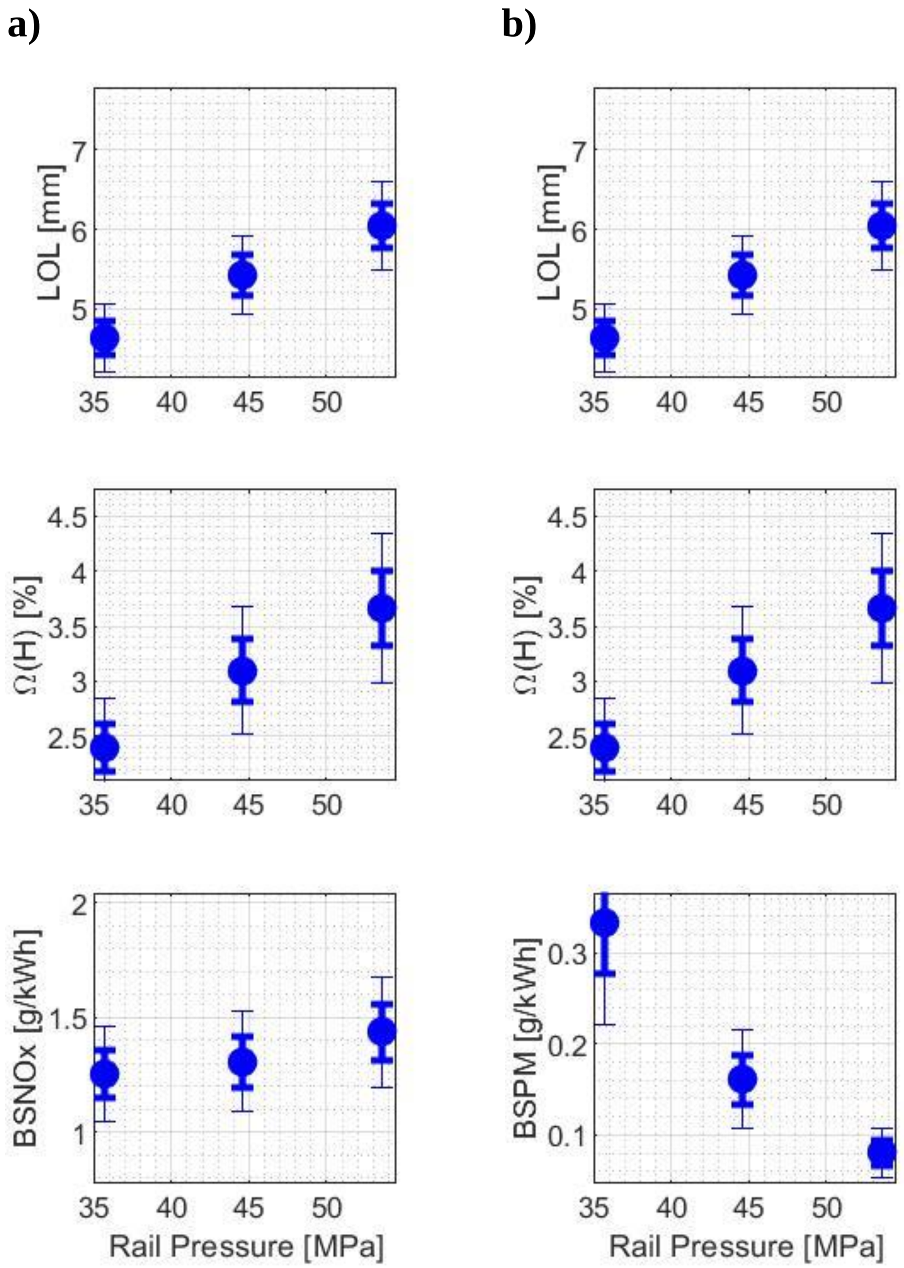

Figure 3.29. Lift-off length and oxygen ratio at the lift-off length during the rail pressure (RP) sweep of the baseline diesel at MM2 with the trend of a) BSNOx, b) BSPM

3.3.1.3 MM3

MM3 is a medium speed-medium load operating condition out of the 6 MM points. The impact of 4 input parameters (i.e., boost pressure (BP), main injection timing (MIT), EGR rate, rail pressure (RP)) on the output parameters (i.e., BFE, BS emissions, and CNL) at MM3 is observed at other mid-speed, mid-load mini-map points such as MM5 in a similar way. This is because the underlying physics for the impact of input parameters at these points is similar to each other. Furthermore, MM3 has the highest weight factor (WF) out of the 6 MM points when estimating the overall performance or emissions for the EPA FTP75 cycle. Thus, it is important to look in detail about the impact of the input parameters on the output parameters and the underlying causes for the results at MM3. The trends of output parameters at MM3 by boost pressure (BP) is first presented in this section, followed by the trends by main injection timing (MIT), EGR rate, then finally by rail pressure (RP).

Figure 3.30a presents the impact of boost pressure (BP) on BFE (top-left), BSNOx (middle-left), BSPM (bottom-left), CNL (top-right), BSTHC (middle-right), BSCO (bottom-right) at MM3 for the baseline diesel. Figure 3.30b presents the trend of the BFE (top-left), BSPM (middle-left), $BSCO_2$ (bottom-left), BSTHC (top-right), BSCO (middle-right) and CNL (bottom-right) by BSNOx during the BP sweep at MM3 with the baseline fuel.

Thick error bars indicate the plus and minus one standard deviation interval (68% confidence interval) while the thin error bars indicate the plus and minus two standard deviations interval (95% confidence interval). In case the difference between two data points is smaller than plus and minus one standard deviation, the difference is not considered to be statistically meaningful. If the difference between two data points is larger than plus and minus one standard deviation, but, smaller than plus and minus two standard deviations, the difference is considered to be statistically meaningful with low statistical confidence (less than 95%). If the difference between two data points is greater than plus and minus two standard deviations, the difference is considered to be statistically meaningful with high statistical confidence (more than 95%).

First, BFE of the baseline diesel (Figure 3.30a, top-left) decreases from 34.3% at low boost pressure (LP) to 33.6% at the default boost pressure (DP), then to 27.9% at high boost pressure (HP). The decrease in BFE with the increase in boost pressure (BP) can be attributed to the increase in pump mean effective pressure (PMEP). The change in different parameters by BP shown in Figure 3.31 can provide the more detailed explanation. The top and second to the top plot in Figure 3.31a show the "Q_{net}/Q_{fuel}" and "IFEg" during the BP sweep of the baseline at MM3, respectively. Both parameters increase with the increase in BP because the main combustion phasing gets closer to TDC with the increase in BP. The main combustion phasing closer to TDC with the increase in BP is well shown in the top plot in Figure 3.31c. When the main SOC gets closer to TDC, the combustion process becomes more like a constant-volume process than a constant-pressure process (less fuel energy is wasted on the volume expansion of the working fluid), thus making the combustion process thermally more efficient. It also results in the higher "actual" compression ratio, thus making the engine cycle thermally more efficient.[48] Thanks to this, IFEg for the baseline increases from 43.0% at LP to 43.7% at DP. However, as shown in the third to the top plot in Figure 3.31a, the increase in PMEP from LP to the higher BP is more significant. PMEP increases from 0.14bar at LP to 0.99bar at HP (i.e., 0.85bar increase), and this corresponds to about 28% of BMEP (3bar) at MM3. The increase in PMEP is more significant than the increase in IFEg, thus resulting in the decrease in BFE with the increase in BP at MM3.

Second, BSNOx of the baseline diesel (Figure 3.30a, middle-left) increases from 0.57g/kWh at LP to 0.60g/kWh at DP, then to 0.65g/kWh at MHP. However, it decreases back from MHP to HP (0.56g/kWh). This concave curve of BSNOx during the boost pressure sweep is due to the competition between the two different NOx generation mechanisms in the combustion chamber. According to the previous studies, there are two NOx generation zones in compression-ignition engines. One is the fuel-rich premixed auto-ignition zone where NOx generation is highly dependent on the local oxygen ratio around the flame stabilization zone (i.e., area nearby lift-off length).[25] The other is the diffusion flame zone where NOx is generated from the reaction of entrained fuel and air at around the stoichiometry. In the diffusion flame zone, NOx generation is dependent on the charge gas temperature, overall charge gas O_2 concentration, and the duration allowed for NOx generation.[25] Charge gas temperature during the ignition delay of the main injection event (T_{IDm}) is one of the parameters representing the overall charge gas temperature relevant for NOx generation while the peak cylinder temperature timing is a parameter to represent the duration allowed for NOx generation.[24] Depending on the engine operating conditions, the degree of the impact of each parameter on NOx generation becomes different, thus requiring a detailed look into each parameter.

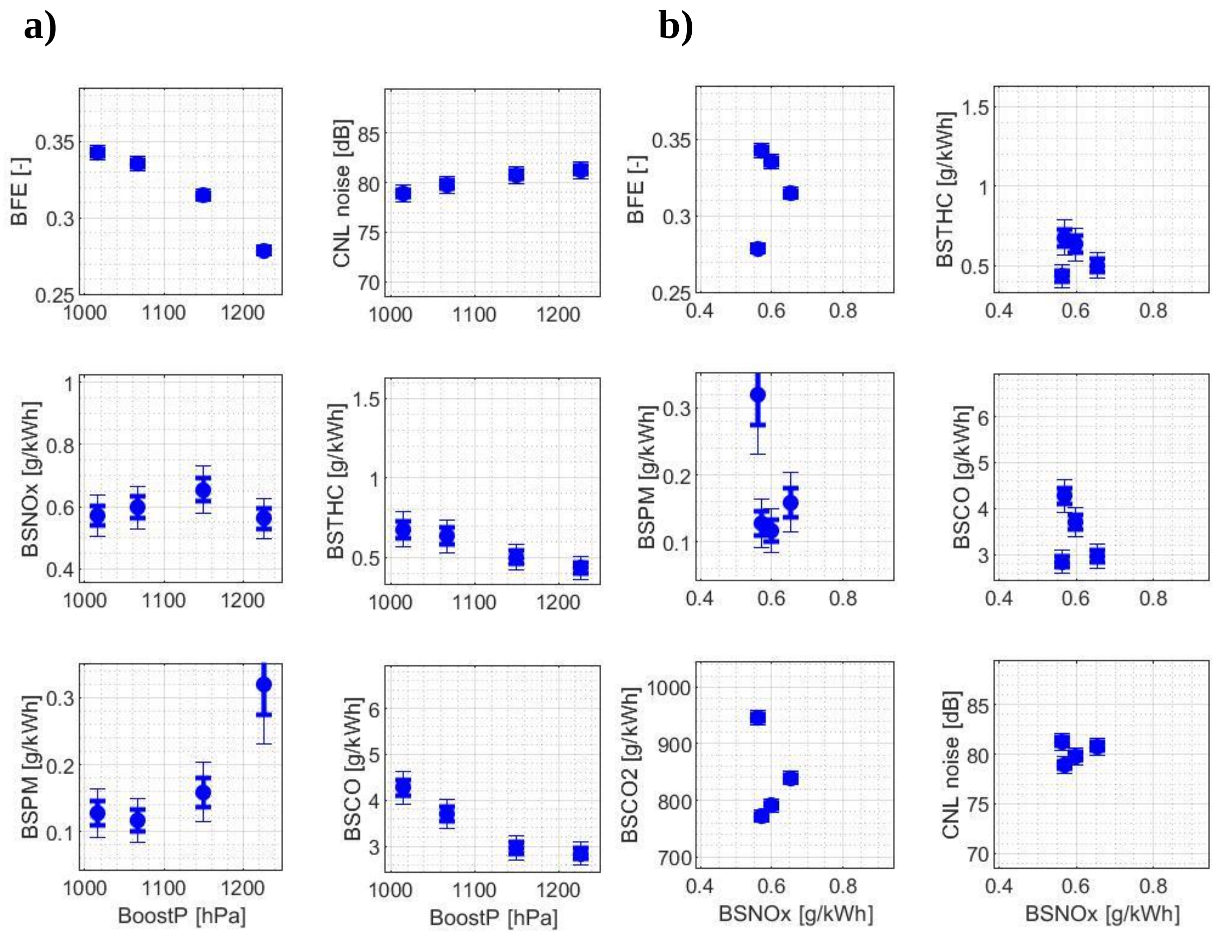

Figure 3.30. Brake fuel conversion efficiency (BFE), BS emissions and CNL of the baseline diesel during the boost pressure (BP) sweep at MM3 as a function of a) BP and b) BSNOx

In Figure 3.31b and 3.31c, the parameters relevant for BSNOx emission during the boost pressure (BP) sweep at MM3 are presented. In Figure 3.31b are intake O_2 concentration (top-plot), peak cylinder temperature timing (second to the top plot), and charge gas temperature during the ignition delay of the main injection (third to the top plot) with the trend of BSNOx at the bottom. The intake O_2 mole concentration increases with the increase in boost pressure due to the increase in overall intake charge density. At the same time, the temperature during the ignition delay of the main injection event (i.e., T_{IDm}) also increases with the increase in BP.

These two factors increase the NOx generation “rate”. Since the final NOx emission is calculated by multiplying the “rate” by the “duration” of NOx generation at high temperature, we should also look into the change in peak cylinder temperature timing. As we can see from Figure 3.31b, peak cylinder temperature timing (i.e., peak T tim.) remains similar for varying BP. Thus, it is reasonable to say that the BSNOx generation from the “diffusion flame” zone, which reflects the overall characteristics of the charge condition, would monotonically increase from LP to HP at MM3.

To describe how the NOx generation from the fuel-rich premixed auto-ignition zone would vary by boost pressure (BP), Figure 3.32a is presented. In Figure 3.32a are the lift-off length trend (top plot) and oxygen ratio at the lift-off length (middle) with the BSNOx trend. The lift-off length decreases with the increase in BP, thus making oxygen ratio at the lift-off length decrease with the increase in BP, as well. The decrease in lift-off length is mainly due to the increase in charge gas temperature and the increase in charge gas density due to BP increase.[36] The oxygen ratio at the lift-off length decreases from 5.74% at low boost pressure (LP) to 3.56% at high boost pressure (HP) (absolute 2.18% decrease), thus potentially decreasing the NOx generation from the auto-ignition zone. The decrease in NOx from the auto-ignition zone competes with the increase in NOx generation from overall charge gas condition represented by charge gas temperature and intake O_2 concentration, thus resulting in the concave trend of BSNOx by the BP change.

Third, BSPM of baseline diesel (Figure 3.30a, bottom-left) increases from 0.12g/kWh in the lower boost pressure range (LP and DP) to 0.320g/kWh at HP. BSPM emission is affected by the intake O_2 concentration (overall availability of O_2 in charge gas) and is also affected by the oxygen ratio at the lift-off length (local availability of O_2 in the fuel-rich premixed auto-ignition zone). At MM3, these two factors compete against each other. However, the degree of decrease in oxygen ratio at the lift-off length caused by the BP increase dominates the increase in intake O_2 concentration at MM3, thus resulting in the increase in BSPM with increasing BP.

Lastly, CNL (Figure 3.30a, top-right), BSTHC (Figure 3.30a, middle-right), and BSCO (Figure 3.30a, bottom-right) trends by boost pressure (BP) are explained here. Combustion noise level (CNL) for the baseline fuel increases from 78.92dB at LP to 79.81dB at DP, then to 81.24dB at HP. BSTHC for the baseline fuel decreases from 0.68g/kWh at LP to 0.63g/kWh at DP, then to 0.43g/kWh at HP. BSCO for the baseline also decreases from 4.27g/kWh at LP to 3.7g/kWh at DP, then to 2.8g/kWh at HP.

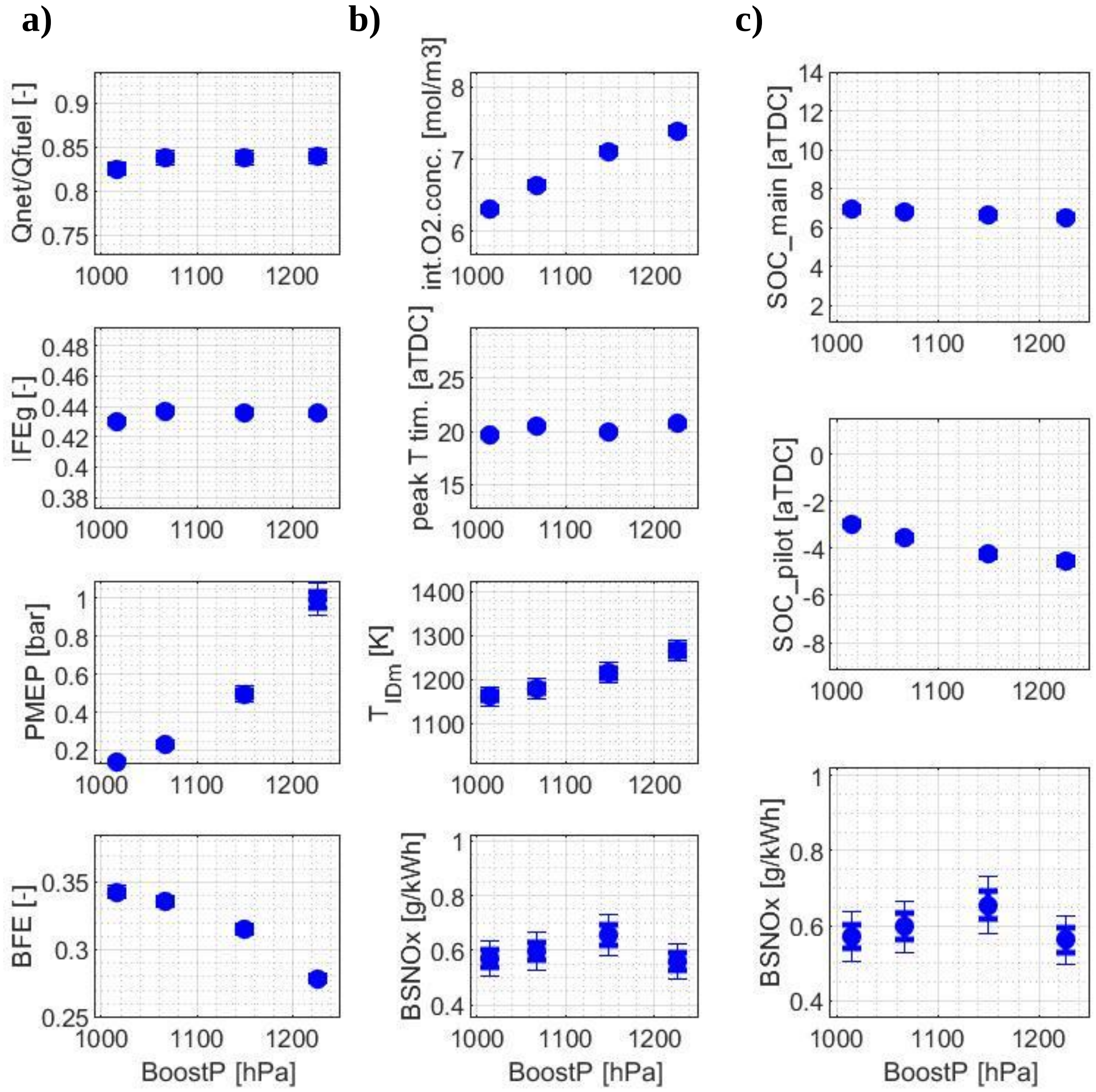

Figure 3.31. The parameters affecting a) BFE and b) and c) BSNOx during the boost pressure (BP) sweep of the baseline diesel at MM3

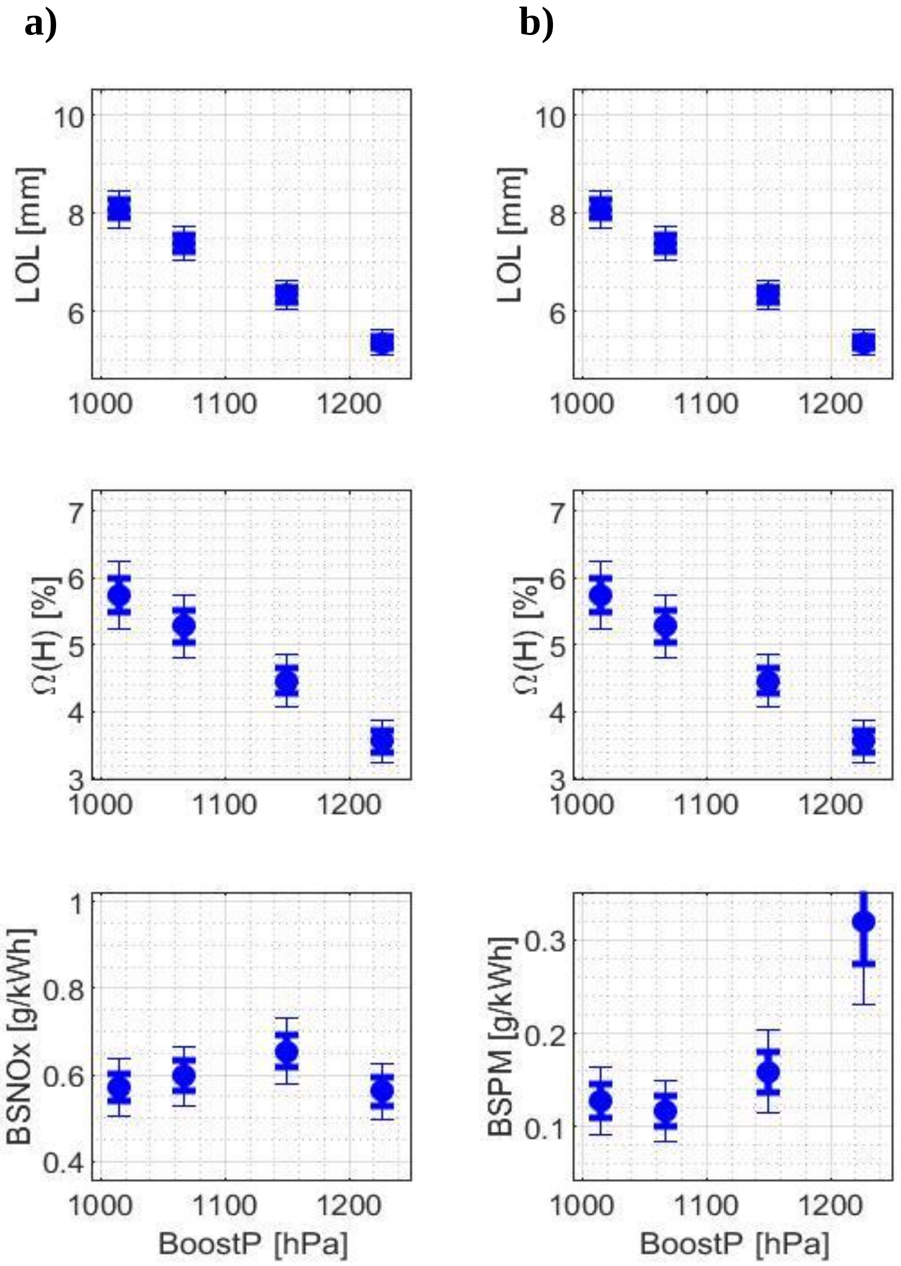

Figure 3.32. Lift-off length and oxygen ratio at the lift-off length during the boost pressure (BP) sweep of the baseline diesel at MM3 with the trend of a) BSNOx, and b) BSPM

Figure 3.33a presents the impact of main injection timing (MIT) on BFE (top-left), BSNOx (middle-left), BSPM (bottom-left), CNL (top-right), BSTHC (middle-right), BSCO (bottom-right) at MM3 for the baseline diesel. Figure 3.33b presents the trend of the BFE (top-left), BSPM (middle-left), $BSCO_2$ (bottom-left), BSTHC (top-right), BSCO (middle-right) and CNL (bottom-right) by BSNOx during the MIT sweep at MM3 with the baseline fuel.

First, BFE of the baseline decreases from 34.4% at 5 degrees advanced injection timing (5A) to 33.9% at the default timing (DF), then to 32.3% at 5 degrees retarded injection timing (5R). The decrease in BFE with the retarded injection timing is due to the worsening in IFEg caused by the less efficient combustion process and lower “actual” compression ratio with retarded combustion phasing.[48] Figure 3.34a shows different parameters that might affect the trend of BFE during the main injection timing (MIT) sweep at MM3. There is no statistically meaningful change in PMEP (Figure 3.34a, third to the top plot) with the change of MIT. However, IFEg (Figure 3.34a, second to the top plot) decreases from 44.8% at 5A to 43.7% at DF, then to 41.8% at 5R. This significant decrease in IFEg is due to the less thermally efficient combustion process caused by the retarding in main combustion phasing. Figure 3.34c shows the SOC of the main injection event (top) and pilot injection event (middle) with the BSNOx trend by MIT (bottom). We can see that the main SOC gets further from TDC with the retarding in MIT while the pilot SOC gets closer to TDC with the retarding in MIT. Thus, the main combustion event will get further from constant-volume combustion process with lower actual compression ratio which will decrease the thermal efficiency while the pilot combustion event will do the opposite. However, at MM3, the fraction of main injection quantity out of the total injection quantity is over 80%, which makes the decrease in the thermal efficiency of main combustion event dominate the increase in thermal efficiency of the pilot combustion event.

Thus, the retarding in SOI eventually decreases IFEg, which, in turn, results in the decrease in BFE.[48]

Second, BSNOx from the baseline fuel decreases from 0.91g/kWh at 5 degrees advanced injection timing (5A) to 0.64g/kWh at the default injection timing (DF), then to 0.42g/kWh at 5 degrees retarded injection timing (5R). The decrease in BSNOx with the retarding in main injection timing (MIT) is mainly due to the retarding in both pilot and main SOCs. The retarding in pilot and main SOCs retards the peak cylinder temperature timing as shown in the second to the top plot in Figure 3.34b. Although the charge gas temperature decreases about 100K over the 10 degrees of the MIT range, the decrease in the duration for NOx generation caused by the peak cylinder temperature timing retarding overwhelmed the impact of increase in charge gas temperature at MM3.

Figure 3.35a shows the lift-off length (top) and oxygen ratio at the lift-off length (middle) with the trend of BSNOx (bottom). The trend of lift-off length generally follows the opposite trend of charge gas temperature during the ignition delay (Figure 3.34b, third to the top plot). Thus, the lift-off length bottoms around 2.5 degrees advanced injection timing (2.5A) and increases for both more advanced (5A) and more retarded (DF, 2.5R, and 5R) conditions. The oxygen ratio at the lift-off length follows this trend of lift-off length by main injection timing (MIT). It increases from about 5% at 2.5A to 6.4% at 5r. Unlike during the boost pressure (BP) sweep, the degree of increase in oxygen ratio at the lift-off length was not large enough to compete with the impact of peak cylinder temperature timing change during the MIT sweep. Since the degree of variation in peak cylinder temperature timing by MIT was significant, the increase in oxygen ratio at the lift-off was simply shadowed, thus eventually resulting in the decrease in BSNOx.

Third, BSPM from the baseline diesel peaked at 0.124g/kWh between 2.5 degrees advanced injection timing (2.5A) and the default injection timing (DF) conditions and decreased for both more advanced (5A) condition and more retarded (2.5R and 5R) conditions. The trend of BSPM during the main injection timing (MIT) sweep resembles the opposite trend of oxygen ratio at the lift-off length. Since the overall intake charge O_2 concentration stays the consistent for different MITs (Figure 3.34b, top plot), it is reasonable to conclude that BSPM trend followed the opposite trend of oxygen ratio at the lift-off length.

Lastly, CNL (Figure 3.33a, top-right), BSTHC (Figure 3.33a, middle-right), and BSCO (Figure 3.33a, bottom-right) trends by main injection timing (MIT) were like the following. CNL peaked around 80dB between 2.5A and DF conditions, and decreased about 1-2dBs for other conditions. BSTHC increased from 0.46g/kWh at 5A through 0.52g/kWh at DF, then to 1.07g/kWh at 5R. BSCO also increased from 3.7g/kWh at advanced and default injection timings to 5.8g/kWh at 5R.

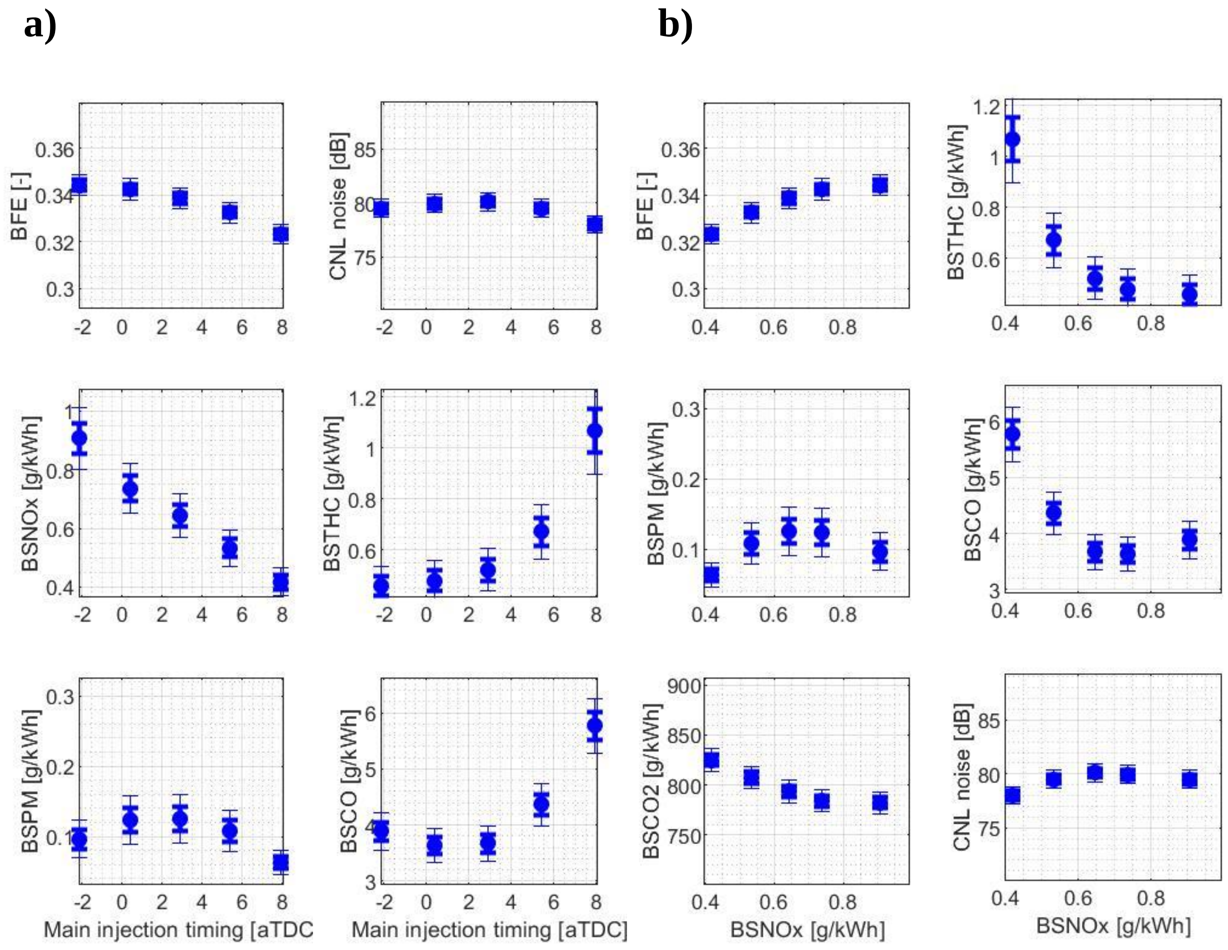

Figure 3.33. BFE, BS emissions and CNL during main injection timing (MIT) sweep of the baseline diesel at MM3 as a function of a) MIT and b) BSNOx

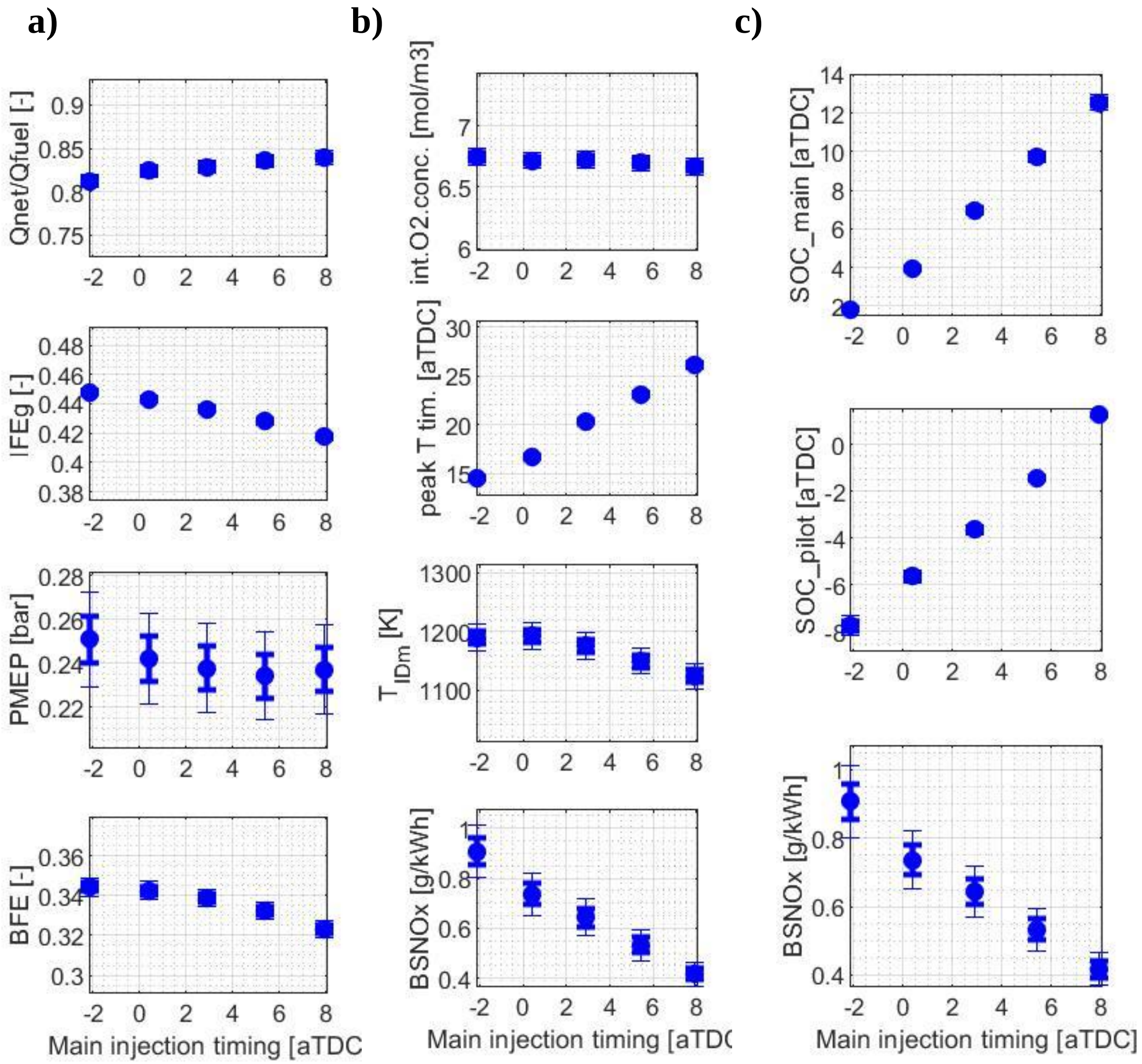

Figure 3.34. The parameters affecting a) BFE, b) and c) BSNOx during the main injection timing (MIT) sweep of the baseline diesel at MM3

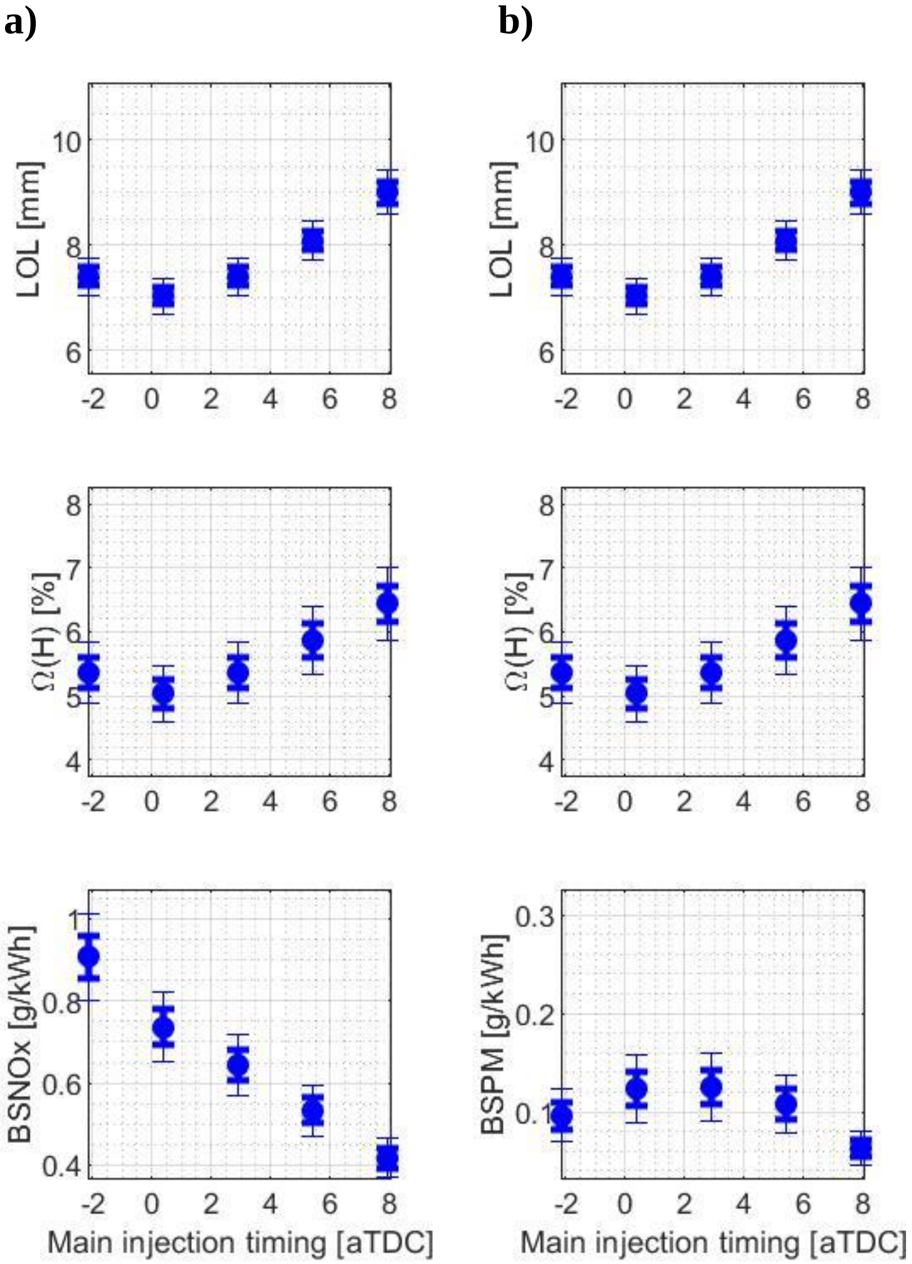

Figure 3.35. Lift-off length and oxygen ratio at the lift-off length during main injection timing (MIT) sweep of the baseline diesel at MM3 with the trend of a) BSNOx b) BSPM

Figure 3.36a presents the impact of EGR on BFE (top-left), BSNOx (middle-left), BSPM (bottom-left), CNL (top-right), BSTHC (middle-right), BSCO (bottom-right) at MM3 for the baseline diesel. Figure 3.36b presents the trend of the BFE (top-left), BSPM (middle-left), $BSCO_2$ (bottom-left), BSTHC (top-right), BSCO (middle-right) and CNL (bottom-right) by BSNOx during the EGR sweep at MM3 with the baseline fuel.

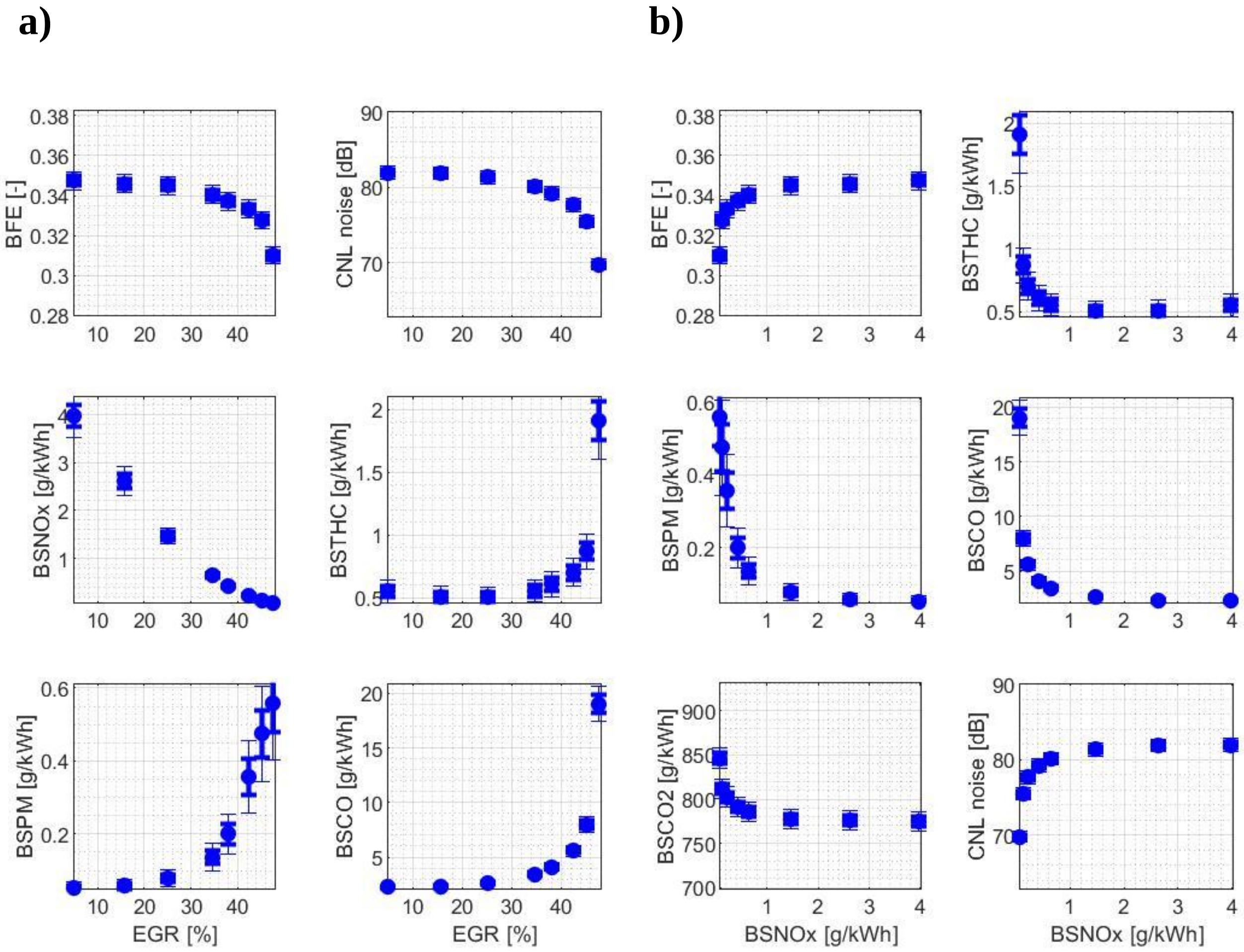

Figure 3.36. BFE, BS emissions, and CNL during EGR sweep of the baseline diesel at MM3 as a function of a) EGR rate, b) BSNOx

First, BFE from the baseline fuel decreases from 34.8% at EGR5% to 34.0% at the default EGR setting (EGR34%), then to 31.0% at EGR47%. The decrease in BFE with increasing EGR rate is mainly due to the increase in PMEP caused by the worsened 2nd law efficiency of the turbine with low mass flow rate of the exhaust gas.[49] Also, the increase in EGR causes retarding in main SOC, thus resulting in less thermally efficient combustion process and lower actual compression ratio worsening the IFEg. Figure 3.37a presents the parameters that might affect BFE during the EGR sweep at MM3. Gross indicated fuel conversion efficiency (IFEg, second to the top plot) decreases from 43.9% at EGR5% to 43.8% at the default EGR settings (EGR34%), then to 41.1% at EGR47% due to the retarded main SOC shown in Figure 3.37c top plot. Pump mean effective pressure (PMEP, Figure 3.37a, third to the top plot) increases from 0.2bar at EGR5% to 0.38bar at EGR37%. These two factors have decreased the BFE with increasing EGR rate at MM3.

Second, BSNOx from the baseline diesel fuel decreased from 3.97g/kWh at EGR5% to 0.65g/kWh at the default EGR settings (EGR34%), then to 0.06g/kWh at EGR47%. The decrease in BSNOx with increasing EGR rate is a well-known effect of the EGR reported in previous publications.[45] When EGR is increased, intake O_2 concentration decreases as shown in Figure 3.37b top plot. Due to the decrease in intake O_2 concentration, the ignition delay for main combustion event gets longer, thus resulting in the retarded main SOC (Figure 3.37c top plot). This retarding in main SOC causes retarding in peak cylinder temperature timing as shown in Figure 3.37b second to the top plot. The degree of retarding in peak cylinder temperature timing between the EGR5% and EGR47% condition is as significant as 7 crank angle degrees (CAs). The significant retarding in peak cylinder temperature timing allows shorter duration for NOx generation. Although there is some increase in charge gas temperature (Figure 3.37b, third to the top plot) from the lower EGR range to higher EGR range, the degree of increase is not enough to overwhelm the retarding in peak cylinder temperature timing.

Figure 3.38a shows the lift-off length (top) and the oxygen ratio at the lift-off length (middle) during the EGR sweep of the baseline fuel with the trend of BSNOx (bottom). Despite the increase in oxygen ratio at the lift-off length at the higher edge of the EGR conditions (EGR40 – 47%), the impact of the increase was overshadowed by the retarding in peak cylinder temperature timing, thus resulting in the decrease in BSNOx with the increase in EGR rate.

Third, BSPM from the baseline diesel increased from 0.053g/kWh at EGR5% to 0.136g/kWh at the default EGR settings (EGR34%), then to 0.557g/kWh at EGR47%. The increase in BSPM during the EGR sweep at MM3 is largely driven by the decrease in intake charge O_2 concentration. Although the oxygen ratio at the lift-off length showed some increase from EGR 40% to EGR 47% range, the degree of the decrease in intake O_2 concentration was more significant, thus resulting in the monotonic increase in BSPM at MM3 during the EGR sweep.

Lastly, CNL (Figure 3.36a, top-right), BSTHC (Figure 3.36a, middle-right), and BSCO (Figure 3.36a, bottom-right) trends are presented. Combustion noise level (CNL) decreased from 81.89dB at EGR5% to 80.09dB at the default EGR settings (EGR34%), then to 69.75dB at EGR 47%. BSTHC monotonically increased from 0.55g/kWh at EGR5% to 1.91g/kWh at EGR47%, and BSCO also monotonically increased from 2.24g/kWh at EGR5% to 19.03g/kWh at EGR47%.

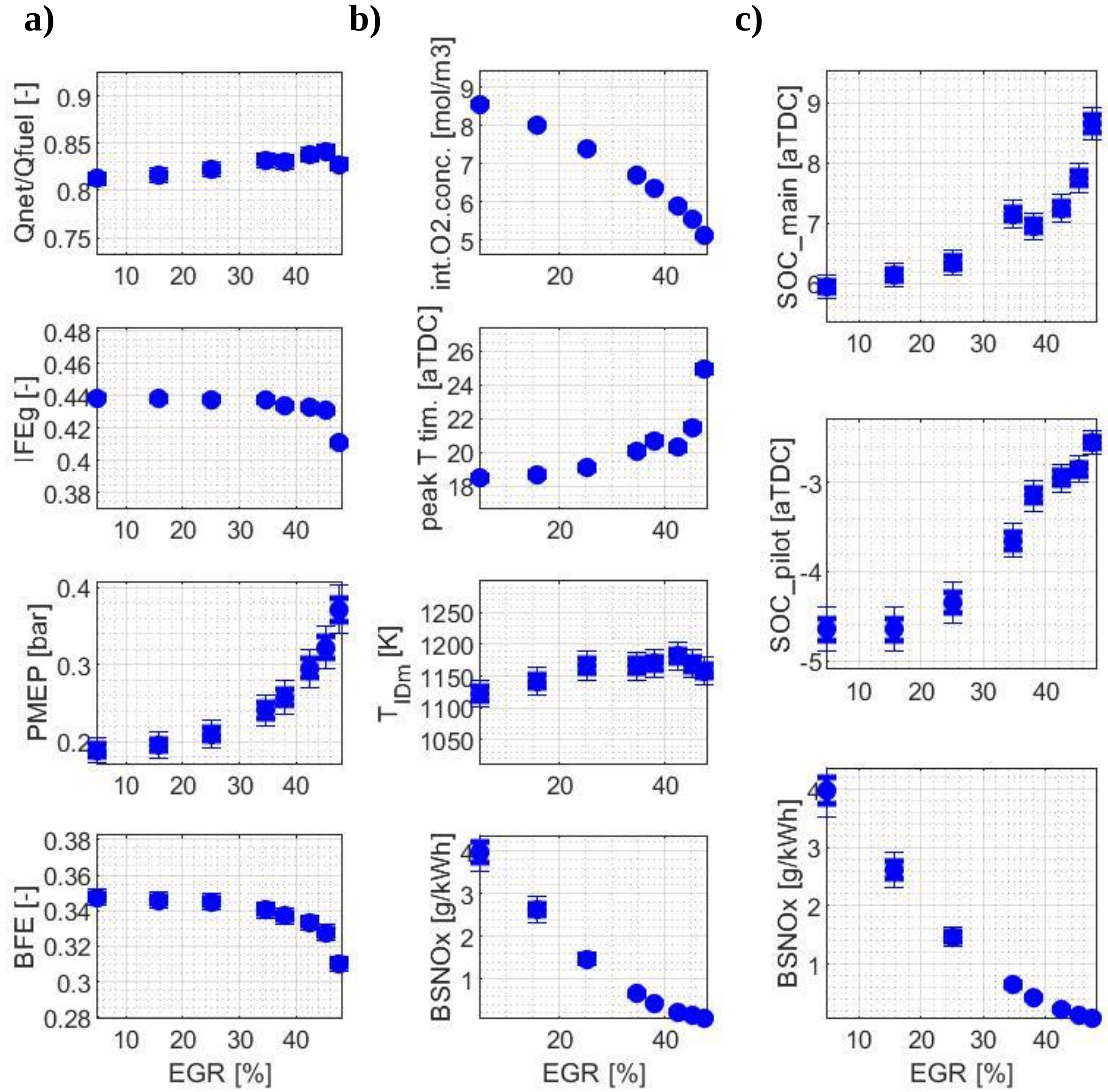

Figure 3.37. The parameters affecting a) BFE, b) and c) BSNOx during EGR sweep of the diesel baseline at MM3.

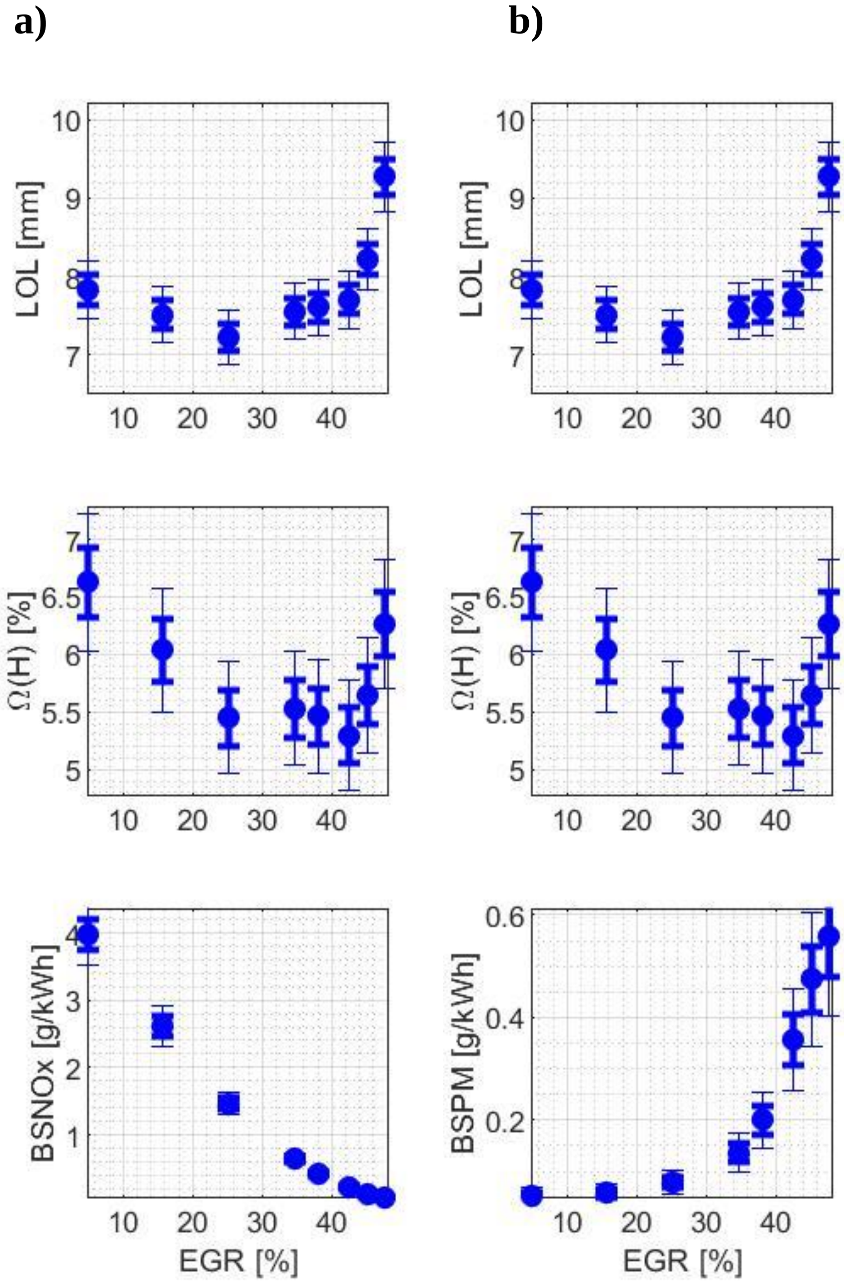

Figure 3.38. Lift-off length and oxygen ratio at the lift-off length during EGR sweep of the diesel baseline at MM3 with the trend of a) BSNOx and b) BSPM

Figure 3.39a presents the impact of rail pressure (RP) on BFE (top-left), BSNOx (middle-left), BSPM (bottom-left), CNL (top-right), BSTHC (middle-right), BSCO (bottom-right) at MM3 for the baseline diesel. Figure 3.39b presents the trend of the BFE (top-left), BSPM (middle-left), $BSCO_2$ (bottom-left), BSTHC (top-right), BSCO (middle-right) and CNL (bottom-right) by BSNOx during the RP sweep at MM3 with the baseline fuel.

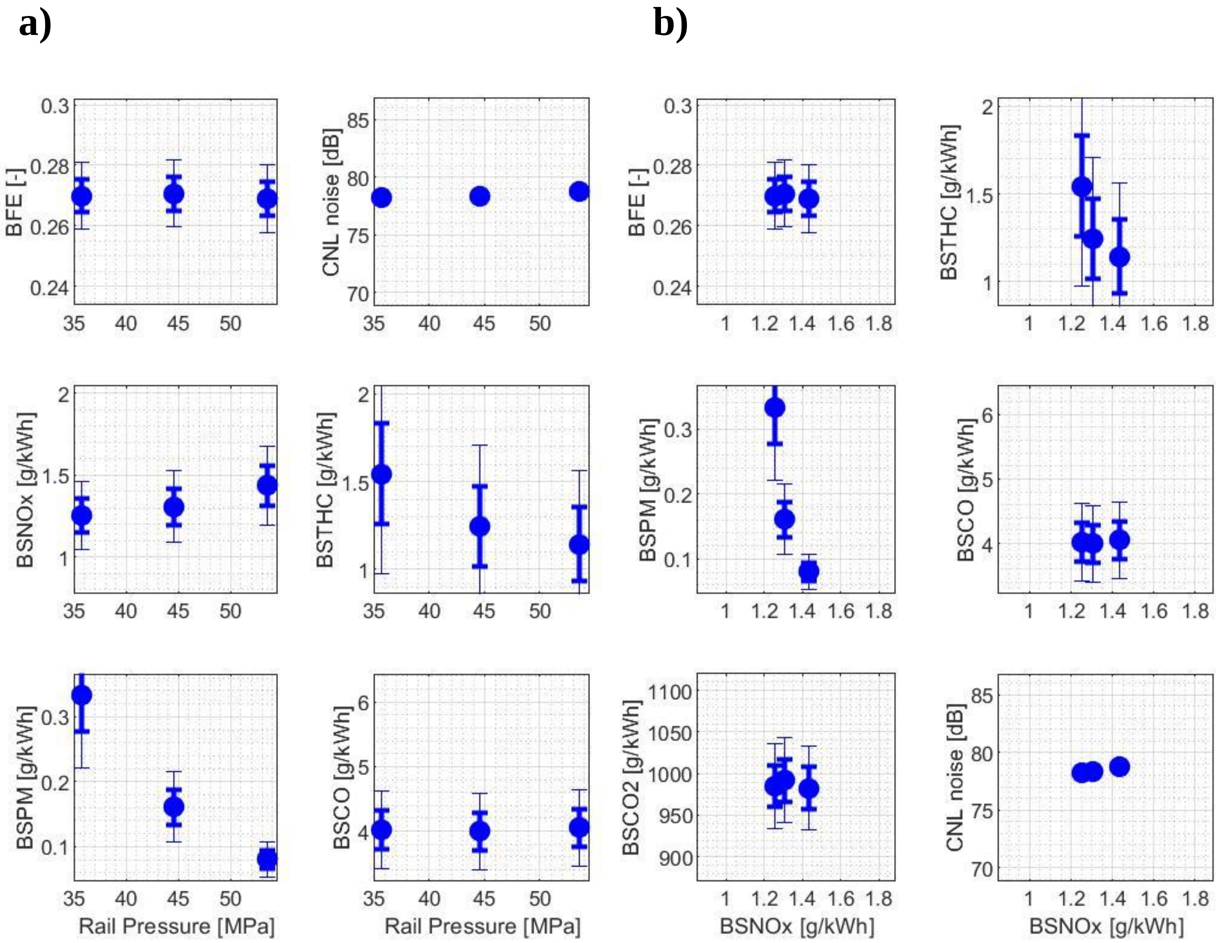

Figure 3.39. BFE, BS emissions, and CNL during rail pressure (RP) sweep of the diesel baseline at MM3 as a function of a) RP and b) BSNOx

First, BFE of the baseline diesel increased from 33.6% at low rail pressure (LRP) to 33.9% at the default rail pressure (DRP), then to 34.1% at high rail pressure (HRP). The increase in BFE with increasing rail pressure (RP) is due to the advance in main SOC caused by the improved atomization of the fuel droplets. Figure 3.40 presents different parameters that can affect BFE during the RP sweep at MM3. Figure 3.40c top plot presents the main SOC during the rail pressure sweep. We can see that the main SOC gets advanced by about 1CA from LRP to HRP. The advance in main SOC results in the advance in peak cylinder temperature timing as shown in Figure 3.40b second to the top plot. We can see that the improved atomization of the fuel advanced the peak cylinder temperature timing even further than it did for the main SOC. The peak cylinder temperature timing is about 4CAs advanced from LRP to HRP. The advance in peak cylinder temperature timing indicates the advance in burn fraction angles, which, in turn, improves the IFEg. Gross indicated fuel conversion efficiency (IFEg, Figure 3.40a- second to the top) increases from 43.2% at LRP to 43.7% at DRP, then to 44.0% at HRP, thus resulting in the increase in BFE with increasing rail pressure at MM3.

Second, BSNOx from the baseline increases from 0.59g/kWh at low rail pressure (LRP) to 0.64g/kWh at the default rail pressure (DRP), then to 0.66g/kWh at high rail pressure (HRP). The increase in BSNOx with the increase in rail pressure (RP) is mainly due to the advance in peak cylinder temperature timing mentioned earlier. It is also due to the increase in oxygen ratio at the lift-off length caused by the increase in fuel jet velocity. When the rail pressure (RP) is increased, the pressure gradient between the fuel injector and the charge gas (ΔP_{inj}) becomes greater, thus making the fuel jet velocity faster. Since the lift-off length linearly correlates with the fuel jet velocity, the increase in rail pressure causes the increase in lift-off length and oxygen ratio at the lift-off length.[36] Figure 3.41a shows the lift-off length (top) and oxygen ratio at the lift-off length (middle) during the rail pressure (RP) sweep of the baseline diesel at MM3 with the trend of BSNOx (bottom). The oxygen ratio at the lift-off length increases about absolute 2% from LRP to HRP, which could have contributed to the increase in BSNOx.

Third, BSPM emission from the baseline diesel decreases from 0.29g/kWh at LRP to 0.125g/kWh at DRP, then to 0.061g/kWh at HRP. This significant decrease in BSPM with increasing rail pressure (RP) is the well-known impact of rail pressure reported in other studies.[50] While the intake O_2 concentration remained the same for different RP conditions (Figure 40b, top), the oxygen ratio at the lift-off length increased by absolute 2% from LRP to HRP. The increase in oxygen ratio at the lift-off length allowed more oxygen in the fuel-rich premixed auto-ignition zone, thus resulting in reduced BSPM emissions at higher RP.

Lastly, CNL (Figure 39a, top-right), BSTHC (Figure 39a, middle-right), and BSCO (Figure 39a, bottom-right) trends by rail pressure (RP) are presented. Combustion noise level (CNL) increases from 79.47dB at LRP to 80.11dB at DRP, then to 80.98dB at HRP. BSTHC decreased from 0.66g/kWh at LRP to 0.52g/kWh at HRP while BSCO increased from 3.37g/kWh at LRP to 4.09g/kWh at HRP.

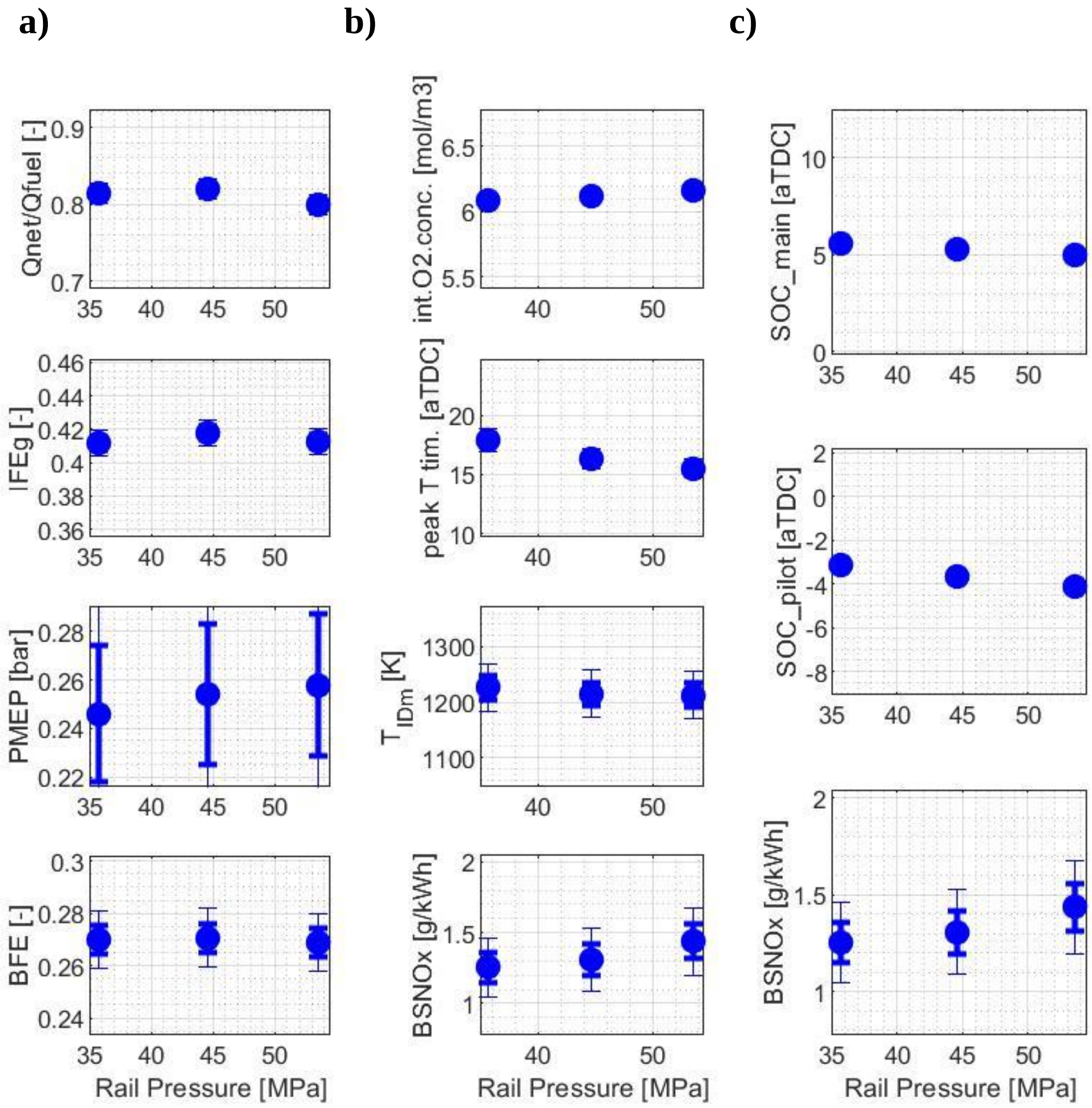

Figure 3.40. The parameters affecting a) BFE, b) and c) BSNOx during rail pressure (RP) sweep of the baseline diesel at MM3

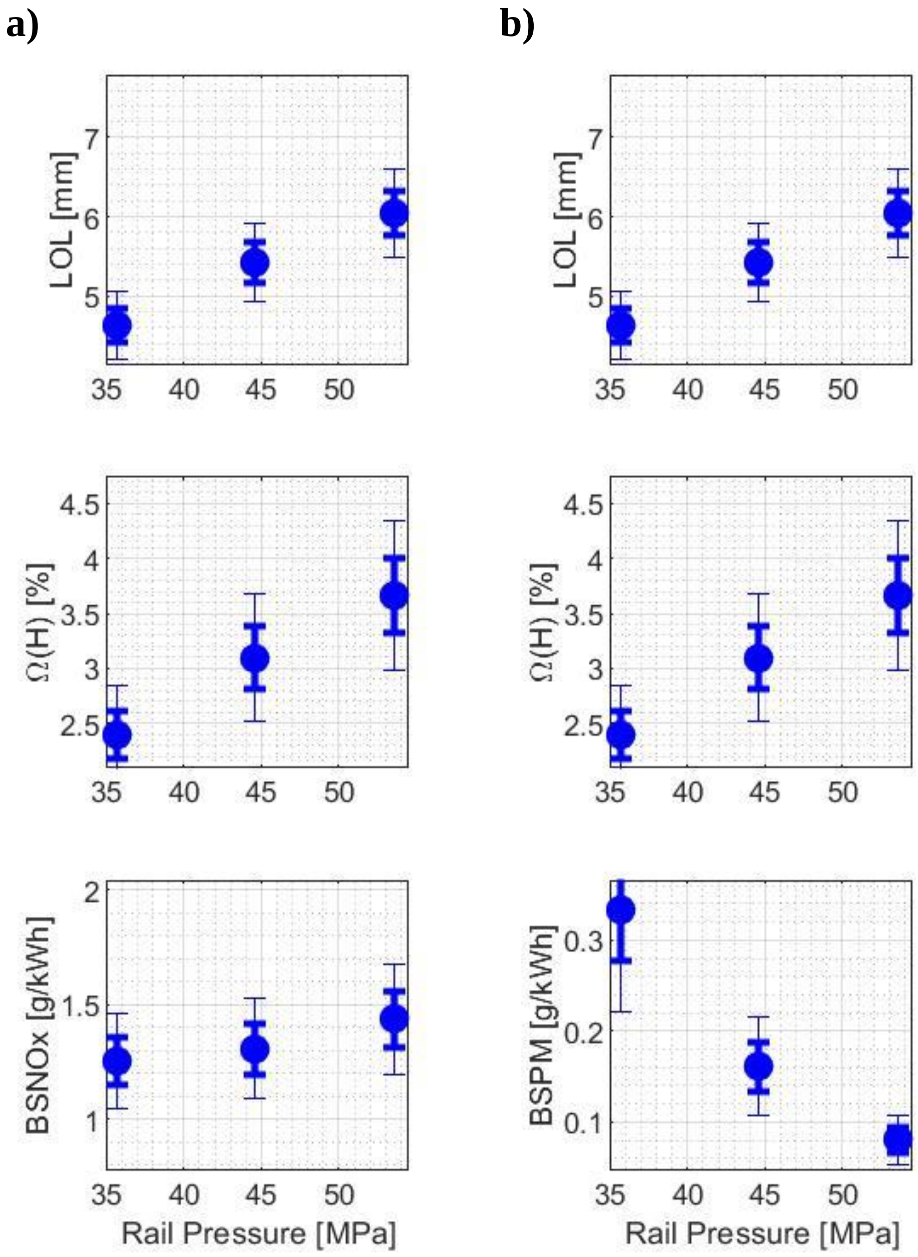

Figure 3.41. Lift-off length and oxygen ratio at the lift-off length during rail pressure (RP) sweep of the baseline diesel at MM3 with the trend of a) BSNOx and b) BSPM

3.3.1.4 MM4

MM4 is a mid-speed, high-load point out of the 6 MM points. The impact of 4 input parameters (i.e., boost pressure (BP), main injection timing (MIT), EGR rate, rail pressure (RP)) on the output results of the primary interest (i.e., BFE, BSNOx, BSPM) at MM4 was very similar to what was observed at MM3. There were only several different trends as compared to MM3: i) the trend of BFE by BP; ii) the trend of BSPM by BP; and iii) the trend of BSPM by MIT. Thus, at MM4, the impact of 4 input parameters on different output results will be shown briefly, and the discussion will be focused on the 3 unique trends observed at MM4.

Figure 3.42a presents the impact of boost pressure (BP) on BFE (top-left), BSNOx (middle-left), BSPM (bottom-left), CNL (top-right), BSTHC (middle-right), BSCO (bottom-right) at MM4 for the baseline diesel. Figure 3.42b presents the trend of the BFE (top-left), BSPM (middle-left), $BSCO_2$ (bottom-left), BSTHC (top-right), BSCO (middle-right) and CNL (bottom-right) by BSNOx during the BP sweep at MM4 with the baseline fuel.

Impact of boost pressure (BP) on all of the primary output parameters of interest was the same as MM3 with two exceptions: i) BFE did not monotonically decrease from low boost pressure (LP) to high boost pressure (HP). Instead, BFE peaked at the default boost pressure (DP), and decreased for both lower BP and higher BP; and ii) BSPM significantly decreased with increasing BP.

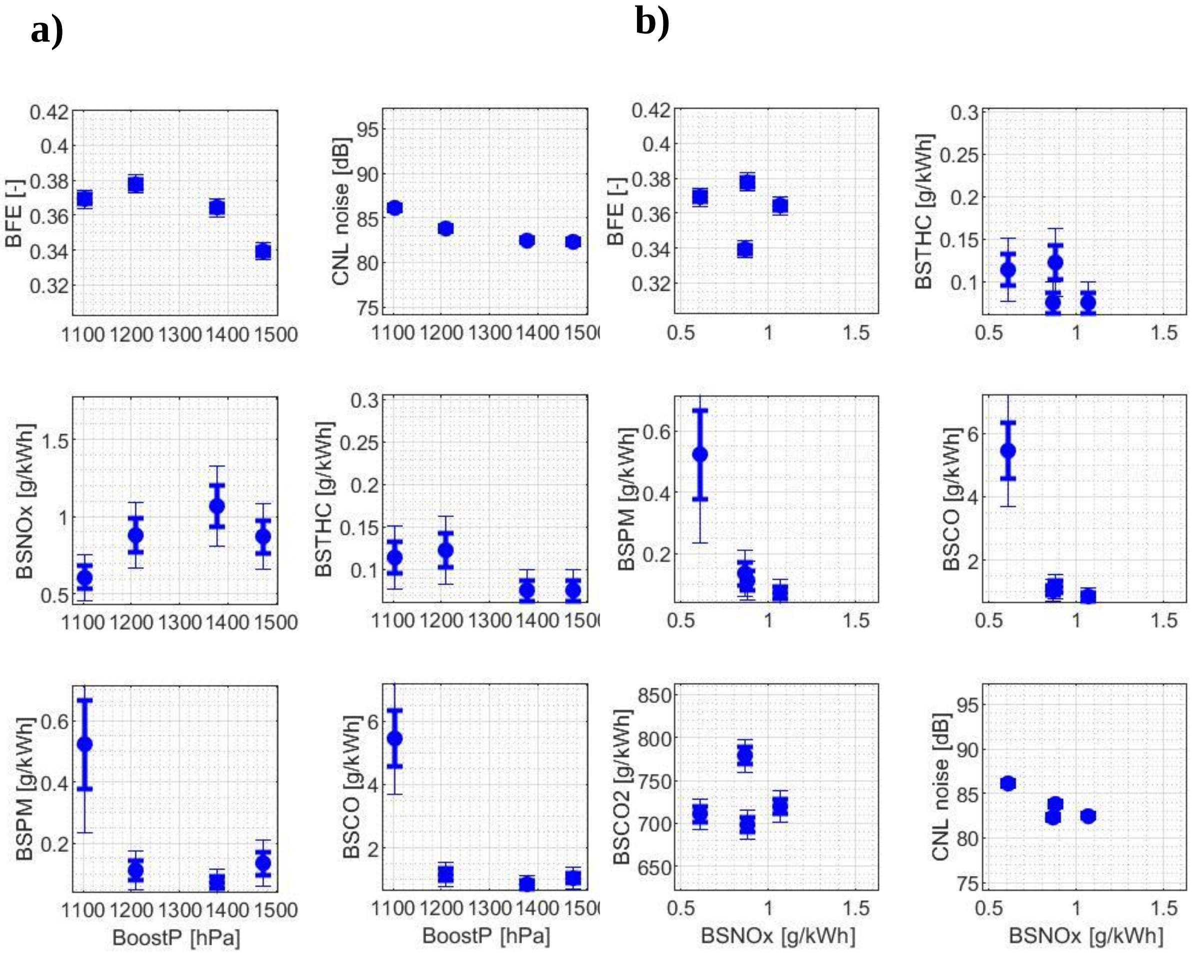

Figure 3.42. BFE, BS emissions and CNL during boost pressure (BP) sweep of the diesel baseline at MM4 as a function of a) BP and b) BSNOx.

First, BFE increases from 36.9% at low boost pressure (LP) to 37.8% at the default boost pressure (DP), then, decreases from the DP to 33.9% at high boost pressure (HP). The increase in BFE from LP to DP is considerable (i.e., absolute 1%, relative 2.7%), thus requiring detailed explanation for the phenomenon. Figure 3.43a presents the parameters that can affect the BFE during the boost pressure (BP) sweep at MM4. Gross indicated fuel conversion efficiency (IFEg, Figure 3.43a, second to the top plot) increases from 41.6% at LP to 43.5% at DP, then to 43.9% at HP. Although the IFEg monotonically increases for the entire range of the boost pressure, the degree of increase is far more intense between LP and DP than the other range of the boost pressure. Meanwhile, the increase in PMEP (Figure 3.43a, third to the top plot) from LP to DP is the least intense throughout the boost pressure sweep. It only increases about 0.1bar from LP to DP which is 2 or 3 factors smaller than the increase in PMEP in other range of the boost pressure. The steep increase in IFEg combined with small increase in PMEP from LP to DP relative to the other boost pressure range makes the default boost pressure the most thermally efficient boost pressure condition at MM4. This is why the trend of BFE during the boost pressure sweep makes the concave curve with its peak at the default boost pressure as shown in Figure 3.42a top plot.

Second, BSPM decreases from 0.522g/kWh at LP to about 0.11g/kWh for DP and the higher BP conditions. The decrease in BPSM with increasing boost pressure at MM4 is because the increase in intake charge O_2 concentration overwhelms the decrease in oxygen ratio at the lift-off length with increasing BP. At MM3, the decrease in oxygen ratio at the lift-off length dominated the increase in intake O_2 concentration with increasing BP. Thus, the difference in BSPM trend by the boost pressure between MM3 and MM4 is not because of the fundamentally different underlying physics, but because of the difference in the degree of the two competing factors at two different operating conditions. Figure 3.43b (top plot) presents the change in intake O_2 concentration during the boost pressure sweep at MM4. The intake O_2 concentration increases from 6.96 mol/m^3 at LP to 9.4 mol/m^3 at HP, which is about 35% increase. At MM3, the increase in intake O_2 concentration between LP and HP was only about 20%.

Figure 3.44b presents the lift-off length (top), oxygen ratio at the lift-off length (middle) during the boost pressure (BP) sweep of the baseline at MM4 with the trend of BSPM (bottom). Because of the increase in charge gas temperature (Figure 3.43b, third to the top) with increasing

BP, lift-off length decreases as shown in Figure 3.44b top plot. Following the trend of lift-off length, oxygen ratio at the lift-off length also drops from 11% at LP to 7.5% at HP (relative 32% decrease). At MM3, from LP to HP, the oxygen ratio at the lift-off length decreased from 5.8% to 3.5% (relative 40% decrease). Thus, at MM4, while the increase in intake O_2 concentration is more significant than at MM3, the decrease in oxygen ratio at the lift-off length is less intense. In conclusion, at MM4, the impact of the increase in intake O_2 concentration just overwhelmed the impact of the decrease in oxygen ratio at the lift-off length while the dominance of one factor over the other was the opposite at MM3.

Although the trend of BSNOx by boost pressure (BP) was the same as at MM3 with the same underlying physics, the values of BSNOx at MM4 was different from those at MM3. Thus, the values of BSNOx are briefly presented here. Also, the values of the other brake specific (BS) emissions and combustion noise level (CNL) during the BP sweep of the baseline fuel at MM4 are briefly presented here. BSNOx increased from 0.61g/kWh at LP to 0.88g/kWh at DP, then peaked at 1.07g/kWh at MHP. Then, it decreased down to 0.87g/kWh at HP. Combustion noise level (CNL) decreased from 86.14dB at LP to 83.82dB at DP, then to 82.29dB. BSTHC emission from MM4 was at negligible level around 0.1g/kWh for the entire range of the BP. BSCO emission decreased from 5.45g/kWh at LP to about 1g/kWh at HP.

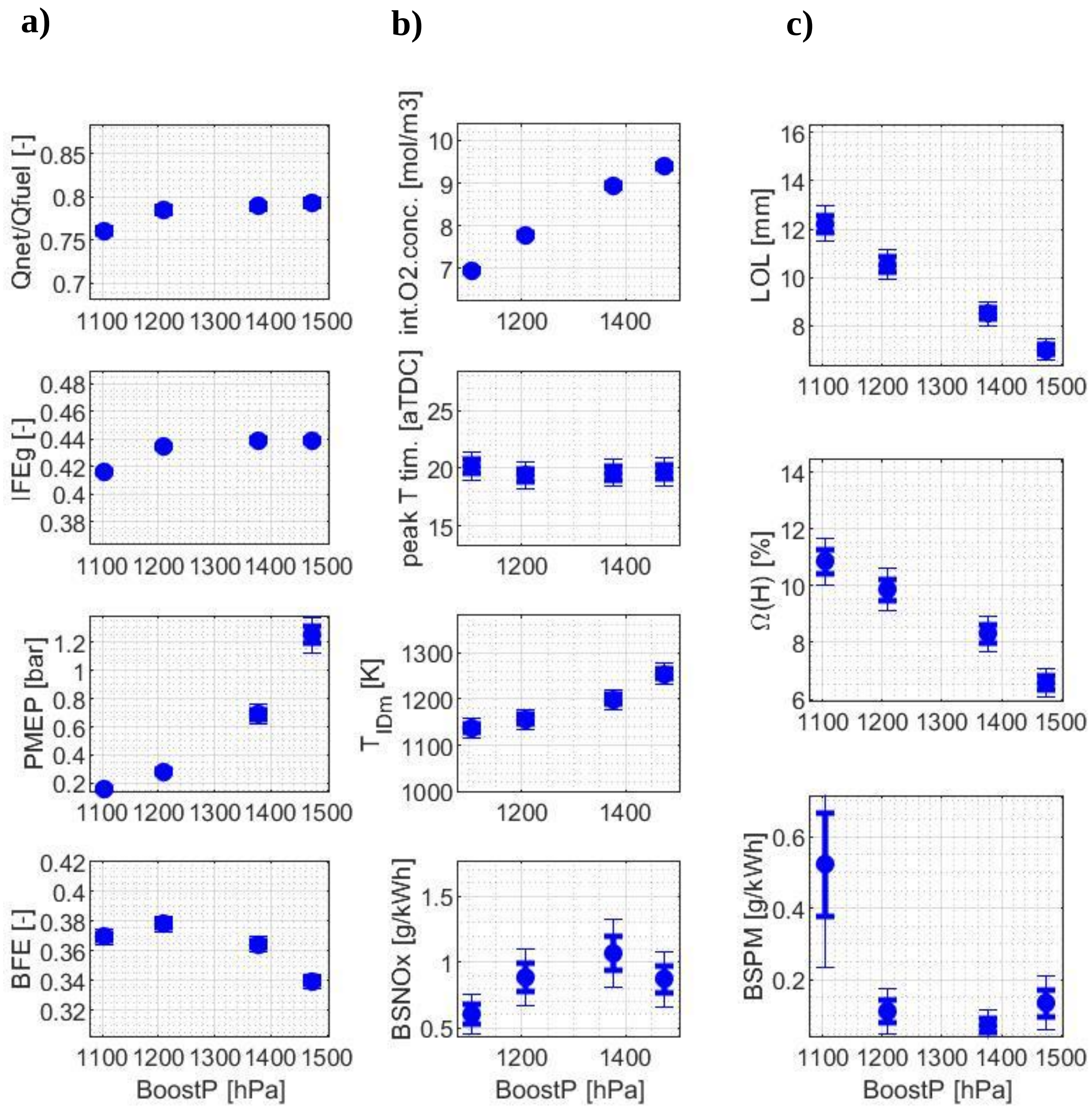

Figure 3.43. The parameters affecting a) BFE, b) and c) BSPM during the boost pressure (BP) sweep of the baseline diesel at MM4

Figure 3.44a presents the impact of main injection timing (MIT) on BFE (top-left), BSNOx (middle-left), BSPM (bottom-left), CNL (top-right), BSTHC (middle-right), BSCO (bottom-right) at MM4 for the baseline diesel. Figure 3.44b presents the trend of the BFE (top-left), BSPM (middle-left), BSCO$_2$ (bottom-left), BSTHC (top-right), BSCO (middle-right) and CNL (bottom-right) by BSNOx during the MIT sweep at MM4 with the baseline fuel.

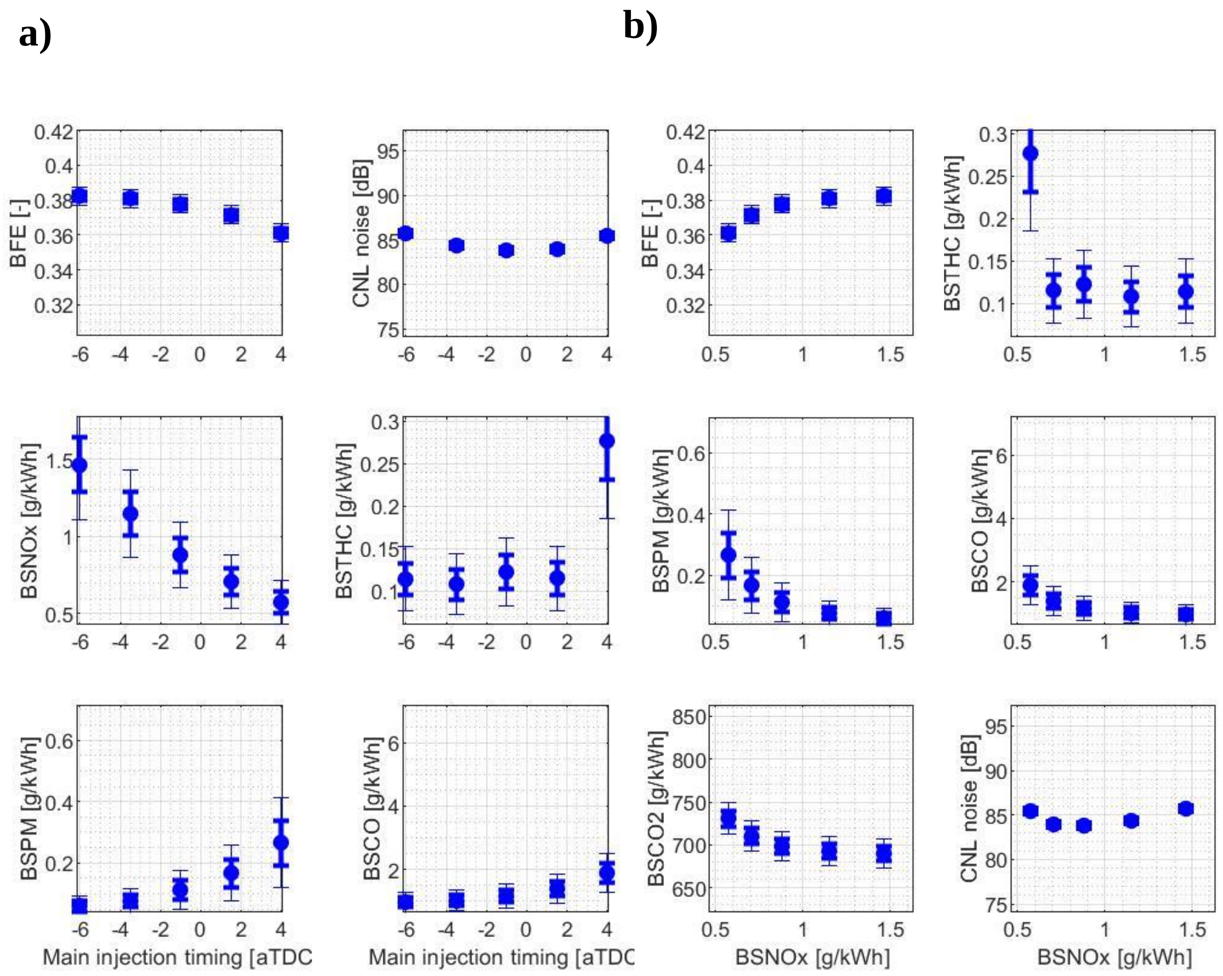

Figure 3.44. BFE, BS emissions, CNL trend during main injection timing (MIT) sweep of the baseline diesel as a function of a) MIT, b) BSNOx at MM4

The impact of main injection timing (MIT) on all of the primary output parameters of interest is the same as MM3 except the impact on BSPM. The BSPM emission monotonically increases with retarded MIT at MM4 while it made a concave curve with its peak around the default injection timing condition at MM3.

Figure 3.45 shows the parameters affecting BSPM during the main injection timing (MIT) sweep at MM4. At the top plot of Figure 3.45a is the intake O_2 concentration during the MIT sweep. The intake O2 concentration remains the same for all of the MIT conditions imposed. However, another important factors affecting BSPM, “oxygen ratio at the lift-off length”, does not remain the same for different MIT conditions. Charge gas temperature (Figure 3.45a, third to the top plot) peaks around the default injection timing, thus causing the lift-off length (Figure 3.45b, top plot) to bottom around the default injection timing. Then, the oxygen ratio at the lift-off length (Figure 3.45b, middle plot) follows the trend of the lift-off length. Oxygen ratio bottoms around the default injection timing (9.5%), and increases for both advanced and retarded injection timings. Given the fact that intake O_2 concentration remains constant for different MIT conditions, it would be more intuitive if BSPM simply followed the opposite trend of the oxygen ratio at the lift-off length. However, the BSPM trend at MM4 does not follow the opposite trend of the oxygen ratio at the lift-off length. This is a unique trend observed only at MM4, and the reason for the trend is hard to be accurately explained. However, the most reasonable guess could be that the increase in oxygen ratio from the default injection timing (DF) to retarded injection timings is not substantial enough at MM4 unlike other mini-map points. At MM4, compared to the 1.7 absolute % decrease in oxygen ratio from 5 degrees advanced injection timing (5A) to the default injection timing (DF), there is only 0.5 absolute % increase in oxygen ratio from the DF to 5 degrees retarded injection timing (5R).

Combined with the small increase in oxygen ratio at retarded injection timings, it is also likely that the impact of pilot injection soot generation was large enough to affect the final BSPM result at MM4. Figure 3.46 shows the lift-off length during the pilot event (left), and oxygen ratio at the lift-off length during the pilot event (right) at MM4 diesel baseline test. Since the pilot injection timing gets closer to TDC with retarded MIT, the charge gas temperature increases with retarded injection timing. Thus, unlike the main combustion event, lift-off length for pilot combustion event monotonically decreases with retarded injection timing as shown in Figure 3.46 (left-plot). Consequently, the oxygen ratio at the lift-off length for the pilot event follows the trend of the lift-off length: oxygen ratio decreases with the retarding in injection timing. Thus, the soot generation from pilot event will monotonically increase with the retarded injection timing. It is possible that the combination of the increase in soot generation from the pilot event and the weak increase in oxygen ratio of the main combustion event at retarded injection timings simply resulted in monotonic increase in BSPM with retarded injection timings.

Although the trend of BFE and BSNOx during the main injection timing (MIT) sweep at MM4 was the same as MM3, the values were different. Thus, the values of BFE and BSNOx during the MIT sweep at MM4 are briefly presented here. Also, the values of BSCO and CNL during the MIT sweep at MM4 are briefly presented here, as well. Brake fuel conversion efficiency (BFE) of the baseline fuel at MM4 decreased from 38.3% at 5 degrees advanced injection timing to 37.8% at the default injection timing, then to 36.1% at 5 degrees retarded injection timing. BSCO increased from 0.96g/kWh at 5 degrees advanced injection timing to 1.17g/kWh at the default injection timing, then to 1.89g/kWh at 5 degrees retarded injection timing. BSTHC emission at MM4 was at negligible level around 0.1g/kWh for most of the imposed main injection timing conditions.

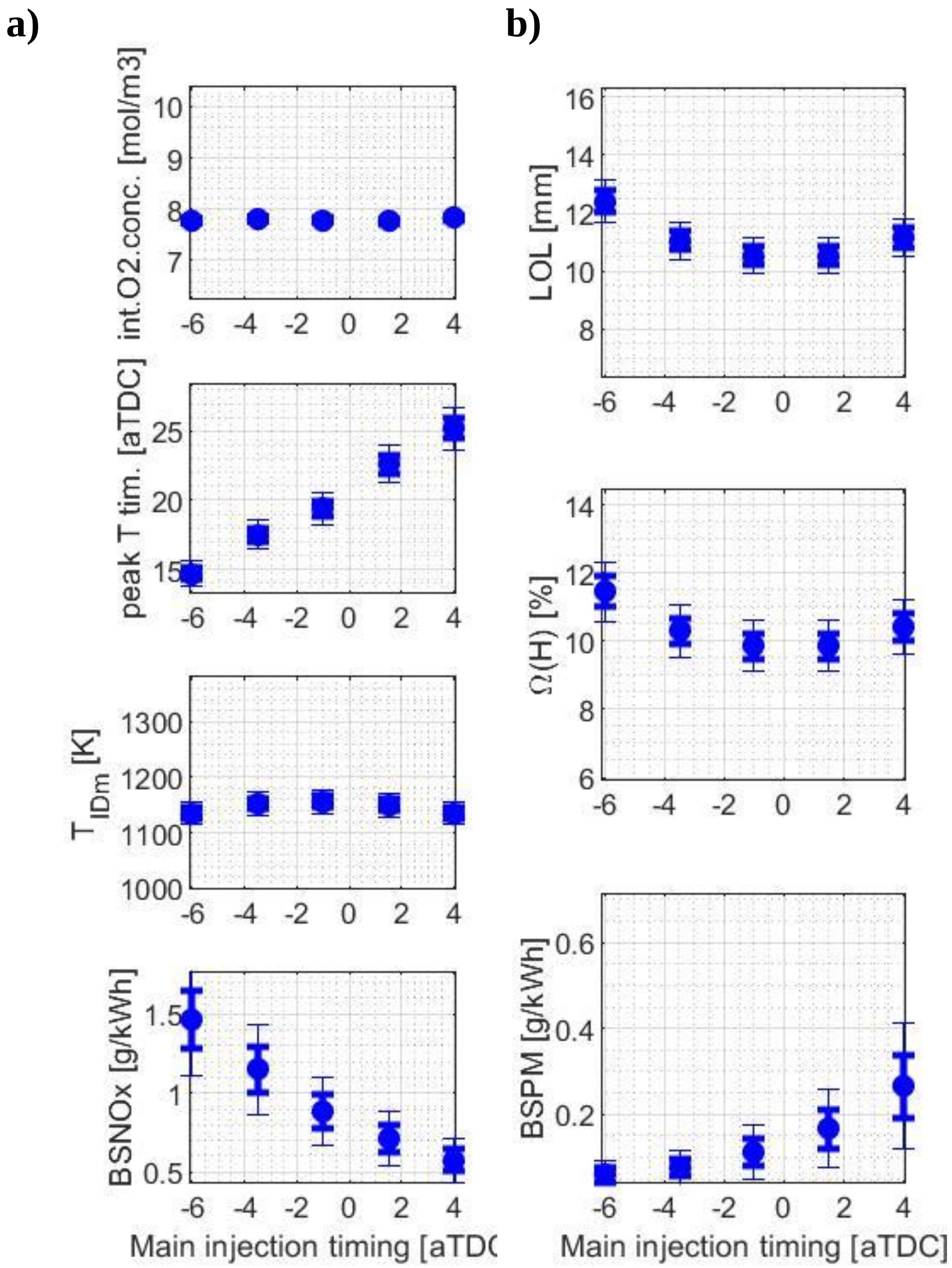

Figure 3.45. The parameters affecting BSPM emission during the main injection timing (MIT) sweep of the baseline diesel at MM4. a) Intake O2 concentration (top), peak cylinder temperature timing (second-to-the-top), charge gas temperature during the main ignition delay (third-to-the-top), and BSNOx (bottom). b) lift-off length (top), oxygen ratio at the lift-off length (middle), BSPM (bottom).

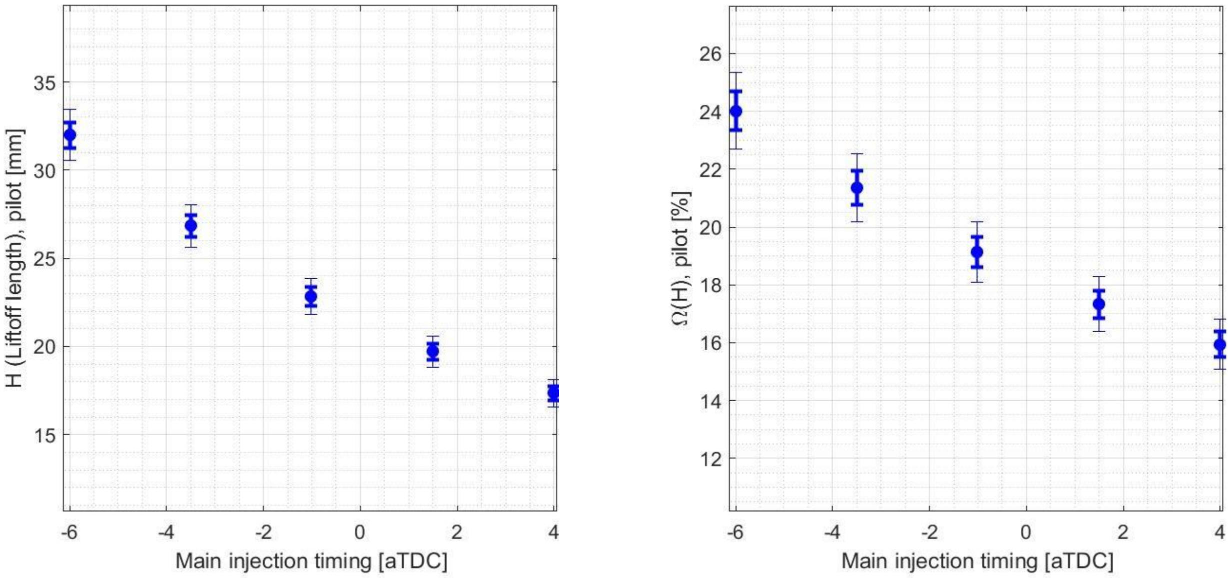

Figure 3.46 Lift-off length (Left) and oxygen ratio at the lift-off length (Right) for pilot injection event during main injection timing (MIT) sweep of the baseline diesel at MM4

Figure 3.47a presents the impact of EGR on BFE (top-left), BSNOx (middle-left), BSPM (bottom-left), CNL (top-right), BSTHC (middle-right), BSCO (bottom-right) at MM4 for the baseline diesel. Figure 3.47b presents the trend of the BFE (top-left), BSPM (middle-left), $BSCO_2$ (bottom-left), BSTHC (top-right), BSCO (middle-right) and CNL (bottom-right) by BSNOx during the EGR sweep at MM4 with the baseline fuel.

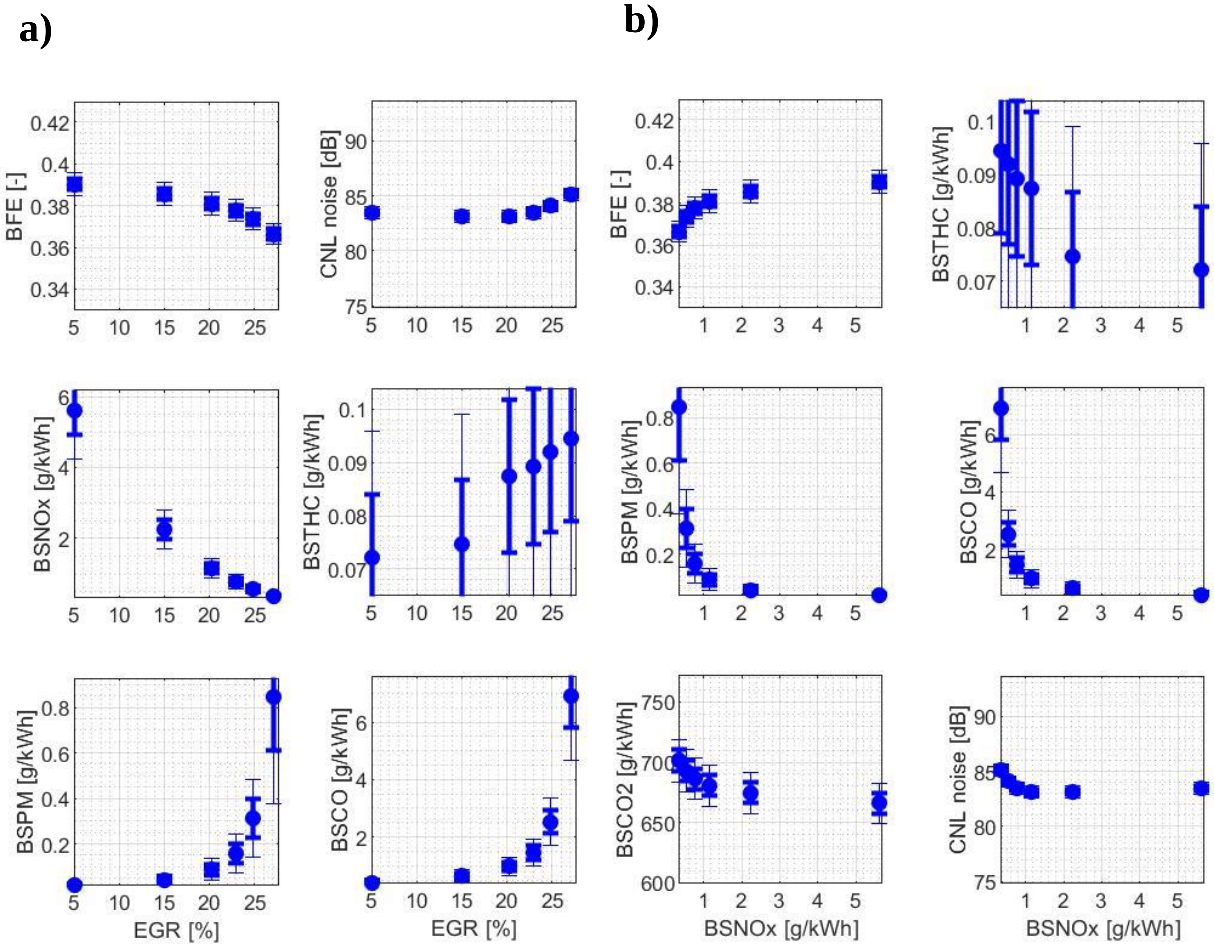

Figure 3.47. BFE, BS emissions and CNL during EGR sweep of the baseline diesel at MM4 as a function of a) EGR rate, b) BSNOx

The impact of EGR rate on all of the primary output parameters of interest at MM4 was the same as at MM3. Thus, in here, the values of BFE, BSNOx, BSPM, and other brake specific (BS) emissions, and CNL will be briefly presented. Brake fuel conversion efficiency (BFE) decreased from 39.0% at EGR5% to 38.1% at the default EGR settings (EGR21%), then to 36.6% at EGR27%. BSNOx decreased from 5.61g/kWh at EGR5% to 1.15g/kWh at the default EGR settings (EGR21%), then to 0.35g/kWh at EGR27%. BSPM increased from 0.018g/kWh at EGR5% to 0.088g/kWh at EGR21%, then to 0.844g/kWh at EGR27%. BSTHC emission at

MM4 was at negligible level around 0.1g/kWh for all of the imposed EGR conditions. BSCO increased from 0.42g/kWh at EGR5% to 0.97g/kWh at EGR21%, then to 6.92g/kWh at EGR27%. Combustion noise level (CNL) increased from 83dB in the lower EGR range to 85.14dB at EGR27%.

Figure 3.48a presents the impact of the rail pressure (RP) on BFE (top-left), BSNOx (middle-left), BSPM (bottom-left), CNL (top-right), BSTHC (middle-right), BSCO (bottom-right) at MM4 for the baseline diesel. Figure 3.48b presents the trend of the BFE (top-left), BSPM (middle-left), BSCO$_2$ (bottom-left), BSTHC (top-right), BSCO (middle-right) and CNL (bottom-right) by BSNOx during the RP sweep at MM4 with the baseline fuel.

The impact of rail pressure (RP) on all of the primary output parameters of interest at MM4 was the same as at MM3. Thus, in here, the values of BFE, BSNOx, BSPM, and other brake specific (BS) emissions, and CNL will be briefly presented. Brake fuel conversion efficiency (BFE) remained constant during all 3 rail pressure conditions at around 38%. BSNOx increased from 0.85g/kWh at low rail pressure (LRP) to 0.99g/kWh at the default rail pressure (DRP), then to 1.12g/kWh at high rail pressure (HRP). BSPM decreased from 0.219g/kWh at LRP to 0.089g/kWh at DRP, then to 1.120g/kWh at HRP. BSTHC emission from MM4 during the rail pressure sweep was all at negligible level around 0.1g/kWh. BSCO decreased from 1.4g/kWh at LRP to 0.9g/kWh at HRP. Combustion noise level (CNL) increased from 80.7dB at LRP to 83.55dB at DRP, then to 86.82dB at HRP.

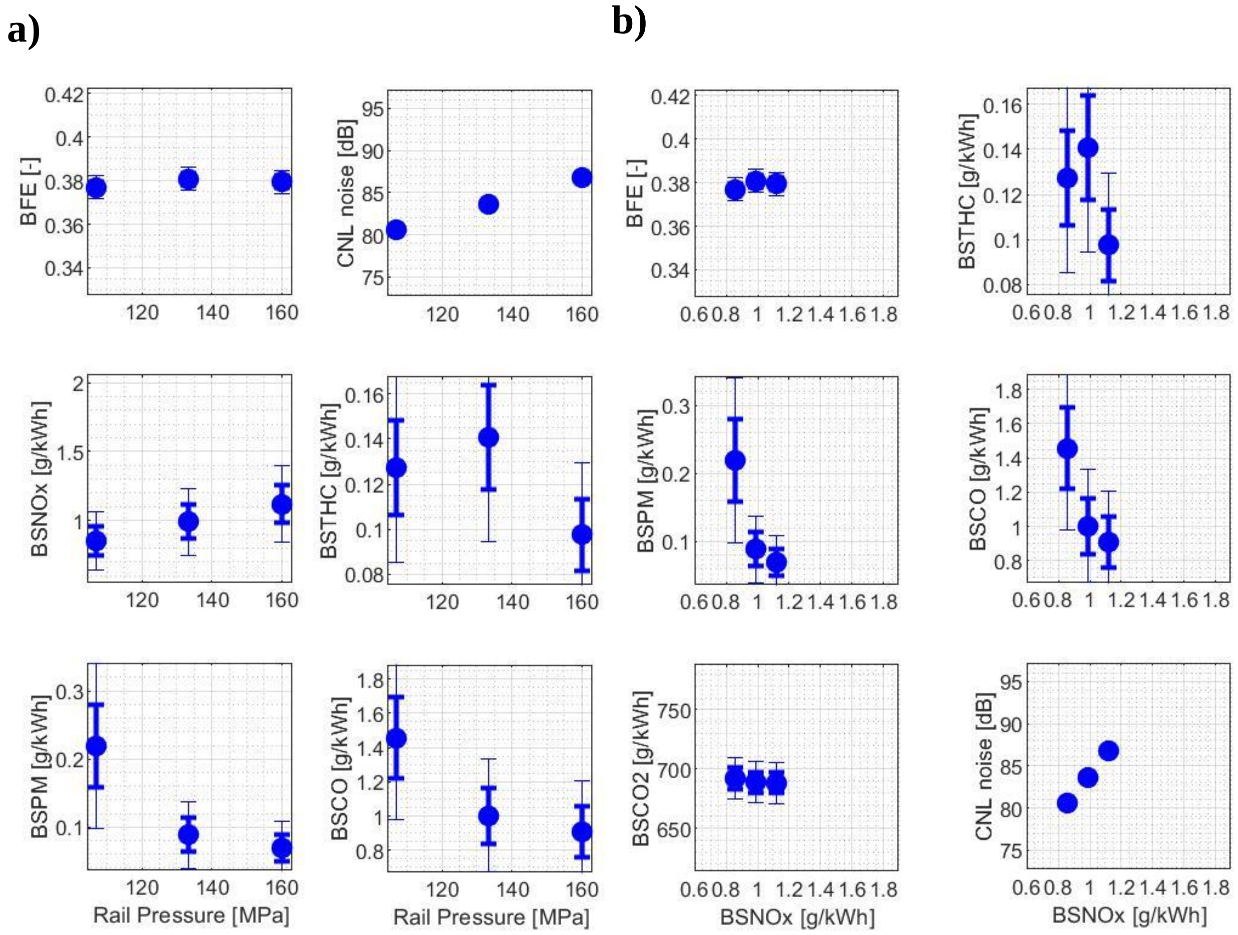

Figure 3.48. BFE, BS emissions, and CNL during the rail pressure (RP) sweep of the baseline diesel at MM4 as a function of a) RP, b) BSNOx

3.3.1.5 MM5

MM5 is a medium-speed, medium-load condition of which performance and emissions trend depending on 4 single sweep parameters (i.e., boost pressure (BP), main injection timing (MIT), EGR rate, rail pressure (RP)) are very similar to those at MM3. Indeed, not only the impact of the 4 input parameters on all output parameters of the primary interest (i.e., BFE, BSNOx, BSPM) was the same as MM3, but also the underlying physics driving the trends was the same as MM3 Thus, in here, just the values of the BFE, brake specific (BS) emissions, and combustion noise level (CNL) obtained from the baseline diesel test at MM5 will be briefly presented with the relevant figures.

Figure 3.49a presents the impact of boost pressure (BP) on BFE (top-left), BSNOx (middle-left), BSPM (bottom-left), CNL (top-right), BSTHC (middle-right), BSCO (bottom-right) at MM5 for the baseline diesel. Figure 3.49b presents the trend of the BFE (top-left), BSPM (middle-left), BSCO$_2$ (bottom-left), BSTHC (top-right), BSCO (middle-right) and CNL (bottom-right) by BSNOx during the BP sweep at MM4 with the baseline fuel.

During the boost pressure (BP) sweep, BFE decreases from 36.8% at low boost pressure (LP) to 36.5% at the default boost pressure (DP), then to 32.8% at high boost pressure (HP). BSNOx increases from 0.52g/kWh at LP to 0.67g/kWh at DP, then to 0.76g/kWh at HP. BSPM decreases from 0.218g/kWh at LP to 0.113g/kWh at DP, then to 0.089g/kWh at mid-high boost pressure (MHP). Then, it increases moderately from MHP to HP (0.109g/kWh). Combustion noise level (CNL) bottoms around the MHP at 81.2dB, and increases for both lower and higher boost pressures. BSTHC emissions at MM5 were at negligible level around 0.2g/kWh for all of the imposed boost pressure conditions. BSCO decreased from 2.34g/kWh at LP to 1.66g/kWh at DP, then to 1.23g/kWh at HP.

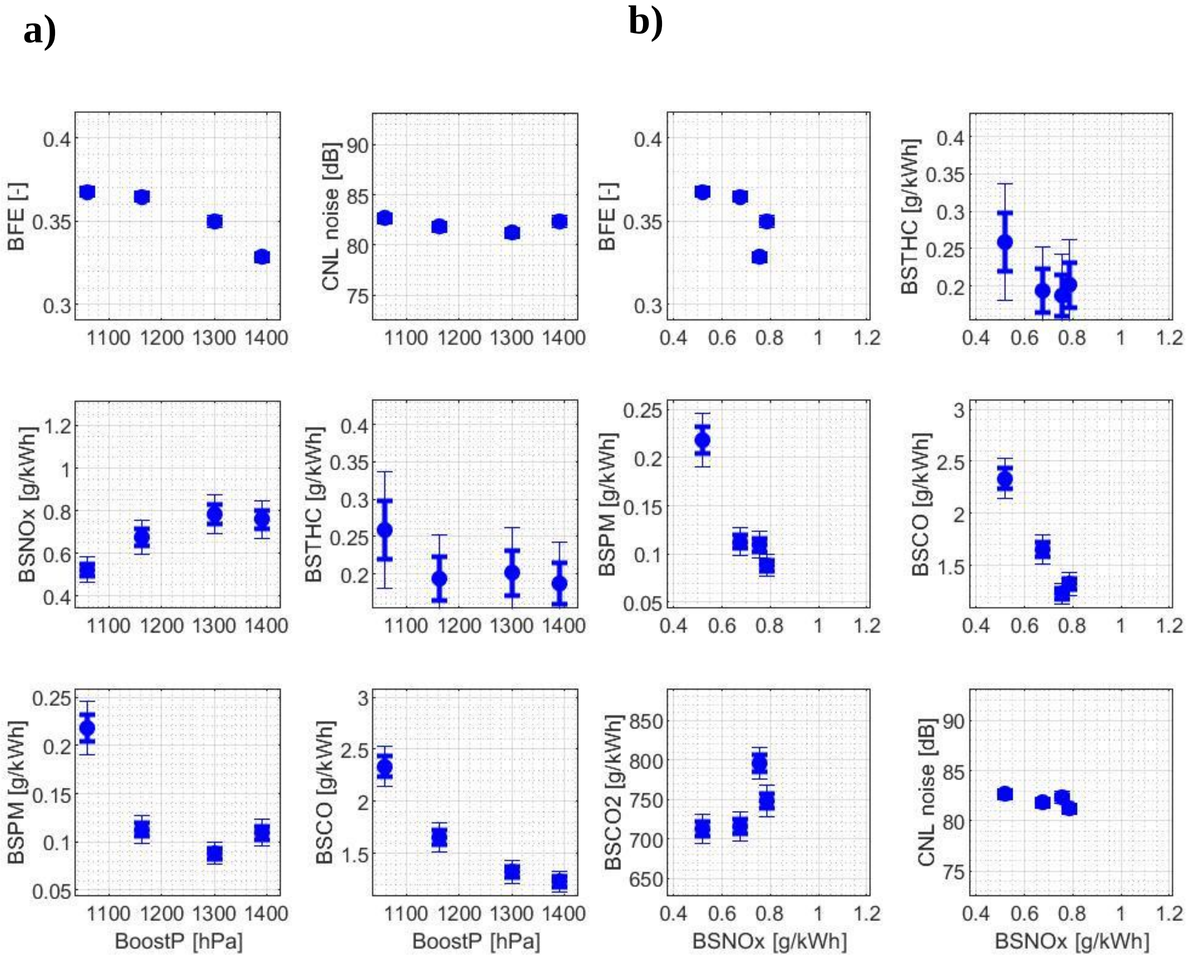

Figure 3.49. BFE, BS emissions, and CNL during the boost pressure (BP) sweep of the baseline diesel at MM5 as a function of a) BP, b) BSNOx

Figure 3.50a presents the impact of main injection timing (MIT) on BFE (top-left), BSNOx (middle-left), BSPM (bottom-left), CNL (top-right), BSTHC (middle-right), BSCO (bottom-right) at MM5 for the baseline diesel. Figure 3.50b presents the trend of the BFE (top-left), BSPM (middle-left), $BSCO_2$ (bottom-left), BSTHC (top-right), BSCO (middle-right) and CNL (bottom-right) by BSNOx during the MIT sweep at MM5 with the baseline fuel.

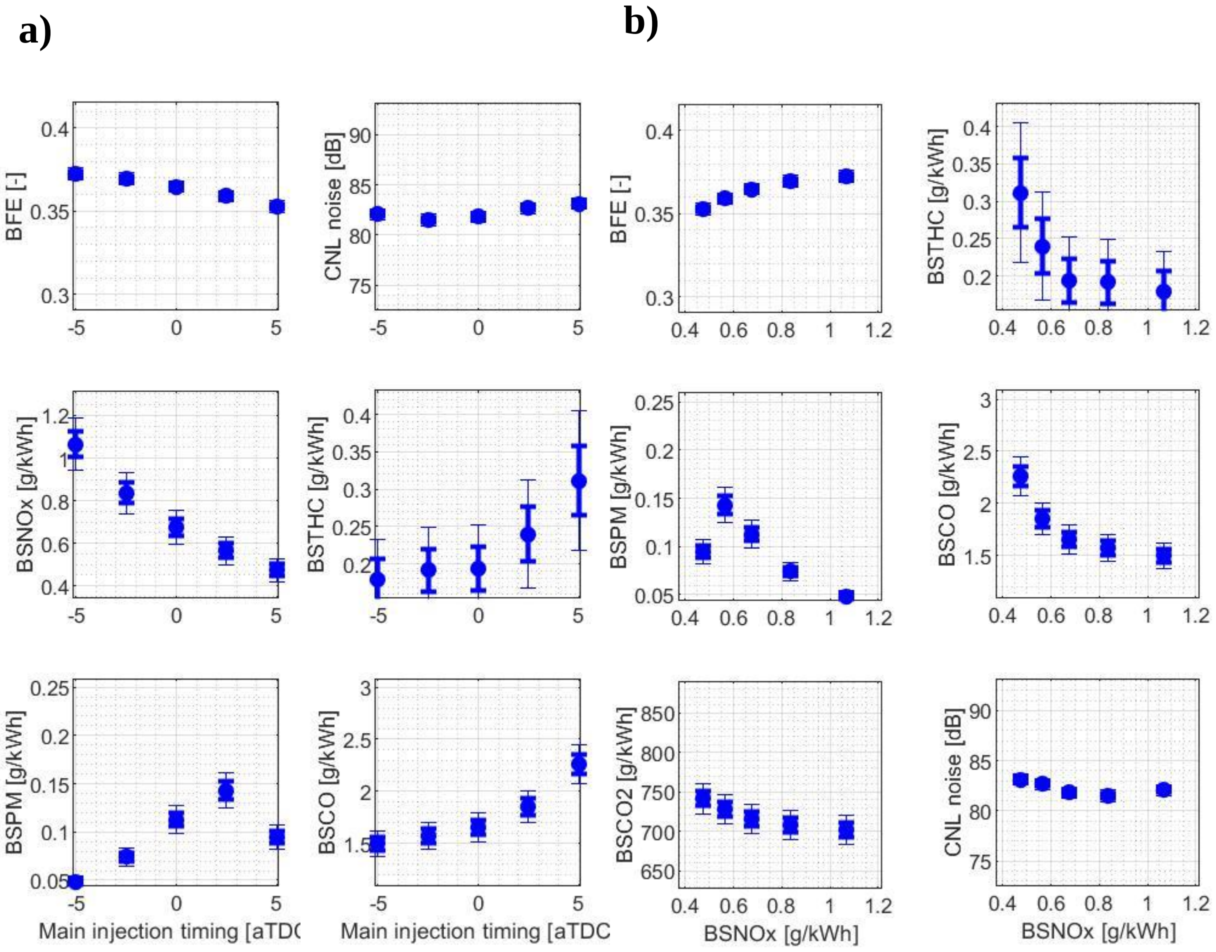

Figure 3.50. BFE, BS emissions, and CNL during main injection timing (MIT) sweep of the baseline diesel at MM5 as a function of a) MIT, b) BSNOx

During the main injection timing (MIT) sweep, BFE decreased from 37.2% at 5 degrees advanced injection timing (5A) to 36.5% at the default injection timing (DF), then to 35.3% at 5 degrees retarded injection timing (5R). BSNOx decreased from 1.07g/kWh at 5A to 0.67g/kWh at DF, then to 0.47g/kWh at 5R. BSPM increased from 0.049g/kWh at 5A to 0.112g/kWh at DF, then peaked at 2.5 degrees retarded injection timing (2.5R), and then, decreased down to 0.094g/kWh at 5 degrees retarded injection timing (5R). Combustion noise level (CNL) was similar for different injection timing conditions around 82dB. BSTHC emissions from MM5 were at negligible level. BSCO increased from 1.50g/kWh at 5A to 1.66g/kWh at DF, then to 2.26g/kWh at 5R.

Figure 3.51a presents the impact of EGR on BFE (top-left), BSNOx (middle-left), BSPM (bottom-left), CNL (top-right), BSTHC (middle-right), BSCO (bottom-right) at MM5 for the baseline diesel. Figure 3.51b presents the trend of the BFE (top-left), BSPM (middle-left), $BSCO_2$ (bottom-left), BSTHC (top-right), BSCO (middle-right) and CNL (bottom-right) by BSNOx during the EGR sweep at MM5 with the baseline fuel.

During the EGR sweep, BFE decreased from 37.6% at EGR0% to 36.8% at the default EGR settings (EGR27%), then to 34.2% at EGR 39%. BSNOx decreased from 5.18g/kWh at EGR0% to 0.66g/kWh at the default EGR settings (EGR27%), then to 0.09g/kWh at EGR39%. BSPM increased from 0.025g/kWh at EGR0% to 0.109g/kWh at EGR27%, then to 1.59g/kWh at EGR39%. BSTHC emissions from MM5 were at negligible level. BSCO increased from 0.99g/kWh at EGR0% to 1.6g/kWh at EGR27%, then to 19.07g/kWh. Combustion noise level (CNL) varied between 80dB and 82.5dB during the EGR sweep depending on the EGR rate.

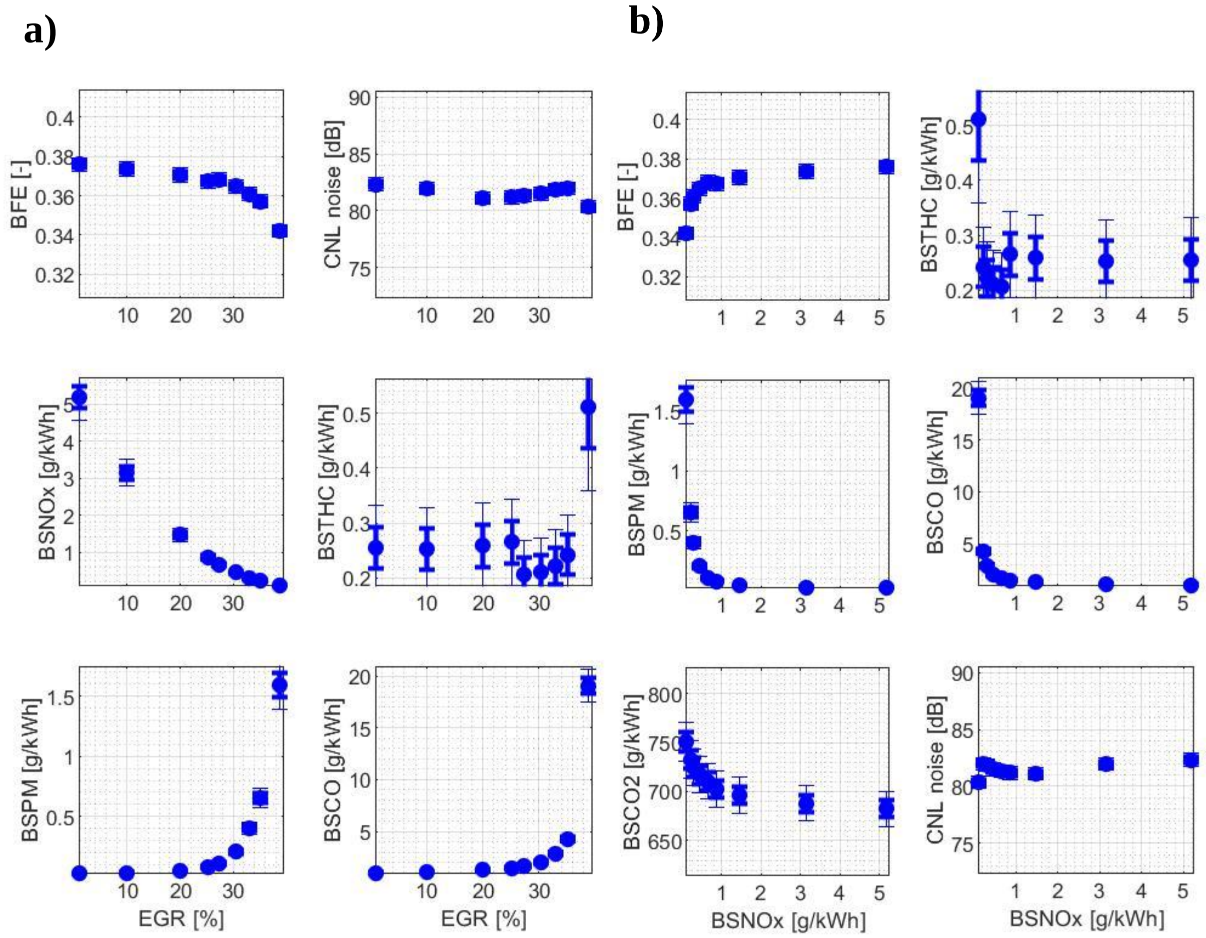

Figure 3.51. BFE, BS emissions, and CNL during EGR sweep of the baseline diesel at MM5 as a function of a) EGR rate, b) BSNOx

Figure 3.52a presents the impact of rail pressure (RP) on BFE (top-left), BSNOx (middle-left), BSPM (bottom-left), CNL (top-right), BSTHC (middle-right), BSCO (bottom-right) at MM5 for the baseline diesel. Figure 3.52b presents the trend of the BFE (top-left), BSPM (middle-left), $BSCO_2$ (bottom-left), BSTHC (top-right), BSCO (middle-right) and CNL (bottom-right) by BSNOx during the RP sweep at MM5 with the baseline fuel.

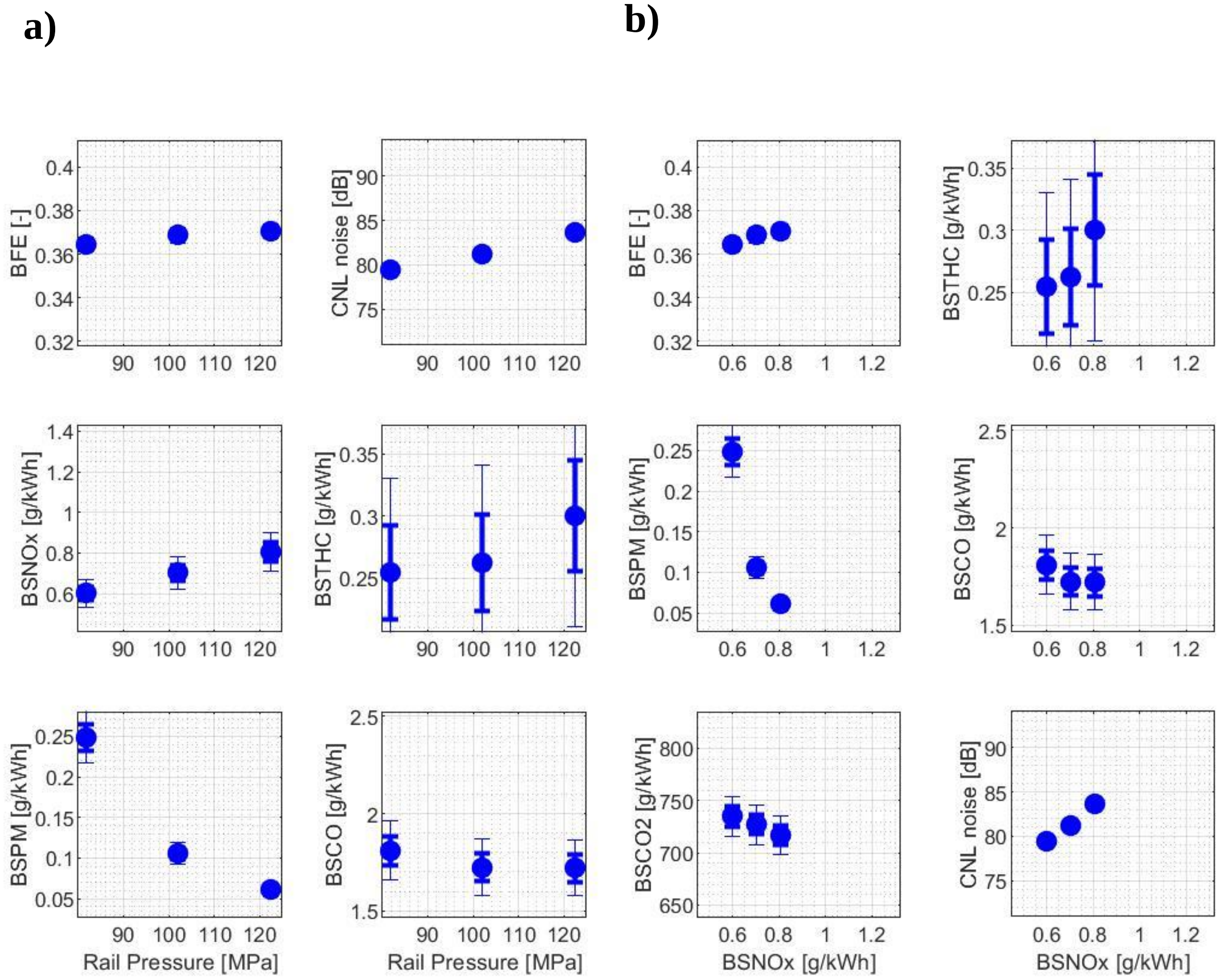

Figure 3.52. BFE, BS emissions, and CNL during rail pressure (RP) sweep of the baseline diesel at MM5 as a function of a) RP, b) BSNOx

During the rail pressure (RP) sweep, BFE increased from 36.4% at low rail pressure (LRP) to 36.9% at the default rail pressure (DRP), then to 37.1% at high rail pressure (HRP). BSNOx increased from 0.60h/kWh at LRP to 0.70g/kWh at DRP, then to 0.80g/kWh at HRP. BSPM decreased from 0.25g/kWh at LRP to 0.106g/kWh at DRP, then to 0.061g/kWh at HRP. Combustion noise level (CNL) increased from 79.48dB at LRP to 81.21dB at DRP, then to 83.7dB at HRP. BSTHC emissions at MM5 during the rail pressure sweep were at negligible level. BSCO decreased from 1.81g/kWh at LRP to 1.72g/kWh at DRP, then to 1.71g/kWh at HRP.

3.3.1.6 MM6

MM6 is a high speed-high load operating conditions out of the 6 MM points. However, the impact of the 4 input parameters (i.e., boost pressure (BP), main injection timing (MIT), EGR rate, rail pressure (RP)) on the output parameters (i.e., BFE, BS emissions, and CNL) at MM6 is generally similar to what is observed at medium-load points such as MM3. Since MM6 is one of the mini-map points with high weight factor when estimating the final performance and emissions of B20 during the EPA FTP75 cycle, it is important to look in detail about the impact of the input parameters on the output parameters and the underlying causes for the results at MM6. However, since the trends are quite similar to those presented at MM3, the explanation will be more focused on the unique trends observed at MM6. The trends of the output parameters at MM6 by boost pressure is first presented in this section, followed by the trends by main injection timing, EGR rate, then finally by rail pressure.

Figure 3.53a presents the impact of boost pressure (BP) on BFE (top-left), BSNOx (middle-left), BSPM (bottom-left), CNL (top-right), BSTHC (middle-right), BSCO (bottom-right) at MM6 for the baseline diesel. Figure 3.53b presents the trend of the BFE (top-left), BSPM (middle-left), BSCO$_2$ (bottom-left), BSTHC (top-right), BSCO (middle-right) and CNL (bottom-right) by BSNOx during the BP sweep at MM6 with the baseline fuel.

Thick error bars indicate the plus and minus one standard deviation interval (68% confidence interval) while the thin error bars indicate the plus and minus two standard deviations interval (95% confidence interval). In case the difference between two data points is smaller than plus and minus one standard deviation, the difference is not considered to be statistically meaningful. If the difference between the two data points is larger than plus and minus one standard deviation, but smaller than plus and minus two standard deviations, the difference is considered to be statistically meaningful with low statistical confidence (less than 95%). If the difference between the two data points is greater than plus and minus two standard deviations, the difference is considered to be statistically meaningful with high statistical confidence (more than 95%).

First, BFE peaks between the default boost pressure (DP) and mid-high boost pressure (MHP), then decreases for both low boost pressure (LP) and high boost pressure (HP). Brake fuel conversion efficiency (BFE) of the baseline fuel during the boost pressure (BP) sweep at MM6 is 37.3% at LP, 37.9% at DP and MHP, and 36.3% at HP. This concave curve of BFE during the BP sweep at MM6 is also observed at MM4. The underlying physics for this trend is identical for the two mini-map points: competition between the increase in IFEg and the increase in PMEP with increasing boost pressure. Figure 3.54a shows the parameters that can affect BFE during the BP sweep at MM6. Gross indicated fuel conversion efficiency (IFEg, Figure 3.54a, second to the top) increases from 43.0% at LP to 43.9% at DP, then to 45.9% at HP. Although the IFEg increases monotonically for the entire range of the boost pressure tested, the degree of the increase is more intense for the lower range of the boost pressure (i.e., from LP to DP) than the higher range of boost pressure. Pump mean effective pressure (PMEP, Figure 3.54a, third to the top) also increases monotonically from 0.21bar at LP to 0.26bar at DP, then to 0.97bar at HP. Unlike IFEg, the degree of increase in PMEP is less intense during the lower range of boost pressure sweep (i.e., LP to DP) than the higher range. Therefore, from LP to DP, the impact of the increase in IFEg dominates the impact of the increase in PMEP, thus resulting in the increase in BFE while the opposite happens for the higher boost pressure range. The cause for the increase in IFEg with increasing boost pressure at MM6 is the advance in main combustion phasing (Figure 3.54c, top) thanks to the increase in the charge density and oxygen concentration. Advanced main SOC makes combustion process to happen more like a constant-volume process than a constant-pressure process, and makes the "actual" compression ratio higher, which, in turn, results in higher IFEg.[48]

Second, BSNOx increases from 0.68g/kWh at low boost pressure (LP) to 0.79g/kWh at the default boost pressure (DP), then to 1.50g/kWh at high boost pressure (HP). The increase in BSNOx during the boost pressure (BP) sweep at MM6 is due to the increase in intake O_2 concentration, advance in peak cylinder temperature timing, and the increase in charge gas temperature during the main ignition delay. Figures 3.54b and 3.54c show the parameters that can affect BSNOx during the BP sweep at MM6. Peak cylinder temperature timing (Figure 3.54b, second to the top) is advanced by about 4CAs from LP to HP, and the charge gas temperature during the main ignition delay (Figure 3.54b, third-to-the-top) increased by about 50K from LP to HP. Intake O_2 concentration (Figure 3.54b, top) also increased from 8.0mol/m^3 at LP to 8.51mol/m^3 at DP, then to 11.58mol/m^3 at HP. The degree of the increase in intake O_2 concentration between LP and HP at MM6 was about 45%, which is more significant than the counterparts of any other mini-map points (e.g., MM3: 20%, MM4: 35%). Due to this significant increase in intake O_2 concentration, the potential impact of the moderate decrease in oxygen ratio at the lift-off length (Figure 3.55a, middle) on BSNOx was overshadowed at all of the boost pressure conditions imposed at MM6.

For the boost pressure (BP) sweep tests among MM3, MM4, and MM6, we can see the change in dominance of the impact from two different oxygen parameters (i.e., intake O_2 concentration vs. oxygen ratio at the lift-off length) on BSNOx and BSPM results. While the degree of decrease in oxygen ratio at the lift-off length with increasing boost pressure remained similar for these three MM points, the degree of increase in intake O_2 concentration was significantly different for the three MM points with the ascending order of MM3, MM4, then MM6. At MM3 where the increase in intake O_2 concentration was about 20% from LP to HP, the BSNOx peaked around MHP and BSPM monotonically increased from LP and HP. This means that, the impact of the increase in intake O_2 concentration was outrun by the impact of the decrease in oxygen ratio for the entire range of boost pressure for the BSPM result. And the impact of increase in intake O_2 concentration was outrun by the impact of decrease in oxygen ratio in partial range of the boost pressure sweep (i.e., from MHP to HP) for the BSNOx result. Thus, in general, the impact of oxygen ratio at the lift-off length was stronger than the impact of overall O_2 concentration. However, when it comes to MM4 where the increase in intake O_2 concentration from LP to HP is about 35%, the dominance between the two different oxygen parameters flips. Now, the impact of increase in intake O_2 concentration outruns the impact of decrease in oxygen ratio for the entire range of boost pressure causing monotonic decrease in BSPM with increasing boost pressure. In regards to BSNOx result, the impact of decrease in oxygen ratio at the lift-off length still dominates the impact of increase in overall O_2 concentration in the partial range of the boost pressure sweep (i.e., from MHP to HP). Finally, when it comes to MM6 where the increase in intake O_2 concentration from LP to HP reaches up to 45%, the dominance of the increase in intake O_2 concentration over the decrease in oxygen ratio exists every boost pressure conditions for both BSNOx and BSPM results. At MM6, despite the decrease in oxygen ratio at the lift-off length with increasing boost pressure, BSNOx monotonically increases while BSPM monotonically decreases from LP to HP.

The intake O_2 concentration represents the availability of oxygen in the overall charge gas while the oxygen ratio at the lift-off length represents the availability of oxygen at specific local area inside the fuel-rich premixed auto-ignition zone. Thus, the change in dominance between these two parameters for different operating conditions can imply the change in importance of the NOx and soot generation from two different regions (i.e., fuel-rich premixed auto-ignition zone vs. diffusion flame zone or mixing-controlled combustion zone) in combustion chamber. In other words, it means that, as the engine load and speed gets higher (i.e., from MM3 through MM4 to MM6), the importance of the overall charge gas oxygen availability becomes more and more significant than the importance of the oxygen availability in the premixed auto-ignition zone when it comes to NOx and soot emissions. This finding is consistent with the observation from Mueller et al.[25] It is reported that one of the important factors causing the increase in NOx emission from biodiesel is the increase in oxygen ratio inside the fuel-rich auto-ignition zone. And the degree of importance of this factor on NOx emissions becomes more evident for lower load conditions with lower charge gas temperature and higher oxygen dilution.[25]

Since the underlying physics governing the change in BSPM during the boost pressure (BP) sweep at MM6 is explained in detail above, the values of BSPM will be briefly presented here with other brake specific (BS) emissions and combustion noise level (CNL). BSPM for the baseline fuel at MM6 decreased from 0.244g/kWh at LP to 0.128g/kWh at DP, then to 0.031g/kWh at HP. BSTHC emissions of the baseline fuel during the boost pressure sweep at MM6 were at negligible level for all of the imposed conditions. BSCO decreased from 2.32g/kWh at LP to 1.17g/kWh at DP, then to 0.54g/kWh at HP. Combustion noise level (CNL) also decreased from 86.33dB at LP to 85.42dB at DP, then to 84.46dB at HP.

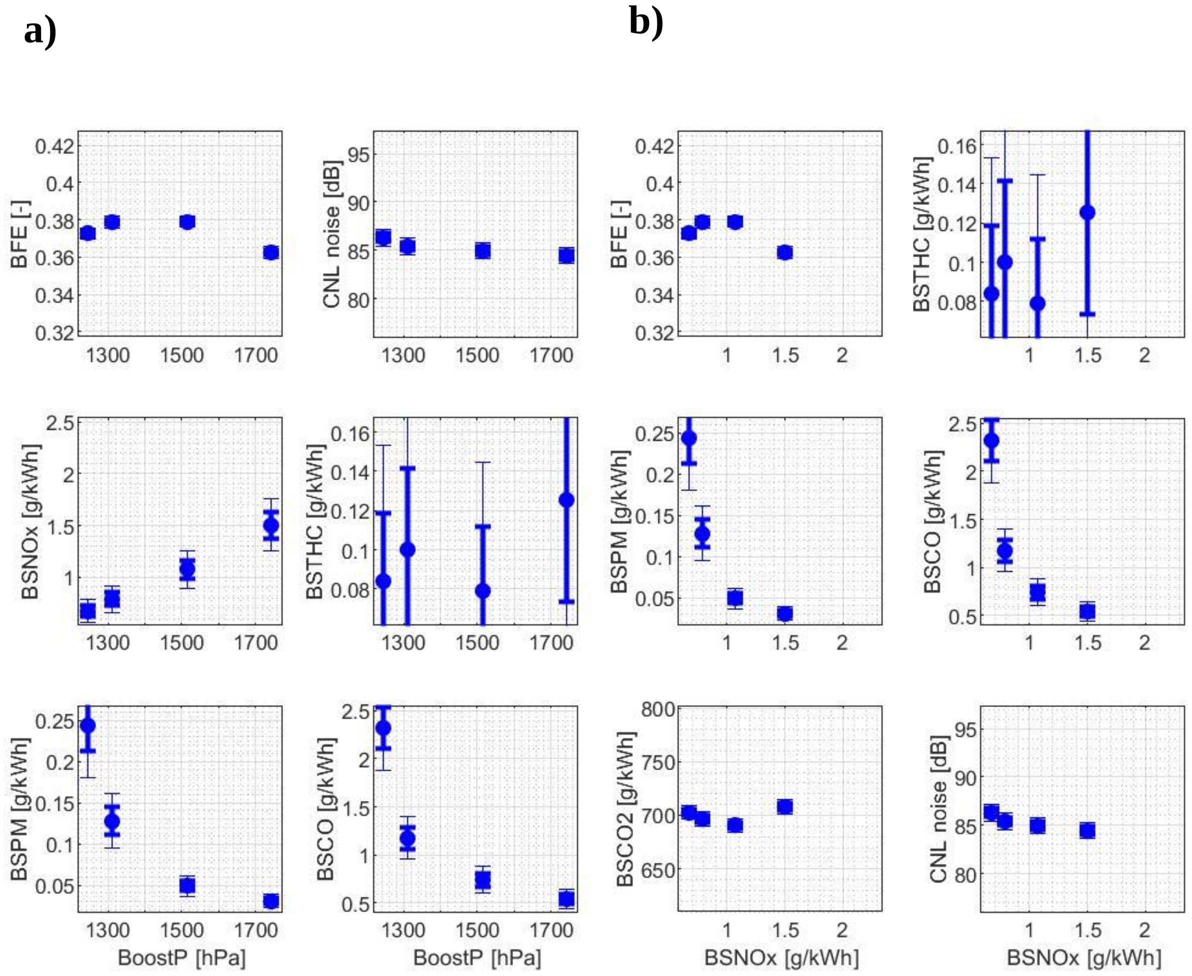

Figure 3.53. BFE, BS emissions, and CNL during boost pressure (BP) sweep of the baseline diesel at MM6 as a function of a) BP, b) BSNOx.

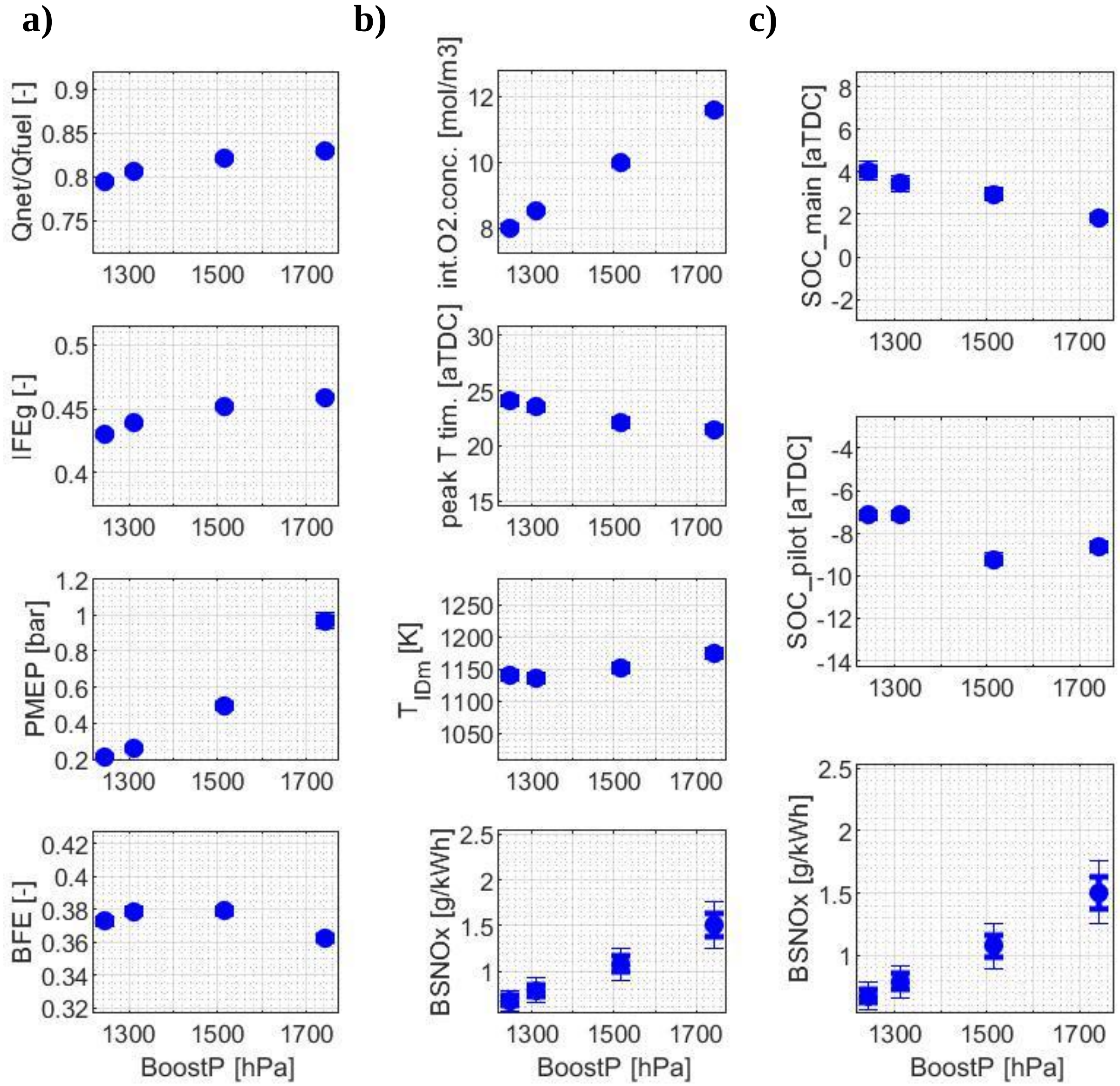

Figure 3.54. The parameters affecting a) BFE, b) and c) BSNOx during boost pressure (BP) sweep of the baseline diesel at MM6

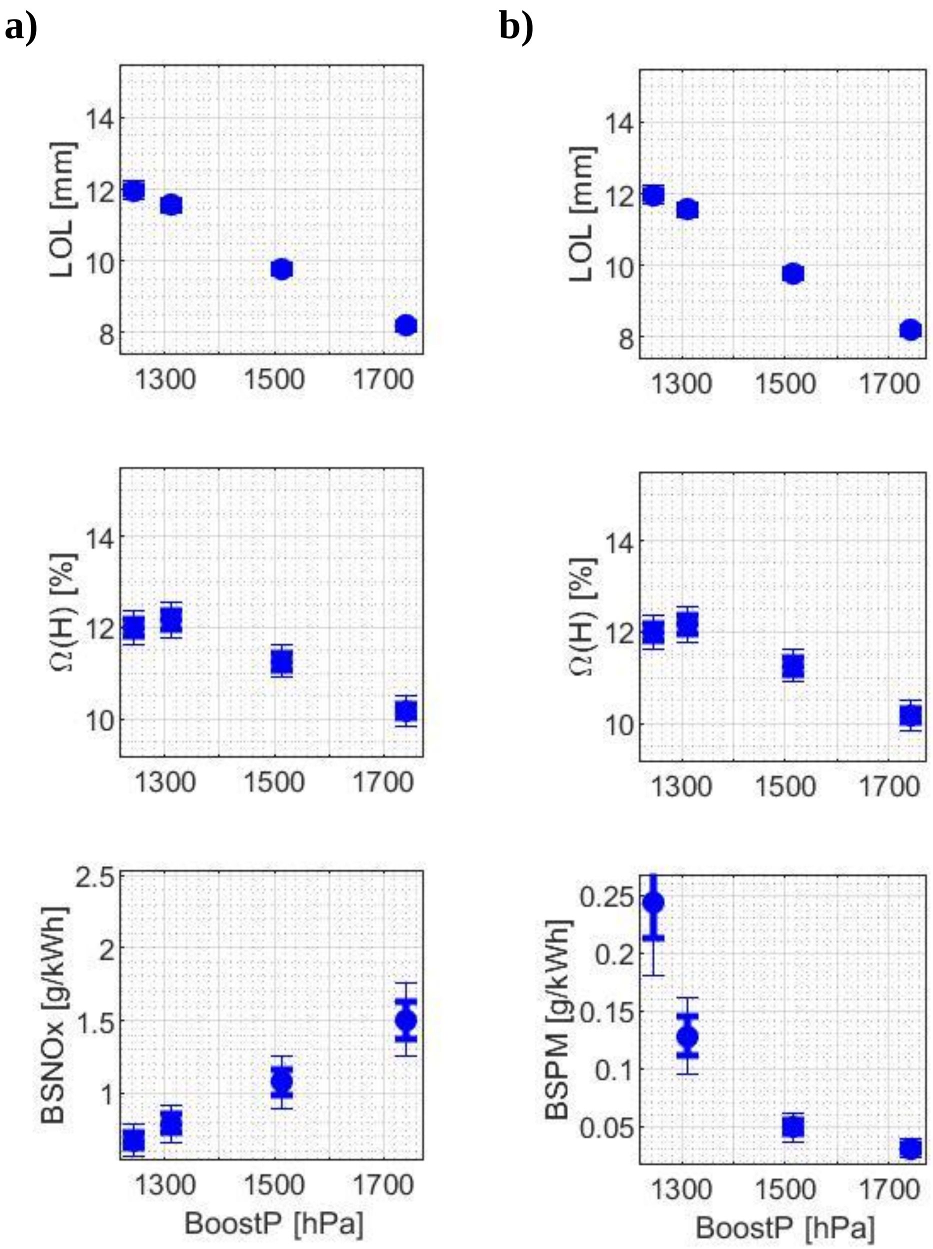

Figure 3.55. Lift-off length and oxygen ratio at the lift-off length during boost pressure (BP) sweep of the baseline diesel at MM6 with the trend of a) BSNOx, b) BSPM

Figure 3.56a presents the impact of main injection timing (MIT) on BFE (top-left), BSNOx (middle-left), BSPM (bottom-left), CNL (top-right), BSTHC (middle-right), BSCO (bottom-right) at MM6 for the baseline diesel. Figure 3.56b presents the trend of the BFE (top-left), BSPM (middle-left), $BSCO_2$ (bottom-left), BSTHC (top-right), BSCO (middle-right) and CNL (bottom-right) by BSNOx during the MIT sweep at MM6 with the baseline fuel.

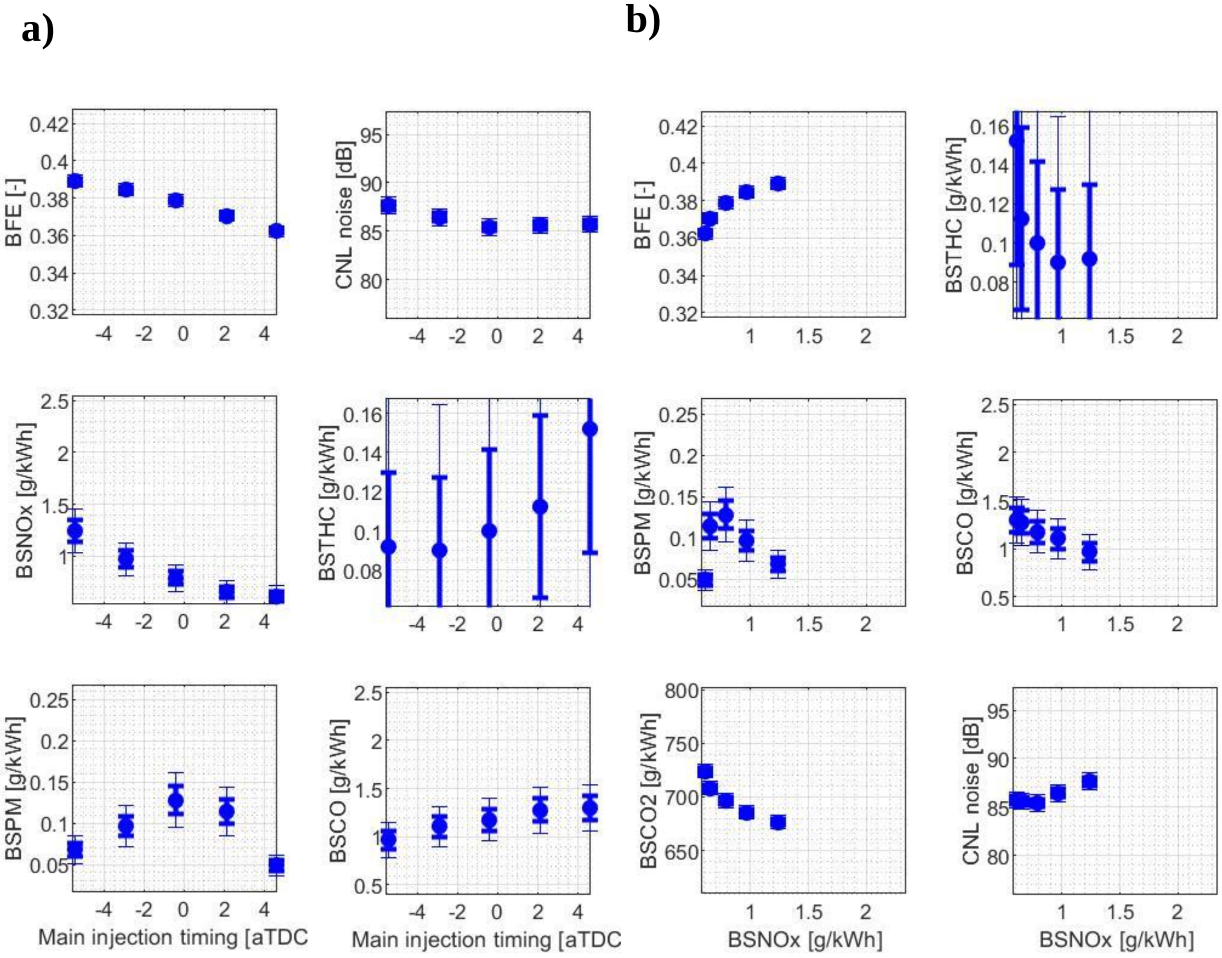

Figure 3.56. BFE, BS emissions, and CNL during main injection timing (MIT) sweep of the baseline diesel at MM6 as a function of a) MIT, b) BSNOx

The impact of main injection timing (MIT) on BFE, BSNOx, and BSPM was the same as that of MM3 with the same underlying physics. Brake fuel conversion efficiency (BFE) and BSNOx monotonically decreased with retarded MIT while BSPM peaked around the default MIT. Thus, in here, the values of BFE, BSNOx, BSPM during the main injection timing sweep at MM6 will be briefly reported. Brake fuel conversion efficiency (BFE) decreased from 38.9% at 5 degrees advanced injection timing (5A) to 37.9% at the default injection timing (DF), then to 36.2% at 5 degrees retarded injection timing (5R). BSNOx decreased from 1.24g/kWh at 5A to 0.79g/kWh at DF, then to 0.61g/kWh at 5R. BSPM increased from 0.068g/kWh at 5A to 0.128g/kWh at DF, but decreased from DF to 0.049g/kWh at 5R. The concave curve of BSPM regarding the main injection timing change is again due to the trend of charge gas temperature shown in Figure 3.57b (third to the top). This trend of charge gas temperature made the lift-off length (Figure 3.58a, top) bottom around the default injection timing, which, in turn, made the oxygen ratio at the lift-off length to bottom around the default injection timing. Since the intake O_2 concentration (Figure 3.57b, top) remained constant over different main injection timing conditions, the oxygen ratio at the lift-off length is almost the only parameter that affected BSPM.

BSTHCs from the baseline fuel during the main injection timing (MIT) sweep at MM6 were at negligible level for all of the imposed main injection timing conditions. BSCO increased from 0.98g/kWh at 5 degrees advanced injection timing (5A) to 1.17g/kWh at the default injection timing (DF), then to 1.30g/kWh at 5 degrees retarded injection timing (5R). Combustion noise level (CNL) decreased from 87.62dB at 5A to 85.5dB for default or retarded injection timings.

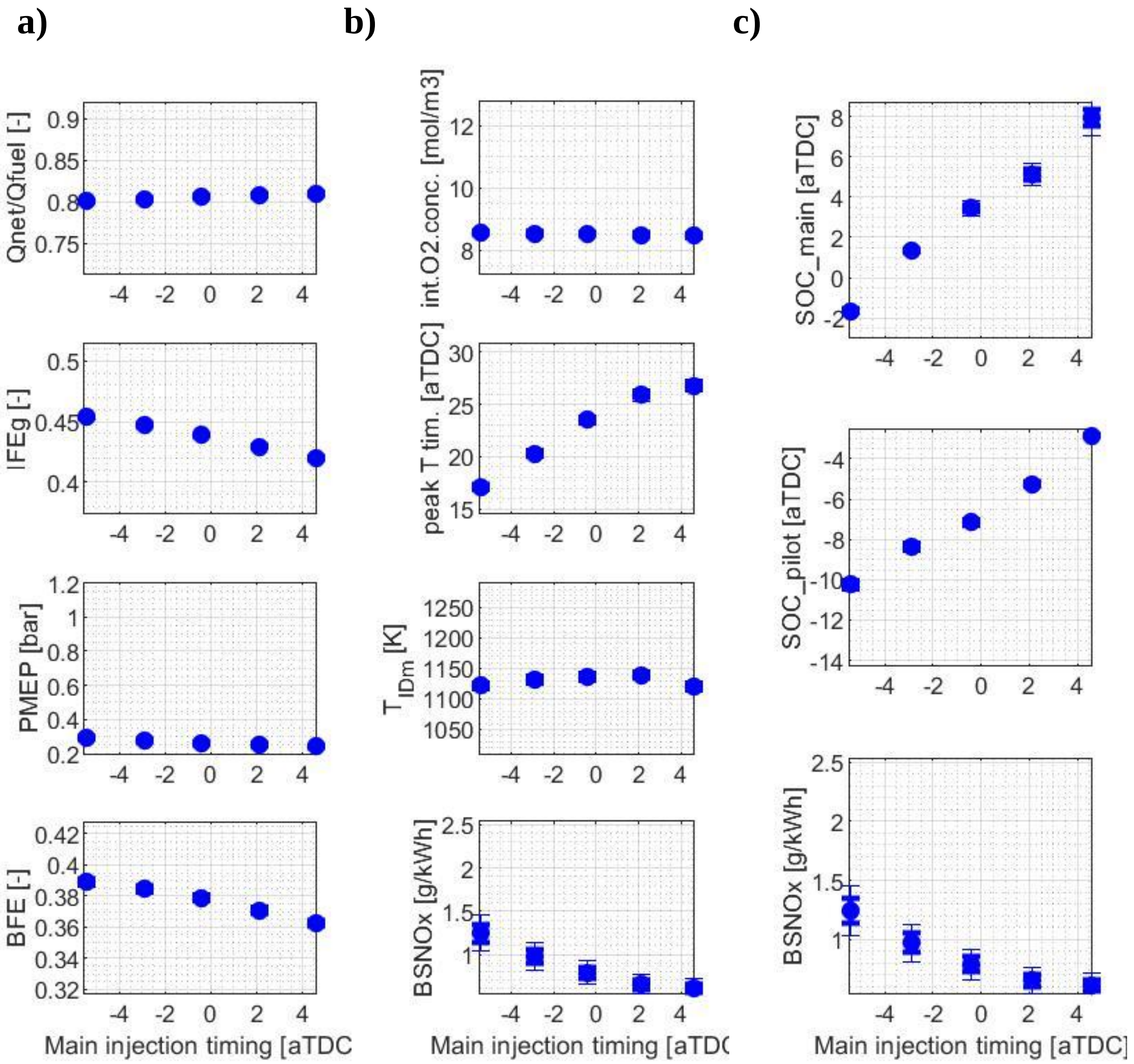

Figure 3.57. The parameters affecting a) BFE, b) and c) BSNOx during main injection timing (MIT) sweep of the baseline diesel at MM6.

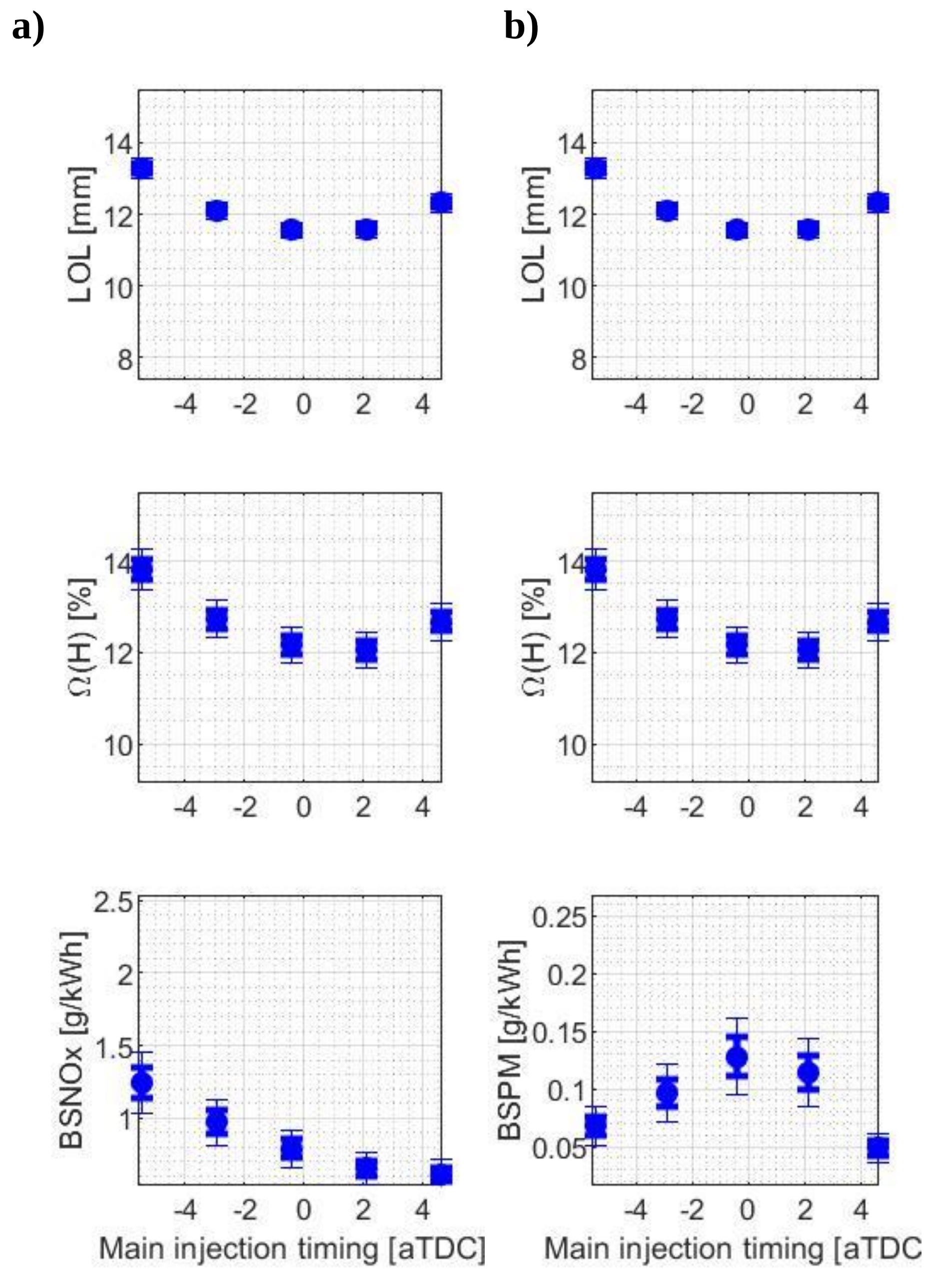

Figure 3.58. Lift-off length and oxygen ratio at the lift-off length with the trend of a) BSNOx and b) BSPM by main injection timing (MIT) at MM6

Figure 3.59a presents the impact of EGR on BFE (top-left), BSNOx (middle-left), BSPM (bottom-left), CNL (top-right), BSTHC (middle-right), BSCO (bottom-right) at MM6 for the baseline diesel. Figure 3.59b presents the trend of the BFE (top-left), BSPM (middle-left), $BSCO_2$ (bottom-left), BSTHC (top-right), BSCO (middle-right) and CNL (bottom-right) by BSNOx during the EGR sweep at MM6 with the baseline fuel.

Figure 3.60 presents the parameters affecting BFE (Figure 3.60a) and BSNOx (Figure 3.60b and 3.60c) during the EGR sweep of the baseline fuel at MM6. As shown in Figure 3.60a, increase in EGR rate decreases IFEg from 43.9% at 0% EGR to 40.0% at 28% EGR because the longer ignition delay makes main SOC (Figure 3.60c, top) further from TDC. Increase in EGR rate also increases the PMEP, which, combined with the decrease in IFEg, results in the decrease in BFE. Brake fuel conversion efficiency (BFE) decreases from 39.1% at 0% EGR to 35.6% at 28% EGR at MM6.

Figures 3.60b and 3.60c present the parameters affecting BSNOx emission. The increase in EGR decreases intake charge O_2 concentration (Figure 3.60b, top) from 10 mol/m^3 at 0% EGR to 7 mol/m^3 at 28% EGR while the increase in EGR rate increases the charge gas temperature during the main ignition delay (Figure 3.60b, third to the top) by about 50K from 0% EGR to 28% EGR. Since two different factors affecting the “rate” of NOx generation are competing against each other, it is unclear whether the rate of NOx generation will increase or decrease just based on these two parameters. However, regardless of the change in the “rate” of NOx generation, the “duration” allowed for NOx generation decreases with the increase in EGR. We can check this in the trend of peak cylinder temperature timing by EGR rate (Figure 3.60b, second-to-the-top). Peak cylinder temperature timing retards with increasing EGR rate, and this makes BSNOx emissions decrease with increasing EGR rate.

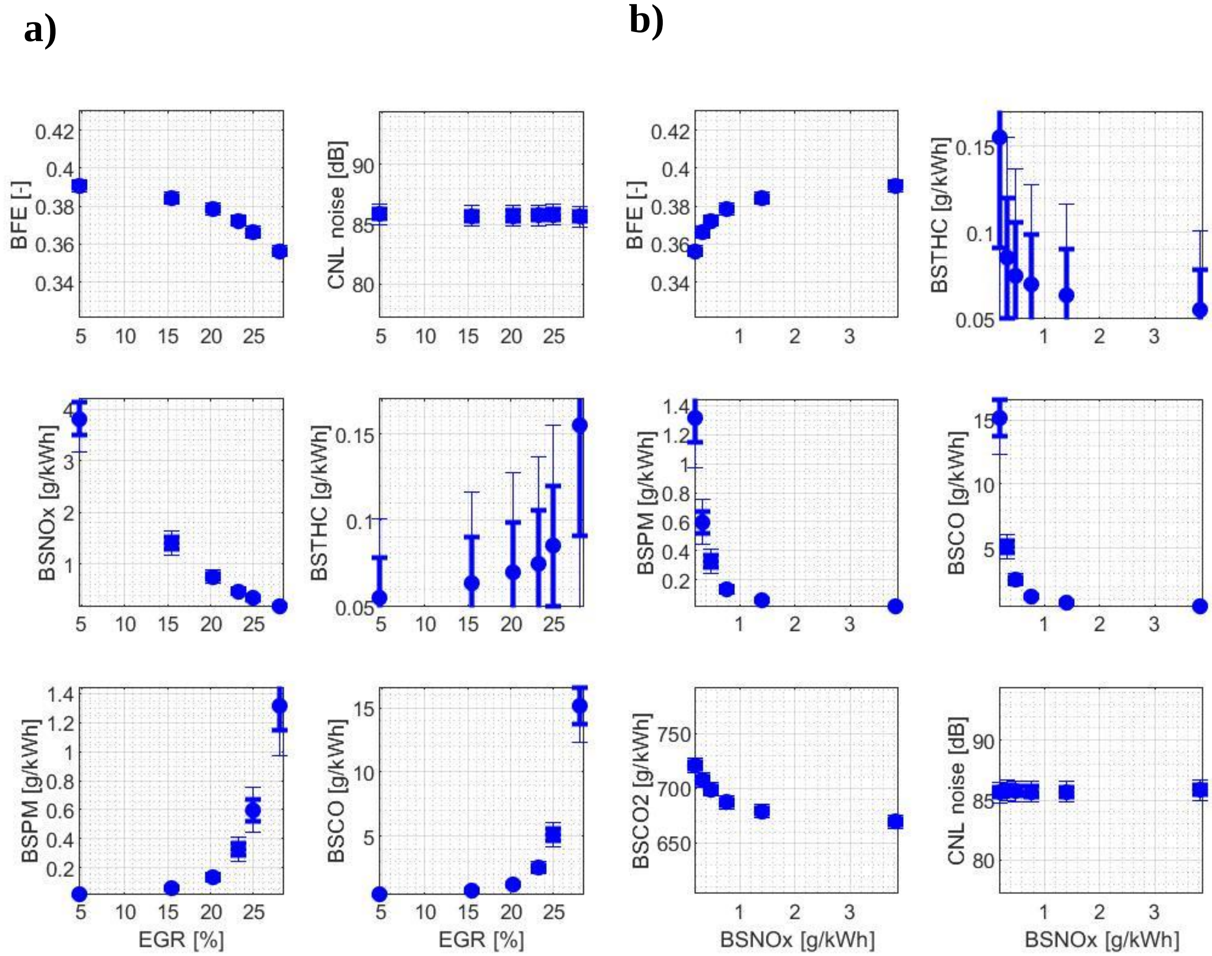

Figure 3.59. BFE, BS emissions, and CNL during EGR sweep of the baseline diesel at MM6 as a function of a) EGR, b) BSNOx

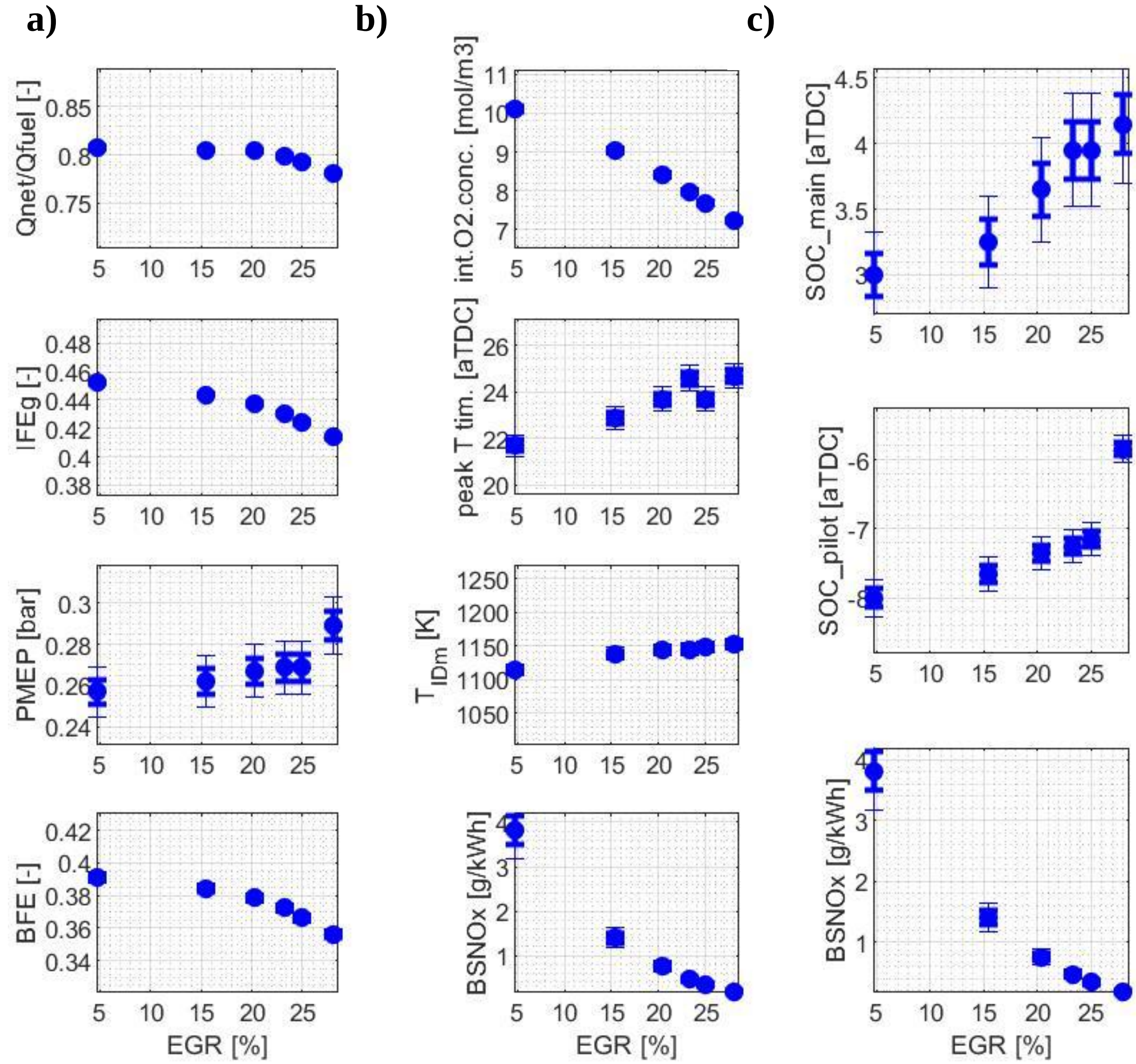

Figure 3.60. Parameters affecting a) BFE, b) and c) BSNOx during EGR sweep of the baseline diesel at MM6.

Figure 3.61 shows the lift-off length (top) and the oxygen ratio at the lift-off length (middle) with the trend of BSNOx (Figure 3.61a, bottom) and BSPM (Figure 3.61b, bottom) during the EGR sweep of the baseline fuel at MM6. It is shown that the lift-off length is minimized around the EGR rate range of 10-15%, then it increases for either lower or higher

EGR rate. However, unlike the observation from the other mini-map points and other sweep tests, the oxygen ratio at the lift-off length does not simply follow the trend of lift-off length during the EGR sweep at MM6. Although the lift-off length bottoms around 10-15% EGR rate range, the oxygen ratio monotonically decreases with the increase in EGR rate. This means that the oxygen ratio at certain axial coordinate (i.e., $\Omega(x)$) decreases at a faster rate with the increasing EGR than the increment rate of the lift-off length with increasing EGR. Figure 3.62 clarifies this phenomenon. Although the lift-off length increases from 11.24mm at EGR15% to 11.87mm at EGR28%, the oxygen ratio at certain axial coordinate decreases at a faster rate from EGR15% to EGR28%. This results in the monotonic decrease in oxygen ratio at the lift-off length (i.e., $\Omega(H)$) from EGR15% to EGR28%.

This discrepancy between the trend of lift-off length and oxygen ratio at the lift-off length occurs because the “stoichiometric charge to fuel ratio (i.e., AF_{st})”, or the ratio of the mass of charge gas required to burn the mass of fuel injected in stoichiometry, increases with increasing EGR. The increase in AF_{st} results in the decrease in $\Omega(x)$. For certain operating conditions like MM6, the degree of decrease in $\Omega(x)$ caused by the increase in AF_{st} simply outweighs the impact of lift-off length variation.

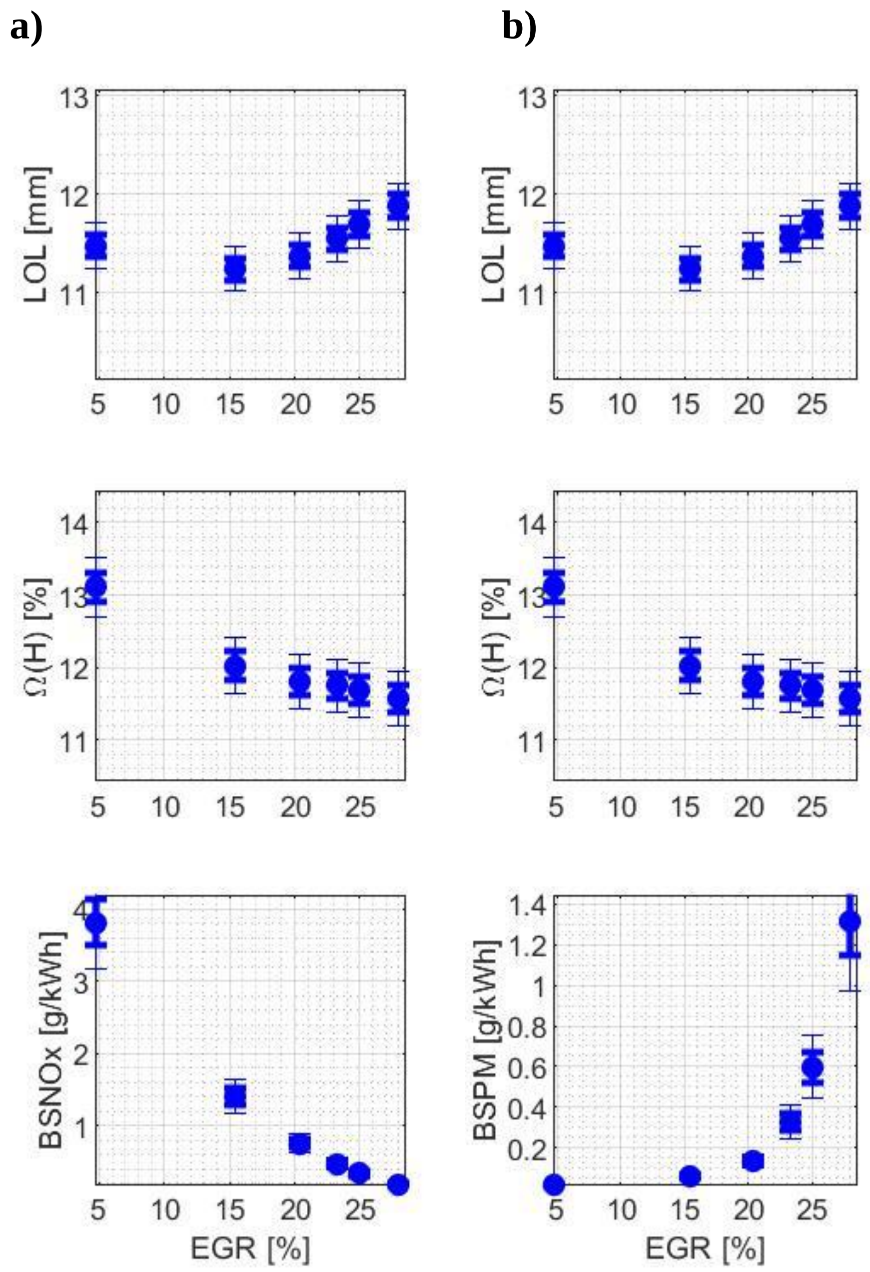

Figure 3.61. Lift-off length and oxygen ratio at the lift-off length during EGR sweep of the baseline diesel at MM6 with the trend of a) BSNOx, b) BSPM

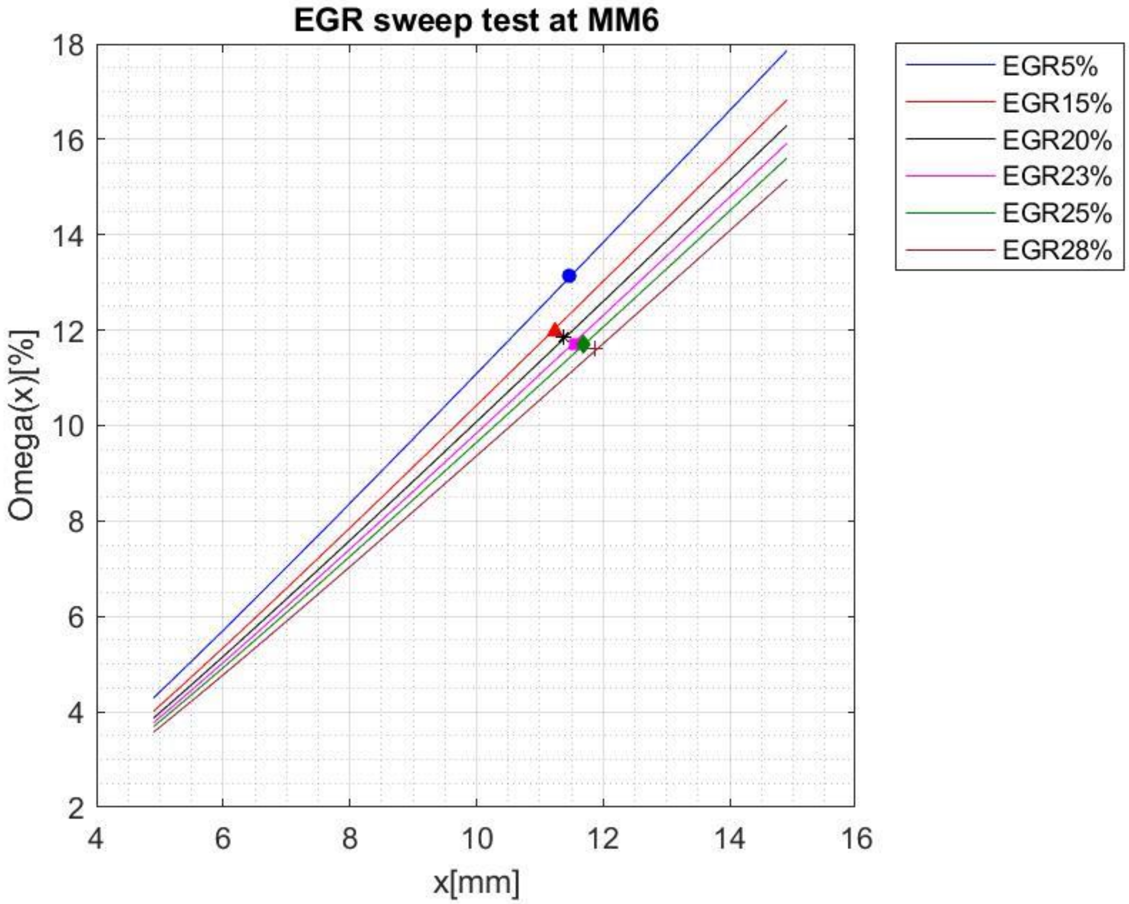

Figure 3.62. Oxygen ratio depending on the axial coordinate (x) by different EGR rate. The markers represent the lift-off length at each EGR rate condition.

Figure 3.63a presents the impact of rail pressure (RP) on BFE (top-left), BSNOx (middle-left), BSPM (bottom-left), CNL (top-right), BSTHC (middle-right), BSCO (bottom-right) at MM6 for the baseline diesel. Figure 3.63b presents the trend of the BFE (top-left), BSPM (middle-left), $BSCO_2$ (bottom-left), BSTHC (top-right), BSCO (middle-right) and CNL (bottom-right) by BSNOx during the RP sweep at MM6 with the baseline fuel.

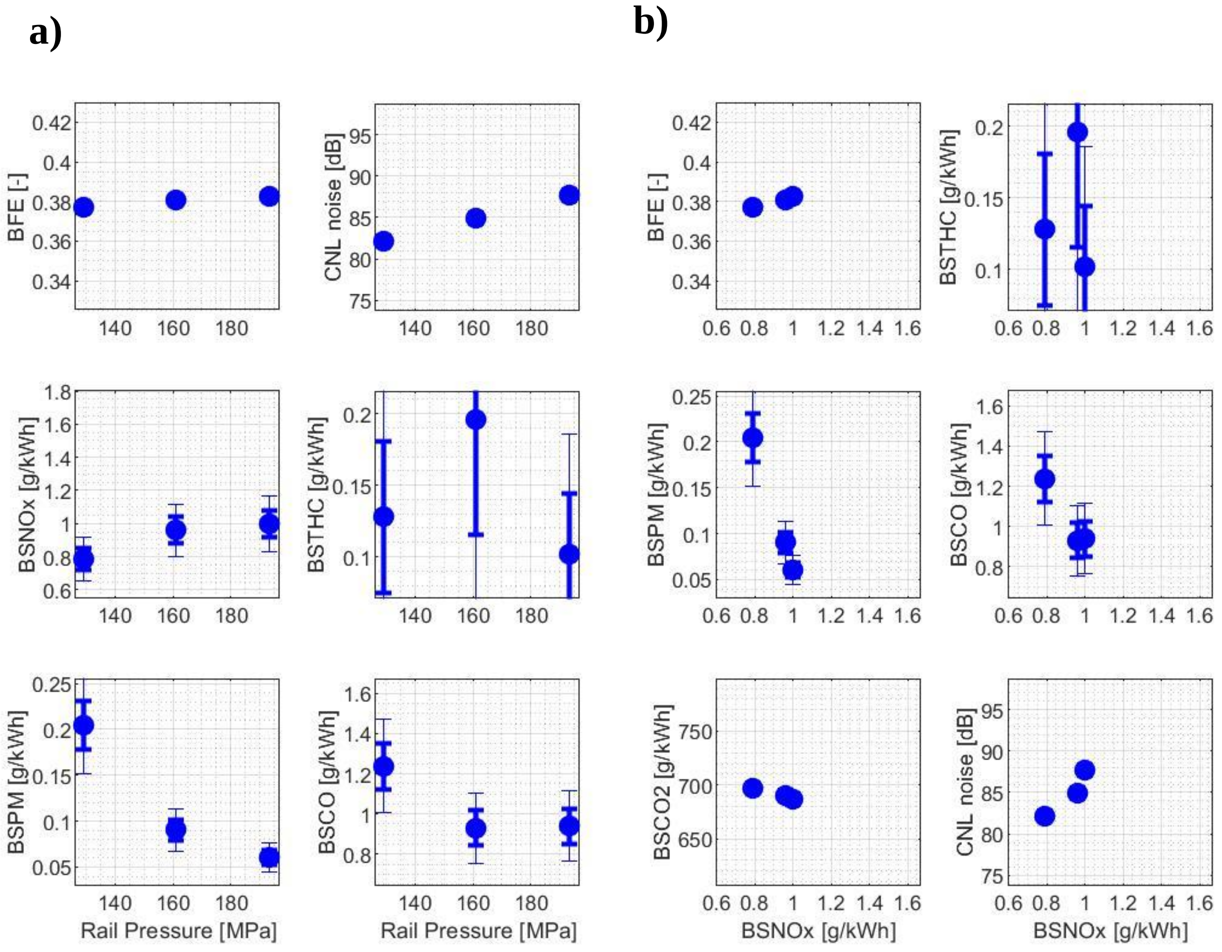

Figure 3.63. BFE, BS emissions, and CNL during rail pressure (RP) sweep of the baseline diesel at MM6 as a function of a) RP, and b) BSNOx

The impact of rail pressure (RP) on BFE, BSNOx, and BSPM observed at MM6 was the same as that of MM3 with the same underlying physics. Thus, in here, the values of the output parameters will briefly be presented with Figures 3.64-3.65. Brake fuel conversion efficiency (BFE) increases from 37.7% at low rail pressure (LRP) to 38.3% at high rail pressure (HRP). This increase in BFE with increasing rail pressure is due to the increase in IFEg (Figure 3.64a, second-to-the-top) caused by the advance in peak cylinder temperature timing (Figure 3.64b, second-to-the-top).

BSNOx increases 0.79g/kWh at LRP to 0.96g/kWh at DRP, then to 1.0g/kWh at HRP. The increase in BSNOx with increasing rail pressure can be mainly attributed to the advance in peak cylinder temperature timing, and the increase in oxygen ratio at the lift-off length (Figure 3.65, middle) caused by the increase in fuel jet velocity. BSPM decreases form 0.204g/kWh at LRP to 0.090g/kWh at DRP, then to 0.06g/kWh at HRP. Given the constant intake O_2 concentration for different rail pressures, the decrease in BSPM can be attributed to the increase in oxygen ratio at the lift-off length.

Combustion noise level (CNL) increases from 82.21dB at LRP to 84.92dB at DRP, then to 87.69dB at HRP. BSTHC emissions from the baseline during the rail pressure sweep at MM6 were at negligible level for all of the imposed rail pressure conditions. BSCO decreased from 1.24g/kWh at LRP to 0.93g/kWh at DRP and HRP.

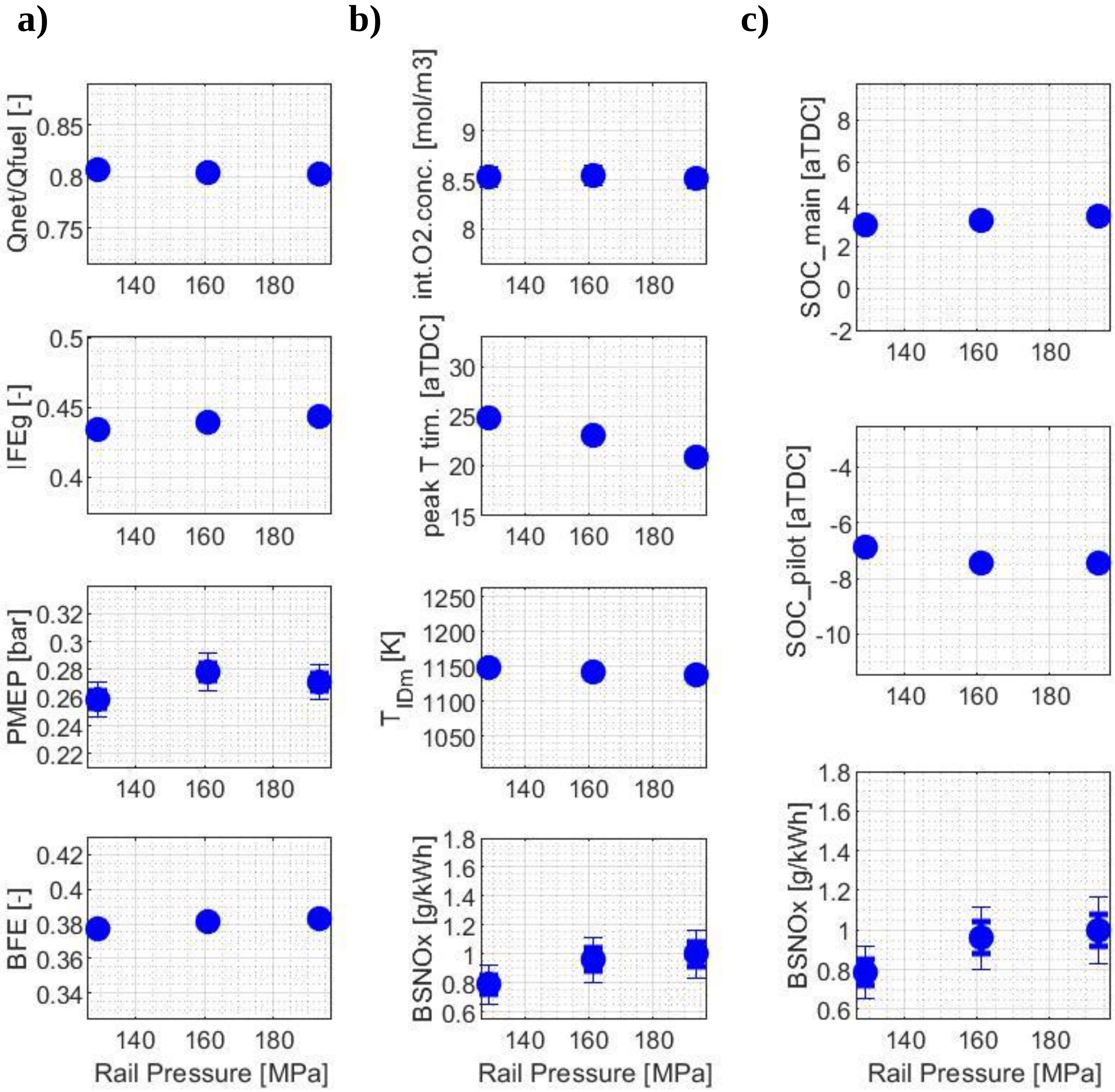

Figure 3.64. The parameters affecting a) BFE, b) and c) BSNOx during rail pressure (RP) sweep of the baseline diesel at MM6

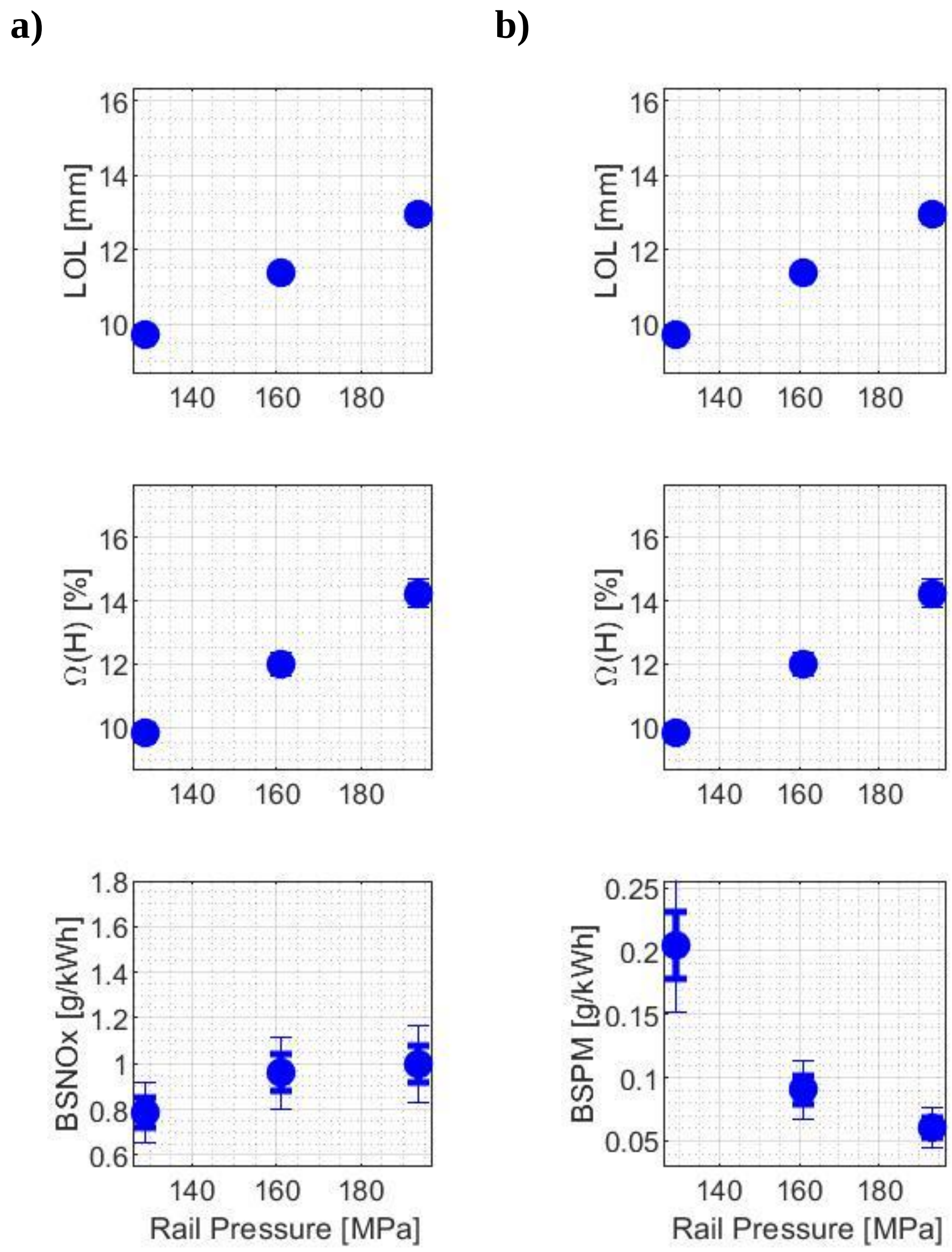

Figure 3.65. Lift-off length and oxygen ratio at the lift-off length with the trend of a) BSNOx and b) BSPM during the rail pressure (RP) sweep of the baseline diesel at MM6

3.3.2 Unintended Shifts in the ECU Setting with B20

The unintended shift in ECU input parameters when B20 is applied with increased pedal angle to compensate for the lower LHV is presented in Figure 3.66. It shows the change in EGR rate (top-left), rail pressure (RP, middle-left), pilot 1 injection quantity (PIQ1, bottom-left), boost pressure (BP, top-right), main injection timing (MIT, middle-right), and relative distance between main injection timing and pilot 1 injection timing (RPIT1, bottom-right) for each MM point. At MM1, the change in pilot 2 injection quantity (PIQ2) and relative distance between pilot 1 injection timing and pilot 2 injection timing (RPIT2) are also measured, but, there was no change in the ECU setting for those two parameters.

We can see that, for all MM points, there is no significant change in MIT, PIQ1, and RPIT1 while there are some changes in other input parameters such as EGR, BP, and RP. In terms of EGR rate, MM3 had highest increase (absolute 4.1%) in EGR rate while most of the other MM points also showed moderate increase (absolute 0.8-2.1%) in EGR rate. MM6 was the only mini-map point where EGR rate was decreased (absolute 0.3%).

Oppositely, boost pressure is decreased for most of the MM points. MM6 experienced the highest decrease in its boost pressure setting (41hPa) while other MM points also experienced moderate to minor degree of decrease (0.6-23.5hPa) in their boost pressure settings. MM1 was the only point that experienced the increase in boost pressure setting (6.2hPa).

Rail pressure setting is increased for most of the MM points, as well. MM6 experienced the highest increase in the rail pressure setting (47.9bar) while medium load points (i.e., MM3, 4 and 5) also experienced some increase in the rail pressure setting (8-28bar). MM1 and 2 did not experience any appreciable change in its rail pressure setting.

Therefore, in general, with the application of B20, the boost pressure (BP) is decreased while the EGR rate and rail pressure (RP) are increased for most MM points. Thus, it is expected that the potential increase in NOx due to the impact of biodiesel might be countered off by the unintended increase in EGR and decrease in BP. This is very different from the potential change in ECU settings reported in Kurtz et al.[22] It is reported that, in a light-duty 0.8L single-cylinder CI engine, the increase in pedal demand with the application of canola-based B100 can decrease the EGR rate, increase the boost pressure, and increase the rail pressure. While the increase in rail pressure happened the same in the current study, the change in BP and EGR in ECU settings with biodiesel applications were the opposite. This could be because of differences in the test engines between the previous study and the current study, and also because of the different response in the ECU for the different blend levels of biodiesel (B20 vs. B100).

However, regardless of the fortunate decrease in BSNOx thanks to the unintended increase in EGR setting and decrease in boost pressure setting, it is still unclear if the BFE from the unintendedly shifted ECU settings is the “best” BFE we can get out of B20. Thus, the comparison between the baseline fuel and B20 at the default ECU calibration with fixed pedal angle is still necessary to investigate the fair impact of B20 and to re-calibrate the ECU for the best BFE.

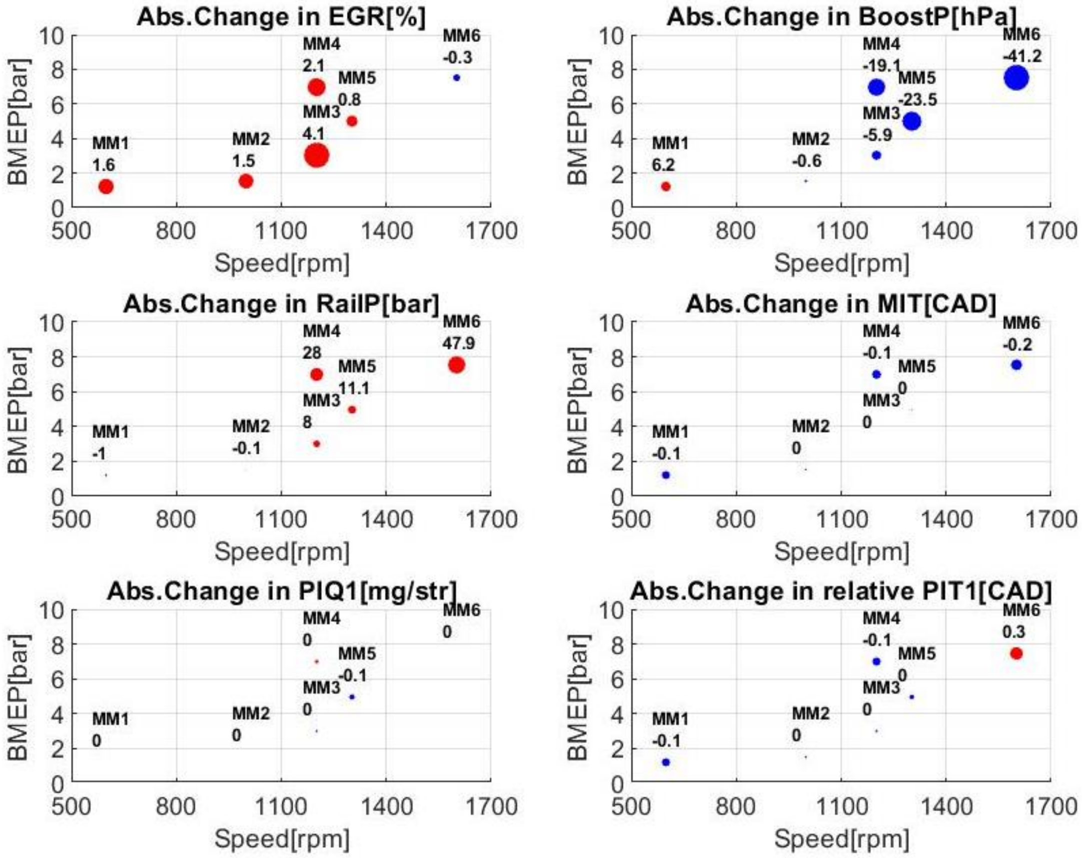

Figure 3.66. The change in the ECU input parameters with B20 with increased pedal angle to compensate for lower LHV. Blue: decrease (advance for MIT), Red: increase (retarding for MIT).

3.3.3 B20 Test Results with Default ECU Calibration

Before discussing the results at each mini-map point, the general trends will be summarized here. At idling (MM1) and medium-to-high load conditions (MM4 and MM5), the fuel properties of B20 did not have any statistically meaningful impact on any of the output parameters of the interest (i.e., BFE, BSNOx, BSPM, etc.). However, at low-to-medium load conditions (MM2, MM3) and a high-load (MM6) condition, increased BSNOx (10-25%) and decreased BSPM (0-10%) are observed for B20 while still no statistically meaningful difference in BFE is observed between the two fuels.

First, regarding BFE, many previous studies report the consistent results with the current observation when biodiesel is compared with diesel at fixed ECU settings. Ye et al.[24,50] report that the BFEs for soy-derived B40 and petroleum-based diesel do not have statistically meaningful difference when important ECU parameters (i.e., EGR rate, boost pressure, rail pressure, main injection timing, etc.) are fixed for the two fuels while compensating for the lower LHV of biodiesel by increasing the fuel injection duration. Kurtz et al.[22] also showed that canola-derived B100 did not have statistically meaningful difference in BFE from the petroleum-based diesel when ECU settings are fixed the same for the two fuels. Based on the current observation, the consistent BFE between B20 and the baseline diesel was due to the negligible difference in ignition delay and pumping loss, which will be presented in detail for each mini-map point in the following sections.

Second, regarding BSNOx and BSPM emissions, previous biodiesel studies report different results from the current study. The previous studies usually report increased NOx and decreased PM emissions for biodiesel for most of the engine operating conditions if the ECU settings are fixed for the two fuels. For example, Kurtz et al.[22] reports increased NOx emissions with decreased PM emissions for the canola-derived B100 at the default ECU calibration, which is consistent with other higher blends biodiesel studies[23-25,35,39,42]. However, since most of these results are taken with higher blends such as B100, the currently observed consistent NOx and PM emissions for the two fuels (B20 vs. petroleum-based diesel) at certain operating conditions (i.e., MM1, MM4, and MM5) may imply that the degree of fuel oxygen content in B20 is not high enough to induce different NOx and PM emissions from its application at certain engine operating conditions. Based on the current observation, the mini-map points showing consistent NOx and PM emissions for the two fuels generally had similar oxygen ratio at the lift-off length while the other mini-map points did not. The importance of oxygen ratio at the lift-off length on the NOx and PM emissions at each mini-map point will be discussed in detail in the following sections with other important parameters affecting these emissions.

3.3.3.1 MM1

At MM1, there was no statistically meaningful impact of B20 on brake fuel conversion efficiency (BFE), brake specific (BS) emissions, and combustion noise level (CNL) during all 4 different single parameter sweep tests. For most imposed conditions, the difference in the output parameters between the two fuels was smaller than one standard deviation of the repeated measurement meaning that the difference is not statistically meaningful. The general trends of the output parameters of B20 by each input parameter was identical to those observed in the baseline test. Here, the comparison between the baseline fuel and B20 at default ECU calibration during the main injection timing (MIT) sweep is presented.

Figure 3.67a presents the impact of main injection timing (MIT) on BFE (top-left), BSNOx (middle-left), BSPM (bottom-left), CNL (top-right), BSTHC (middle-right), BSCO (bottom-right) at MM1 for the baseline diesel (blue filled dots) and B20 (red empty rectangles) at default ECU calibration. Figure 3.67b presents the trend of the BFE (top-left), BSPM (middle-left), BSCO$_2$ (bottom-left), BSTHC (top-right), BSCO (middle-right) and CNL (bottom-right) by BSNOx during the MIT sweep of the baseline fuel and B20 at default calibration at MM1.

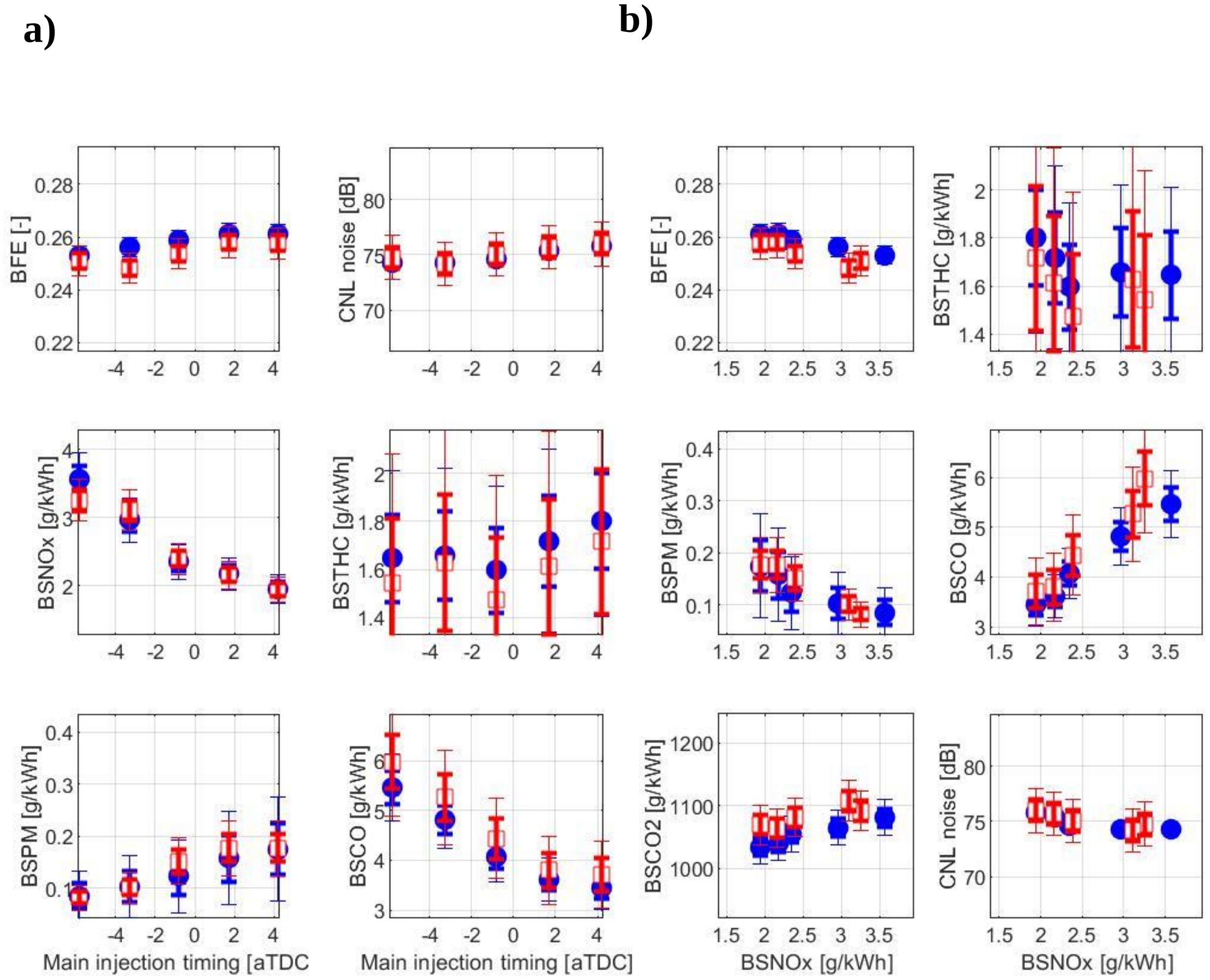

Figure 3.67. BFE, BS emissions, and CNL during the main injection timing (MIT) sweep at MM1 (●: Diesel, □: B20) with the default ECU calibration as a function of a) MIT, b) BSNOx

First, BFE from B20 at the default calibration increases from 25% at 5 degrees advanced injection timing to 25.4% at the default timing, then to 25.8% at 5 degrees retarded injection timing. Except for the 2.5 degrees advanced injection timing which had absolute 1% decrease in BFE for B20, the BFE for B20 at default calibration did not have statistically meaningful difference from the baseline result. In general, the BFE of B20 at default calibration was about absolute 0.25 - 0.5% lower than that of the baseline fuel, but the standard deviation from the repeated measurement was about 0.5%. This means that there is less than 68% probability that the BFE of the baseline fuel will be measured to be higher than B20 when another set of data is obtained.

Second, BSNOx from B20 at the default calibration decreases from 3.26g/kWh at 5 degrees advanced injection timing to 2.40g/kWh at the default timing, then to 1.94g/kWh at 5 degrees retarded injection timing. Like BFE, BSNOx from B20 at MM1 also does not have statistically meaningful difference from the baseline fuel.

Third, BSPM from B20 at default calibration increases from 0.082g/kWh at 5 degrees advanced injection timing to 0.152g/kWh at the default timing, then to 0.177g/kWh at 5 degrees retarded timing. Again, there was no statistically meaningful difference between the BSPM from B20 and diesel at default ECU calibration.

Combustion noise level (CNL), BSTHC, and BSCO from B20 at default calibration are presented in the top, middle, and bottom-right plots in Figure 3.67a. All three output parameters also did not show meaningful statistical difference between the two fuels.

3.3.3.2 MM2

The key points of the impact of B20 on BFE, BS emissions, and CNL can be summarized as follows. First, BFE of B20 with default ECU calibration does not have statistically meaningful difference from that of the baseline fuel. The PMEP remained same for the two fuels, and IFEg also remained same for the two fuels due to the similar combustion phasing.

Second, BSNOx emission for B20 is increased from that of the baseline fuel for all of the imposed conditions during the 4 different single parameters sweeps. The degree of the increase in BSNOx due to B20 varied depending on the imposed conditions, but in general, there was 15-

20% increase in BSNOx for B20. The main contributors for the increase in BSNOx were the increase in intake O_2 concentration and the increase in oxygen ratio at the lift-off length caused by the fuel oxygen content in B20 and the lower charge gas temperature.

Third, BSPM emission from B20 is decreased from that of the baseline fuel for all of the imposed conditions during 4 different sweep tests. The degree of the decrease in BSPM varied for different imposed conditions, but in general, BSPM decreased about 20%. The decrease in BSPM for B20 can be attributed to the increase in intake O_2 concentration and the increase in oxygen ratio at the lift-off length. In other words, we could see the PM-NOx trade-off due to the B20's impact at MM2.

The general impact of B20 on other brake specific (BS) emissions and combustion noise level (CNL) at MM2 is as follows. BSTHC and BSCO emissions decreased for B20 at most of the imposed conditions, but CNL increased for B20 at most imposed conditions. The degree of decrease in BSTHC and BSCO for B20 varied for different imposed conditions, but they both decreased about 10-20% in general. Combustion noise level (CNL) generally increased about 0.5dB when B20 is applied as compared to the diesel baseline result.

More detailed investigation on the impact of B20 on BFE, BSNOx, and BSPM will be presented in the following paragraphs. The impact of B20 on output parameters during the four different parameter sweeps is similar to each different sweep test, and the main injection timing sweep at MM2 shows the impact of B20 on BFE, BS emissions, and CNL very well. Thus, the experimental results of the B20 main injection timing (MIT) sweep with the default ECU calibration at MM2 are presented in Figures 3.68, 3.69 and 3.70.

Figure 3.68a presents the impact of main injection timing (MIT) on BFE (top-left), BSNOx (middle-left), BSPM (bottom-left), CNL (top-right), BSTHC (middle-right), BSCO (bottom-right) at MM2 for the baseline diesel (blue filled dots) and B20 (red empty rectangles) at default ECU calibration. Figure 3.68b presents the trend of the BFE (top-left), BSPM (middle-left), BSCO$_2$ (bottom-left), BSTHC (top-right), BSCO (middle-right) and CNL (bottom-right) by BSNOx during the MIT sweep of the baseline and B20 at default calibration at MM2.

First, BFE of B20 during main injection timing (MIT) sweep at MM2 remained same as that of the baseline fuel. It decreased from 27.4% at 5 degrees advanced injection timing (5A) to 26.8% at 5 degrees retarded injection timing (5R). These values have no statistically meaningful difference from the baseline fuel. Figure 3.69a shows the reason for this consistent BFEs for the two fuels. Gross indicated fuel conversion efficiency (IFEg, Figure 3.69a, second-to-the-top) of B20 is 42.5% at 5 degrees advanced injection timing, and 41.0% at 5 degrees retarded injection timing, which has no statistically meaningful difference from the baseline fuel. Also, although the mean value of the PMEP (Figure 3.69a, third-to-the-top) for repeated measurements of B20 is lower than the baseline fuel, the difference in the mean is smaller than the standard deviation of the repeated measurements. Thus, PMEP for the two fuels also does not have statistically meaningful difference. Due to the consistent IFEg and PMEP, BFE of B20 remained the same as diesel.

Second, BSNOx of B20 during main injection timing (MIT) sweep is generally higher than the baseline fuel. It decreases from 1.96g/kWh at 5 degrees advanced injection timing (5A) to 1.09g/kWh at 5 degrees retarded injection timing (5R). Although there are some specific injection timing conditions where the BSNOx difference in B20 and the baseline is not statistically meaningful (e.g., 2.5 degrees advanced injection timing), BSNOx emissions from B20 is higher than diesel by about 15% at most of the other imposed conditions. The increase in

BSNOx at MM2 can be attributed to two factors: i) the increase in intake O_2 concentration; ii) and the increase in oxygen ratio at the lift-off length.

Figure 3.69b and 3.69c show the parameters affecting BSNOx during the main injection timing (MIT) sweep at MM2. Intake O_2 concentration (Figure 69b, top) for B20 is always about 2% higher than diesel. This is one of the peculiar observations made only at MM2. At other mini-map points, the difference in intake O_2 concentration between B20 and the baseline fuel was simply too small to call it statistically meaningful. Higher intake O_2 concentration allows more oxygen available in the overall charge gas, thus providing higher O_2 concentration in the vicinity of the diffusion flame. This is one of the two main reasons of the BSNOx increase in B20 applications at MM2. Another factor for BSNOx increase for B20 at MM2 is the increased oxygen ratio at the lift-off length.

Figure 3.70 shows the lift-off length (top) and oxygen ratio at the lift-off length (middle) during the main injection timing (MIT) sweep at MM2. The lift-off length of B20 is estimated to be longer than diesel about 0.3-1mm depending on different injection timings thanks to the decrease in charge gas temperature (Figure 3.69b, third-to-the-top) and increase in fuel oxygen content. This increase in lift-off length resulted in the increase in oxygen ratio (Figure 3.70a, middle). The oxygen ratio at the lift-off length of B20 is about absolute 1.0-1.5% higher than diesel. This much increase in oxygen ratio is also peculiar feature only observed at MM2. At other mini-map points, oxygen ratio at the lift-off length either increased less than 1% or just did not have statistically meaningful difference from the baseline fuel. The more apparent increase in oxygen ratio at the lift-off length at MM2 which is the low load point with high EGR rate (default EGR rate at 41%) than MMs 3-6 re-confirms what has been reported in Mueller et al.:

the impact of the local physics of the fuel-rich premixed auto-ignition zone is more apparent at lower loads than higher loads.[25]

Third, due to the increase in oxygen ratio at the lift-off length and overall intake O_2 concentration for B20, BSPM emission decreased for B20 from the baseline fuel. BSPM emission from B20 is 0.099g/kWh at 5 degrees advanced injection timing (5A), 0.143g/kWh at the default injection timing (DF), and 0.086g/kWh at 5 degrees retarded injection timing (5R). Compared to the baseline result (i.e., 0.127g/kWh at 5A, 0.161g/kWh at DF, 0.107g/kWh at 5R), the BSPM emission decreased by 20-25% depending on the injection timings imposed.

Lastly, the values of other brake specific (BS) emissions and combustion noise level (CNL) from B20 during the main injection timing (MIT) sweep at MM2 will be briefly stated here. BSTHC for B20 generally increases as the injection timing is retarded. It was 1.03g/kWh at 5 degrees advanced injection timing (5A) and was 1.47g/kWh at 5 degrees retarded injection timing (5R) for B20, which is about 10-20% decrease as compared to the baseline fuel. BSCO for B20 also generally increased with retarded injection timing. BSCO for B20 was 3.92g/kWh at 5A, and 5.1g/kWh at 5R. This was about 10-20% decrease from the baseline result. Combustion noise level (CNL) for B20 was 78.6dB at 5A, 79.0dB at DF, and 78.07dB at 5R.

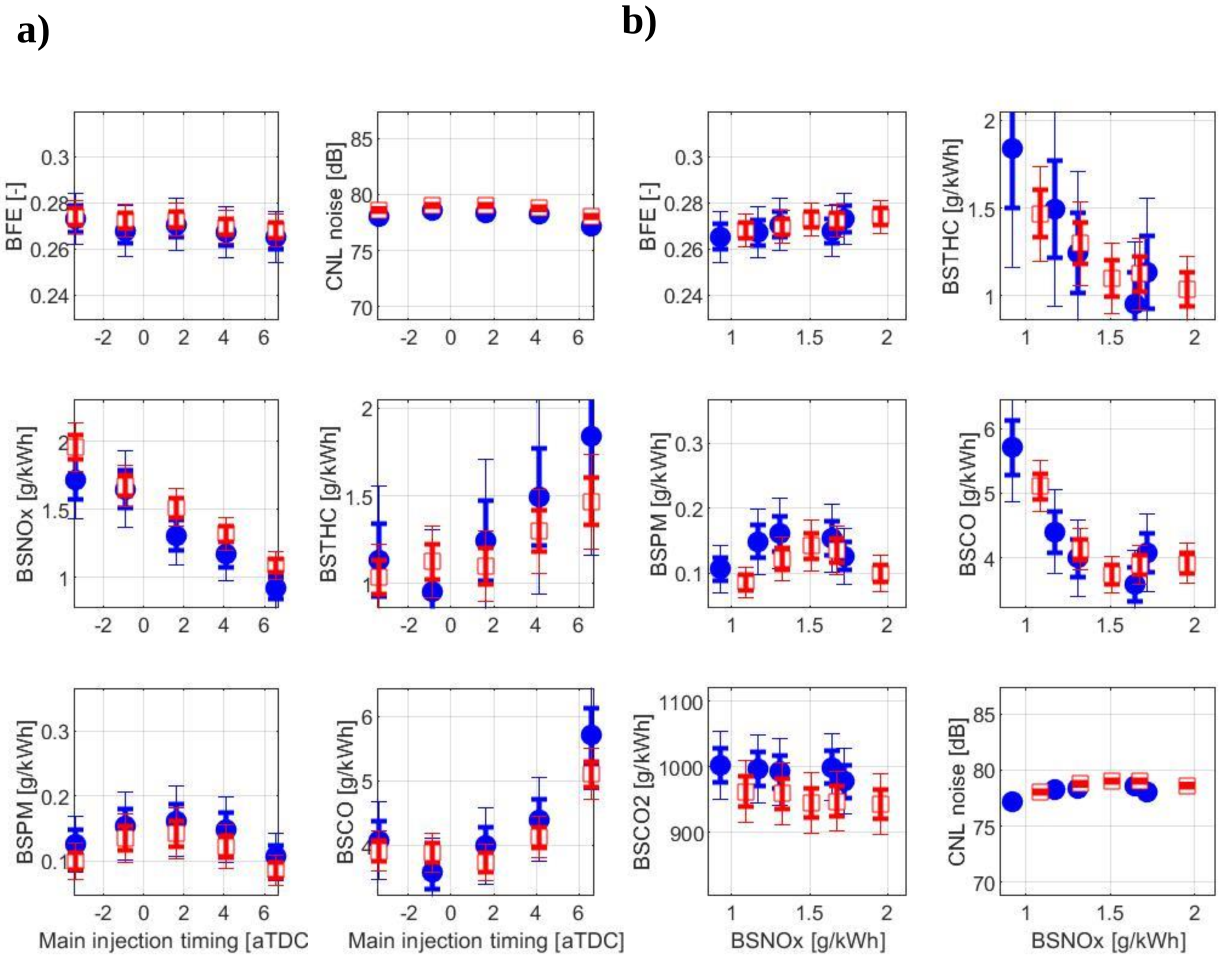

Figure 3.68. BFE, BS emissions, and CNL during the main injection timing (MIT) sweep at MM2 (●: Diesel, □: B20) with the default ECU calibration as a function of a) MIT and b) BSNOx

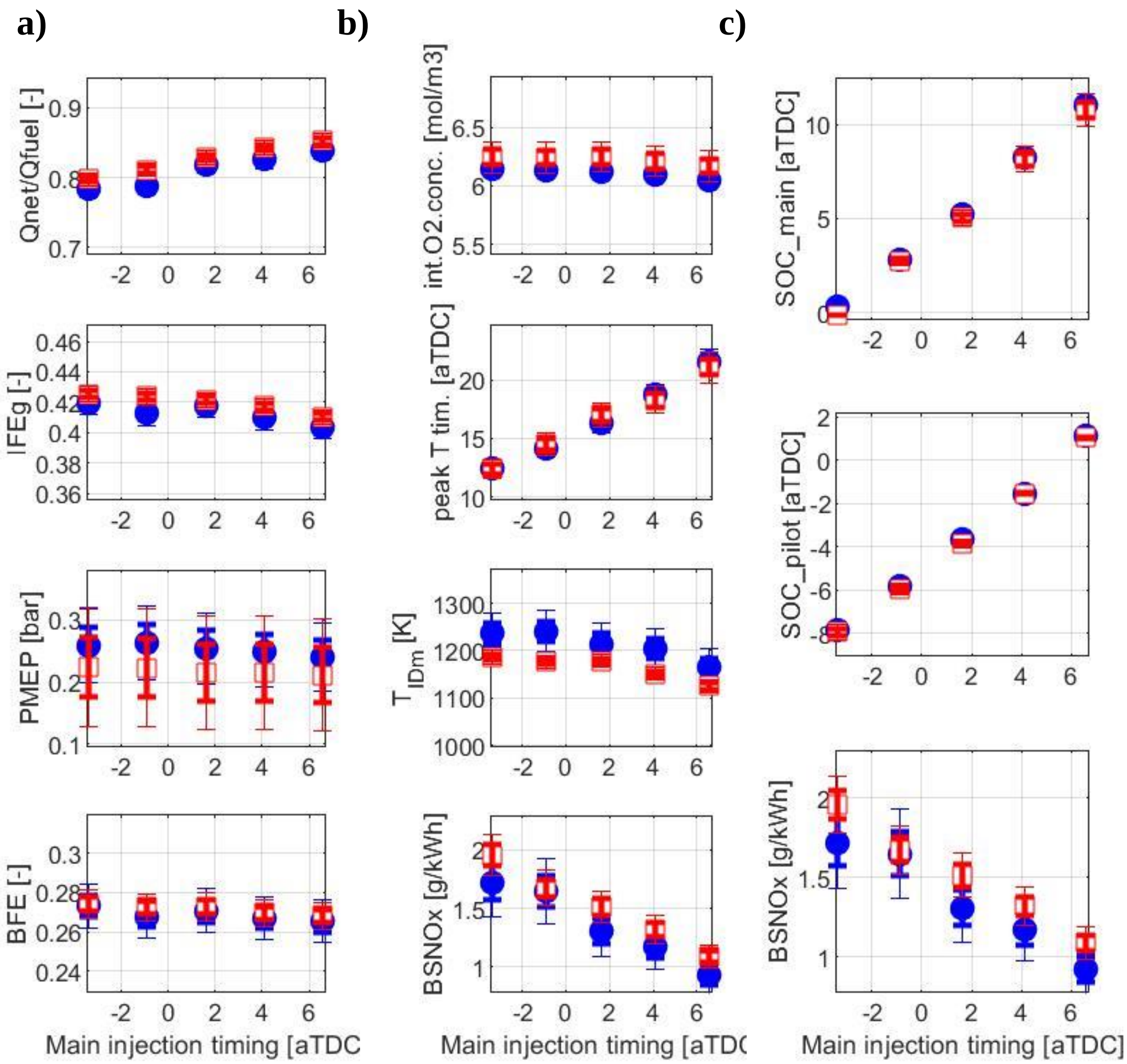

Figure 3.69. The parameters affecting a) BFE, b) and c) BSNOx during the main injection timing (MIT) sweep at MM2 (●: Diesel, □: B20) with the default ECU calibration

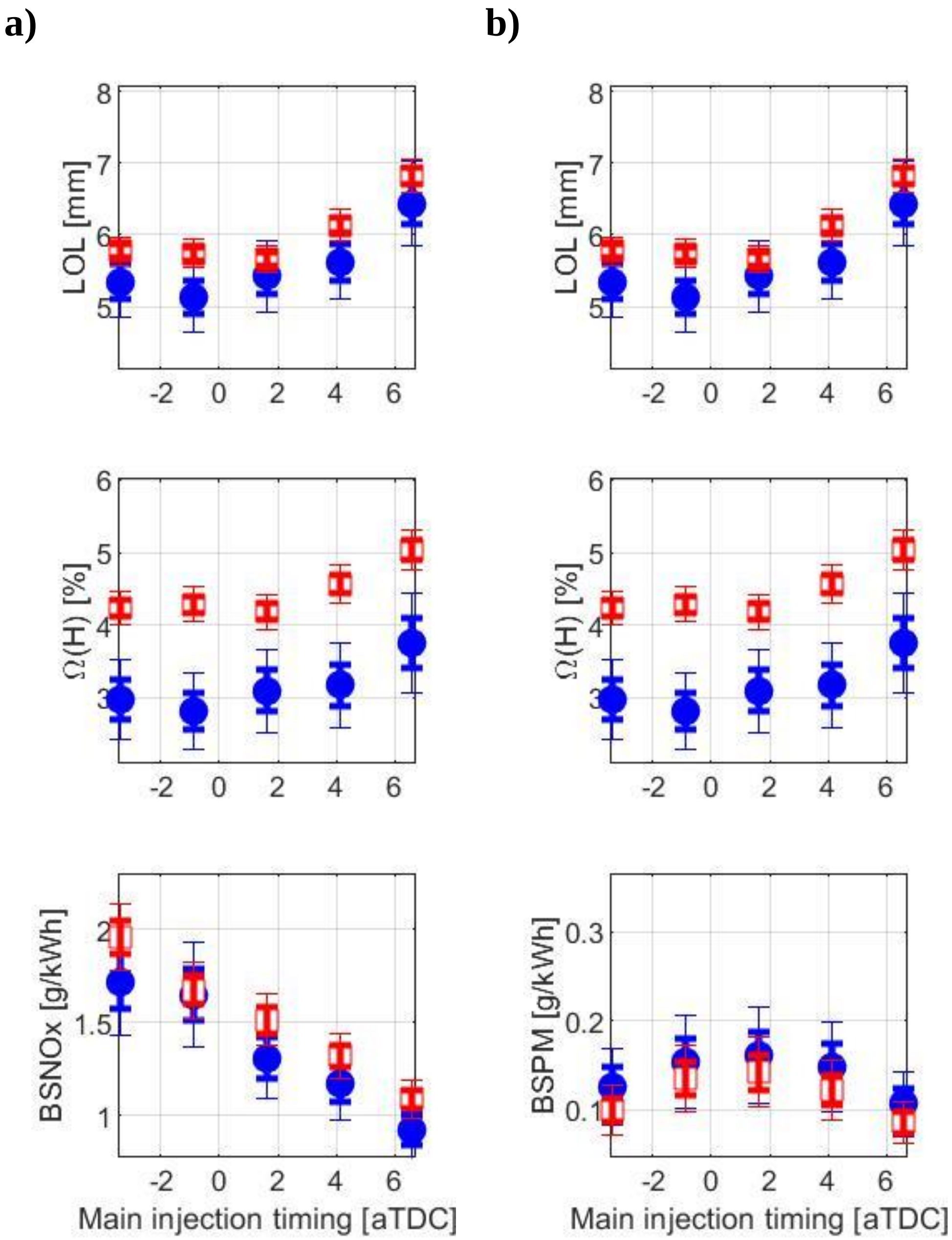

Figure 3.70. Lift-off length and oxygen ratio at the lift-off length (●: Diesel, □: B20) during the main injection timing (MIT) sweep at MM2 with the trend of a) BSNOx and b) BSPM

3.3.3.3 MM3

The key points of the impact of B20 on brake fuel conversion efficiency (BFE), brake specific (BS) emissions, and combustion noise level (CNL) at MM3 with the default ECU calibration can be summarized as follows. First, BFE for B20 and the baseline fuel does not have statistically meaningful difference at all of the imposed conditions during the 4 different single parameter sweeps. The underlying physics leading to the same BFE for the two fuels was the same for 4 different single parameter sweeps. It is because B20 did not show any statistically meaningful difference in PMEP while IFEg also remained same for the two fuels. There was no statistically meaningful difference in ignition delay for the two fuels at MM3, which led to the consistent combustion phasing for the given main injection timing (MIT). This eventually led to the same IFEg for the two fuels.

Second, BSNOx for B20 with the default ECU calibration increased about 10-20% as compared to the baseline fuel while the degree of the increase varied depending on the specific imposed conditions. However, the underlying physics that led to the increase in BSNOx for B20 was the same for all of the imposed conditions during 4 different single parameter sweeps. The increase in BSNOx was mainly due to the increase in oxygen ratio at the lift-off length. There was about absolute 0.3-1.0% increase in oxygen ratio at the lift-off length for B20 as compared to the baseline diesel, and this increased the NOx generation from the fuel-rich premixed auto-ignition zone.

Third, BSPM for B20 with the default calibration did not have statistically meaningful difference from the baseline fuel for all of the imposed conditions during the 4 single parameter sweeps. Although the increase of the oxygen ratio at lift-off length did increase BSNOx for B20 at MM3, the degree of the increase in oxygen ratio at the lift-off length was not enough to decrease the BSPM for B20 at MM3.

Lastly, BSTHC and BSCO emissions for B20 with default ECU calibration, in general, decreased 10-20% from the baseline fuel while CNL increased up to 1dB for B20 at default calibration from the baseline fuel.

Thus, B20 without re-calibration in the ECU did not meet the BSNOx and CNL bound criteria while BFE is not improved at all. Although BSPM is kept the same as the baseline fuel and there was some decrease in secondary BS emissions such as BSTHC and BSCO, the excessive BSNOx emission from B20 necessitated the ECU re-calibrations at MM3 for B20. The following paragraphs describe the impact of B20 with default calibration at MM3 in a more detail. Since the impact of B20 and its underlying physics apply the same for 4 different single parameter sweeps, comparison of B20 and the baseline fuel at default calibration during the main injection timing (MIT) sweep is selected to be presented in this study.

Figure 3.71a presents the impact of main injection timing (MIT) on BFE (top-left), BSNOx (middle-left), BSPM (bottom-left), CNL (top-right), BSTHC (middle-right), BSCO (bottom-right) at MM3 for the baseline diesel (blue filled dots) and B20 (red empty rectangles) at the default ECU calibration. Figure 3.71b presents the trend of the BFE (top-left), BSPM (middle-left), BSCO$_2$ (bottom-left), BSTHC (top-right), BSCO (middle-right) and CNL (bottom-right) by BSNOx during the MIT sweep of the baseline fuel and B20 at default calibration at MM3.

First, BFE for B20 with default ECU calibration remained same as the baseline fuel at each main injection timing (MIT) condition. Brake fuel conversion efficiency (BFE) for B20 decreases from 34.3% at 5 degrees advanced injection timing (5A) to 33.6% at the default injection timing (DF), then to 32.4% at 5 degrees retarded injection timing (5R). At the same injection timings, BFEs for the baseline fuel are all within the plus and minus one standard deviation interval as compared to the B20 measurements, which means that any differences in BFEs for the two fuels are not statistically meaningful.

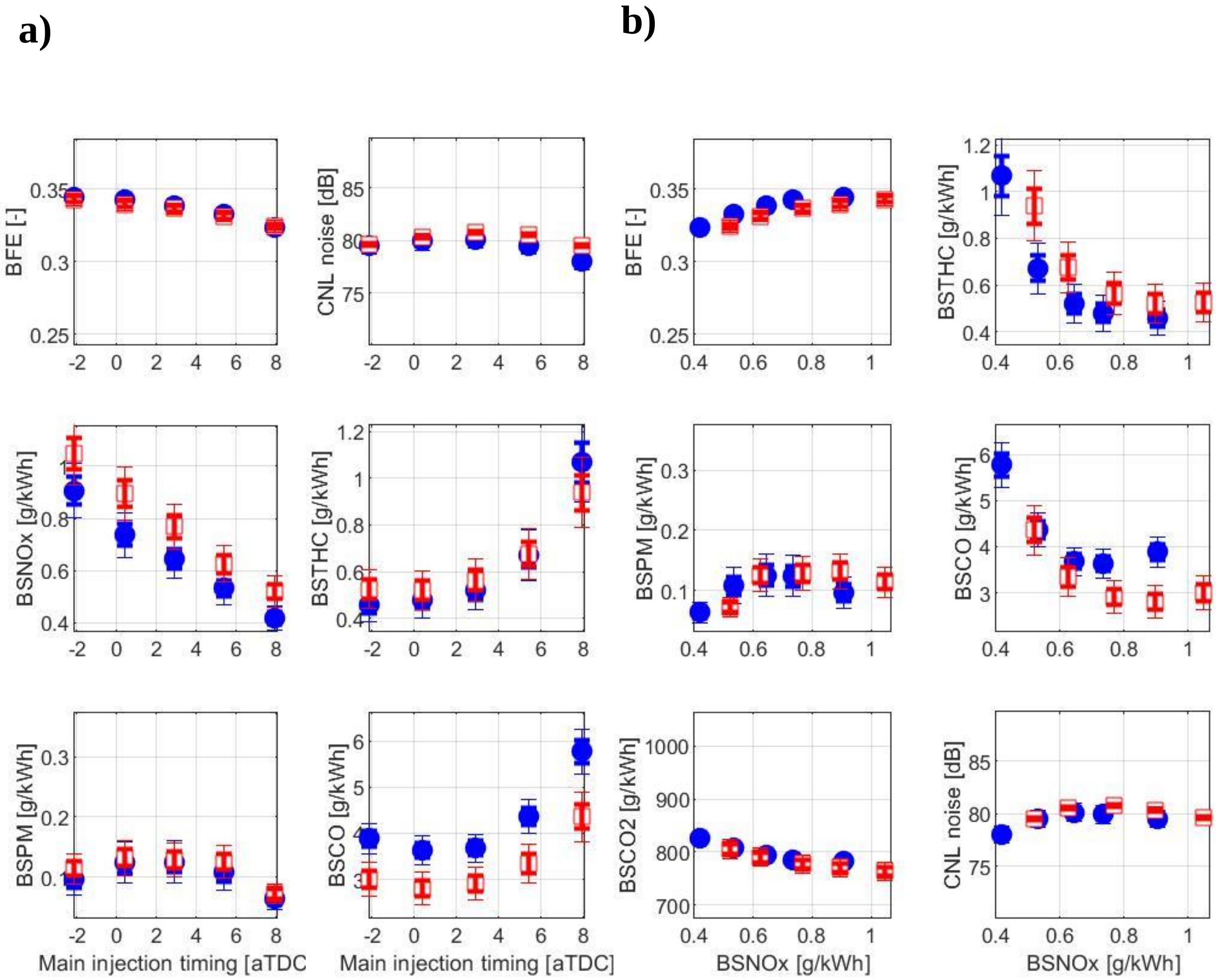

Figure 3.71. BFE, BS emissions, and CNL during the main injection timing (MIT) sweep at MM3 (●: Diesel, □: B20) with default ECU calibration as a function of a) MIT, b) BSNOx.

The consistent BFE for the two fuels is due to the consistent PMEP and IFEg at each injection timing condition. Figure 3.72a presents the fundamental parameters that can affect BFE during the main injection timing (MIT) sweep at MM3 for the two fuels. As shown in the second to the top plot, IFEg for B20 with default calibration remains same as the baseline fuel at each of the injection timing imposed. Pump mean effective pressure (PMEP) for B20 with default calibration (Figure 3.72a, third to the top plot) also remains same as the baseline fuel, thus resulting in the same BFE for the two fuels.

Second, BSNOx emission is increased for B20 with the default ECU calibration. As shown in the middle-left plot in Figure 3.71a, BSNOx from B20 decreases from 1.04g/kWh at 5 degrees advanced injection timing (5A) to 0.77g/kWh at the default injection timing (DF), then to 0.52g/kWh at 5 degrees retarded injection timing (5R) condition. At these injection timings, BSNOx from the baseline fuel is 0.91g/kWh at 5A, 0.64g/kWh at DF, and 0.42g/kWh at 5R condition. Thus, there was about 13-19% increase in BSNOx depending on the main injection timing when B20 is applied with the default ECU calibration. The cause of the increase in BSNOx is the increase in oxygen ratio at the lift-off length.

Figure 3.73a shows the lift-off length (top) and the oxygen ratio at the lift-off length (middle) during the main injection timing (MIT) sweep at MM3 for the two fuels at the default ECU calibration with the trend of BSNOx (bottom). The oxygen ratio at the lift-off length for B20 is absolute 0.5-1.0% higher than the baseline fuel due to the fuel oxygen content in B20. This increase in oxygen ratio at the lift-off length allows more oxygen available in the fuel-rich premixed auto-ignition zone, thus resulting in more NOx generation.

There are some other factors that could have potentially affected BSNOx from B20: intake charge O_2 concentration (Figure 3.72b, top), peak cylinder temperature timing (Figure

3.72b, second to the top) and charge gas temperature during the main ignition delay (Figure 3.72b, third to the top). However, all these factors remained same for the two fuels, eliminating the possibility of BSNOx difference between the two fuels due to these factors.

Third, BSPM emission from B20 with default ECU calibration did not have statistically meaningful difference from the baseline fuel. This is very important point to note because BSNOx emission is increased for B20 due to the increased oxygen ratio at the lift-off length. The increase in BSNOx emission without any statistically meaningful decrease in BSPM means that the degree of increase in oxygen ratio at the lift-off length was not enough to achieve meaningful reduction in PM while it was able to increase NOx. Thus, it is worth to run the ECU re-calibration at MM3 to avoid this un-optimized ECU settings from the aspect of NOx parity BSPM emission.

Lastly, CNL (Figure 3.71a, top-right), BSTHC (Figure 3.71a, middle-right), and BSCO (Figure 3.71a, bottom-right) from B20 with the default ECU calibration are as follows. BSCO emissions decreased about 20-25% for B20 while BSTHC from B20 did not have statistically meaningful difference from the baseline fuel. Combustion noise level (CNL) was increased for B20, and the degree of increase was about 1dB.

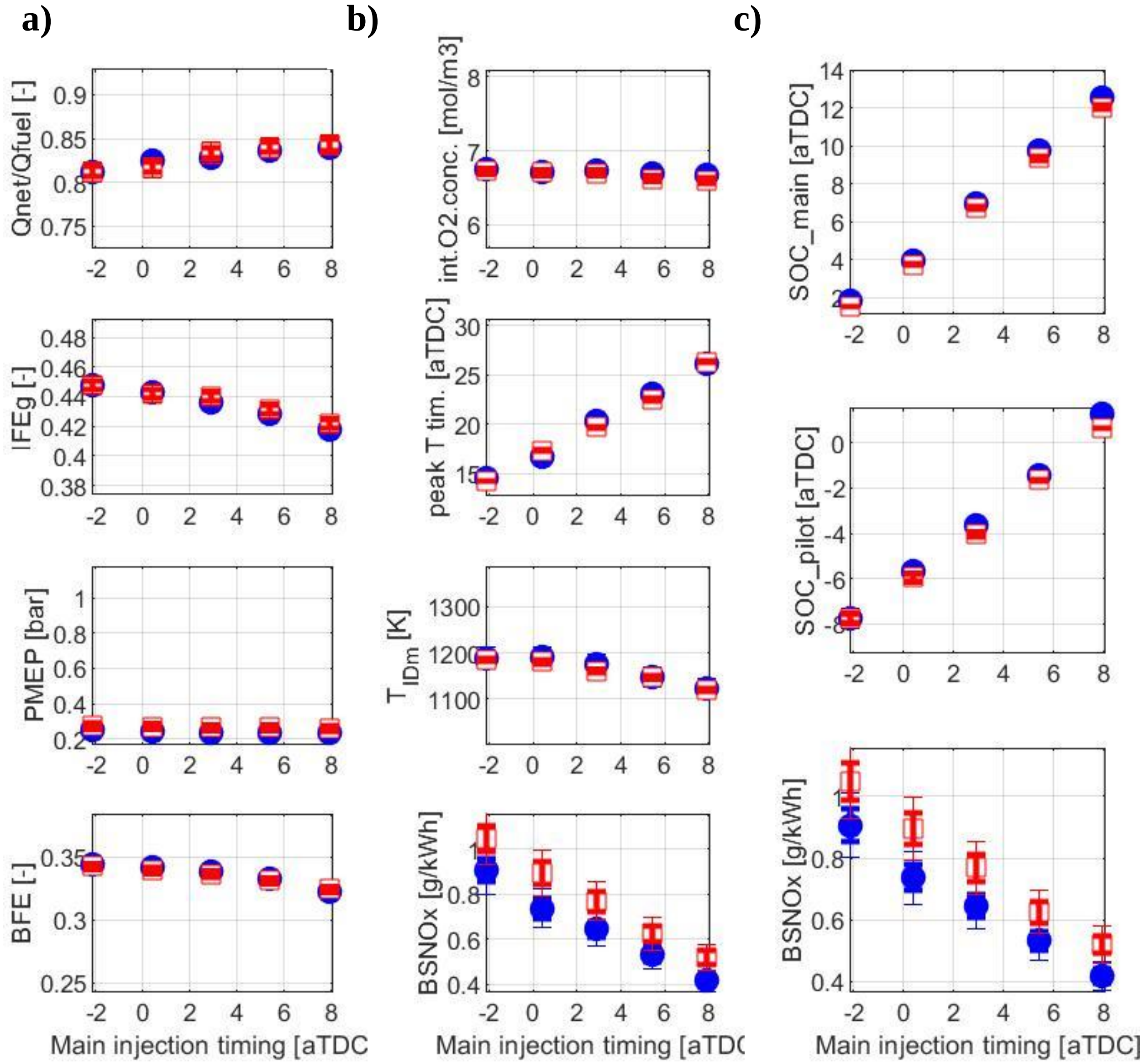

Figure 3.72. The parameters affecting a) BFE, b) and c) BSNOx during the main injection timing (MIT) sweep at MM3 with default ECU calibration (●: Diesel, □: B20) .

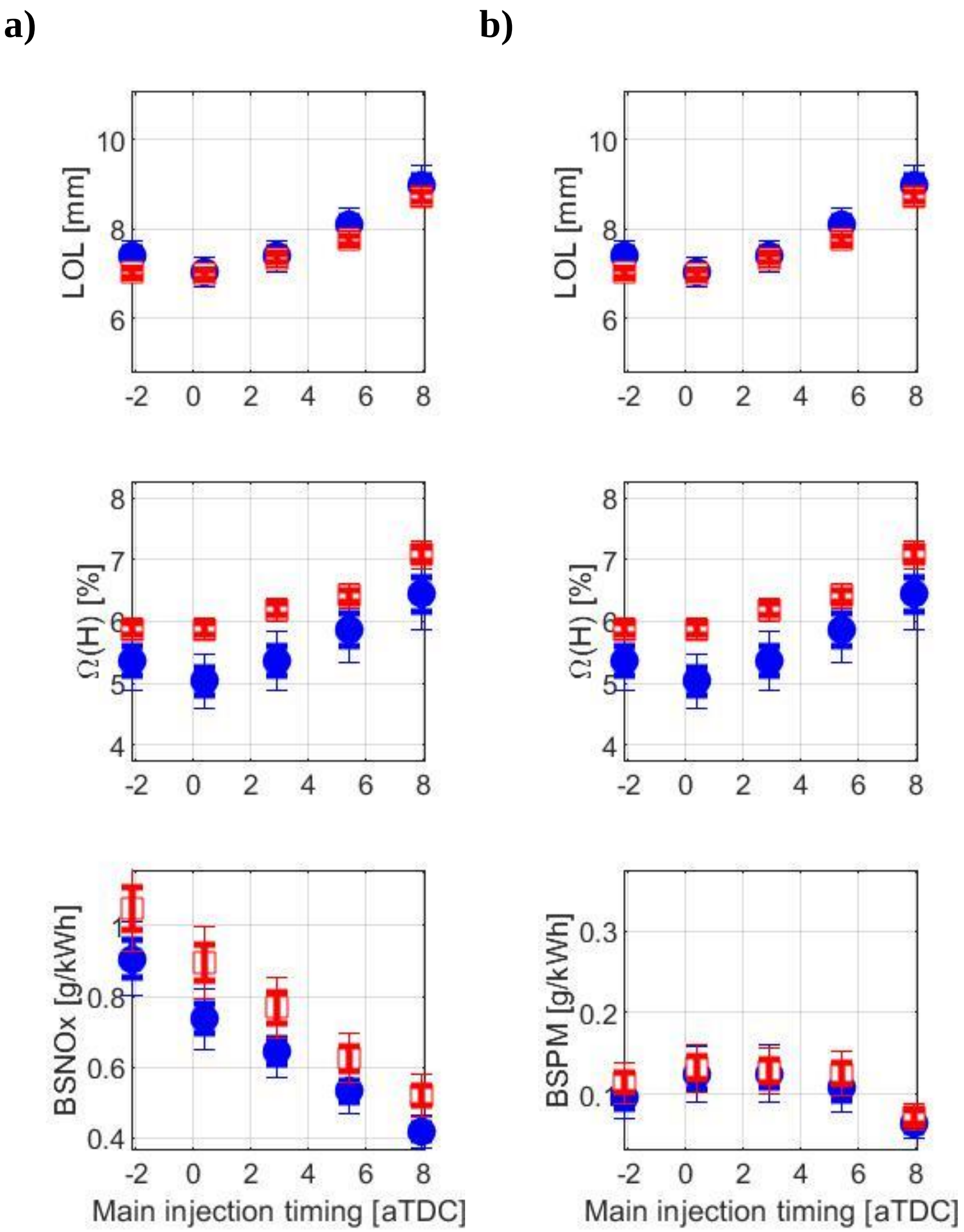

Figure 3.73. Lift-off length and oxygen ratio at the lift-off length during the main injection timing (MIT) sweep at MM3 with default ECU calibration (●: Diesel, □: B20) with the trend of a) BSNOx and b) BSPM

3.3.3.4 MM4

The key points of the impact of B20 on the output parameters at MM4 can be summarized as follows. First, BFE for B20 and the baseline fuel did not show statistically meaningful difference in all of the conditions imposed during the 4 single parameter sweep tests. The reason for consistent BFE for the two fuels with the default ECU setting at MM4 was the same for 4 different single parameter sweeps: no statistically meaningful difference in both IFEg and PMEP.

Second, BSNOx for B20 and the baseline fuel did not show statistically meaningful difference in all of the imposed conditions during 4 single parameter sweep tests. The parameters determining the NOx generation from diffusion flame zone (i.e., intake charge O_2 concentration, peak cylinder temperature timing, and charge gas temperature during the ignition delay) remained constant for the two fuels. Furthermore, the oxygen ratio at the lift-off length was also consistent for the two fuels at all of the imposed conditions during the 4 different sweeps.

Third, BSPM for B20 and the baseline fuel did not show statistically meaningful difference in most of the conditions imposed during the 4 sweep tests. At two of the imposed conditions, “5 degrees retarded injection timing condition (5R)” and “Low boost pressure condition (LP)”, the BSPM from B20 was lower than that from the baseline fuel with low statistical confidence. However, even this difference could be due to the higher measurement inaccuracy from the smoke meter measurements at those certain imposed conditions (i.e., 5R and LP conditions).

Lastly, the impact of B20 on CNL and other BS emissions with the default ECU calibration at MM4 is as follows. BSTHC emissions were at negligible level for B20 as they were for the baseline fuel. BSCO emission for the two fuels did not show any statistically meaningful difference at all of the imposed conditions. Combustion noise level (CNL) for B20 with the default ECU settings generally decreased from that for the baseline fuel. The degree of decrease in CNL for B20 varied depending on the imposed conditions, but in general, there was about 1-1.5dB decrease in CNL for B20.

Although B20 does not worsen BFE or BS emissions with the default ECU calibration at MM4 significantly, it is still worthwhile to investigate the better ECU settings that can improve BFE at MM4. More detailed explanation for the consistent BFE and BS emissions for the two fuels with the default ECU calibration will be presented in the following paragraphs. Since all 4 sweep tests showed the same impact of B20, one of the single parameter sweep tests is chosen to be presented: main injection timing (MIT) sweep.

Figure 3.74a presents the impact of main injection timing (MIT) on BFE (top-left), BSNOx (middle-left), BSPM (bottom-left), CNL (top-right), BSTHC (middle-right), BSCO (bottom-right) at MM4 for the baseline diesel (blue filled dots) and B20 (red empty rectangles) at default ECU calibration. Figure 3.74b presents the trend of the BFE (top-left), BSPM (middle-left), $BSCO_2$ (bottom-left), BSTHC (top-right), BSCO (middle-right) and CNL (bottom-right) by BSNOx during the MIT sweep of the baseline diesel and B20 at default calibration at MM4.

As shown in the top-left plot in Figure 3.74a, BFE for B20 with the default ECU calibration does not have statistically meaningful difference from the baseline fuel. It decreases from 37.8% at 5 degrees advanced injection timing (5A) to 36.2% at 5 degrees retarded injection timing (5R). Figure 3.75a shows the parameters affecting BFE during the main injection timing (MIT) sweep at MM4. Both IFEg (second to the top plot) and PMEP (third to the top) for the two fuels remain the same for the two fuels during the main injection timing sweep. As shown in

Figure 3.75c, main SOC (top) and pilot SOC (middle) both remained the same for the two fuels, which contributed to the consistent IFEg for the two fuels.

BSNOx for B20 with the default ECU calibration, as shown in the middle-left plot in Figure 3.74a, does not have statistically meaningful difference from the baseline fuel. The parameters that might affect NOx during the main injection timing (MIT) sweep are presented in Figures 3.75b, 3.75c, and 3.76a. We can see that all of the parameters relevant for NOx generation (i.e., intake O_2 concentration (Figure 3.75b, top), peak cylinder temperature timing (Figure 3.75b, second-to-the-top), charge gas temperature (Figure 3.75b, third-to-the-top), and oxygen ratio at the lift-off length (Figure 3.76a, middle)) remained the same for the two fuels at MM4.

BSPM for B20 with the default ECU calibration, as shown in the bottom-left plot in Figure 3.74a, also does not have statistically meaningful difference from the baseline fuel. Given the fact that both the intake O_2 concentration and oxygen ratio at the lift-off remained the same for the two fuels at MM5, the consistency in BSPM for the two fuels is reasonable.

Combustion noise level (CNL) for B20 with the default ECU calibration, as shown in the top-right plot in Figure 3.74a, is in general, 1-1.5dB lower than that for baseline diesel. BSTHC for B20 with the default ECU calibration, as shown in the second to the top-right plot in Figure 3.74a, was at negligible level as it was for baseline diesel. BSCO for B20 with the default ECU calibration, as shown in the bottom-right plot in Figure 3.74a, did not have statistically meaningful difference from the baseline fuel.

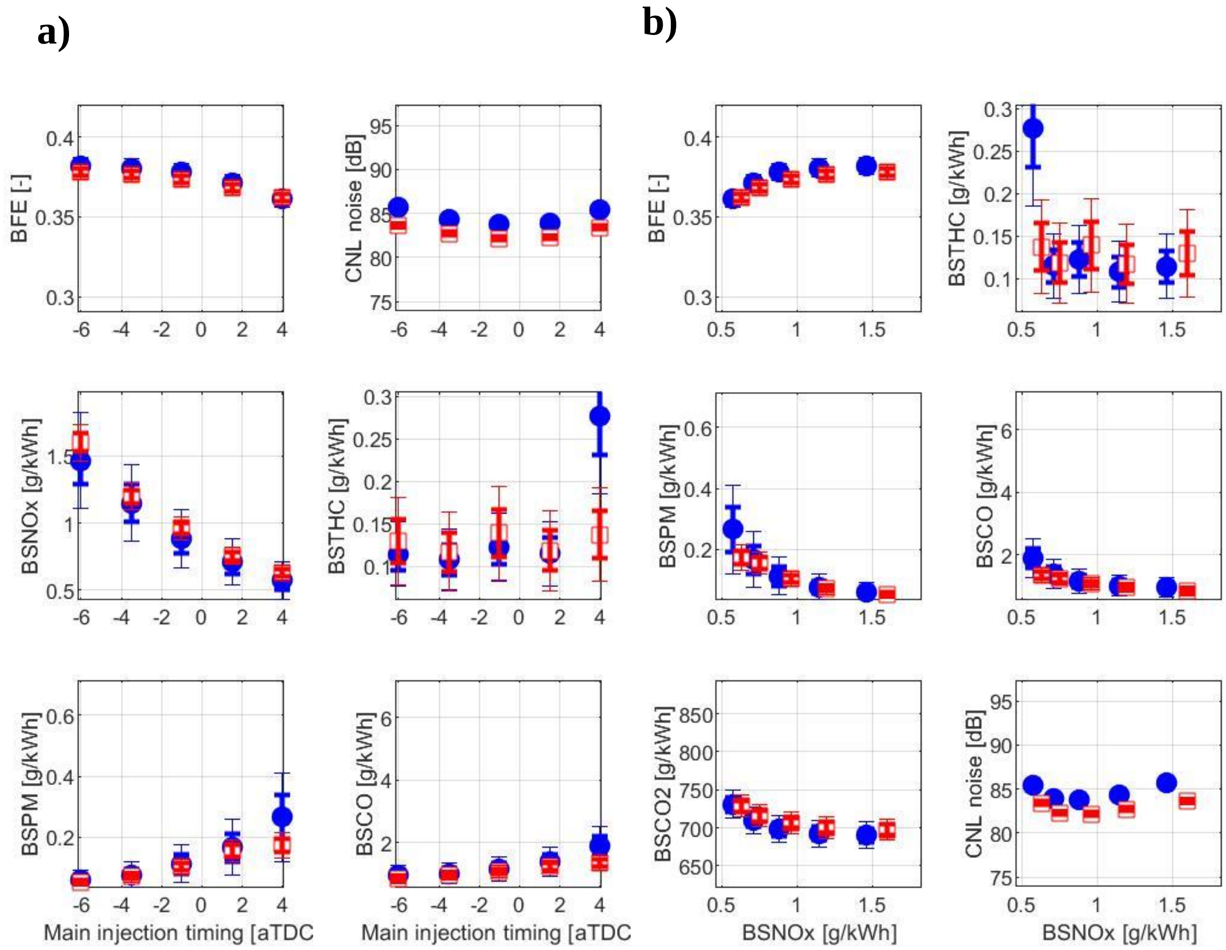

Figure 3.74. BFE, BS emissions, and CNL during the main injection timing (MIT) sweep at MM4 (●: Diesel, □: B20) as a function of a) MIT and b) BSNOx

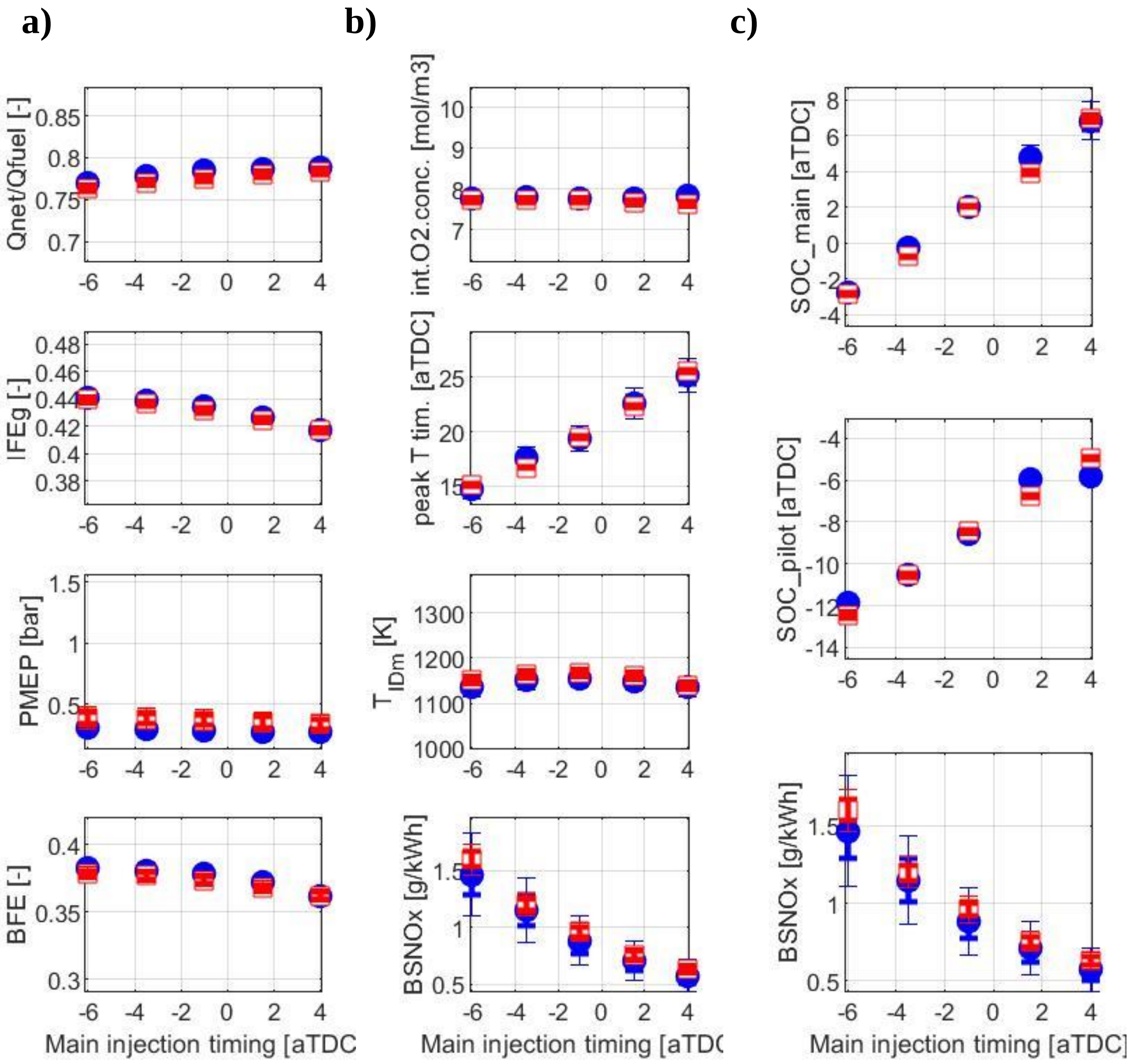

Figure 3.75. The parameters affecting a) BFE, b) and c) BSNOx during the main injection timing (MIT) sweep at MM4 (●: Diesel, □: B20)

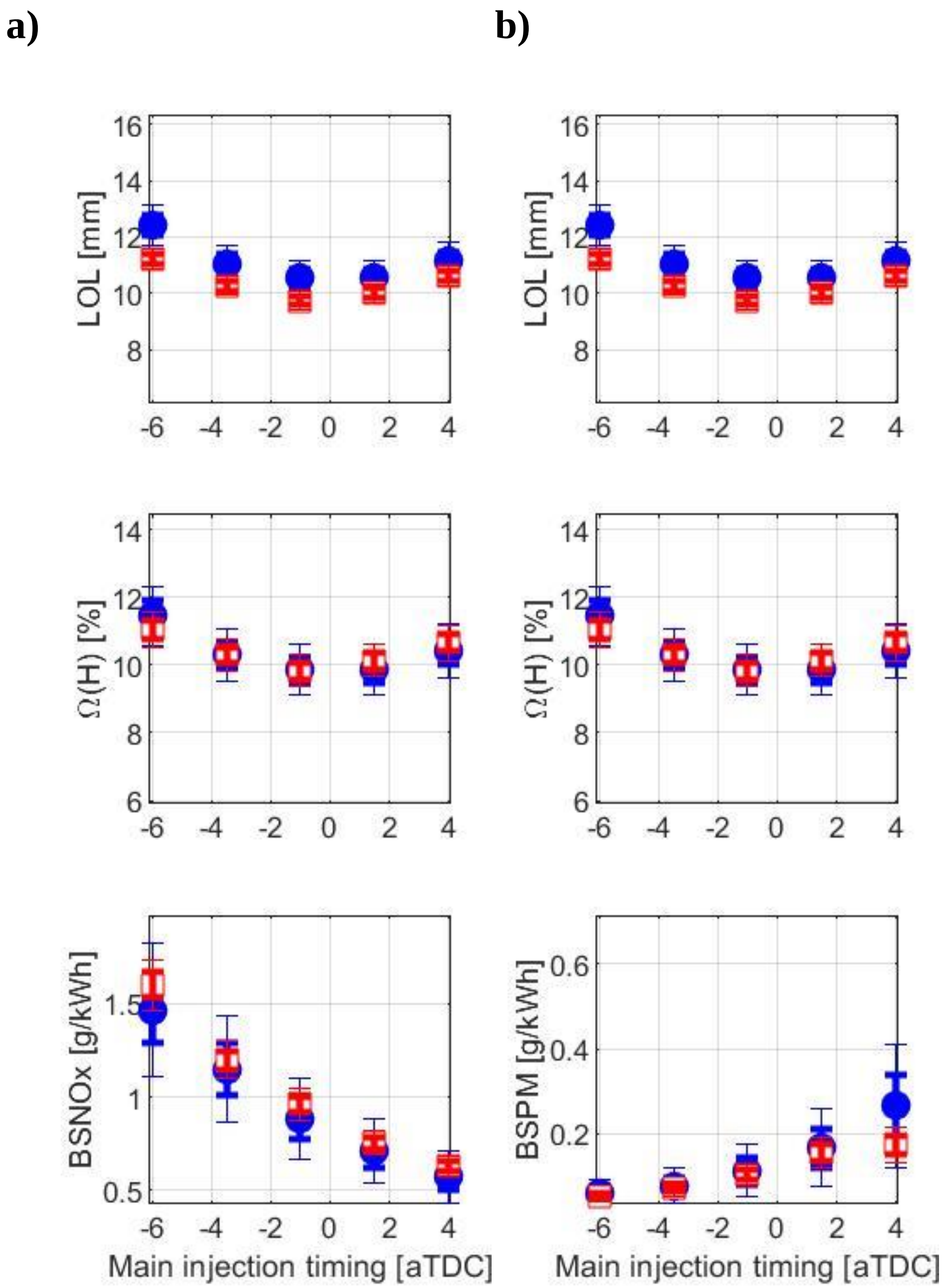

Figure 3.76. Lift-off length and oxygen ratio at the lift-off length during the main injection timing (MIT) sweep at MM4 (●: Diesel, □: B20) with the trend of a) BSNOx and b) BSPM

3.3.3.5 MM5

No statistically meaningful difference in BFE, BSNOx, BSPM, and CNL between the baseline fuel and B20 with the default ECU calibration could be observed at MM5 at any of the imposed conditions during 4 different single parameter sweeps. Meanwhile, BSCO emission from B20 with default ECU calibration was lower than that from the baseline fuel with low statistical confidence. BSTHC emissions from B20 with the default ECU calibration at MM5 were at negligible level as they were for the baseline fuel at the mini-map point. The result of the main injection timing (MIT) sweep test is presented here.

Figure 3.77a presents the impact of main injection timing (MIT) on BFE (top-left), BSNOx (middle-left), BSPM (bottom-left), CNL (top-right), BSTHC (middle-right), BSCO (bottom-right) at MM5 for the baseline diesel (blue filled dots) and B20 (red empty rectangles) at default ECU calibration. Figure 3.77b presents the trend of the BFE (top-left), BSPM (middle-left), $BSCO_2$ (bottom-left), BSTHC (top-right), BSCO (middle-right) and CNL (bottom-right) by BSNOx during the MIT sweep of the baseline fuel and B20 at the default calibration at MM5.

As mentioned earlier, no statistically meaningful difference in BFE, BSNOx, BSPM, and CNL could be observed between the two fuels with the default ECU settings. Figures 3.78 and 3.79 are presented to show the parameters affecting BFE, BSNOx, and BSPM during the main injection timing (MIT) sweep.

As shown in Figure 3.78a, the IFEg (second-to-the-top plot) and PMEP (third-to-the-top plot) for the two fuels with the default ECU calibration are the same at all imposed main injection timing (MIT) conditions, guaranteeing the same BFE for the two fuels. As shown in Figure 3.78b, intake O_2 concentration (top), peak cylinder temperature timing (second-to-the-top), and charge temperature during the main ignition delay (third-to-the-top) all remained the same for the two fuels. Furthermore, the oxygen ratio at the lift-off length (Figure 3.79a, middle) also remained the same for the two fuels at all of the imposed main injection timing conditions, guaranteeing the consistent BSNOx for the two fuels with the default ECU calibration. The consistent BSPM for the two fuels is also a reasonable result given the consistent intake O_2 concentration and oxygen ratio at the lift-off length for the two fuels. BSCO for B20 generally decreased, but the degree of decrease varied depending on the imposed conditions.

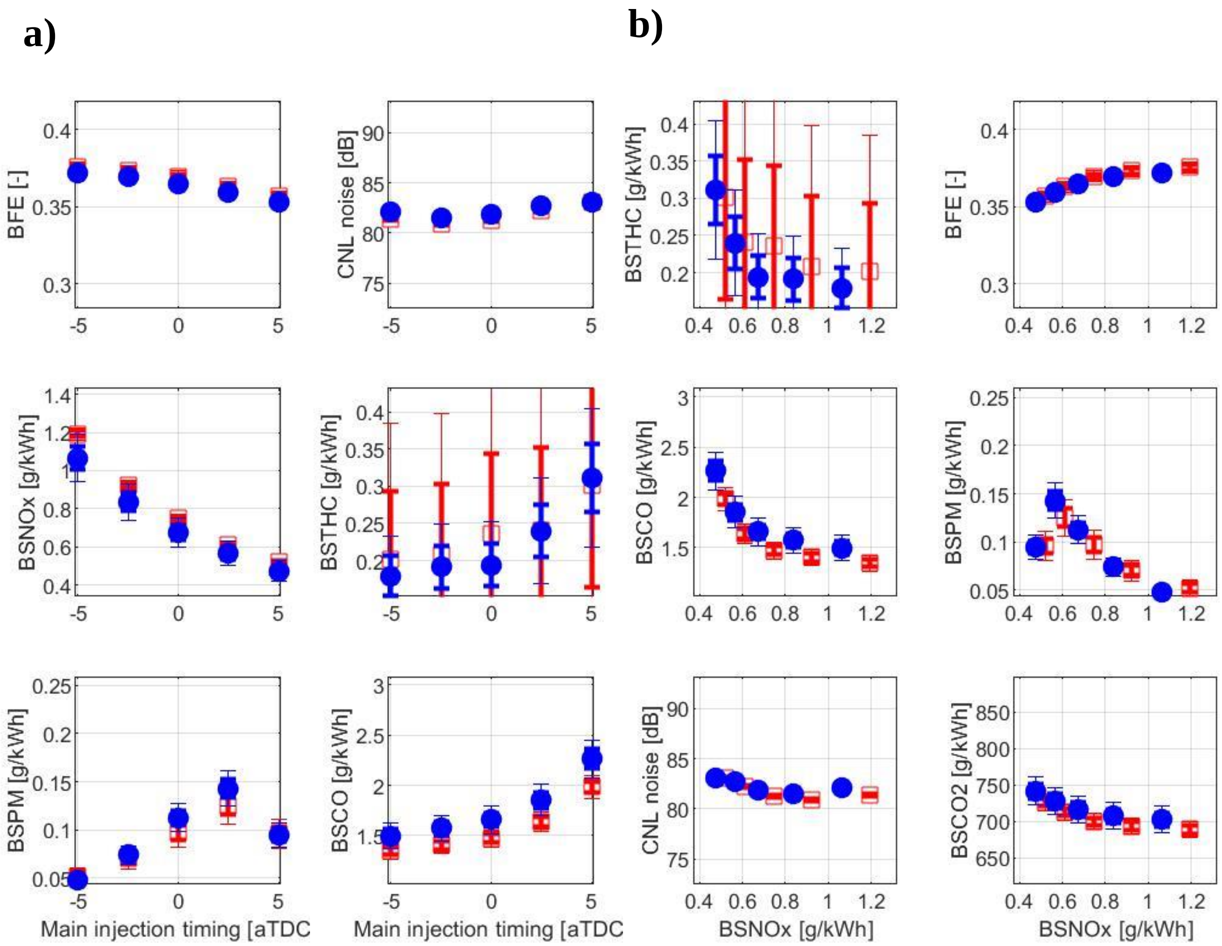

Figure 3.77. BFE, BS emissions, and CNL during main injection timing (MIT) sweep at MM5 (●: Diesel, □: B20) as a function of a) MIT, b) BSNOx

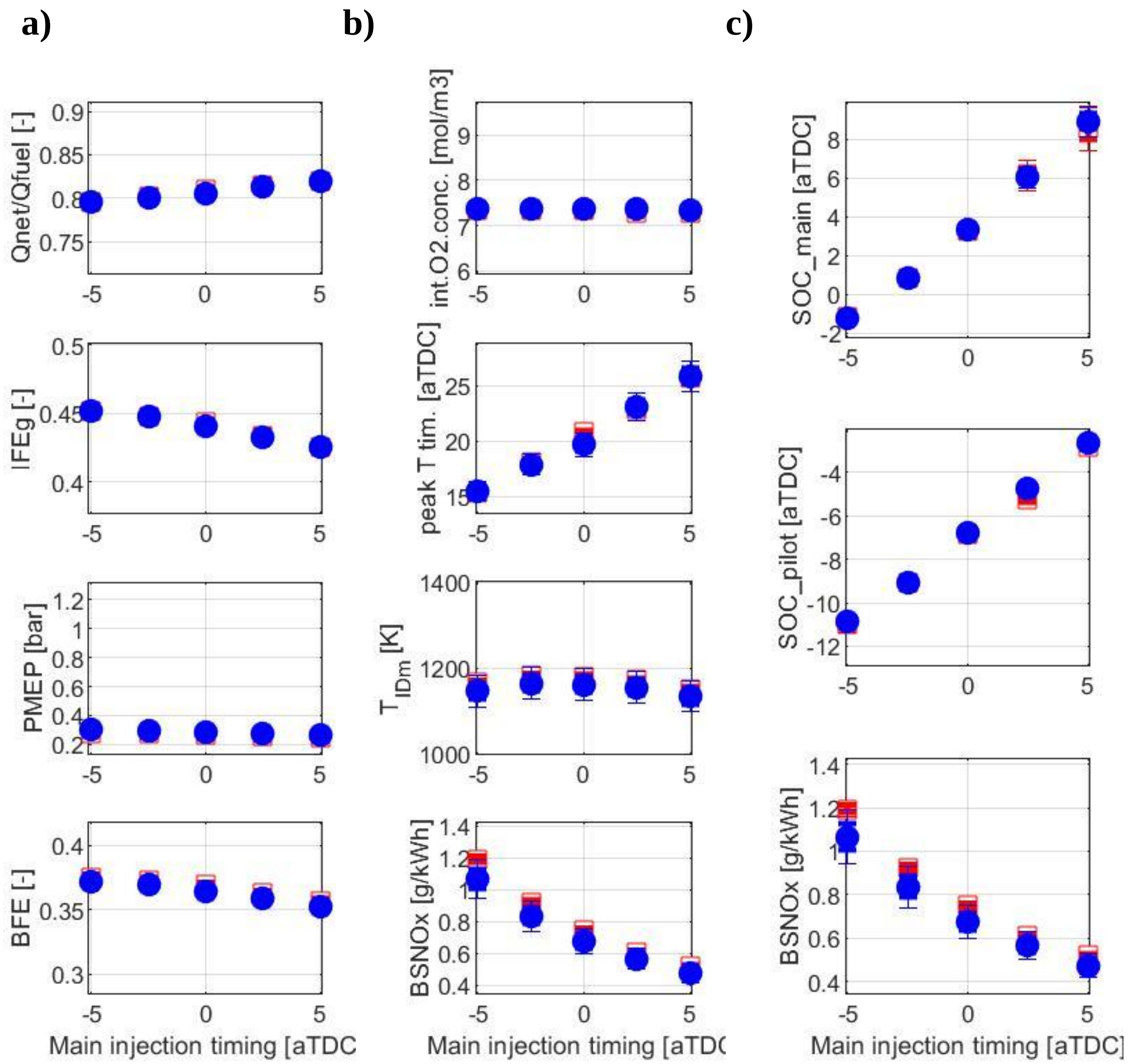

Figure 3.78. The parameters affecting a) BFE, b) and c) BSNOx during MIT sweep at MM5 (●: Diesel, □: B20)

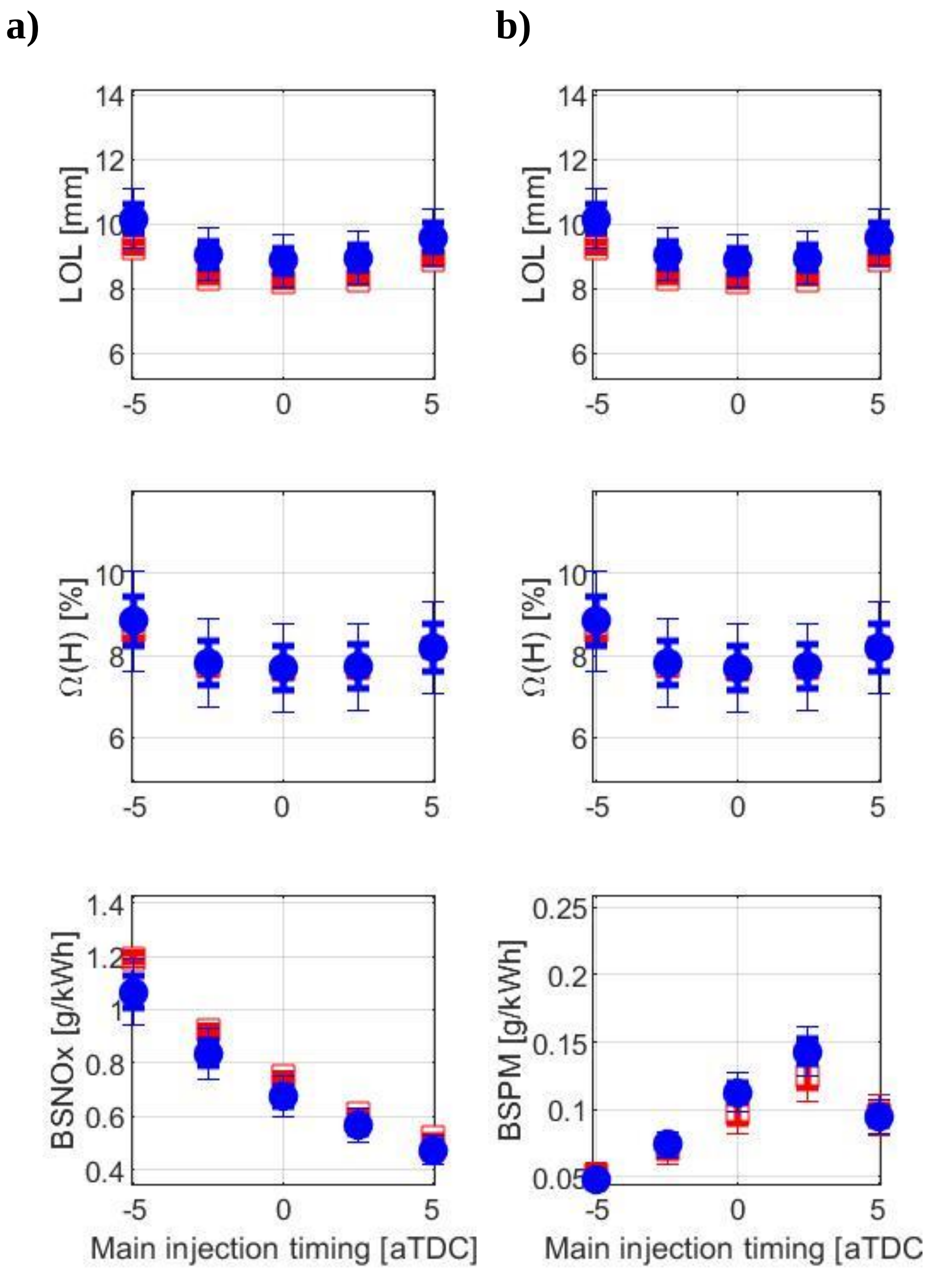

Figure 3.79. Lift-off length and oxygen ratio at the lift-off length during MIT sweep at MM5 (●: Diesel, □: B20) with the trend of a) BSNOx b) BSPM

3.3.3.6 MM6

The impact of B20 on BFE and BS emissions at MM6 can summarized as follows. First, BFE for B20 at the default ECU calibration does not show statistically meaningful difference from the baseline fuel for all of the conditions imposed during the 4 different single parameter sweeps. The IFEg and PMEP remained the same for the two fuels, thus resulting in the consistent BFE for the two fuels.

Second, BSNOx emission increased for B20 at most of the imposed conditions during the 4 different single parameter sweeps. The main contributor for the increase in BSNOx varied depending on the imposed conditions. However, in general, either the advance in peak cylinder temperature timing or the increase in charge gas temperature during the main ignition delay was the main reason for the BSNOx increase.

Third, BSPM emission decreased for B20 at most of the imposed conditions during the 4 different single parameter sweeps. However, the fundamental cause for the decrease in BSPM for B20 could not be clearly defined in the current study. It is likely that the accuracy of the lift-off length estimation model was not high enough to calculate the correct oxygen ratio at the lift-off length at this particular MM point.

Although it was unclear to show why BSPM emission from B20 was lower than that from the baseline fuel at MM6 based on the current measurements for the fundamental parameters, some of the previous studies report the more intense decrease in BSPM from B20 at higher load conditions. Thus, the observation of the lower BSPM emission from B20 at higher load conditions such as MM6 is not unique for the current study. Ye et al.[24] compared the PM emission from the conventional petroleum-based diesel and soy-derived B40 at three different load conditions, and the highest-load condition experienced the most intense decrease in PM emissions for B40. Furthermore, it is also reported that the reactivity of the soot particles has also been increased the most at the highest-load condition with B40. Thus, it is likely that the current work has confirmed this tendency at MM6.

Lastly, the impact of B20 on other BS emissions and CNL was as follows. Combustion noise level (CNL) generally decreased for B20 for most of the imposed conditions by about 1dB. BSTHC emissions for B20 at MM6 were at negligible level for all of the imposed conditions during the 4 single parameter sweeps. BSCO decreased by about 20-25% for most of the imposed conditions at MM6.

Since the impact of B20 on the primary output parameters of interest (i.e., BFE, BSNOx, and BSPM) was identical for the 4 different single parameter sweep tests, the result of main injection timing (MIT) sweep test will only be presented in this study to compare the two fuels in a more detail.

Figure 3.80a presents the impact of main injection timing (MIT) on BFE (top-left), BSNOx (middle-left), BSPM (bottom-left), CNL (top-right), BSTHC (middle-right), BSCO (bottom-right) at MM6 for the baseline diesel (blue filled dots) and B20 (red empty rectangles) at the default ECU calibration. Figure 3.80b presents the trend of the BFE (top-left), BSPM (middle-left), BSCO$_2$ (bottom-left), BSTHC (top-right), BSCO (middle-right) and CNL (bottom-right) by BSNOx during the MIT sweep of the baseline fuel and B20 at the default ECU calibration at MM6.

First, BFE for B20 at the default ECU calibration did not have statistically meaningful difference from that for the baseline fuel (Figure 3.80a, top-left). It decreases from 38.9% at 5 degrees advanced injection timing (5A) to 38.0% at the default injection timing (DF), then to 36.4% at 5 degrees retarded injection timing (5R). At the same main injection timing (MIT), the

BFE for the baseline diesel was 38.9% at 5A, 37.9% at DF, and 36.2% at 5R. The consistent BFEs for the two fuels can be explained by the consistent IFEg and PMEP as shown in Figure 3.81a.

Figure 3.81a shows the parameters affecting the BFE during the main injection timing (MIT) sweep at MM6. On its second to the top plot is the IFEg during the MIT sweep at MM6. Gross indicated fuel conversion efficiency (IFEg) for B20 decreases from 45.3% at 5 degrees advanced injection timing (5A) to 42.1% at 5 degrees retarded injection timing (5R), which does not have statistically meaningful difference from the IFEg of the baseline diesel (i.e., 45.4% at 5A and 42.0% at 5R). The third to the top plot in Figure 3.81a shows the PMEP of B20 during the main injection timing sweep at MM6. Pump mean effective pressure (PMEP) for B20 does not change appreciably during the main injection timing sweep at MM6 around 0.3bar, and this is the same case for the baseline fuel.

Second, BSNOx emission for B20 increased from the baseline result for all of the injection timings imposed. BSNOx for B20 decreases from 1.52g/kWh at 5 degrees advanced injection timing (5A) to 0.95g/kWh at the default injection timing (DF), then to 0.68g/kWh at 5 degrees retarded injection timing (5R). The BSNOx emission from the baseline diesel was 1.25g/kWh at 5A, 0.79g/kWh at DF, and 0.61g/kWh at 5R. Thus, the increase in BSNOx for B20 was the highest at 5 degrees advanced injection timing by 22.6%, then, 16.8% increase at the default injection timing, and finally the least increase at 5 degrees retarded injection timing by 11.3%. This more intensive increase in BSNOx at the advanced injection timings can be "partially" attributed to the more intensive decrease in "pilot" ignition delay at advanced injection timings.

Figure 3.81c shows the combustion phasing of the main injection event (top plot) and pilot injection event (middle plot) for B20 during the main injection timing (MIT) sweep at MM6. There is no appreciable difference in the main combustion phasing for the two fuels. However, MM6 is peculiar in that the pilot combustion phasing for B20 is not only advanced from the baseline diesel in general, but also gets more intensely advanced at the advanced injection timings. At 5 degrees retarded injection timing, the difference in the pilot start of combustion (SOC) between B20 and the baseline diesel is only 0.4CA, but the difference becomes greater at 5 degrees advanced injection timing as 1.1CA. This more advanced pilot combustion phasing at the advanced injection timings resulted in the advanced peak cylinder temperature timing at some of the advanced injection timing conditions (i.e., 2.5 degrees advanced injection timing) as shown in the second to the top plot in Figure 3.81b. The peak cylinder temperature timing for B20 is about 0.5CA advanced than that for the baseline diesel for the 2.5 degrees advanced injection timing (2.5A).

Third, BSPM for B20 decreased from the baseline result for most of the imposed injection timings at MM6 except for the 5 degrees retarded injection timing (5R). BSPM is well-known to generally decrease with the increase in oxygen ratio at the lift-off length or with the increase in overall charge O_2 concentration. However, at MM6, none of these two factors have changed in a way to decrease BSPM for B20. Figure 3.81b top plot shows that the intake O_2 concentration for B20 and the baseline diesel were the same for all of the imposed injection timings. Figure 3.82b shows the oxygen ratio at the lift-off length (middle) for B20 and the baseline diesel during the main injection timing sweep at MM6, and it was either the same for the two fuels or was rather decreased for B20.

The primary cause for either the same or the lower oxygen ratio estimated for B20 at MM6 is its shorter estimated lift-off length than the baseline diesel as shown in Figure 3.82b top plot. Based on the fact that the engine speed and load at MM6 are appreciably different from the other mini-map points, it is possible that the lift-off length estimation method worked well in the other mini-map points simply did not worked well at MM6. And this might have resulted in inaccurate estimation of the oxygen ratio at the lift-off length, thus making the cause of the decrease in BSPM for B20 at MM6 unclear.

Lastly, the impact of B20 on other brake specific (BS) emissions and combustion noise level (CNL) is presented here. BSTHCs from B20 during the main injection timing sweep at MM6 were at negligible level. BSCO emission was about 20-25% lower for B20 than for the baseline diesel. Combustion noise level (CNL) was decreased for B20 at all of the main injection timing conditions. The maximum decrease in CNL for B20 as compared to diesel was at the 5 degrees advanced injection timing (5A) by 1.3dB.

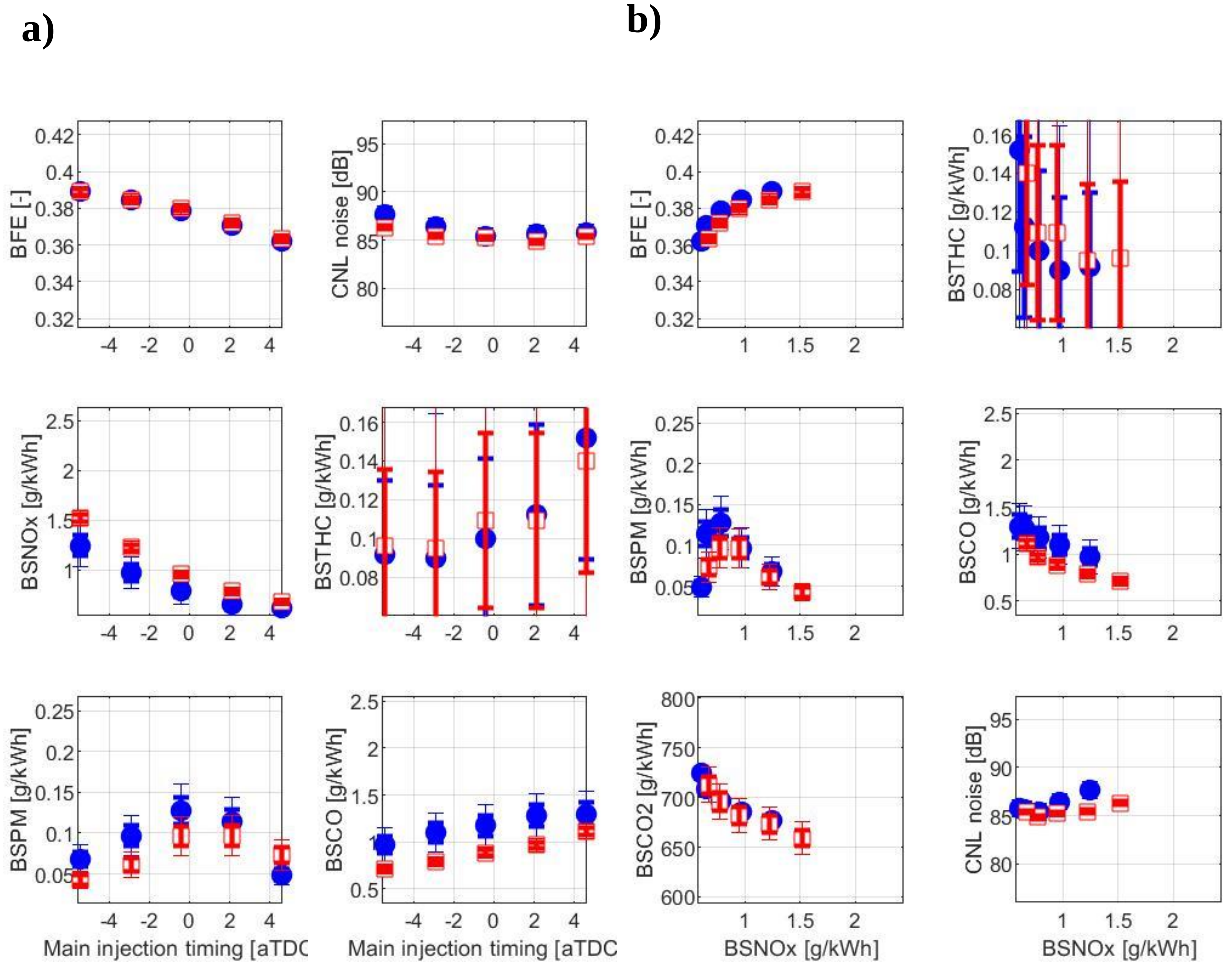

Figure 3.80. BFE, BS emissions, and CNL during the main injection timing (MIT) sweep at MM6 (●: Diesel, □: B20) with default ECU calibration as a function of a) MIT, b) BSNOx

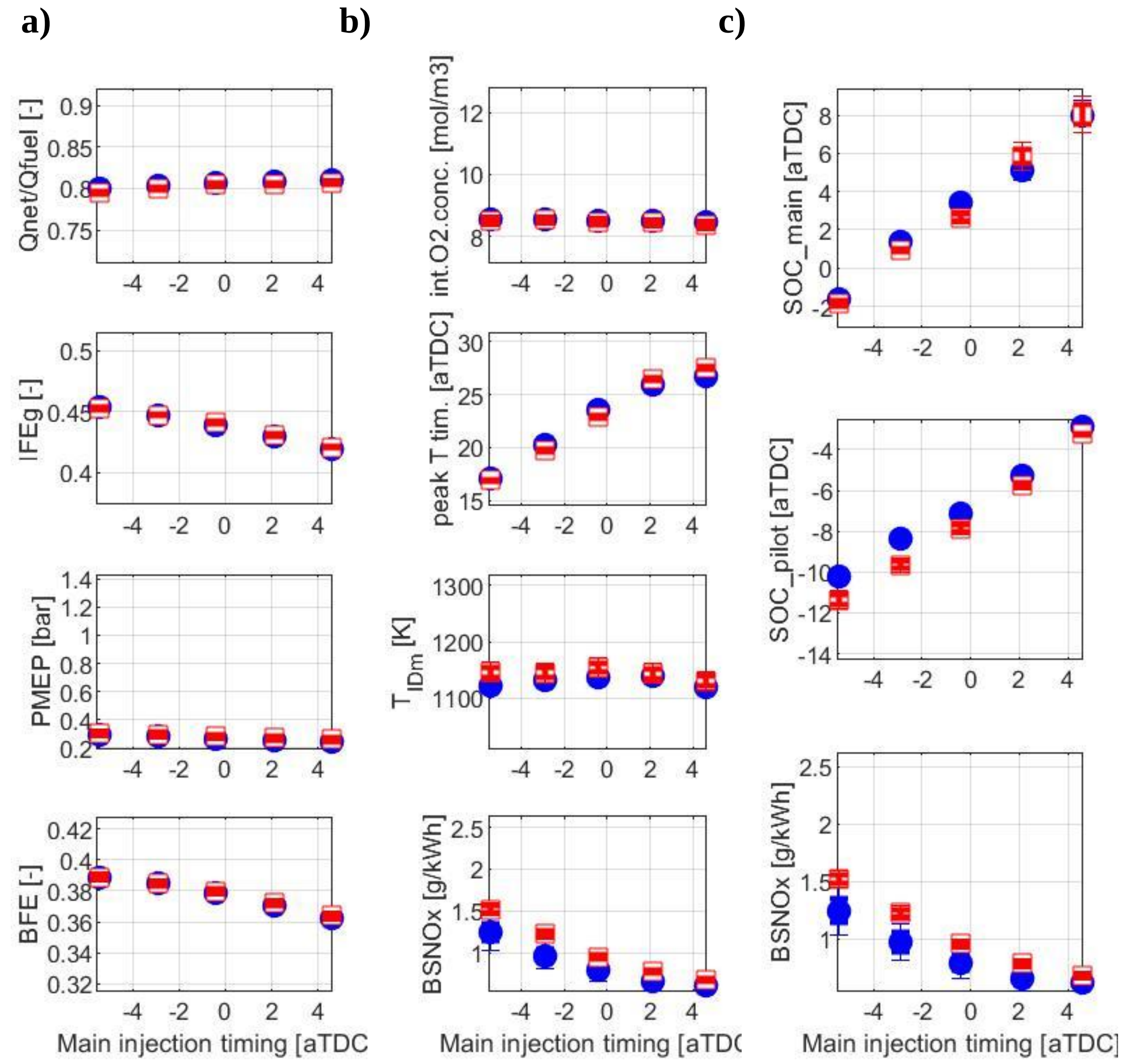

Figure 3.81. The parameters affecting a) BFE, b) and c) BSNOx during the main injection timing (MIT) sweep at MM6 (●: Diesel, □: B20) with default ECU calibration.

a) b)

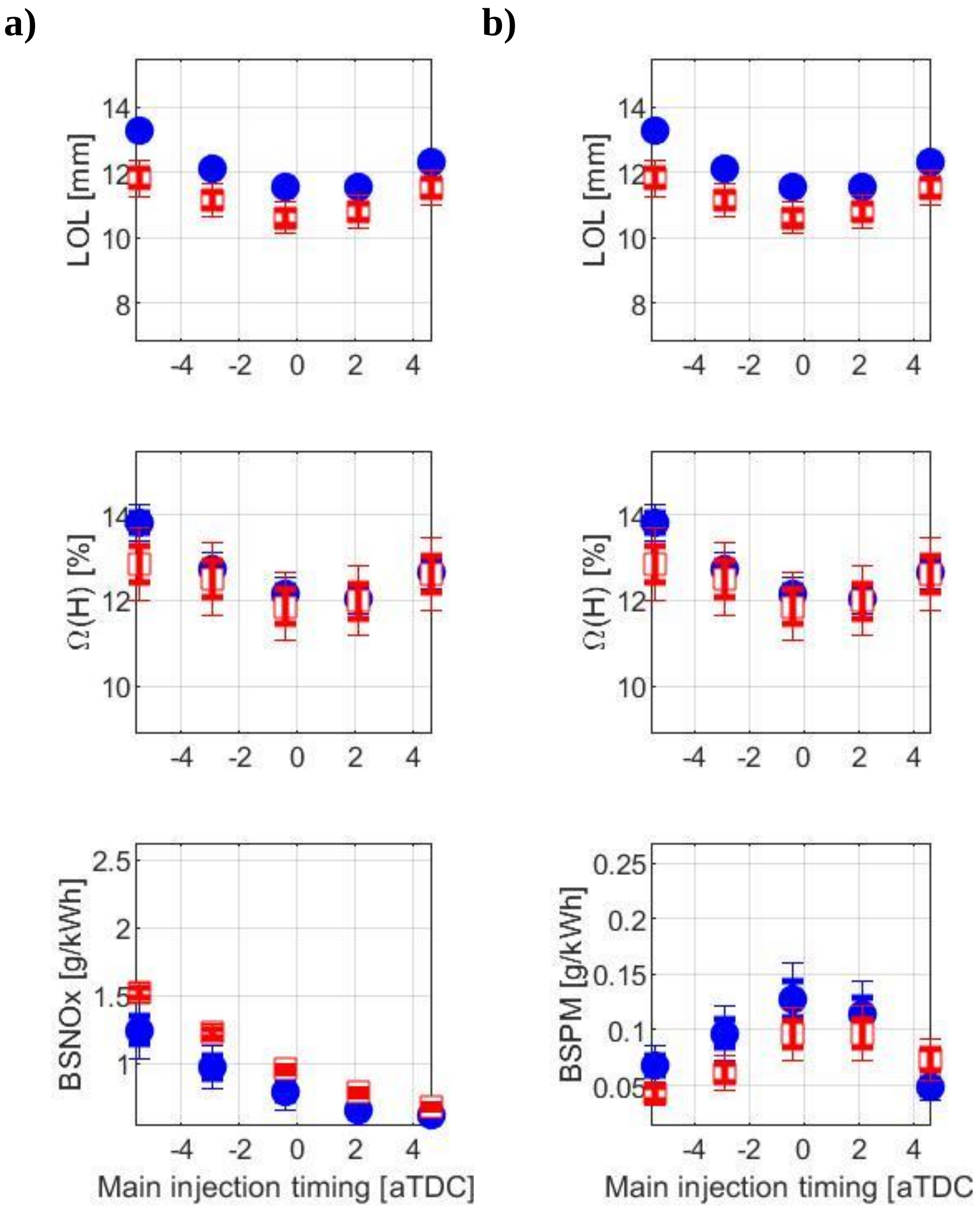

Figure 3.82. Lift-off length and oxygen ratio at the lift-off length during the main injection timing (MIT) sweep at MM6 (●: Diesel, □: B20) at the default ECU calibration with the trend of a) BSNOx b) BSPM

3.3.4 B20 Test Results with Adjusted ECU Calibration

Before the results at each mini-map point are discussed, the general trends will be summarized here.

First, regarding BFE, at idling (MM1), low-to-medium load (MM2-3) and a high load condition (MM4), the final BFE for B20 did not show statistically meaningful difference from the baseline results. However, at a medium load (MM5) and the highest load (MM6) condition, there was small improvement in BFE for B20. At MM5, the BFE is improved by 1.31%. At MM6, the BFE is improved by 1.08%. The results for each MM point are available with detailed explanation and discussion in the following sections (3.3.4.1 – 3.3.4.6). The improvement in BFEs at different MM points is also used to calculate the final improvement in “MJ/mile” for B20 with the optimized ECU calibration. This results and discussion is also available in the following section (3.3.6).

Second, regarding BSNOx and BSPM emissions, the significant reduction in BSNOx emissions (up to 53%) with either fixed or moderately decreased BSPM emissions were available at most mini-map points. At some of the mini-map points, significant reduction in BSPM (up to 37%) was available with fixed BSNOx emissions. Based on the current observation, one of the notable reasons that enabled these reductions in BSNOx or BSPM was the optimized ECU calibration that fully utilized the benefit of the increased fuel injection volume for B20, which, in turn, caused significant decrease in charge gas temperature. This decreased charge gas temperature subsequently caused significant reduction in lift-off length to result in greater PM benefit at NOx parity. The details of the BSNOx and BSPM results for each MM point will be covered in the following sections (3.3.4.1 – 3.3.4.6).

3.3.4.1 MM1

Table 3.12 shows the change in the ECU input parameters at MM1 as a result of the re-calibration of ECU for B20 to maximize the BFE (or minimize $BSCO_2$) while satisfying the other bound criteria such as brake specific (BS) emissions and combustion noise level (CNL). The greyed rows are the fixed target operating conditions imposed same for the baseline diesel and B20. The red/blue colored rows are the input variables increased/decreased for B20 in the new calibration settings. For main injection timing (MIT), if the MIT is advanced/retarded, the row is colored blue/red.

First input parameter to discuss from Table 3.12 is the EGR rate. EGR rate is increased by absolute 11% from 42% at the default ECU calibration to 53% for the final B20 calibration. This significant increase in EGR rate settings at MM1 was mainly to counter off the potential increase in BSNOx due to the impact of the advanced injection timing and increased rail pressure at the adjusted ECU calibration.

Boost pressure is decreased about 20hPa from the default calibration (979hPa at 78% turbovane closing) to the B20 final calibration (956hPa at 71% turbovane closing). The decrease in boost pressure was one of the main reasons that led to better BFE at the final B20 calibration.

Rail pressure is increased about 30bars from the default ECU calibration (282bar) to the B20 final calibration (314bar). The increase in rail pressure is another reason that led to better BFE at the final B20 calibration.

Despite the potential increase in BFE led by the decreased boost pressure (BP) and increased rail pressure (RP), MM1 did not show statistically meaningful improvement in BFE at its final ECU calibration. This is because other input parameters are also changed to offset the increase in other BS emissions and CNL while sacrificing BFE. One of the examples is the change in main injection timing (MIT) settings at MM1. The main injection timing setting is advanced by 0.9CA from -0.8aTDC at the default calibration to -1.7aTDC at the B20 final calibration. The advance in the MIT setting was mainly to reduce the CNL which have potentially decreased the BFE based on the observation from Figure 3.11a.

Pilot 1 injection quantity (PIQ1) is decreased by 1.6mg/stroke from the default calibration (3.3mg/stroke) to the B20 final calibration (1.69mg/stroke), while pilot 2 injection quantity (PIQ2) is increased by 0.6mg/stroke from the default calibration (1.85mg/stroke) to the B20 final calibration (2.52mg/stroke). Relative distance between MIT and PIT1 is increased from 8.31CA at the default calibration to 9.62CA at the B20 final calibration while the relative distance between PIT1 and PIT2 is increased from 8.31CA at the default calibration to 9.62CA at the B20 final calibration.

MM1	Diesel (DSL) at default ECU calibration	B20 at final adjusted ECU calibration
Engine speed [rpm]	600	600
Brake torque [N·m]	66	66
BMEP [bar]	1.2	1.2
EGR rate [%]	42	53
Turbovane closing [%]	78	71
Boost pressure [hPa]	979	956
Rail pressure [bar]	282	314
Main injection timing [aTDC]	-0.79	-1.71
Pilot 1 injection quantity [mg/stroke]	3.30	1.69
Pilot 2 injection quantity [mg/stroke]	1.85	2.52
Relative distance between MIT and PIT1 [CA]	8.31	9.62
Relative distance between PIT1 and PIT2 [CA]	8.0	5.54

Table 3.12. Comparison between the default ECU calibration for the baseline diesel and the adjusted ECU calibration for B20. Grey: Fixed conditions, Red: Increase (Retarding for main injection timing), Blue: Decrease (Advance for main injection timing)

The comparison of BFE, BS emissions, and CNL between the baseline diesel and B20 at the final ECU calibration is shown in Table 3.13. Brake fuel conversion efficiency (BFE) is increased by absolute 0.01% (relative 0.04%) from the baseline diesel. However, this mean difference in BFE between the two fuels was much smaller than one standard deviation (0.48%) of the repeated measurements, which meant that the two fuels did not have statistically meaningful difference in BFE. Meanwhile, $BSCO_2$ of B20 with the final calibration was 46.55g/kWh higher than that of the baseline diesel, which was actually higher than one standard deviation (33.99g/kWh) of the repeated measurements. The discrepancy in the trends of BFE and $BSCO_2$ at MM1 is likely due to the relatively high measurement inaccuracy of the fuel mass flow rate at the idling condition. Since the measurement capacity of the fuel mass flow meter had to cover the highest engine load of the test engine (i.e., max power: 328kW vs. MM1 power: 4.2kW), the measurement inaccuracy of the fuel mass flow rate is increased up to 5-7% at MM1. Also, due to the low target brake torque (66N·m) at MM1, even the small variation in the brake torque settings affected emissions characteristics significantly causing relatively higher measurement inaccuracy in the emissions measurement. Considering the result of BFE and $BSCO_2$ together, it is concluded that, at MM1, B20 at final calibration did not show statistically meaningful improvement in BFE, or GHG emissions.

Second, BSNOx for B20 at the final ECU calibration decreased by 0.96g/kWh from the baseline diesel value of 2.29g/kWh (relative 41.9% reduction). This decrease in BSNOx was higher than two standard deviations of the repeated BSNOx measurements at MM1, guaranteeing over 95% statistical confidence.

Third, BSPM for B20 at the final ECU calibration decreased by 0.002g/kWh from the baseline diesel value of 0.105g/kWh, but, the degree of decrease was smaller than one standard deviation (0.050g/kWh) of the repeated BSPM measurements at MM1. Thus, BSPM for B20 at the final ECU calibration did not have statistically meaningful difference from the baseline fuel.

Lastly, other brake specific (BS) emissions and combustion noise level (CNL) from the B20 at the final ECU calibration are addressed here briefly. Combustion noise level (CNL) from B20 is increased by 0.82dB from the baseline fuel value of 74.77dB. However, the degree of increase was considered to be in acceptable range, requiring no further change in the ECU calibration. BSTHC for B20 decreased by 0.64g/kWh from the baseline fuel value of 1.81g/kWh (relative 35.4% decrease). This was significant decrease in BSTHC with statistical confidence over 68%. BSCO for B20 decreased by 0.17g/kWh from the baseline fuel value of 4.37g/kWh, but, the standard deviation (0.51g/kWh) of the repeated BSCO measurements at MM1 was greater than the mean difference in BSCO.

MM1	DSL at default calibration	B20 at final calibration	Difference in [%] $[(\frac{B20-DSL}{DSL})\cdot 100]$	Difference in absolute quantity [B20-DSL]	Standard deviation (σ)
BFE [%]	25.85	25.86	+0.04	+0.01	0.48
$BSCO_2$ [g/kWh]	1059	1106	+4.40	+46.55	33.99
BSNOx [g/kWh]	2.29	1.33	-41.9	-0.96	0.257
BSPM [g/kWh]	0.105	0.103	-1.9	-0.002	0.050
BSTHC [g/kWh]	1.81	1.17	-35.4	-0.64	0.513
BSCO [g/kWh]	4.37	4.20	-3.9	-0.17	0.51
CNL [dB]	74.77	75.59	[-]	0.82	0.39

Table 3.13. The comparison of BFE, BS emissions, and CNL between the baseline fuel and B20 at the final ECU calibration at MM1

Figure 3.83a compares the BFE (top-left), BSNOx (middle-left), BSPM (bottom-left), CNL (top-right), BSTHC (middle-right), BSCO (bottom-right) during the EGR sweep of the diesel fuel at the default ECU calibration (blue filled dots) and at B20 final ECU calibration (green star). Figure 3.83b presents the comparison of the BFE (top-left), BSPM (middle-left), BSCO2 (bottom-left), BSTHC (top-right), BSCO (middle-right) and CNL (bottom-right) by BSNOx for the baseline fuel and for the B20 final calibration at MM1.

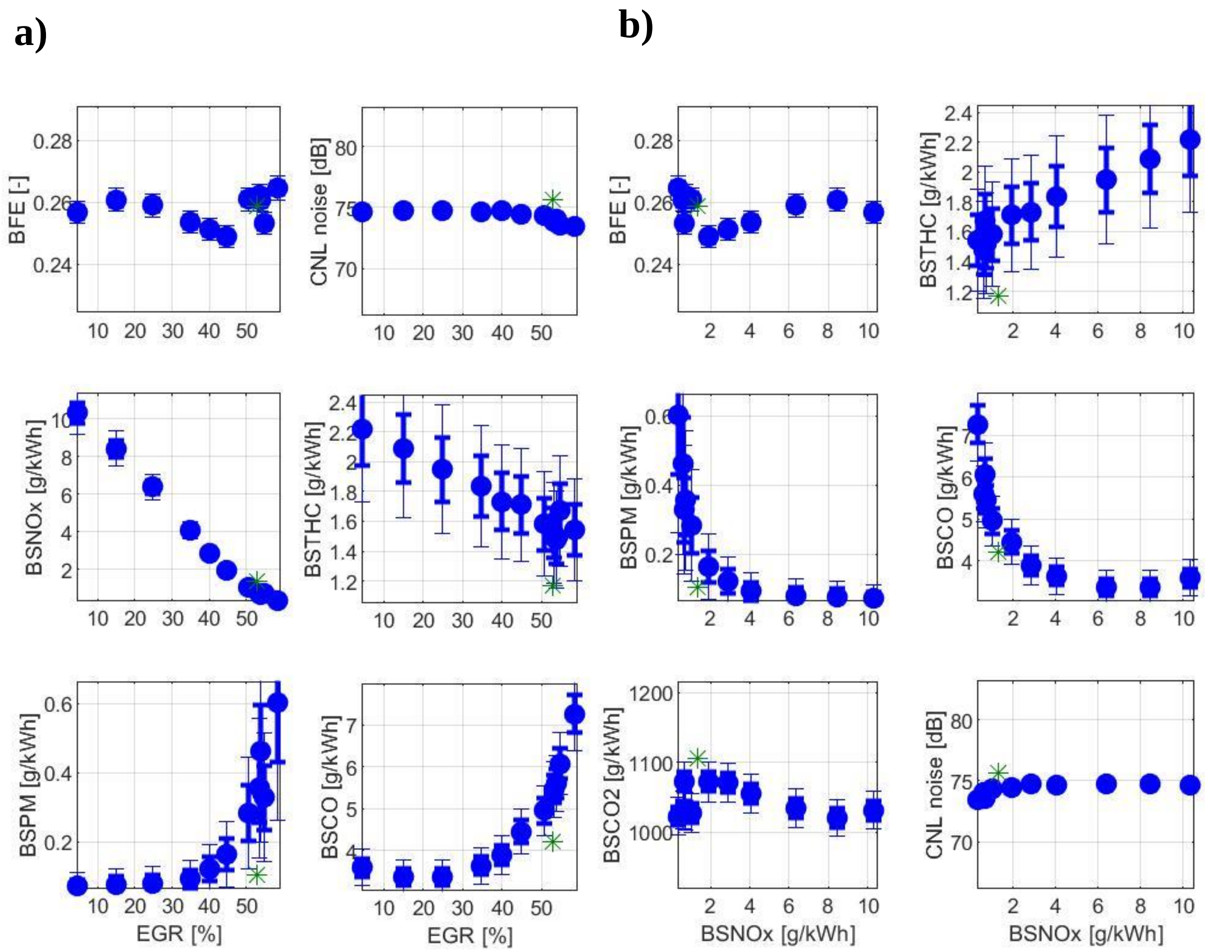

Figure 3.83. BFE, BS emissions, and CNL during the EGR sweep (●: Diesel at default ECU calibration, *: B20 at final calibration) at MM1 as a function of a) EGR rate, b) BSNOx

3.3.4.2 MM2

Table 3.14 shows the change in the ECU input parameters at MM2 as a result of the re-calibration of ECU for B20 to maximize the BFE (or minimize $BSCO_2$) while satisfying the other bound criteria such as BS emissions and CNL. The greyed rows are the fixed target operating conditions imposed the same for the baseline fuel and B20. The red/blue colored rows are the input variables increased/decreased for B20 in the new ECU calibration. For main injection timing (MIT), if the MIT is advanced/retarded, the row is colored blue/red. There are two sets of the B20 calibration shown in Table 3.14. One is the "first" adjusted calibration for B20 with "un-optimized" pilot injected quantity. This is the calibration at which the EGR sweep test is conducted for B20 of which result is shown in Figures 3.84-3.86. After running the EGR sweep test, combustion noise level (CNL) is measured to exceed the bound criterion set by the baseline fuel value, thus requiring further change in the ECU calibration. From the first adjusted ECU calibration, the pilot injection quantity is decreased by 0.25mg/stroke from 2.5mg/stroke to 2.25mg/stroke (underlined in Table 3.14), and the output parameters are measured again at this single point. The result is presented in Figures 3.84-3.86. The other input parameters were all fixed the same between the first and final adjusted ECU calibrations.

First input parameter to discuss from Table 3.14 is the EGR rate. EGR rate is increased by absolute 9.5% from 41% at the default ECU calibration to 50.5% for the adjusted B20 calibrations. The increase in EGR rate at MM2 was mainly to counter off the increased NOx emission due to the impact of B20 at the default calibration and the impact of advanced injection timing at the adjusted ECU calibration.

Boost pressure is decreased by 40hPa from 1030hPa at the default calibration to 990hPa at B20 calibration. Main injection timing (MIT) is advanced by 2.5CAs from 1.6aTDC at the default calibration to -0.9aTDC at the adjusted calibration for B20. The decrease in boost pressure and advance in MIT are the main reasons for the increase in BFE at the adjusted ECU calibration for B20 at MM2.

Rail pressure is decreased by 60bars from 446bar at the default ECU calibration to 385bar at the adjusted ECU calibration for B20. Pilot injection quantity (PIQ) is decreased by 0.6mg/stroke from 3.1mg/stroke at the default ECU calibration to 2.5mg/stroke at the "first" adjusted ECU calibration. However, the combustion noise level (CNL) bound criteria could not be met with the first adjusted pilot injection quantity (PIQ) settings. Thus, PIQ is additionally reduced by 0.25mg/stroke from the first adjusted ECU calibration to the "final" B20 calibration. The relative distance between MIT and PIT decreased by 3.4CAs from 12.3CA at the default ECU calibration to 8.9CA at the adjusted B20 calibration.

MM2	Diesel at default ECU calibration	B20 at first adjusted ECU calibration	B20 at final adjusted ECU calibration
Engine speed [rpm]	1000	1000	1000
Brake torque [N·m]	80	80	80
BMEP [bar]	1.5	1.5	1.5
EGR rate [%]	41	50.5	50.5
Boost pressure [hPa]	1030	990	990
Rail pressure [bar]	446	385	385
Main injection timing [aTDC]	1.6	-0.9	-0.9
Pilot injection quantity [mg/stroke]	3.1	2.5	**2.25**
Relative distance between MIT and PIT [CA]	12.3	8.9	8.9

Table 3.14. Comparison between the default ECU calibration for the baseline diesel and the first/final adjusted ECU calibration for B20. The only difference between the first and final adjusted calibration is the pilot injection quantity (underlined). Grey: Fixed conditions, Red: Increase (Retarding for main injection timing), Blue: Decrease (Advance for main injection timing)

The comparison of BFE, BS emissions, and CNL between the baseline fuel and B20 at the final ECU calibration is shown in Table 3.15. Brake fuel conversion efficiency (BFE) is increased by absolute 0.07% (relative 0.25%) from the baseline fuel. However, this mean difference in BFE between the two fuels was much smaller than one standard deviation (1.02%) from the repeated measurements of BFE, which meant that the two fuels did not have statistically meaningful difference in BFE. Furthermore, $BSCO_2$ of B20 with the final adjusted ECU calibration was only 2g/kWh higher than the baseline fuel, which was much smaller than one standard deviation from the repeated $BSCO_2$ measurements (51.12g/kWh). Considering the results of BFE and $BSCO_2$ together, it can be concluded that, at MM2, B20 at final calibration did not show statistically meaningful improvement in BFE, or GHG emissions.

BSNOx from B20 at the final ECU calibration decreased by 0.67g/kWh from the baseline BSNOx of 1.27g/kWh. This was 52.8% mean decrease in BSNOx, and the mean decrease was much higher than two standard deviations of the repeated BSNOx measurements, which means significant reduction in NOx with statistical confidence over 95%.

BSPM from B20 at the final ECU calibration increased by 0.009g/kWh from the baseline BSPM of 0.169g/kWh. However, the standard deviation in the repeated BSPM measurements at MM2 was 0.050g/kWh, which is much higher than the mean difference in BSPM from the two fuels. Thus, it is concluded that BSPM from B20 at MM2 did not have statistically meaningful difference from the baseline result.

BSTHC from B20 at the final ECU calibration increased by 0.07g/kWh from the baseline value. However, the standard deviation (0.62g/kWh) from the repeated BSTHC measurements at MM2 was much higher than the mean difference in BSTHC between the two fuels. Thus, BSTHC from B20 at the final ECU calibration did not have statistically meaningful difference from the baseline result. BSCO from B20 at the final ECU calibration increased by 0.73g/kWh from the baseline value. This increase was higher than one standard deviation (0.69g/kWh) of the repeated BSCO measurements at MM2, thus ensuring more than 68% confidence in the increase in BSCO for B20. However, the degree of increase in BSCO for B20 was within acceptable range, as a consequence, further change in ECU calibration was not required. Combustion noise level (CNL) from B20 at final calibration increased by 0.19dB from the baseline value. This much increase in CNL could be considered as statistically not meaningful.

The underlying physics causing either the consistency or the change in BFE, BSNOx and BSPM between the two fuels at MM2 will be discussed in detail in the following paragraphs.

MM2	DSL at default calibration	B20 at final calibration	Difference in [%] $[(\frac{B20-DSL}{DSL}) \cdot 100]$	Difference in absolute quantity [B20-DSL]	Standard deviation (σ)
BFE [%]	27.14	27.21	+0.25	+0.07	1.02
$BSCO_2$ [g/kWh]	979	981	+0.2	+2	51.12
BSNOx [g/kWh]	1.27	0.60	-52.8	-0.67	0.134
BSPM [g/kWh]	0.169	0.178	+5.3	+0.009	0.050
BSTHC [g/kWh]	1.39	1.46	+5.0	+0.07	0.62
BSCO [g/kWh]	4.12	4.85	+17.7	+0.73	0.69
CNL [dB]	78.28	78.47	[-]	+0.19	0.29

Table 3.15. Comparison of BFE, BS emissions, and CNL for the baseline fuel and B20 at the final ECU calibration at MM2

Figure 3.84a compares the BFE (top-left), BSNOx (middle-left), BSPM (bottom-left), CNL (top-right), BSTHC (middle-right), BSCO (bottom-right) during the EGR sweep for the diesel fuel at the default ECU calibration (blue filled dots) and for the B20 with the first adjusted ECU calibration (orange empty diamonds) at MM2. The B20 result with the final adjusted ECU calibration is also included in the figure (green star). Figure 3.84b presents the comparison of the BFE (top-left), BSPM (middle-left), $BSCO_2$ (bottom-left), BSTHC (top-right), BSCO (middle-right) and CNL (bottom-right) by BSNOx during the EGR sweep of the diesel fuel at the default ECU calibration and B20 at the first and final adjusted ECU calibrations at MM2.

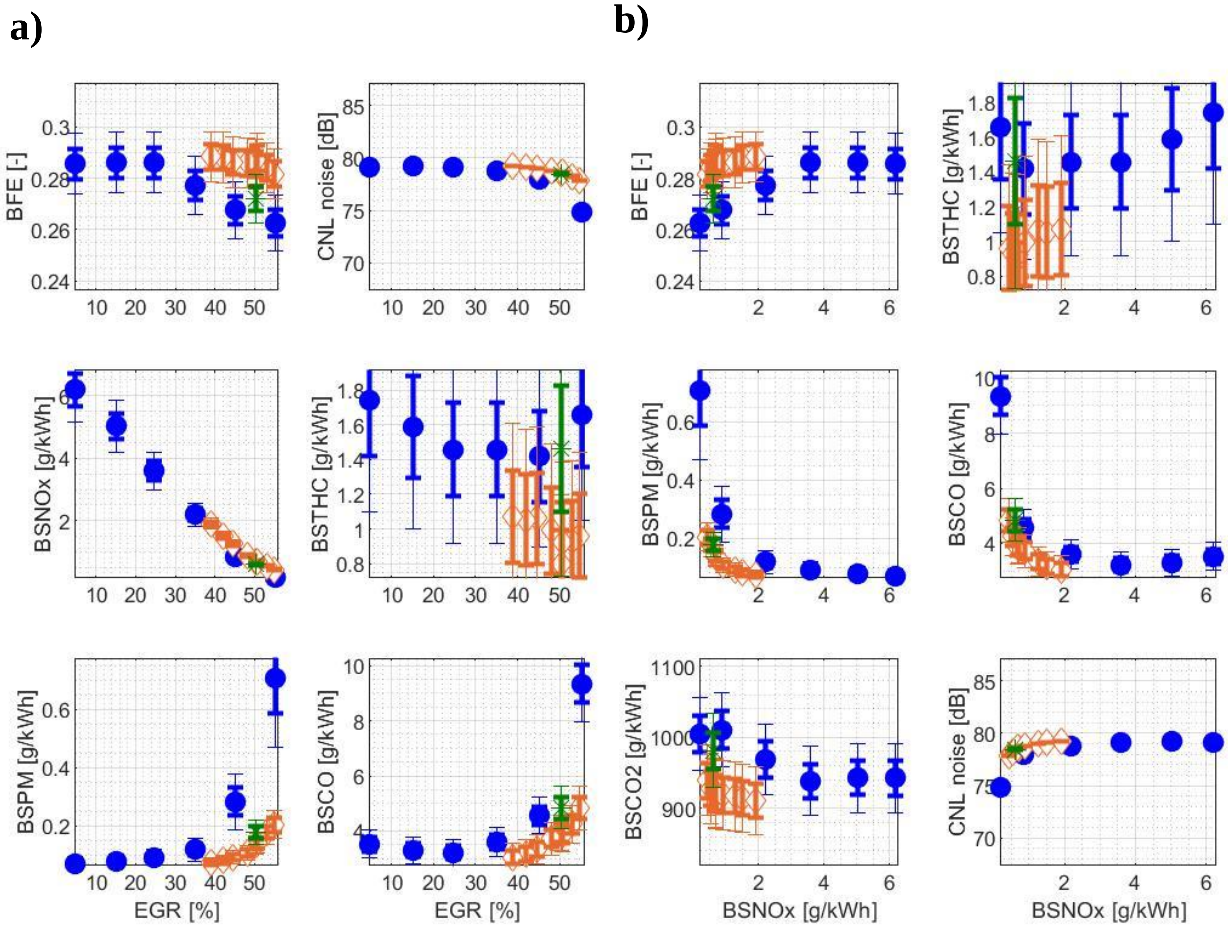

Figure 3.84. BFE, BS emissions, and CNL during EGR sweep (●: Diesel at the default ECU calibration, ◊: B20 at first adjusted ECU calibration, *: B20 at the final calibration) at MM2 as a function of a) EGR rate, b) BSNOx

First, BFE for B20 at the first adjusted ECU calibration (Figure 3.84a, top-left) is increased from the baseline result when compared at the same EGR rate. Brake fuel conversion efficiency (BFE) for B20 at the first adjusted ECU calibration decreases from 28.84% at EGR39% to 28.17% at EGR55%. This is about absolute 1.0-2.0% increase in BFE from the baseline results at the same EGR rate. The main contributor for the increase in BFE at fixed EGR rate is the decrease in PMEP thanks to the decrease in the boost pressure settings for B20. Despite the advance in main injection timing (MIT) at the first adjusted calibration and the subsequent advance in main combustion phasing, IFEg for B20 did not have statistically meaningful improvement from the baseline results.

Figure 3.85a shows the parameters that can affect BFE during the EGR sweep at MM2. Gross indicated fuel conversion efficiency (IFEg, Figure 3.85a, second-to-the-top) for B20 at first adjusted ECU calibration does not show statistically meaningful difference from the baseline result when compared at fixed EGR rates. However, PMEP (Figure 3.85a, third-to-the-top) for B20 at the first adjusted ECU calibration is 0.1-0.2bar lower than that for the baseline fuel at fixed EGR rates, thus confirming the decrease in PMEP as the main cause of improvement in BFE at MM2.

However, the final ECU calibration for B20 could not fully take advantage of the increase in BFE due to the combustion noise level (CNL) bound criterion. As shown in Figure 3.84a (top-right), CNL from B20 at the first adjusted calibration is generally 0.8-1.2dB higher than that from the baseline diesel at fixed EGR rate. To counter off the increase in CNL, the pilot injection quantity (PIQ) is decreased by 0.25mg/stroke from the first adjusted calibration (orange diamond) to the final adjusted calibration (green star). At the final calibration, BFE was 27.2%, which is only absolute 0.07% higher than that for the baseline diesel.

Second, BSNOx emission for B20 at the first adjusted calibration did not have statistically meaningful difference from the baseline value at fixed EGR rate. It decreases from 1.9g/kWh at EGR39% to 0.44g/kWh at EGR55%. The difference of BSNOx values between the two fuels was smaller than the standard deviation of the repeated BSNOx measurements at MM2, which means there is no statistically meaningful difference between the two fuels in terms of BSNOx emissions. Although BSNOx emission was consistent for the baseline diesel and B20 at the adjusted ECU calibrations, the values of the fundamental parameters affecting BSNOx for the two fuels were different. Thus, it is likely that the different impacts from different parameters affecting BSNOx countered off each other resulting in the same BSNOx for the two fuels.

Figures 3.85b, 3.85c, and 3.86a present the parameters affecting BSNOx emission during the EGR sweep at MM2. Intake O_2 concentration (Figure 3.85b, top) for B20 at the adjusted ECU calibrations did not have statistically meaningful difference from the baseline results at each EGR rate. However, peak cylinder temperature timing (Figure 3.85b, second-to-the-top) was advanced for B20 at the adjusted ECU calibrations. It was advanced by about 2CAs from the baseline results for most of the imposed EGR conditions, with more intense degree of advance in the higher EGR range. This advance in peak cylinder temperature timing for B20 competed with the decrease in charge gas temperature during the main ignition delay for B20 (Figure 3.85b, third-to-the-top). The charge gas temperature decreased for B20 by 100-150K from the baseline value depending on the EGR rate imposed. As the EGR rate is increased, the degree of decrease in the charge gas temperature became more intense. Thus, it is reasonable to conclude that these two factors (i.e., peak cylinder temperature timing and charge gas temperature during the main ignition delay) have countered each other off, thus resulting in the consistent BSNOx level for the two fuels. From the viewpoint of the change in input parameter settings at MM2, the advance in main injection timing (MIT) can be regarded as the primary factor for the advance in peak cylinder temperature timing for B20 while the decrease in boost pressure can be regarded as the main reason for the decrease in the charge gas temperature for B20.

One interesting phenomenon to note here is that the trend of charge gas temperature by EGR rate for the two fuels is very different. The slope and range of decrease in charge gas temperature by EGR increase is greater in B20 than in the baseline diesel. This is because, at the adjusted ECU calibration for B20, the decrease in total charge gas molar concentration with increasing EGR rate was less apparent while the decrease in cylinder pressure with increasing EGR rate remained similar to the baseline case.

Figure 3.87 shows the cylinder pressure and total number of moles of charge gas (i.e., sum of the number of moles of fresh air, EGR gas, and injected fuel contained in the combustion chamber) during the ignition delay of the EGR sweep tests of the two fuels. Based on the ideal gas law (i.e., $\frac{PV}{nR} = T$), charge gas temperature during the main ignition delay varies depending on the ratio of cylinder pressure to the total number of moles of charge gas. For the baseline diesel, the cylinder pressure decreased from 45.2bar at 35% EGR to 42.0bar at 55% EGR (7% decrease) while it has decreased from 42.3bar at 38% EGR to 40.6bar at 53% EGR (4% decrease) for B20 with the first adjusted ECU calibration. Considering that the 7% decrease in cylinder pressure for the baseline diesel occurred for 20% increase in EGR rate while the 4% decrease in cylinder pressure for B20 occurred for 15% increase in EGR rate, it is reasonable to say that the degree of cylinder pressure drop with increasing EGR rate for the two fuels was similar. However, the degree of decrease in the total number of moles of charge gas with increasing EGR rate for the two fuels was significantly different. For the baseline fuel, the total number of moles of charge gas has decreased from $2.49 \cdot 10^{-5}$ kmol at 35% EGR to $2.29 \cdot 10^{-5}$ kmol at 55% EGR (8%

decrease) while it only decreased from $2.59 \cdot 10^{-5}$ kmol at 38% EGR to $2.55 \cdot 10^{-5}$ kmol at 53% EGR (1.5% decrease) for B20 with the first adjusted ECU calibration. This less intensive drop in the total number of moles of charge gas with increasing EGR rate for B20 is partially due to the unintended increase in boost pressure (~3hPa) at higher EGR conditions at the adjusted ECU calibrations. However, there is a more fundamental reason for this phenomenon.

The total number of moles of charge gas is simply the sum of the total moles of fresh air, EGR gas, and injected fuel. Since B20 has lower LHV, more mass (or more moles) of fuel must be injected to meet the same fuel energy flow. This increase in the number of moles of injected fuel also increases its share out of the total number of moles of charge gas: simply put, the change in the number of moles of fuel caused by the EGR rate increase plays greater role for B20 than the baseline diesel. When EGR rate is increased, the average molecular weight of the intake gas increases due to the heavier molecules (i.e., CO_2 and H_2O) contained in the EGR gas compared to O_2 and N_2 contained in the fresh air. This increased average molecular weight results in the decrease in the number of moles of fresh air and EGR gas since the total mass of intake gas must be conserved for fixed boost pressure and engine speed. The drop in the number of moles of intake gas competes with the increased number of moles of fuel with increasing EGR rate. However, the degree of increase in the number of moles of fuel usually gets overshadowed by the decrease in the number of moles of intake gas, thus resulting in the decrease in the total number of moles of charge gas with increasing EGR rate. Yet, when B20 is applied, the impact of the number of moles of fuel becomes greater than for the baseline diesel, thus resulting in the less apparent decrease in the total number of moles of charge gas with increasing EGR rate. In conclusion, at MM2, B20 application makes the total number of moles of charge gas drop less apparent with increasing EGR rate while the cylinder pressure drop remains similar to the baseline case. This results in the more intensive decrease in charge gas temperature with increasing EGR rate for B20 as shown in Figure 3.85b (third-to-the-top).

This significant decrease in charge gas temperature during the main ignition delay for B20 results in the significant decrease in lift-off length. Figure 3.86b shows the lift-off length (top) and oxygen ratio at the lift-off length (middle) with the trend of BSPM (bottom) for the two fuels with different ECU calibration. Due to the decrease in charge gas temperature, lift-off length for B20 is 3-4mm longer than the baseline case, thus resulting in the absolute 4-5% increase in oxygen ratio at the lift-off length. Considering that the variation in oxygen ratio across the whole EGR range at MM2 for the baseline fuel was just around absolute 2%, the absolute 4-5% increase in oxygen ratio due to B20 application is such a significant improvement that can affect BSPM emission. As a result, despite the consistent intake O_2 concentration for the two fuels, the BSPM emission for B20 with the adjusted ECU calibrations is significantly lower than the baseline case. BSPM emission for B20 at the first adjusted ECU calibration increases from 0.074g/kWh at EGR39% to 0.204g/kWh at EGR55%. As compared to the baseline case, this is 37-71% reduction in BSPM at the fixed EGR rate.

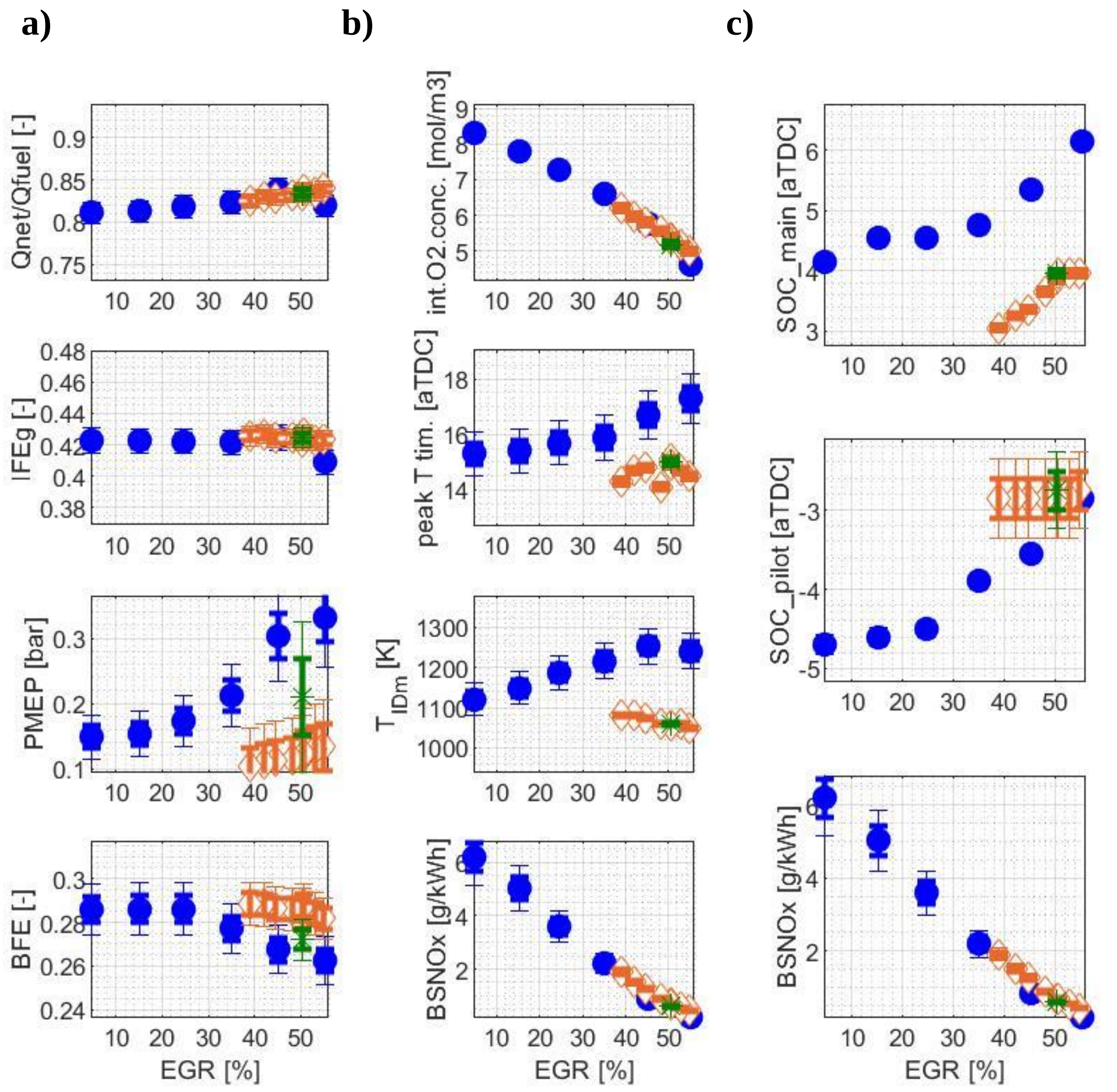

Figure 3.85. The parameters affecting a) BFE, b) and c) BSNOx during EGR sweep at MM2 (●: Diesel at the default ECU calibration, ◊: B20 at first adjusted ECU calibration, *: B20 at the final calibration)

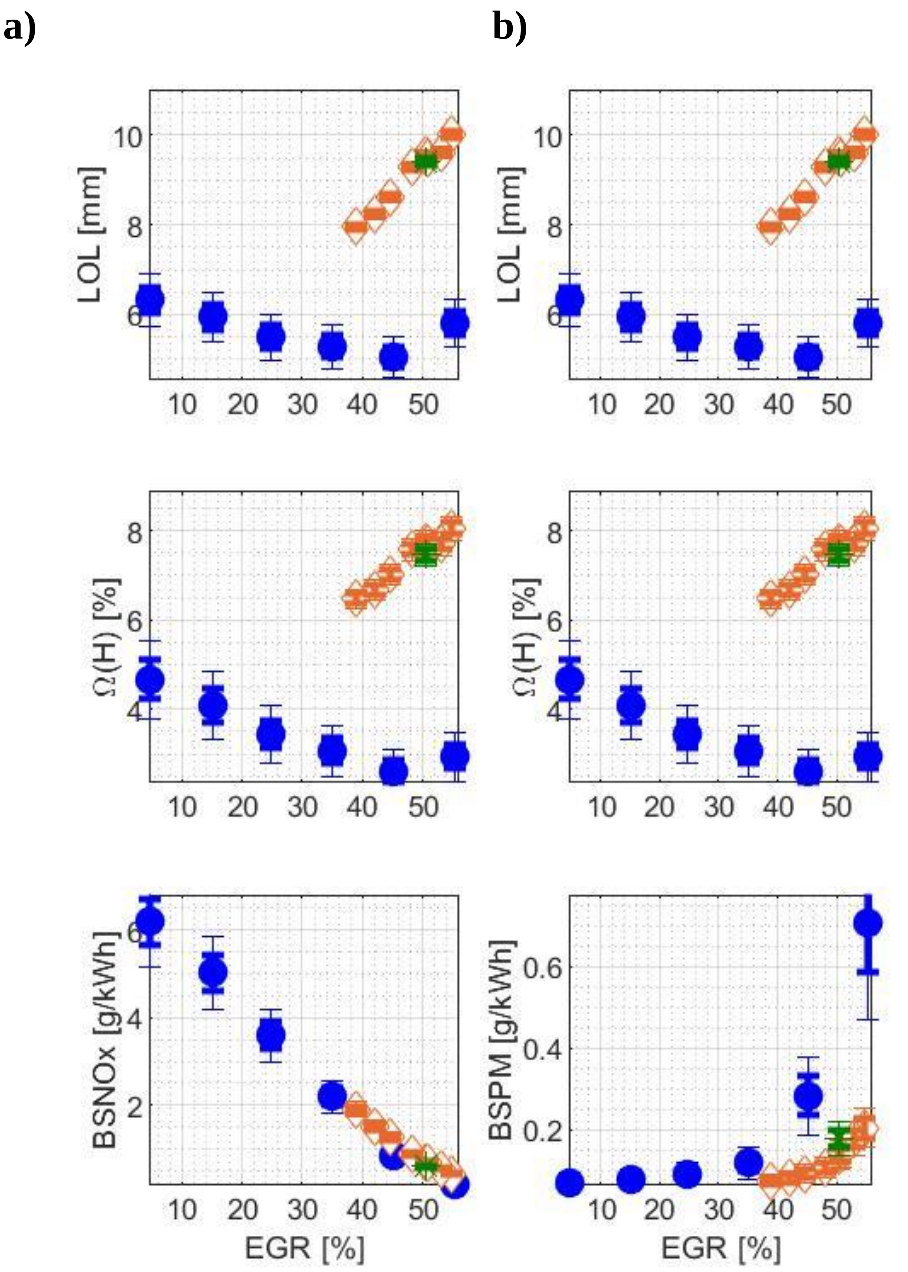

Figure 3.86. The lift-off length and oxygen ratio at the lift-off length during EGR sweep (●: Diesel at the default ECU calibration, ◊: B20 at first adjusted ECU calibration, *: B20 at the final calibration) at MM2 with the trend of a) BSNOx and b) BSPM

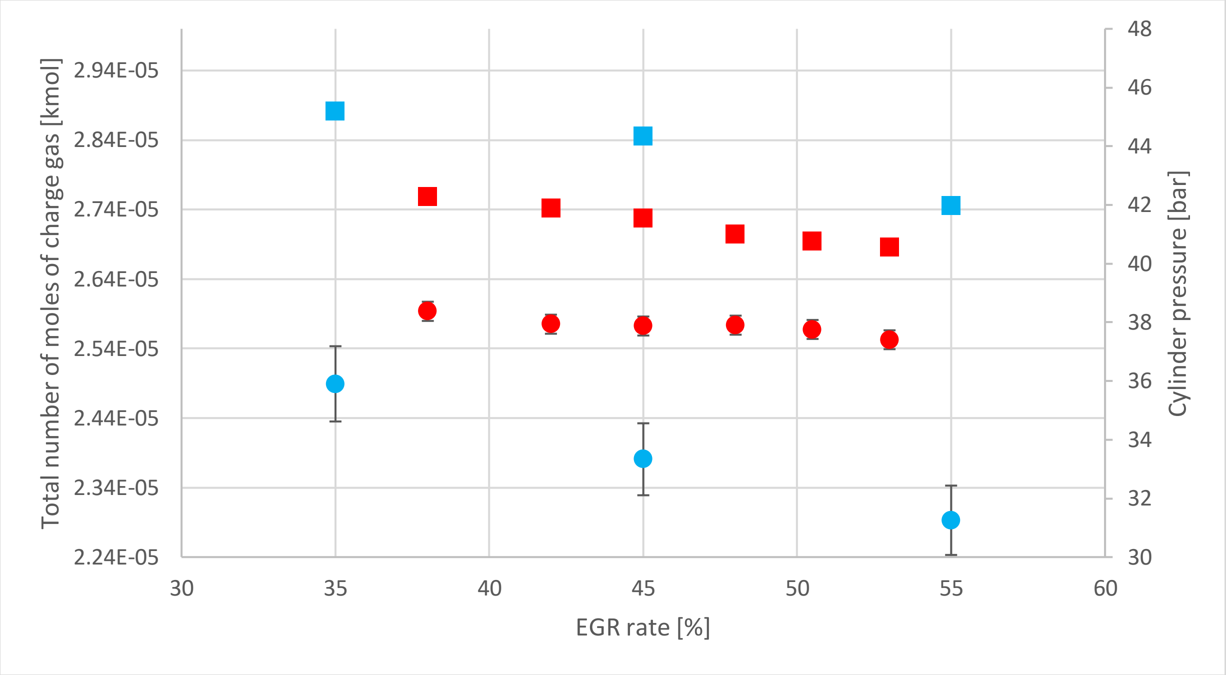

Figure 3.87 Cylinder pressure and total number of moles of charge gas by EGR rate at MM2 (🟦: Cylinder pressure (Baseline diesel), 🟥: Cylinder pressure (B20 at the first adjusted ECU calibration), ●: Total number of moles of charge gas (Baseline diesel), ●: Total number of moles of charge gas (B20 at the first adjusted ECU calibration))

3.3.4.3 MM3

Table 3.16 shows the change in ECU input parameters at MM3 as a result of the re-calibration of ECU for B20 to maximize the BFE (or minimize $BSCO_2$) while satisfying the other bound criteria such as BS emissions and CNL. The greyed rows are the fixed target operating conditions imposed the same for the baseline fuel and B20. The red/blue colored rows are the input variables increased/decreased for B20 in the new calibration settings. For main injection timing (MIT), if the MIT is advanced/retarded, the row is colored blue/red.

First input parameter to discuss from Table 3.16 is the EGR rate. Exhaust gas recirculation (EGR) rate is increased by absolute 8% from 34% at the default ECU calibration to 42% for the adjusted B20 calibration. The increase in EGR rate at MM3 was mainly to counter off the increased NOx emission due to the impact of B20 at the default calibration and the impact of the advanced injection timing at the adjusted ECU calibration for B20. The other reason for the increase in EGR rate was to meet the combustion noise level (CNL) upper limit. This will be explained in detail later in this section. Rail pressure is also increased for the new ECU calibration for B20 at MM3, but the degree of increase was small (i.e., 1.3% increase from the default rail pressure).

Boost pressure is decreased by 40hPa from 1070hPa at the default ECU calibration to 1030hPa at the adjusted ECU calibration for B20. The decrease in boost pressure partially contributed to the increase in BFE which would have been decreased otherwise due to the increase in EGR rate at the adjusted ECU calibration for B20. The decrease in boost pressure also contributed to the decrease in BSNOx.

Main injection timing (MIT) is advanced from 2.9aTDC at the default ECU calibration to 1.7aTDC (i.e., 1.2CA advance) at the adjusted B20 calibration. The advance in MIT was the primary factor that compensated for the BFE decrease caused by EGR increase at the new ECU calibration for B20. Pilot injection quantity is decreased from 3.9mg/stroke at the default ECU calibration to 3.78mg/stroke at the new ECU calibration for B20. The relative distance between MIT and pilot injection timing (PIT) has also decreased from 14.4CA at the default calibration to 9.4CA at the adjusted ECU calibration for B20.

MM3	Diesel at default ECU calibration	B20 at final adjusted ECU calibration
Engine speed [rpm]	1200	1200
Brake torque [N·m]	159	159
BMEP [bar]	3	3
EGR rate [%]	34	42
Boost pressure [hPa]	1070	1030
Rail pressure [bar]	711	720
Main injection timing [aTDC]	2.9	1.7
Pilot injection quantity [mg/stroke]	3.9	3.78
Relative distance between MIT and PIT [CA]	14.4	9.4

Table 3.16. Comparison between the default ECU calibration for baseline diesel and the final adjusted ECU calibration for B20 at MM3. Grey: Fixed conditions, Red: Increase (Retarding for main injection timing), Blue: Decrease (Advance for main injection timing)

The comparison of BFE, BS emissions, and CNL between the baseline fuel and B20 with the final ECU calibration is shown in Table 3.17. Brake fuel conversion efficiency (BFE) is increased by absolute 0.03% (relative 0.1%) from the baseline result. However, this mean difference in BFE between the two fuels was much smaller than one standard deviation (0.36%) of the repeated measurements of BFE, which meant that the two fuels did not have statistically meaningful difference in BFE. In the meanwhile, $BSCO_2$ of B20 with the final calibration was 14g/kWh lower than the baseline result. The standard deviation in $BSCO_2$ was 8.72g/kWh during the repeat point tests, thus meaning the statistically meaningful decrease in $BSCO_2$ for B20 with the final ECU calibration with low statistical confidence. Considering the result of BFE and $BSCO_2$ together with more weight on BFE, it is concluded that, at MM3, B20 with the adjusted calibration did not show statistically meaningful improvement in BFE, or GHG emissions.

BSNOx from B20 at the final ECU calibration decreased by 0.29g/kWh from the baseline BSNOx of 0.64g/kWh. This was 45.3% decrease in BSNOx, and the mean decrease in BSNOx was much higher than plus and minus two standard deviations, which means significant reduction in NOx with statistical confidence over 95%. BSPM from B20 at the final ECU calibration decreased by 0.060g/kWh from the baseline BSPM of 0.136g/kWh. This was 44.1% decrease in BSPM, and the mean decrease in BSPM was much higher than plus and minus two standard deviations, which meant significant reduction in PM with statistical confidence over 95%. The underlying physics that led to the significant reduction in BSNOx and BSPM for B20 at MM3 will be discussed in detail later in this section.

The BSTHC and BSCO both increased for B20 at the final ECU calibration. BSTHC increased by 0.11g/kWh from the baseline value of 0.57g/kWh. BSCO increased by 1.05g/kWh from the baseline value of 3.53g/kWh. These increases in BSTHC and BSCO were 19.3% and 29.7% increase from the baseline values. However, the degree of increase was in the acceptable range, as a consequence, further ECU calibration was not required. Combustion noise level (CNL) for B20 at final calibration increased by 0.33dB from the baseline value of 80.17dB, which could also be considered as the increase within acceptable range.

MM3	DSL at default calibration	B20 at final calibration	Difference in [%] $[(\frac{B20-DSL}{DSL})\cdot 100]$	Difference in absolute quantity [B20-DSL]	Standard deviation (σ)
BFE [%]	33.77	33.80	+0.1	+0.03%	0.36
$BSCO_2$ [g/kWh]	787	773	-1.8	-14	8.72
BSNOx [g/kWh]	0.64	0.35	-45.3	-0.29	0.043
BSPM [g/kWh]	0.136	0.076	-44.1	-0.060	0.023
BSTHC [g/kWh]	0.57	0.68	+19.3	+0.11	0.060
BSCO [g/kWh]	3.53	4.58	+29.7	+1.05	0.21
CNL [dB]	80.17	80.50	[-]	+0.33	0.52

Table 3.17. Comparison of BFE, BS emissions, and CNL for the baseline fuel with the default ECU settings and B20 with final ECU calibration at MM3

Figure 3.88a compares the BFE (top-left), BSNOx (middle-left), BSPM (bottom-left), CNL (top-right), BSTHC (middle-right), BSCO (bottom-right) during the EGR sweep of the diesel fuel at the default ECU calibration (blue filled dots) and of the B20 with the adjusted ECU calibration (orange empty diamonds) at MM3. One of the data points obtained during the EGR sweep test of B20 is the result at the final ECU calibration for B20 (i.e., EGR 42%). Figure 3.88b presents the comparison of the BFE (top-left), BSPM (middle-left), $BSCO_2$ (bottom-left), BSTHC (top-right), BSCO (middle-right) and CNL (bottom-right) by BSNOx during the EGR sweep of the baseline diesel at the default ECU calibration and B20 at the adjusted ECU calibration at MM3.

First, BFE of B20 at the adjusted ECU calibration is increased from the baseline value at fixed EGR rate. Brake fuel conversion efficiency (BFE) for B20 decreases from 34.4% at EGR34% to 33.4% at EGR45% during the EGR sweep. During the same range of EGR, the BFE for the baseline diesel decreased from 34.0% at EGR 34% to 32.8% at EGR45%. Thus, there is about absolute 0.5% increase in BFE for B20 for most of the EGR conditions imposed. This is thanks to the increase in IFEg and the decrease in PMEP.

Figure 3.89a presents the parameters relevant to BFE during the EGR sweep for the two fuels at MM3. Gross indicated fuel conversion efficiency (IFEg, Figure 3.89a, second to the top plot) for B20 at the adjusted ECU calibrations is generally about absolute 0.8% higher than the baseline results at each EGR rate. This increase in IFEg for B20 is thanks to the advanced main SOC driven by the advanced SOI command in the adjusted calibration as shown in Figure 3.89c top plot. We can also see that the pilot SOC got closer to TDC for B20 at adjusted ECU calibration (Figure 3.89c, middle plot) thanks to the decrease in relative distance between main injection timing and pilot injection timing. The advance in main SOC and retarding in pilot SOC resulted in the improvement in the thermal efficiency of both pilot and main combustion events and the higher “actual” compression ratio, which led to the increase in IFEg. Pump mean effective pressure (PMEP, Figure 3.89a, third to the top plot) is also decreased for B20 at adjusted ECU calibration. It is about 0.15bar lower for B20 at the adjusted ECU calibration due to the decrease in boost pressure settings. Therefore, the increase in IFEg and decrease in PMEP resulted in the increase in BFE for B20 with the adjusted ECU calibration when compared at the fixed EGR rate.

However, the final calibration for B20 cannot fully take advantage of the increase in BFE at fixed EGR rate due to its increased EGR rate settings. The final calibration for B20 uses 42% EGR rate while the default calibration use only 34% EGR rate. The increase in EGR rate setting is mainly because BSNOx emission from B20 exceeds the bound criteria at the default EGR rate settings (i.e., EGR 34%). As shown in the middle-left plot in Figure 3.88a, BSNOx emission from B20 at the adjusted ECU calibration at EGR 34% is 0.85g/kWh while BSNOx emission from the baseline diesel with default calibration was 0.64g/kWh (i.e., 33% increase). To meet the BSNOx bound criteria, the EGR rate had to be increased, at least, to 38% for B20.

There is another reason for the increase in EGR rate settings for B20 calibration: combustion noise level (CNL) bound criteria. Although BSNOx bound criteria can be met at EGR 38% at the adjusted ECU calibration for B20, CNL at EGR 38% was 81.9dB for B20, which is about 1.5dB higher than the baseline CNL. Thus, EGR rate had to be increased further. At EGR 42%, CNL could be reduced to the acceptable level (80.5dB). Therefore, the final EGR rate settings for B20 at MM3 became 42%, resulting in the same BFE performance as the baseline fuel.

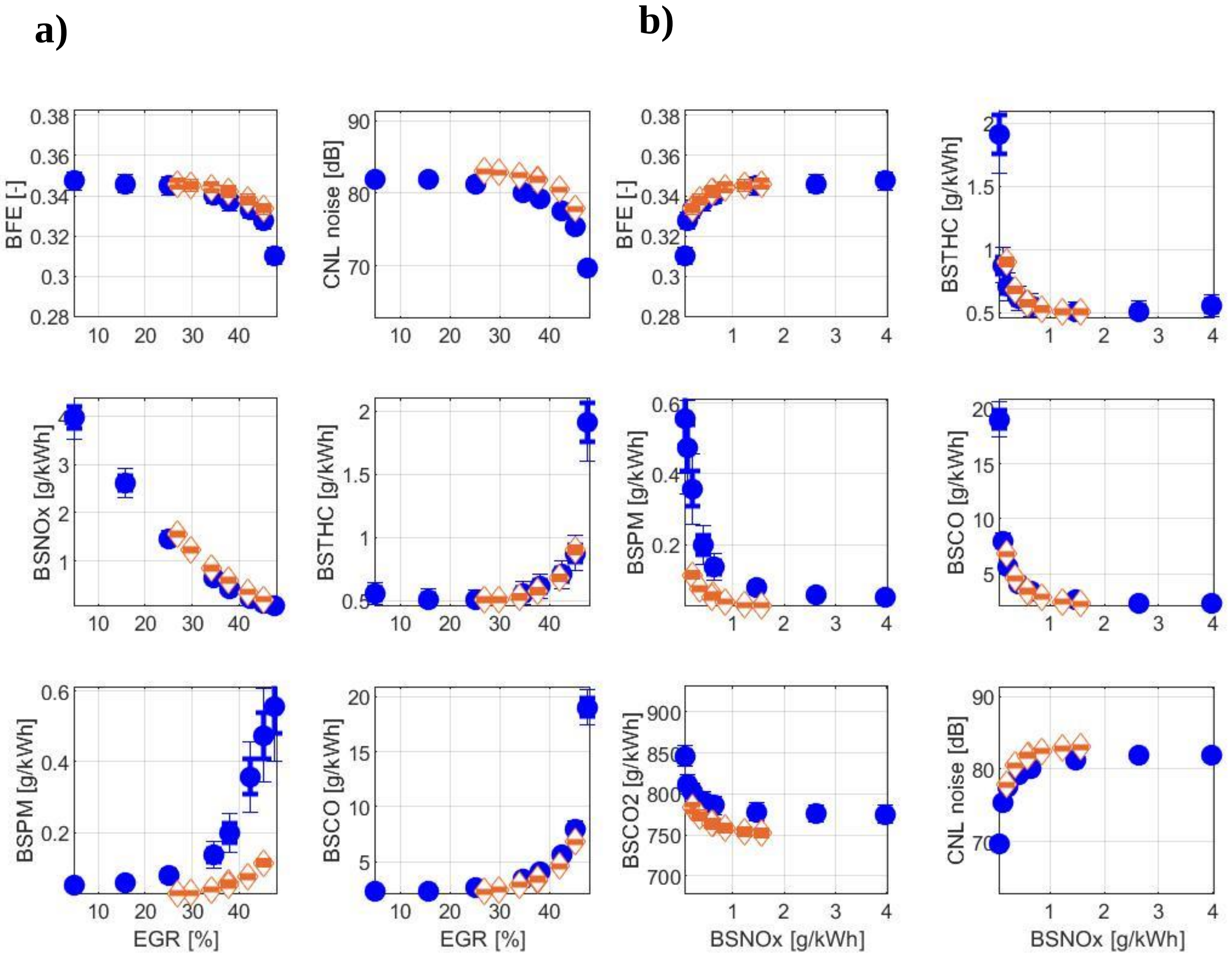

Figure 3.88. BFE, BS emissions, and CNL during EGR sweep (●: Diesel at default ECU calibration, ◊: B20 at adjusted ECU calibration) at MM3 as a function of a) EGR rate, b) BSNOx

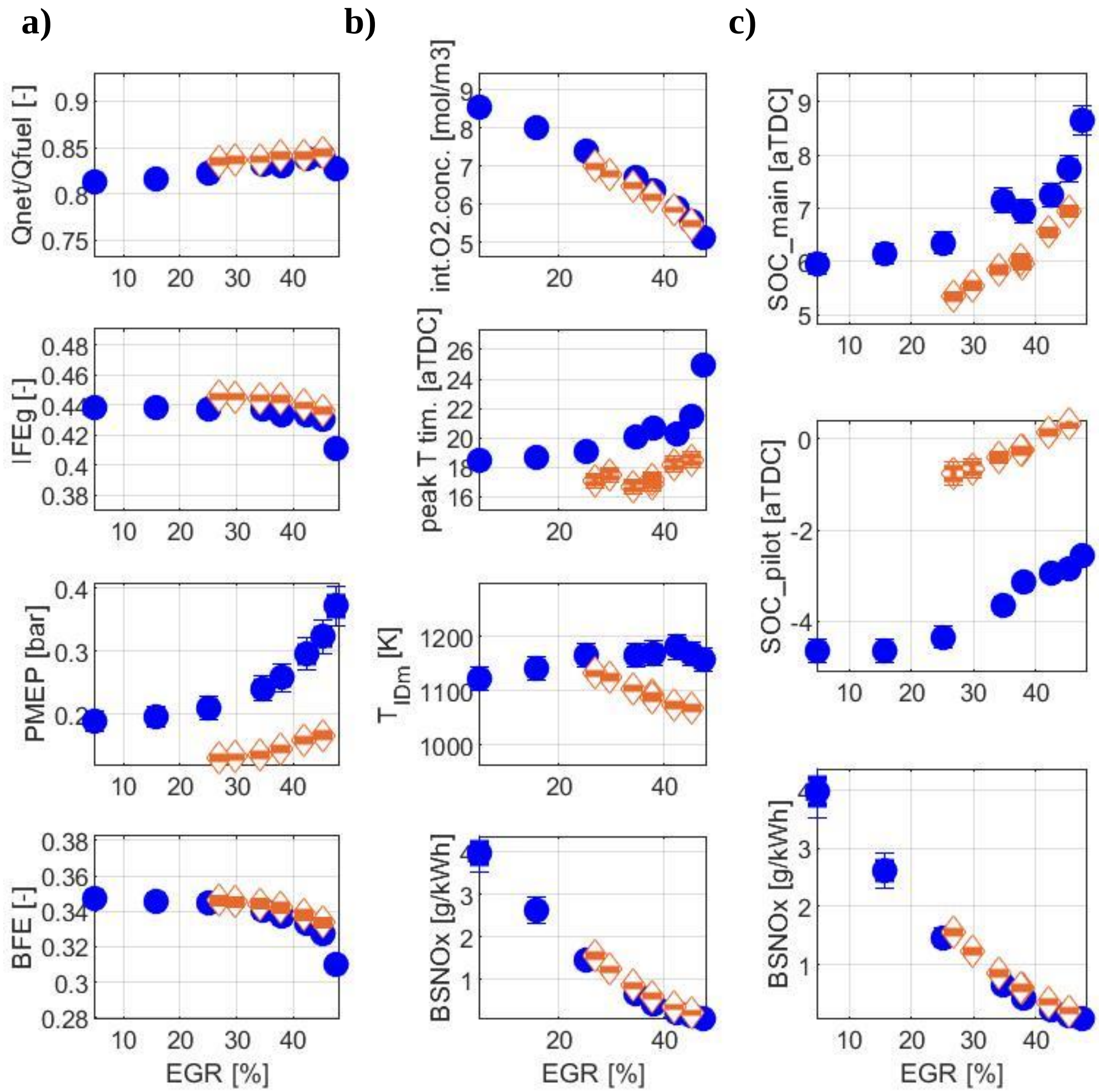

Figure 3.89. The parameters affecting a) BFE, b) and c) BSNOx during EGR sweep (●: Diesel at default ECU calibration, ◊: B20 at adjusted ECU calibration) at MM3

Second, BSNOx from B20 at the adjusted ECU calibration did not have statistically meaningful difference from the baseline result at each EGR rate. However, the increase in EGR rate settings has greatly contributed to the decrease in final BSNOx emission from B20, and this is the main reason for significant BSNOx reduction (45%) from B20 with the final ECU calibration.

One interesting phenomenon to note here is the decrease in charge gas temperature for B20 with the adjusted ECU calibration with increased sensitivity of charge gas temperature to the EGR rate. Figure 3.89b third to the top plot shows the comparison of the charge gas temperature of the two fuels at different ECU calibrations. B20 generally has the decreased charge gas temperature during the ignition delay than the baseline fuel, and the degree of decrement becomes significantly greater as the EGR rate is increased (i.e., higher sensitivity to EGR rate for B20). For example, at EGR 34%, the charge gas temperature for B20 is about 60K lower than the baseline fuel, but, the difference increases to about 100K at 45% EGR. This is because, for B20, the cylinder pressure drops more apparent while the total charge gas mole count drops less apparent with increasing EGR rate.

Figure 3.90 shows the cylinder pressure and total number of moles of charge gas (i.e., sum of the number of molecules of fresh air, EGR gas, and injected fuel) during the main ignition delay for the two fuels. Based on the ideal gas law (i.e., $\frac{PV}{nR} = T$), charge gas temperature during the ignition delay (Figure 3.89b, third to the top plot) varies based on the ratio of cylinder pressure to total number of moles of charge gas. For the baseline fuel, the cylinder pressure decreased from 46.4bar at 34% EGR to 44.5bar at 45% EGR (4% decrease) while it has decreased from 43.7bar at 34% EGR to 41.2bar at 45% EGR (5.7% decrease) for B20 with the adjusted ECU calibration: the lower boost pressure settings for the B20 calibration made the percentage of cylinder pressure drop more intense with increasing EGR rate. Furthermore, while the total number of moles of charge gas has decreased from $2.73 \cdot 10^{-5}$ kmol at 34% EGR to $2.63 \cdot 10^{-5}$ kmol at 45% EGR (3.7% decrease) for the baseline diesel, it only decreased from $2.68 \cdot 10^{-5}$ kmol at 34% EGR to $2.64 \cdot 10^{-5}$ kmol at 45% EGR (1.5% decrease) for B20 with the adjusted ECU calibration. This less intensive drop in the total number of moles of charge gas for B20 is partially due to the unintended increase in boost pressure (~5hPa) at higher EGR conditions with new ECU calibration, but there is more fundamental reason for this phenomenon.

The total number of moles of charge gas is simply the sum of the number of moles of fresh air, EGR gas, and injected fuel. Since B20 has lower LHV, more mass (or more moles) of fuel must be injected to meet the same fuel energy flow. When EGR rate is increased, the average molecular weight of the intake gas increases due to the heavier molecules (i.e., CO_2 and H_2O) contained in EGR gas compared to O_2 and N_2 contained in the fresh air. This increased average molecular weight results in the decrease in the number of moles of fresh air and EGR gas since the total mass of intake gas must be conserved for certain boost pressure and engine speed. However, since BFE decreases with increasing EGR rate, the number of moles of injected fuel increases with increasing EGR. Thus, when EGR is increased, the drop in the number of moles of intake gas competes with the increase in the number of moles of injected fuel. Often, the degree of increase in the number of moles of fuel gets overshadowed by the decrease in the number of moles of intake gas, thus resulting in the overall decrease in total number of moles of charge gas as EGR is increased. However, when B20 is applied, the impact of the number of moles of fuel becomes greater than it was for the baseline diesel, thus resulting in less apparent decrease in the total number of moles of charge gas.

Therefore, B20 application makes cylinder pressure drop more apparent, but also makes the drop in the total number of moles of charge gas less apparent when EGR is increased. This results in significant decrease in charge gas temperature with higher sensitivity to EGR rate as shown in Figure 3.89b (third-to-the-top plot). Then, this decrease in charge gas temperature results in significant increase in lift-off length, which, in turn, results in significant increase in oxygen ratio at the lift-off length.

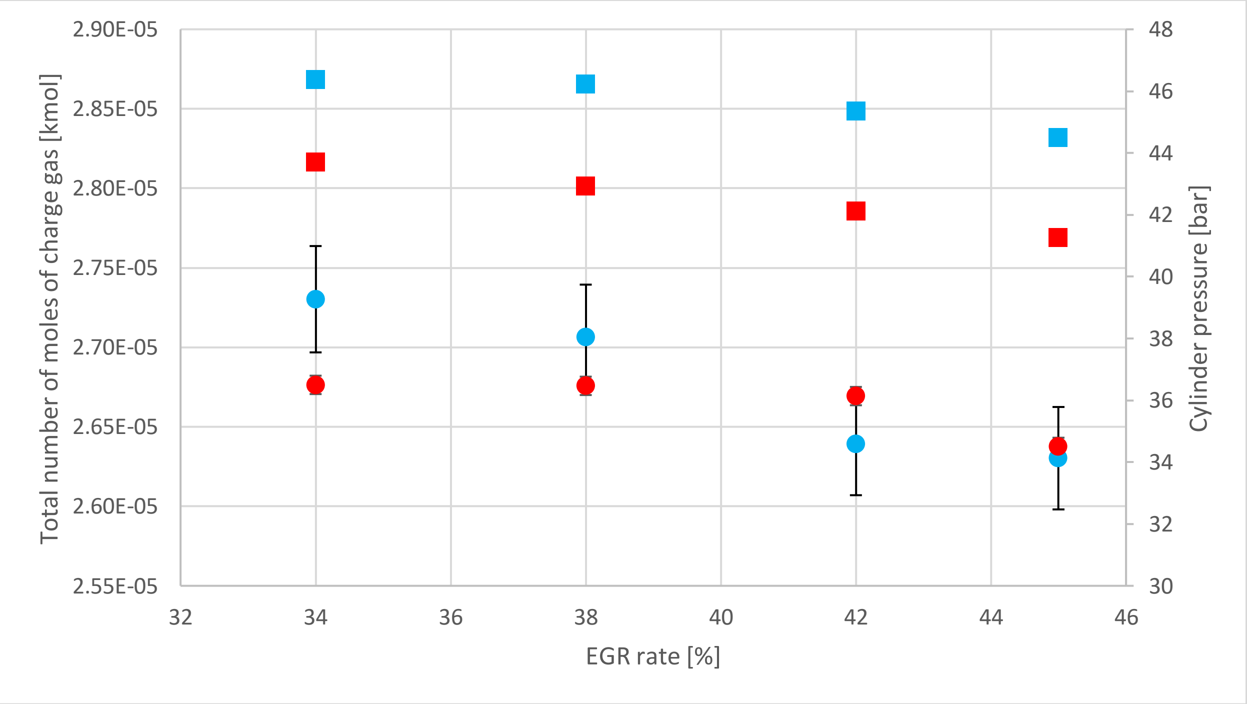

Figure 3.90 Cylinder pressure and total number of moles of charge gas by EGR rate at MM3 (🟦: Cylinder pressure (Baseline diesel), 🟥: Cylinder pressure (B20 at the adjusted ECU calibration), 🔵: Total number of moles of charge gas (Baseline diesel), 🔴: Total number of moles of charge gas (B20 at the adjusted ECU calibration))

Figure 3.91a shows the lift-off length (top) and oxygen ratio at the lift-off length (middle) during the EGR sweep of the two fuels at MM3 with the trend of BSNOx (bottom). Lift-off length for B20 at the adjusted ECU calibration increases from 8.5mm to 13mm between EGR 27% condition and EGR45% condition. Oxygen ratio at the lift-off length for B20 at the adjusted

ECU calibration also increases from 7.5% at EGR27% to 11% at EGR 45%. This is significant increase in oxygen ratio for B20 in the average standpoint and also from the perspective of sensitivity to the EGR rate. In the end, this increase in oxygen ratio for B20 counters off the decrease in charge gas temperature, thus resulting in the same level of BSNOx for the two fuels.

However, when it comes to the BSPM emission, this decrease in charge gas temperature and increase in the sensitivity of the charge gas temperature to the EGR rate significantly decreases the emission. Since the oxygen ratio at the lift-off length is increased for B20 due to the decrease in charge gas temperature, the more oxygen becomes available in the fuel-rich premixed auto-ignition zone. This results in the decrease in BSPM for B20 at fixed EGR rate. Given the fact that intake O_2 concentration remains the same for the two fuels (Figure 3.89b top plot), it is reasonable to conclude that the increase in oxygen ratio for B20 is the main cause for the decrease in BSPM. As a result, at fixed EGR rate, BSPM for B20 at the adjusted ECU calibration is about 50-80% lower than the baseline values. This allows the increase in EGR rate settings to reduce the NOx and CNL while achieving the 44% reduction in BSPM at the final ECU calibration for B20.

Figure 3.88a also shows other brake specific (BS) emissions and combustion noise level (CNL) from B20 at the adjusted ECU calibration. BSTHC and BSCO are the same for the two fuels at fixed EGR rate while CNL is about 2 dB higher for B20 at the adjusted ECU calibration. As mentioned earlier with Table 3.17, the final BSTHC and BSCO for B20 with the final ECU calibration were just moderately higher than the baseline results, which did not require further ECU adjustment. The 2dB increase in CNL at fixed EGR rate is compensated by the increase in EGR rate settings, which resulted in satisfactory CNL result (80.5dB) for B20, as well.

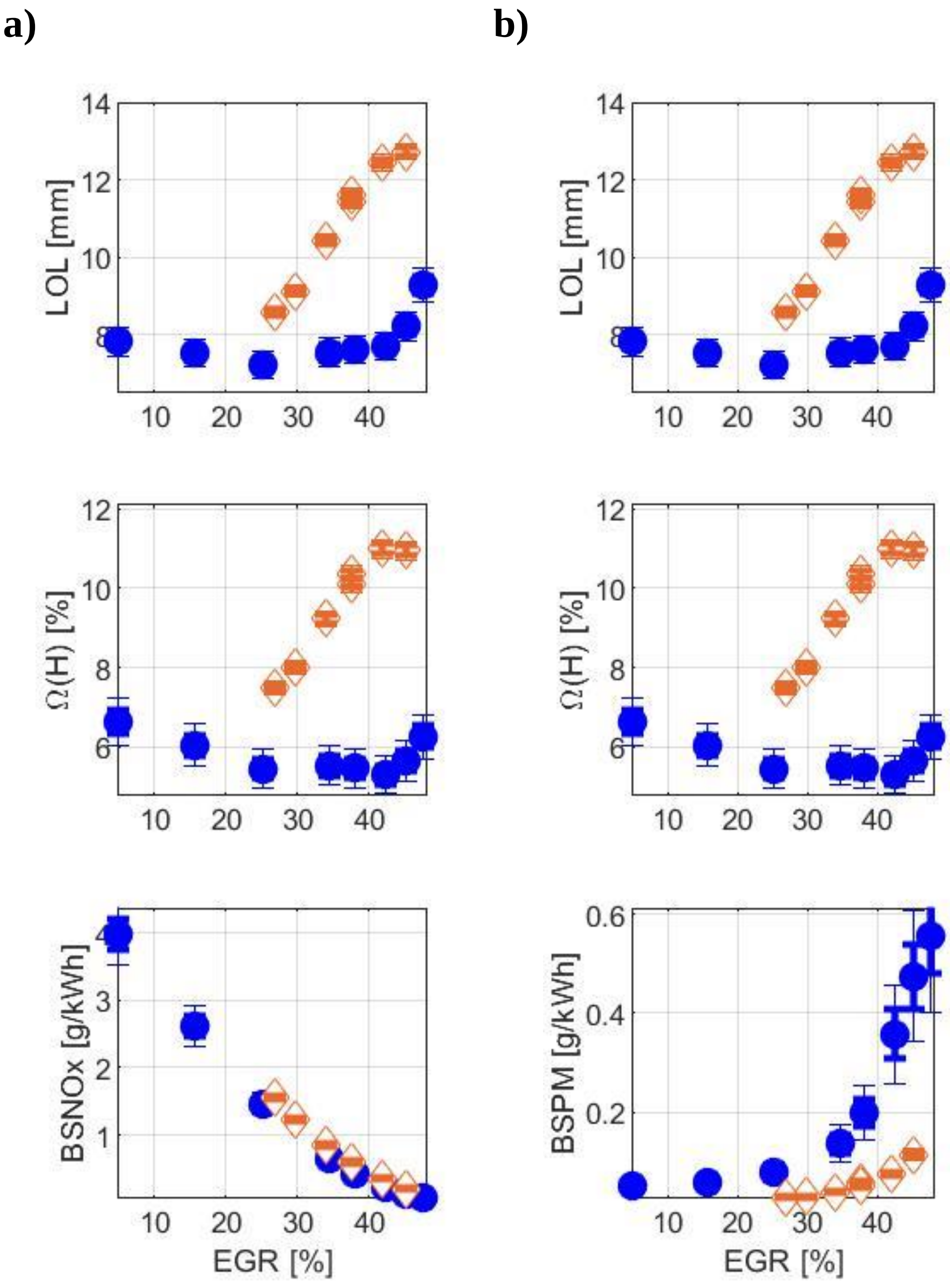

Figure 3.91. Lift-off length and oxygen ratio at the lift-off length during EGR sweep at MM3 (●: Diesel at default ECU calibration, ◊: B20 at adjusted ECU calibration) with the trend of a) BSNOx and b) BSPM

3.3.4.4 MM4

Table 3.18 shows the change in ECU input parameters at MM4 as a result of the re-calibration of ECU for B20 to maximize the BFE (or minimize $BSCO_2$) while satisfying the other bound criteria such as brake specific (BS) emissions and combustion noise level (CNL). BSTHC is not included as a bound criterion at MM4 because the level of emission was negligible. The greyed rows are the fixed target operating conditions imposed the same for the baseline fuel and B20. The red/blue colored rows are the input variables increased/decreased for B20 in the new calibration settings. For main injection timing (MIT), if the MIT is advanced/retarded, the row is colored blue/red. There are two sets of the B20 calibrations shown in Table 3.18. One is the "first" adjusted calibration for B20 with "un-optimized" rail pressure. This is the calibration at which the EGR sweep test is conducted for B20 of which results are shown in Figures 3.92-3.94. After running the EGR sweep test, CNL is measured to be higher the value from the baseline fuel, thus requiring further change in the calibration. From the first adjusted ECU calibration, the rail pressure is decreased by 46bar from 1486bar to 1440bar (underlined in Table 3.18), and the output parameters are measured again at this single point. The result is presented in Figures 3.92-3.94. The other input parameters were kept the same between the first and final ECU calibration settings.

First input parameter to discuss from Table 3.18 is the EGR rate. Exhaust gas recirculation (EGR) rate is increased by absolute 2% from 21% at the default ECU calibration to 23% for the first or final adjusted ECU calibrations for B20. The increase in EGR rate at MM4 was mainly to counter off the increased NOx emission due to the impact of the advanced injection timing and the increased rail pressure at the adjusted ECU calibration for B20.

Boost pressure is decreased by 27hPa from 1210hPa at the default ECU calibrations to 1183hPa at the adjusted calibrations for B20, and main injection timing is advanced by 2.2CAs from -1aTDC at the default ECU calibration to -3.2aTDC at the adjusted calibration for B20. The rail pressure was increased by about 150bars for the first adjusted ECU calibration and 105bars for the final adjusted ECU calibration. Although the decrease in boost pressure potentially contributed to the "decrease" in BFE (see Figure 3.42a), the advance in main injection timing and increase in rail pressure both contributed to the increase in BFE. Eventually, the competition between the changes in these three input parameters resulted in the moderate increase in BFE for B20 at fixed EGR rate.

Pilot injection quantity is increased by 0.85mg/stroke from 2.15mg/stroke at the default ECU calibration to 2.9mg/stroke at the adjusted ECU calibration for B20. Relative distance between the main injection timing (MIT) and pilot injection timing (PIT) is decreased by about 2.3CAs from 14CAs at the default calibration to 11.65CAs at the adjusted calibration for B20. The decrease in relative distance between MIT and PIT kept the pilot injection timing of the adjusted calibration the same as that of the default calibration while advancing main injection timing only. This was the secondary contributor for the improvement in BFE at the adjusted ECU calibrations for B20 at fixed EGR rate.

MM4	Diesel at default ECU calibration	B20 at first adjusted ECU calibration	B20 at final adjusted ECU calibration
Engine speed [rpm]	1200	1200	1200
Brake torque [N·m]	371	371	371
BMEP [bar]	7	7	7
EGR rate [%]	21	23	23
Boost pressure [hPa]	1210	1183	1183
Rail pressure [bar]	1335	1486	**1440**
Main injection timing [aTDC]	-1	-3.2	-3.2
Pilot injection quantity [mg/stroke]	2.15	2.9	2.9
Relative distance between MIT and PIT [CA]	14	11.65	11.65

Table 3.18. Comparison between the default ECU calibration for the baseline diesel and the first and final adjusted ECU calibration for B20. The only difference in the first and final B20 calibrations is the rail pressure at MM4. Grey: Fixed conditions, Red: Increase (Retarding for main injection timing), Blue: Decrease (Advance for main injection timing)

The comparison of BFE, BS emissions, and CNL between the baseline fuel and B20 with the final ECU calibration is shown in Table 3.19. Brake fuel conversion efficiency (BFE) is decreased by absolute 0.28% (relative 0.74%) from the baseline fuel. However, this mean difference in BFE between the two fuels was only about the half of one standard deviation (0.48%) from the repeated measurements of BFE at MM4, which meant that B20 did not have statistically meaningful difference in BFE from the baseline fuel. Meanwhile, $BSCO_2$ of B20 with the final ECU calibration was 19g/kWh higher than that of the baseline fuel. The standard deviation in $BSCO_2$ was 18.52g/kWh from the repeated measurements of $BSCO_2$ at MM4. This meant that the 19g/kWh increase in $BSCO_2$ for B20 was statistically meaningful, but with low statistical confidence barely over 68%. Considering the result of BFE and $BSCO_2$ together with more weight on BFE, it is concluded that, at MM4, B20 with final ECU calibration did not show statistically meaningful improvement in BFE, or GHG emissions.

BSNOx from B20 at the final ECU calibration decreased by 0.15g/kWh from the baseline BSNOx of 0.97g/kWh. This was 15.5% decrease in BSNOx, and the mean decrease in BSNOx was much higher than plus and minus two standard deviations of repeated BSNOx measurements at MM4. Thus, it is concluded that the final ECU calibration for B20 achieved the moderate 15.5% reduction in BSNOx with statistical confidence over 95%. BSPM from B20 at the final ECU calibration increased by 0.034g/kWh from the baseline BSPM of 0.113g/kWh. The standard deviation of the repeated BSPM measurements was 0.028g/kWh. Thus, the increase in BSPM at the final ECU calibration for B20 was statistically meaningful with low statistical confidence. Relative to the baseline fuel, there was 30% increase in BSPM from B20 at the final ECU calibration. The underlying physics that led to these changes in final BFE, BSNOx, and BSPM at MM4 will be discussed in detail later in this section.

BSCO for B20 at the final ECU calibration increased by 0.56g/kWh from the baseline value of 1.14g/kWh. This was 49.1% increase relative to the baseline result. However, the degree of increase in BSCO was considered to be in the acceptable range that could be treated by the after-treatment system, so, further ECU calibration was not required. Combustion noise level (CNL) for B20 at final ECU calibration increased by 0.1dB from the baseline value of 83.54dB, which could also be considered as acceptable increase.

MM4	DSL at default calibration	B20 at final calibration	Difference in [%] $[(\frac{B20-DSL}{DSL})\cdot 100]$	Difference in absolute quantity [B20-DSL]	Standard deviation (σ)
BFE [%]	37.85	37.57	-0.74	-0.28	0.48
BSCO$_2$ [g/kWh]	693	712	+2.7	+19	18.52
BSNOx [g/kWh]	0.97	0.82	-15.5	-0.15	0.043
BSPM [g/kWh]	0.113	0.147	+30.0	+0.034	0.028
BSCO [g/kWh]	1.14	1.70	+49.12	+0.56	0.33
CNL [dB]	83.54	83.64	[-]	0.1	0.07

Table 3.19. Comparison of BFE, BS emissions, and CNL for the baseline fuel and B20 at final ECU calibration at MM4

Figure 3.92a compares the BFE (top-left), BSNOx (middle-left), BSPM (bottom-left), CNL (top-right), BSTHC (middle-right), BSCO (bottom-right) during the EGR sweep of the diesel fuel at default ECU calibration (blue filled dots) and of the B20 with first adjusted ECU calibration (orange empty diamonds) at MM4. The results at the final adjusted ECU calibration with B20 is also included in the figure (green star). Figure 3.92b presents the comparison of the BFE (top-left), BSPM (middle-left), BSCO$_2$ (bottom-left), BSTHC (top-right), BSCO (middle-right) and CNL (bottom-right) by BSNOx during the EGR sweep of the baseline fuel at default ECU calibration and B20 at first and final adjusted ECU calibrations at MM4.

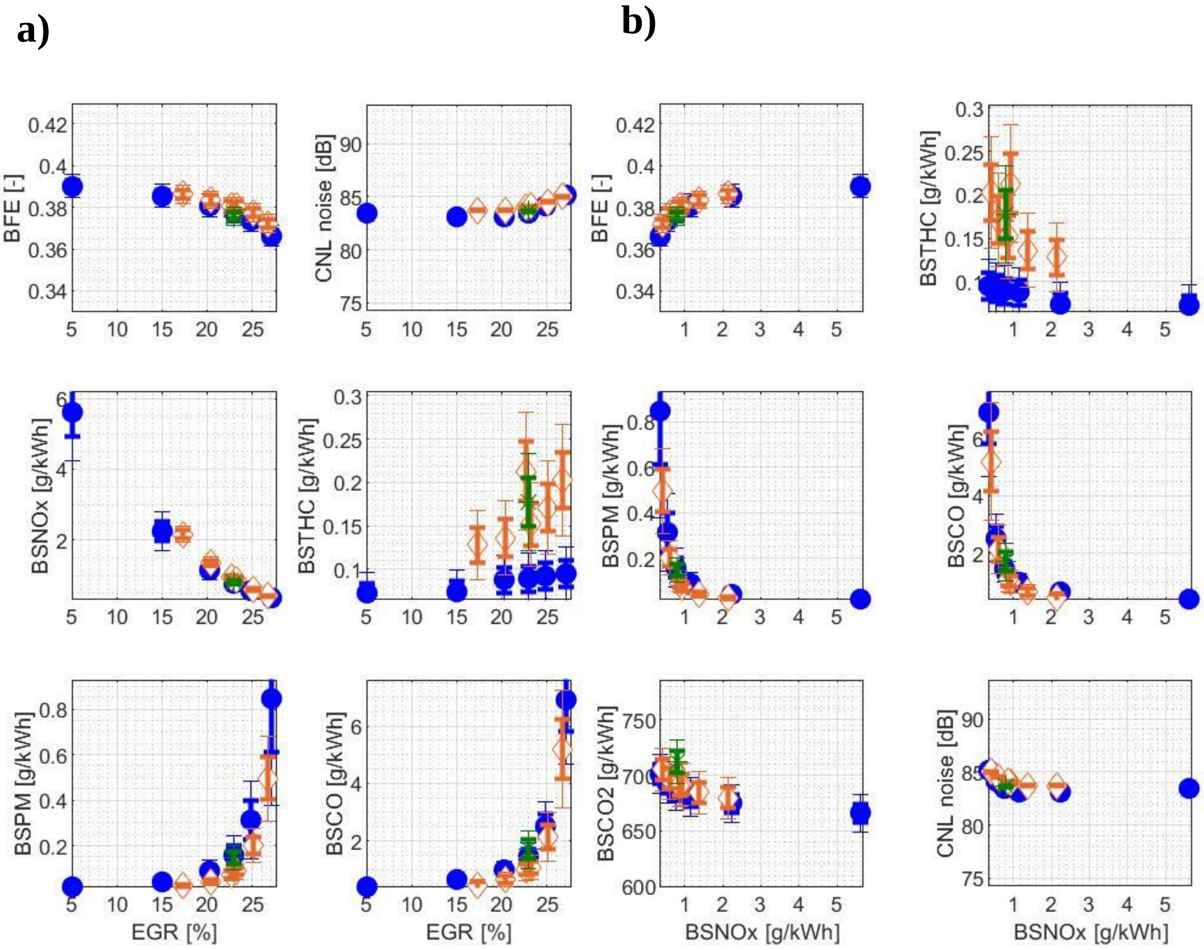

Figure 3.92. BFE, BS emissions, and CNL during the EGR sweep at MM4 (●: Diesel at default ECU calibration, ◊: B20 at first adjusted ECU calibration, *: B20 at final adjusted ECU calibration) as a function of a) EGR rate, b) BSNOx

First, BFE of B20 at the first adjusted ECU calibration is increased from the baseline result at fixed EGR rate. Brake fuel conversion efficiency (BFE) for B20 decreases from 38.6% at EGR17% to 37.2% at EGR27% during the EGR sweep. During the similar range of EGR, the BFE for the baseline fuel decreases from 38.6% at EGR15% to 36.6% at EGR27%. Thus, there is about absolute 0.3-0.6% increase in BFE for B20 at fixed EGR conditions in general. The BFE increase for B20 is because of the shifts in both main and pilot SOC closer to TDC thanks to the advance in main injection timing (MIT), increase in rail pressure (RP), and decrease in relative distance between MIT and pilot injection timing (PIT). The shifts of main and pilot SOCs closer to TDC made the combustion process more like a constant-volume process than a constant-pressure process, thus making the process thermally more efficient. Furthermore, the closer SOCs to TDC increased the actual compression ratio, which also contributed to the increase in IFEg.[48]

Figure 3.93a shows the parameters that might affect BFE during the EGR sweep tests at MM4. In the second-to-the-top plot in Figure 3.93a is the comparison of the IFEg for the baseline fuel and B20 at the adjusted ECU calibrations. Gross indicated fuel conversion efficiency (IFEg) for B20 at the first adjusted calibration decreases from 44.3% at EGR17% to 43.0% at EGR27%. In the similar range of EGR rate, the IFEg for the baseline fuel was 43.7% at EGR15% and 41.8% at EGR27%. Thus, B20 at the first adjusted ECU calibration has about absolute 0.6-1.2% higher IFEg than the baseline fuel. This improvement in IFEg is due to the advance in main SOC (Figure 3.93c, top) and the retarding in pilot SOC (Figure 3.93c, middle). While the main injection timing (MIT) is advanced with the adjusted ECU calibration, relative distance between the pilot injection timing and main injection timing is decreased about the same degrees, thus making both SOCs of the main and pilot events getting closer to TDC.

However, the final adjusted ECU calibration of B20 at MM4 could not fully take advantage of the improvement in BFE at fixed EGR rate since its EGR rate setting had to be increased to meet the BSNOx bound criteria. Therefore, the absolute 0.3-0.6% improvement in BFE at fixed EGR rate is offset by the increase in EGR rate settings at the final ECU calibration, thus resulting in no statistically meaningful difference in BFE between the two fuels.

Second, BSNOx from B20 at the first adjusted ECU calibration generally increases from the baseline values when compared at fixed EGR rate. BSNOx emission for B20 at the first adjusted ECU calibration decreases from 2.16g/kWh at EGR17% to 0.42g/kWh at EGR27%. In the similar range of EGR rate, the baseline BSNOx emission was 2.24g/kWh at EGR15% and 0.35g/kWh at EGR27%. Thus, the degree of increase in BSNOx for B20 depended on each EGR rate. However, within the usual EGR rate settings range at MM4 (i.e., EGR20-23%), BSNOx emission is increased by about 15% for B20. The main contributor for the increase in BSNOx is the advance in main injection timing and increase in rail pressure.

Figure 3.93b shows the parameters that might affect BSNOx during the EGR sweep at MM4. While the intake O_2 concentration (top) and charge gas temperature (third-to-the-top) during the main ignition delay remained the same for the two fuels at fixed EGR rate, the peak cylinder temperature timing (second-to-the-top) is about 1-2CAs advanced for B20 at fixed EGR rate. This allows longer duration of NOx generation at high cylinder temperature. Furthermore, the oxygen ratio at the lift-off length is also increased for B20 as compared to the baseline value when compared at fixed EGR rate.

Figure 3.94a shows the lift-off length (top) and oxygen ratio at the lift-off length (middle) for the baseline fuel and B20 at the adjusted ECU calibrations with the trend of BSNOx (bottom) during the EGR sweep at MM4. There is about 0.5-1mm increase in lift-off length for B20 due to the increase in fuel jet velocity caused by the increase in rail pressure. The increase in lift-off length, then, causes the increase in oxygen ratio at the lift-off length. There is about absolute 2% increase in oxygen ratio at the lift-off length for B20 when compared at fixed EGR rate. The increase in oxygen ratio allows more oxygen molecules available in the fuel-rich premixed auto-ignition zone, thereby increasing the NOx generation. This could have played the secondary role in the increase in final BSNOx emissions at fixed EGR rate for B20.

Now, the increase in EGR rate settings for the adjusted B20 calibrations could be understood as follows. To counter off the 15% increase in BSNOx from B20 at the adjusted ECU calibration at fixed EGR rate, the increase in EGR settings was necessary at the adjusted calibration. Furthermore, on top of the increase in EGR settings, the rail pressure had to be decreased by moderate amount (46bars) from the first adjusted ECU calibration to the final ECU calibration to meet the combustion noise level (CNL) bound criteria. The decrease in rail pressure resulted in further decrease in BSNOx, which, indeed, resulted in 15% reduction in BSNOx for B20 at the final ECU calibration compared to the baseline result.

Third, BSPM decreased for B20 at the adjusted ECU calibrations when compared at fixed EGR rate with the baseline fuel. BSPM emission from B20 at the first adjusted ECU calibration increases from 0.024g/kWh at EGR17% to 0.495g/kWh at EGR27%. In the similar rage of EGR rate, the BSPM emission from the baseline fuel was 0.042g/kWh at EGR15% and 0.844g/kWh at EGR27%. The degree of decrease in BSPM varies depending on the EGR rate imposed, but, in general, there was about 40-50% reduction in BSPM for B20 at the fixed EGR rate. The advance in the main injection timing is one of the factors decreased BSPM for B20 at the first adjusted ECU calibration. However, the more dominant contributor for the decrease in BSPM is the increase in rail pressure settings at the adjusted ECU calibrations. The increase in rail pressure increased the fuel jet velocity, which, in turn, increased the lift-off length for B20 (Figure 3.94b, top). Then, this increase in lift-off length increased the oxygen ratio at the lift-off length (Figure 3.94b, middle), and finally resulted in the reduction in PM (Figure 3.94b, bottom). Also, the increase in rail pressure is well-known to improve the atomization of fuel droplets, which reduces the rate of soot particle growth.

However, at the final ECU calibration, due to the increase in the EGR rate settings to meet the BSNOx bound criteria and the decrease in rail pressure settings to meet the CNL bound criteria, the PM benefit for B20 at fixed EGR rate is largely offset. Indeed, the effect of those two changes at the final ECU calibration was strong enough to make BSPM from B20 increase by 30% than the baseline result.

Figure 3.91a also shows other brake specific (BS) emissions and combustion noise level (CNL) from B20 at the adjusted ECU calibrations. BSTHC from B20 at the adjusted ECU calibrations was at negligible level as it was for the baseline fuel. BSCO from B20 at the adjusted ECU calibrations decreased from the baseline result when compared at the fixed EGR rate. However, similar to the BSPM result, the increase in EGR rate settings to meet the BSNOx bound criteria and the decrease in rail pressure to meet the CNL bound criteria increased the BSCO from B20 at the final ECU calibration. Combustion noise level (CNL) for B20 at the first adjusted ECU calibration was about 1dB higher than the baseline result, which necessitated the decrease in the rail pressure settings at the final ECU calibration for B20. As a result, at the final adjusted ECU calibration, B20 did not show statistically meaningful difference in CNL from the baseline fuel.

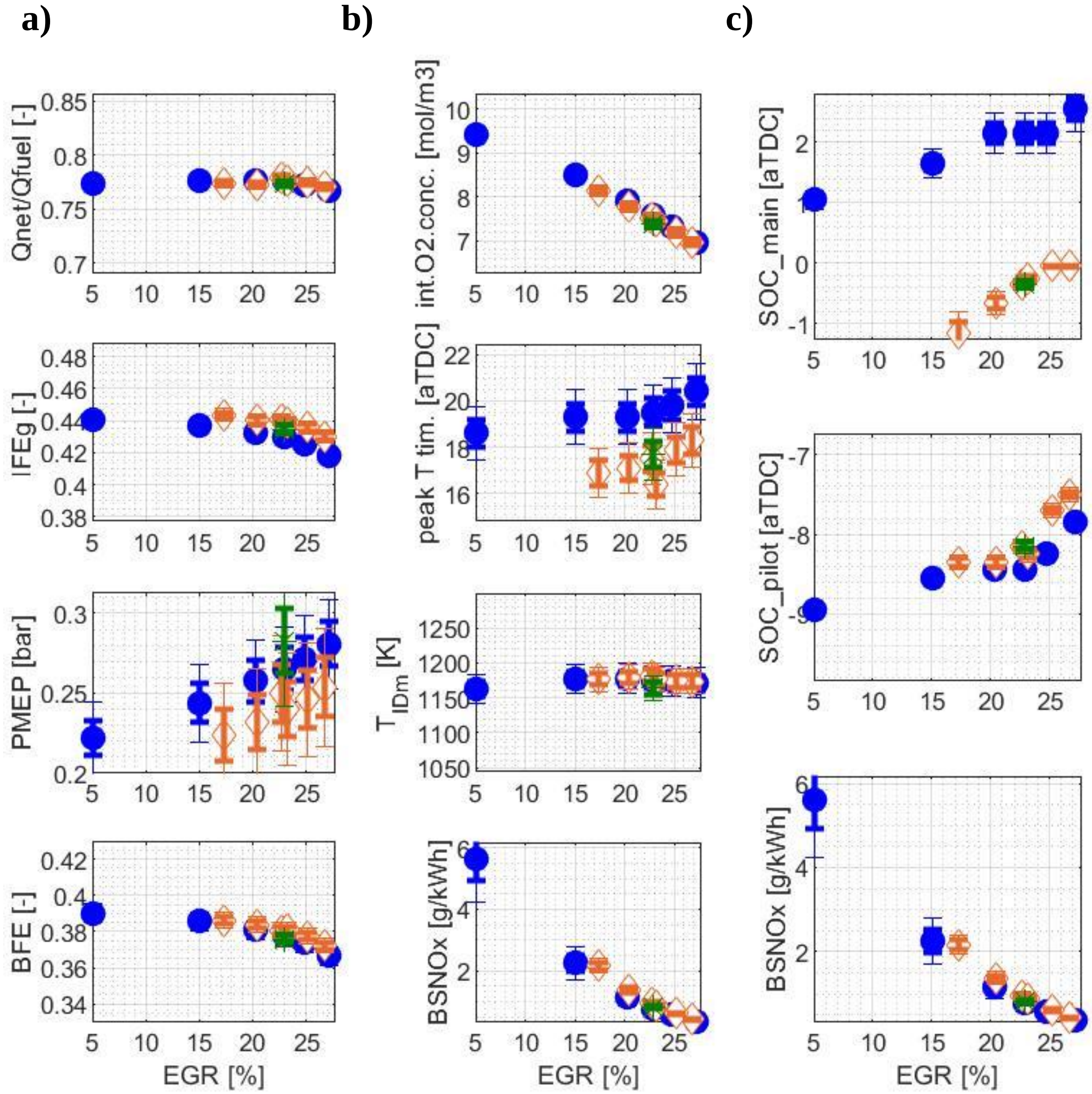

Figure 3.93. The parameters affecting a) BFE, b) and c) BSNOx during EGR sweep at MM4 (●: Diesel at default ECU calibration, ◊: B20 at first adjusted ECU calibration, *: B20 at final adjusted ECU calibration)

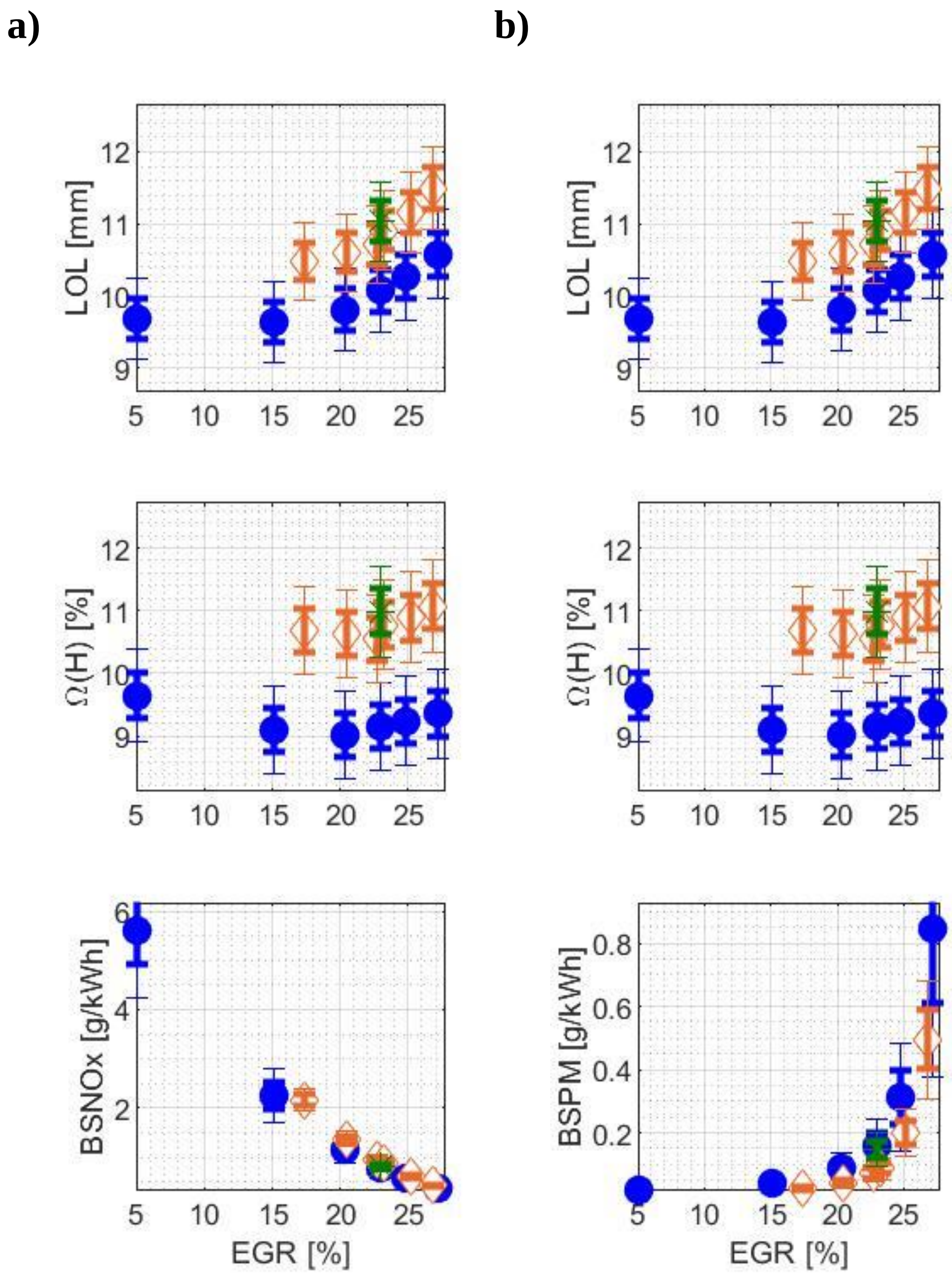

Figure 3.94. Lift-off length and oxygen ratio at the lift-off length during EGR sweep at MM4(●: Diesel at default ECU calibration, ◊: B20 at first adjusted ECU calibrations, *: B20 at final adjusted ECU calibration) with the trend of a) BSNOx and b) BSPM

3.3.4.5 MM5

Table 3.20 shows the change in ECU input parameters at MM5 as a result of the re-calibration of ECU for B20 to maximize the BFE (or minimize $BSCO_2$) while satisfying the other bound criteria such as brake specific (BS) emissions and combustion noise level (CNL). BSTHC is not included as a bound criterion because the level of BSTHC emission at MM5 was negligible. The greyed rows are the fixed target operating conditions imposed the same for the baseline fuel and B20. The red/blue colored rows are the input variables increased/decreased for B20 in the new calibration settings. For main injection timing (MIT), if the MIT is advanced/retarded, the row is colored blue/red.

The first input parameter to discuss from Table 3.20 is the EGR rate. Exhaust gas recirculation (EGR) rate is decreased by absolute 1% from 27% at the default ECU calibration to 26% for the adjusted B20 calibration. The decrease in EGR rate at MM5 was mainly to increase the BFE.

Boost pressure is decreased by 94hPa from 1164hPa at the default ECU calibration to 1070hPa at the final calibration. The decrease in boost pressure contributed to the increase in BFE by reducing the pumping loss in parallel with the decrease in EGR rate. The decrease in boost pressure also contributed to the decrease in BSNOx at the final ECU calibration.

Rail pressure is decreased by about 60bars from 1021bar at the default calibration to 960bar at the final calibration. The decrease in rail pressure potentially contributed to the decrease in BFE, which is, however, countered and dominated by the impact of decrease in EGR rate and boost pressure settings. The decrease in rail pressure helped decreasing BSNOx in parallel with the decrease in boost pressure.

Main injection timing is advanced by small amount (0.18CA) from TDC at the default ECU calibration to -0.18aTDC at the final ECU calibration. The small advance in the main injection timing secondarily contributed to the improvement in BFE. Pilot injection quantity is increased by 0.47mg/stroke from 2.9mg/stroke at the default calibration to 3.37mg/stroke at the final calibration. The relative distance between main injection timing and pilot injection timing is increased by 1.73CA from 14.9CA at the default calibration to 16.63CA at the final calibration.

MM5	Diesel at default ECU calibration	B20 at final ECU calibration
Engine speed [rpm]	1300	1300
Brake torque [N·m]	265	265
BMEP [bar]	5	5
EGR rate [%]	27	26
Boost pressure [hPa]	1164	1070
Rail pressure [bar]	1021	960
Main injection timing [aTDC]	0	-0.18
Pilot injection quantity [mg/stroke]	2.9	3.37
Relative distance between MIT and PIT [CA]	14.9	16.63

Table 3.20. Comparison between the default ECU calibration for the baseline diesel and the final ECU calibration for B20 at MM5. Grey: Fixed conditions, Red: Increase (Retarding for main injection timing), Blue: Decrease (Advance for main injection timing)

The comparison of BFE, BS emissions, and CNL between the baseline fuel and B20 with the final ECU calibration at MM5 is shown in Table 3.21. Brake fuel conversion efficiency (BFE) is increased by absolute 0.36% (relative 0.97%) from the baseline fuel. This improvement in BFE for B20 was slightly higher than one standard deviation (0.34%) of the repeated measurements of BFE at MM5. Thus, it can be concluded that the BFE for B20 is improved from the baseline fuel with low statistical confidence of about 68%. Furthermore, $BSCO_2$ for B20 with the final ECU calibration was 12.03g/kWh lower than that for the baseline fuel. The standard deviation from the repeated $BSCO_2$ measurements at MM5 was 12.01g/kWh. Since the reduction in $BSCO_2$ from B20 with the final ECU calibration was in similar degree as one standard deviation, it can be concluded that B20 reduced BSCO$_2$ from the baseline result with the statistical confidence of about 68%. Considering the result of BFE and BSCO$_2$ together, it is concluded that, at MM5, B20 with the final ECU calibration had BFE improvement (or GHG emissions reduction) of 0.97 – 1.67% with about 68% statistical confidence.

BSNOx from B20 at the final ECU calibration decreased by 0.06g/kWh from the baseline BSNOx of 0.70g/kWh. This was 8.6% decrease in BSNOx. The mean decrease in BSNOx was higher than one standard deviation (0.046g/kWh), but, lower than two standard deviations of the repeated measurements of BSNOx at MM5. Thus, we can conclude that the B20 final calibration achieved the moderate 8.6% reduction in BSNOx with low statistical confidence. BSPM from B20 at the final ECU calibration decreased by 0.002g/kWh from the baseline BSPM value of 0.113g/kWh. The standard deviation of the repeated BSPM measurements at MM5 was 0.009g/kWh, which is much higher than the mean difference in BSPM between the two fuels. Thus, the decrease in BSPM at the B20 final calibration was not statistically meaningful. The underlying physics that led to these changes or consistency in final BFE, BSNOx, and BSPM at MM5 will be discussed in detail later in this section.

The BSCO for B20 at the final ECU calibration increased by 0.18g/kWh from the baseline value of 1.67g/kWh. This was 10.8% increase relative to the baseline result. However, the degree of increase in BSCO was considered to be in the acceptable range that could be treated by the after-treatment system, so, further adjustment in the ECU calibration was not required. Combustion noise level (CNL) for B20 at the final ECU calibration decreased by 0.34dB from the baseline value of 81.34dB.

MM5	DSL at default calibration	B20 at final calibration	Difference in [%] $[(\frac{B20-DSL}{DSL})\cdot 100]$	Difference in absolute quantity [B20-DSL]	Standard deviation (σ)
BFE [%]	36.81	37.17	+0.97	+0.36	0.34
BSCO$_2$ [g/kWh]	715	703	-1.67	-12.03	12.01
BSNOx [g/kWh]	0.70	0.64	-8.6	-0.06	0.046
BSPM [g/kWh]	0.113	0.111	-1.7	-0.002	0.009
BSCO [g/kWh]	1.67	1.85	+10.8	+0.18	0.07
CNL [dB]	81.34	81.00	[-]	-0.34	0.29

Table 3.21. Comparison of BFE, BS emissions, and CNL for baseline and B20 at final ECU calibration at MM5.

Figure 3.95a compares the BFE (top-left), BSNOx (middle-left), BSPM (bottom-left), CNL (top-right), BSTHC (middle-right), BSCO (bottom-right) during the EGR sweep of the diesel baseline at the default ECU calibration (blue filled dots) and of the B20 with the final adjusted ECU calibration (orange empty diamonds). Figure 3.95b presents the comparison of the BFE (top-left), BSPM (middle-left), BSCO$_2$ (bottom-left), BSTHC (top-right), BSCO (middle-right) and CNL (bottom-right) by BSNOx during the EGR sweep of the diesel baseline at the default ECU calibration and B20 at the adjusted calibration at MM5.

First, BFE for B20 at the adjusted ECU calibration is increased from the baseline result when compared at the fixed EGR rate. Brake fuel conversion efficiency (BFE) for B20 at the adjusted ECU calibration decreases from 36.1% at EGR35% to 37.3% at EGR26%, then to 37.7% at EGR20%. These numbers are generally absolute 0.5% higher than the baseline results at the same EGR rate. The increase in BFE for B20 with the adjusted ECU calibration at MM5 is mainly due to the reduction in pumping loss thanks to the reduced boost pressure settings.

Figure 3.96a shows the parameters affecting BFE during the EGR sweep at MM5. We can see in the third-to-the-top plot that PMEP for B20 with the adjusted ECU calibration is 0.1-

0.15bar lower than the baseline results while IFEg shown in the second to the top plot in Figure 3.96a remains the same for the two fuels. The 0.1 bar decrease in PMEP is about 2% of the BMEP (i.e., 5bar) at MM5, which is significant enough to cause meaningful BFE increase for the adjusted ECU calibration for B20. Thus, the decrease in boost pressure settings for B20 was one of the main factors achieving the increase in BFE.

Although boost pressure decrease at the adjusted ECU calibration can be attributed for the primary cause of the increase in BFE for B20, there are some other factors that might have contributed to the increase in BFE. Based on the impact of main injection timing on BFE at MM5 presented earlier in this study (i.e., BFE increases when main injection timing is advanced), the 0.2 degree advance in the main injection timing at the adjusted ECU calibration can be thought as the secondary contributor for the increase in BFE.

While the BFE has increased for B20 at the fixed EGR rate with the adjusted ECU calibration, the EGR rate settings also decreased for the final calibration of B20. And this additionally contributed to the improvement in BFE for B20 at the final ECU calibration. There was absolute 1% decrease in EGR rate settings at the final ECU calibration whose combined effect with the decrease in boost pressure and advance in main injection timing achieved the absolute 0.36% improvement in the final BFE for B20.

Second, BSNOx emissions from B20 at the adjusted ECU calibration did not show statistically meaningful difference from the baseline results at the fixed EGR rate. BSNOx decreases from 1.25g/kWh at EGR 20% to 0.19g/kWh at EGR35%. This is generally the same level of BSNOx as the baseline results at fixed EGR rate. This consistent NOx emissions between the baseline fuel and B20 at the adjusted ECU calibration is in line with what is observed during the comparison tests between the baseline fuel and B20 at the default ECU calibration. Therefore, it can be thought that the potential increase in BSNOx due to the advance in main injection timing settings was countered off by the potential decrease in BSNOx due to the decrease in rail pressure and boost pressure settings.

Figures 3.96b and 3.96c show the parameters relevant for the NOx emissions during the EGR sweep at MM5. Peak cylinder temperature timing (second to the top) and charge gas temperature during the main ignition delay (third to the top) remains the same for the two fuels at fixed EGR rate. Although the intake O_2 concentration is lower for B20 (Figure 3.96b, top) than that for the baseline diesel, the degree of decrease is less than 8%. This moderate degree of decrease in intake O2 concentration seemed to be countered off by the small advance in pilot SOCs shown in Figure 3.96c (middle) and small increase in oxygen ratio at the lift-off length shown in Figure 3.97a (middle).

Third, BSPM from the B20 at the adjusted ECU calibration did not show statistically meaningful difference from the baseline result when compared at fixed EGR rate. BSPM emission for B20 at the adjusted ECU calibration increases from 0.05g/kWh at EGR20% to 0.70g/kWh at EGR35%, which is same as the baseline BSPM values at each EGR rate. This is consistent with the trend seen when the baseline result is compared to B20 result at the default ECU calibration: BSPM from B20 at the default ECU calibration did not have statistically meaningful difference from the baseline result. Thus, it can be concluded that the re-calibration of the ECU happened in a way that the impact from the changes in different input parameter settings counterbalanced with each other to maintain the original BSPM emissions from B20.

Lastly, combustion noise level (CNL) and other brake specific (BS) emissions from B20 at the adjusted ECU calibration are compared to the baseline results at the fixed EGR rate. Combustion noise level (CNL) for B20 at the adjusted ECU calibration did not show statistically meaningful difference from the baseline result at fixed EGR rate (Figure 3.95a, top-right). BSTHC from B20 with adjusted ECU calibration at MM5 was at negligible level as it was for the baseline result. BSCO from B20 with the adjusted ECU calibration decreased from the baseline values when compared at the fixed EGR rate. BSCO from B20 increased from 1.44g/kWh at EGR20% to 5.86g/kWh at EGR35%. This was about 15-20% increase from the baseline results at each EGR rate. However, at the final calibration, the EGR setting was decreased by absolute 1% from the baseline settings, resulting in only 10.8% increase in BSCO from the baseline value. This much increase was considered to be acceptable, thus not requiring further change in the ECU calibration.

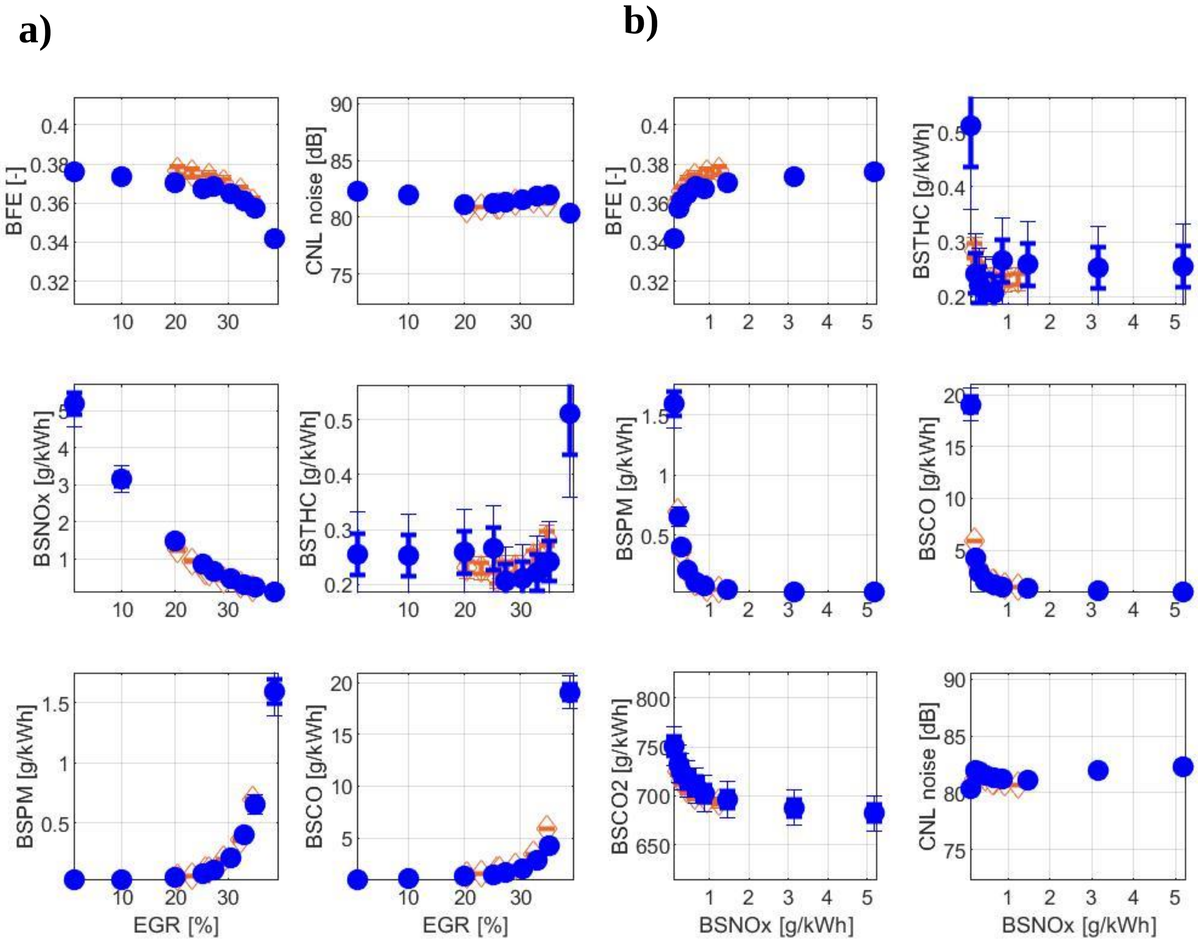

Figure 3.95. BFE, BS emissions, and CNL during EGR sweep (●: Diesel at default ECU calibration, ◊: B20 at adjusted ECU calibration) at MM5 as a function of a) EGR rate, b) BSNOx

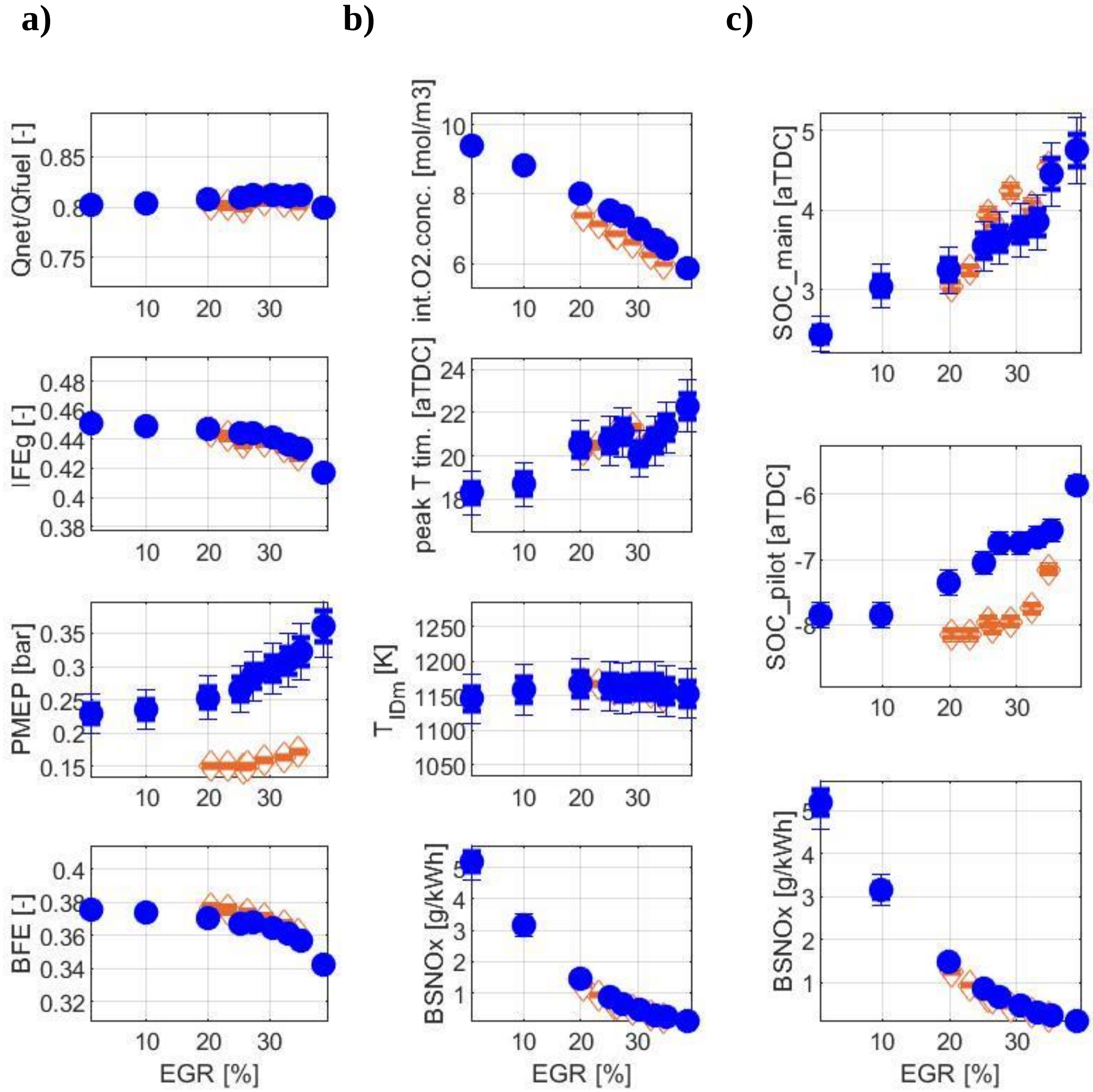

Figure 3.96. The parameters affecting a) BFE, b) and c) BSNOx during the EGR sweep (●: Diesel at default ECU calibration, ◊: B20 at adjusted ECU calibration) at MM5

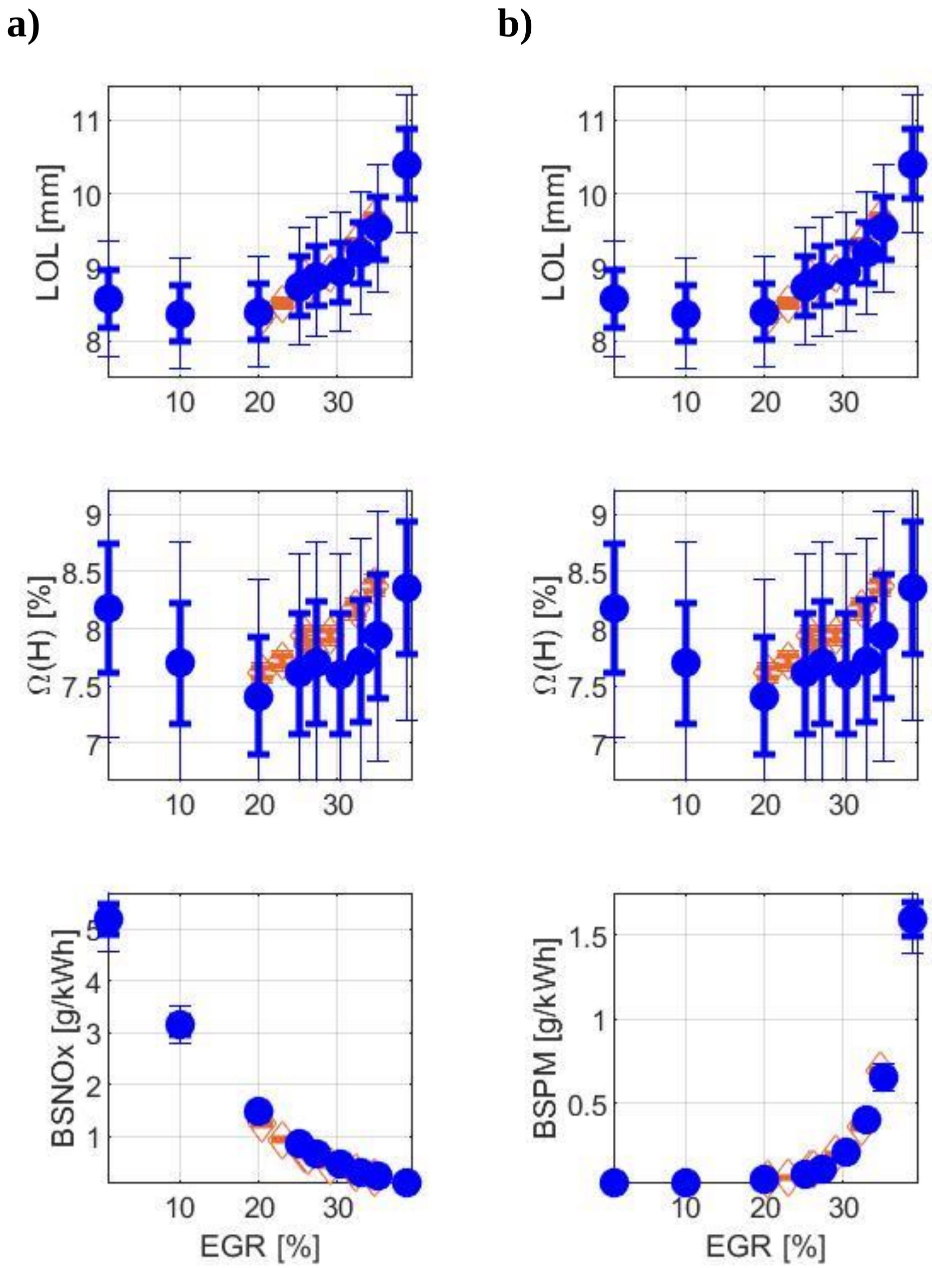

Figure 3.97. Lift-off length and oxygen ratio at the lift-off length during the EGR sweep at MM5 (●: Diesel at default ECU calibration, ◊: B20 at adjusted ECU calibration) with the trend of a) BSNOx, b) BSPM

3.3.4.6 MM6

Table 3.22 shows the change in ECU input parameters at MM6 as a result of the re-calibration of ECU for B20 to maximize the BFE (or minimize $BSCO_2$) while satisfying the other bound criteria such as brake specific (BS) emissions and combustion noise level (CNL). BSTHC is not included as a bound criterion because the level of BSTHC emission at MM6 was at negligible level. The greyed rows are the fixed target operating conditions imposed the same for the baseline and B20. The red/blue colored rows are the input variables increased/decreased for B20 in the new calibration settings. For main injection timing (MIT), if the MIT is advanced/retarded, the row is colored blue/red.

As shown in Table 3.22, EGR rate was increased by absolute 4% from 20% at the default ECU calibration to 24% at the final B20 calibration. The increase in EGR rate settings was mainly to offset the increase in BSNOx at the default ECU calibration due to the impact of B20.

The boost pressure is increased by about 50hPa from 1317hPa at the default calibration to 1365hPa at the final ECU calibration for B20. Unlike other MM points, at MM6, BFE is improved with moderate increase in boost pressure from the default boost pressure (DP, see Figure 53). Thus, the 50hPa increase in the boost pressure settings contributed to the improvement in BFE.

The rail pressure is increased by 250bar from 1612bar at the default ECU calibration to 1863bar at the final B20 calibration. The increase in rail pressure was one of the two main contributors for the improvement in BFE. The other important contributor for BFE improvement was the advance in main injection timing (MIT). The main injection timing is advanced by about 2.5 CA from -0.4aTDC at the default calibration to -2.9aTDC at the final ECU calibration for B20.

Pilot injection quantity is increased by about 2mg/stroke from 1.8mg/stroke at the default calibration to 3.9mg/stroke at the final ECU calibration for B20 while relative distance between the main injection timing and pilot injection timing has increased slightly by 0.15CA from 14.35CA at the default ECU calibration to 14.5CA at the final ECU calibration for B20.

MM6	Diesel at default ECU calibration	B20 at final adjusted ECU calibration
Engine speed [rpm]	1600	1600
Brake torque [N·m]	397	397
BMEP [bar]	7.5	7.5
EGR rate [%]	20	24
Boost pressure [hPa]	1317	1365
Rail pressure [bar]	1612	1863
Main injection timing [aTDC]	-0.4	-2.9
Pilot injection quantity [mg/stroke]	1.8	3.9
Relative distance between MIT and PIT [CA]	14.35	14.5

Table 3.22 Comparison between the default ECU calibration for the baseline diesel and the adjusted ECU calibration for B20 at MM6. Grey: Fixed conditions, Red: Increase (Retarding for main injection timing), Blue: Decrease (Advance for main injection timing)

The comparison of BFE, BS emissions, and CNL between the baseline fuel and B20 with the final ECU calibration at MM6 is shown in Table 3.23. Brake fuel conversion efficiency (BFE) is increased by absolute 0.33% (relative 0.87%) from the baseline result. This improvement in BFE for B20 was similar to two standard deviations of the repeatability error. Thus, BFE for B20 at MM6 achieved the relative 0.87% improvement with statistical confidence of about 95%. Furthermore, $BSCO_2$ of B20 with the final ECU calibration was 9g/kWh lower than the baseline result. The standard deviation in repeated $BSCO_2$ measurements at MM6 was 3.47g/kWh. Since the reduction in $BSCO_2$ from B20 at the final ECU calibration was greater than two standard deviations of the repeated measurements of $BSCO_2$ at MM6, it can be concluded that B20 reduces $BSCO_2$ from the baseline result with statistical confidence higher than 95%. Considering the result of BFE and $BSCO_2$ together, it is concluded that, at MM6, B20 with the final ECU calibration shows BFE improvement (or GHG emissions reduction) of 0.87 – 1.30% with more than 95% statistical confidence.

BSNOx is increased by 0.02g/kWh from the baseline value of 0.84g/kWh. However, the increased amount was much smaller than the standard deviation (0.072g/kWh) of the repeated test results. Thus, BSNOx emission from B20 at the final ECU calibration does not have statistically meaningful difference from the baseline result.

BSPM from B20 at the final ECU calibration decreased by 0.044g/kWh from the baseline value of 0.12g/kWh. This decrement was greater than two standard deviations of the repeated measurements of BSPM at MM6, thus guaranteeing statistical confidence of more than 95%.

Lastly, BSCO from B20 at the final ECU calibration decreased by 0.17g/kWh from the baseline value of 1.11g/kWh with standard deviation of 0.11g/kWh. This was relative 15.3% reduction from the baseline value with low statistical confidence. Combustion noise level (CNL) from B20 at the final ECU calibration decreased by 0.02dB, but, the standard deviation (0.49dB) of the repeated measurements of CNL at MM6 was greater than the degree of decrease in CNL. Thus, CNL from B20 at the final ECU calibration did not have statistically meaningful difference from the baseline result. More detailed comparison between the two fuels at different ECU calibrations will be covered in the following paragraphs.

MM6	DSL at default calibrations	B20 at final calibrations	Difference in [%] $[(\frac{B20-DSL}{DSL}) \cdot 100]$	Difference in absolute quantity [B20-DSL]	Standard deviation (σ)
BFE [%]	37.87	38.20	+0.87	+0.33	0.17
$BSCO_2$ [g/kWh]	691	682	-1.3	-9	3.47
BSNOx [g/kWh]	0.84	0.86	+2.3	+0.02	0.072
BSPM [g/kWh]	0.12	0.076	-36.7	-0.044	0.018
BSCO [g/kWh]	1.11	0.94	-15.3	-0.17	0.11
CNL [dB]	85.41	85.39	[-]	-0.02	0.49

Table 3.23. Comparison of BFE, BS emissions, and CNL for the baseline fuel and B20 at the final ECU calibration at MM6

Figure 3.98a compares the BFE (top-left), BSNOx (middle-left), BSPM (bottom-left), CNL (top-right), BSTHC (middle-right), BSCO (bottom-right) during the EGR sweep of the diesel fuel at default ECU calibration (blue filled dots) and of the B20 with the adjusted ECU calibration (orange empty diamonds). Figure 3.98b presents the comparison of the BFE (top-left), BSPM (middle-left), $BSCO_2$ (bottom-left), BSTHC (top-right), BSCO (middle-right) and CNL (bottom-right) by BSNOx during the EGR sweep of the baseline diesel at default ECU calibration and B20 at adjusted calibration at MM6.

First, BFE of B20 at the adjusted calibration (Figure 3.98a, top-left) is increased from the baseline result when compared at fixed EGR rate. Brake fuel conversion efficiency (BFE) for B20 at the adjusted calibration decreases from 38.8% at EGR 17% to 37.9% at EGR 26%. This is about absolute 0.5-1.0% increase in BFE at the fixed EGR rate from the baseline result. The increase in boost pressure settings, advance in main injection timing settings, and the increase in rail pressure settings are the contributors for this improvement in BFE at fixed EGR rate.

As shown earlier in Figures 3.53 and 3.54, BFE at MM6 does not decrease between the default boost pressure (DP) and mid-high boost pressure (MHP) due to the competition between the increase in IFEg and increase in PMEP. In other words, despite the increase in PMEP from DP (1317hPa) to MHP (1515hPa), thanks to the more intense degree of increase in IFEg from DP to MHP, BFE actually increases from DP to MHP. The adjusted ECU calibration takes advantage of this peculiar range of the boost pressure at MM6 to improve BFE. The boost pressure is increased just about 50hPa from the default boost pressure settings, which potentially contributes to the better BFE at the final ECU calibration.

Another factor improving IFEg for B20 at the adjusted ECU calibration is the advanced main injection timing. The 2.5CAs advance in the main injection timing advanced both the main combustion phasing and cylinder peak temperature timing, thus bringing the combustion process closer to a constant-volume process than a constant-pressure process. Furthermore, when main SOC is advanced to be closer to TDC, the actual compression ratio increases, which, in turn, improves BFE, as well.

Figure 3.99 presents the parameters mentioned very well. As shown in the second to the top plot in Figure 3.99a, IFEg for B20 at the adjusted ECU calibration is higher than the baseline results at the fixed EGR rate. Gross indicated fuel conversion efficiency (IFEg) for B20 decreases from 45.6% at EGR17% to 44.9% at EGR26%, which is about absolute 1.0-1.5% higher than the baseline results. The primary cause of this improvement in IFEg is the advance in main combustion phasing as shown in the Figure 3.99c top plot. The main start of combustion (SOC) for B20 is advanced about 2.5-3.0CAs at the adjusted ECU calibration. This advance in main SOC also resulted in the advance in peak cylinder temperature timing as shown in the second to the top plot in Figure 3.99b, which, in turn, resulted in the improvement in IFEg and BFE for B20.

Figure 3.99a third-to-the-top plot presents the comparison of PMEP for the baseline fuel and B20 at the adjusted ECU calibration. Pump mean effective pressure (PMEP) increases by 0.1bar for B20 at the adjusted ECU calibration when compared to the baseline fuel at fixed EGR rate, but the degree of increase is not as significant as the increase in IFEg. Therefore, the increase in PMEP is simply overshadowed by the increase in IFEg, thus resulting in the increase in BFE for B20 at the adjusted ECU calibration at fixed EGR rate.

The final ECU calibration does not fully take advantage of the improvement in BFE at fixed EGR rate because its EGR rate settings is increased significantly (by absolute 4%) from the default settings to meet the BSNOx bound criteria. However, the improvement in BFE at fixed EGR rate is not "fully" offset by the increase in EGR rate settings. There was still absolute 0.33% improvement in BFE at the final ECU calibration for B20.

Second, BSNOx emissions from B20 at the adjusted ECU calibration is increased from the baseline result when compared at fixed EGR rate. BSNOx (Figure 3.98a, left-middle) from B20 at the adjusted calibration decreases from 1.46g/kWh at EGR17% to 0.63g/kWh at EGR26%, which corresponds to about 4% to 90% increase from the baseline results at the fixed EGR rate. The increase in BSNOx for B20 can be contributed mainly to the advance in peak cylinder temperature timing shown in the second to the top plot of Figure 3.99b. The increase in boost pressure setting by 50hPa also resulted in the increase in intake O_2 concentration as shown in Figure 3.99b (top). Intake O_2 concentration for B20 at the adjusted ECU calibration was generally 5-6% higher than the baseline result, and this can also be considered as another factor for BSNOx increase in B20. The increase in charge gas temperature during the ignition delay by 50K as shown in the third to the top plot in Figure 3.99b is another factor contributed to the increase in BSNOx emission from B20 at the adjusted ECU calibration.

This significant increase in BSNOx necessitated the increase in EGR rate settings for B20 at the adjusted ECU calibration. However, despite the significant increase in EGR rate settings from the default settings, BSPM emission from the adjusted ECU calibration has decreased from the baseline result. The bottom-left plot in Figure 3.98a shows the BSPM emission from B20 at the adjusted ECU calibration. BSPM emission from B20 increases from 0.018g/kWh at EGR17% to 0.145g/kWh at EGR26%, which is about 50% to 75% decrease from the baseline results at the fixed EGR rate. Furthermore, the degree of decrease in BSPM gets more intense at higher EGR rates. The primary cause for this significant decrease in BSPM is the increase in intake oxygen concentration. Intake O_2 concentration from B20 at the adjusted ECU calibration is 2-6% higher than the baseline result, and the degree of increase becomes greater at the higher EGR rate. The fact that the rail pressure setting has increased by 250bar from the default calibration has also contributed to the decrease in BSPM from B20 at the adjusted calibration.

Figure 3.98a also shows the other brake specific (BS) emissions and combustion noise level (CNL) from B20 at the adjusted ECU calibration. BSTHC emission from B20 at MM6 was at negligible range at all imposed conditions. BSCO emission from B20 generally decreased from the baseline results. The degree of decrease was 50-75% depending on the EGR rate. Combustion noise level (CNL) from B20 at the adjusted ECU calibration did not have statistically meaningful difference from the baseline result.

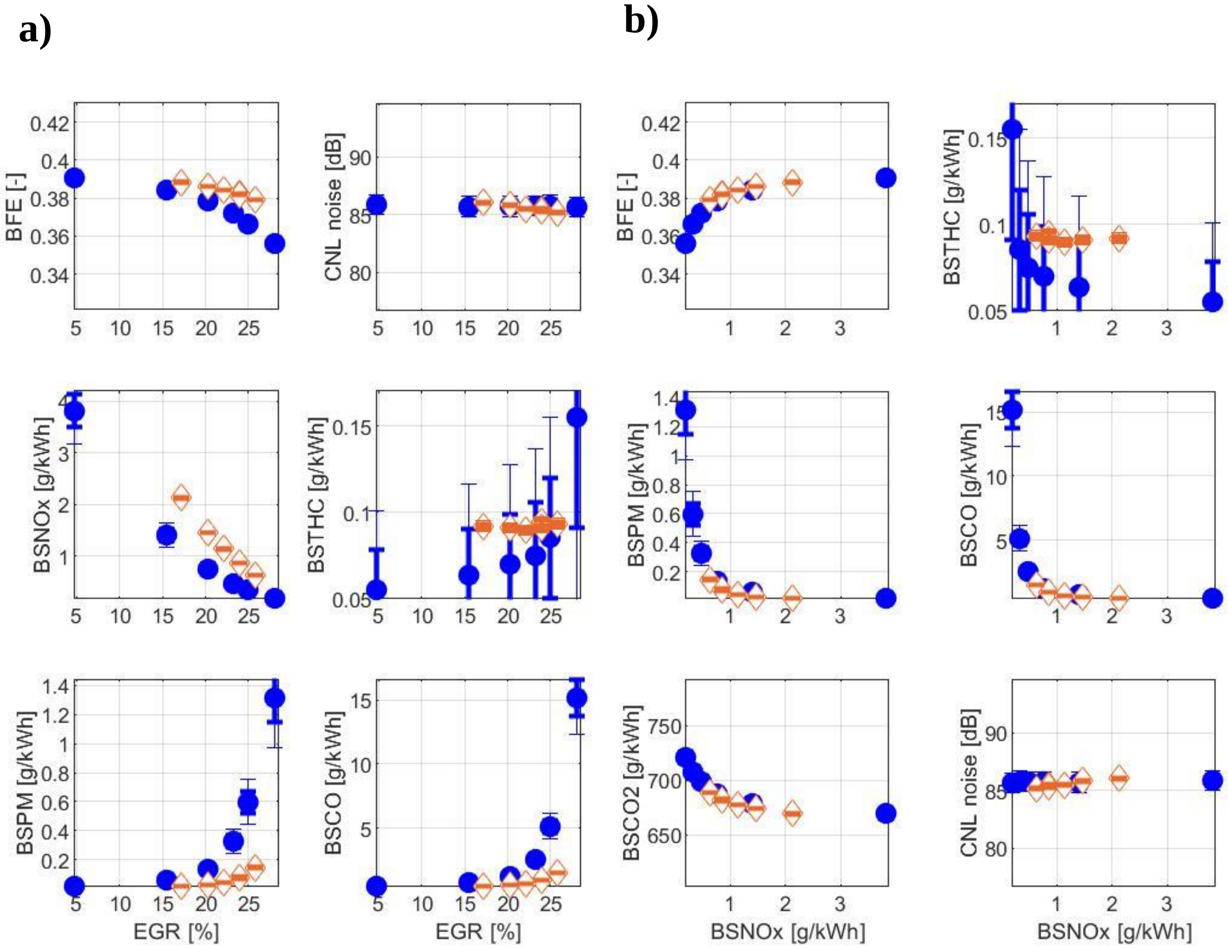

Figure 3.98. BFE, BS emission, and CNL during EGR sweep (●: Diesel at default ECU calibration, ◊: B20 at adjusted ECU calibration) at MM6 as a function of a) EGR rate, b) BSNOx

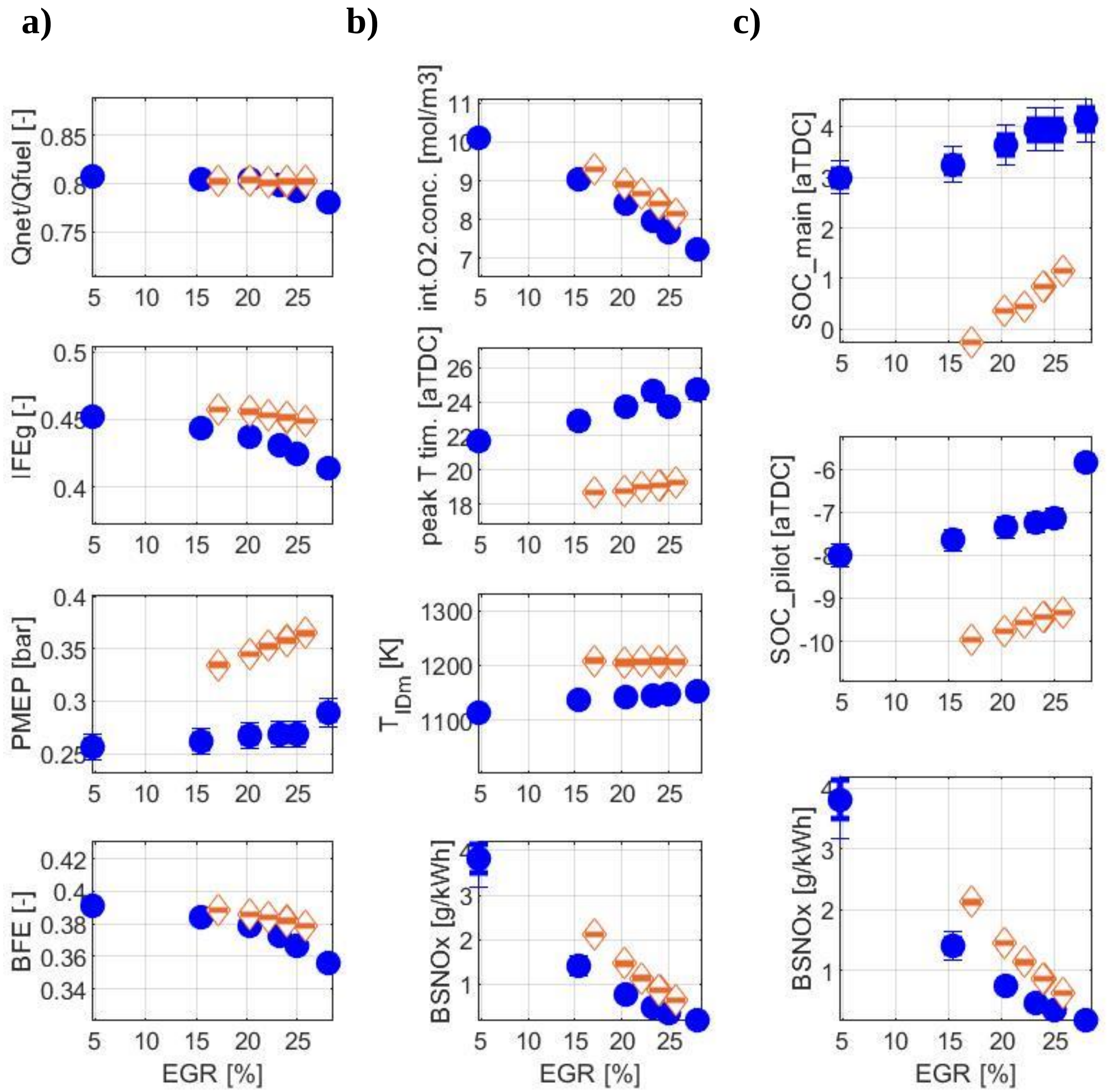

Figure 3.99. The parameters affecting a) BFE, b) and c) BSNOx during the EGR sweep (●: Diesel at default ECU calibration, ◊: B20 at adjusted ECU calibration) at MM6

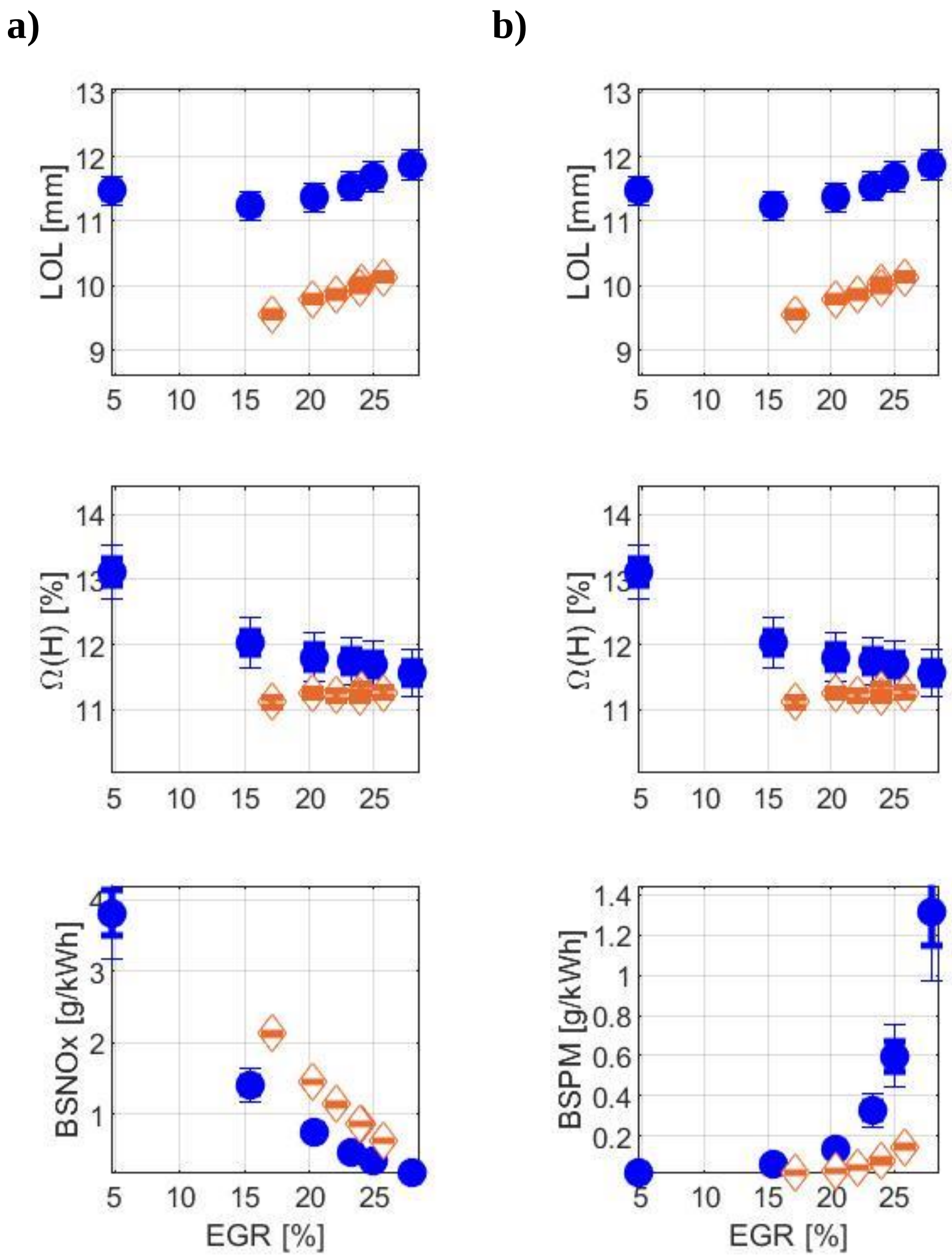

Figure 3.100. Lift-off length and oxygen ratio at the lift-off length during the EGR sweep at MM6 (●: Diesel at default ECU calibration, ◊: B20 at adjusted ECU calibration) with the trend of a) BSNOx, b) BSPM

3.3.5 Final ECU Optimization Results for B20

Figure 3.101 shows the final change in the ECU input settings with B20 application at 6 MM points. Figure 3.101a shows the change in EGR rate (top-left), rail pressure (middle-left), pilot 1 injection quantity (bottom-left), boost pressure (top-right), main injection timing (middle-right), and relative distance between the main injection timing and pilot 1 injection timing (bottom-right) at 6 different MM points. Figure 3.101b shows the change in pilot 2 injection quantity and relative distance between pilot 1 injection timing and pilot 2 injection timing at MM1.

First, EGR rate is increased at most MM points. It was increased the most at MM1 (absolute 10.6%) while other lower load points such as MM2 (absolute 9.4%) and MM3 (absolute 7.6%) also experienced significant increase in EGR rate. Mini-map point 5 (MM5) was the only mini-map point where the EGR rate was decreased. However, even at MM5, the degree of decrease in the EGR rate was relatively small (absolute 0.7%).

Second, boost pressure is decreased at most MM points. It was most intensively decreased at MM5. At MM5, the boost pressure decreased by 90.5hPa from the default ECU settings. The only mini-map point at which the boost pressure is increased was MM6. At MM6, the boost pressure is increased about 50hPa from the default ECU settings.

Third, main injection timing is advanced at all 6 MM points with different degrees of advance (0.2-2.5CAs) depending on the mini-map points. MM6 and MM2 experienced the most intensive advance in main injection timings (2.5CAs) while MM5 experienced the least advance in main injection timing (0.2CA).

The change in rail pressure settings at the final B20 calibration varied depending on the MM points. At MM2 and MM4, the rail pressure settings decreased by moderate amount

(~60bars) while the rail pressure settings increased for the other MM points. The most intensive increase in the rail pressure was conducted at MM6 (251.1bar).

The change in relative distance between main injection timing and pilot 1 injection timing (RPIT1) also varied depending on each mini-map point. For MM2-4, relative distance between main injection timing (MIT) and pilot 1 injection timing (PIT1) was decreased (which means retarding in PIT1) while it was increased for MM1, MM5, and MM6.

Pilot 1 injection quantity (PIQ1) is increased for higher load points (MMs 4-6) while it was decreased for lower-load points (MMs 1-3). The degree of the increase or decrease in PIQ1 was highest for highest (MM6)/lowest (MM1) load conditions. Since the default PIQ1 was generally low for higher load points and generally high for lower load points, the final PIQ1 settings became more even for different mini-map points than the default settings.

At MM1, the pilot 2 injection quantity (PIQ2) is increased by 0.7mg/stroke while the relative distance between PIT1 and PIT2 (RPIT2) is decreased by 2.5CAs.

The general trend in the change of ECU input parameters at different MM points provides a good understanding on how the new calibration was able to achieve better BFE while satisfying other bound criteria such as brake specific (BS) emissions and combustion noise level (CNL). In terms of maximizing BFE, boost pressure and main injection timing are actively utilized in a way to improve BFE. At most MM points (MM1-5), the boost pressure setting is decreased almost down to the lowest boost pressure level achievable at the imposed EGR rate settings so that the BFE improvement from the boost pressure adjustment can be maximized. Even at MM6, the boost pressure is not increased to “sacrifice” BFE. Since, at MM6, BFE uniquely increases from the default boost pressure (DP) to mid-high boost pressure (MHP), the calibration was actually taking advantage of the unique range of the boost pressure where BFE can still be increased. Meanwhile, main injection timing is advanced at all of the 6 MM points since the advance in the main injection timing improves BFE at most MM points.

While boost pressure and main injection timing are mainly used to improve BFE, the shift in EGR settings is more focused on countering off the BSNOx increase caused by the B20's impact and/or by the impact of the change in other ECU input parameters (e.g., advance in main injection timing). This is why EGR rate is increased in most mini-map points while it could be decreased exceptionally at MM5. Since MM5 had neither an aggressive advance in main injection timing nor statistically meaningful increase in NOx due to B20 at the default ECU calibration, the EGR rate could be rather reduced at MM5 to get further improvement in BFE.

a)

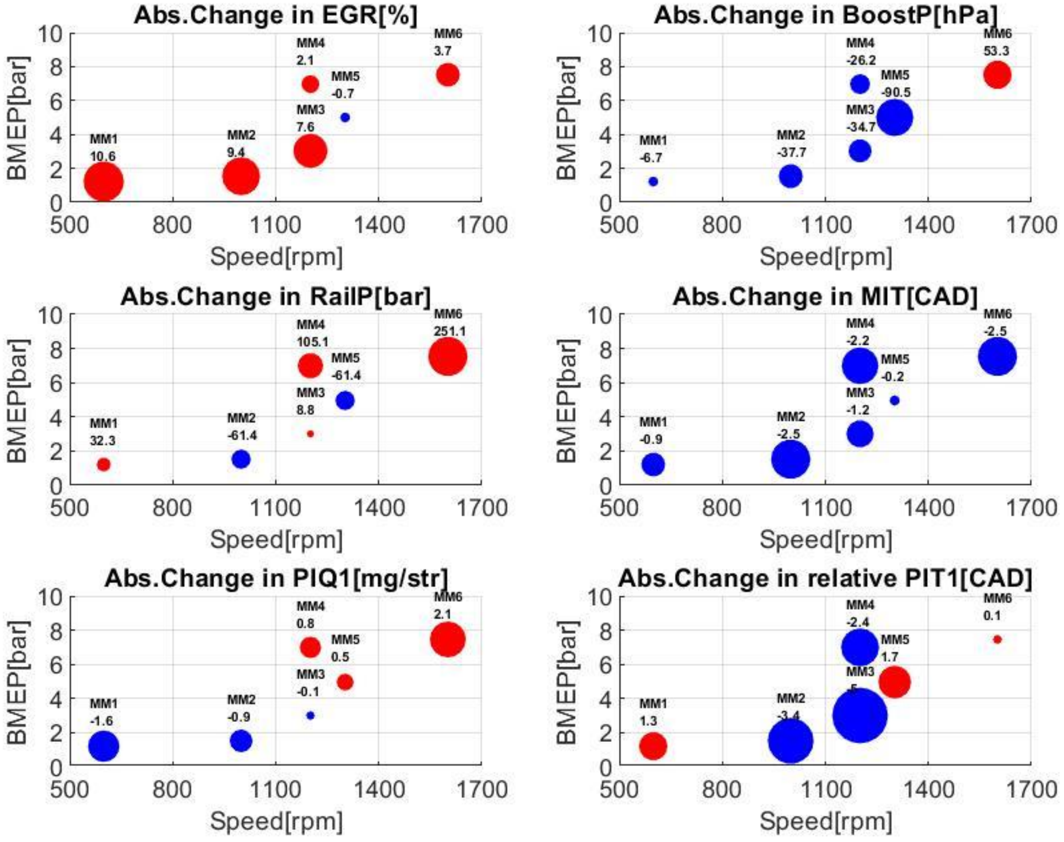

b)

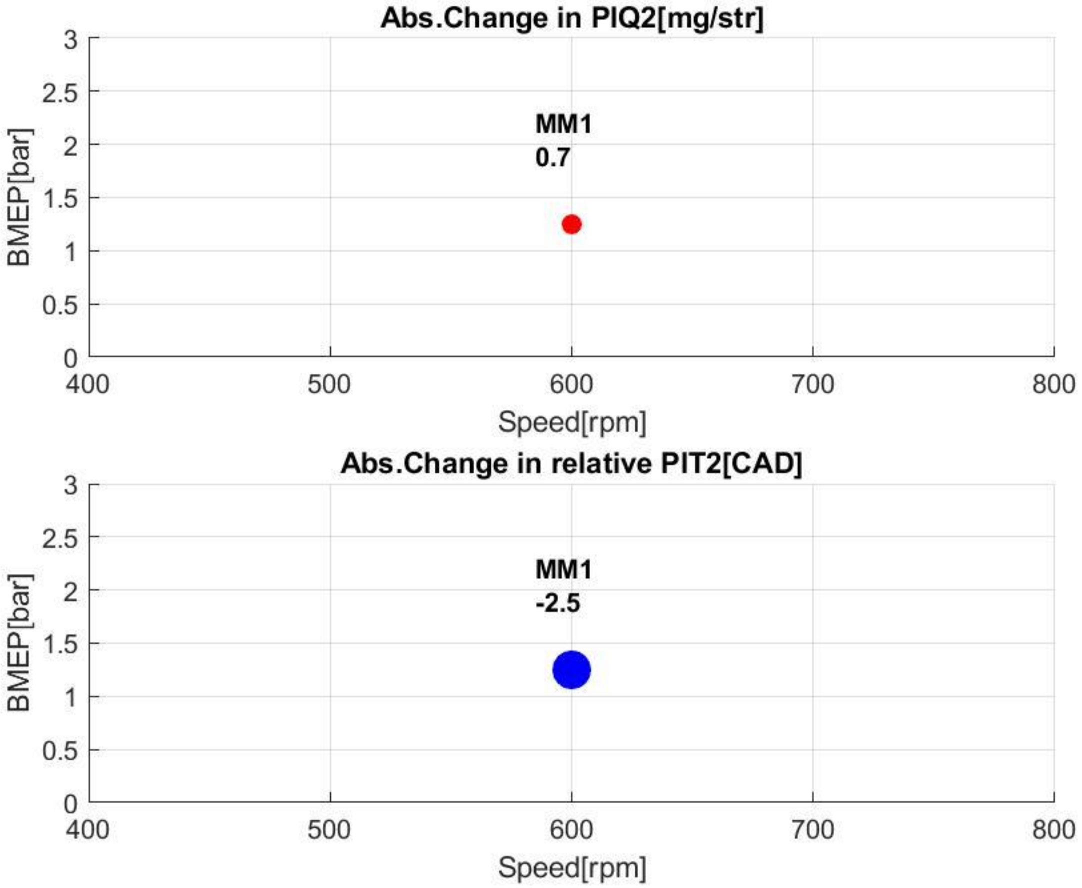

Figure 3.101. The final change in ECU input parameters for B20 (blue: decrease or advance, red: increase or retarding). a) Change in EGR, rail pressure (RP), boost pressure (BP), main injection timing (MIT), pilot 1 injection quantity (PIQ1), and relative distance between main injection timing and pilot 1 injection timing (RPIT1) for MMs 1-6, b) Change in pilot 2 injection quantity (PIQ2) and relative distance between pilot 1 injection timing and pilot 2 injection timing (RPIT2) for MM1

3.3.6 Implication on Life-Cycle GHG Reduction

3.3.6.1 Implication on GHG Reduction from Pump-to-Wheels (PTW) Combustion Process

Table 3.24 shows the comparison in BFE and $BSCO_2$ for the two fuels at the different ECU calibrations (i.e., baseline diesel at the default ECU calibration vs. B20 at the final adjusted ECU calibration) at each MM point. The mean difference in BFE and $BSCO_2$ between the two fuels is provided in the table in both absolute value of the difference and the relative difference in percentage. The standard deviation given in the table is the sum of the standard deviation of the multiple (3-8 points) repeat points measurements for the baseline diesel at the default ECU calibration and the standard deviation of the multiple (3-4 points) repeat points measurements for B20 with the final ECU calibration. It is the measure of the degree of difference in BFE or $BSCO_2$ between the two fuels guaranteeing 68% statistical confidence: if the mean difference in BFE or $BSCO_2$ between the two fuels is greater than the standard deviation, it is more than 68% sure that the difference will be repeated in the next data set obtained. For each MM point, if there was no statistically meaningful (less than 68% statistical confidence) difference in BFE or $BSCO_2$ between the two fuels, the mini-map point is colored with grey. If BFE or $BSCO_2$ is improved or worsened with statistical significance, the mini-map point is colored with blue or red.

As a result, MMs 1-4 turned out to have no statistically meaningful difference in BFEs between the two fuels. Thus, these four mini-map points are concluded to have no difference in the energy requirement per unit travelling distance (i.e., “MJ/mile”) between the two fuels.

MM5 achieved absolute 0.36% improvement in BFE for B20, which is greater than or the same as the standard deviation of the repeated measurements of BFE at the mini-map point (i.e., 0.34%). The absolute 0.36% improvement in BFE at MM5 corresponds to relative 0.98%

improvement in BFE as compared to the baseline result. Also, $BSCO_2$ from MM5 for B20 was 12.03g/kWh lower than the baseline result, which was greater than or the same as the standard deviation of the repeated measurements of $BSCO_2$ at the mini-map point (i.e., 12.01g/kWh). Therefore, at MM5, it is concluded that the PTW GHG emission is improved for B20 by relative 0.98 (based on BFE measurements)-1.64% (based on $BSCO_2$ measurements) from the baseline case with low statistical confidence (~68%). In conclusion, there was relative 1.31% (average of the BFE result and $BSCO_2$ result) improvement in the PTW GHG emission for B20 with the final ECU calibration at MM5 with statistical confidence of 68%.

At MM6, both BFE and $BSCO_2$ had statistically meaningful improvement with high statistical confidence when B20 is applied with the final ECU calibration. Brake fuel conversion efficiency (BFE) was increased by absolute 0.33% for B20 with the final ECU calibration, which was relative 0.87% improvement from the baseline result. The degree of improvement in BFE was almost twice of the standard deviation of the repeated BFE measurements at MM6, thus guaranteeing statistical confidence of about 95%. $BSCO_2$ emission for B20 with the final ECU calibration was decreased by 8.83g/kWh, which was also greater than twice of the standard deviation of the repeated $BSCO_2$ measurements at MM6. Therefore, it is concluded that, at MM6, B20 achieved the relative 0.87-1.28% improvement (1.08% in average) in PTW GHG emission as compared to the baseline case with statistical confidence of about 95%.

One thing to note in Table 3.24 is that, at MM1, there is a noticeable difference between when BFE is compared for the two fuels and when $BSCO_2$ is compared for the two fuels. Although the BFE for B20 is improved by relative 0.04% at MM1, $BSCO_2$ for B20 is rather increased by 4.4% at MM1. This is because of the particularly high measurement inaccuracy for both BFE and $BSCO_2$ at MM1 (idling). At idling condition, the fuel flow rate becomes much lower than other operating conditions, which results in the increase in fuel flow rate measurement inaccuracy. This, in turn, increases inaccuracy in the BFE calculation. Also, the variation in brake torque setting becomes greater at MM1 causing greater noise in emissions measurement including CO_2. This increases inaccuracy in the $BSCO_2$ measurement, as well. There was also the difference in the degree of BFE measurement errors for B20 and baseline diesel fuel. Based on a carbon balance error calculation, fuel mass flow rate was more intensely underestimated with B20 than with diesel. The more intensive underestimation in the fuel flow rate with B20 could have made a positive bias on the BFE for B20 over the baseline diesel fuel.

To account for this difference in BFE and $BSCO_2$, it is concluded that the mini-map points with statistically meaningful change in “both” BFE and $BSCO_2$ are considered to have the change in PTW GHG emissions for B20, which only leaves MM5 and 6 as the mini-map points with PTW GHG emissions change from the baseline diesel.

	Baseline BFE at def. cal. [%]	B20 BFE at final cal. [%]	Absolute mean difference [%]	Difference in [%]	Standard deviation (σ) [%]
MM1	25.85	25.86	+0.01	+0.04	0.48
MM2	27.14	27.21	+0.07	+0.26	1.02
MM3	33.77	33.80	+0.04	+0.12	0.36
MM4	37.85	37.57	-0.28	-0.74	0.48
MM5	36.81	37.17	+0.36	+0.98	0.34
MM6	37.87	38.20	+0.33	+0.87	0.17
	Baseline $BSCO_2$ at def. cal. [g/kWh]	B20 $BSCO_2$ at final cal. [g/kWh]	Absolute mean difference [g/kWh]	Difference in [%]	Standard deviation (σ) [g/kWh]
MM1	1059	1106	+46.55	+4.40	33.99
MM2	979	981	+2.36	+0.24	51.12
MM3	787	773	-13.07	-1.66	8.72
MM4	693	712	+19.57	+2.82	18.52
MM5	715	703	-12.03	-1.64	12.01
MM6	691	682	-8.83	-1.28	3.47

Table 3.24. Comparison of BFE and $BSCO_2$ for the two fuels at the optimized ECU calibrations of each fuel. (Grey: no statistically meaningful difference between the two fuels, blue: statistically meaningful (≥68% statistical confidence) improvement for B20, red: statistically meaningful worsening for B20)

Table 3.25 provides the weight factors for each mini-map point used to estimate the performance and emissions from the Environmental Protection Agency (EPA) Federal Test Protocol 75 (FTP75) certification cycle. Mini-map point 3 (MM3) has the highest weight on the certification cycle followed by MM6, MM5, MM2, MM1, and lastly by MM4. The pump-to-wheels GHG emissions reduction from the transient certification cycle can be estimated by the linear combination of the improvement in PTW GHG emissions at each mini-map point with these weight factors (WF).

	MM1	MM2	MM3	MM4	MM5	MM6
Weight factor [%]	9.1	11.3	27.3	8.8	23.6	20.0

Table 3.25. Weight factors applied to each mini-map point to emulate the EPA FTP75 certification cycle.

Equation 3.42 is used to estimate the reduction in the energy required per unit travelling distance (i.e., MJ/mile), or the PTW GHG emissions reduction, from FTP75 transient cycle based on the performances at different MM points. “WF” denotes the weight factor at each mini-map point while the subscript “i” denotes the mini-map point “i”.

$$relative\ improvement\ in\ "MJ/mile"\ for\ FTP75\ cycle\ [\%] =$$

$$\sum_{i=1}^{6}(relative\ improvement\ in\ "MJ/mile"\ \ at\ MM_i\ [\%]) \cdot (WF_i) \qquad \text{(Eq. 3.42)}$$

If there is no statistically meaningful difference in “MJ/mile” between the two fuels at certain MM point, the “MJ/mile” improvement is assumed to be zero at that MM point. The only two mini-map points with statistically meaningful “MJ/mile” difference between the two fuels were MM5 and MM6. By combining the relative 1.31% improvement at MM5 and 1.08% improvement at MM6 with the weight factors presented in Table 3.25, there was relative 0.53% improvement in “MJ/mile” (i.e., PTW GHG emissions) for B20 during the EPA FTP75 certification cycle.

The improvement or worsening in BSNOx and BSPM emissions for B20 with the optimized ECU setting as compared to the baseline diesel during the EPA FTP75 certification cycle could also be calculated using the B20's BSNOx and BSPM change for each MM point (Tables 3.13, 3.15, 3.17, 3.19, 3.21, and 3.23) and the same weight factors shown in Table 3.25. There was 25.5% reduction in BSNOx and 16.7% reduction in BSPM for B20 with the final optimized ECU setting as compared to the baseline diesel. This was a significant co-benefit of the current ECU optimization in parallel with the 0.5% PTW GHG emissions improvement.

The previous studies similar to the current study include the work by Millo et al.[51] and Omari et al.[19] Millo et al.[51] compares the criteria pollutant emissions between different biodiesel blends (i.e., B30s and B100s from Rapeseed oil and Jatropha oil) and petroleum-based diesel at the optimized ECU calibration for each fuel. However, their ECU optimization was focused on maximizing the PM reduction at NOx parity than maximizing the BFE to minimize the GHG emissions from the PTW combustion processes. Thus, the improvement in BFE with their optimized ECU calibration was not available from their work. Omari et al.[19] compared the BFE and emissions for hydrotreated vegetable oils (HVO) with those for the petroleum-based diesel at the optimized ECU calibrations for each fuel. However, due to the differences in the fuel properties between HVO and biodiesel, the implication on BFE or the GHG emissions improvement from HVO reported in their research should not be extended to the case of biodiesel.

Therefore, as far as I am concerned, the current work is the first-in-the-field experimental results showing how much improvement in BFE or PTW GHG emissions is possible for B20 with the comprehensively adjusted ECU calibration (i.e., including the adjustment in 6-8 input parameters at different operating conditions covering the whole range of chassis-dyno certification) while achieving the significant reduction in some of the other criteria pollutant (i.e., NOx, PM) emissions from the baseline case.

3.3.6.2 Implication on GHG Reduction from Well-to-Wheels (WTW) Process

The relative 0.53% improvement in "MJ/mile" means that the optimized ECU calibration for B20 reduced the energy required for unit travelling distance (i.e., MJ/mile) by 0.53% when compared to the conventional petroleum-based diesel. To account for the overall GHGs reduction from well-to-wheels (WTW) process on a "gCO_{2e}/mile" basis, we also need to assess the GHGs reduction from the production and combustion of B20 on a "gCO_{2e}/MJ" basis.

The well-to-wheels (WTW) carbon intensity of B100 per unit energy is 30gCO2e/MJ (including the biogenic benefit of biodiesel) while it is 95gCO2e/MJ for the petroleum-based diesel.[8] Based on these values, the WTW carbon intensity of B20 per unit energy (i.e., gCO_{2e}/MJ) can be calculated as follows.

First of all, the mass fraction of biodiesel in B20 is calculated using Equation 3.43.

$$Y_B = \frac{\rho_B \cdot X_B}{\rho_B \cdot X_B + \rho_D \cdot X_D} \quad \text{(Eq. 3.43)}$$

In Equation 3.43, Y_B is the mass fraction of biodiesel in B20, *X* is a volume fraction while the subscript "*B*" denotes for biodiesel, and "*D*" denotes for petroleum-based diesel. Then, the fraction of energy from biodiesel in B20 is calculated using Equation 3.44.

$$Z_B = \frac{LHV_B \cdot Y_B}{LHV_B \cdot Y_B + LHV_D \cdot Y_D} \quad \text{(Eq. 3.44)}$$

In Equation 3.44, Z_B is the fraction of energy from biodiesel in B20. Based on the density and LHV values of petroleum-based diesel and biodiesel presented in Tables 3.2 and 3.3, the mass fraction of biodiesel in B20 is calculated to be 20.7%, and the fraction of energy from biodiesel in B20 is calculated to be 18.6%. Now, the WTW carbon intensity of B20 per unit energy could be calculated using Equation 3.45.

$$CI_{B20} = CI_B \cdot Z_B + CI_D \cdot Z_D \quad \text{(Eq. 3.45)}$$

As a result, the WTW carbon intensity of B20 per unit energy is calculated to be 82.91gCO_{2e}/MJ, which is 12.7% reduction from the petroleum-based diesel.

Regarding the WTW GHG emissions per unit travelling distance (i.e., gCO_{2e}/mile), we need to account for the 0.53% savings in “MJ/mile” in addition to the 12.7% reduction in “gCO_{2e}/MJ”. Therefore, there is 13.2% reduction in final WTW GHG emissions per unit travelling distance (i.e., gCO_{2e}/mile) for B20 application with the final optimized ECU calibration.

3.4 Summary and Conclusions

The GHG emissions reduction impact of the application of B20 in a production CI engine (6.7L Ford Powerstroke engine) is investigated in the current work. Four different single parameter sweep tests (i.e., EGR sweep, boost pressure sweep, rail pressure sweep, main injection timing sweep) are conducted for the baseline petroleum-based diesel and B20 at the default ECU calibrations of the six different engine operating conditions (6 MM points) simulating EPA FTP75 certification cycle to investigate the impact of 4 different input parameters and the impact of B20 fuel on the output parameters of the interest (i.e., BFE, BSNOx, BSPM, BSTHC, BSCO, and CNL). The comprehensiveness of the operating conditions and input parameters covered by the current study is unprecedented by the previous B20 studies in a production CI engine. While the results from the 4 single parameter sweep tests re-confirm most of the well-known impacts of the EGR, boost pressure, rail pressure, and main injection timing on BFE, BS emissions, and CNL from the previous studies (e.g., BFE increase with decreasing EGR, advanced main injection timing, and BSNOx increase with decreasing EGR, increasing rail pressure, and advanced main injection timing, etc.), a couple of notable findings that have not been reported or emphasized in the previous studies are also reported in the current study.

First, for both petroleum-based diesel and B20, BSPM peaks around the default injection timing for most engine operating conditions, then decreases for both advanced and retarded main injection timings due to the decreased charge gas temperature, which fundamentally led to the increase in lift-off length and oxygen ratio at the lift-off length to reduce PM generation in the fuel-rich premixed auto-ignition zone. Second, the competition of overall charge O_2 concentration and the oxygen ratio at the lift-off length existed in most MM points to result in different NOx and PM trends at different MM points with different load conditions. At higher load conditions, the impact of the overall charge O_2 concentration increased over the impact of the oxygen ratio at lift-off length on BSPM and BSNOx emissions, implying the importance of mixing-controlled emissions formation mechanism over the importance of the emissions formation inside the fuel-rich premixed auto-ignition zone.

The impact of B20 fuel properties on BFE and BS emissions could also be quantified from the current study for unprecedentedly comprehensive range of engine operating conditions and the ECU settings. At idling (MM1) and medium-to-high load conditions (MM4 and MM5), the fuel properties of B20 did not have any statistically meaningful impact on any of the output parameters of the interest, but at low-to-medium load conditions (MM2, MM3) and a high-load

(MM6) condition, the fuel properties of B20 did increase BSNOx (10-25%) and decrease BSPM (0-10%) depending on the mini-map points while still not affecting BFE. The consistent BFE between the two fuels was due to the negligible difference in ignition delay and pumping loss between the two fuels while the increase/decrease in BSNOx/BSPM was mainly due to the increase in oxygen ratio at the lift-off length caused by the fuel oxygen content of B20. This observation corroborated the need for ECU optimization for the B20 application to maximize the BFE while satisfying other bound criteria such as BSNOx and CNL by utilizing the PM benefits of B20.

The final GHG emissions reduction for B20 with the optimized ECU calibration is measured and the underlying mechanism used by the optimization software to maximize BFE is also suggested in the current study. At idling (MM1), low-to-medium load (MM2-3) and a high load condition (MM4), the final BFE for B20 did not show statistically meaningful difference from the baseline result. However, at a medium load (MM5) and the highest load (MM6) condition, there was small improvement in BFE for B20. At MM5, the BFE is improved by 1.31%. At MM6, the BFE is improved by 1.08%. Combined with the weight factors to simulate the EPA FTP75 cycle from these 6 MM points, 0.53% improvement in the energy requirement per unit travelling distance (i.e., MJ/mile) is achieved for B20 with the final ECU calibration. Although the degree of improvement in pump-to-wheels energy savings (i.e., MJ/mile) was relatively smaller than the degree of GHG emissions reduction on a “gCO_{2e}/MJ” basis (i.e., ~12.5% reduction in gCO_{2e}/MJ), this study proved that the application of B20 in a production CI engine with “optimized” calibrations can actually reduce GHG emissions in pump-to-wheels combustion processes. Also, 25.5% reduction in BSNOx and 16.7% reduction in BSPM were achieved for B20 with the optimized ECU setting as co-benefits.

The optimization software mainly used “the decrease in boost pressure” and “the advance in main injection timing” to maximize BFE and reduce GHG emissions while mainly used “the increase in EGR rate” to counter off the potential NOx increase due to the fuel oxygen content in B20 and the impact of the change in the other ECU input settings. Other ECU variables such as rail pressure, pilot injection quantity, and relative distance between main injection timing and pilot injection timings seem to be used as secondary means to further improve BFE (e.g., by increasing rail pressure) or to reduce other bound criteria parameters such as BS emissions and CNL. One of the notable observation made during the B20 testing with the final ECU calibration was that the sensitivity of the charge gas temperature on EGR rate is significantly increased. This was because the increased injected fuel moles for B20 has partially countered off the decrease in the intake gas mole count with increasing EGR, thus resulting in the less apparent drop in total charge gas mole count with increasing EGR when B20 is applied. Then, the less apparent decrease in charge gas mole count significantly decreased the charge gas temperature with increasing EGR rate, which eventually increased the lift-off length and oxygen ratio at the lift-off length to result in significant reduction in BSPM emissions. It is suggested that the optimization software was able to locate this optimized ECU settings where the impact of increased fuel injection volume of B20 could be exaggerated enough to bring the best PM benefits, which, in turn, could be used to maximize the BFE while satisfying BSNOx bound criteria.

To further reduce the GHG emissions from the pump-to-wheels combustion processes of B20 in CI engines, the future work is suggested to be focused on the following two directions. First, the application of higher blends of biodiesel (i.e., >B20) is recommended because it provides more aggressive fuel oxygen content from biodiesel and the more aggressive increase in fuel injection volume, both of which can increase the oxygen ratio at the lift-off length more intensely to result in further PM benefit. Then, this increased PM benefit could potentially be used to further improve the BFE. This strategy would work the best for the lower load conditions due to the importance of oxygen ratio in the fuel-rich premixed auto-ignition zone for the lower load conditions. Second, the application of B20 or the higher level of blends at higher engine loads not covered in the current study (e.g., higher load conditions relevant to the engine-dyno certification) is recommended because the highest engine load covered in the current study (i.e., MM6) is still around 35% of the peak torque at its engine speed. According to Ye et al.[24], high load conditions at around 75% of the peak torque showed the most exaggerated PM reduction effect of which underlying mechanism is different from the PM reduction observed in low-to-medium load conditions reported in the current work. Thus, investigating B20's impact on such high load conditions will also narrow the research gap left from the current work.

3.5 References

[1] Campbell, P.; Beer, T.; Batten, D. Life cycle assessment of biodiesel production from microalgae in ponds, *Bioresource Technology*, **2011**, 102, 50-56.

[2] Huo, H.; Wang, M.; Bloyd, C.; Putsche, V. *Life-Cycle Assessment of Energy and Greenhouse Gas Effects of Soybean-Derived Biodiesel and Renewable Fuels*; ANL/ESD/08-2; Argonne National Laboratory: Lemont, IL, March 12, 2008.

[3] Thanh, L.T.; Okitsu, K.; Van Boi, L.; Maeda, Y. Catalytic Technologies for Biodiesel Fuel Production and Utilization of Glycerol: A Review, *Catalysts*, **2012**, 2, 191-222.

[4] *Monthly Biodiesel Production Report (with data for May 2020)*; U. S. Energy Information Administration (EIA) in U. S. Department of Energy (DOE): Washington, D.C., July 2020.

[5] Scott, S.A.; Davey, M.P.; Dennis, J.S.; Horst, I.; Howe, C.J.; Lea-Smith, D.J.; Smith, A.G. Biodiesel from algae: challenges and prospects, *Current Opinion in Biotechnology*, **2010,** 21, 277-286.

[6] Nautiyal, P.; Subramanian, K.A.; Dastidar, M.G. Production and Characterization of biodiesel from algae, *Fuel Processing Technology*, **2014**, 120, 79-88.

[7] Piloto-Rodriguez, R.; Sanchez-Borroto, Y.; Melo-Espinosa, E.A.; Verhelst, S. Assessment of diesel engine performance when fueled with biodiesel from algae and microalgae: An overview, *Renewable and Sustainable Energy Reviews*, **2017**, 69, 833-842.

[8] Chen, R.; Qin, Z.; Han, J.; Wang, M.; Taheripour, F.; Tyner, W.; O'Connor, D.; Duffield, J. Life cycle energy and greenhouse gas emission effect of biodiesel in the United States with induced land use change impacts, *Bioresource Technology*, **2018**, 251, 249-258.

[9] Wallington, T.; Anderson, J.; Kurtz, E.; Tennison, P. Biofuels, vehicle emissions, and urban air quality, *Faraday Discuss.*, **2016**, 189, 121-136.

[10] Lapuerta, M.; Armas, O.; Rodriguez-Fernandez, J. Effect of biodiesel fuels on diesel engine emissions, *Progress in Energy and Combustion Science*, **2008**, 34, 198-223.

[11] Lapuerta, M.; Oliva, F.; Agudelo, J.; Boehman, A. Effect of fuel on the soot nanostructure and consequences on loading and regeneration of diesel particulate filters, *Combustion and Flame*, **2012**, 159, 844-853.

[12] Graboski, M.; McCormick, R. Combustion of fat and vegetable oil derived fuels in diesel engines, *Progress in Energy and Combustion Science*, **1998**, 24, 125-164.

[13] Sappok, A.; Wong, V. Impact of Biodiesel on Ash Emissions and Lubricant Properties Affecting Fuel Economy and Engine Wear: Comparison with Conventional Diesel Fuel, SAE Technical Paper (2008), 2008-01-1395.

[14] Ye, P.; Prabhakar, B.; Boehman, A.L. Experimental investigation of the impact of post-injection on emissions, combustion and lubricant dilution in a diesel engine with B20 fuel, *International Journal of Engine Research*, **2013**, 14, 12-22.

[15] Fang, H.; McCormick, R. Spectroscopic study of biodiesel degradation pathways, SAE Technical Paper (2006)**,** 2006-01-3300.

[16] Hermitte, E.; Lunati, A.; Delebinski, T. Onboard Optimisation of Engine Emissions and ConsumptionAccording to Diesel Fuel Quality, SAE Technical Paper (2012), 2012-01-1694.

[17] Senatore, A.; Cardone, M.; Buono, D.; Rocco, V.; Allocca, L.; Vitolo, S. Performances and Emissions Optimization of a CR Diesel Engine Fuelled with Biodiesel, SAE Technical Paper (2006), 2006-01-0235.

[18] Murr, F.; Winklhofer, E.; Friedl, H. Reducing Emissions and Improving Fuel Economy by Optimized Combustion of Alternative Fuels , SAE Technical Paper (2011), 2011-28-0050.

[19] Omari, A.; Pischinger, S.; Bhardwaj, O. P.; Holderbaum, B.; Nuottimaki, J.; Honkanen, M. Improving Engine Efficiency and Emission Reduction Potential of HVO by Fuel-Specific Engine Calibration in Modern Passenger Car Diesel Applications, SAE Technical Paper (2017), 2017-01-2295.

[20] Mejia, A.; Leiva, M.; Rincon-Montenegro, A.; Gonzalez-Quiroga, A.; Duarte-Forero, J. Experimental assessment of emissions maps of a single-cylinder compression ignition engine powered by diesel and palm oil biodiesel-diesel fuel blends, *Case Studies in Thermal Engineering*, **2020**, 19, 100613.

[21] Larsson, M.; Denbratt, I. Combustion of Fischer-Tropsch, RME and Conventional Fuels in a Heavy-Duty Diesel Engine, SAE Technical Paper (2007), 2007-01-4009.

[22] Kurtz, E.; Kuhel, D.; Anderson, J.; Mueller, S. A Comparison of Combustion and Emissions of Diesel Fuels and Oxygenated Fuels in a Modern DI Diesel Engine, SAE Technical Paper (2012), 2012-01-1695.

[23] Yehliu, K.; Boehman, A.; Armas, O. Emissions from different alternative diesel fuels operating with single and split fuel injection, *Fuel*, **2010**, 89, 423-437.

[24] Ye, P.; Boehman, A. An investigation of the impact of injection strategy and biodiesel on engine NOx and particulate matter emissions with a common-rail turbocharged DI diesel engine, *Fuel*, **2012**, 476-488.

[25] Mueller, C.; Boehman, A.; Martin, G. An Experimental Investigation of the Origin of Increased NOx Emissions when Fueling a Heavy-Duty Compression-Ignition Engine with Soy Biodiesel, SAE Technical Paper (2009), 2009-01-1792.

[26] ASTM D7668-17. “Standard Test Method for Determination of Derived Cetane Number (DCN) of Diesel Fuel Oils—Ignition Delay and Combustion Delay Using a Constant Volume Combustion Chamber Method”.

[27] Heywood, J. Chapter 10: Combustion in Compression-Ignition Engines. *Internal Combustion Engine Fundamentals*, International Edition, McGraw Hill: Singapore, 1988, pp. 509-514.

[28] Shahlari, A.; Kurtz, E.; Hocking, C.; Antonov, S., Correlation of cylinder pressure–based engine noise metrics to measured microphone data, *International Journal of Engine Research*, **2015**, 16(7), 829-850.

[29] U. S. Environmental Protection Agency (EPA) Home Page. https://www.epa.gov/criteria-air-pollutants (Accessed on August 19th, 2020).

[30] Heywood, J. Chapter 2: Engine Design and Operating Parameters. *Internal Combustion Engine Fundamentals*, International Edition, McGraw Hill: Singapore, 1988, pp. 45-50.

[31] Naber, J.; Siebers, D. Effects of Gas Density and Vaporization on Penetration and Dispersion of Diesel Sprays, SAE Technical Paper (1996), 960034.

[32] Siebers, D. Scaling Liquid-Phase Fuel Penetration in Diesel Sprays Based on Mixing-Limited Vaporization, SAE Technical Paper (1999), 1999-01-0528.

[33] Siebers, D.; Higgins, B. Flame Lift-Off on Direct-Injection Diesel Sprays Under Quiescent Conditions, SAE Technical Paper (2001), 2001-01-0530.

[34] Siebers, D.; Higgins, B.; Pickett, L. Flame Lift-Off on Direct-Injection Diesel Fuel Jets: Oxygen Concentration Effects, SAE Technical Paper (2002), 2002-01-0890.

[35] Ye, P.; Boehman, A.L. Investigation of the Impact of Engine Injection Strategy on the Biodiesel NOx Effect with a Common-Rail Turbocharged Direct Injection Diesel Engine, *Energy & Fuels*, **2010**, 24, 4215-4225.

[36] Pickett, L.; Siebers, D.; Idicheria, C. Relationship Between Ignition Processes and the Lift-Off Length of Diesel Fuel Jets, SAE Technical Paper (2005), 2005-01-3843.

[37] Pickett, L.; Siebers, D. Soot formation in diesel fuel jets near the lift-off length, *Int. J. Engine. Res.* **2006,** 7, 103-130.

[38] Heywood, J. Chapter 6: Gas Exchange Processes. *Internal Combustion Engine Fundamentals*, International Edition, McGraw Hill: Singapore, 1988, pp. 249-253.

[39] Colban, W.F.; Miles, P.C.; Oh, S. Effect of Intake Pressure on Performance and Emissions in an Automotive Diesel Engine Operating in Low Temperature Combustion Regimes, SAE Technical Paper (2007), 2007-01-4063.

[40] Benajes, J.; Molina, S.; Garcia, J.M.; Novella, R. Influence of Boost Pressure and Injection Pressure on Combustion Process and Exhaust Emissions in a HD Diesel Engine, SAE Technical Paper (2004), 2004-01-1842.

[41] Pulkrabek, W. Chapter3: Engine Cycles, *Engineering Fundamentals of the Internal Combustion Enigne*, 2nd international edition, Pearson: Upper Saddle River, NJ., 2004, pp. 113-118.

[42] Szybist, J.; Song, J.; Alam, M.; Boehman, A. Biodiesel combustion, emissions and emission control, *Fuel Processing Technology*, **2007**, 88, 679-691.

[43] De Serio, D.; de Oliveira, A.; Sodre, J.R. Effects of EGR rate on performance and emissions of a diesel power generator fueled by B7, *Journal of Brazilian Society of Mechanical Sciences and Engineering*, **2017**, 39, 1919-1927.

[44] Divekar, P.; Yang, Z.; Ting, D.; Chen, X.; Zheng, M.; Tjong, J. Efficiency and Emission Trade-Off in Diesel-Ethanol Low Temperature Combustion Cycles, SAE Technical Paper (2015), 2015-01-0845.

[45] Al-Qurashi, K.; Zhang, Y.; Boehman, A. Impact of Intake CO2 Addition and Exhaust Gas Recirculation on NOx Emissions and Soot Reactivity in a Common Rail Diesel Engine, *Energy & Fuels*, **2012**, 26, 6098-6105.

[46] Szybist, J.; Kirby, S.; Boehman, A. NOx Emissions of Alternative Diesel Fuels: A Comparative Analysis of Biodiesel and FT Diesel, *Energy & Fuels*, **2005**, 19, 1484-1492.

[47] Al-Qurashi, K.; Lueking, A.; Boehman, A. The deconvolution of the thermal, dilution, and chemical effects of exhaust gas recirculation (EGR) on the reactivity of engine and flame soot, *Combustion and Flame*, **2011**, 158, 1696-1704.

[48] Heywood, J. Chapter 5. Ideals models of engine cycles, *Internal Combustion Engine Fundamentals*, McGraw Hill International Edition, McGraw Hill Book Company: Singapore, 1988; pp173-175.

[49] Edara, G.; Murthy, S.; Srinivas, P.; Nayar, J.; Ramesh, M. Effect of cooled EGR on modified light duty diesel engine for combustion, performance and emissions under high pressure split injection strategies, *Case Studies in Thermal Engineering*, **2018**, 12, 188-202.

[50] Ye, P.; Boehman, A. Investigation of the Impact of Engine Injection Strategy on the Biodiesel NOx Effect with a Common-Rail Turbocharged Direct Injection Diesel Engine, *Energy & Fuels*, **2010**, 24, 4215-4225.

[51] Millo, F.; Vezza, D.; Vlachos, T. Effects of Rapeseed and Jatropha Methyl Ester on Performance and Emissions of a Euro 5 Small Displacement Automotive Diesel Engine, SAE Technical Paper (2011), 2011-24-0109.

Chapter 4

Greenhouse Gas Emissions Reduction via Development of Optimized Dimethyl Ether (DME) Blend for Mixing-Controlled Compression-Ignition Engines

4.1 Introduction

Dimethyl ether (DME) is a low carbon fuel that can be produced from a number of renewable feedstocks because it can be produced from renewable feedstocks that are convertible to syngas. Gasification of lignocellulosic biomass[1] and reforming of biogas from animal manure[2-4] and landfill gas[5,6] are the practical examples of this kind of process. Well-to-wheel (WTW) greenhouse gas (GHG) emissions of DME from these production pathways are significantly lower than diesel fuel: -1gCO$_2$e/MJ (DME from animal manure) and 6gCO$_2$e/MJ (DME from landfill gas) as compared to 92gCO$_2$e/MJ (Diesel from petroleum).[7] DME can be also produced from the process called "Carbon Recycling" where the carbon dioxide captured either from a combustion source or from the atmosphere is combined with renewable hydrogen to produce methanol, then, dehydrated into DME. In this case, DME can be a carbon-negative fuel.[8-10]

In addition, DME has other benefits as an alternative fuel for compression ignition (CI) engines. It has appropriate ignition quality (i.e., CN: 55-60) for CI engine applications, which is moderately higher than conventional diesel fuel (i.e., CN: 40-50).[11] It burns soot-free with no significant rise in NOx emission.[12] It is also non-toxic and non-carcinogenic.[13] Thus, much research has been conducted for the past three decades to apply DME as a CI engine alternative fuel.[14-18]

However, the application of DME in CI engines poses challenges due to the different physicochemical properties of DME from conventional petroleum-based diesel.[19] Table 4.1 compares the key physicochemical properties of DME with diesel. Low lower heating value (LHV) and low density of DME necessitate larger fuel tank for the same travel range per fueling. High vapor pressure of DME demands modifications in fuel return system to prevent cavitation.[17] DME also has extremely low lubricity and low viscosity, both of which cause premature wear on the surface of the reciprocating components of the fuel injection systems.[20] The extremely low viscosity of DME also causes internal leakage in the fuel pump or fuel injector.[21] Although the lubricity of DME could be improved by adding around 1000ppm level of commercial lubricity enhancing agents (e.g., Lubrizol 539N), the viscosity of DME was difficult to be improved to the diesel level with the similar dose of the lubricity enhancing agent or other materials such as Castor oil.[20] The extremely low viscosity of DME has been the hardiest technological problem to solve because, unlike lubricity, viscosity is a bulk physical property instead of being a surface property. Surface properties such as lubricity or surface tension are relatively easier to be changed with additives because the amount of additive molecules just to cover the boundary layer between the fuel liquid and other substances (i.e., metal surface of the injector or pump plunger in case of lubricity of DME) was needed to alter them.[20-22]

Property	Unit	DME	Diesel
Formula	[-]	CH_3OCH_3	$C_{14}H_{30}$
CAS number	[-]	115-10-6	-
Molecular weight	[kg/kmol]	46.07	198.4[a]
Carbon content	[wt. %]	52.2	87[a]
Oxygen content	[wt. %]	34.8	0[a]
Hydrogen content	[wt. %]	13	13[a]
Liquid Density @25°C	[kg/m^3]	655.97*[b]	856[a]
Normal boiling point	[°C]	-24.84[b]	125-400[a]
Vapor pressure @25°C	[kPa]	592.80[b]	<10[c]
Vapor pressure @40°C	[kPa]	893.67[b]	-
Kinematic Viscosity @40°C	[cSt]	0.150*	No.1 grade: 1.3-2.4[d]
			No.2 grade: 1.9-4.1[d]
LHV	[MJ/kg]	28.62[a]	41.66[a]
Energy density	[MJ/L]	18.92[a]	35.66[a]
Cetane Number (CN)	[-]	55-60[c]	40-50[c]

Table 4.1. Physicochemical properties of DME and diesel. (*: at the vapor pressure of the corresponding temperature, a: Semelsberger et al.[12], b: DIPPR project 801[23], c: Park et al.[11], d: ASTM D975[24])

To resolve the viscosity-related mechanical problems of DME in CI engines, researchers have taken two approaches. The first kind is to devise a new fuel injection system that can accommodate the low viscosity and lubricity of DME. McCandless et.al. developed a fuel pump, injector and common-rail that can alleviate the wear and leakage with DME and integrated those components into the system called “Novel Fuel Injection System (NFIS)”.[19] The system has gone through further upgrades in its mechanical design and has achieved further improvement in its durability to date.[25,26] However, the durability still remains lower than the conventional petro-diesel fuel injection system. Furthermore, upgrading of the fuel injection systems to accommodate neat DME has an inherent limitation that it requires intensive modifications to the fuel injection systems installed in the pre-existing CI engines, which, in turn, significantly limits the number of

CI engines to which DME can be applied. This was why researchers have also tried to improve the viscosity of DME by adding other chemical species, which is the second approach to resolve the viscosity-related mechanical problems of DME. Sivebaek et.al. tested commercial lubricity enhancers, seed oils, seed oil derived esters, candle and lard as “viscosity” improving agents in DME.[21] Bhide et.al. blended seed oils, biodiesel and petroleum-based diesel in a wide range of pressure (0-2500psig) to improve the viscosity of DME.[22] However, the viscosity of DME did not improve to an acceptable range with small amounts of additives. The two most effective additives reported in the previous studies are rapeseed oil and castor oil, demanding about 75 wt. % addition in DME to reach the regular diesel viscosity (i.e., 4.48cSt at 25ºC or 2.0cSt at 40ºC). Since all of the additives used in the previous studies were composed of the molecular species (e.g., tryglycerides, polymethacrylates, etc.) generating significant level of soot particles at high dose, blending these additives in DME at high ratio could degrade one of the best merits of using DME.[27] Moreover, the additives were often more costly than DME itself, potentially increasing the cost of the blend at high doses of the additives.

Yet, if there is a molecular species of which production cost is reasonable and properties are not degrading the original merits of DME, high ratio blending (>30%) with DME will be still worthwhile to be studied. The following are the primary criteria for the ideal blendstock for DME. First, the blendstock should be non-toxic like DME. Second, it should be or expected to be soot-free to not degrade the soot-free combustion characteristic of DME. Third, the production of the blendstock should be available from renewable feedstocks at large scale to permit reasonable production cost and WTW GHG emissions. Lastly, it should have appropriate ignition quality in a mixture state with DME for CI engine application. A chemical species satisfying most of these criteria listed above is “glycerol”.

Table 4.2 presents some of the important properties of glycerol. High viscosity (i.e., 229cSt at 40ºC) is the first reason to consider glycerol as a DME viscosity improving agent. Its high oxygen mass content (>50%) and non-toxicity[28] could maintain the combustion soot-free even at high blending ratio. Its reasonable volumetric energy density (20.17MJ/L) will improve the low volumetric energy density of DME (18.92MJ/L), although the degree of the improvement in the energy density will not be enough to make it similar to that of petroleum-based diesel. Its low vapor pressure will improve the cavitation issues of DME in fuel injection systems. Since glycerol is a co-product of biodiesel, its supply is abundant resulting in low market price (i.e., crude glycerin: 0.48 $/gal. as of 2012)[29] with low carbon emissions (i.e., 31gCO_2e/MJ-glycerol from soy feedstock)[30]. Furthermore, glycerol can be produced potentially from a carbon-negative pathway. An algae species, "*Dunaliella",* when the salt concentration of the water outside the algae gets higher, overproduces glycerol to protect itself from the osmotic pressure. When producing glycerol, the algae uses atmospheric carbon dioxide and sunlight as resources, and the amount of glycerol produced from the algae reaches up to 50% on a dry mass basis.[31-33] Researchers are reporting continuous improvement in the yield of glycerol through this method. Combined with the "Carbon Recycling" production pathway of DME, direct synthesis of glycerol from the algae species will also maintain the carbon negative characteristic of DME.

Property	Unit	
Nomenclature	[-]	Glycerol, Propane-1,2,3-triol
CAS number	[-]	56-81-5
Molecular weight	[kg/kmol]	92.09
Carbon content	[wt. %]	39.1
Oxygen content	[wt. %]	52.2
Hydrogen content	[wt. %]	8.7
Normal boiling point	[°C]	287.85[a]
Normal melting point	[°C]	18.18[a]
Freezing point	[ºC]	-50[*]

Liquid density @25°C	[kg/m^3]	1258.0[a]
Kinematic viscosity @25°C	[cSt]	688.64[b]
Kinematic viscosity @40°C	[cSt]	228.94[b]
Vapor pressure @25°C	[Pa]	0.0223[a]
Vapor pressure @40°C	[Pa]	0.1249[a]
Heat of vaporization @25°C	[MJ/kg]	0.959[a]
LHV @25°C	[MJ/kg]	16.04[a]
Energy density @25°C	[MJ/L]	20.17[a]
Price	[$/gal]	Crude: 0.48 (in 2012)[c] USP grade: 3.59 (in 2012)[c]

Table 4.2. Properties of glycerol (*: Due to the unique metastable behavior of glycerol around its freezing point, its freezing point is not necessarily the same as its melting point, a: DIPPR project 801[23], b: Segur et al.[34], c: Chen et al.[31])

However, despite all the benefits of blending glycerol with DME, DME and glycerol are immiscible. Phase separation occurs with about 1-2 wt. % addition of glycerol in DME. This is because of the huge difference in polarity between the two species. To make DME and glycerol blend without phase separation at higher blending ratio, a third chemical species (i.e., co-solvent) with intermediate polarity between the two species must be included in the mixture. If the phase separation problem of DME and glycerol could be resolved by a proper co-solvent, DME blends with improved viscosity can be applied to pre-existing CI engines without intensive modification while maintaining most of the merits of the neat DME, eventually reducing GHG emissions from CI engines on a large scale.

In this chapter, the selection criteria for the co-solvent of DME-glycerol blend is established. Then, the selection criteria is applied to different molecular species, and a couple of final co-solvents are selected: Propylene glycol and Di-propylene glycol. Then, the viscosity of two final DME-glycerol blends (i.e., Michigan DME I and Michigan DME II) are measured at different blending ratios of glycerol and co-solvent. Finally, life-cycle GHG emissions assessment is conducted for one of the two final DME blends (i.e., Michigan DME II) to show the potentials of GHG reduction by applying the DME blend in CI engines. Engine operation with the Michigan DME blend is also conducted with a Yanmar Genset 3700W, and the findings from the operation is briefly addressed here.

4.2. Experimental

4.2.1. Selection Criteria for Co-solvent

Establishment of the selection criteria for the co-solvent of the DME-glycerol blend was based on the two primary objectives: 1. Improvement of the viscosity of DME without phase separation, 2. No or Minimal degradation in the main merits of neat DME as an alternative fuel for CI engines.

To fulfill the first objective, kinematic viscosity of the co-solvent candidates was investigated first. Second, to evaluate the effectiveness of the phase-separation prevention of co-solvents, a parameter called the "averaged solubility distance" is defined based on the Hansen Solubility Parameter theory, and the averaged solubility distance was calculated for different co-solvent candidates. Details of the definition of the averaged solubility distance is covered in section 4.2.3.

To fulfill the second objective, first of all, oxygen mass content of the co-solvent candidates are investigated to ensure the soot-free combustion characteristics. Westbrook et al.[35] reports that the oxygen mass content of fuel is one of the most significant parameters affecting soot production and the fuel burns soot-free when the fuel oxygen mass content is over 30 wt. %. This has been confirmed by many other previous studies.[36,37] Second, production availability from renewable feedstocks is investigated to ensure the low carbon fuel characteristics of neat DME. A techno-economic assessment (TEA) report from National Renewable Energy

Laboratory (NREL)[38] is used as a main reference to see which chemical species can be cost-effectively and stably produced from renewable feedstocks at large scale. Different factors including technology readiness level (TRL), annual production capacity and consumption, and price range are reviewed from the report. Life cycle GHG emissions of some selected co-solvent candidates are also investigated. Different LCA reports from Argonne National Laboratory (ANL)[39,40] and Greenhouse gases, Regulated Emissions and Energy use in Transportation (GREET) software are used as primary references. Third, health impact and environmental impact of the selected candidate species are investigated to ensure the non-toxic, non-carcinogenic merits of DME. Globally Harmonized System of Classification and Labelling of Chemicals (GHS) categories[41] of the selected co-solvent candidates are used as the main evaluation criteria for this item.

Flash point was not included in the final selection criteria since it was obvious that such a molecular species increasing the viscosity of DME up to diesel oil level would have much stronger intermolecular interaction than DME, which, in turn, would make its flash point much higher than DME (-80ºC). Cetane number (CN) was also not included in the final selection criteria because of the limitation in previously published values of the CNs of the species of interest.

4.2.2 0th level Co-solvent Candidate Species

Based on the background knowledge relevant to the solubility and polarity of DME and glycerol, initial co-solvent candidate groups are determined. These chemical groups and species are defined as “0th level co-solvent candidate groups/species”. The chemical groups and species included are listed in Table 4.3. Different chemical groups containing hydroxyl functional groups are included in the 0th level candidate groups based on the fact that methanol dissolves in both DME and glycerol.[42,43] Those chemical groups include alcohols with a single hydroxyl functionality (i.e., Mono-ols), alcohols with two hydroxyl functionality (i.e., Di-ols), glycols resulting from the etherification of more than two di-ols (i.e., poly-glycols), glycols resulting from the etherification of glycols and a single mono-ol (i.e., glycol mono-ethers), or two mono-ols (i.e., glycol di-ethers). Other chemical groups such as lactates and glycerol acetates are also included in the 0th level candidate groups because they exhibit high viscosity and they can be produced from renewable feedstocks. The total number of species determined as 0th level candidate species was 53.

Chemical Group	Molecular species	Acronym	CAS number
Mono-ols (9)	Methanol	MEOH	67-56-1
	Ethanol	ETOH	64-17-5
	1-Propanol	PROH1	71-23-8
	2-Propanol	PROH2	67-63-0
	n-butanol	BUOH	71-36-3
	n-pentanol	PTOH	71-41-0
	2-ethyl butanol	EBOH	97-95-0
	2-ethyl hexanol	EHOH	104-76-7
	Cyclohexanol	CHOH	108-93-0
Di-ols (5)	Ethylene glycol	EG	107-21-1
	Propylene glycol	PG	57-55-6
	1,2-butanediol	BG12	584-03-2
	1,3-butanediol	BG13	107-88-0
	1,4-butanediol	BG14	110-63-4
Poly-glycols (2)	Diethylene glycol	DEG	111-46-6
	Dipropylene glycol	DPG	25265-71-8
Glycol monoethers (22)	Propylene glycol monomethyl ether	PGME	107-98-2
	Propylene glycol monoethyl ether	PGMEE	609847-69-0
	Propylene glycol n-propyl ether	PGMNPE	1569-01-3
	Propylene glycol iso-propyl ether	PGMIPE	110-48-5
	Propylene glycol n-butyl ether	PGMNBE	29387-86-8
	Propylene glycol iso-butyl ether	PGMIBE	23436-19-3
	Propylene glycol tert-butyl ether	PGMTBE	80763-10-6
	Dipropylene glycol monomethyl ether	DPGME	13588-28-8
	Dipropylene glycol mono n-propyl ether	DPGMNPE	29911-27-1

	Dipropylene glycol mono n-butyl ether	DPGMNBE	29911-28-2
	Tripropylene glycol monomethyl ether	TPGME	10213-77-1
	Ethylene glycol monomethyl ether	EGME	109-86-4
	Ethylene glycol monoethyl ether	EGMEE	110-80-5
	Ethylene glycol mono n-propyl ether	EGMNPE	2807-30-9
	Ethylene glycol n-butyl ether	EGMNBE	111-76-2
	Ethylene glycol n-hexyl ether	EGMNHE	112-25-4
	Diethylene glycol monomethyl ether	DEGME	111-77-3
	Diethylene glycol monoethyl ether	DEGMEE	111-90-0
	Diethylene glycol mono n-propyl ether	DEGMNPE	6881-94-3
	Diethylene glycol mono n-butyl ether	DEGMNBE	112-34-5
	Diethylene glycol mono n-hexyl ether	DEGMNHE	112-59-4
	Triethylene glycol monomethyl ether	TEGME	112-35-6
Glycol diethers (9)	Dipropylene glycol dimethyl ether	DPGDME	89399-28-0
	Ethylene glycol dimethyl ether	EGDME	110-71-4
	Ethylene glycol diethyl ether	EGDEE	629-14-1
	Ethylene glycol di-n-butyl ether	EGDNBE	112-48-1
	Ethylene glycol di-tert-butyl ether	EGDTBE	26547-47-7
	Ethylene glycol methyl n-butyl ether	EGDMBE	13343-98-1
	Ethylene glycol ethyl n-butyl ether	EGDEBE	4413-13-2
	Diethylene glycol diethyl ether	DEGDEE	112-36-7
	Diethylene glycol di-n-butyl ether	DEGDBE	112-73-2
Lactates (1)	Ethyl lactate	EL	97-64-3
Glycerol acetates (2)	Glycerol monoacetate	GMA	106-61-6
	Glycerol diacetate	GDA	102-62-5
Carboxylic Acids (3)	Acetic acid	AA	64-19-7
	Propionic acid	PA	79-09-4
	Butyric acid	BA	107-92-6

Table 4.3. List of 0th level co-solvent candidate groups and species. Numbers in the parenthesis of each chemical group shows the number of chemical species in the chemical group.

4.2.3 Definition of Averaged Solubility Distance

To maintain the original merits of both DME and glycerol as cost-effective, low carbon, soot-free combustion fuels, adding less co-solvent into the DME-glycerol blend is preferred. In other words, being an effective co-solvent means preventing phase separation at low dose. In the context of HSP, this means that the HSP of the mixture of co-solvent and DME becomes similar enough to the HSP of the glycerol to be miscible at low dose of the co-solvent, and likewise for the opposite case (i.e., the HSP of the mixture of co-solvent and glycerol becomes similar enough to the HSP of DME to be miscible at low dose of the co-solvent). Figure 4.1a describes the case in which the co-solvent and DME are first mixed and then that binary mixture is mixed with glycerol as a second step. HSP of the binary mixture of DME and co-solvent (i.e., $\delta_{i,m}$) can be estimated by linear interpolation of the HSP of neat DME (i.e., $\delta_{i,d}$) and co-solvent (i.e., $\delta_{i,c}$) depending on the mixture composition.[44] Then, the solubility distance between the DME/co-solvent binary mixture and glycerol ($R_{a,1}$) can be calculated. According to the HSP theory, the relative energy difference (RED), or the ratio of the solubility distance to the interaction radius of glycerol ($R_{o,g}$), is used as a measure to predict the solubility of the DME/co-solvent binary mixture in glycerol.[44]

Figure 4.1b describes the opposite case in which the co-solvent and glycerol is first mixed, and then, that binary mixture is mixed subsequently with DME. The HSP value of the binary mixture, solubility distance between the binary mixture and DME, and the RED of the corresponding case are shown in the figure.

Since the blending ratio between DME and glycerol of interest in this work is near or over 50/50, both of the cases presented in Figures 4.1a and 4.1b should be accounted for when evaluating the effectiveness of a co-solvent for preventing phase-separation. Thus, the relative importance of one case over the other is evaluated as follows.

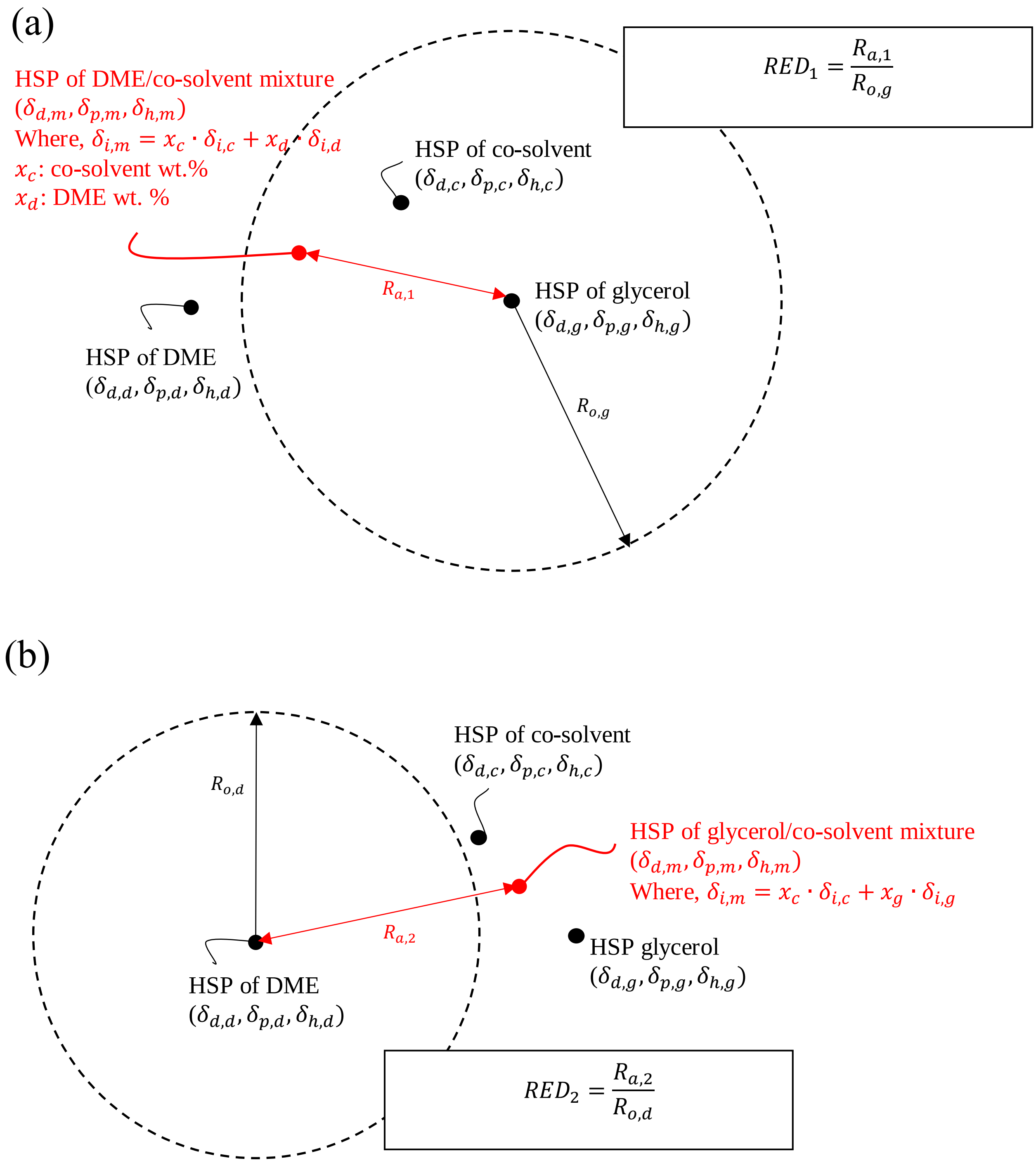

Figure 4.1. Two different cases of mixing among DME, co-solvent, and glycerol. **(a)** DME and co-solvent first mixed, then the DME/co-solvent binary mixture subsequently mixed with glycerol. **(b)** Glycerol and co-solvent first mixed, then the glycerol/co-solvent binary mixture subsequently mixed with DME.

between co-solvent and glycerol because we have more room of solubility allowed for the case (a) (i.e., RED1 value is lower than RED2 when R_a values for the two cases are the same).

Thus, to see if there is appreciable difference in the interaction radius of glycerol and DME which will make either case (a) or (b) more important than the other, interaction radii of glycerol and DME are investigated through experiment. Different molecular species with known HSP are mixed with DME and glycerol by varying mixing ratio. The result is presented in Table 4.4.

Glycerol				
Species mixed with glycerol	PGME	DPGME	EHOH	TPGME
Ra [MPa$^{1/2}$]	18.97	19.57	19.82	20.46
Solubility by mass ratio [%]	100	30	0	0
DME				
Species mixed with DME	MEOH	PG	1,2,3-benzenetriol	EG
Ra [MPa$^{1/2}$]	17.69	18.17	19.45	21.17
Solubility by mass ratio [%]	100	100	40	0

Table 4.4. Solubility distance (*Ra*) between different molecular species and glycerol (Top) or DME (bottom), and the experimental solubility result of the species by mass ratio [%] $(i.e. \frac{mass\ of\ species\ mixed}{mass\ of\ glycerol\ or\ DME} \cdot 100)$.

For glycerol, it is perfectly miscible with a species (PGME) having 18.97 MPa$^{1/2}$ of solubility distance, and is immiscible with a species (EHOH) having 19.82 MPa$^{1/2}$ of solubility distance. It is 30% miscible with a species (DPGME) with 19.57 MPa$^{1/2}$ solubility distance. Thus, the interaction radius of glycerol is between 18.97 and 19.82. Similarly, DME is perfectly miscible with PG while immiscible with EG, and it is 40% soluble in 1,2,3-benzenetriol. Thus, we can say that R_o of DME is between 18.17 and 21.17. Thus, the range of interaction radius of DME covers the range of interaction radius of glycerol. Also, since both DME and glycerol are about 30-40% miscible in the species with solubility distance of about 19.5 MPa$^{1/2}$, it is reasonable to assume that the interaction radius of DME and glycerol must not have a significant difference.

Thus, when we evaluate the effectiveness of the co-solvent, it is reasonable to weigh the case (a) and (b) in Figure 4.1 equally. This simply means that the effectiveness of the co-solvent can be measured by the solubility distance between the co-solvent and the middle HSP point of DME and glycerol. In other words, such a co-solvent in the middle of the HSP of DME and glycerol will bring the HSP of the different components closer to each other most effectively. Thus, the solubility distance between the middle point of DME, glycerol and co-solvent is defined as lambda (λ) in Figure 4.2.

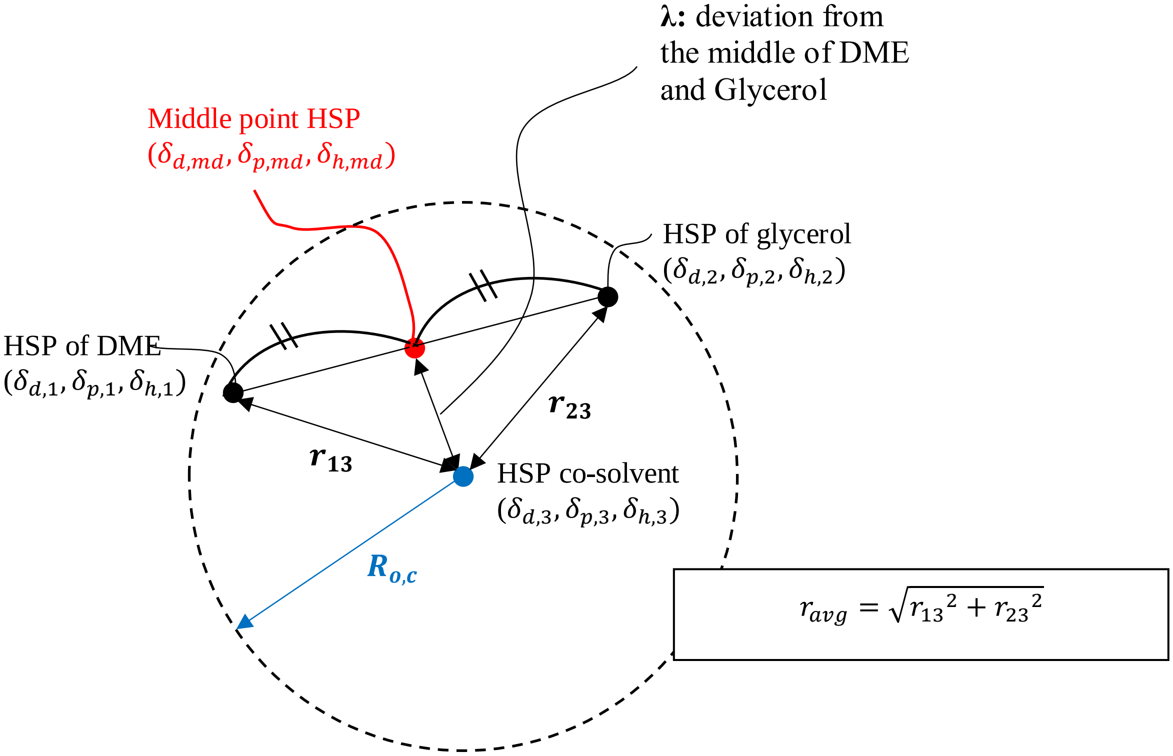

Figure 4.2. Description of averaged solubility distance (r_{avg}) and parameter lambda (λ)

Furthermore, since the root mean squared average (i.e., $\sqrt{{r_{13}}^2 + {r_{23}}^2}$) of the solubility distance between co-solvent and two blendstocks (i.e., DME and glycerol) decreases as lambda decreases, this root mean squared average value can be also used as a measure to evaluate the effectiveness of the co-solvent instead of lambda. In this work, the root mean squared average of the solubility distance between co-solvent and two blendstocks is defined as the "averaged solubility distance" ($\boldsymbol{r_{avg}}$), and is calculated for each co-solvent candidate.

It is more rigorous to set the criteria parameter as the RED of the co-solvent (i.e., $\frac{r_{avg}}{R_{o,c}}$) rather than the averaged solubility distance, since each co-solvent candidate species would have different interaction radius. However, there were the following limitations that led to opt for r_{avg} instead of RED. First, the interaction radius values of the many molecular species of interest were not available from the literature. Thus, the limitation in time and resources to determine a number of different species' interaction radius through experimental measurement was critical. Also, since the interaction radius is known to increase as the molar volume of the species decreases[45], which usually accompanies the decrease in viscosity, being lenient on the species with greater interaction radius did not seem to match the original purpose of the current work.

The result of the co-solvent selection will be presented first in section 4.3 (Results and Discussion). The following sections (i.e., sections 4.2.4 – 4.2.5) will present the experimental methods used to measure the optimal ratio of the finally selected co-solvents (i.e., PG and DPG) and glycerol and the viscosity of the final blends (i.e., Michigan DME Blend I (DME, DPG, and glycerol) and Michigan DME Blend II (DME, PG, and glycerol)).

4.2.4 Minimum Co-solvent to Glycerol Ratio

For the selected two co-solvents (i.e., PG and DPG), the minimum mass ratio of the co-solvent to glycerol required to prevent phase-separation of the ternary solution (i.e., DME/glycerol/co-solvent mixture) is measured at different wt. % of DME. The minimum mass ratio is defined as the “minimum co-solvent to glycerol ratio” (MCR). Lower MCR at certain wt. % of DME means the increase in glycerol concentration relative to co-solvent while ensuring no phase separation, which, in turn, improves many different properties of the blend including viscosity. Experimental measurement for MCR is conducted as follows.

First, the binary mixture of glycerol and co-solvent with different mixing ratio is produced by mixing 30g of glycerol with the corresponding mass of co-solvent. A Sartorius weighing scale with 1mg accuracy and 1200g capacity is used for taring the weight of a glass beaker and for measuring the net weight of glycerol and co-solvent each. Then, the known mass of glycerol and co-solvent are mixed in the beaker by using a glass rod. Since glycerol is very hygroscopic, the beaker with prepared binary solution is covered with plastic wrap or aluminum foil to prevent water absorption into the solution. Then, the binary solution of glycerol and co-solvent is injected into the 150mL sample cylinder (Swagelok, 304L-HDF4-150) by using a hypodermic syringe. The mass of the sample cylinder with binary solution is measured by using the weighing scale.

Now, the main mixing chamber is prepared by purging the chamber with 10psig helium. Figure 4.3 shows the main mixing chamber and the configuration of other experimental components during the MCR measurement. The main mixing chamber (Jerguson gage, 14-RL-10 stainless steel) is a pressure-resistant (up to 1000psig) vessel with 3cm thick transparent quartz windows allowing visual inspection inside the vessel. For more detailed information about the pressure-resistant vessel, refer to a previous publication.[46]

Then, the binary mixture of glycerol and co-solvent in the 150mL sample cylinder is injected into the mixing chamber by applying the helium back pressure of about 20 psig. After fully emptying the sample cylinder, the valves are closed and the sample cylinder is decoupled from the main chamber. The decoupled sample cylinder is weighed again to confirm the exact mass of the injected co-solvent/glycerol binary solution. After that, the valve at the top of the main mixing chamber is slowly opened to release the internal pressure down to 3psig. This pressure relief process allowed the easier injection of liquid DME into the mixing chamber with reasonable helium pressure (~80psig).

Then, depending on the target wt. % of the DME in the ternary solution, the corresponding mass of liquefied DME is injected into a different 150mL sample cylinder from its original packaging (i.e., 20 pound DOT compatible cylinder, DOT-4BA240). Then, the DME is injected from the sample cylinder into the main mixing chamber. Since the vapor pressure of DME at 20ºC is around 75psig, helium back pressure of about 80-85psig is applied to prevent flash vaporization of DME. Lastly, the chamber is agitated manually to mix the blendstocks well. The quartz window allowed visual inspection inside the vessel to check for the occurrence of phase separation. If the homogeneous solution is maintained over 1 day, the solution is deemed to be phase-separation free.

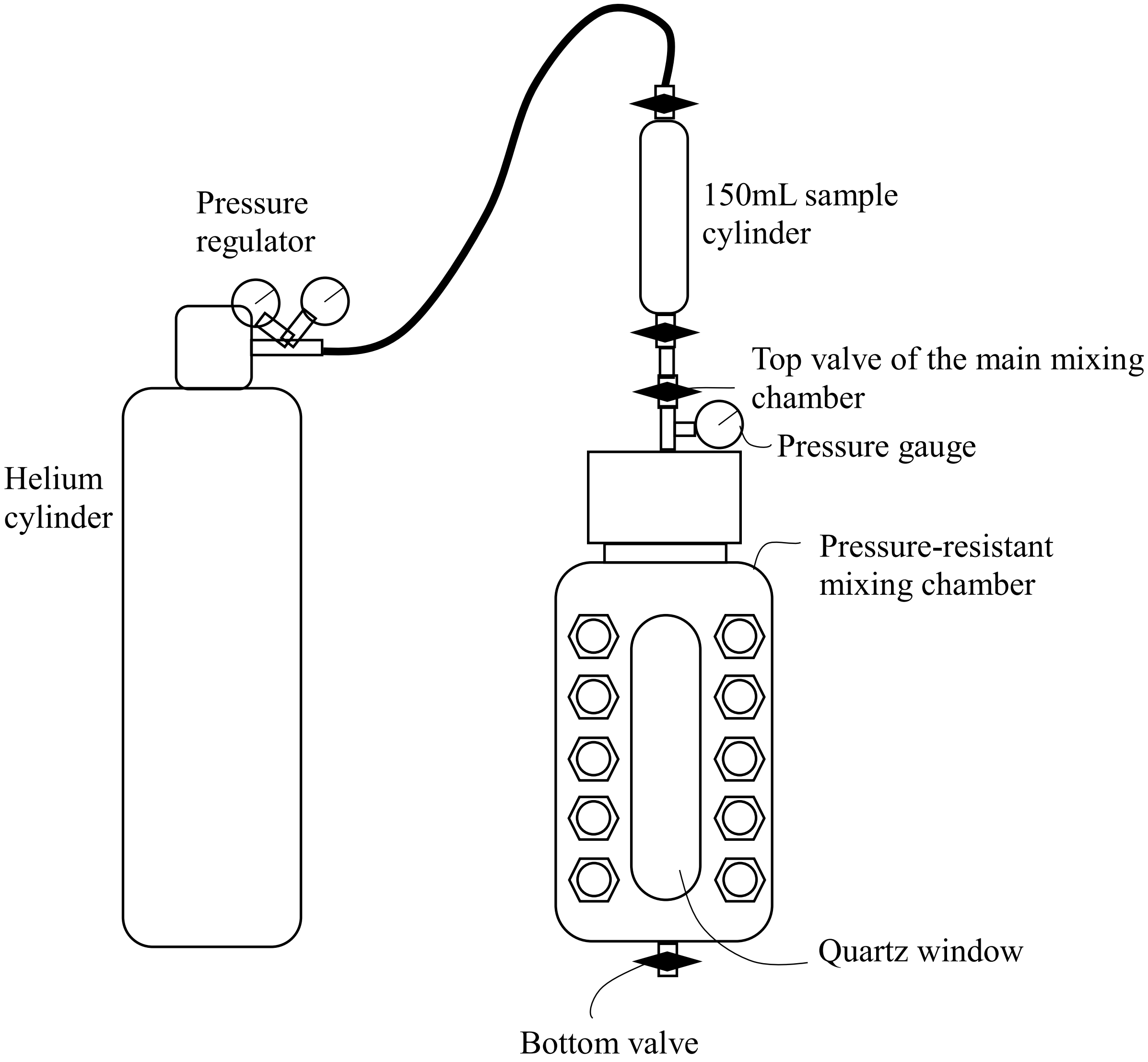

Figure 4.3. Experimental setup for minimum co-solvent to glycerol ratio (MCR) measurement

4.2.5 Kinematic Viscosity Measurement of Michigan DME Blends

Kinematic viscosity measurement of Michigan DME blends is conducted at the minimum co-solvent to glycerol ratio (MCR) of each different DME wt. %. Volatile Fuel Viscometer (VFVM) reported in Sivebaek et al.[21] is used. The details of the VFVM and the measurement procedure could be referred from Sivebaek et al.[21] The basic principles of the measurement and some additional information not available from Sivebaek et al.[21] will be briefly addressed here.

Figure 4.4 is presented to explain the experimental setup used for the viscosity measurement. After ensuring that there is no phase separation in the blends from MCR experiment, the blend contained in the main mixing chamber is transferred into the VFVM by opening the valve at the bottom of the mixing chamber and the valve at the top of the VFVM. Then, the VFVM and mixing chamber is disconnected. Next, VFVM is put inside a water bath. The water bath temperature is controlled constant at 40ºC (±0.3ºC) by using a heating rod connected to a temperature controller. A water circulator is also used inside the water bath to ensure the uniform temperature inside the bath. After waiting about half an hour to ensure the uniformity of the temperature inside the water bath, the kinematic viscosity measurement is started. The temperature 40ºC is chosen to make a fair comparison between the measured blend viscosity and the ASTM D975 diesel viscosity standard.[24]

For kinematic viscosity measurement, the time elapsed for the liquid to pass through the timing bulb (i.e., between the top and bottom red markers) is measured following the procedure established in Sivebaek et al.[21] The procedure is based on the standard measurement method ASTM D446 in which the kinematic viscosity of a liquid is calculated from the multiplication of the measured time interval by the pre-defined viscometer constant provided from the viscometer manufacturer.[47] Difference between the Sivebaek's method and the ASTM D446 is that Sivebaek's test rig and method (i.e., VFVM) enabled the measurement of viscosity of "volatile" liquid while preventing the flash vaporization by covering the Cannon-Manning viscometer with a glass tube and metal covers as shown in Figures 4.4 and 4.5[21].

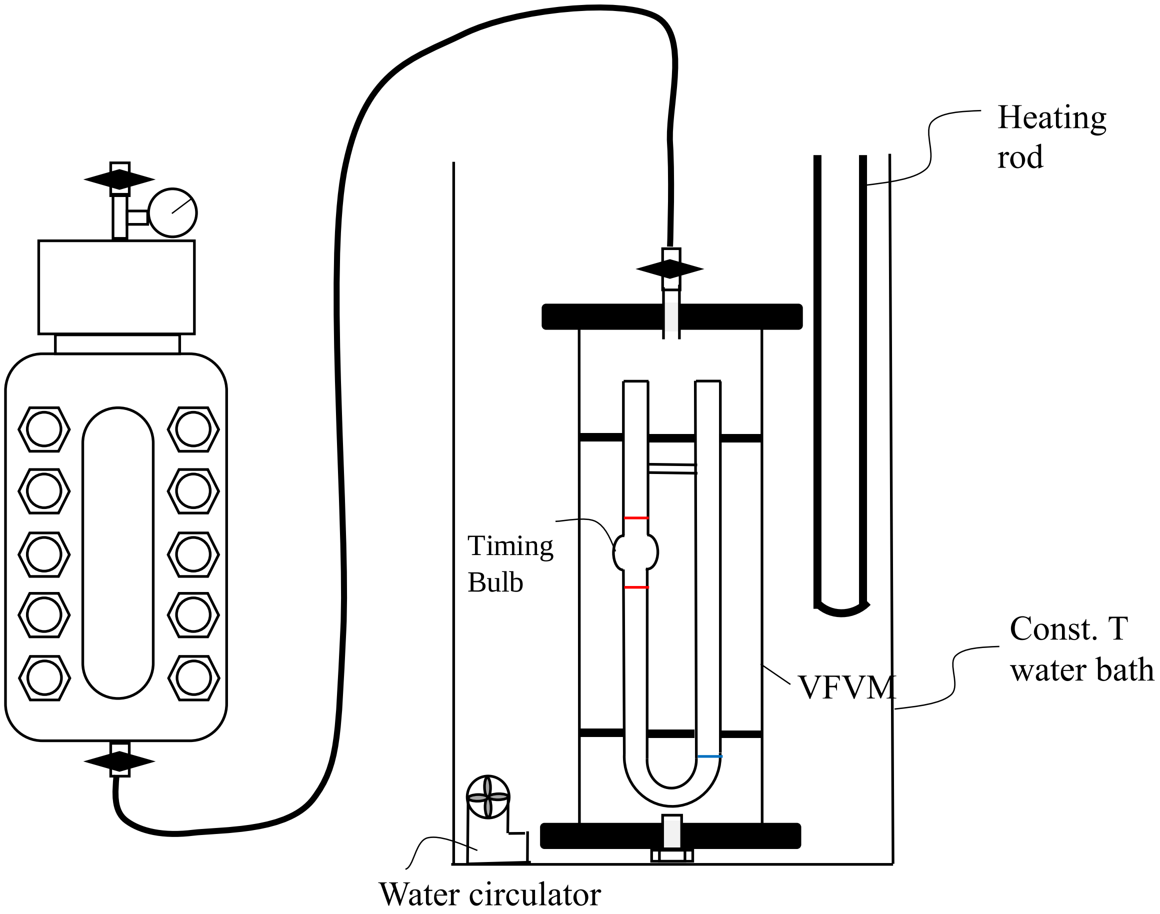

Figure 4.4. Experimental setup for kinematic viscosity measurement

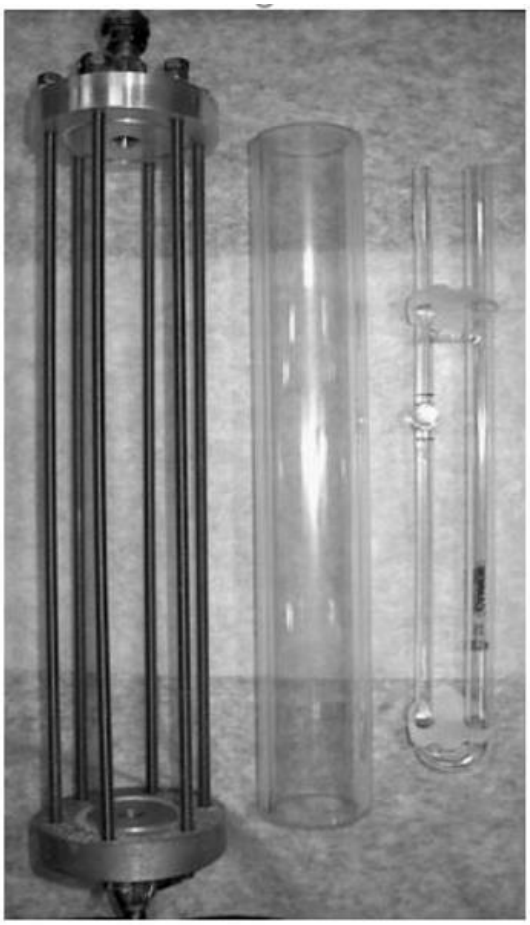

Figure 4.5. VFVM components (from Sivebaek et al., 2001)[21]

The minimum co-solvent to glycerol ratio (MCR) and viscosity measurement results are presented in the Results and Discussion section (i.e., section 4.3). The following sections (i.e., sections 4.2.6 – 4.2.8) will provide the approach and assumptions used for the life-cycle GHG emissions assessment of the selected final blend (i.e., Michigan DME Blend II).

4.2.6 System Boundary of the Life-Cycle GHG Emissions Assessment of Michigan DME II (DME/PG/Glycerol Blend)

The WTW GHG emissions from the production and use of 1kg of Michigan DME II (MDME II, DME/PG/glycerol blend) are calculated as follows. For life-cycle GHG emissions assessment, it is assumed that DME wt. % in the blend varies between 40% and 50% with the ratio of co-solvent to glycerol being MCR at each DME wt. %. This assumption is based on the fact that the viscosity of MDME II reached at the level of either No. 1 or No.2 diesel oil when its DME wt. % was between 40% and 50%. Section 4.2.7 deals with more details about the composition and properties of MDME II that went through the life-cycle GHG emissions assessment.

Figure 4.6 shows the system boundary of the life-cycle GHG emissions assessment conducted on the MDME II. The overall system boundary is composed of 7 different processes. Some of the processes such as the glycerol purification (i.e., process 2) and DME production (i.e., process 4) have different cases with different process inputs (i.e., feedstocks, material inputs and energy inputs), which, in turn, results in different GHG emissions for each case. For example, “Cases 1 and 2” of the DME production process use natural gas as the feedstock for DME production whereas “Case 3” of the DME production process uses landfill gas as the feedstock. As a result, the GHG emissions from the DME production process alone becomes significantly higher for Cases 1 and 2 than for Case 3.

Since three cases for the glycerol purification process and four cases for the DME production process have been addressed in the current work, 12 different combinations of the processes were addressed in this study. Each combination of the processes is defined as a “pathway”. Different cases for the glycerol purification process are labelled as A, B, and C while different cases for the DME production process is labelled as 1,2,3 and 4, which eventually formed a code from A1 to C4 as shown in the right-bottom corner of Figure 4.6. Also, in case a process is composed of multiple steps, each step constituting a process is defined as a “sub-procedure”. For example, the Case A of the glycerol purification process is composed of multiple sub-procedures, and the details are available in the section 4.2.8.

To state the overall MDME II production and its use briefly, a pathway starts with the crude glycerol production. This process takes exactly the same feedstock, materials, and energy input parameters used for soy biodiesel (BD) production as its input parameters. The GHG emissions burden allocated to BD based on the energy-allocation method (i.e., gCO_2e/MJ) is the same as the crude glycerol production. Then, the crude glycerol product (CGP) undergoes a purification process into the technical grade glycerol (TGP), or the purified glycerol over 98 wt. % purity. For the glycerol purification process, a number of different cases with different GHG emissions were available from the previous studies and patents. Thus, to interpret those different purification processes into a few representative cases, three different cases of the glycerol purification are defined as the Cases A, B, and C. These cases use different methods (e.g., simple distillation vs. vacuum distillation) and different materials and feedstocks (e.g., different purity of CGP, different kinds of catalysts and filter materials), which results in different overall process efficiency and GHG emissions.

After TGP is produced, the product is divided into two different streams. One is the TGP stream as an input to produce PG through hydrogenolysis (i.e., PG production), and the other is the TGP input directly into the MDME II blending (i.e., Michigan DME blending).

The left-bottom corner in Figure 4.6 shows the DME production process, and this process has multiple cases. Cases 1 and 2 use natural gas as the feedstock to produce DME whereas the

Case 3 uses landfill gas and Case 4 uses animal manure. All of these 4 Cases are referenced from Lee et al.[7] Then, three components of the MDME II blends (i.e., DME, TGP, and PG) are mixed together in the Michigan DME Blending process.

After MDME II is mixed, it is transported to fuel stations. The sum of GHG emissions from the 1st process (crude glycerol production) through the 6th process (MDME transportation) is defined as the Well-to-Pump (WTP) GHG emissions. Then, the last process is the pump-to-wheel (PTW) combustion of the MDME II blend in a vehicle (7th process). A complete combustion of every carbon atom contained in the fuel is assumed (i.e., no potent GHG emissions such as CH_4 and N_2O are formed as the combustion product) in this work, which did not require any engine tests to calculate "gCO_{2e}/MJ" for PTW combustion process. Investigation of how much mass (or energy) of MDME II is required to travel a unit distance (i.e., kg-fuel/mile, MJ-fuel/mile) can be conducted in future work.

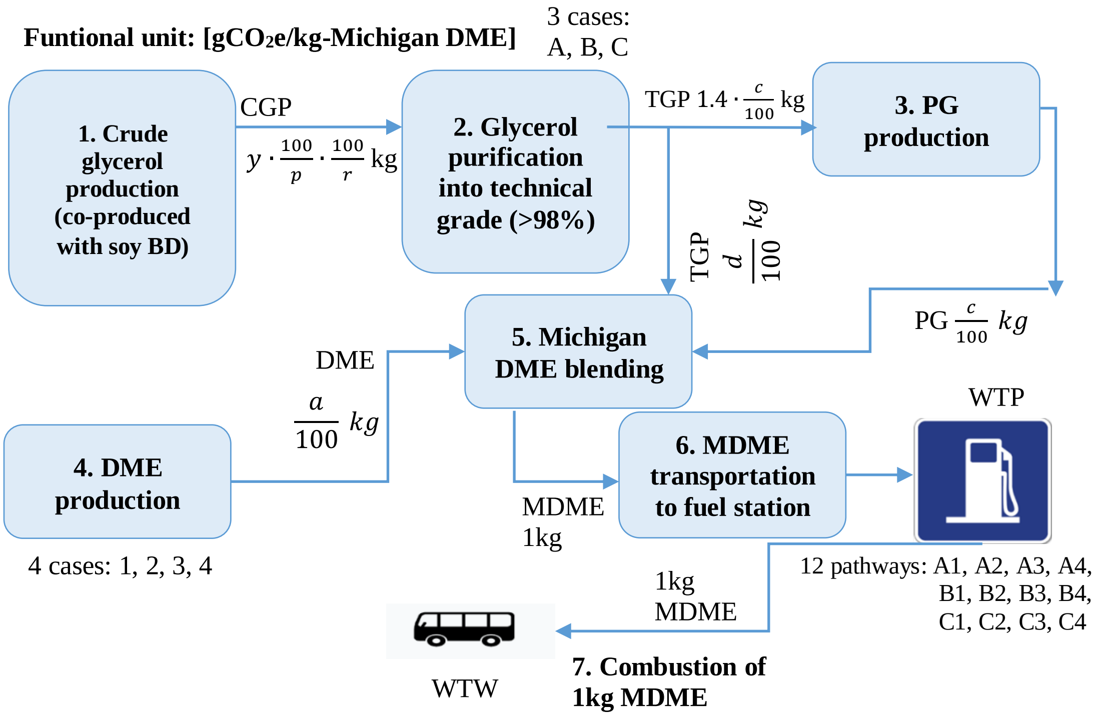

Figure 4.6. System boundary of the life-cycle GHG emissions assessment of the Michigan DME Blend II (DME/PG/Glycerol blend). For the definitions of the notations used (e.g., y, p, r), see Table 4.5.

4.2.7 Composition and Properties of Michigan DME Blend II for Life-Cycle GHG Assessment

Since the Michigan DME Blend II includes a variety of solutions with different mass fractions of its components (i.e., DME/glycerol/PG), the range of solutions of interest for the life-cycle GHG assessment is defined in this section. As stated in section 4.2.6, since MDME II exhibits the diesel level viscosity at DME mass fractions between 40% and 50%, GHG life-cycle assessment is conducted for MDME II solutions with 40-50 wt. % DME. Table 4.5 shows how the minimum co-solvent to glycerol mass ratio (MCR) (i.e., b), mass fraction of PG (i.e., c) and glycerol (i.e., d) are determined depending on the wt. % of DME (i.e., a).

The MCR linearly increases from 1.65 (at 40% DME) to 1.90 (at 50% DME). Thus, a linear regression is used to estimate the MCR at arbitrary DME wt. % between 40% and 50%. This is a reasonable assumption based on the linear trend of MCR by wt. % DME between 40% and 80% shown in the Results and Discussion section (i.e., section 4.3).

The mass fraction of PG and glycerol are calculated based on the wt. % of DME and the corresponding MCR. Both PG and glycerol mass fractions decrease as the DME wt. % increases, but, PG mass fraction relative to glycerol mass fraction increases as the DME wt. % increases due to the increase in MCR.

The density of the MDME II (ρ_{MDME}) at certain wt. % of DME is calculated using the linear combination of the pure density and the mass fractions of the three components. For the density of the pure components ($\rho_G, \rho_{PG}, \rho_{DME}$), the density value of glycerol at 8bar, 298K (1259kg/m^3) is referenced from Prieto et al.[48], density of PG at 8bar 298K (1033kg/m^3) is referenced from Sagdeev et al.[49], and the density of DME at 8bar, 298K (662kg/m^3) is referenced from Ihmels et al[50].

The lower heating value (LHV) of MDME II (LHV_{MDME}) is calculated using the linear interpolation of the LHVs of the pure components ($LHV_{DME}, LHV_{PG}, LHV_G$). The LHV of DME is referenced from Lee et al. (28.87MJ/kg)[7], the LHV of PG is referenced from DIPPR project 801 (22.16MJ/kg)[23], and the LHV of glycerol is presented in Table 4.2.

The mass of technical glycerol product (TGP) required for the production of PG amount required to produce 1kg of MDME II, or "x", is also presented in Table 4.5. Since 1.4 times the mass of TGP is required to produce a unit mass (1kg) of PG, the corresponding TGP mass is simply the multiplication of the mass fraction of PG in MDME II and 1.4.

Then, the total mass of TGP required downstream of the glycerol purification process, or "*y*", is presented in the table. It is simply the sum of the mass of TGP required to produce PG and the mass of TGP required to be directly mixed with DME.

Lastly, the total mass of CGP required to produce 1kg of MDME II is presented in the table, as well. It is calculated from the purity (*p* wt.%) of the CGP input into the glycerol purification process, and the recovery rate (*r* wt.%) of the glycerol purification process.

DME wt. %	MCR (b)	PG wt.% (c)	Glycerol wt. % (d)	Density [kg/m^3]
a	$b = 1.65 + 0.025(a - 40)$	$c = (100 - a) \cdot \frac{b}{b+1}$	$d = (100 - a) \cdot \frac{1}{b+1}$	$\rho_{MDME} = \rho_{DME} \cdot a + \rho_{PG} \cdot c + \rho_G \cdot d$
40	1.65	37.38	22.62	936
45	1.78	35.19	19.81	911
50	1.90	32.76	17.24	886
DME wt. %	LHV [MJ/kg]	Mass [kg] of TGP for PG production per 1kg of MDME (x)	Total mass [kg] of TGP from glycerol purification per 1kg of MDME (y)	Total mass [kg] of CGP required per 1kg of MDME
a	$LHV_{MDME} = LHV_{DME} \cdot a + LHV_{PG} \cdot c + LHV_G \cdot d$	$x = 1.4 \cdot \frac{c}{100}$	$\mathrm{y} = x + \frac{d}{100}$	$z = y \cdot \frac{100}{p} \cdot \frac{100}{r}$
40	23.65	0.523	0.749	[-]
45	24.13	0.493	0.691	[-]
50	24.61	0.459	0.631	[-]

Table 4.5. The composition and properties of MDME II depending on the wt. % of DME

4.2.8 Detailed Process Parameters and Assumptions for Life-Cycle GHG Assessment

The methods and key parametric assumptions used to calculate the GHG emissions for each process constituting the life-cycle of MDME II blend will be presented in this section.

4.2.8.1.Crude Glycerol Production Process

Figure 4.7 is the schematic of the crude glycerol production process assumed in the current work. GHG emissions from the crude glycerol production process is calculated as follows.

$$GHG\ emissions\ from\ CGP\ production\ per\ 1kg\ of\ MDME\left[\frac{gCO_{2e}}{kgMDME}\right]$$

$$= GHG\ emissions\ per\ unit\ mass\ of\ CGP\ \left[\frac{gCO_{2e}}{kgCGP}\right]$$

$$\cdot\ mass\ of\ CGP\ per\ 1kg\ of\ MDME\ \left[\frac{kgCGP}{kgMDME}\right]$$

First, the GHG emissions per unit mass of CGP is calculated from the GHG emissions from the production of soy biodiesel. This is based on the fact that most of the crude glycerol in the U. S. is produced as a co-product of soy biodiesel production process.[29] The life-cycle GHG emissions of soy biodiesel is referenced from previous studies.[30,51,52] Based on the most recent publication addressing the GHG emissions from soy biodiesel production (i.e., Chen et al.[30]), 30.1gCO_2e of GHG emissions are emitted per 1MJ production of biodiesel. This value is based on the co-product allocation method of the mass allocation for soymeal and the energy allocation for glycerol. The current work assumes the same co-product allocation methods between soymeal and soy-oil, and between biodiesel and glycerol. Thus, the crude glycerol production emits the same GHG emissions per unit energy (i.e., 30.1 gCO_2e/MJ-CGP) as biodiesel, which is then converted into GHG emissions per unit mass by multiplying the LHV of glycerol (LHV_G).

Secondly, the mass of CGP required to produce unit mass (1kg) of MDME II blend is shown in Table 4.5 (i.e., *z kg*). It is a function of DME wt. % in MDME II blend and the type of the glycerol purification process. DME wt. % determines the mass fractions of PG (c) and glycerol (d), which, in turn, determines the total mass of TGP required (y). Then, depending on the purity of the glycerol in CGP input (*p %*) and the recovery rate of the purification process (*r %*), the mass of CGP input (z) is determined from the mass of TGP required (y).

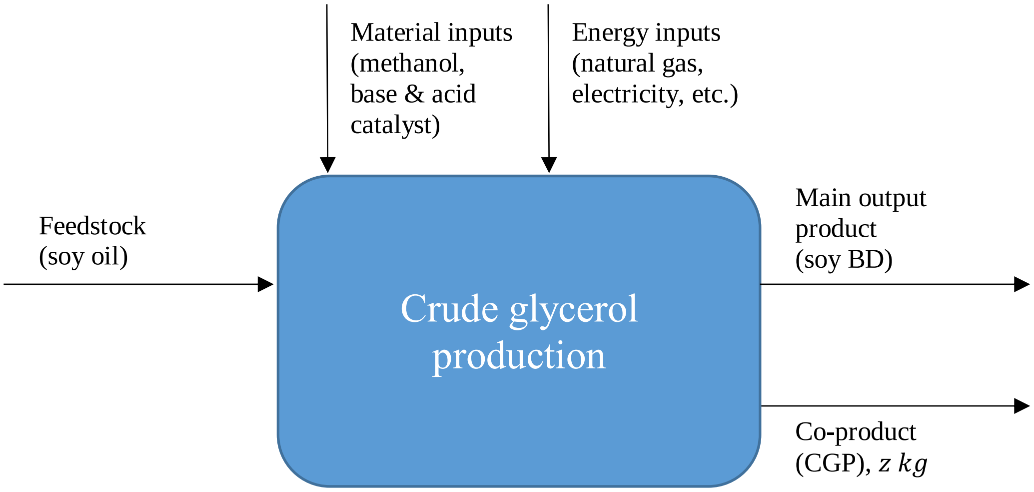

Figure 4.7. Schematic of the crude glycerol production process

4.2.8.2.Glycerol Purification Process

Figure 4.8 is the schematic of the glycerol purification process assumed in the current work. During the glycerol purification process, CGP is purified into the technical grade glycerol product (TGP) with purity over 98%. This process is necessary for both the PG production and MDME mixing process since both processes require at least 98% purity glycerol to ensure the quality of the output product. Greenhouse gas emissions from the glycerol purification process is analyzed based on three different “Cases” (i.e., Cases A, B, and C). The three cases are based on three different previous studies and patents with different parametric assumptions and overall efficiency. Case A is based on Nanda et al.[53], Case B is based on Rodriguez-Kabana et al.[54], and Case C is based on Aiken’s patent.[55]

The first difference among the three purification cases is the composition and temperature of the CGP input for the purification. Table 4.6 presents the input CGP properties assumed for the current work. In Case A, low purity CGP with glycerol concentration of about 13% is used as the input CGP as reported in Nanda et al.[53] Concentration of water, ash, methanol, and total

Material Organic Non-Glycerol (MONG) are also referenced from Nanda et al.[53] The study also reports the seven main molecular species constituting the MONG content: 1-propanol, hexanoic acid, octanoic acid, dodecanoic acid, methyl tetradecanoate, 7-hexadecanoic acid, octadecanoic acid. However, the study does not report the exact mass percentage of each molecular species in CGP. Thus, in the current work, it is assumed that each of the seven species take the same share out of the total MONG content. The input temperature of the CGP in Case A is assumed to be at ambient (298K). The recovery rate (*r*) of Case A is assumed to be 100%.

Case A					
Group	Species	Mass fraction [%]	Normal boiling point [K]	Input temperature [K]	Recovery rate (*r*) [%]
Glycerol	-	12-14	561	298	100
Water	-	10-12	373		
Ash	-	6	-		
Methanol	-	0	338		
MONG (Material Organic Non-Glycerol)	1-propanol	10	370		
	Hexanoic acid	10	479		
	Octanoic acid	10	513		
	Dodecanoic acid	10	572		
	Methyl tetradecanoate	10	570		
	7-hexadecanoic acid	10	623		
	Octadecanoic acid	10	647		
Case B					
Group	Species	Mass fraction [%]	Normal boiling point [K]	Input temperature [K]	Recovery rate [%]
Glycerol	-	60	561	298	100
Water	-	7	373		
Ash/Salts	-	7.5	-		
Methanol	-	15	338		
	Methyl oleate	4.4	617		

MONG (Material Organic Non-Glycerol) or FFA (Free Fatty acids)	Methyl palmitate	2.5	598		
	Palmitic acid	0.9	623		
	Oleic acid	0.8	633		
	Methyl stearate	0.8	624		
	Methyl taurate	0.4	540		
	Methyl myristate	0.3	570		
	Methyl palmitoleate	0.3	594		
Case C					
Group	Species	Mass fraction [%]	Normal boiling point [K]	Input temperature [K]	Recovery rate [%]
Glycerol	-	86.7	561	398	86.5
Water	-	1	373		
Ash/Salts	-	-	-		
Methanol	-	12	338		
MONG (Material Organic Non-Glycerol) or FFA (Free Fatty acids)	Methyl oleate	0.13	617		
	Methyl palmitate	0.07	598		
	Palmitic acid	0.03	623		
	Oleic acid	0.02	633		
	Methyl stearate	0.02	624		
	Methyl taurate	0.01	540		
	Methyl myristate	0.01	570		
	Methyl palmitoleate	0.01	594		

Table 4.6. Composition of CGP input used for three different Cases A, B and C of the glycerol purification process

For Case B, medium purity CGP is used. The purity of the CGP is determined based on the information reported in Rodriguez-Kabana et al.[54] The patent reports that, after soap splitting, about 10-15% of the initial CGP volume turned into the soap residue, then, 73 vol. % of the treated glycerol stream was molecular glycerol. Thus, it was reasonable to assume that Case B uses CGP with 60% glycerol concentration.

To determine the composition of the rest of the CGP, two other studies presenting the similar glycerol content (i.e., 60%) are referenced because of the lack of information from Rodriguez-Kabana et al.[54] First, for the concentration of water, salts, methanol, and MONG contents, the values from Quispe et al.[29] on methylated CGP are used: water (~7%), ash/salts (7.5%), methanol (15%), and MONG or Free Fatty Acids (FFA) (10.5%). Then, the molecular composition of MONG and FFA are assumed to be the same as reported in Manosak et al.[56] The final composition of the CGP input for Case B is presented in Table 4.6. The temperature of the CGP is assumed to be at ambient (298K), and the recovery rate of the purification process is assumed to be 100%.

For Case C, high purity CGP with the glycerol concentration of 86.7% is used as the input CGP. The composition of the CGP input for Case C is based on Aiken's patent.[55] The patent reports the CGP input with 86.7 wt. % glycerol, 12% methanol, 1% water, and rest of the fractions being fatty acid methyl esters (FAME) or FFAs. The molecular composition of the FAME or FFAs are again assumed to be the same as reported in Manosak et al.[56] due to the lack of information from Aiken's patent.[55] The temperature of the CGP input for Case C is 398K, which means that the CGP is not fed into the purification process after being fully cooled down from the biodiesel transesterification process. The remnant heat from the biodiesel transesterification process is partly kept in the CGP to save the thermal energy required for the purification process. The recovery rate of the purified glycerol is assumed to be 86.5%.

Table 4.7 presents the sub-procedures of the three different cases of the glycerol purification process. For Case A, the CGP is first preheated from the input temperature (298K) to 328K to decrease the viscosity and density of CGP to facilitate the fluid motion. As shown in Table 4.8, the thermal energy for preheating is provided from a natural gas (NG) boiler with overall efficiency of 80%.[39] WTW carbon intensity of NG is assumed to be 68.8gCO_2e/MJ.[57] This applies the same for all of the thermal energy inputs required for the three different cases of the glycerol purification process.

The preheated glycerol, then, goes through soap splitting and neutralization. Phosphoric acid and potassium hydroxide are added into the preheated glycerol. An electric agitator is assumed to be used to help the blending of CGP with the added acid/base. The mass of phosphoric acid and potassium hydroxide used for the production of unit mass of TGP in Case A is presented in Table 4.9. Presented together in Table 4.9 are the GHG emissions from the production of each of the material input as referenced from GREET software (Phosphoric acid: Johnson et al.[58], Potassium hydroxide: Lampert et al.[59], Methanol: Cai et al.[60], Activated Carbon: Wang et al.[61], Nitrogen gas: Dunn et al.[39]). For electric agitator, a commercial mixer (Amixon Conical Mixer Type AM) with volumetric capacity of 1m^3 is assumed to be used at 11kW for 50 minutes. The GHG emissions from the use of 1MJ electricity is referenced from Cai et al.[62] (Table 4.10) with the average mix of sources for electricity in the U. S. distribution.

Then, the neutralized glycerol went through simple distillation. During the distillation, the neutralized glycerol is heated from 55ºC to 110ºC while evaporating the molecular species with normal boiling point lower than 110ºC (i.e., 1-propanol and water). For the next step, solvent extraction is conducted on the glycerol stream with methanol solvent. The mass of methanol used per ton production of TGP, and the GHG emissions from unit mass production of methanol are presented in Table 4.9. Lastly, de-colorization and de-odorization are conducted on the glycerol stream by using activated carbon bed. The mass of activated carbon material used per ton production of TGP and the GHG emissions per unit mass production of activated carbon are presented in Table 4.9.

For Case B, the glycerol purification process starts with the addition of phosphoric acid for soap splitting and neutralization. The mass of phosphoric acid required for a ton production of TGP is presented in Table 4.9. The value is based on the required volume of phosphoric acid per unit volume of CGP presented in Rodriguez-Kabana et al.[54]: phosphoric acid (14mL) used to treat 500mL CGP. Then, the volume ratio is converted into the mass ratio presented in Table 4.9 based on the density of the two compounds. The phosphoric acid input in Case B is only 7% of the Case A.

The neutralized bioglycerine (NBG) goes through "volatilization" where 100% of water and methanol in NBG is evaporated. This sub-procedure can be distinguished into 3 items: 1) Agitation of the NBG to facilitate the evaporation of water and methanol, 2) Vacuuming of the NBG to lower the boiling point, 3) Heating NBG. The first two items require electricity input, while the third item requires thermal energy input from natural gas. Tables 4.8 and 4.10 present the GHG emissions from 1MJ use of electricity and natural gas. For electric agitator, the same model used in Case A is assumed to be used. For vacuum pump, an electric high-vacuum pump operating at 600W (8460K64, McMaster-Carr) is assumed to be used for 30 minutes to keep the pressure at -700 mmHg-gauge (60 Torr). The detailed assumptions regarding the use of the electricity and thermal energy are presented in Table 4.9.

The last sub-procedure for Case B is the "vacuum distillation". The sub-procedure contained three items: 1) Agitation of the glycerin to facilitate the distillation of impurities, 2) Vacuuming to lower the boiling point, 3) Heating. The type of the electric agitator, vacuum pump, and natural gas boiler used for this sub-procedure was the same as for the "volatilization" sub-procedure. However, the devices were used for the longer time (75 minutes) than for the volatilization sub-procedure (30minutes).

Case A			
Sub-procedure	Material input	Energy input type	Methanol recovery
1. Preheating of CGP	[-]	Thermal energy	None
2. Soap split and Neutralization	Phosphoric acid	Electricity	None
	Potassium hydroxide		
3. Distillation	[-]	Thermal energy	None
4. Solvent extraction	Methanol	[-]	None
5. De-colorization & De-odorization	Activated Carbon (AC)	[-]	None
Case B			
Sub-procedure	Material input	Energy input type	Methanol recovery
1. Soap split and Neutralization	Phosphoric acid	[-]	None
2. Volatilization	[-]	Thermal energy	Methanol recovered. Then, it displaces the input required for biodiesel production.
		Electricity	
3. Vacuum Distillation	[-]	Thermal energy	None
		Electricity	
Case C			
Sub-procedure	Material input	Energy input type	Methanol recovery
1. Soap split and Neutralization	Phosphoric acid	[-]	None
2. 1st - stage evaporation.	N_2 gas	Thermal energy	Methanol recovered. Then, it displaces the input required for biodiesel production.
3. 2nd - stage evaporation	N_2 gas	Thermal energy	Methanol recovered. Then, it displaces the input required for biodiesel production.
4. Vacuum distillation	[-]	Thermal energy	None
		electricity	
5. De-colorization & De-odorization	Activated Carbon	[-]	None

Table 4.7. Sub-procedures of the three different cases of the glycerol purification process

Thermal energy resource	Combustion device	Boiler efficiency	WTW Carbon intensity of NG [gCO_2e/MJ]
Natural gas	Boiler	80%	68.8

Table 4.8. Key parametric assumptions for thermal energy input[39,57]

Case A			
Material input	Mass [kg] per kg purification of CGP	Mass [kg] per ton production of TGP	GHG emissions per unit mass of material input [gCO_2e/kg]
Phosphoric acid	0.1604	1070	539.41
Potassium hydroxide	0.029	200	1744.78
Methanol	0.199	1330	463.31
Activated Carbon	0.010	70	9440
Energy type	Specific purpose	Other key assumptions	
Electricity	Soap splitting agitation	Use of a $1m^3$ capacity industrial mixer at 11kW (~13rpm) for 50 minutes	
Thermal Energy	Preheating	Boiler heating from 25ºC to 55ºC	
	Simple distillation	Boiler heating from 55ºC to 110ºC while evaporating 1-propanol and water contents	
Case B			
Material input	Mass [kg] per kg purification of CGP	Mass [kg] per ton production of TGP	GHG emissions per unit mass of material input [gCO_2e/kg]
Phosphoric acid	0.042	70.24	539.41
Energy type	Specific purpose	Other key assumptions	
Electricity	Agitator for volatilization	Use of a $1m^3$ capacity industrial mixer at 11kW (~13rpm) for 30 minutes	
	Vacuum pump for volatilization	Use of a $1m^3$ capacity vacuum pump at 600W for 30 minutes (vacuum P at 60 Torr)	
	Agitator for vacuum distillation	Use of a $1m^3$ capacity industrial mixer at 11kW (~13rpm) for 75 minutes	
	Vacuum pump for vacuum distillation	Use of a $1m^3$ capacity vacuum pump at 600W for 75 minutes (vacuum P at 60 Torr)	
Thermal Energy	Volatilization	Boiler heating from 25ºC to 90ºC while evaporating methanol and water contents	
	Vacuum distillation	Boiler heating from 90ºC to 250ºC while evaporating methyl laurate and glycerol contents	
Material recovered	Mass [kg] recovered per ton of TGP produced	Displacement rate [%]	Reduced GHG emissions per kg of displaced material [gCO_2e/kg]
Recovered methanol	250	100% displacement for methanol input for biodiesel transesterification	463.31

Case C			
Material input	Mass [kg] per kg purification of CGP	Mass [kg] per ton production of TGP	GHG emissions per unit mass of material input [gCO$_2$e/kg]
Phosphoric acid	0.042	56.19	539.41
N$_2$ gas	1st stage evaporation	30.67	192.41
	2nd stage evaporation	22.67	
Activated Carbon	[-]	13.99	9440
Energy type	Specific purpose	Other key assumptions	
Electricity	Vacuum pump for vacuum distillation	Use of a 1m^3 capacity vacuum pump at 600W for 90 minutes (vacuum P at 12.5 Torr)	
Thermal Energy	1st stage evaporation	Boiler heating from 125ºC to 160ºC while evaporating 92% of methanol and 53% of water contents.	
	2nd stage evaporation	Boiler heating to evaporate 8% of methanol contents.	
	Vacuum distillation	Boiler heating from 160ºC to 185ºC while evaporating remnant water, methyl laurate and glycerol contents	
Material recovered	Mass [kg] recovered per ton of TGP produced	Displacement rate [%]	Reduced GHG emissions per kg of displaced material [gCO$_2$e/kg]
Recovered methanol	160	100% displacement for methanol input for biodiesel transesterification	463.31

Table 4.9. Material and energy input for the three different cases of the glycerol purification process.

Carbon intensity of electricity [gCO$_2$e/MJ]	Electricity mix
140	Average mix for U. S. distribution[62]

Table 4.10. Key parametric assumptions for electric energy input

For Case C, the glycerol purification process starts with the neutralization which splits soap residues and salts out of the CGP. It is assumed that the same mass of phosphoric acid is required to treat unit mass of CGP as Case B: 0.042kg/kg-CGP. However, due to the higher purity (*p*) of the CGP, Case C required less mass of phosphoric acid per ton production of TGP than Case B.

The neutralized CGP goes through 1st-stage evaporation where the 92% of methanol content and 53% of water content are evaporated by nitrogen sparging and heat. During the 1st stage evaporation, the temperature was increased from 125ºC to 160ºC. The mass of nitrogen gas used for sparging unit mass (1kg) of CGP is 0.115kg, with nitrogen gas reuse times of 5, thus resulting in 30.67kg nitrogen used per ton of TGP. The GHG emissions from the production of unit mass of nitrogen gas is set to be 192.41gCO_2e/kg as referenced from Dunn et al.[39] The 2nd – stage evaporation involves the vaporization of the rest of methanol while maintaining the temperature at 160ºC with nitrogen sparging.

Then, the vacuum distillation is conducted. The vacuum pressure is assumed to be 12.5 mmHg (Torr) while the temperature is increased from 160ºC to 185ºC. Water, methyl laurate are evaporated out of the stream in the early stage of the sub-procedure, then, the glycerol is distilled and isolated. The vacuum pump is assumed to consume 600W power during 90 minutes.

Lastly, the de-colorization and de-odorization sub-procedure is conducted by flowing glycerol through activated carbon bed. Since Aiken's patent[55] did not specify the mass of activated carbon (AC) used to treat unit mass of glycerol, it is assumed that the same mass ratio of AC and glycerol is used in Case C as it was for Case A (i.e., 0.01kg AC/kg-CGP). Thus, 13.98kg of AC is used to produce one ton of purified glycerol in Case C.

The methanol recovered from the 1st and 2nd stage volatilization sub-procedure is assumed to be reused as the input material for biodiesel transesterification process. Thus, the amount of methanol recovered from those sub-procedures could displace the same mass of methanol used in the biodiesel transesterification process which reduced overall GHG emissions. The mass of methanol recovered per ton of TGP is also presented in Table 4.9.

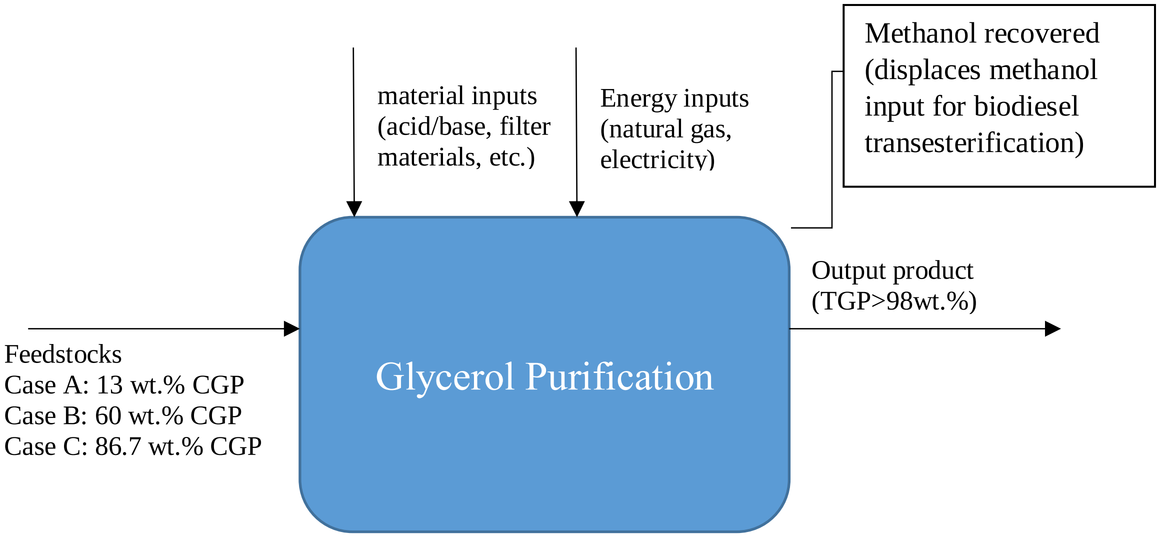

Figure 4.8. Schematic of the glycerol purification process

4.2.8.3. PG Production Process

Figure 4.9 is the schematic of the PG production process assumed in the current work. GHG emissions from the PG production process is calculated as follows.

$$GHG\ emissions\ from\ PG\ production\ per\ 1kg\ MDME\ II\ \left[\frac{gCO_{2e}}{kgMDME}\right]$$

$$=\ GHG\ emissions\ from\ 1kg\ PG\ production\ \left[\frac{gCO_{2e}}{kgPG}\right]$$

$$\cdot\ mass\ of\ PG\ per\ 1kg\ MDME\ II\ \left[\frac{kgPG}{kgMDME}\right]$$

In this work, a fraction of TGP stream after the glycerol purification process is converted to PG through hydrogenolysis reaction in a high temperature, high pressure reactor. The rest of the TGP stream after glycerol purification process does not go through PG production process, and is directly mixed into the Michigan DME II blend. The mass of TGP used for PG production is equal to *x* kg as shown in Table 4.5.

The GHG emissions from the production of unit mass of PG is referenced from Dunn et al.[39] Table 4.11 shows the material and energy inputs used for the production of 1 ton of PG. For each unit mass production of PG, 1.4 times the mass of TGP is required. The mass of hydrogen required to produce unit mass (1ton) of PG is 0.035ton.

Material input [ton/ton-PG]		Energy input [MMBtu/ton-PG]	
Hydrogen	TGP	Natural gas	Electricity
$3.5 \cdot 10^{-2}$	1.4	7.2	0.36

Table 4.11. Material and energy input to produce unit mass of PG (Dunn et al., 2015[39])

The detailed process input parameters (e.g., boiler efficiency, reactor conditions, etc.) are also assumed to be the same as the one reported in Dunn et al.[39], which assumed the natural gas boiler overall efficiency of 80%.

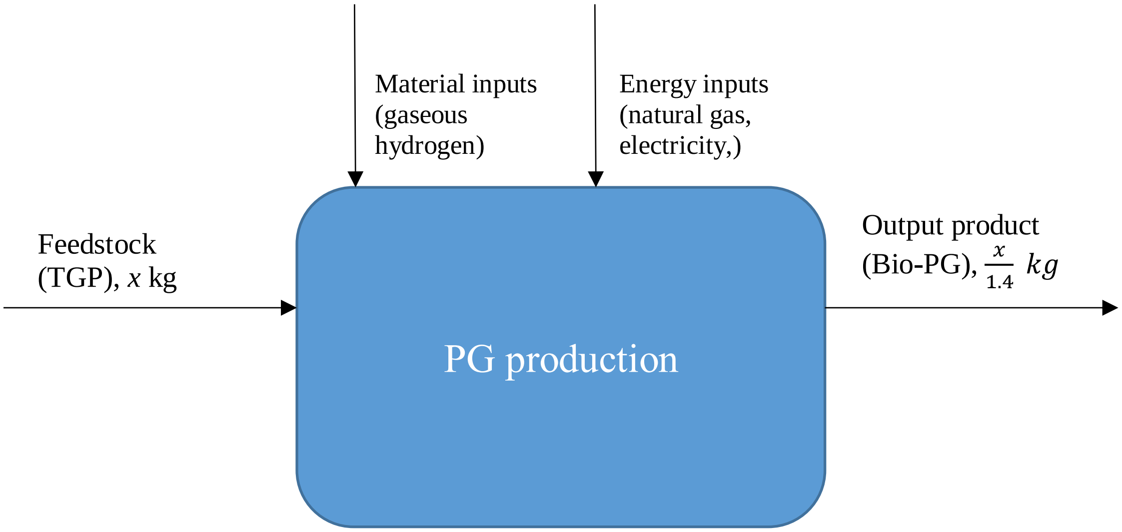

Figure 4.9. Schematic of the PG production process

4.2.8.4. DME Production Process

Figure 4.10 is the schematic of the DME production process assumed in the current work. The GHG emissions from the DME production process is calculated as follows.

$$GHG\ emissions\ from\ DME\ production\ per\ 1kg\ of\ MDME\ II\ \left[\frac{gCO_{2e}}{kgMDME}\right]$$

$$= GHG\ emissions\ from\ unit\ mass\ of\ DME\ \left[\frac{gCO_{2e}}{kgDME}\right]$$

$$\cdot\ mass\ of\ DME\ per\ 1kg\ of\ MDME\ II\ \left[\frac{kgDME}{kgMDME}\right]$$

First, the mass of DME required to produce 1kg of MDME II is shown in Table 4.5 (i.e., *a* kg). Depending on the mass fraction of DME in MDME II blend, the mass of DME for 1kg of MDME II varied between 0.4 kg (40 wt. % DME) and 0.5 kg (50 wt. % DME).

The GHG emissions from the production of unit mass (or energy) of DME is referenced from Lee et al.[7] The study reports four different pathways of producing neat DME: 1) DME production from natural gas in a large scale plant, 2) DME production from "natural-gas-derived" methanol which is produced in a separate plant from the DME production plant, 3) DME production from landfill gas, 4) DME production from animal manure. These 4 different DME production pathways reported in Lee et al.[7] are defined as the 4 different "Cases" of the DME production process in the current work. Table 4.12 presents the GHG emissions from the production of DME by unit energy.

Case #	Production method	[gCO_2e/MJ-DME]	Carbon resource
1	NG (single plant)	29.97	Fossil fuel
2	NG (two plants)	29.56	Fossil fuel
3	Landfill gas	6	Biogenic
4	Animal manure	-1	Biogenic

Table 4.12. GHG emissions from the production of 1MJ neat DME in 4 different cases.

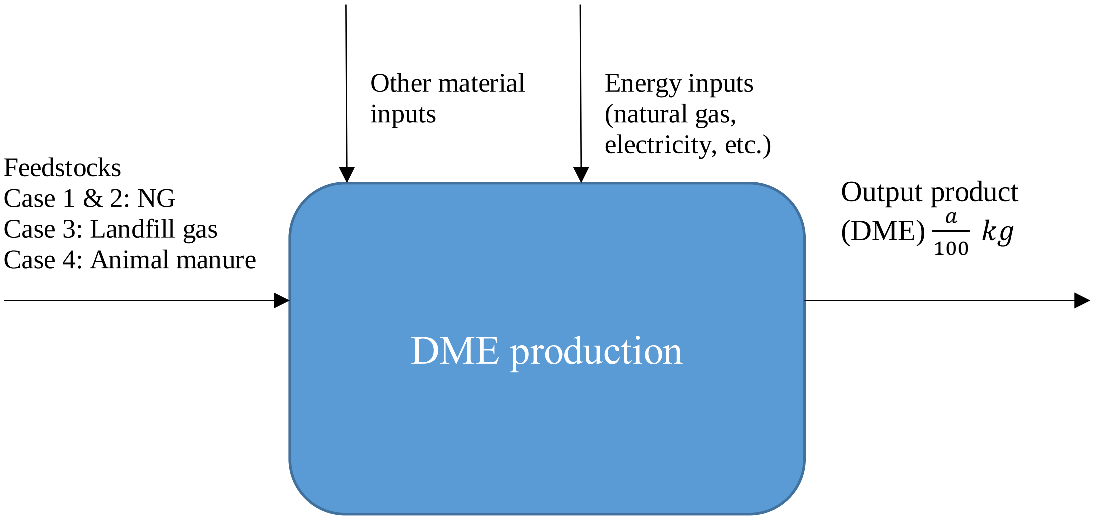

Figure 4.10. Schematic of the DME production process

4.2.8.5. Michigan DME II Blending Process

Figure 4.11 is the schematic of the Michigan DME II Blending process assumed in the current study. During the Michigan DME II blending process, three different pure components of the blend (i.e., DME/PG/Glycerol) are injected into a pressure-resistant vessel, and mixed by an electric mixer. Then, the top part of the container is pressurized and blanketed with nitrogen gas at 8bar to prevent vaporization of DME. Therefore, to calculate the GHG emissions from the MDME II blending process, two items are analyzed: 1. GHG emissions from the production of the nitrogen gas used to compress and blanket MDME II blends, 2. GHG emissions from the use of electricity to mix DME, PG, and glycerol.

First, to calculate the GHG emissions from nitrogen gas, the GHG emissions per unit mass production of nitrogen are referenced from Dunn et al.[39] (i.e., 210gCO_2e/kg-N_2) and the mass of nitrogen used per 1kg of MDME II blend is calculated.

The mass of nitrogen gas required for 1kg of MDME II blend is calculated as follows. First, the mass of nitrogen gas required to blanket unit volume (1m^3) of MDME II blend is calculated by assuming that the volume fraction of the nitrogen gas in the container is 10%, which means that 1/9 m^3 of nitrogen gas is used to blanket 1m^3 of MDME II. The container pressure is assumed to be 8bar. Then, the mass of nitrogen gas occupying 1/9 m^3 at that pressure and ambient temperature (298K) could be calculated by using the ideal gas law: 1.004kg/m^3-MDME II. Then, the value is converted into the mass of nitrogen required per unit mass of MDME II by using the density of the MDME II blend shown in Table 4.5.

As a result, the mass of nitrogen gas required for the unit mass of MDME II can be expressed as Equation 4.1. It is 1.07 grams of nitrogen gas per kg of MDME II for 40 wt. % DME blend, and is 1.13grams of nitrogen per kg of MDME II for 50 wt. % DME blend.

$$mass\ of\ N_2\ per\ kg\ MDME\ II = \frac{1.004}{\rho_{MDME}\left[\frac{kg}{m^3}\right]} \quad \text{(Eq. 4.1)}$$

To estimate the GHG emissions from the electricity used for the mixing of the pure components, GHG emissions per unit electric energy is first referenced from Cai et al. (i.e., 140gCO_2e/MJ, average mix for the U. S. distribution).[62] Then, the amount of electric energy required for the mixing process is estimated based on the energy requirement for a commercial chemical mixer with 1m^3 capacity. Amixon industrial chemical mixer (Conical Mixer Type AM) for 1m^3 capacity provided 13-48 rpm rotational mixing with 11-35kW (23kW in avg.) power requirement. Based on the fact that the sample MDME II blend during the minimum co-solvent to glycerol ratio (MCR) measurement could be easily mixed by manual agitation within 30 seconds, it is assumed that just one minute is required to mix the blend. Thus, the electric energy required to mix the unit volume (1m^3) of MDME II blend is assumed to be 1380kJ. Again, to convert this number to the electric energy per unit mass of MDME II, the density of MDME II shown in Table 4.5 is used.

$$electricity\ for\ 1kg\ MDME\ II\ mixing\ \left[\frac{kJ}{kg}\right] = \frac{1380\ \left[\frac{kJ}{m_3}\right]}{\rho_{MDME}\ \left[\frac{kg}{m^3}\right]}$$

Eventually, the GHG emissions from the MDME II mixing process is like below.

$$GHG\ from\ mixing\ process\ \left[\frac{gCO2e}{kgMDME}\right] = \frac{211}{\rho_{MDME}\ \left[\frac{kg}{m^3}\right]} + \frac{193.2}{\rho_{MDME}\ \left[\frac{kg}{m^3}\right]} = \frac{404.2}{\rho_{MDME}\ \left[\frac{kg}{m^3}\right]}$$

For DME 40% blend, GHG emissions from the blending process is 0.432gCO_2e/kg-MDME II. For DME 50% blend, it is 0.456gCO_2e/kg-MDME II. As compared to other processes, the blending process has insignificant GHG emissions burden.

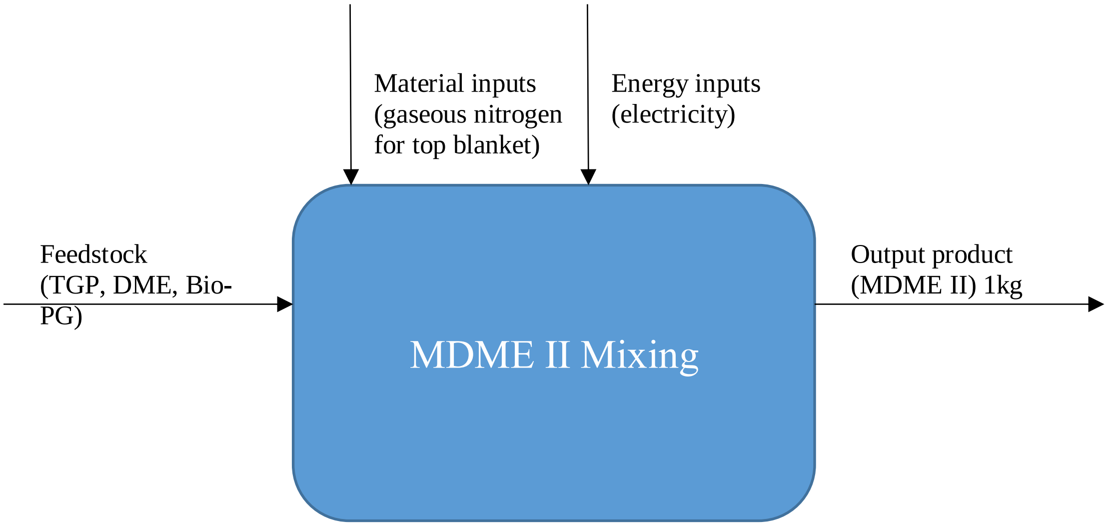

Figure 4.11. Schematic of the Michigan DME II blending process

4.2.8.6. Michigan DME II Transportation Process

Figure 4.12 is the schematic of the MDME II transportation process assumed in the current work. During the Michigan DME II transportation process, the blend is transported from the mixing plant to fuel stations. Thus, the input material is 1kg of MDME II blend "before" distribution, and the output is 1kg of MDME II blend "after" distribution. The parameters used to define the transportation path is assumed to be the same as neat DME. This is a reasonable assumption in that Michigan DME blending will likely to take place near DME production plant. Furthermore, since the vapor pressure of MDME II is similar to neat DME, it will be packed in the similar pressure resistant containers, which in turn, makes the energy required to migrate the unit mass of MDME II for certain distance be similar to that of neat DME. Lee et al.[7] reported a typical transportation process for neat DME in the U.S., which combines the 800 miles of railroad shipping and 30 miles of truck delivery. This combination results in 32.98gCO_2e for the transportation of 1kg neat DME, and the value is used in the current work for 1kg of MDME II blend, too.

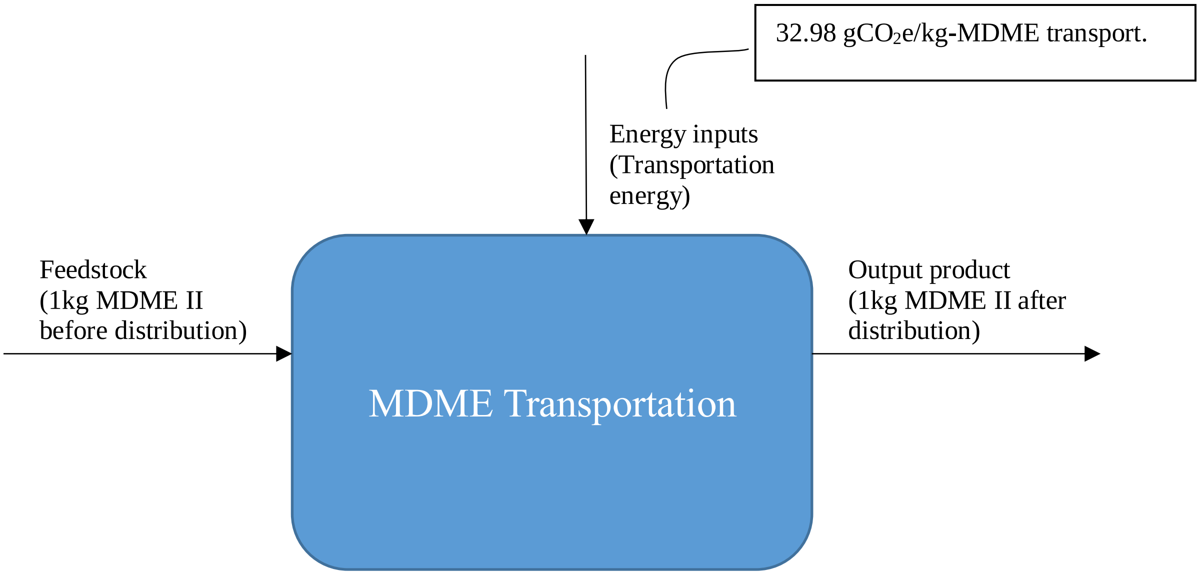

Figure 4.12. Schematic of the Michigan DME II Transportation process

4.2.8.7. Pump-To-Wheels (PTW) Combustion Process

Figure 4.13 is the schematic of the PTW combustion process assumed in the current study. The GHG emissions from the combustion of unit mass (1kg) of carbon containing fuel, or simply "gCO_{2e}/kg-fuel", can be calculated by multiplying the weight percentage of carbon atoms in the fuel and the ratio of the molecular weight of carbon dioxide and atomic weight of carbon. Then, the value can be converted into the carbon intensity (i.e., gCO_2e/MJ) by using the LHV of the fuel. Table 4.13 presents the GHG emissions from the direct combustion of different fuels.

Fuel	Carbon wt. %	LHV [MJ/kg]	PTW Carbon intensity [gCO_2e/MJ]
Gasoline Blendstock	86.0	43.45	72.58
Natural Gas	72.4	47.14	56.31
Coal	58.6	20.04	107.13
ULSD	87.1	42.78	74.66
Biodiesel	77.6	37.66	75.55
DME	52.2	28.87	66.29
Glycerol	39.1	16.88	85.00
PG	47.4	22.16	78.38

Table 4.13 GHG emissions from the PTW combustion of different fuels regardless of the sources of the carbon

When a fuel is produced from a renewable feedstock, the carbon atoms contained in the fuel is considered as biogenic carbon, which is part of the natural carbon cycle that does not cause excessive global warming. Thus, the “anthropogenic” GHG emissions from the combustion of fuel should be re-adjusted by the fraction of biogenic carbon in a fuel.

In the current work, glycerol is assumed to be produced 100% from soybean, and PG is produced from that glycerol. Thus, all of the carbon atoms contained in glycerol and PG are biogenic carbons. However, regarding DME, the carbon can be either fossil carbon or biogenic carbon based on its production process. If DME is produced through Cases 1 or 2, the carbon is from natural gas. Thus, in this case, the PTW carbon emissions should be added to the WTP carbon emissions. However, for the Cases 3 and 4 where DME is produced from either landfill gas or animal manure, the carbon atoms contained in DME is assumed to be 100% biogenic, and the carbon emissions from PTW combustion are not added to the WTP carbon emissions.

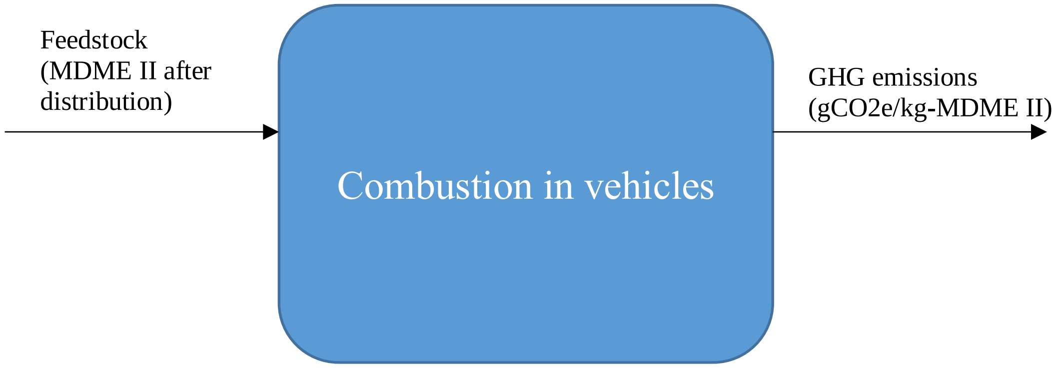

Figure 4.13. Schematic of the PTW combustion process

4.2.9 Engine Operation with Michigan DME Blend I (DME/DPG/Glycerol Blend)

A brief engine operation with Michigan DME blend I (DME/DPG/Glycerol) with 40 wt. % DME is attempted in the current work. Figure 4.14 is the schematic of the test setup. A Yanmar Genset 3700W with a single-cylinder, naturally aspirated compression ignition engine with a pump-line-nozzle type fuel injection system is used as the test engine. The engine has a fuel governor that keeps the engine speed around 3600rpm (±150rpm) regardless of the engine load, but the governor cannot maintain the engine speed normal when the rate of the fuel energy flow is simply not sufficient to maintain that engine speed. The fuel injection timing could be manually adjusted by changing the fuel pump shim thickness, and the fuel injection pressure (i.e., injector nozzle opening pressure) could also be manually adjusted by changing the fuel injector shim thickness. The pump-line-nozzle injection system controls the start of pumping (SOP) to indirectly control the start of injection (SOI) timing. However, the difference between SOI and SOP exists, and the degree of it can be different depending on the fuel type. Boehman et al.[63] reports the retarding in “actual” start of injection timing at fixed start of pumping timing when the fuels with lower bulk modulus than petroleum diesel are applied in a pump-line-nozzle type fuel injection system.

To compensate for the lower bulk modulus and cetane number (CN) of the Michigan DME blend I as compared to those of conventional petro-diesel of which combined effect is known to cause unintended retarding in start of combustion (SOC) at fixed SOP, the start of pumping timing is advanced by 4 crank angle degrees (maximum advance possible in the test engine) from the default timing setting. Fuel injection pressure is varied between 100 and 200bar to find the optimal injection pressure for the blend. To compensate for the lower LHV of the Michigan DME blend I compared to the petro-diesel, the original fuel injector (i.e., 3700W-standard) is replaced by the standard injector for a Yanmar Genset 5500W. The nozzle diameter of the 5500W-standard injector was greater than that of the 3700W-standard. The increase in fuel injector nozzle diameter increased the fuel injection volume, which partially compensated for the lower LHV of the Michigan DME I blend.

Compressed helium gas (~120psig) is applied to the fuel supply line to prevent vaporization of Michigan DME blend I in the fuel injection system. The fuel return line is disconnected and is replaced by a fuel disposal line to dispose of the returning fuel in a dumpster, which prevented potential cavitation inside the fuel tank.

To further compensate for the low cetane number of the Michigan DME I, a heat gun was applied upstream of the engine intake to increase the intake air temperature. The experiment was conducted with no heat applied (~25ºC, no intake air temperature boost), low heat applied (~40ºC intake temperature), medium heat applied (~55ºC), and high heat applied (~70ºC).

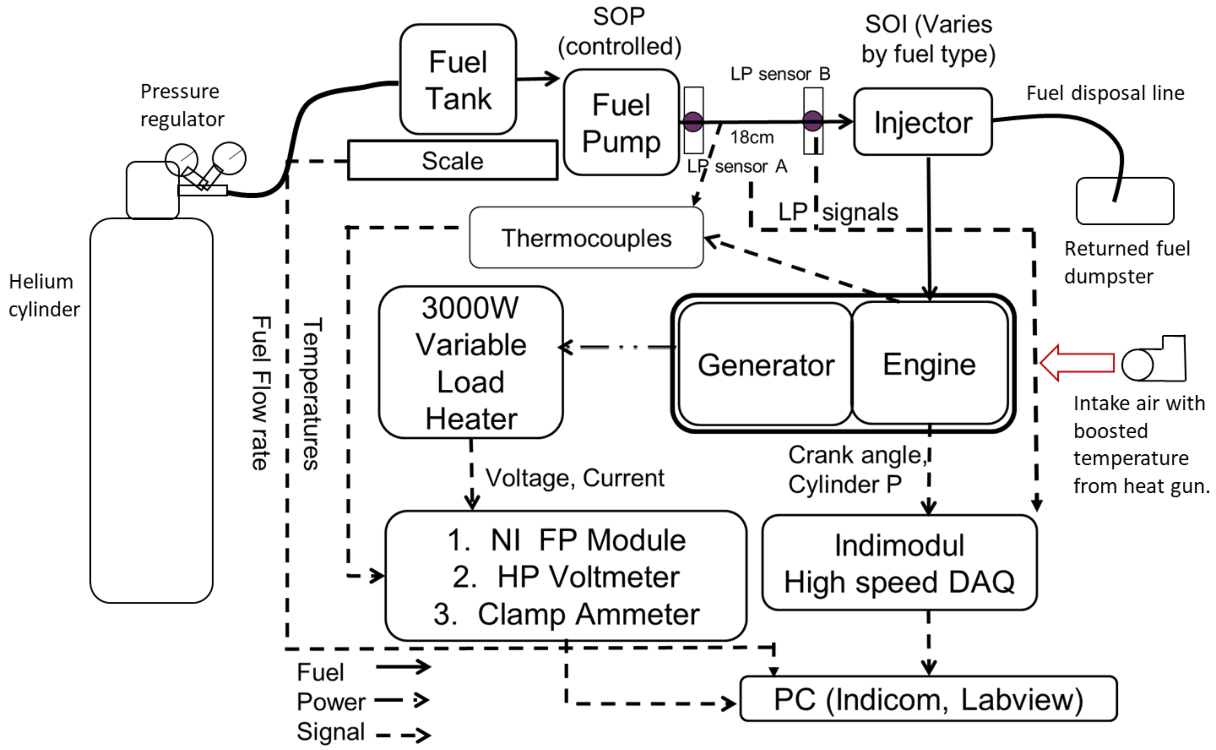

Figure 4.14. Schematic of the test setup for Michigan DME blend I (DME/DPG/Glycerol) application in a production compression-ignition engine (i.e., Yanmar Genset 3700W).

4.3. Results and Discussion

In this section, the results for the selection criteria application on the fifty-three “0th level co-solvent candidates” will be first covered in sections 4.3.1 – 4.3.4. Next, the results for the minimum co-solvent to glycerol ratio measurement will be covered in section 4.3.5 followed by the results for the viscosity measurement of the final DME blend (i.e., Michigan DME blend I and II) in section 4.3.6. The life-cycle GHG emissions assessment for the Michigan DME blend II production is covered in section 4.3.7. The section 4.3.8 provides a brief summary of the engine operations with Michigan DME blend I with 40 wt. % DME. The engine test results in this work is primarily presented for the purposes for future development.

4.3.1. First Level Candidate Species

Out of the 0th level candidate species, those species with shorter solubility distance than the interaction radius of both DME and glycerol (i.e., those species expected to be soluble in both DME and glycerol based on the HSP method) are chosen and defined as the 1st level candidate species. Out of the fifty-three 0th level candidates, thirty-three species are selected as the 1st level candidate species which are presented in Table 4.14.

4.3.2. Averaged Solubility Distance, Kinematic Viscosity, and Oxygen Mass Content of the 1st Level Candidates

The averaged solubility distance (r_{avg}) of the 1st level candidate species was calculated and presented in Table 4.14 in the ascending order. The averaged solubility distance calculation was based on the Hansen Solubility Parameter values reported in Appendix A in "*Hansen Solubility Parameters: A User's Handbook*".[64] Kinematic viscosity of the species at 40ºC is estimated based on the DIPPR project 801[23], and oxygen mass content is calculated based on Equation 4.2.

$$oxygen\,mass\,content\;[\%] = \frac{atomic\;mass\;of\;oxygen\;atoms\;in\;a\;molecule}{molecular\;weight} \cdot 100 \qquad \text{(Eq. 4.2)}$$

Species	EGME	DPG	ETOH	PROH1	EGMEE	GDA	PROH2	BG12
r_{avg} [MPa$^{1/2}$]	17.55	17.61	17.75	17.81	18.06	18.10	18.13	18.27
ν [cSt]	1.23	42.34	1.05	1.77	1.43	N/A	1.75	21.08
Oxygen mass [%]	42.11	35.82	34.78	26.66	35.56	45.45	26.66	35.56
Species	BUOH	EGMNPE	BG13	DEG	PTOH	GMA	DEGME	TEGME
r_{avg} [MPa$^{1/2}$]	18.33	18.39	18.43	18.52	18.81	18.82	18.90	18.99
ν [cSt]	2.25	1.99	40.69	13.93	2.87	N/A	2.43	4.10
Oxygen mass [%]	21.62	30.77	35.56	38.30	18.18	47.76	40.00	39.02
Species	EL	DEGMEE	AA	PG	MEOH	EBOH	DEGMNPE	EGMNBE
r_{avg} [MPa$^{1/2}$]	19.00	19.03	19.14	19.36	19.57	19.66	19.77	19.83
ν [cSt]	1.61	2.76	0.88	18.78	0.58	3.57	2.75	2.16
Oxygen mass [%]	40.68	35.82	53.33	42.11	50.00	15.68	32.21	27.11
Species	PGME	CHOH	PA	DEGMNBE	DPGMNPE	PGMIPE	DPGME	EGMNHE
r_{avg} [MPa$^{1/2}$]	19.88	19.96	20.19	20.27	20.31	20.34	20.34	20.38
ν [cSt]	1.33	23.60	0.86	3.60	2.84	N/A	2.58	3.14
Oxygen mass [%]	35.56	16.00	43.24	29.63	27.27	27.12	32.43	21.92
Species	BG14							
r_{avg} [MPa$^{1/2}$]	20.43							
ν [cSt]	60.56							
Oxygen mass [%]	35.56							

Table 4.14. Averaged solubility distance (r_{avg}), kinematic viscosity (ν), and oxygen mass content of the 1st level co-solvent candidates.

Since the viscosity improvement of DME is the most critical objective of this work, the co-solvent candidate species with viscosity lower than 10cSt at 40°C were first screened out. Also, to ensure the soot-free combustion, those candidate species with oxygen mass content lower than 30% are screened out. After applying these two criteria, 8 species were left: DPG, GDA, BG12, BG13, DEG, GMA, PG, BG14 (in the ascending order of the averaged solubility distance). These eight species are defined as the “2nd level co-solvent candidate species”, and a more comprehensive investigation is conducted on these species.

4.3.3. Health and Environmental Impacts of the 2nd Level Candidate Species

Since non-toxicity and non-carcinogenicity are the important merits of DME and glycerol, a co-solvent with better or similar health and environmental impact than or to DME and glycerol should be regarded as better co-solvent. Thus, different categories of health and environmental impacts based on the GHS are investigated for the 2nd level candidate species and the result is presented in Table 4.15.

	DPG	GDA	BG12	BG13
Acute toxicity	NH (Not Hazardous)	NH	NH	NH
Skin corrosion/irritation	NH	NH	NH	NH
Serious eye damage/irritation	NH	NH	NH	Mild eye irritation from rabbit test
Respiratory sensitizer	NH	NH	NH	NH
Germ cell mutagenicity	NH	NH	NH	NH
Carcinogenicity	NH	NH	NH	NH
Reproductive toxicity	NH	NH	NH	NH
STOT*** single exposure	NH	NH	NH	NH
STOT repeated exposure	NH	NH	NH	NH
Aspiration hazard	NH	NH	NH	NH
Acute hazard to aquatic environment	NH	NH	NH	Toxic to algae

Long-term hazard to aquatic environment	NH	NH	NH	NH
Biodegradability	RD (readily degradable)*	RD	RD	RD**
	DEG	GMA	PG	BG14
Acute toxicity	Grade 4 Hazmat	NH	NH	Grade 4 Hazmat
Skin corrosion/irritation	NH	NH	NH	NH
Serious eye damage/irritation	NH	NH	NH	NH
Respiratory sensitizer	NH	NH	NH	NH
Germ cell mutagenicity	NH	Mutagenicity reported for some lab animals	NH	NH
Carcinogenicity	NH	NH	NH	NH
Reproductive toxicity	NH	NH	NH	NH
STOT single exposure	NH	NH	NH	Grade 3 Hazmat (CNS)****
STOT repeated exposure	Grade 2 Hazmat (Kidney)	NH	NH	NH
Aspiration hazard	NH	NH	NH	NH
Acute hazard to aquatic environment	NH	NH	NH	NH
Long-term hazard to aquatic environment	NH	NH	NH	NH
Biodegradability	RD	RD	RD	RD

Table 4.15. Health and environmental impacts of the 2nd level co-solvent candidates (* >84.8 wt. % degraded within 28 days of aerobic exposure based on OECD 301F test, ** >81 wt. % degraded within 29 days of aerobic exposure based on OECD 301B test, *** Specific target organ toxicity (STOT), **** Central nervous system (CNS))

As shown in Table 4.15, DEG and BG14 exhibit acute toxicity. These two species also exhibit specific target organ toxicity (STOT) either through single exposure or repeated exposure. When mixed with DME and glycerol, these two species have a potential to degrade the non-toxic characteristics of the DME and glycerol. BG13 does not have acute toxicity to humans, but it does have toxicity on aquatic life such as algae. Other 5 species (DPG, GDA, BG12, GMA, PG) did not show critical health and environmental impacts. Thus, these 5 species are considered as better co-solvents, and defined as the "3rd level candidate species".

4.3.4. Renewable Production Availability of the 3rd Level Candidate Species

One of the important merits of DME and glycerol is that they can be produced from renewable feedstocks with significantly lower WTW GHG emissions. To maintain the low carbon fuel characteristic of the final blend, the co-solvent must be available from renewable feedstock at scalable production pathways, as well. Thus, renewable production availability of the 3rd level co-solvent candidates is investigated and summarized in this section. Investigation was conducted separately for three categories of the candidates: 1) BG12, 2) PG and DPG, 3) GMA and GDA.

4.3.4.1. 1,2-Butanediol (BG12)

To state the conclusion first, there is no BG12 production from renewable feedstocks at large scale yet. BG12 is usually produced as a byproduct of BG14 production either from petroleum feedstock or renewable feedstock.[38] One of the main renewable production pathways of BG14 is the hydrogenolysis (i.e., hydrocracking) of sorbitol. BG12 and BG13 are produced as byproducts of this BG14 production process. However, the wt. % of BG12 in the output stream is less than 10% in this production method. Since BG14 and BG13 have toxicity, BG12 will have to be separated from the product stream. However, research on the economic feasibility and additional environmental burden of the purification process is not available at this moment.

Although there is no renewable production pathway at scale targeting BG12 as a main product, there are some recent publications reporting the production at lab scale. One of the pathways is using *Escherichia Coli* (E. Coli) to convert C_2 –C_4 olefins from bio-syngas to BG12. Thus, renewable production of BG12 at commercial scale might be possible in future, which will, in turn, make this species more attractive as a co-solvent for DME/glycerol blend.

4.3.4.2. Propylene Glycol (PG) and Dipropylene Glycol (DPG)

PG is one of the few chemical species that is reported to have near-term economic feasibility from renewable feedstocks based on Biddy et al.[38] Based on this study, PG from renewable feedstock has technology readiness level (TRL) of 9, which is the highest TRL grade meaning that it is fully operational at large scale commercial plants with sufficient engineering background. It is one of the commodity chemicals produced at large scale (global production of 2.2 million metric tons in 2013), and both the production capacity and demand have increased annually to date. The average price of PG during the three-year period of 2014-2016 was $5.48/gal, which is more expensive than that of petroleum-based diesel ($3.65/gal)[38], but the price can decrease as the process efficiency of the bio-PG increases.

There are two different production pathways of PG from renewable feedstocks with different economic feasibility and WTW GHG emissions. The less feasible kind is the production through the hydration of the bio-propylene oxide which is obtained from the bio-propylene available either from the 1st generation bio-feedstocks (i.e., sugarcane) or the 2nd generation bio-feedstocks (i.e., lignocellulosic biomass) as suggested by Machado et al.[65] The production pathway is presented in Figure 4.15. The cost of bio-PG production through this pathway depends greatly on that of the bio-propylene oxide production. Machado et al.[65] evaluated the potentially achievable cost range of the bio-propylene oxide production process by using a parameter called Minimum Bio-Propylene Selling Price (MBSP). The MBSP was estimated to be 1.8 times higher than the conventional petroleum-based propylene production pathway, which, in turn, has made the wide-spread adoption of this process in the propylene industry difficult.

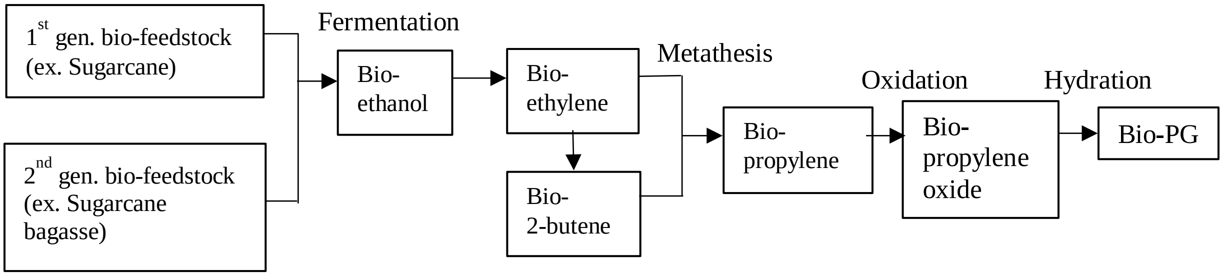

Figure 4.15. Renewable production pathway of PG from bio-propylene

The other production pathway of bio-PG is shown in Figure 4.16: Bio-PG production from bio-glycerol through hydrogenolysis. This pathway is more economically feasible and reduces GHG emissions more than previous one, and as a consequence, is accepted widely in the PG industry. Any pathways that make biodiesel through transesterification process produces glycerol as a co-product, then the glycerol co-product is used as an input material for the hydrogenolysis process into bio-PG. Hydrogenolysis process requires compressed hydrogen gas input and thermal/electrical energy of which the amount depends on the details of the catalysts and the practical reaction conditions used. Typically, the conversion rate of glycerol is around

90% with the selectivity into bio-PG around 90%. Bio-PG produced through this pathway can reduce WTW GHG emissions by 66% as compared to its counterpart pathway from fossil-fuel[40], with great economic viability that enabled companies like Archer Daniels Midland (ADM) to start commercial production. Furthermore, since a great portion of WTW GHG emissions from this PG production pathway depends on the GHG burdens on hydrogen production, further reduction of GHG emissions is possible when hydrogen is produced from less carbon intensive resources.

DPG, a dimer of PG molecules, can be produced from the etherification reaction between two PG molecules.[66] The reaction involves acid catalyst such as sulfuric acid, and high temperature around 200°C. Thus, the WTW GHG emissions of DPG would be higher than PG.

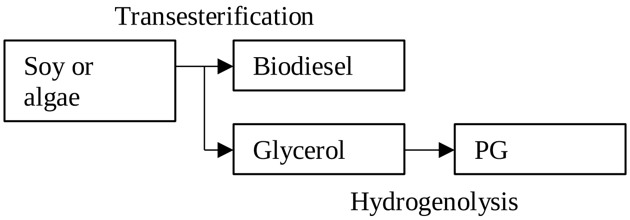

Figure 4.16. Renewable production pathway of PG from bio-glycerol

4.3.4.3. Glycerol Mono-Acetate (GMA) and Glycerol Di-Acetate (GDA)

Although GMA and GDA are not the commodity chemicals produced at large scale, its precursor, glycerol, is a commodity chemical produced 1500MMTs (million metric ton) annually of which 88% is from renewable resources. As mentioned in the previous section, glycerol is produced as a co-product of biodiesel of which production has significantly increased during the mid-2000s. As a result, TRL of glycerol from renewable feedstock such as algae is 9 based on Biddy et al.[38] In addition, the global glycerol production increased two folds between 2001 and

2011, which resulted in very low crude glycerin price which has motivated many researchers to pursue development of new uses for glycerol.[29]

One of the uses could be esterifying glycerol into the mono- or di-esters of glycerol: GMA and GDA. The production of GMA and GDA from glycerol are available through esterification reaction by using different catalytic reactions. Okoye et al. reported a successful (>99%) conversion of glycerol into three different kinds of glycerol acetates (i.e., GMA, GDA, and glycerol triacetin) using glycerol-based carbon catalysts.[67] They could easily adjust the ratio of the output of GMA and GDA by controlling the reaction temperature. Other publications also present high conversion ratio and selectivity into GMA and GDA with feasible energy use. [68,69]

Based on the comprehensive research on the 3rd level co-solvent candidates, it is concluded that PG and DPG are the most attractive co-solvent options for DME-glycerol blend at this moment. In summary, PG and DPG are soluble in both DME and glycerol with small averaged solubility distance (r_{avg}) values, viscosity over 10 cSt at 40ºC, oxygen mass content over 30% and non-toxicity. Their production is available from bio-glycerol produced either from algae or soybean at large-scale commercial plant with competitive cost while emitting low WTW GHG emissions. Glycerol esters (i.e., GMA, GDA) also have potentials to be good co-solvents. However, the increase in annual production capacity and more research on their fundamental properties including viscosity must be preceded. For BG12, the separation from the other isomers of butanediol (i.e., BG13 and BG14) that are toxic to either humans or aquatic life must be available at large scale with low cost.

The two final co-solvents (i.e., PG and DPG) are blended with DME and glycerol to create each different DME blend. The blends are named as Michigan DME blend I (i.e., DME/DPG/Glycerol blend) and Michigan DME blend II (i.e., DME/PG/Glycerol blend). The minimum co-solvent to glycerol ratio (MCR) measurement and kinematic viscosity measurement results conducted on these two final blends will be presented in the following sections.

4.3.5 Minimum Co-solvent to Glycerol Ratio (MCR) Results for Michigan DME Blends

Minimum co-solvent to glycerol ratio (MCR) is measured for Michigan DME blend I (MDME I) and blend II (MDME II) at different wt. % of DME. The result is presented in Figure 4.17. For both blends, MCR increases from the 40% DME blends to the 80% DME blends. It peaks at 80% DME blends, then, decreases between the 80% DME blends and 90% DME blends. Thus, the trend of MCR can be distinguished into two different regions based on the mass % of DME. When DME wt. % is higher than 80% (i.e., high DME ratio region), the HSP difference between DME and glycerol is greater than the effect of the co-solvent. So, more co-solvent is required to prevent phase separation as the glycerol concentration increases. However, after the binary mixture of co-solvent and glycerol is blended over 20% (i.e., at 80% DME), thanks to the decrease in HSP disparity between DME and glycerol achieved, less co-solvent is required to prevent the phase separation from then on. Thus, MCR decreases with decrease in DME wt. %. Linear regression models for two different regions of MCR trends are also posted with Figure 4.17. To provide a quantitative explanation of why does that regime change occurs at DME 80% solutions instead of other wt. %, liquid-liquid phase equilibrium[70] calculation must be conducted for the two Michigan DME blends. In this work, the experimental measurement of the MCRs and the application of the measured MCRs in viscosity improvement were the primary interest. Thus, a quantitative explanation based on liquid-liquid phase equilibrium is left for future work.

To compare MDME I and MDME II, MDME I generally has higher MCR than MDME II except for the DME 50% and 40% solutions. For DME 50% solution, the two MDME blends exhibit the same MCR, whereas, for DME 40% solutions, MDME I has lower MCR than MDME II. Although MCRs based on mass were similar for the two MDME blends, minimum co-solvent to glycerol ratio on a molar basis was different for MDME I and MDME II. On a molar basis, minimum ratio of co-solvent to glycerol for MDME I ranged between 1.0 and 2.6 while it ranged between 2.0 and 4.2 for MDME II. Due to the heavier molecular weight of DPG (134kg/kmol) than PG (76.09kg/kmol), MCRs on a mass basis are similar for the two blends despite the difference in minimum ratio of co-solvent to glycerol on a molar basis.

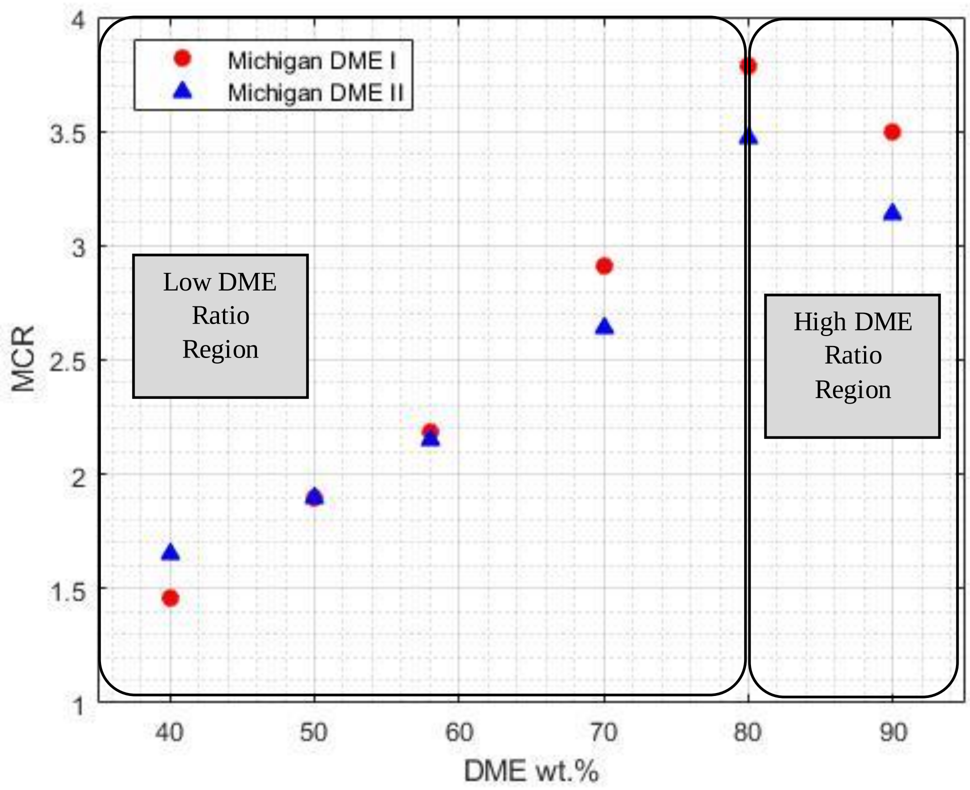

Low DME Ratio Region Linear Regression: $\boldsymbol{MCR = a \cdot (DME\ wt.[\%]) + b}$

MDME I: $a_1 = 0.05716,\ b_1 = -0.9592,\ R^2 = 0.9633$

MDME II: $a_2 = 0.0441,\ b_1 = -0.2641,\ R^2 = 0.9417$

High DME Ratio Region Linear Regression: $\boldsymbol{MCR = c \cdot (DME\ wt.[\%]) + d}$

MDME I: $c_1 = -0.02914,\ d_1 = 6.119$

MDME II: $c_2 = -0.03305,\ d_1 = 6.114$

Figure 4.17. Minimum mass ratio of co-solvent to glycerol (MCR) required to prevent phase separation for Michigan DME blends.

4.3.6. Kinematic Viscosity Measurement Results for Michigan DME Blends

Kinematic viscosity measurements were conducted for MDME I and MDME II at minimum co-solvent to glycerol ratios (MCRs) of different DME wt. %. The results are presented in Table 4.16 with corresponding mass fractions of the component species of MDME blends and corresponding MCRs.

Michigan DME Blend I (DME/DPG/Glycerol)							
DME wt.%	100	90	80	70	58	50	40
DPG wt.%	0	7.78	15.82	22.34	28.82	32.72	35.58
Glycerol wt.%	0	2.22	4.18	7.66	13.18	17.28	24.42
MCR	-	3.50	3.79	2.91	2.48	2.19	1.89
ν [cSt]	0.150	0.215	0.279	0.358	0.665	0.960	1.840
Michigan DME Blend II (DME/PG/Glycerol)							
DME wt.%	100	90	80	70	58	50	40
PG wt.%	0	7.58	15.53	21.77	28.66	32.76	37.38
Glycerol wt.%	0	2.42	4.47	8.23	13.34	17.24	22.62
MCR	-	3.14	3.47	2.64	2.15	1.90	1.65
ν [cSt]	0.150	0.222	0.301	0.434	0.745	1.103	2.428

Table 4.16. Mixture composition, MCR, and the corresponding kinematic viscosity of the two Michigan DME Blends.

The viscosity measurements are presented in Figure 4.18 with the comparison to the ASTM D975 viscosity standards of the regular petroleum-based diesel oils.[24] The red dotted line at 1.9cSt represents No.2 Diesel oil while the blue line at 1.3cSt represents No.1 Diesel oil. Power law regression models fitting the data trend for each MDME blend are also presented. Based on the regression models, MDME I achieves the ASTM viscosity standard limit of No.1 and No.2 diesel oils at DME 45.2% and 39.5%, respectively. MDME II achieves the same viscosities at DME 48.6% and 43.1%, respectively. Thus, both MDME blends achieve the lower limit of No.2 diesel with 40-43% of DME content. One of the best improvements in DME viscosity reported in previous studies is from Sivebaek et al.[21] Rapeseed oil addition of ~75 wt. % (i.e., DME 25%) improved the viscosity of DME up to regular petroleum-based diesel oil level, and Rapeseed oil ester (RME) addition of ~95 wt. % improved the viscosity up to the diesel oil level. The Michigan DME blends achieve the better viscosity with lower amount of blending. Thus, it is the best viscosity improvement result for DME reported by far.

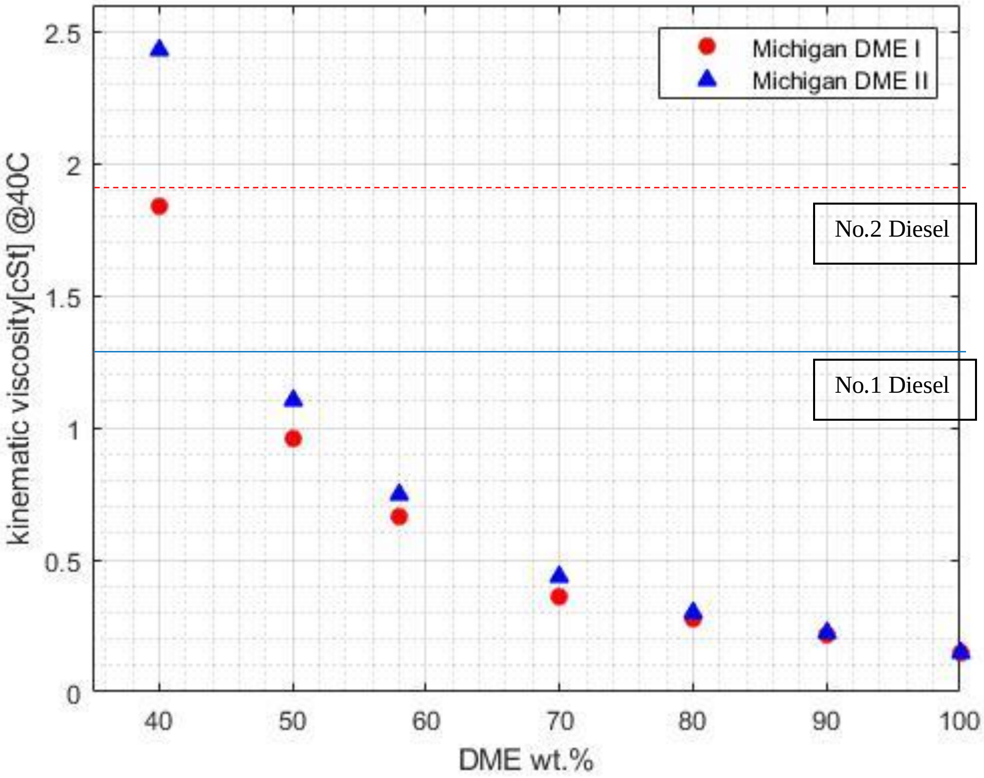

Power law regression model: $\nu\ [cSt] = a(DME\ wt.[\%])^b$

MDME I: $a_1 = 5.381 \cdot 10^4,\ b_1 = -2.789,\ R^2 = 0.9987$

MDME II: $a_2 = 2.867 \cdot 10^5\ ,\ b_2 = -3.169,\ R^2 = 0.9966$

Figure 4.18. Kinematic viscosity of Michigan DME blends measured at 40ºC in comparison with ASTM standards limits of regular petroleum-based diesel oils.

4.3.7. Life-cycle GHG Emissions Assessment Results for Michigan DME Blend II

The WTW GHG emissions from 12 different pathways of MDME II blend are calculated. The LCA result for MDME II at DME 40 wt. % is shown in Table 4.17. The pathway with lowest GHG emissions was the "Case C4": Glycerol purification process based on Aiken's patent[55] (Case C) with DME production from animal manure[7] (Case 4).

When the same DME production process is used, the glycerol purification process based on Aiken's patent[55] (Case C) always reduced the GHG emissions the most, followed by the purification process based on Rodriguez-Kabana et al.[54] (Case B), and then Nanda et al.[53] (Case A). The difference in GHG emissions between Case A and other two cases (Case B and Case C) was about the factor of three when DME is produced from natural gas (Cases 1 and 2), and was about the factor of 4.8 when DME is produced from renewable feedstocks (Cases 3 and 4).

It is proven in the current work that, depending on the GHG emissions from the glycerol purification process, the WTW GHG emissions from Michigan DME blend II can be significantly different. Also, the impact of the purification process on the final WTW GHG emissions could be more intense when DME is produced from renewable feedstocks since one of the main sources of the GHG emissions for "natural-gas-based" DME (i.e., GHG from DME combustion) does not exist for DME from renewable resources.

This is a very meaningful result because most crude glycerin is discarded in the current industrial practice, thus requiring no or insufficient improvement in the efficiency of the glycerol purification process. However, it seems to be necessary to make the glycerol purification more energy efficient and carbon neutral to make the GHG reduction impact greater through the use of Michigan DME blends.

[gCO2e/MJ-MDME II]	Case 1	Case 2	Case 3	Case 4
Case A	283.91	283.71	239.83	236.41
Case B	95.84	95.64	51.76	48.35
Case C	93.32	93.12	49.24	45.82

Table 4.17. WTW GHG emissions from 12 different pathways of MDME II (DME 40 wt. %).

Figure 4.19 shows the GHG emissions from each process of the life-cycle of MDME II with comparison to other fuels (i.e., USLD, Biodiesel, and Bio-DME). Here, GHG emissions of MDME II blend based on the Case A glycerol purification process are not included because the values were significantly higher than the other cases. The values of the GHG emissions for ULSD and bio-DME (DME from animal manure) are from Lee et al.[7] while the emissions of biodiesel (U.S. soy-ate) is from Chen et al[30].

For MDME II blends based on the DME produced from natural gas (i.e., Cases 1 and 2), PTW combustion process emits 32.37gCO_2e/MJ of GHG emissions, which accounts for about a third of WTW GHG emissions. This is greater than GHG emissions from any other processes. Next to the PTW combustion are the emissions from crude glycerol production: 26.8gCO_2e/MJ for Case B and 21.5gCO_2e/MJ for Case C. Since Case C requires less amount of CGP to produce unit mass (energy) of MDME II thanks to the use of higher purity CGP, GHG emissions for CGP production is lower for Case C. For glycerol purification process itself, Case C emits more GHG emissions than Case B: 3.8gCO_2e/MJ for Case B and 7.0gCO_2e/MJ for Case C. However, the increment in the GHG emissions from the glycerol purification process in Case C is less than the decrement in the GHG emissions from the CGP production process, thus making Case C a less carbon intensive glycerol purification method than the Case B.

PG production process also accounts for an appreciable portion of WTW GHG emissions, 15.3gCO_2e/MJ of GHG emissions.

If MDME II blends are based on the DME produced from renewable feedstocks (i.e., landfill gas: Case 3, animal manure: Case 4), no anthropogenic carbon emissions exist in the PTW combustion process because the carbon atoms contained in the MDME II blend is 100% biogenic. Furthermore, the GHG emissions from the DME production process is significantly lower than DME from natural gas: 14.5gCO_2e/MJ for Case 1 and 2, 2.9gCO_2e/MJ for Case 3, and -0.49gCO_2e/MJ for Case 4.

MDME II blending process and transportation process did not have a significant impact on the final WTW GHG emissions: 0.02gCO_2e/MJ for MDME II blending process, and 1.39gCO_2e/MJ for MDME II transportation process.

As compared to the regular ULSD (92gCO_2e/MJ), the MDME II blend with the best GHG emissions performance (i.e., Case C4) reduced WTW GHG emissions by 50.2%. Although its WTW GHG emissions per unit energy are higher than for BD (30.1gCO_2e/MJ) or bio-DME (-1gCO_2e/MJ), the overall impact of MDME II can be potentially greater than them because MDME II can be applied to a greater number of the pre-existing CI engines without intensive modifications.

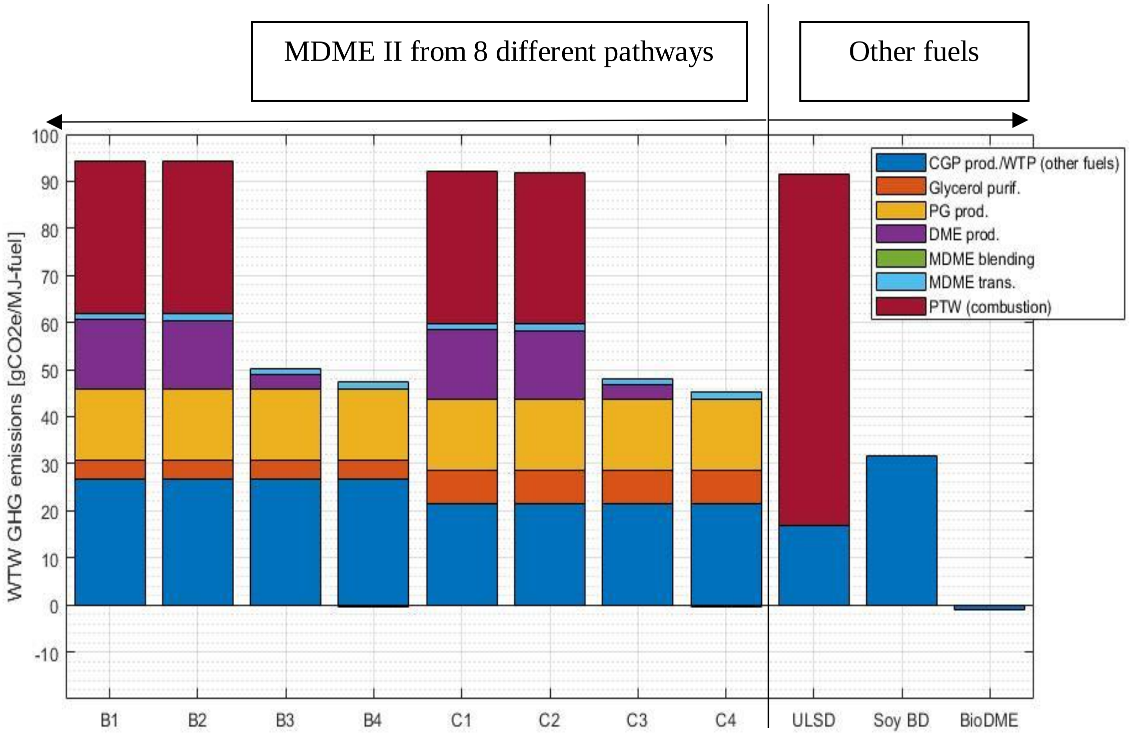

Figure 4.19. Well-to-wheels (WTW) life-cycle GHG emissions assessment results for 8 different pathways of MDME II blends compared to other diesel engine fuels. The dark blue bar at the bottom is for CGP production for MDME II cases, and for total WTP process for other fuels (ULSD, Soy Biodiesel, and BioDME).

4.3.8 Engine Operation Results with Michigan DME Blend I

A brief summary on the engine operation results with Michigan DME blend I (DME/DPG/glycerol) with 40 wt. % DME is presented in this section. To state the conclusion first, the engine did operate with Michigan DME blend I without the internal fuel leakage in the fuel pump, which is confirmed from the fact that the fuel supply line pressure of Michigan DME blend I was similar to that of the conventional petroleum-diesel. However, the engine could not maintain the normal engine speed (i.e., 3600rpm) even at idling condition (i.e., a condition with no generator load). This is partially due to the low LHV of the Michigan DME blend I which is not fully compensated by sizing the fuel injector up (i.e., from 3700W-standard injector to

5500W-standard injector). However, it is also suggested that the low cetane number of the blend causes difficulties in proper fuel ignition inside the combustion chamber. Following are the qualitative descriptions of what has been observed during the engine test. The observation is presented in three sections: engine operations with i) a 3700W-standard fuel injector with no intake air temperature boost; ii) a 5500W-standard fuel injector with no intake air temperature boost and; iii) a-5500W standard fuel injector with intake air temperature boost. The result presented here is all at idling condition.

First, with a 3700W-standard fuel injector with no intake air temperature boost, a lower injector nozzle opening pressure increased the amount of fuel injected into the combustion chamber, which, in turn, resulted in a moderate increase in engine speed: from 900rpm at 200bar injection pressure through 1100rpm at 150bar to 1500rpm at 100bar. However, despite the increase in the engine speed, the frequency of misfiring or incomplete firing was higher at lower injector nozzle opening pressure. At the same time, when a complete combustion happens for a lower injection pressure condition, the combustion peak pressure was higher (~60bar) than normal (45-50bar), which made the engine operation generally more unstable and noisy. It is suggested that the lower injector nozzle opening pressure worsens the quality of atomization of the fuel, thus resulting in poor ignition in most of the combustion cycles. Then, the unburned fuel or hydrocarbons from the incomplete combustion cycles burn during the next combustion cycle, thus making the combustion peak pressure higher than normal and engine operations more unstable.

Second, with a 5500W-standard fuel injector with no intake air temperature boost, the engine speed increased by about 300rpm from the 3700W-standard fuel injector counterpart. The difference in engine speed due to the injector nozzle opening pressure was maintained the same with the upgraded fuel injector as the 3700W-standard fuel injector counterpart. It is suggested that the use of the fuel injector with greater injector nozzle diameter partially compensates for the lack of fuel energy flow, but the degree of compensation is not enough.

Third, with a 5500W-standard fuel injector with boosted intake air temperature, the engine speed generally increased with increasing intake air temperature. As compared to the case with no intake air temperature boost (1500rpm at injection pressure of 150 bar), the engine speed was improved up to 2400rpm when the intake air temperature was boosted to be around 70ºC. This suggests that the low engine speed is significantly related to the low cetane number of the Michigan DME I blend, which seems to be partially improved by increasing the intake air temperature.

4.4. Summary and Conclusions

Two novel, stable DME blends (i.e., Michigan DME I and II) of which viscosity is improved up to the level of conventional petroleum-based diesel oils (i.e., ~1.9cSt at 40ºC) are developed in this work to expand the adoption of DME in CI engines without intensive modifications to the fuel injection system. Michigan DME blend I is based on blending DME, glycerol, and DPG while Michigan DME blend II is based on blending DME, glycerol, and PG. Both of the Michigan DME blends are verified to achieve No.1 or No.2 diesel oil viscosity levels with 40-50 wt. % of DME in the blends, which is the highest ratio of DME in a mixture reported by far. The MDME blends exhibit such high oxygen mass content that they are expected to guarantee soot-free emissions (>30 wt. % oxygen content). Furthermore, the blends maintain the non-toxicity and non-carcinogenicity which were the main merits of DME over petroleum-based diesel or some of the other diesel alternative fuels such as methanol. All of the molecular components of the MDME blends can be produced from renewable feedstocks at large scale with low cost with significant reduction in WTW GHG emissions as compared to the petroleum-based diesel (e.g., 50.2% reduction at best-case scenario). Throughout the WTW production and use of MDME blends, the crude glycerol production process, the glycerol purification process, and the PG production process are found to be the three most important processes determining the final life-cycle performance of the blends. Developing feedstocks for glycerol production that have less land use change impact (e.g., algae) and employing more energy efficient and less carbon intensive glycerol purification process, and less carbon intensive hydrogen for PG production will further improve the life-cycle GHG emissions from the blends. Although the reduction in WTW GHG emissions per unit mass or energy of MDME blends is less significant than neat DME, the practical carbon emissions benefit from the adoption of the blends in CI engines can be more significant than that of the neat DME since MDME blends are expected to be adopted in "pre-existing" CI engines with moderate modifications to the fuel injection system, which is not possible for the neat DME.

Future work is recommended to be focused on verifying the operation of the CI engines with Michigan DME blends. The improvement on fuel injection system durability with the blends should be verified based on measurable parameters. One of the options could be comparing the wear scar diameter on important reciprocating parts in the fuel injection system (i.e., pump plunger) with neat DME and the Michigan DME blends. Ignition of the blends in combustion chamber must also be verified since the blends contain glycols and glycerol which are known to have very low cetane number. The preliminary engine test conducted in the current work suggested that the Michigan DME blend must be applied to a fuel injection system with higher injection pressure to achieve better atomization, and larger injector nozzle diameter to fully compensate for the lower LHV of the blend. The engine test also indicated that boosted intake air temperature can compensate for the lower CN of the blend, thus resulting in better engine operations. Thus, an engine with a common-rail type fuel injection system with turbocharged air-intake system is recommended to test the Michigan DME Blend in future. Other disadvantages of using neat DME such as low LHV or elastomer swelling issue with Viton could also be checked with the blends developed here to see if the blends will resolve these issues.

4.5 References

[1] Alauddin, Z.; Lahijani, P.; Mohammadi, M.; Gasification of lignocellulosic biomass in fluidized beds for renewable energy development: A review, *Renewable and Sustainable Energy Reviews*, **2010**, 14, 2852-2862.

[2] Gordillo, G.; Annamalai, K. Gasification of coal and dairy manure with air-steam as oxidizing agent, ASME-JSME Thermal Engineering Summer Heat transfer conference, July8-12, 2007, Vancouver, British Columbia, Canada, HT2007-32128.

[3] Wu, H.; Hanna, M.; Jones, D. Fluidized-bed gasification of dairy manure by Box–Behnken Design, *Waste Management & Research*, **2012**, 30, 506-511.

[4] Fernandez-Lopez, M.; Pedroche, J.; Valverde, J.L.; Sanchez-Silva, L. Simulation of the gasification of animal wastes in a dual gasifier using Aspen Plus, *Energy Conversion and Management*, **2017**, 140, 211-217.

[5] Kohn, M.; Castaldi, M.; Farrauto, R. Auto-thermal and dry reforming of landfill gas over a Rh/γAl2O3 monolith catalyst, *Applied Catalysis B Environmental*, **2010**, 94, 125-133.

[6] Yang, L.; Ge, X.; Wan, C.; Yu, F.; Li, Y. Progress and perspectives in converting biogas to transportation fuels, *Renewable and Sustainable Energy Review*, **2014**, 40, 1133-1152.

[7] Lee, U.; Han, J.; Wang, M.; Ward, J.; Hicks, E.; Goodwin, D.; Boudreaux, R.; Hanarp, P.; Salsing, H.; Desai, P.; Varenne, E.; Kilntbom, P.; Willems, W.; Winkler, S.; Mass, H.; De Kleine, R.; Hansen, J.; Shim, T.; Furusjo, E.; Well-to-Wheels Emissions of Greenhouse Gases and Air Pollutants of Dimethyl Ether from Natural Gas and Renewable Feedstocks in

Comparison with Petroleum Gasoline and Diesel in the United States and Europe, SAE Technical Paper (2016), 2016-01-2209.

[8] Olah, G.; Goeppert, A.; Surya Prakash, G. Chemical Recycling of Carbon Dioxide to Methanol and Dimethyl Ether: From Greenhouse Gas to Renewable, Environmentally Carbon Neutral Fuels and Synthetic Hydrocarbons, *Journal of Organic Chemistry*, **2009**, 74, 487-498.

[9] Pontzen, F.; Liebner, W.; Gronemann, V.; Rothaemel, M.; Ahlers, B. CO2-based methanol and DME – Efficient technologies for industrial scale production, *Catalysis Today*, **2011**, 171, 242-250.

[10] Centi, G.; Perathoner, S. Opportunities and prospects in the chemical recycling of carbon dioxide to fuels, *Catalysis Today*, **2009**, 148, 191-205.

[11] Park, S.; Lee, C. Combustion performance and emission reduction characteristics of automotive DME engine system, *Progress in Energy and Combustion Science*, **2013**, 39, 147-168.

[12] Semelsberger, T.; Borup, R.; Greene, H.; Dimethyl ether (DME) as an alternative fuel, *Journal of Power Sources*, **2006**, 156, 497-511.

[13] DuPont, *Robust summary for Dimethyl Ether;* report to environmental protection agency (EPA); Dupont Safety, Health, and Environment Commitment Excellence Center, 11 Octover 2000.

[14] Fleisch, T.; McCarthy, C.; Basu, A.; Udovich, C.; Charbonneau, P.; Slodowske, W.; Mikkelsen, S-E. A New Clean Diesel Technology: Demonstration of ULEV Emissions on a Navistar Diesel Engine Fueled with Dimethyl Ether, SAE Technical Paper (1995), 950061.

[15] Kapus, P.; Ofner, H. Development of Fuel Injection Equipment and Combustion System for Dl Diesels Operated on Dimethyl Ether, SAE Technical Paper (1995), 950062.

[16] Hansen, J.; Voss, B.; Joensen, F.; Siguroardottir, I. D. Large Scale Manufacture of Dimethyl Ether - a New Alternative Diesel Fuel from Natural Gas, SAE Technical Paper (1995), 950063.

[17] Sorenson, S.C.; Mikkelsen, S-E. Performance and Emissions of a 0.273 Liter Direct Injection Diesel Engine Fuelled with Neat Dimethyl Ether, SAE Technical Paper (1995), 950064.

[18] Chen, K-C.; Dewitte, K.; Cheng, W. K. Fuel Effects and Enrichment Effects on Engine Starting and Warm-Up Behavior, SAE Technical Paper (1995), 950065.

[19] McCandless, J.; Li, S. Development of a Novel Fuel Injection System (NFIS) for Dimethyl Ether-and Other Clean Alternative Fuels, SAE Technical Paper (1997), 970220.

[20] Sivebaek, I.;Sorenson, S. Dimethyl Ether (DME) – Assessment of Lubricity Using the Medium Frequency Pressurised Reciprocating Rig Version 2 (MFPRR2), SAE Technical Paper (2000), 2000-01-2970.

[21] Sivabaek, I.; Sorenson, S.; Jakobsen, J. Dimethyl Ether (DME) – Assessment of Viscosity Using the New Volatile Fuel Viscometer (VFVM), SAE Technical Paper (2001), 2001-01-2013.

[22] Bhide, S.; Morris, D.; Leroux, J.; Wain, K.; Perez, J.; Boehman, A. Characterization of the Viscosity of Blends of Dimethyl Ether with Various Fuels and Additives, *Energy & Fuels*, **2003**, 17, 1126-1132.

[23] *DIPPR project 801*: Design Institute for Physical Properties (DIPPR)-Sponsored by American Institute of Chemical Engineers (AICHE), Last updated September 7th 2019, https://app.knovel.com/web/toc.v/cid:kpDIPPRPF7/viewerType:toc/root_slug:dippr-project-801-full/url_slug:dippr-project-801-full/ (Accessed on July 14th 2020).

[24] ASTM D975-20a. “Standard Specification for Diesel fuel”.

[25] McCandless, J.; Teng, H.; Schneyer, J. Development of a Variable-Displacement, Rail-Pressure Supply Pump for Dimethyl Ether, SAE Technical Paper (2000), 2000-01-0687.

[26] Xu, S.; Wang, Y.; Zhang, X.; Zhen, X.; Tao, C. Development of a novel common-rail type Dimethyl ether (DME) injector, *Applied Energy*, **2012**, 94, 1-12.

[27] Wain, K., A study of alternative diesel fuel lubricity, deposit formation, and material compatibility: Dimethyl Ether, biodiesel and ultra-low sulfur diesel fuels, PhD Thesis, Pennsylvania State University, State College, PA, May 2004.

[28] *Glycerol*; MSDS No. G9012; Sigma-Aldrich; St. Louis, MO., January, 2020.

[29] Quispe, C.; Coronade, C.; Carvalho Jr., J.; Glycerol: Production, consumption, prices, characterization and new trends in combustion, *Renewable and Sustainable Energy Reviews***,** **2013**, 27, 475-493.

[30] Chen, R.; Qin, Z.; Han, J; Wang, M.; Taheripour, F.; Tyner, W.; O’Connor, D.; Duffield, J. Life cycle energy and greenhouse gas emission effects of biodiesel in the United States with induced land use change impacts, *Bioresource Technology*, **2018**, 251, 249-258.

[31] Chen, B.; Chi, C. Process development and evaluation for algal glycerol production, *Biotechnology and Bioengineering*, **1981**, 23, 1267-1287.

[32] Chitlaru, E.; Pick, U. Regulation of Glycerol Synthesis in Response to Osmotic Changes in Dunaliella, *Plant Physiology*, **1991,** 96, 50-60.

[33] Chen, H.; Jiang, J., Osmotic responses of Dunaliella to the changes of salinity, *Journal of Cellular Physiology*, **2009**, 219, 251-258.

[34] Segur, J.; Oberstar, H. Viscosity of Glycerol and Its Aqueous Solutions, *Industrial and Engineering Chemistry*, **1951**, 43, 2117-2120.

[35] Westbrook, C.; Pitz, W.; Curran, H.; Chemical Kinetic Modeling Study of the Effects of Oxygenated Hydrocarbons on Soot Emissions from Diesel Engines, *Journal of Physical Chemistry A*, **2006**, 110, 6912-6922.

[36] Boot, M.; Frijters, P.; Luijten, C.; Somers, B.; Baert, R.; Donkerbroek, A.; Klein-Douwel, R.; Dam, N. Cyclic Oxygenates: A New Class of Second-Generation Biofuels for Diesel Engines?, *Energy & Fuels*, **2009**, 23, 1808-1817.

[37] Boot, M.; Frijters, P.; Klein-Douwel, R.; Baert, R. Oxygenated Fuel Composition Impact on Heavy-Duty Diesel Engine Emissions, SAE Technical Paper (2007), 2007-01-2018.

[38] Biddy, M.; Scarlata, C.; Kinchin, C.; *Chemicals from Biomass: A Market Assessment of Bioproducts with Near-Term Potential*; NREL/TP-5100-65509; National Renewable Energy Laboratory (NREL): Golden, CO, March 2016.

[39] Dunn, J.; Adom, F.; Sather, N.; *Life-cycle Analysis of Bioproducts and Their Conventional Counterparts in GREET*; ANL/ESD-14/9 Rev.; Argonne National Laboratory: Lemont, IL, September 2015.

[40] Adom, F.; Dunn, J.; Han, J.; Sather, N. Life-Cycle Fossil Energy Consumption and Greenhouse Gas Emissions of Bioderived Chemicals and Their Conventional Counterparts, *Environ. Sd. Technol.*, **2014**, 48, 14624-14631.

[41] Globally Harmonized System of Classification and Labelling of Chemicals (GHS): 8th Revised Edition, Classification and labelling summary tables, DOI: https://doi.org/10.18356/b02cb806-en, 2019.

[42] Kuramochi, H.; Maeda, K.; Osako, M.; Nakamura, K.; Sakai, S. Superfast Transesterification of Triolein Using Dimethyl Ether and a Method for High-Yield Transesterification, *Ind. Eng. Chem. Res.*, **2008**, 47, 10076-10079.

[43] Maeda, K.; Kuramochi, H.; Asakuma, Y.; Fukui, K.; Tsuji, T.; Osako, M.; Sakai, S. De-emulsification of mixtures containing glycerin and fatty acid methyl ester promoted by dimethyl ether co-solvent, *Chemical Engineering Journal*, **2011**, 169, 226-230.

[44] Kaas, M.; Daw, C.; Compatibility of Dimethyl Ether (DME) and Diesel Blends with Fuel System Polymers: A Hansen Solubility Analysis Approach, SAE Technical Paper (2016), 2016-01-0835.

[45] Hansen, C. M. Chapter 1: Solubility Parameters – An Introduction, *Hansen Solubility Parameters: A User's Handbook*, 2nd Ed.; CRC Press: Boca Raton, FL. June 2007.

[46] O'Brien, J. Precise measurement of liquid bulk modulus, Master's Thesis, Pennsylvania State University: State College, PA, March 1963.

[47] ASTM D446-12. "Standard Specifications and Operating Instructions for Glass Capillary Kinematic Viscometers".

[48] Prieto, N.; Souza, T.; Egas, A.; Ferreira, A.; Lobo, L.; Portugal, A. Liquid glycerol: Experimental densities at pressures of up to 25 MPa, and some derived thermodynamic properties, *J. Chem. Thermodynamics*, **2016**, 101, 64-77.

[49] Sagdeev, D.; Fomina, M.; Abdulagatov, I. Density and viscosity of propylene glycol at high temperatures and high pressures, *Fluid Phase Equilibria*, **2017**, 450, 99-111.

[50] Ihmels, E.; Lemmon, E. Experimental densities, vapor pressures, and critical point, and a fundamental equation of state for dimethyl ether, *Fluid Phase Equilibria*, **2007**, 260, 36-48.

[51] Huo, H.; Wang, M.; Bloyd, C.; Putsche, V. Life-Cycle Assessment of Energy Use and Greenhouse Gas Emissions of Soybean-Derived Biodiesel and Renewable Fuels, *Environ. Sci. Technol.*, **2009**, 43, 750-756.

[52] Omni Tech International, *Life Cycle Impact of Soybean Production and Soy Industrial Products*; Technical report for The United Soybean Board by Omni Tech International: Midland, MI, February, 2010.

[53] Nanda, MR.; Yuan, Z.; Qin, W.; Poirier, M.; Chunbao, X. Purification of Crude Glycerol using Acidification: Effects of Acid Types and Product Characterization, *Austin Journal of Chemical Engineering*, **2014**, 1, 1-7.

[54] Rodriguez-Kabana, R.; Walker, R. Treated Biodiesel Glycerin. US 2008/0214679 A1, September 4th, 2008.

[55] Aiken, J. Purification of Glycerin, U. S. Patent 7126032 B1, October 24th, 2006.

[56] Manosak, R.; Limpattayanate, S.; Hunsom, M. Sequential-refining of crude glycerol derived from waste used-oil methyl ester plant via a combined process of chemical and adsorption, *Fuel Processing Technology*, **2011**, 92, 92-99.

[57] Clark, C.; Han, J.; Burnham, A.; Dunn, J.; Wang, M. *Life-Cycle Analysis of Shale Gas and Natural Gas*; ANL/ESD/11-11; Argonne National Laboratory: Lemont, IL. December 2011.

[58] Johnson, M.C.; Palou-Rivera, I.; Frank, E.D. Energy consumption during the manufacture of nutrients for algae cultivation, *Algal research*, **2013**, 2, 426-436.

[59] Lampert, D.J.; Cai, H.; Wang, Z.; Keisman, J.; Wu, M.; Han, J.; Dunn, J.; Sullivan, J.; Elgowainy, A.; Wang, M. *Development of a Life Cycle Inventory of Water Consumption Associated with the Production of Transportation Fuels*; ANL/ESD-15/27; Argonne National Laboratory: Lemont, IL. Octover 2015.

[60] Cai, H.; Han, J.; Forman, G.; Divita, V.; Elgowainy, A.; Wang, M. *Analysis of petroleum refining energy efficiency of U. S. refineries*, Argonne National Laboratory: Lemont, IL. October, 2013.

[61] Wang, Z.; Benavides, P.T.; Dunn, J.; Cronauer, D.C. *Development of GREET Catalyst Module*; ANL/ESD-14/12 Rev,; Argonne National Laboratory: Lemont, IL. August 2015.

[62] Cai, H.; Wang, M.; Elgowainy, A.; Han, J. *Updated Greenhouse Gas and Criteria Air Pollutant Emission Factors and Their Probability Distribution Functions for Electric Generating Units*; ANL/ESD/12-2; Argonne National Laboratory: Lemont, IL. May 2012.

[63] Boehman, A.L.; Morris, D.; Szybist, J. The Impact of the Bulk Modulus of Diesel Fuels on Fuel Injection Timing, *Energy & Fuels*, **2004**, 18(6), 1877-1882.

[64] Hansen, C. M. Appendix A, *Hansen Solubility Parameters: A User's Handbook*, 2nd Ed.; CRC Press: Boca Raton, FL. June 2007.

[65] Machado, P.; Walter, A.; Cunha, M. Bio-based propylene production in a sugarcane biorefinery: A techno-economic evaluation for Brazilian conditions, *Biofuels, Bioprod. Bioref.*, **2016**, 10, 623-633.

[66] Bloom, P.; Venkitasubramanian, P. Method for producing bioderived dipropylene and tripropylene glycols without propylene oxide, United States Patent, US20140107380A1, 2014.

[67] Okoye, P.; Abdullah, A.; Hameed, B. Synthesis of oxygenated fuel additives via glycerol esterification with acetic acid over bio-derived carbon catalyst, *Fuel*, **2009**, 209, 538-544.

[68] Zhang, J.; He, D.; Synthesis of glycerol carbonate and monoacetin from glycerol and carbon dioxide over Cu catalysts: the role of supports, *J. Chem. Technol. Biotechnol.*, **2015**, 90, 1077-1085.

[69] Rastegari, H.; Ghaziaskar, H.; Yalpani, M. Valorization of Biodiesel Derived Glycerol to Acetins by Continuous Esterification in Acetic Acid: Focusing on High Selectivity to Diacetin and Triacetin with No Byproducts, *Ind. Eng. Chem. Res.,* **2015**, 54, 3279-3284.

[70] Kuramochi, H.; Maeda, K.; Osako, M.; Nakamura, K.; Sakai, S. Superfast Transesterification of Triolein Using Dimethyl Ether and a Method for High-Yield Transformation, *Ind. Eng. Chem. Res.,* **2008**, 47, 10076-10079.

Chapter 5

Experimental Measurement of the Isothermal Bulk Modulus and Speed of Sound of Conventional and Alternative Jet Fuels

5.1 Introduction

The bulk modulus of compressibility and the speed of sound of a fuel are important physical properties that directly affect fuel injection behavior in internal combustion engines. Particularly, in mechanically-driven fuel injection systems, the difference of bulk modulus and speed of sound in different fuels can cause unintended shifts in the start of injection timing, which can impede the optimal operation, performance and exhaust emissions of internal combustion engines.[1-5]

Currently, about 30% of the ground vehicles and ground equipment used by the United States Army operate with a mechanically-driven fuel injection system called a "pump-line-nozzle" system[6], and these vehicles are operating on jet fuel, an unconventional fuel that has fairly different physical properties from conventional diesel fuel.[7] The operation of compression-ignition engines on jet fuel requires the re-adjustment of the injection parameters based on the physical properties of jet fuel,[8] which necessitates the thorough characterization on the physical properties of the jet fuels used. Furthermore, various new alternative jet fuels are recently under development and are being introduced to the market, and these fuels have limited published information on their physical properties. These new fuels include: Farnesane (2,6,10-trimethyldodecane), Hydrogenated renewable jet fuel (HRJ), and Alcohol-to-jet fuel (ATJ). These alternative jet fuels are reported to have 55-85% well-to-wheels (WTW) GHG emissions reduction as compared to the petroleum-based jet or diesel.[9] Thus, the wider adoption of these alternative jet fuels in the U. S. Army ground vehicles with pump-line-nozzle type fuel injection system will help reducing GHG emissions from U. S. Army fleet operations. Considering these facts altogether, the characterization of jet fuel is very timely and needed at this moment.

In addition, due to the elevated pressure and temperature applied to liquid fuels in a pump-line-nozzle type fuel injection system (>150bar, >45ºC), investigating the impact of the elevated pressure and temperature on the bulk modulus of compressibility and the speed of sound of these jet fuels is also important. Bridgman presented the general impact of pressure and temperature on the bulk modulus of different hydrocarbon molecular species[10], which has been confirmed by many other studies: the bulk modulus and speed of sound can significantly increase with elevated pressure and decreased temperature.[11-15] Thus, the characterization of the jet fuels mentioned earlier at elevated pressure and temperature range, not to mention at standard state, is also needed.

Thus, this work focuses on measurement of the bulk modulus of compressibility and of the speed of sound of the six different jet fuels that could potentially be applied to military ground vehicles. The isothermal bulk modulus (B_T) of three petroleum-based jet fuels (i.e., POSF 4658, POSF 6169, POSF 10325) is measured at 313K (0.1-27.7MPa), and the isothermal bulk modulus of three alternative jet fuels (i.e., Farnesane, Hydrogenated renewable jet fuel derived from camelina (HRJC), Alcohol to jet (ATJ)) is measured at 308K (0.1-27.7MPa). The specific heat ratio (γ) of the selected test fuels is calculated by comparing the isothermal bulk modulus measurement obtained from the current study and the isentropic bulk modulus (B_s) values obtained from other published work. We also measured the pseudo-isothermal speed of sound (a_p) of the six jet fuels (i.e., POSF 4658, POSF 6169, POSF 10325, Farnesane, HRJC, 50/50 wt. % blend of ATJ and Farnesane) and the baseline diesel (i.e., No. 2 ultra-low-sulfur diesel (ULSD)) in a pump-line-nozzle type fuel injection system of a single cylinder compression-ignition engine via a pair of fuel line pressure sensors. The pseudo-isothermal coefficient (α) of the fuel injection processes corresponding to different test fuels is calculated by comparing the pseudo-isothermal speed of sound measurement and the isothermal speed of sound (a_T) calculated from the isothermal bulk modulus measurement. Lastly, the isentropic speed of sound (a_s) of the selected test fuels is estimated from the pseudo-isothermal speed of sound measurement by applying the pseudo-isothermal coefficient and specific heat ratio as conversion factors.

5.2 Experimental

5.2.1 Difference between Isothermal and Isentropic Bulk Modulus

The bulk modulus of compressibility is distinguished into two different sub-types depending on the thermodynamic process under which density increase of a material occurs: (1) isentropic bulk modulus (B_s); and (2) isothermal bulk modulus (B_T). The isothermal bulk modulus, the sub-type measured in this work, is less commonly reported in the field of study. Furthermore, there are few published resources that articulate the fundamental difference between isentropic and isothermal bulk moduli and how much those two sub-types are different for hydrocarbon molecular species and fuels in practice. Thus, we articulate the fundamental and practical difference between isentropic bulk modulus and isothermal bulk modulus here. In so doing, measurement data of the two different sub-types of the bulk modulus can be compared.

The mathematical definition of the isentropic bulk modulus and isothermal bulk modulus is presented in Equations 5.1 and 5.2, respectively, where B is bulk modulus, γ is specific heat ratio ($\frac{C_p}{C_v}$), ρ is density, v is specific volume, a is speed of sound, and κ is compressibility.[5,16] The subscripts "S" and "T" refer to the isentropic and isothermal property, respectively.

$$B_S \equiv \rho \left(\frac{\partial P}{\partial \rho}\right)_S = -v \left(\frac{\partial P}{\partial v}\right)_S = \rho {a_S}^2 = \frac{1}{\kappa_S} \qquad \text{(Eq. 5.1)}$$

$$B_T \equiv \rho \left(\frac{\partial P}{\partial \rho}\right)_T = -v \left(\frac{\partial P}{\partial v}\right)_T = \rho {a_T}^2 = \frac{1}{\kappa_T} = \frac{B_S}{\gamma} \qquad \text{(Eq. 5.2)}$$

As shown in Equation 5.2, isothermal bulk modulus is the same as the isentropic bulk modulus divided by specific heat ratio. For hydrocarbon molecular species, the specific heat ratio is very different from unity even in the liquid-phase, which leads to a significant difference between the isentropic and isothermal bulk moduli.[17] Furthermore, the value of γ also differs significantly for different molecular species. Appendix B shows how and why the value of γ varies by molecular structure and molecular weight based on different thermophysical properties of hydrocarbon molecular species in the liquid phase.

5.2.2 Instrument and Measurement Methods

5.2.2.1 Isothermal Bulk Modulus (B_T) Measurement

Figures 5.1a – 5.1c and 5.2 show the instrument used for isothermal bulk modulus measurements. This experimental instrument is identical to that used in previous work.[3,5,18] The details of the instrument are well-described therein. Thus, a brief explanation of the instrument and measurement procedure is presented here.

The isothermal bulk modulus is measured as follows. First, a liquid sample is injected into a pycnometer (Figure 5.1a) and the pycnometer is placed into a high-pressure vessel (Figure 5.1b).

Then, the high-pressure vessel is placed into a bath filled with water (Figure 5.1c-(2)) and the water temperature is maintained constant within ±0.3°C. High-pressure helium gas (Figure 5.1c-(1)) is used to raise the pressure inside the high-pressure vessel. From 0.1MPa to 6.3MPa (0-900psig), the pressure is directly controlled by the pressure regulator on the helium gas cylinder. From 6.3MPa to 27.7MPa (900-4000psig), a hydraulic oil pump (Figure 5.1c-(3)) is used to control the pressure inside the piston bomb (Figure 5.1c-(4)) which is connected to the high-pressure vessel. As the pressure inside the high-pressure vessel is increased, the volume of the liquid sample inside the pycnometer contracts. When the meniscus of the liquid sample hits each graduation mark of the pycnometer, the corresponding pressure is measured. The pressure and volume measured are used to calculate the isothermal bulk modulus. The overall pressure range of the measurement was 0.1-27.7MPa (0-4000psig).

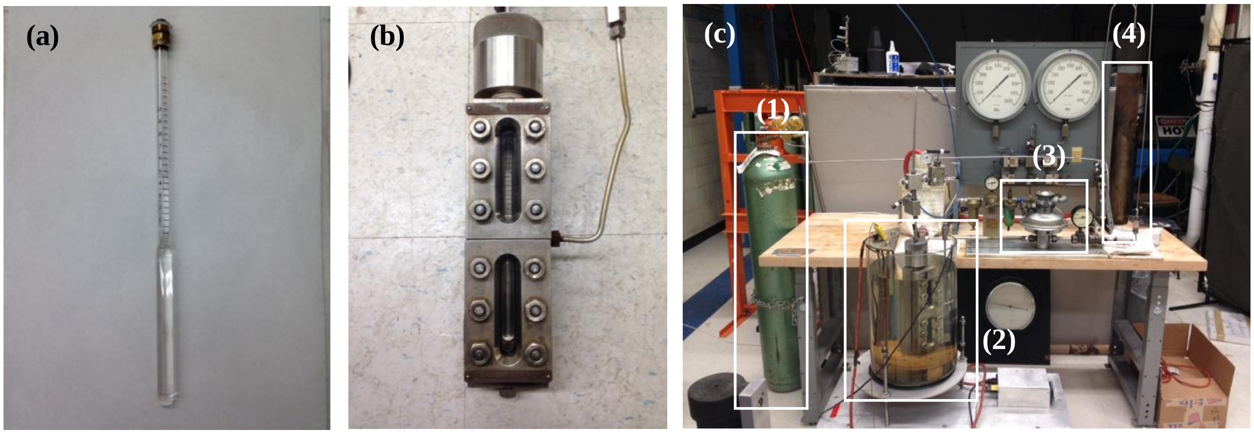

Figure 5.1. (a) Pycnometer (b) High-pressure vessel (Modified 21-R-30 Jerguson Gauge, operation range: 0-5000psig) (c) Isothermal bulk modulus measurement setup: (1) Helium gas cylinder, (2) Water bath, (3) Sprague hydraulic oil pump, (4) Piston bomb.

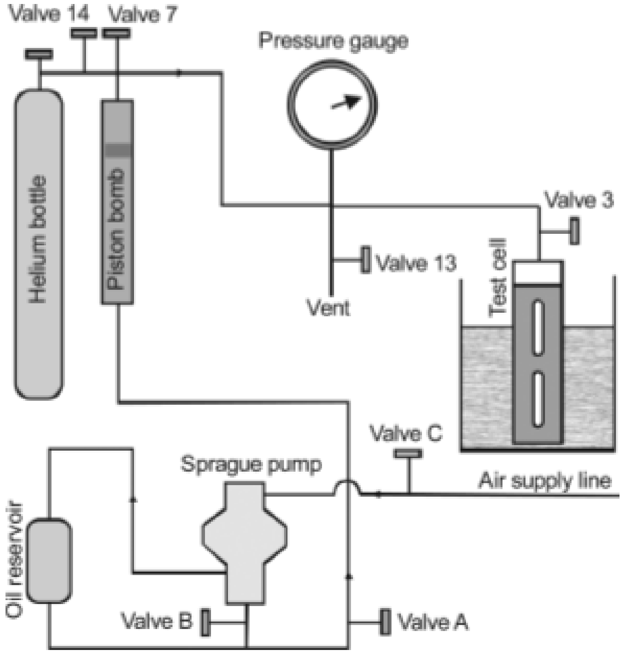

Figure 5.2 Schematic of the isothermal bulk modulus measurement instrument. (From Lapuerta et al.)[5]

Based on the pressure and volume measured, the bulk modulus can be calculated in two different ways: tangent bulk modulus (B_{tan}); and secant bulk modulus (B_{sec}). Tangent bulk modulus is calculated by using two adjacent measurement points whereas secant bulk modulus is calculated by using one measurement point and a reference point. Equations 5.3 and 5.4 show the definition of the tangent bulk modulus and secant bulk modulus, respectively.[5] Subscript "i" means each measurement point at which the volume and pressure are measured, while subscript "*ref*" means the reference point.

$$B_{tan} = \left(\frac{\rho_i+\rho_{i+1}}{2}\right)\frac{P_{i+1}-P_i}{\rho_{i+1}-\rho_i} = -\left(\frac{v_i+v_{i+1}}{2}\right)\frac{P_{i+1}-P_i}{v_{i+1}-v_i} \quad \text{(Eq. 5.3)}$$

$$B_{sec} = \rho_{ref}\frac{P-P_{ref}}{\rho-\rho_{ref}} = -v_{ref}\frac{P-P_{ref}}{v-v_{ref}} \quad \text{(Eq. 5.4)}$$

As expected from Equations 5.3 and 5.4, the tangent bulk modulus gives more accurate value of the bulk modulus at a given pressure than the secant bulk modulus. The secant bulk modulus is the “average” bulk modulus between the reference pressure and the measurement pressure, so it can get gradually more and more off from the real value of the bulk modulus at the given pressure as the pressure measurement gets further from the reference pressure. Thus, there should be an accurate means of readjusting the secant bulk modulus to tangent bulk modulus when dealing with measurement pressure far from the reference pressure.

In this work, due to the limited measurement accuracy of the device, secant bulk modulus is first calculated from the measured pressure and volume. Then, we applied the conversion factor between the secant bulk modulus and tangent bulk modulus at the given pressure to obtain the tangent bulk modulus. The calibration procedure to obtain the conversion factor between the two different bulk modulus properties is as follows.

We selected one of the petroleum-based Jet-A fuels, POSF 4658, as the calibration standard because the National Institute of Standard and Technology (NIST) has provided very accurate liquid density data of this fuel over a wide range of pressure along the isotherm.[19] We used the Tait equation for the compressed liquid density for POSF 4658 established in this work to calculate its isothermal “tangent” bulk modulus. Then, we compared the isothermal tangent bulk modulus to the isothermal “secant” bulk modulus obtained from the current measurement.

Figure 5.3 shows the comparison between the isothermal “secant” bulk modulus measurement of POSF 4658 obtained from the current study and the isothermal “tangent” bulk modulus of POSF 4658 obtained from Outcalt et al.[19] As expected, the discrepancy between two data sets increases at higher pressure. Table 5.1 is presented to show the exact values of the discrepancy between the tangent and secant bulk modulus over the pressure range of 0.1-30MPa.

The isothermal secant bulk modulus presented in Table 5.1 is obtained by using the pressure-dependent linear regression equation presented in Figure 5.3. The secant bulk modulus and tangent bulk modulus agrees within 1% up to 4MPa. However, at 5MPa, the offset between the two properties becomes greater than 1% (1.18%), and becomes 6.4% 30MPa.

For all of the fuels tested in this study, we re-calculated the tangent bulk modulus from the initial secant bulk modulus calculation by using the discrepancy chart shown in Table 5.1. For example, for the calculation of the tangent bulk modulus at 5MPa, we calculated it by adding 1.18% of the secant bulk modulus to its own value. At 30MPa, 6.40% of the secant bulk modulus is added to its own value to obtain the tangent bulk modulus.

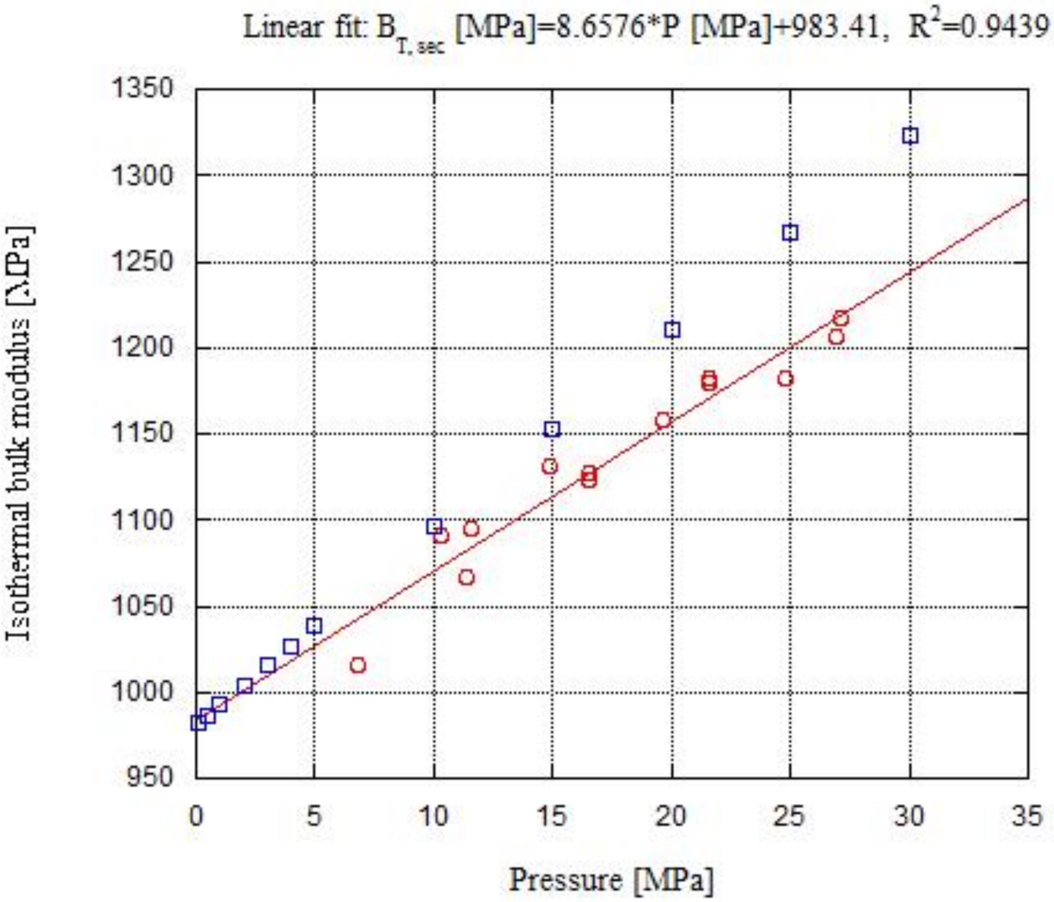

Figure 5.3 Comparison between (○) isothermal secant bulk modulus measurement ($B_{T,sec}$) and (□) isothermal tangent bulk modulus ($B_{T,\tan}$) data[19] for POSF 4658. Both data are at T=313K.

Pressure [MPa]	$B_{T,sec}$ (based on the linear regression) [MPa]	$B_{T,tan}$ (Outcalt, et al, 2009) [MPa]	% of discrepancy $(\frac{(B_{T,sec}-B_{T,tan})}{B_{T,sec}} \times 100)$
0.1	984.26	981.98	+0.23
0.5	987.72	986.87	+0.09
1	992.05	992.74	-0.07
2	1000.7	1004.2	-0.36
3	1009.3	1015.8	-0.64
4	1018.0	1027.2	-0.90
5	1026.6	1038.7	-1.18
10	1069.9	1096.1	-2.44
15	1113.2	1153.0	-3.57
20	1156.5	1209.8	-4.61
25	1199.8	1266.3	-5.55
30	1243.1	1322.7	-6.40

Table 5.1 Discrepancy between the isothermal secant bulk modulus measurement and the isothermal tangent bulk modulus data[19] for POSF 4658. Both data are at 313K.

The reference pressure used for the calculation of the secant bulk modulus slightly varied (i.e., 0.1-2.5MPa) for different measurement trials due to the unavoidable inaccuracy of the amount of the sample injected. To set the reference pressure constant as atmospheric pressure, it is required to inject the sample with such an amount that the meniscus of the sample sits right at the graduation mark of the pycnometer. However, because some amount of the injected sample formed a thin liquid film on the pycnometer surface, and was accumulated on top of the meniscus after the sample is pressurized, it was very hard to inject the exact amount of sample for every measurement trial. Therefore, we conducted an experiment to verify that the degree of the variation in reference pressure shown in this study (i.e., 0.1-2.5MPa) does not significantly affect the result of the secant bulk modulus measurement. The experiment is conducted as follows.

For the first measurement for a given sample, if the meniscus of the sample does not exactly sit at the graduation mark of the pycnometer at atmospheric pressure, the pressure is increased until the meniscus hits the closest pycnometer graduation. Then, the corresponding pressure and volume is determined as the reference pressure and reference volume of the first measurement ($P_{ref,1}$ and $v_{ref,1}$ in Equation 5.5). For the second measurement, the measurement is repeated with the same amount of sample in the pycnometer, which guarantees the same reference pressure and reference volume as those of the first measurement ($P_{ref,2}$ and $v_{ref,2}$ in Equation 5.6). Then, the measurement error between the first and second measurement is attributed to the other sources of the experimental error than the variation of the reference pressure (e.g., the inaccuracy in pressure gauge reading, the inaccuracy in reading the volume of the sample due to eye-to-meniscus error). Next, for the third measurement, a small amount of additional sample is injected into the pycnometer so that the reference pressure for the third measurement ($P_{ref,3}$ in Equation 5.7) will be slightly higher than the reference pressure for the first two measurements. Then, the cause of the measurement error between the third and second measurement includes the variation of the reference pressure. Thus, if the measurement error between the third and second measurement is not noticeably greater than the measurement error between the first two measurements, we can say that the variation of the reference pressure does not add significant inaccuracy to the measurement.

$$B_{T,\mathrm{sec1}} = -v_{ref,1}\frac{P-P_{ref,1}}{v-v_{ref,1}} \qquad \text{(Eq. 5.5)}$$

$$B_{T,\mathrm{sec2}} = -v_{ref,2}\frac{P-P_{ref,2}}{v-v_{ref,2}}\text{, } P_{ref,2} = P_{ref,1},\ v_{ref,2} = v_{ref,1} \qquad \text{(Eq. 5.6)}$$

$$B_{T,\mathrm{sec3}} = -v_{ref,3}\frac{P-P_{ref,3}}{v-v_{ref,3}}\text{, } P_{ref,3} \neq P_{ref,1},\ v_{ref,3} = v_{ref,1} \qquad \text{(Eq. 5.7)}$$

Figures 5.4a and 5.4b show the isothermal secant bulk modulus measurement result of two molecular liquid samples (i.e., n-dodecane, iso-cetane) using the measurement method explained above. Symbols represent the measurement points while the lines represent the least-square linear regressions of each measurement. Red solid line is the linear regression of the first measurement, red dotted line is for the second measurement, and the black solid line is for the third measurement. Although we can observe the discrepancy between the third and second measurement, the discrepancy is not greater than the discrepancy between the first two measurements. This means that the slight variation in reference pressure involved in this work does not add significant inaccuracy to the measurement result.

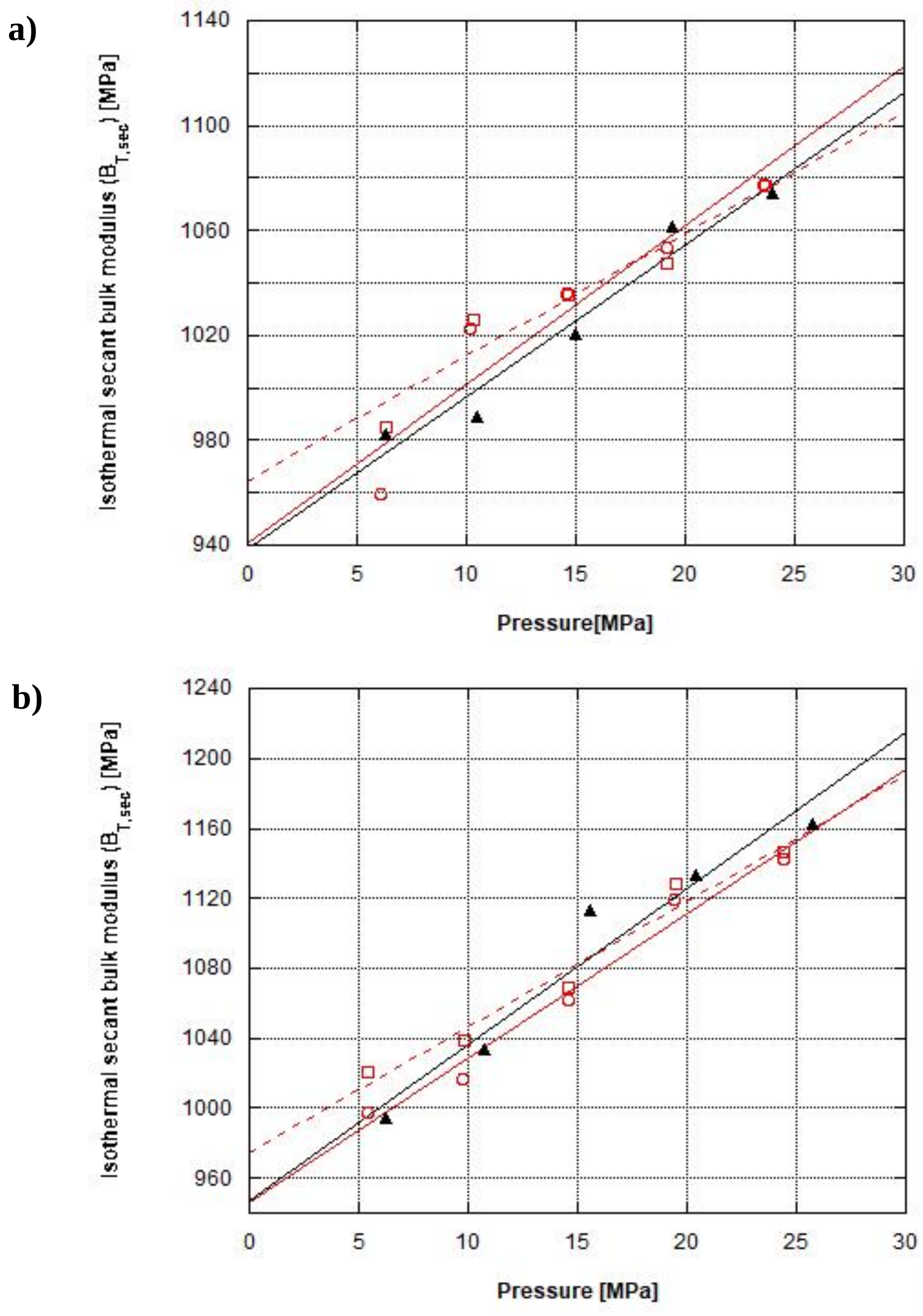

Figure 5.4 Isothermal secant bulk modulus measurement of **(a)** n-dodecane **(b)** iso-cetane. (All measurements are at 313K, (○) 1st measurement, (□) 2nd measurement, (▲) 3rd measurement. For n-dodecane, $P_{ref,1}$=$P_{ref,2}$=1.8MPa, $P_{ref,3}$=2.45MP. For iso-cetane, $P_{ref,1}$=$P_{ref,2}$=0.52MPa, $P_{ref,3}$=2.08MPa.

5.2.2.2 Pseudo-Isothermal Speed of Sound (a_p) Measurement and Isentropic Speed of Sound (a_s) Estimation

Depending on the thermodynamic process that causes the density perturbation in a material, and in turn, the propagation of the perturbed density in a medium, the wave speed in the medium (i.e., $\sqrt{\frac{\partial P}{\partial \rho}}$) can be defined in three different ways, the speed of the density perturbation wave under: (1) an isentropic process (i.e., $\sqrt{\left(\frac{\partial P}{\partial \rho}\right)_s}$); (2) an isothermal process (i.e., $\sqrt{\left(\frac{\partial P}{\partial \rho}\right)_T}$); and (3) a pseudo-isothermal process (i.e., an arbitrary process which is neither isentropic nor isothermal, $\sqrt{\left(\frac{\partial P}{\partial \rho}\right)_p}$). By the rigorous scientific definition, only the speed of the wave under an isentropic process (i.e., $\sqrt{\left(\frac{\partial P}{\partial \rho}\right)_s}$) is defined as the "speed of sound", and the wave speeds relevant to the other thermodynamic processes (i.e., $\sqrt{\left(\frac{\partial P}{\partial \rho}\right)_T}$ and $\sqrt{\left(\frac{\partial P}{\partial \rho}\right)_p}$) are not named with a specific terminology.[20]

In this work, we measured the wave speed under a pseudo-isothermal process (i.e., $\sqrt{\left(\frac{\partial P}{\partial \rho}\right)_p}$) and the measurement is compared to the wave speeds under isothermal (i.e., $\sqrt{\left(\frac{\partial P}{\partial \rho}\right)_T}$) and isentropic processes (i.e., $\sqrt{\left(\frac{\partial P}{\partial \rho}\right)_s}$). This necessitated distinguishing wave speeds under three different thermodynamic processes, and to name each term differently. Despite the fact that the wave speeds under non-isentropic processes are not called the "speed of sound" by the rigorous definition, in this work, we refer to the wave speed under isothermal process as the "isothermal speed of sound (a_T)" and under pseudo-isothermal process as the "pseudo-isothermal speed of sound (a_p)" for the sake of keeping the analogy between the three wave speeds. Consequently, the wave speed under an isentropic process, which is generally accepted as the “speed of sound”, is defined as “isentropic speed of sound (a_s)” in this work.

The pseudo-isothermal speed of sound for the six jet fuels (i.e., POSF 4658, POSF 6169, POSF 10325, Farnesane, HRJC, 50/50 wt. % blend of Farnesane and ATJ) and the baseline diesel fuel (i.e., No.2 ULSD) are measured by using a Yanmar Diesel Genset 3700W (YDG3700EV-6EI) with a single-cylinder, naturally-aspirated, direct-injection, air-cooled, compression ignition engine (engine model: L70V6HJ1C9GAYG). Table 5.2 shows the selected features of the test engine.

Engine model	Yanmar L70V Diesel	Engine weight	41kg
No. of strokes/cycle	4 stroke	Cooling system	Forced air by flywheel fan
No. of cylinders	1	Fuel injection system	Pump-line-nozzle system with direct injection
Bore × Stroke	78 × 67 mm	Fuel injection pump	BOSCH-type with upper lead plunger
Displacement	0.320 L	Fuel injection nozzle	P-size, VCO
Compression ratio	21.1	Fuel injection timing	Default @16°BTDC, controlled by the fuel pump shim thickness (1 degree retarding/+0.1mm)
Continuous rated output	5.8hp (4.3kW) @ 3600rpm	Fuel injection pressure	Default @19.6MPa, Controlled by the fuel injector shim thickness (+1.96MPa/+0.1mm)
Max. rated output	6.4hp (4.8kW) @ 3600rpm	Generator phase	Single-phase
Generator rated output	3.5 AC kVA or 12VDC – 8.3A	Generator frequency	60Hz

Table 5.2 Specification of the Yanmar 3700W Diesel Genset (model: YDG3700EV-6EI)

Figures 5.5 shows the schematic of the experimental setup of the test engine. As shown in Figure 5.5, four signals (i.e., in-cylinder pressure, crank angle, injector needle lift, line pressure) are acquired by an AVL Indimodul high-speed data acquisition system, and analyzed in AVL Indicom software. The in-cylinder pressure is measured by a Kistler 6052B1 piezoelectric pressure-transducer, and an AVL 365.01 crank angle encoder is used for the crank angle measurement. The injector needle lift timing is measured by a Hall-effect sensor prepared by Wolff Controls, and the pressure inside the fuel supply line is measured by a pair of piezoresistive pressure sensors (Kistler 406A3000).

For each test fuel, three different load conditions (i.e., low load (1000W), mid-load (2000W), and midhigh-load (2500W)) are tested while the injector nozzle opening pressure and fuel injection timing are kept constant. Engine speed is also controlled within the range of 3450-3750rpm. Different engine loads are achieved by using a circulation heater (max. power: 3000W) with a variable AC transformer. The temperature of the fuel supply line is measured by a K-type thermocouple, and the fuel supply line temperature is ensured to be stabilized within ±0.5°C during the pseudo-isothermal speed of sound measurement. The fuel flow rate is measured by using a Sartorius weighing scale (capacity: 30kg, accuracy: 1g). The temperature and weighing scale signals are acquired by Labview software with the data acquisition frequency of 1Hz.

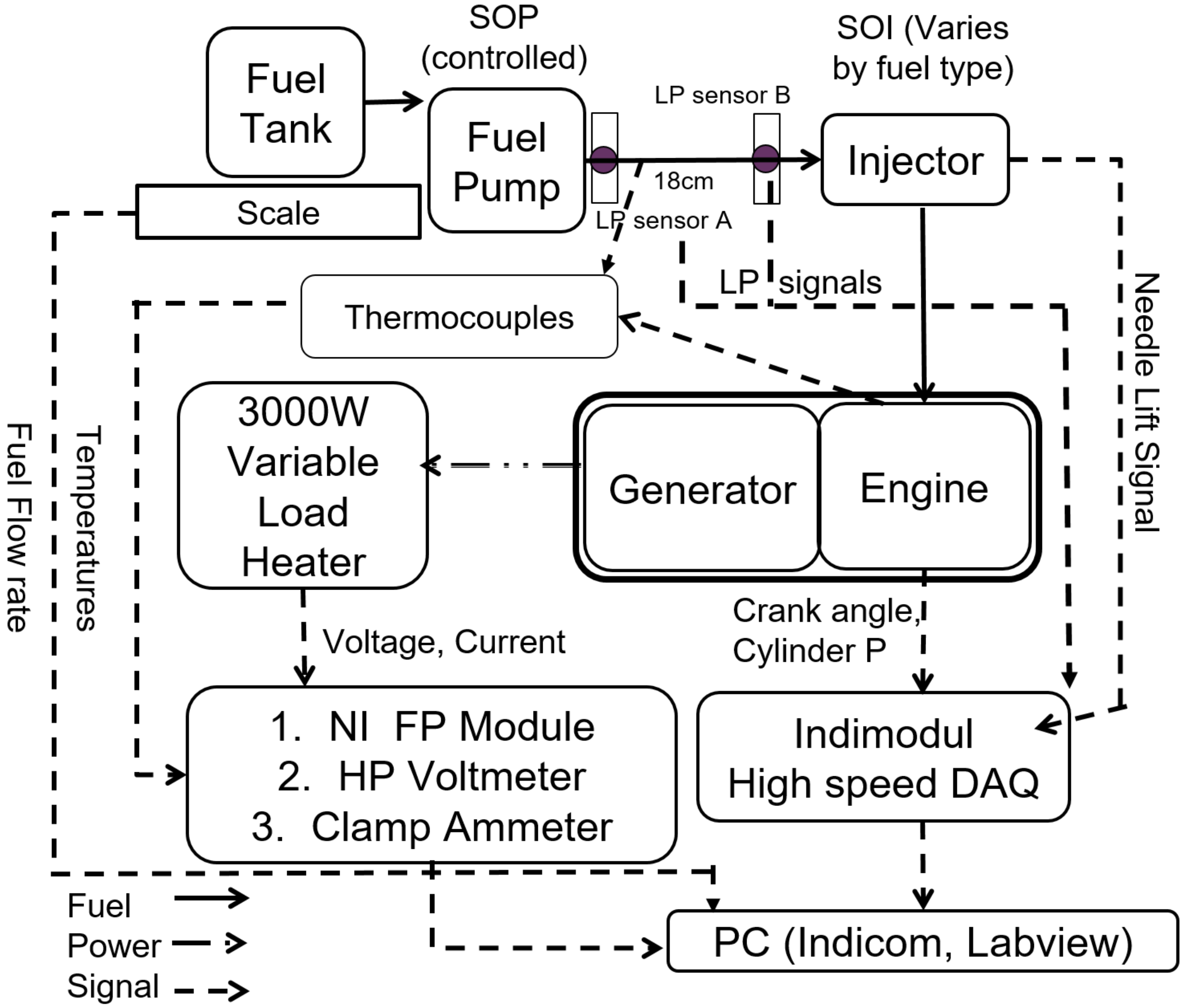

Figure 5.5 Schematic of the Yanmar engine experimental setup

Figure 5.6 shows an example of the line pressure sensor signals. The crank angle at which the gradient of the pressure wave measured by LP sensors A and B becomes greater than “2bar/0.1CA” is defined as “CA_A” and “CA_B”, respectively. Then, the crank angle difference between CA_A and CA_B is defined as “ΔCA_1”. This crank angle difference is converted to the time scale (t_1) by using the engine speed (Equation 5.8). The distance between LP sensors A and B is measured (179.86mm) and denoted as "d_1" in Equation 5.9. Then, the pseudo-isothermal speed of sound (a_p) of the test fuel is calculated by dividing d_1 by t_1 (Equation 5.9).

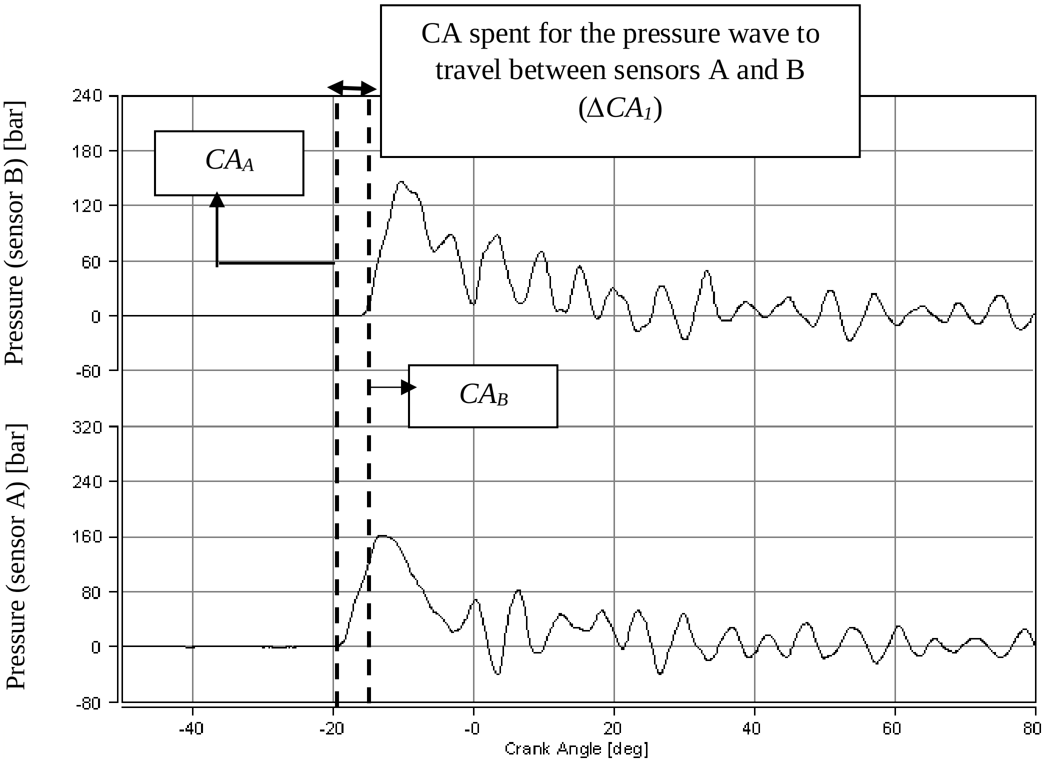

Figure 5.6. Example of line pressure sensor signals (low load, ULSD fuel)

$$t_1 = \frac{\Delta CA_1}{6 \cdot rpm} \quad \text{(Eq. 5.8)}$$

$$a_p = \frac{d_1}{t_1} \quad \text{(Eq. 5.9)}$$

Here, it should be noted that the pseudo-isothermal wave speed calculated by Equation 5.9 is not necessarily the same as the isentropic speed of sound (a_s) because the fuel compression process of the practical fuel injection system generally involves irreversibility. In our case, the fuel supply line was not insulated, and the fuel injection frequency was very high (i.e., ~30Hz). These two factors generated irreversibility respectively by the heat transfer from the fuel supply line to atmosphere and by the friction inside the fuel pump.

Also, the pseudo-isothermal wave speed should not be assumed to be the same as the isothermal speed of sound (a_T). Although the fuel supply line temperature is ensured to be within the range of ±0.5°C during the pseudo-isothermal speed of sound measurement, the data acquisition frequency (1Hz) of the temperature signal was much lower than the fuel injection frequency (30Hz). This leaves the possibility that the fuel compression process happens very fast with a certain amount of temperature increase that can be dissipated within a short period of time which could not be captured by the data acquisition system.

Thus, a reliable conversion method from the pseudo-isothermal speed of sound to the isentropic speed of sound is required. In this work, we calculated the specific heat ratio (γ) and pseudo-isothermal coefficient (α) of each test fuel and used these values to convert pseudo-isothermal speed of sound to the isentropic speed of sound. Figure 5.7 shows the algorithm of this conversion method. First, the isothermal speed of sound (a_T) is calculated by using the isothermal bulk modulus (B_T) measurement and density (ρ) obtained from the reference. Also, the specific heat ratio (γ) is calculated by comparing the isentropic bulk modulus (B_s) value obtained from other published work and the isothermal bulk modulus measurement obtained in the current study. Then, the "pseudo-isothermal coefficient" (α) is calculated by comparing the calculated value of the isothermal speed of sound and pseudo-isothermal speed of sound measurement. Finally, the isentropic speed of sound (a_s) is calculated from the pseudo-isothermal speed of sound by using the specific heat ratio and pseudo-isothermal coefficient.

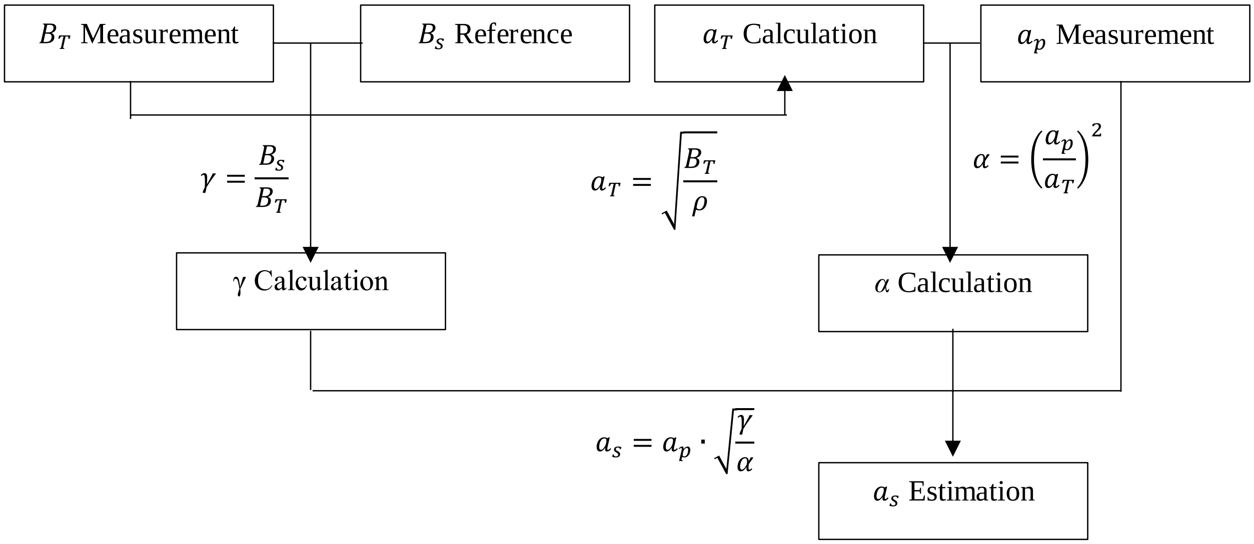

Figure 5.7. Algorithm of the isentropic speed of sound (a_s) estimation from the pseudo-isothermal speed of sound (a_p) measurement

5.2.3 Liquid Samples and Test Matrix

Three different petroleum-based Jet-A and JP-8 fuels (i.e., POSF4658, POSF6169, POSF10325) and three different alternative jet fuels (i.e., Farnesane (POSF10370), HRJC (POSF11714), ATJ (POSF11498)) were provided by the Air Force Research Lab (AFRL) at Wright Patterson Air Force Base (WPAFB). The fuel identification number designated by the AFRL is code-named as “POSF#”. No. 2 ULSD is used as the baseline test fuel for the pseudo-isothermal speed of sound measurement in the Yanmar engine. For the pseudo-isothermal speed of sound measurement of ATJ, instead of applying neat ATJ into the test engine, 50/50 wt. % blend of Farnesane and ATJ is used because the engine could not operate on neat ATJ due to its low cetane number (i.e., CN≈18). Then, the result of the 50/50 wt. % blend of Farnesane and ATJ is used to extrapolate the pseudo-isothermal speed of sound of the ATJ. Table 5.3 summarizes the test fuels and test conditions of this research.

		Isothermal bulk modulus measurement		Pseudo-isothermal speed of sound measurement		
Test fuel category	Test fuel name	Temperature	Pressure	Temperature	Load	Controlled variables
Diesel	No.2 ULSD	-		T=318-338K	Low load (1000W) Mid load (2000W) Mid-high load (2500W)	Pressure (@0.1MPa) Engine speed (3600±150rpm) Fuel injector nozzle opening pressure Fuel injection timing
Petroleum-based Jet-A and JP-8	POSF 4658	313K	0.1-27.7MPa (0-4000psig)			
	POSF 6169					
	POSF 10325					
Alternative jet fuels	Farnesane	308K				
	HRJC					
	ATJ†					

Table 5.3. Test matrix of the isothermal bulk modulus (B_T) measurement and the pseudo-isothermal speed of sound (a_p) measurement. † Neat ATJ is used for the isothermal bulk modulus measurement, and 50/50 wt. % blend of ATJ and Farnesane is used for the pseudo-isothermal speed of sound measurement.

5.2.4 Calibration of the Isothermal Bulk Modulus Measurement Instrument

The bulk modulus instrument is calibrated by using water as the calibration standard. The compressed liquid density of water is calculated based on the isothermal bulk modulus measurement obtained from the current study. Then, the calculated compressed liquid density of water is compared to the water density data obtained from other work.[21,22] As shown in Figure 5.8, the liquid water density calculated from the isothermal bulk modulus measurement agrees very well with the data reported previously, confirming the reliability of the measurement device.

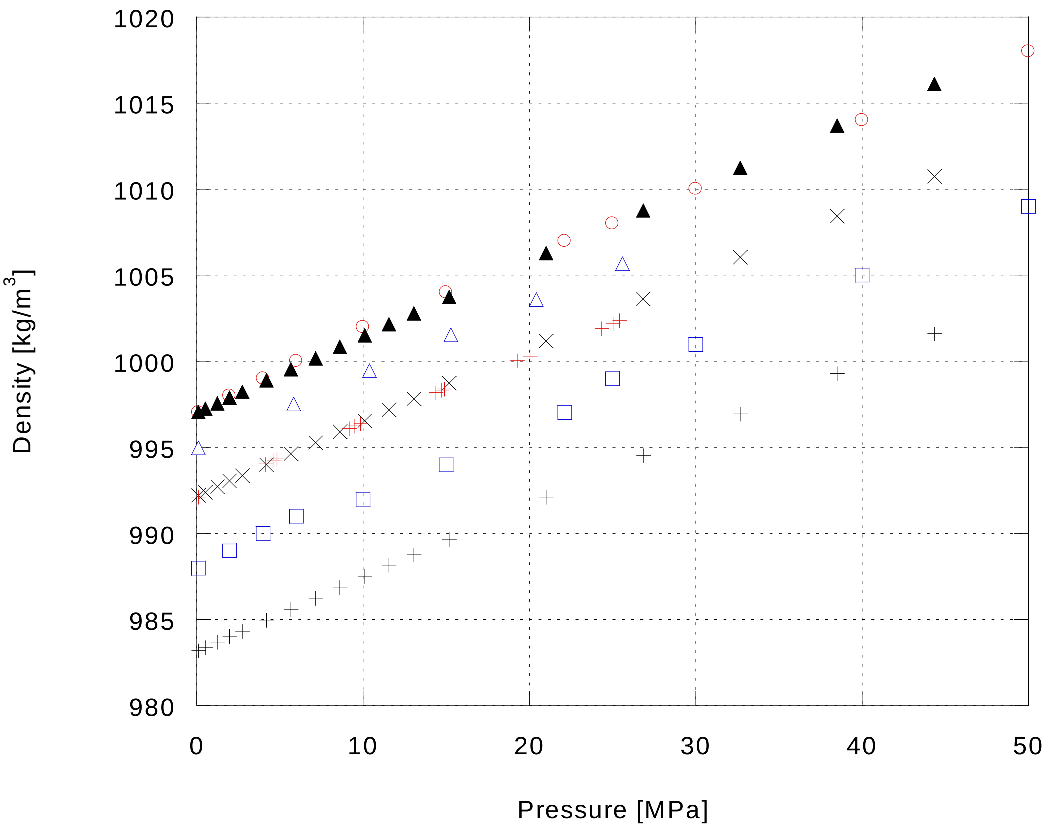

Figure 5.8. Compressed liquid density of water calculated from the current isothermal bulk modulus measurement ((△) 32°C, (+) 40°C) and from references (Haywood[22]: (○) 25°C, (□) 50°C, Kell et al.[21]: (▲) 25°C, (×) 40°C, (+) 60°C)

5.3 Results and Discussion

5.3.1. Isothermal Bulk Modulus Measurement and Specific Heat Ratio (γ) Calculation

5.3.1.1 Petroleum-Based Conventional JP-8/Jet-A Fuels

Figures 5.9a and 5.9b, respectively, show the isothermal secant and tangent bulk modulus measurement of the three different petroleum-based jet fuels (i.e., POSF 4658, POSF 6169, POSF 10325) at 313K over the pressure range of 0.1MPa (0psig) - 27.7MPa (4000psig). The isothermal tangent bulk modulus of "ISO 4113 Normafluid" at the same temperature is referenced from the work of Chorazewski et al.[23] and presented in Figure 5.9 for comparison purposes. ISO 4113 Normafluid is the standardized fuel used for the calibration of diesel fuel injectors because of its similar physical properties to commercial No.2 ULSD.[23] In Figure 5.9a, the symbols represent the measurement points while the lines represent the least-square linear regressions of the measurement of each fuel. We can observe that the difference between the isothermal bulk modulus of the ISO 4113 Normafluid and petroleum-based jet fuels increases at higher pressure. This is because the presented sub-type of the bulk modulus of ISO 4113 Normafluid (tangent) is different from the presented sub-type of the bulk modulus of the jet fuels (secant) in Figure 5.9a. Thus, for the more precise comparison, we converted the secant bulk modulus of the jet fuels into the tangent bulk modulus using the conversion ratio presented in Table 5.1. Figure 5.9b shows the isothermal tangent bulk modulus of the three petroleum-based jet fuels and ISO 4113 Normafluid. We can see that the difference between the bulk modulus of Normafluid and jet fuels no longer increases at higher pressure. Compared to Normafluid, the three petroleum-based jet fuels have about 20-25% lower isothermal bulk modulus. According to the chemical composition analysis reported in previous studies, the percentage of the aromatic compounds in No.2 ULSD[24-26] is about absolute 10-15% higher than the petroleum-based jet fuels[26-29], and the major paraffinic molecular species constituting No.2 ULSD has greater carbon number (C_{12}-C_{18}) than those of the petroleum-based jet fuels (C_8-C_{12}).[26,27] Assuming that ISO 4113 Normafluid can be interpreted as the surrogate of the commercial No.2 ULSD, the lower bulk modulus of the jet fuels compared to ISO 4113 Normafluid can be attributed to the two reasons mentioned above (i.e., lower aromatic content and lower carbon number of the major paraffinic molecular species), which is consistent with Bridgman[10] and other researcher's finding.[11-15,17,19] Among the petroleum-based jet fuels, POSF 4658 has slightly greater bulk modulus than the other two jet fuels (i.e., POSF 10325 and POSF 6169).

In Table 5.8, the pressure dependent linear regression equations for the isothermal bulk modulus of the three petroleum-based jet fuels are presented with their R-squared values and the maximum deviation between the linear regression and measurement. The R-squared values of all linear regression models presented are above 0.90, confirming the reliability of the regression models and measurement repeatability. The maximum deviation between the linear regression and the measurement is 25.7MPa, 26.5MPa and 16.4MPa for POSF 4658, POSF 6169, and POSF 10325, respectively. These values of deviation corresponds to 2.6%, 2.8%, and 1.7% of the value of isothermal bulk modulus of POSF 4658, POSF 6169, and POSF 10325 measured at atmospheric pressure.

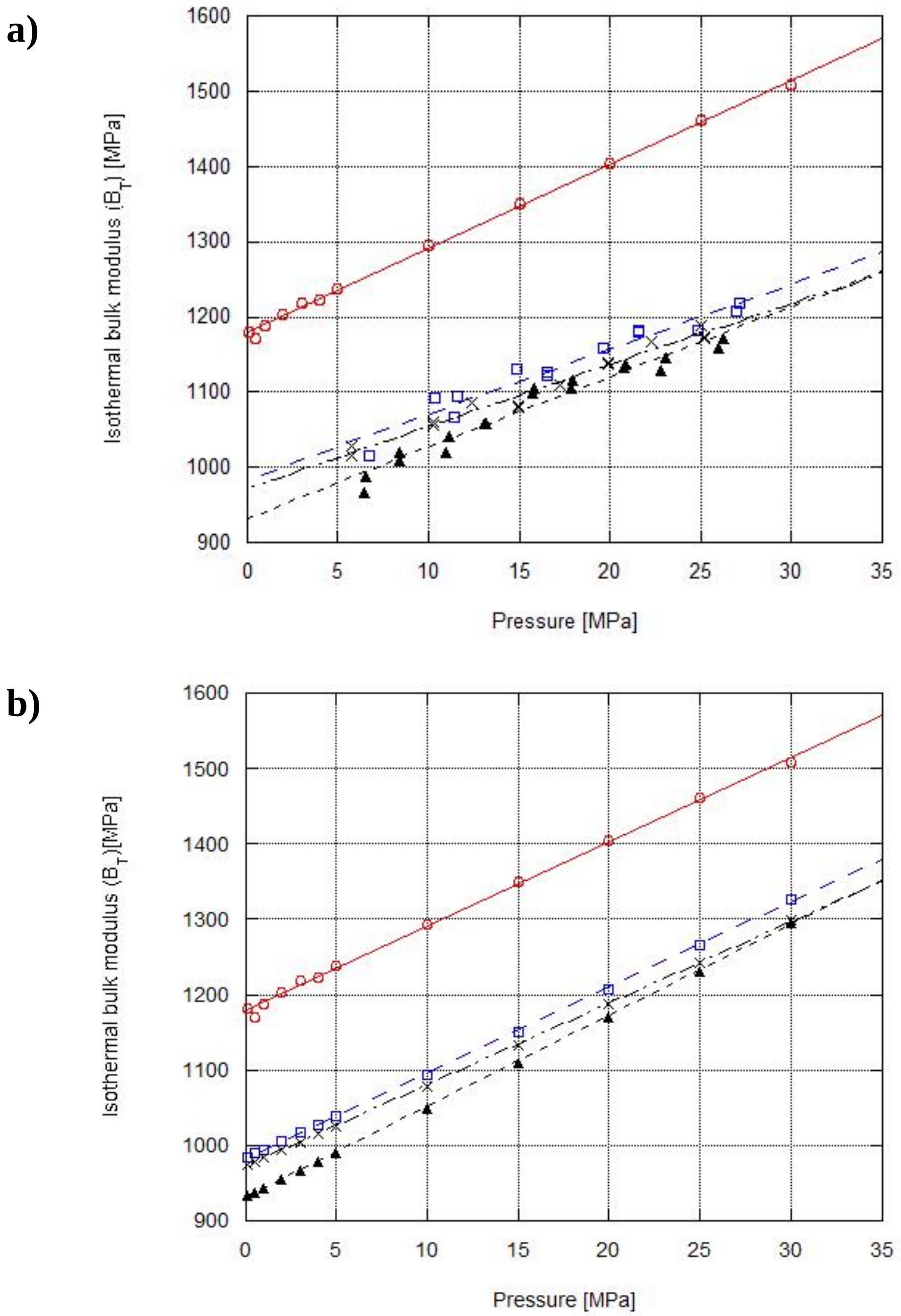

Figure 5.9 Isothermal **(a)** secant bulk modulus measurement of (□) POSF 4658, (▲) POSF 6169, (×) POSF 10325, and the isothermal tangent bulk modulus of (○) ISO 4113 Normafluid (diesel fuel injector calibration oil) referenced from Chorazewski et al.[23] **(b)** tangent bulk modulus measurement of (□) POSF 4658, (▲) POSF 6169, (×) POSF 10325, and the isothermal tangent bulk modulus of (○) ISO 4113 Normafluid from Chorazewski et al.[23] (All data are at T=313K)

<table>
<tr><th colspan="3">POSF 4658</th><th colspan="3">POSF 10325</th></tr>
<tr><td>Linear regression (secant)</td><td>R-squared</td><td>Max. deviation [MPa]</td><td>Linear regression (secant)</td><td>R-squared</td><td>Max. deviation</td></tr>
<tr><td>$B_{T,sec}\ [MPa] = 8.658 \cdot P[MPa] + 983.4$</td><td>0.944</td><td>25.7</td><td>$B_{T,sec}\ [MPa] = 8.177 \cdot P[MPa] + 972.7$</td><td>0.977</td><td>16.4</td></tr>
<tr><td colspan="3">Linear regression (tangent)</td><td colspan="3">Linear regression (tangent)</td></tr>
<tr><td colspan="3">$B_{T,tan}\ [MPa] = 11.36 \cdot P[MPa] + 982.5$</td><td colspan="3">$B_{T,tan}\ [MPa] = 10.82 \cdot P[MPa] + 971.9$</td></tr>
<tr><td colspan="3">POSF 6169</td><td colspan="3" rowspan="5"></td></tr>
<tr><td>Linear regression (secant)</td><td>R-squared</td><td>Max. deviation</td></tr>
<tr><td>$B_{T,sec}\ [MPa] = 9.408 \cdot P[MPa] + 931.4$</td><td>0.953</td><td>26.5</td></tr>
<tr><td colspan="3">Linear regression (tangent)</td></tr>
<tr><td colspan="3">$B_{T,sec}\ [MPa] = 12.04 \cdot P[MPa] + 930.3$</td></tr>
</table>

Table 5.4. Pressure dependent linear regression equation, R-squared value, and the maximum deviation between the linear regression and measurement for the isothermal bulk modulus of POSF 4658, POSF 6169, and POSF 10325 at 313K.

The specific heat ratios (γ) of the No.2 ULSD and some of the petroleum-based jet fuels (i.e., POSF 4658 and POSF 10325) at 313K are calculated using Equation 5.2 by dividing B_S by B_T. The isentropic bulk modulus data of the No.2 ULSD, POSF 4658, and POSF 10325 at 313K are referenced from previous work (i.e., No.2 ULSD from Tat et al.[1] and Payri et al.[30], POSF 4658 from Outcalt et al.[19], POSF 10325 from Edwards et al.[28]). For the isothermal bulk modulus, the measurements obtained from the current study are used for POSF 4658 and POSF 10325, and the isothermal bulk modulus data of ISO 4113 Normafluid referenced from Chorazewski et al.[23] is used for the isothermal bulk modulus of No.2 ULSD. Figures 5.10a – 5.10c present the comparison between the isentropic bulk modulus and isothermal bulk modulus for No.2 ULSD, POSF 4658, and POSF 10325, respectively. The specific heat ratios calculated for No.2 ULSD, POSF 4658, and POSF 10325 are presented in Table 5.9. The specific heat ratio of the No.2 ULSD is calculated based on two different isentropic bulk modulus data obtained from two different references[1,30] to ensure the reliability of the specific heat ratio of the baseline diesel. The specific heat ratio of No.2 ULSD is calculated to be 1.19-1.20 at atmospheric pressure with slight decrease at higher pressure range (i.e., 1.15-1.16 at 30MPa). Based on the values of the specific heat ratio of the major paraffinic species constituting No.2 ULSD (i.e., C_{12}-C_{18}, see Table B.3), "1.19" is a reasonable value for the specific heat ratio of No.2 ULSD. The slight decrease of the specific heat ratio at higher pressure is attributed to the relative increase in isothermal bulk modulus to isentropic bulk modulus at higher pressure. The specific heat ratios of POSF 4658 and POSF 10325 are calculated to be similar to each other as 1.23 at around atmospheric pressure due to their similar molecular composition.[27,29] Compared to No.2 ULSD, the specific heat ratio of the petroleum-based jet fuels is about 3% greater. The result suggests that the lower carbon number of the major paraffinic species constituting the petroleum-based jet fuels (i.e., C_8-C_{12}) than that of No.2 ULSD (i.e., C_{12}-C_{18}) has largely contributed to the greater value of the specific heat ratio in the petroleum-based jet fuels.

a)

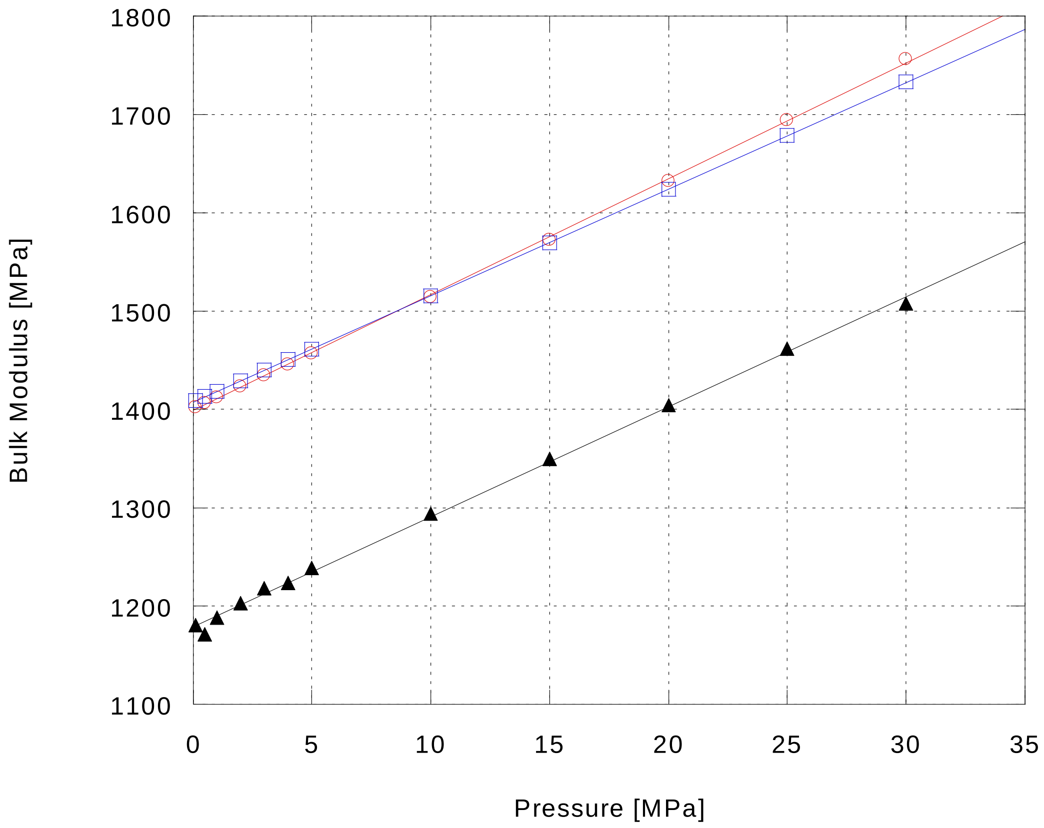
1800
1700
1600
1500
1400
1300
1200
1100
Bulk Modulus [MPa]
0
5
10
15
20
25
30
35
Pressure [MPa]

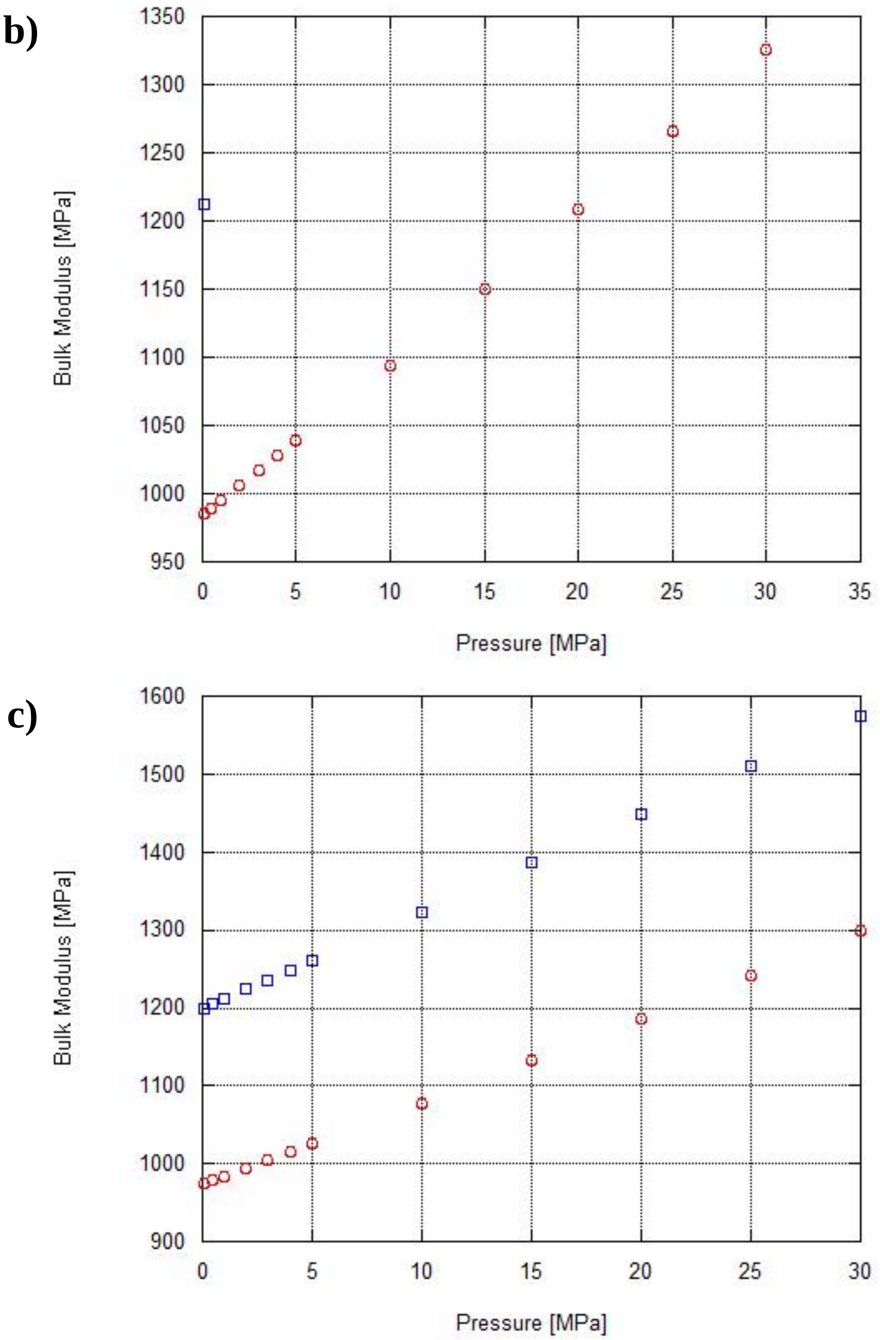

Figure 5.10 Comparison between **(a)** (▲) the isothermal tangent bulk modulus of No.2 ULSD obtained from Chorazewski et al.[23] and the isentropic tangent bulk modulus of No.2 ULSD from (☐) Payri et al.[30] and (○) Tat et al.[1] **(b)** (○) the isothermal tangent bulk modulus measurement of POSF 4658 and (☐) the isentropic tangent bulk modulus data of POSF 4658 obtained from Outcalt et al.[19] **(c)** (○) the isothermal tangent bulk modulus measurement of POSF 10325 and (☐) the isentropic tangent bulk modulus data of POSF 10325 obtained from Edwards et al.[28] (All data are at 313K).

	Fuel Type			
	ULSD (B_s from Payri et al.[30])	ULSD (B_s from Tat et al.[1])	POSF 4658	POSF 10325
Pressure [MPa]	$\gamma = {B_{s,Payri}}/{B_T}$	$\gamma = {B_{s,Tat}}/{B_T}$	γ	γ
0.1	1.19	1.19	1.23	1.23
0.5	1.20	1.20	-	1.23
1	1.19	1.19		1.23
2	1.19	1.18		1.23
3	1.18	1.18		1.23
4	1.18	1.18		1.23
5	1.18	1.18		1.23
10	1.17	1.17		1.23
15	1.16	1.16		1.22
20	1.16	1.16		1.22
25	1.15	1.16		1.21
30	1.15	1.16		1.21

Table 5.5. The specific heat ratio of No.2 ULSD, POSF 4658, and POSF 10325 at 313K.

5.3.1.2 Alternative Jet Fuels

Figures 5.11a and 5.11b, respectively, show the isothermal secant and tangent bulk modulus measurement of the three alternative jet fuels (i.e., Farnesane, HRJC, ATJ) at 308K (0.1-27.7MPa). The isothermal tangent bulk modulus of ISO 4113 Normafluid at 308K obtained from Chorazewski et al.[23] is also presented in Figure 5.11 for the comparison purposes. Like Figure 5.9a, we can observe in Figure 5.11a that the difference between the bulk modulus of ISO 4113 Normafluid and alternative jet fuels increases at higher pressure due to the difference between the secant and tangent bulk modulus. Thus, we converted the isothermal secant bulk modulus of the three alternative jet fuels to the tangent bulk modulus using Table 5.1, and presented the isothermal tangent bulk modulus of the three alternative jet fuels and ISO 4113 Normafluid in Figure 5.11b. In Figure 5.11b, we can observe that the isothermal bulk modulus of the three alternative jet fuels are all smaller than that of ISO 4113 Normafluid with the decreasing order of Farnesane, HRJC, and ATJ. Low aromatic content and low carbon number of the major component species of the alternative jet fuels are the reasons for the lower bulk modulus of alternative jet fuels compared to ISO 4113 Normafluid.[28,31,32] The isothermal bulk modulus of Farnesane is very similar to that of the petroleum-based jet fuels. Considering that Farnesane is not a mixture of hundreds of different hydrocarbon species like the petroleum-based jet fuels, but is a single molecular species (i.e., 2,6,10-trimethyldodecane)[31], it is reasonable to say that Farnesane could be used as a "bulk modulus surrogate fuel" for the petroleum-based jet fuels.

The isothermal bulk modulus of HRJC is 4% lower than that of Farnesane. In order to account for this slight decrease in the bulk modulus of HRJC compared to Farnesane, we need to compare the chemical composition of the two fuels. According to Edwards et al.[28], HRJC is composed of 90% paraffinic alkanes (i.e., n-alkanes + br-alkanes) and 10% cycloalkanes, and the major paraffinic species have a carbon number between C_8 and C_{12}. While the low carbon number of the major paraffinic species of HRJC is the factor decreasing its bulk modulus compared to that of Farnesane, the existence of some cycloalkane species in HRJC partly compensates the reduced bulk modulus, thus resulting in only 4% decrease.

In fact, the bulk modulus of HRJC is higher than that of ATJ even though the carbon number of its major paraffinic component is lower than that of ATJ. The isothermal bulk modulus of ATJ is 14% lower than that of Farnesane. Luning Prak et al.[32] provides the estimated chemical composition of ATJ by comparing the physical properties of the mixture of iso-cetane (i.e., 2,2,4,4,6,8,8-heptamethylnonane) and iso-dodecane (i.e., 2,2,4,6,6-pentamethylheptane) to the physical properties of commercial ATJ. In this work, ATJ is composed of about 75 wt.% iso-dodecane and 25 wt.% iso-cetane, which results in a lower average carbon number (i.e., $\sim C_{13}$) than Farnesane (i.e., C_{15}). In addition, the number of methyl substitutions in iso-cetane and iso-dodecane are greater than in Farnesane, and this also contributes to the lower bulk modulus of

ATJ. Figure 5.12 shows the isentropic bulk modulus of the paraffinic molecular species with different number of methyl substitution as a function of carbon number (the isentropic bulk modulus data used in Figure 5.12 is the same as the one presented in Table B.3). We can observe that, for the species with fixed carbon number, it is generally acceptable that more methyl substitution causes the decrease in bulk modulus.[10]

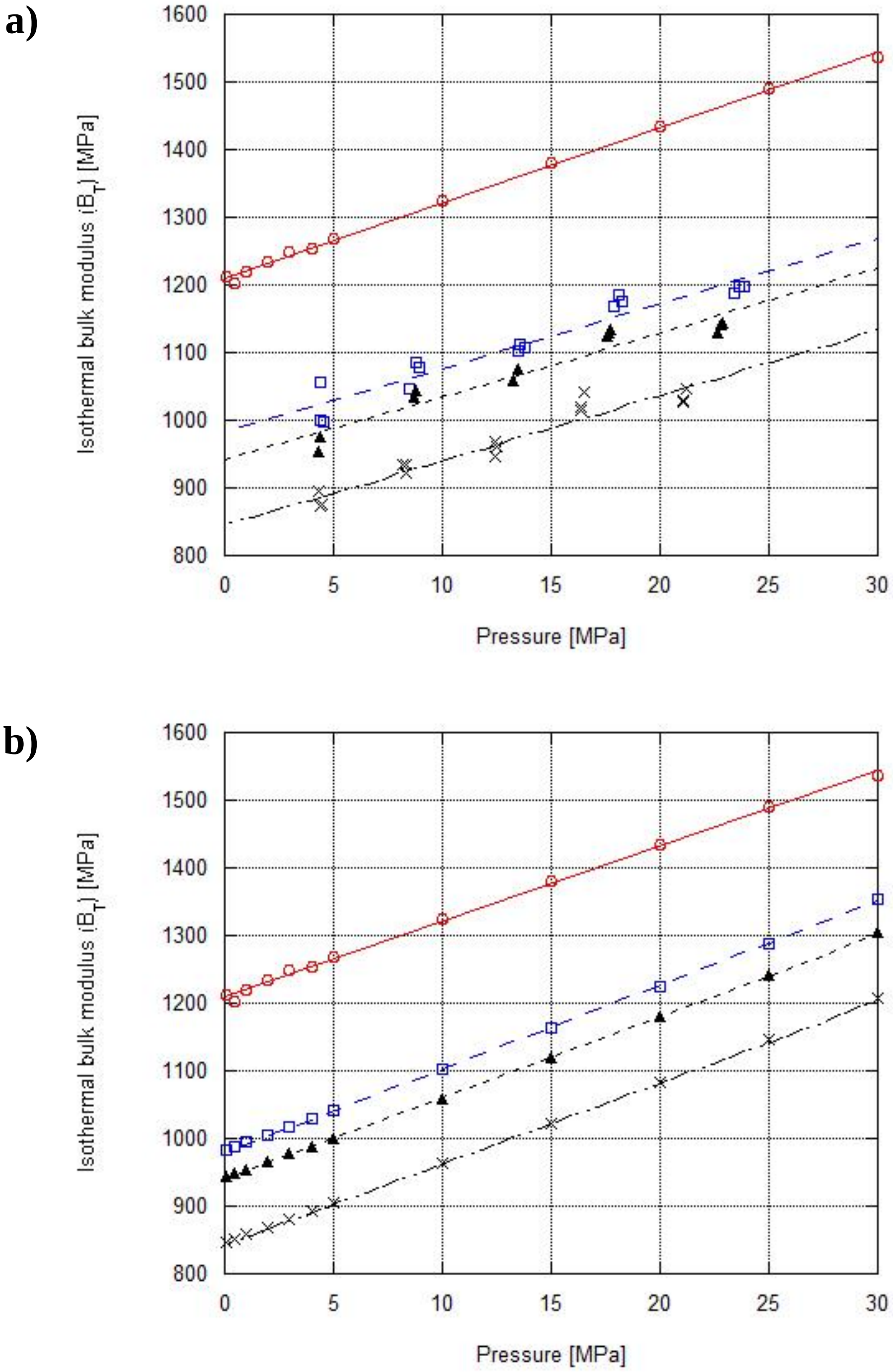

Figure 5.11 Isothermal **(a)** secant bulk modulus measurement of (□) Farnesane, (▲) HRJC, and (×) ATJ and (○) the isothermal tangent bulk modulus of ISO 4113 Normafluid obtained from Chorazewski et al.[23] **(b)** tangent bulk modulus of (□) Farnesane, (▲) HRJC, and (×) ATJ and (○) the isothermal tangent bulk modulus of ISO 4113 Normafluid obtained from Chorazewski et al.[23] (All data are at T=308K)

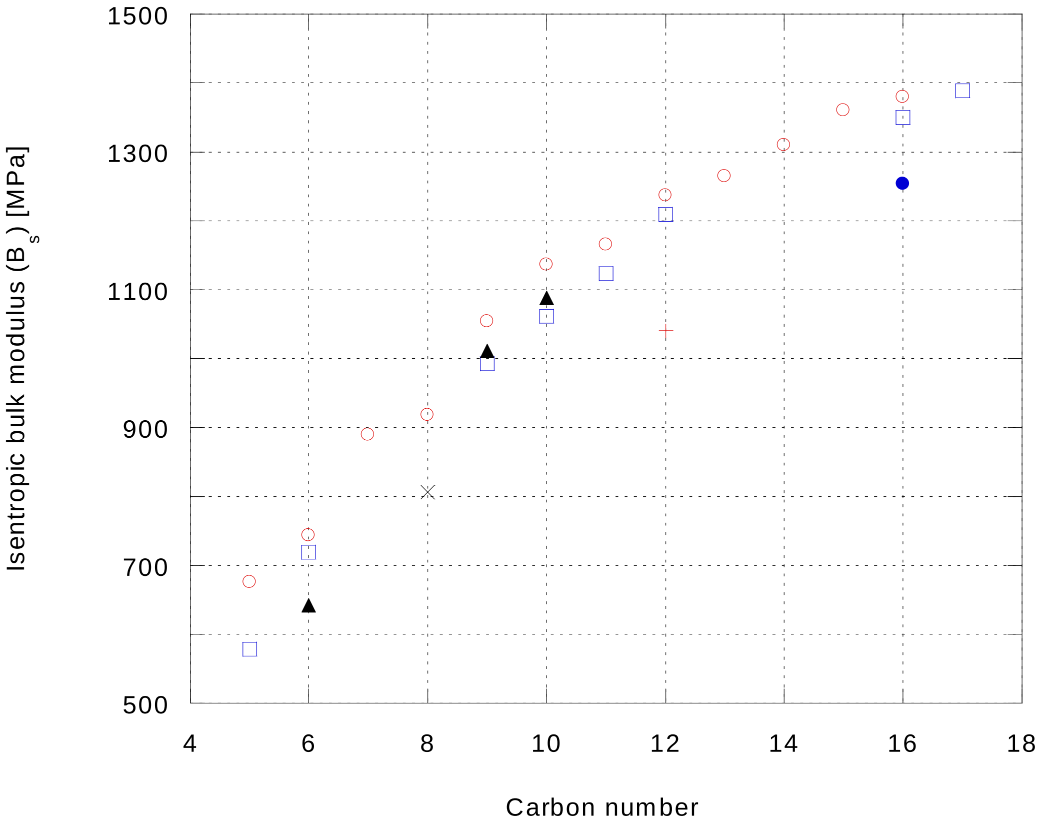

Figure 5.12 Isentropic bulk modulus of (○) n-alkanes, (□) alkanes with single methyl substitution (2-methylbutane, 2-methylpentane, 2-methyloctane, 2-methylnonane, 2-methyldecane, 3-methylundecane, 2-methylpentadecane, 7-methylhexadecane), (▲) alkanes with two methyl substitutions (2,2-dimethylbutane, 3,5-dimethylheptane, 3,6-dimethyloctane), (×) alkane with three methyl substitutions (2,2,4-trimethylpentane (iso-octane)), (+) alkane with five methyl substitutions (2,2,4,6,6-pentamethylheptane (iso-dodecane)), (●) alkane with seven methyl substitutions (2,2,4,4,6,8,8-heptamethylnonane (iso-cetane)).

Table 5.6 shows the pressure dependent linear regression equations, R-squared value, and the maximum deviation between the linear regression and the measurement of the isothermal bulk modulus of the three alternative jet fuels. The R-squared values for all regression models are over 0.90, ensuring the reliability of the models and the repeatability of measurement. The maximum deviation between the linear regression and the measurement is 32.6MPa, 27.7MPa and 37.0MPa for Farnesane, HRJC, and ATJ, respectively. These values of deviation corresponds to 3.3%, 2.9%, and 4.3% of the value of isothermal bulk modulus of Farnesane, HRJC, and ATJ measured at atmospheric pressure.

<table>
<tr><th colspan="3">Farnesane (2,6,10-trimethyldodecane)</th><th colspan="3">HRJ-Camelina (HRJC)</th></tr>
<tr><td>Linear regression (secant)</td><td>R-squared</td><td>Max. deviation [MPa]</td><td>Linear regression (secant)</td><td>R-squared</td><td>Max. deviation</td></tr>
<tr><td>$B_{T,sec}[MPa] = 9.5628 \cdot P[MPa] + 981.89$</td><td>0.9216</td><td>32.6</td><td>$B_{T,sec}[MPa] = 9.3808 \cdot P[MPa] + 942.15$</td><td>0.9309</td><td>27.7</td></tr>
<tr><td colspan="3">Linear regression (tangent)</td><td colspan="3">Linear regression (tangent)</td></tr>
<tr><td colspan="3">$B_{T,tan}[MPa] = 12.313 \cdot P[MPa] + 980.79$</td><td colspan="3">$B_{T,tan}[MPa] = 12.032 \cdot P[MPa] + 941.06$</td></tr>
<tr><th colspan="3">Alcohol-to-jet fuel (ATJ)</th><td colspan="3" rowspan="5"></td></tr>
<tr><td>Linear regression (secant)</td><td>R-squared</td><td>Max. deviation</td></tr>
<tr><td>$B_{T,sec}[MPa] = 9.5943 \cdot P[MPa] + 845.48$</td><td>0.9319</td><td>37.0</td></tr>
<tr><td colspan="3">Linear regression (tangent)</td></tr>
<tr><td colspan="3">$B_{T,tan}[MPa] = 12.046 \cdot P[MPa] + 844.31$</td></tr>
</table>

Table 5.6. Pressure dependent linear regression equation, R-squared value, and the maximum deviation between the linear regression and the measurement of the isothermal bulk modulus for Farnesane, HRJC, ATJ at 308K (0.1-27.7MPa).

The specific heat ratios of the alternative jet fuels (i.e., Farnesane, HRJC, ATJ) are calculated at 308K based on the isentropic bulk modulus data obtained from previous work (i.e., Farnesane from Luning Prak et al.[31], HRJC from Luning Prak et al.[33], ATJ from Edwards et al.[34]) and the isothermal bulk modulus measurement obtained in the current study. It should be noted that the isentropic bulk modulus data obtained for Farnesane is not the value of the neat Farnesane but the value of "Direct Sugar to Hydrocarbon Diesel (i.e., DSH-76)" which is the mixture of 92.7 wt. % Farnesane and other n-alkanes as balance.[31] Thus, the calculated specific heat ratio of Farnesane in the current work can be slightly different from the real value. Table 5.7 shows the specific heat ratios of the alternative jet fuels (i.e., Farnesane, HRJC, ATJ) at 308K. The specific heat ratio of Farnesane is calculated to be 1.21 at atmospheric pressure, which is between the value of No.2 ULSD (i.e., 1.19) and petroleum-based jet fuels (i.e., POSF4658 and POSF 10325: 1.23). In comparison with the specific heat ratio of the petroleum-based jet fuels, the smaller specific heat ratio of Farnesane is a reasonable result because Farnesane is composed of the molecular species with higher carbon number (i.e., C_{15}) than those of the petroleum-based jet fuels (i.e., C_8-C_{12}) and does not have any cyclic species which contribute to increase the specific heat ratio. However, in comparison with the specific heat ratio of No.2 ULSD, the specific heat ratio of Farnesane does not seem very reasonable because No.2 ULSD contains more cyclic species than Farnesane while the average carbon number of the two fuels are similar to each other. Theoretically, the specific heat ratio of Farnesane should be similar to or slightly lower than that of No.2 ULSD. This unexpected high specific heat ratio of Farnesane can be attributed to the error of the isothermal and isentropic bulk modulus values used for the calculation of the specific heat ratio. As mentioned earlier, the isentropic bulk modulus value referenced from the work of Luning Prak et al.[31] will generate some degree of error in specific heat ratio calculation because the isentropic bulk modulus value is not the value of neat Farnesane. Furthermore, the isothermal bulk modulus values used for the calculation of the specific heat ratio are based on the linear regression equation of the measurement. As also mentioned earlier, the linear regression has a maximum deviation from the real measurement of 3.3%, which, in turn, causes the commensurate degree of error in the specific heat ratio calculation.

The specific heat ratio of HRJC is calculated to be 1.24. It is suggested that the higher specific heat ratio in HRJC compared to Farnesane is because of the lower carbon number of the major paraffinic components of HRJC (i.e., C_8-C_{12}) compared to Farnesane (i.e., C_{15}) and the presence of cycloalkane components in HRJC (~10%).

The specific heat ratio of ATJ is calculated to be 1.18, which is lower than the specific heat ratio of the petroleum-based jet fuels (i.e., 1.23) and HRJC (i.e., 1.24), and is similar to the value of No.2 ULSD (i.e., 1.19). The reason for the lower value of specific heat ratio in ATJ compared to the petroleum-based jet fuels and HRJC is suggested to be the absence of the cyclic species in the fuel mixture and the higher carbon number of the major paraffinic species. In comparison with No.2 ULSD, the value of the specific heat ratio of ATJ is also reasonable because the carbon number of its component species is similar to that of No.2 ULSD while ATJ does not contain any cyclic hydrocarbon species. It is suggested that these two factors resulted in the slightly lower value of the specific heat ratio in ATJ compared to that of No.2 ULSD.

	Fuel Type		
	Farnesane	HRJC	ATJ
Pressure [MPa]	Specific heat ratio (γ)		
0.1	1.21	1.24	1.18
0.5	-	-	1.18
1			1.18
2			1.18
3			1.18
4			1.17
5			1.17
10			1.17
15			1.16
20			1.15
25			1.14
30			1.14

Table 5.7. Specific heat ratios of Farnesane, HRJC, and ATJ at 308K

5.3.2 Pseudo-Isothermal Speed of Sound Measurement and Pseudo-Isothermal Coefficient (α) Calculation

5.3.2.1 Petroleum-Based Conventional JP-8/Jet-A Fuels

The pseudo-isothermal speed of sound measurement of the three petroleum-based JP-8/Jet-A fuels (i.e., POSF 4658, POSF 6169, POSF 10325) and the baseline diesel (i.e., No.2 ULSD) is presented in Figure 5.13 as a function of temperature within the temperature range of 45℃-65℃ at 0.1MPa. Here, the symbols represent the measurement points while the lines represent the least-square linear regressions of the measurement for each test fuel. As expected from the isothermal bulk modulus measurement, the pseudo-isothermal speed of sound of all three petroleum-based jet fuels are lower than No.2 ULSD. Among the three petroleum-based jet fuels, POSF 4658 has the highest value of pseudo-isothermal speed of sound, which is 3.9% lower than that of No.2 ULSD at 40℃. The pseudo-isothermal speed of sound of POSF 10325 and POSF 6169 are similar to each other as 1148m/s at 40ºC. Similar to the case of the isothermal bulk modulus, the lower aromatic content and the lower carbon number of the major component species of the petroleum-based jet fuels contributed to their lower pseudo-isothermal speed of sound compared to No.2 ULSD.[10,17]

Table 5.8 shows the temperature dependent linear regression equations and their R-squared values for the pseudo-isothermal speed of sound measurement of the petroleum-based jet fuel (i.e., POSF 4658, POSF 6169, POSF 10325) and the baseline diesel (i.e., No.2 ULSD) at 0.1MPa. The R-squared values of all linear regression models are over 0.90, ensuring the reliability of the model and the repeatability of the measurement.

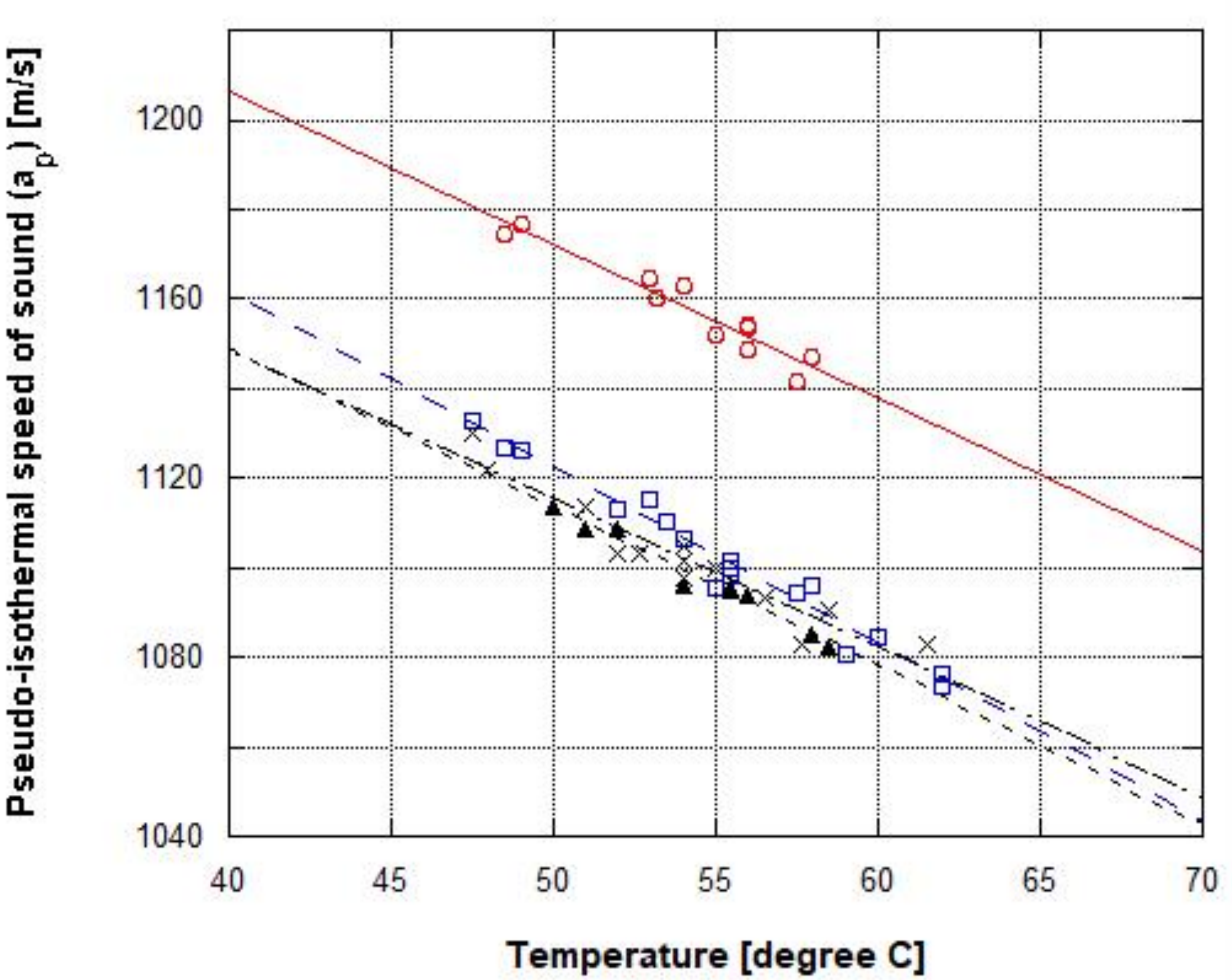

Figure 5.13 Pseudo-isothermal speed of sound (a_p) measurement of the (□) POSF 4658, (▲) POSF 6169, (×) POSF 10325 and (○) No.2 ULSD at 0.1MPa.

ULSD		POSF4658	
Linear regression	R-squared	Linear regression	R-squared
$a_p[m/s] = -3.4356 \cdot T[℃] + 1344$	0.924	$a_p[m/s] = -3.9521 \cdot T[℃] + 1319.9$	0.967
POSF 6169		POSF 10325	
Linear regression	R-squared	Linear regression	R-squared
$a_p[m/s] = -3.5433 \cdot T[℃] + 1290.7$	0.975	$a_p[m/s] = -3.3228 \cdot T[℃] + 1281.4$	0.912

Table 5.8. Temperature dependent linear regression equations and the R-squared values for the pseudo-isothermal speed of sound (a_p) measurement of the petroleum-based jet fuel (POSF 4658, POSF 6169, POSF 10325) and the baseline diesel (No.2 ULSD) at 0.1MPa.

As mentioned in section 5.2, the pseudo-isothermal speed of sound measurement obtained in the current study is not necessarily the same as the isentropic speed of sound. Thus, we calculated the pseudo-isothermal coefficients of some of the test fuels, and utilized the pseudo-isothermal coefficients to convert the pseudo-isothermal speed of sound measurement to the isentropic speed of sound (see Fig. 5.7). Starting from Equations 5.1 and 5.2, we can derive an equation that expresses the pseudo-isothermal coefficient in terms of the isothermal speed of sound and pseudo-isothermal speed of sound. First, we know from Equation 5.2 that specific heat ratio is equal to the ratio of the isentropic bulk modulus to the isothermal bulk modulus. Thus, if we express B_s and B_T in terms of density and speed of sound, the specific heat ratio can be expressed as Equation 5.10.

$$\gamma = \left(\frac{a_s}{a_T}\right)^2 \qquad \text{(Eq. 5.10)}$$

Now based on the definition of the pseudo-isothermal coefficient shown in a set of equations 5.11 – 5.13, we can simply replace the specific heat ratio and isentropic speed of sound in Equation 5.10 with the pseudo-isothermal coefficient and pseudo-isothermal speed of sound, respectively, which results in Equation 5.14.[35]

$$PV = C\ (isothermal\ process) \qquad \text{(Eq. 5.11)}$$

$$PV^{\alpha} = C\ (pseudo - isothermal\ process, \alpha{:}\ pseudo - isothermal\ coefficient, 1 < \alpha < \gamma) \qquad \text{(Eq. 5.12)}$$

$$PV^{\gamma} = C\ (isentropic\ process, \gamma{:}\ specific\ heat\ ratio) \qquad \text{(Eq. 5.13)}$$

$$\alpha = \left(\frac{a_p}{a_T}\right)^2 \qquad \text{(Eq. 5.14)}$$

In Table 5.9, the calculated pseudo-isothermal coefficients of the selected test fuels are presented. For POSF 4658 and POSF 10325, the isothermal bulk modulus measurement obtained in this work and the density data obtained from the previous studies (i.e., POSF 4658 from Outcalt et al.[19] and POSF 10325 from Edwards et al.[34]) are used to first calculate the isothermal speed of sound using Equation 5.2. For the pseudo-isothermal speed of sound values used for the calculation of the pseudo-isothermal coefficient, the temperature dependent linear regression equation presented in Table 5.12 is used. The pseudo-isothermal coefficient of POSF 4658 and POSF 10325 at 313K is calculated to be 1.08 and 1.05, respectively.

	Fuel Type				
	POSF 4658	POSF 10325	Farnesane	HRJC	ATJ
T[K]	Pseudo-isothermal coefficient (α)				
308	-	-	1.05	1.06	1.06
313	1.08	1.05	-	-	-

Table 5.9. Pseudo-isothermal coefficient of the fuel compression process corresponding to each test fuel (POSF 4658, POSF 10325, Farnesane, HRJC, ATJ) at 0.1MPa.

5.3.2.2 Alternative Jet Fuels

Figure 5.14 shows the pseudo-isothermal speed of sound measurement of three alternative jet fuels (i.e., Farnesane, HRJC, and 50/50 wt. % blend of ATJ/Farnesane). The pseudo-isothermal speed of sound of the neat ATJ is extrapolated from the two linear regression equations of Farnesane and 50/50 wt. % blend of ATJ/Farnesane, and is also presented in Figure 5.14. The pseudo-isothermal speed of sound measurement of the baseline diesel fuel (i.e., No.2 ULSD) is presented together in Figure 5.14 for comparison purposes. As expected from the isothermal bulk modulus measurement result, the pseudo-isothermal speed of sound of all three alternative jet fuels are lower than No.2 ULSD with the decreasing order of Farnesane, HRJC, and 50/50 wt.% blend of ATJ/Farnesane. The pseudo-isothermal speed of sound of Farnesane is about 4% lower than No.2 ULSD at 40ºC, which is very similar to the values of the three petroleum-based jet fuels. The lower pseudo-isothermal speed of sound of Farnesane compared to No.2 ULSD is due to the absence of the cyclic hydrocarbon species in Farnesane.[10] HRJC has about 1.2% lower pseudo-isothermal speed of sound compared to that of Farnesane at 40ºC. This can be attributed to the lower carbon number of the major paraffinic component species of HRJC compared to Farnesane.[3,5] The extrapolated pseudo-isothermal speed of sound of neat ATJ is about 6.3% lower than that of Farnesane at 40ºC, and this is due to the greater number of methyl substitutions and the lower carbon number of the major paraffinic component of ATJ compared to Farnesane.[3,5,17]

Table 5.10 shows the temperature dependent linear regression equations and their R-squared values for the pseudo-isothermal speed of sound (a_p) measurement for the alternative jet fuels (i.e., Farnesane, HRJC, 50/50 wt.% blend of ATJ and Farnesane, and neat ATJ). The linear regression equation of neat ATJ is extrapolated from the linear regressions of Farnesane and 50/50 wt. % blend of ATJ/Farnesane. The R-squared values of the regression models are all over 0.90, ensuring the reliability of the models and the repeatability of the measurement.

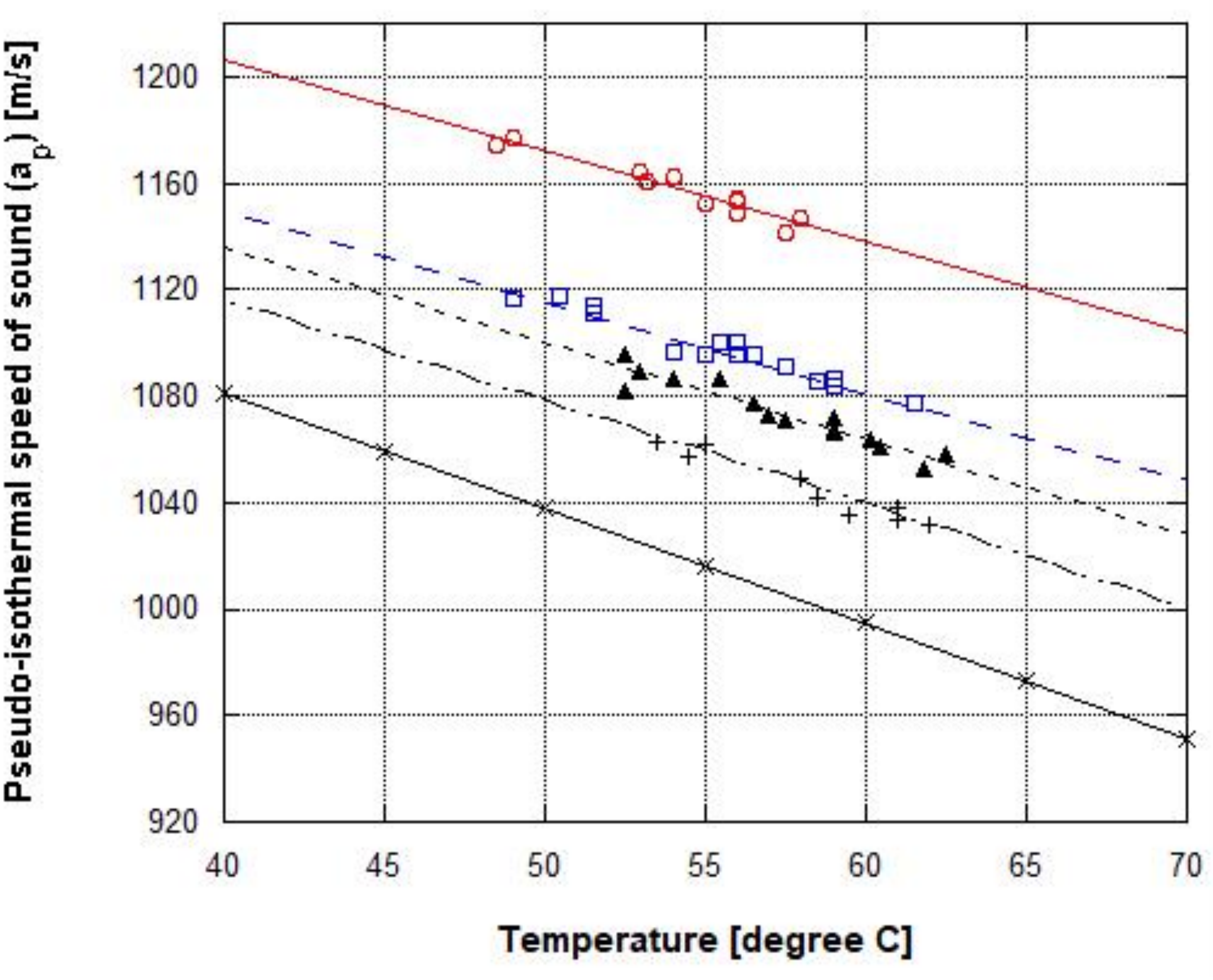

Figure 5.14 Pseudo-isothermal speed of sound (a_p) measurement of the (□) Farnesane, (▲) HRJC, (+) 50/50 wt. % blend of ATJ and Farnesane, (×) neat ATJ and (○) No.2 ULSD at 0.1MPa.

Farnesane (2,6,10-trimethyldodecane)		HRJC	
Linear regression	R-squared	Linear regression	R-squared
$a_p[m/s] = -3.3801 \cdot T[℃] + 1285.1$	0.950	$a_p[m/s] = -3.5845 \cdot T[℃] + 1279.0$	0.905
50/50 wt. % blend of ATJ/Farnesane		**Neat ATJ***	
Linear regression	R-squared	Linear regression	R-squared
$a_p[m/s] = -3.8487 \cdot T[℃] + 1269.4$	0.941	$a_p[m/s] = -4.3173 \cdot T[℃] + 1253.7$	1.00

Table 5.10 Temperature dependent linear regression equations and their R-squared values for the pseudo-isothermal speed of sound measurement of the alternative jet fuels (Farnesane, HRJC, 50/50 wt. % blend of ATJ/Farnesane, and neat ATJ) at 0.1MPa. *Linear regression of neat ATJ is obtained by extrapolating the linear regression equations of Farnesane and 50/50 wt. % blend of ATJ/Farnesane.

The pseudo-isothermal coefficients of the fuel compression processes corresponding to Farnesane, HRJC, and neat ATJ are calculated using Equation 5.14, and are presented in Table 5.9. The isothermal bulk modulus measurement obtained in the current study and the density data obtained from previous work (i.e., Farnesane from Luning Prak et al.[31], HRJC from Luning Prak et al.[33], and ATJ from Edwards et al.[34]) are used to first calculate the isothermal speed of sound using Equation 5.2. For the pseudo-isothermal speed of sound used for the calculation of the pseudo-isothermal coefficient, the linear regression equations presented in Table 5.10 is used. The pseudo-isothermal coefficients of Farnesane, HRJC, and neat ATJ are calculated to be 1.05, 1.06, and 1.06, respectively. In Table 5.9, one can notice that the pseudo-isothermal coefficients of the fuel compression processes corresponding to different types of fuels fall into the range of 1.05-1.08, which indicates the consistency of the pseudo-isothermal coefficients during the pseudo-isothermal speed of sound measurement.

5.3.3 Isentropic Speed of Sound Estimation

By combining Equation 5.10 and 5.14, we can write the isentropic speed of sound in terms of the pseudo-isothermal speed of sound, specific heat ratio, and pseudo-isothermal coefficient as shown in Equation 5.15.

$$a_s = a_p \cdot \sqrt{\frac{\gamma}{\alpha}} \quad \text{(Eq. 5.15)}$$

Then, the isentropic speed of sound of each test fuel is estimated based on Equation 5.15. For the value of the pseudo-isothermal speed of sound used in Equation 5.15, the linear regression equations presented in Tables 5.8 and 5.10 are used for petroleum-based jet fuels and alternative jet fuels, respectively. For the value of the pseudo-isothermal coefficient used in Equation 5.15, the average value of the 5 different pseudo-isothermal coefficients (i.e., 1.06) of different test fuels shown in Table 5.9 is used based on the fact that the fuel compression processes corresponding to different test fuels have very similar pseudo-isothermal coefficient to each other. For the value of the specific heat ratio used in Equation 5.15, we used the specific heat ratio corresponding to each test fuel at atmospheric pressure as shown in the first row of Table 5.5 (for POSF 4658 and POSF 10325) and Table 5.7 (Farnesane, HRJC, and ATJ). This is based on the assumption that the specific heat ratio of the test fuels is constant over the measurement temperature range of this study (i.e., 35°C-65°C). This assumption can be justified by the isobaric and isochoric heat capacity data presented in Perry's Chemical Engineers' Handbook[36]. The isobaric and isochoric heat capacity of 12 hydrocarbon molecular species are reviewed from Perry's Chemical Engineers' Handbook over the temperature range of 300-350K, and the specific heat ratios of the species are calculated over the same temperature range. In average, the specific heat ratios of these molecular species decrease only about 1% over the temperature range.

Figures 5.15a and 5.15b show the estimated isentropic speed of sound of the petroleum-based jet fuels (i.e., POSF 4658, POSF 10325) and the alternative jet fuels (i.e., Farnesane, HRJC, ATJ), respectively. The estimated isentropic speed of sound of all five jet fuels generally agrees well with the isentropic speed of sound data reported in previous studies.

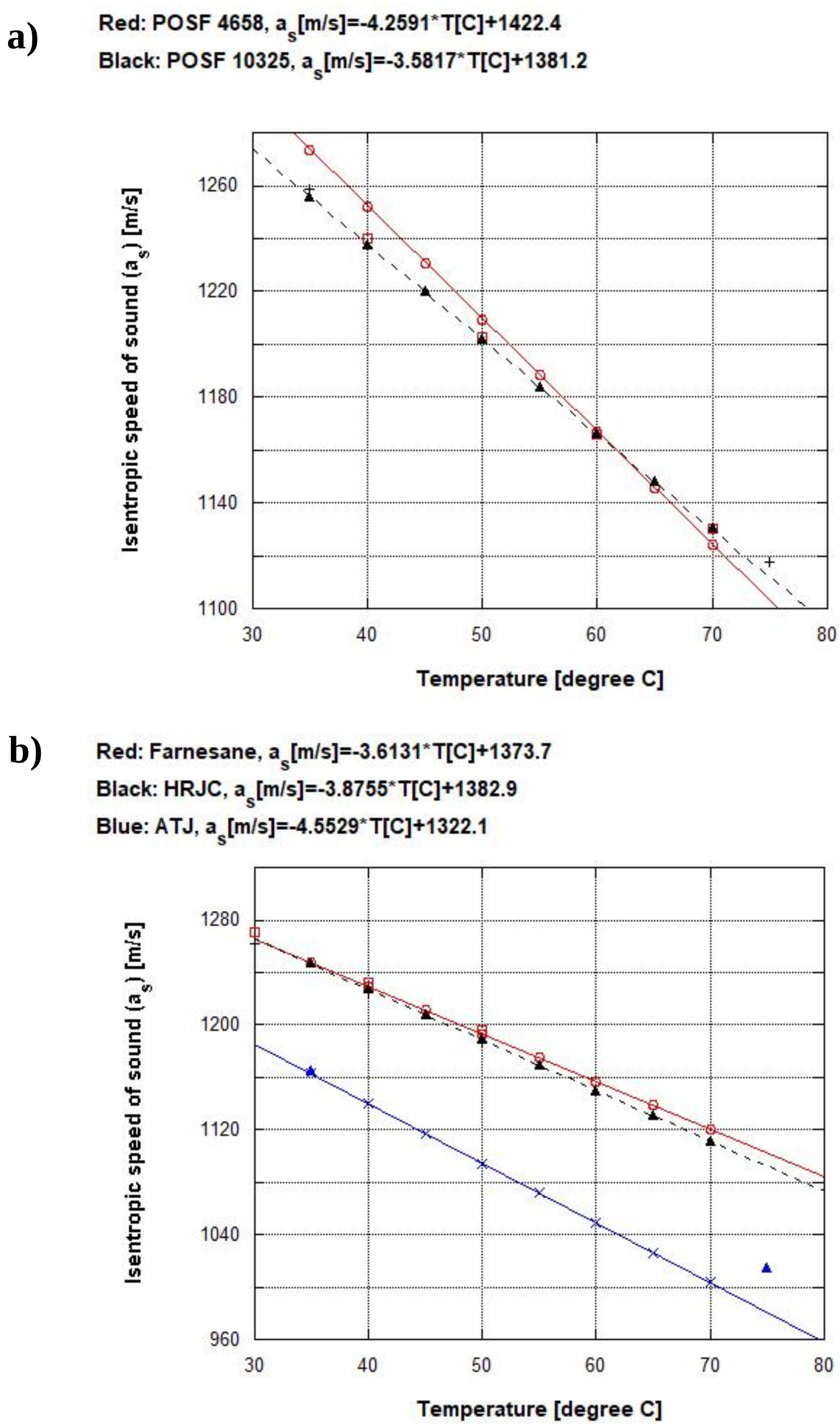

Figure 5.15 The estimated isentropic speed of sound of **(a)** (○) POSF 4658 and (▲) POSF 10325 compared to the reported data of (□) POSF 4658 from Outcalt et al.[19] and (+) POSF 10325 from Edwards et al.[34] **(b)** (○) Farnesane, (▲) HRJC, and (×) ATJ compared to the reported data of (□) Farnesane from Luning Prak et al.[31], (+) HRJC from Luning Prak et al.[33], (▲) ATJ from Edwards et al.[34]

5.4 Summary and Conclusions

In this work, the isothermal bulk modulus of 3 different petroleum-derived JP-8/Jet-A fuels (i.e., POSF 4658, POSF 6169, POSF 10325) is measured at 313K (0.1-27.7MPa), and the isothermal bulk modulus of 3 different alternative jet fuels (i.e., Farnesane, HRJC, ATJ) is measured at 308K (0.1-27.7MPa) using a high-pressure vessel immersed in a constant temperature water bath. The specific heat ratio of the test fuels is calculated by comparing the isothermal bulk modulus measurement obtained from the current work and the isentropic bulk modulus data obtained from other published work. Furthermore, the pseudo-isothermal speed of sound of 3 different petroleum-based jet fuels (i.e., POSF 4658, POSF 6169, POSF 10325), 3 different alternative jet fuels (i.e., Farnesane, HRJC, ATJ) and No.2 ULSD is measured at 0.1MPa over the measurement temperature range between 45°C and 65°C using a pair of line pressure sensors on a pump-nozzle-line fuel injection system of a single cylinder compression ignition engine. The pseudo-isothermal coefficient of the fuel compression processes corresponding to the test fuels is calculated based on the pseudo-isothermal speed of sound measurement and the isothermal bulk modulus measurement. Lastly, the isentropic speed of sound of the selected test fuels (i.e., POSF 4658, POSF 10325, Farnesane, HRJC, ATJ) is estimated from the pseudo-isothermal speed of sound measurement using the pseudo-isothermal coefficient and specific heat ratio. This method of speed of sound estimation is unique in that it can be conducted within a test engine while taking other performance and emissions measurements without a complicated device dedicated for the speed of sound measurement. Previous work with similar approach includes Armas et al.[37] and Payri et al.[38]

The isothermal bulk modulus and the pseudo-isothermal speed of sound of the jet fuels were all lower than those of No.2 ULSD in the decreasing order of POSF 4658 > POSF 10325 ≈

POSF 6169 ≈ Farnesane > HRJC > ATJ. Quantitatively speaking, the isothermal bulk modulus of the three petroleum-based jet fuels and Farnesane was 20-25% lower than that of the petroleum-based diesel while the isothermal bulk modulus of HRJC was about 4% lower than the Farnesane. The isothermal bulk modulus of ATJ was about 14% lower than that of the Farnesane. Given the fact that the decrease in bulk modulus and speed of sound unintendedly retards the actual fuel injection timing in the pump-line-nozzle type fuel injection system, the advance in nominal fuel injection timing is recommended when using these jet fuels in the U. S. Army legacy vehicles with pump-line-nozzle type fuel injection system.

The pressure-dependent linear regression equation is established for the isothermal bulk modulus of the tested jet fuels, and the temperature-dependent linear regression equation is established for the pseudo-isothermal speed of sound of the tested fuels. The linear regression equations presented in this study all achieved the R-squared value higher than 0.90. The specific heat ratios of the test fuels were calculated to be 1.19, 1.23, 1.23, 1.21, 1.24, and 1.18 at 0.1MPa for No.2 ULSD, POSF 4658, POSF 10325, Farnesane, HRJC, and ATJ, respectively. The pseudo-isothermal coefficients of the selected test fuels all fell into the narrow range of 1.05-1.08, which guaranteed the consistency of the fuel compression processes for different types of the test fuel. Thus, we could estimate the isentropic speed of sound of selected test fuels (i.e., POSF 4658, POSF 10325, Farnesane, HRJC, ATJ), and compare the estimated values to the reported data obtained from previous works. The estimated isentropic speed of sound of the jet fuels matched very well with the previous data.

In addition, the effect of molecular structure and molecular weight on the specific heat ratio of different molecular species is investigated in this study, and the details are presented in Appendix B. In general, the specific heat ratio was greater in the molecular species with the lower carbon number and cyclic molecular structure. The knowledge can serve as the important scientific background to explain the difference in the specific heat ratio observed in different molecular species in the current work. However, more study is also recommended to establish a "quantitative" model to estimate specific heat ratio from the relevant thermophysical properties (e.g., dielectric constant, isobaric thermal expansivity, etc.) that are more readily available from previous literature to enable the conversion of pseudo-isothermal speed of sound to isentropic speed of sound for a species with unknown isentropic bulk modulus value.

5.5 References

[1] Tat, M. E; Van Gerpen, J. H. *Measurement of biodiesel speed of sound and its impact on injection timing-Final report (report 4 in series of 6)*; NREL/SR-510-31462; National Renewable Energy Laboratory (NREL): Golden, CO, Feb. 2003; pp.1-3.

[2] Szybist, J.P.; Boehman, A.L. Behavior of a Diesel Injection System with Biodiesel Fuel, SAE Technical Paper (2003), 2003-01-1039.

[3] Boehman, A. L.; Morris, D.; Szybist, J. P. The Impact of the Bulk Modulus of Diesel Fuels on Fuel Injection Timing, *Energy & Fuels*, **2004**, 18, 1877-1882.

[4] Szybist, J. P.; Kirby, S. R.; Boehman, A. L. NOx Emissions of Alternative Diesel Fuels: A Comparative Analysis of Biodiesel and FT Diesel, *Energy & Fuels*, **2005**, 19, 1484-1492.

[5] Lapuerta, M.; Agudelo, J. R.; Prorok, M.; Boehman, A. L. Bulk Modulus of Compressibility of Diesel/Biodiesel/HVO Blends, *Energy & Fuels*, **2012**, 26, 1336−1343.

[6] Eric Sattler, U.S. Army Tank Automotive Research Development and Engineering Center (TARDEC), Personal Communication, 2014.

[7] *DoD management policy for energy commodities and related services*; Directive 4140.25; U.S. Department of Defense (DoD): Arlington County, VA, U.S.A, 2004; pg.3.

[8] Kim, D.; Martz, J.; Violi, A. *Combust. Flame*, **2014**, 161, 1489-1498.

[9] Elgowainy, A.; Han, J.; Wang, M.; Carter, N.; Stratton, R.; Hileman, J., Malwitz, A.; Balasubramanian, S. *Life-Cycle Analysis of Alternative Aviation Fuels in GREET*; ANL-ESD-12/8; Argonne National Laboratory: Lemont, IL, June 2012.

[10] Bridgman, P. W. *The Physics of High Pressure*; G. Bell and Sons: London, 1958; pp 116-149.

[11] Varde, K.S. Bulk modulus of vegetable oil-diesel fuel blends, *Fuel*, **1984,** 63, 713-715.

[12] Daridon, J.L.; Carrier, H.; Lagourette, B. Pressure Dependence of the Thermophysical Properties of n-Pentadecane and n-Heptadecane, *International Journal of Thermophysics*, **2002**, 23(3), 697-708.

[13] Takagi, T.; Sakura, T.; Guedes, H.J.R. Speed of sound in liquid cyclic alkanes at temperatures between (283 and 343)K and pressures up to 20MPa, *J. Chem. Thermodynamics*, **2002**, 34, 1943-1957.

[14] Khasanshin, T.S.; Shchamialiou, A.P.; Poddubskij, O.G. Thermodynamic properties of heavy n-alkanes in the liquid state: n-tridecane, *High Temperatures - High Pressures*, **2003/2004**, 35/36, 227-235.

[15] Bessieres, D.; Plantier, F. Thermodynamic Consistency Between Calorimetric Acoustic and Volumetric Measurements: Application to n-undecane, *Journal of Thermal Analysis and Calorimetry*, **2007**, 89, 81-85.

[16] Borgnakke, C.; Sonntag, R.E. Chapter 14: Thermodynamic property relations. *Fundamentals of Thermodynamics*, 7th ed.; Wiley: New Delhi, 2009; pp. 511-512.

[17] Marcus, Y.; Hefter, G.T. The Compressibility of Liquids at Ambient Temperature and Pressure, *Journal of Molecular Liquids*, **1997**, 73, 61-74.

[18] O'Brien, J. A. Precise Measurement of Liquid Bulk Modulus. Master's Thesis, Pennsylvania State University: University Park, PA, March 1963.

[19] Outcalt, S.; Laesecke, A.; Freund, M. B. Density and Speed of Sound Measurements of Jet A and S-8 Aviation Turbine Fuels, *Energy & Fuels*, **2009**, 23, 1626-1633.

[20] Borgnakke, C.; Sonntag, R.E. Chapter 12: Thermodynamic Relations. *Fundamentals of Thermodynamics*, 8th ed.; Wiley: New Delhi, 2009; pp. 517-572.

[21] Kell, G.S.; Whalley, E. Reanalysis of the density of liquid water in the range 0–150 °C and 0–1 kbar, *J. Chem. Phys.*, **1975**, 62, 3496-3503.

[22] Haywood, R.W., *Thermodynamic tables in SI(metric) Units*, Cambridge University Press: Cambridge, UK, 1972, pg.18.

[23] Chorazewski, M.; Dergar, F.; Sawaya, T.; Mokbel, I.; Grolier, J-P. E.; Jose, J. Thermophysical properties of Normafluid (ISO 4113) over wide pressure and temperature ranges, *Fuel*, **2013**, 105, 440-450.

[24] Ivanova, L.V.; Koshelev, V.N.; Burov, E.A. Influence of the hydrocarbon composition of diesel fuels on their performance characteristics, *Pet. Chem.*, **2014**, 54, 466-472.

[25] Smagala, T.G.; Christensen, E.; Christison, K.M.; Mohler, R.; Gjersing, E.; McCormick, R. Hydrocarbon Renewable and Synthetic Diesel Fuel Blendstocks: Composition and Properties, *Energy & Fuels*, **2013**, 27, 237-246.

[26] Chapter3: Chemical and physical information. *Toxicological profile for fuel oils*; U.S. Department of Health and Human Services, Public Health Service Agency for Toxic Substances and Disease Registry: Atlanta, GA, 1995; pp. 105-109.

[27] Bruno, T.J.; Huber, M.; Laesecke, A.; Lemmon, E.; McLinden, M.; Outcalt, S.; Perkins, R.; Smith, B.; Widegren, J. *Thermodynamic, transport, and chemical properties of "Reference" JP-8* ; NISTIR 6659; National Institute of Standards and Technology: Boulder, CO, 2010; pp. 48-49.

[28] Edwards, J.T.; Shafer, L.M.; Klein, J.K. *U.S. Air Force hydroprocessed renewable jet (HRJ) fuel research*; AFRL-RQ-WP-TR-2013-0108; Air Force Research Laboratory: Wright-Patterson Air Force Base, OH, July 2012; pp.6-10.

[29] Lovestead, T.M.; Burger, J.L.; Schneider, N.; Bruno, T.J. Comprehensive Assessment of Composition and Thermochemical Variability by High Resolution GC/QToF-MS and the Advanced Distillation-Curve Method as a Basis of Comparison for Reference Fuel Development, *Energy & Fuels*, **2016**, 30, 10029-10044.

[30] Payri, R.; Salvador, F.J.; Gimeno, J.; Bracho, G. The effect of temperature and pressure on thermodynamic properties of diesel and biodiesel fuels, *Fuel*, **2011,** 90, 1172-1180.

[31] Luning Prak, D.J.; Morris, R.E.; Cowart, J.S.; Hamilton, L.; Trulove, P. Density, Viscosity, Speed of Sound, Bulk Modulus, Surface Tension, and Flash Point of Direct Sugar to Hydrocarbon Diesel (DSH-76) and Binary Mixtures of N-Hexadecane and 2,2,4,6,6-Pentamethylheptane, *J. Chem. Eng. Data*, **2013**, 58, 3536-3544.

[32] Luning Prak, D.J.; Jones, M.H.; Trulove, P.; McDaniel, A.; Dickerson, T.; Cowart, J. Physical and Chemical Analysis of Alcohol-to-Jet (ATJ) Fuel and Development of Surrogate Fuel Mixtures, *Energy & Fuels*, **2015,** 29, 3760-3769.

[33] Luning Prak, D.J.; Brown, E.K.; Trulove, P.C. Density, Viscosity, Speed of Sound, and Bulk Modulus of Methyl Alkanes, Dimethyl Alkanes, and Hydrotreated Renewable Fuels, *J. Chem. Eng. Data*, **2013,** 58, 2065-2075.

[34] Edwards, J.T.; Hutzler, S.A.; Morris, R.E.; Muzzell, P.A. *Tri-service jet fuel characterization for DOD applications:Fit-for-purpose and trace impurity evaluations task 2 & 3 final report*; Southwest Research Institute: San Antonio, TX, March 20, 2014, pp. A-12.

[35] Borgnakke, C.; Sonntag, R.E. Chapter 8: Entropy for a control mass. *Fundamentals of Thermodynamics*, 7th ed.; Wiley: New Delhi, 2009; pp. 269-273.

[36] Poling, B.E.; Thomson, G.H.; Friend, D.G.; Rowley, R.; Wilding, W. V. Section 2-Physical and chemical data. *Perry's chemical engineers' handbook*, 8th ed.; McGraw-Hill: New York, 2008; pp. 2-229, 2-252, 2-254, 2-261, 2-274, 2-276, 2-300, 2-302, 2-316, 2-318, 2-324, 2-410.

[37] Armas, O.; Martinez-Martinez, S.; Mata, C.; Pacheco, C. Alternative method for bulk modulus estimation of Diesel fuels, *Fuel*, **2016**, 167, 199-207.

[38] Payri, R.; Armas, O.; Bracho, G.; Soriano, J.A.; Fernandez-Yanez, P. Nozzle rate of injection estimation from hole to hole momentum flux data with different fossil and renewable fuels, *Fuel,* **2020**, 279, 118404, DOI: 10.1016/j.fuel.2020.118404.

Chapter 6

Summary and Conclusions

This study covers greenhouse gas (GHG) emissions reduction via co-optimization of three different alternative diesel fuels (i.e., B20, DME, and jet fuels) with compression ignition (CI) engines.

Chapter 3 presents GHG emissions reduction via optimization of the calibration of the engine control unit (ECU) for B20 application in a medium-duty compression ignition engine. The optimization of ECU calibration for B20 application resulted in a relative 0.53% improvement in brake fuel conversion efficiency from the conventional petroleum-based diesel (i.e., 0.53% decrease in "MJ/mile"), which, in turn, resulted in the same percentage of decrease in GHG emissions in the pump-to-wheels (PTW) stage. Combining the well-to-pump (WTP) GHG emissions reduction from B20 (i.e., ~12.7% reduction compared to petroleum-based diesel on a "gCO_{2e}/MJ" basis), the application of B20 in a medium-duty compression ignition engine reduces GHG emissions by about 13.2% throughout its entire life-cycle (i.e., well-to-wheels) on a "gCO_{2e}/mile" basis. This satisfies the criteria for the State of California's Low Carbon Fuel Standard, which requires, at least, 10% reduction in WTW GHG emissions from the production and use of the transportation fuel. In addition, the use of B20 with the optimized ECU setting achieved 25.5% reduction in BSNOx and 16.7% reduction in BSPM emissions. Thus, the wider adoption of B20 in compression ignition engines with optimized ECU calibration is a feasible means to reduce GHG emissions cost-effectively.

Studies of higher biodiesel blends (>B20) are suggested for future work to achieve a greater degree of GHG reduction through the adoption of biodiesel. Studies at higher load conditions relevant to an engine-dyno certification test are also suggested to explore the potential increase in the GHG reductions that are not investigated in the current research.

Chapter 4 presents GHG emissions reduction via development of two novel DME blends optimized for the fuel injection systems of mixing controlled compression ignition engines. The two novel DME blends, or Michigan DME blend I (DME/glycerol/DPG blend) and II (DME/glycerol/PG blend), are successfully developed achieving a viscosity of that of No. 2 diesel fuel (i.e., 1.9cSt at 40°C) at around 45 wt. % DME content. Both blends did not show phase separation thanks to the presence of the well-chosen co-solvents (i.e., DPG for blend I and PG for blend II) while maintaining most of the main merits of neat DME (i.e., soot-free combustion, non-toxicity and benign health and environmental impact, and renewable production availability at commercial scale with low carbon intensity). A well-to-wheels (WTW) life-cycle GHG assessment is conducted for 1kg production and use of Michigan DME blend II, and the result showed that the Michigan DME blend II reduces GHG emissions by 50.2% compared to the conventional petroleum-based diesel fuel. A preliminary engine test with Michigan DME blend I with 40 wt. % DME was also conducted in the study showing the promise of adopting Michigan DME blend I in the production CI engines in the future.

A more extensive engine demonstration with the Michigan DME blends is recommended for future work in compression-ignition engines with higher injection pressure and better injection timing control capability (i.e., common-rail fuel injection system) and a turbocharged intake air system to apply boosted intake air temperature to compensate for the low cetane number of the blends. Extended engine tests with the blends to ensure the durability of the fuel injection systems are also suggested for future work.

Chapter 5 presents experimental measurements of the isothermal bulk modulus of compressibility and speed of sound of conventional and alternative jet fuels to provide a fundamental guideline for the co-optimization of pump-line-nozzle (PLN) type fuel injection systems installed in the U. S. Army ground vehicles with a wide variety of jet fuels. The study showed that all of the jet fuels measured have both an isothermal bulk modulus and a speed of sound that are lower than those of the conventional petroleum-based diesel fuel, with the descending order of: petroleum-based diesel fuels > petroleum-based jet fuels ≈ Farnesane > HRJC > ATJ. Quantitatively speaking, the isothermal bulk modulus of the three petroleum-based jet fuels and Farnesane was about 20-25% lower than that of the petroleum-based diesel. The HRJC had around 4% lower isothermal bulk modulus as compared to Farnesane while ATJ had 14% lower isothermal bulk modulus as compared to Farnesane. The lower bulk modulus and speed of sound of jet fuels suggested that advance in the start of pumping timing settings is required in the pump-line-nozzle type fuel injection systems to ensure optimal operation of the U. S. Army ground vehicles with such legacy PLN fuel injection systems. The wider adoption of the three different alternative jet fuels (i.e., Farnesane, HRJC, and ATJ) with adjusted start of pumping timings based on the current study’s guideline from their bulk modulus and speed of sound is expected to reduce GHG emissions from Army fleet operations by enabling optimal engine operation with these unconventional fuels.

The establishment of a quantitative correlation between the bulk modulus and speed of sound of fuels and the unintended injection timing shifts in pump-line-nozzle type fuel injection system is suggested for future work. Further fundamental research on the estimation of specific heat ratios of different liquid hydrocarbon molecular species from their readily available fundamental properties such as dielectric constant is also suggested for future work.

Appendix A

Net Heat Release Rate Calculation

A.1 Detailed Description of Net Heat Release Rate (Q_{net}) Calculation

The net heat release rate (Q) calculated from Equation 3.19 is based on the general 1st law of thermodynamics. There are only two assumptions applied to the general form of 1st law when Equation 3.19 is derived: 1. The work process should be a reversible process or an irreversible process that can be approximated by reversible polytropic process, 2: The working fluid is an ideal gas.

The well-known general form of the 1st law is presented in Equation A.1.[1] The sign convention for the heat term (Q) and the work term (W) is "positive-in" and "positive-out" for each. Here, the change of the "thermodynamic properties" (i.e., properties that only depend on the initial and final states) is denoted with differential "d" whereas the change of other properties is denoted with "δ". Since work is not a thermodynamic property (i.e., it depends not only on the initial and final states, but also on the process between the two states), the process should be assumed to be "reversible" to make the work term equal to the volume expansion work term (i.e., PdV). If we apply this reversible work assumption in hand with the definition of the enthalpy (H), Equation A.1 could be re-written as Equation A.2.

$$\delta Q = dU + \delta W \qquad \text{(Eq. A.1)}$$

$$\delta Q = dU + PdV = dH - VdP \quad \text{(Eq. A.2)}$$

(H: enthalpy)

Now, the second assumption applied is that the working fluid is ideal gas. Equation A.3 is only justifiable when the working fluid is ideal gas.^{1} If we apply the ideal gas working fluid assumption, Equation A.2 can go through the algebraic rearrangement shown in Equations A.4-A.8, and finally results in Equation A.9 which is the analytical version of the Equation 3.19. The only difference between Equation A.9 and Equation 3.19 is that, in Equation 3.19, the specific heat ratio in Equation A.9 is replaced by the polytropic coefficient estimated from the iteration method in Indicom in order to account for the irreversibility of the piston work done to or given from the working fluid.

$$dH = C_p dT \quad \text{(Eq. A.3)}$$

(C_p: isobaric heat capacity)

$$\delta Q = C_p dT - VdP \quad \text{(Eq. A.4)}$$

$$= \gamma C_v dT - VdP \quad \text{(Eq. A.5)}$$

(γ: specific heat ratio, C_v: isochoric heat capacity)

$$= \frac{\gamma}{\gamma-1} \cdot (\gamma - 1) \cdot C_v dT - VdP \quad \text{(Eq. A.6)}$$

$$= \frac{\gamma}{\gamma-1} \cdot (dH - dU) - VdP \quad \text{(Eq. A.7)}$$

$$= \frac{\gamma}{\gamma-1} \cdot (PdV + VdP) - VdP \quad \text{(Eq. A.8)}$$

$$= \frac{\gamma}{\gamma-1} \cdot PdV - \frac{1}{\gamma-1} VdP \quad \text{(Eq. A.9)}$$

Thus, the net heat release rate (Q_i) obtained from Equation 3.19 is simply the sum of the change in internal energy and work done to or given from the working fluid with reasonable assumption that the working fluid is ideal gas. Therefore, the net heat release rate term accounts for the net increase in the internal energy of the working fluid captured by the change in cylinder pressure and cylinder volume and also accounts for the volume compression/expansion work given to/provided from the working fluid. In other words, the net heat release rate (Q_i) term is not the gross amount of heat generated from the fuel mass burnt. It is the net heat input rate into the working fluid after accounting for all sources of heat losses (e.g., convective/conductive/radiative heat losses from the working fluid to the chamber wall and valves, evaporative cooling due to liquid fuel vaporization, heat losses due to the mass transfer inside the combustion chamber through crankcase blow-by or crevice volume effect) during the CA duration of the analysis. This difference between the net heat release rate and gross heat release rate is clarified in the next paragraph with the clarification on other terms of the energy with different steps and levels of conversion from the original fuel energy.

Now, having clarified the net heat release rate term, additional understandings can be obtained from the Figure 3.4a. We can see that the net heat release rate gradually decreases from -30aTDC to around -10aTDC. This is because the compression work done to the working fluid is accounted into the net heat release rate with negative value. It is also because of the small amount of heat losses to the chamber wall before the fuel injection event. Then, at around -9aTDC, the net heat release rate suddenly drops and bottoms at around -8aTDC. This drop in net heat release rate is due to the evaporation of the injected liquid fuel. Then, between -8aTDC and pilot SOC (~ -2aTDC), there is a small increase in heat release rate. Based on the findings regarding the low temperature diesel fuel combustion, this small increase in heat release rate observed before the pilot combustion peak can be considered as the cool-flame heat release (i.e., 1st stage heat release).[2]

A.2 References

[1] Borgnakke, C.; Sonntag, R. Chapter 5: The First Law of Thermodynamics, The Fundamentals of Thermodynamics, 7th ed., John Wiley & Sons: Hoboken, NJ., 2009, pp. 127-131.

[2] Zhang, Y.; Boehman, A. *Combustion and Flame*, **2012**, 159, 1619-1630.

Appendix B

Specific Heat Ratios of Hydrocarbon Liquids

B.1 List of the References for Thermophysical Properties of Hydrocarbon Liquids

The investigation on the specific heat ratios of different hydrocarbon molecular species in liquid phase is presented in this appendix, which provides supplementary argument and information to Chapter 5. Due to the great amount of the referenced data presented in this appendix, the list of the references for thermophysical properties of the referenced molecular species in Tables B.2 – B.4 and Figures B.2 – B.7 are summarized in Table B.1.

			Table B.2		Table B.3			
Group	Species	CAS no.	ρ	a	B_s	B_T	C_p	C_v
Normal alkanes	n-pentane	109-66-0	a	a	†	t	a	a
	n-hexane	110-54-3	a	a	†	t	a	a
	n-heptane	142-82-5	a	a	†	t	a	a
	n-octane	111-65-9	a	a	†	t	a	a
	n-nonane	111-84-2	a	a	†	t	a	a
	n-decane	124-18-5	a	a	†	t	a	a
	n-undecane	1120-21-4	b	c	†	t	-	
	n-dodecane	112-40-3	a	a	†	t	a	a
	n-tridecane	629-50-5	d	e	†	t	d	d

	n-tetradecane	629-59-4	f	e	†	t	-	
	n-pentadecane	629-62-9	g	g	†	t	-	
	n-hexadecane	544-76-3	h	h	†	t	-	
Branched alkanes	iso-pentane (2-methylbutane)	78-78-4	a	a	†	t	a	a
	iso-hexane (2-methylpentane)	107-83-5	a	a	†	t	a	a
	3-methylpentane	96-14-0	-		u	t	-	
	2,2-dimethylbutane	75-83-2	i	j	†	t	-	
	iso-octane (2,2,4-trimethylpentane)	540-84-1	k	k	†	t	-	
	iso-cetane (2,2,4,4,6,8,8-heptamethylnonane)	4390-04-9	l	l	†	v	-	-
Aromatics	benzene	71-43-2	a	a	†	t	a	a
	toluene	108-88-3	a	a	†	t	a	a
	o-xylene	95-47-6	m	m	†	t	-	
	m-xylene	108-38-3	m	m	†	t	-	
	p-xylene	106-42-3	m	m	†	t	-	
	ethylbenzene	100-41-4	n	o	†	t	-	
	mesitylene	108-67-8	p	p	†	t	-	
	cumene	98-82-8	q	q	†	t	-	
Cycloalkanes	cyclopentane	287-92-3	r	r	†	w	-	
	cyclohexane	110-82-7	a	a	†	w	a	a
	methylcyclohexane	108-87-2	r	r	†	w	-	
	tr-decalin	91-17-8	s	s	†	t	-	

			Table B.4	Fig. B.2	Fig. B.3	Fig. B.4	Fig. B.5	Fig. B.6	Fig. B.7
Group	Species	CAS no.	B.P.	ε_r	VDW Vol.	V_m	B_s	α_p	C_p
Normal alkanes	n-pentane	109-66-0	x	x	x	x	†	x	A
	n-hexane	110-54-3	x	x	x	x	†	x	A
	n-heptane	142-82-5	x	x	x	x	†	x	A
	n-octane	111-65-9	x	x	x	x	†	x	A

	n-nonane	111-84-2	x	x	x	x	†	x	A
	n-decane	124-18-5	x	-	x	x	†	x	A
	n-undecane	1120-21-4	x	x	x	x	†	x	A
	n-dodecane	112-40-3	x	x	x	x	†	x	A
		CAS no.	Table B.4	Fig. B.2	Fig. B.3	Fig. B.4	Fig. B.5	Fig. B.6	Fig. B.7
	n-tridecane	629-50-5	x	x	x	x	†	x	A
	n-tetradecane	629-59-4	x	x	x	x	†	x	A
	n-pentadecane	629-62-9	x	x	x	x	†	x	A
	n-hexadecane	544-76-3	x	x	x	x	†	x	A
Branched alkanes	iso-pentane (2-methylbutane)	78-78-4	-				†	-	
	iso-hexane (2-methylpentane)	107-83-5	-			x	†	x	B
	3-methylpentane	96-14-0	-			x	u	x	B
	2,2-dimethylbutane	75-83-2	-			x	†	x	B
	2-methylhexane	591-76-4	-			x	-	x	B
	3-methylhexane	589-34-4	-			x	-	x	B
	2,4-dimethylpentane	108-08-7	-			x	-	x	B
	2,2-dimethylpentane	590-35-2	-			x	-	x	B
	3,3-dimethylpentane	562-49-2	-			x	-	x	B
	3-methylheptane	589-81-1	-			x	-	x	B
	2-methylheptane	592-27-8	-			x	-	x	B
	3,3-dimethyhexane	563-16-6	-			x	-	x	B
	2,5-dimethylhexane	592-13-2	-			x	-	x	B
	iso-octane (2,2,4-trimethylpentane)	540-84-1	-			x	†	x	B
	3,5-dimethylheptane	926-82-9	-				y	-	
	2-methyloctane	3221-61-2	-				y	-	
	4-methyloctane	2216-34-4	-				y	-	
	3,6-dimethyloctane	15869-94-0	-				y	-	

	2-methylnonane	871-83-0	-			x	y	x	B
	3-methylnonane	5911-04-6	-			x	-	x	B
	2-methyldecane	6975-98-0	-			x	y	x	B
	3-methylundecane	1002-43-3	-				y	-	
		CAS no.	Table B.4	Fig. B.2	Fig. B.3	Fig. B.4	Fig. B.5	Fig. B.6	Fig. B.7
	2-methylpentadecane	1560-93-6	-				y	-	
	iso-cetane	4390-04-9	-				z	-	
	7-methylhexadecane	26730-20-1	-				y	-	
Aromatics	benzene	71-43-2	x	x	x	x	†	x	C
	toluene	108-88-3	-			x	†	x	C
	o-xylene	95-47-6	-			x	†	x	C
	m-xylene	108-38-3	-			x	†	x	C
	p-xylene	106-42-3	-			x	†	x	C
	ethylbenzene	100-41-4	-			x	†	x	D
	mesitylene	108-67-8	-			x	†	x	C
	cumene	98-82-8	-			x	†	x	E
	n-butylbenzene	104-51-8	-			x	-	x	B
	naphthalene	91-20-3	x	x	x	-			
	anthracene	120-12-7	x	x	x	-			
	pyrene	129-00-0	x	x	x	-			
Cycloalkanes	cyclopentane	287-92-3	x	x	x	x	†	x	A
	methylcyclopentane	96-37-7	-			x	-	x	B
	cyclohexane	110-82-7	x	x	x	x	†	x	A
	1,1-dimethylcyclopentane	1638-26-2	-			x	-	x	B
	ethylcyclopentane	1640-89-7	-			x	-	x	B
	methylcyclohexane	108-87-2	-			x	†	x	B
	cycloheptane	291-64-5	x	x	x	x	-	x	B

	n-propylcyclopentane	2040-96-2	-			x	-	x	B
	1,1-dimethylcyclohexane	590-66-9	-			x	-	x	B
	ethylcyclohexane	1678-91-7	-			x	-	x	B
	cyclooctane	292-64-8	x	x	x	x	-	x	A
		CAS no.	Table B.4	Fig. B.2	Fig. B.3	Fig. B.4	Fig. B.5	Fig. B.6	Fig. B.7
	n-butylcyclopentane	2040-95-1	-			x	-	x	B
	n-propylcyclohexane	1678-92-8	-			x	-	x	B
	n-butylcyclohexane	1678-93-9	-			x	-	x	B
	tr-decalin	91-17-8	x	x	x	x	†	x	F
	cyclodecane	293-96-9	-						A
	cyclododecane	294-62-2	x	-					A

Table B.1. List of the references for the thermophysical properties presented in appendix B (Tables B.2 – B.4 and Figures B.2 – B.7). a: Poling et al.[1], b: Giuliano et al.[2], c: Bessieres et al.[3], d: Khasanshin et al.[4], e: Daridon et al.[5], f: Bernardo et al.[6], g: Daridon et al.[7], h: Outcalt et al.[8], i: Brooks et al.[9], j: Kumaran et al.[10], k: Koravkova et al.[11], l: Luning Prak et al.[12], m: Gahlyan et al.[13], n: Calvar et al.[14], o: Gonzalez et al.[15], p: Gonzalez-Olmos et al.[16], q: Gragoescu et al.[17], r: Gonzalez et al.[18], s: Miyake et al.[19], t: Marcus et al.[20], u: Tamura et al.[21], v: Bessieres et al.[22], w: Takagi et al.[23], x: DIPPR Project 801[24], y: Luning Prak et al.[25], z: Luning Prak et al.[26], A: Huang et al.[27], B: Domalski et al.[28], C: Ali et al.[29], D: Sastry et al.[30], E: NIST Chemistry web-book[31], F: Miyake et al.[32], †B_s is calculated using Equation 5.1 based on the referenced density and speed of sound, -: Not available from previous studies

B.2 Specific Heat Ratio of Hydrocarbon Liquids

To start the discussion on the specific heat ratio of different hydrocarbon molecular species, Tables B.2 and B.3 are first presented. Table B.2 shows the density and speed of sound of different hydrocarbon molecular species in four different hydrocarbon groups (i.e., linear alkanes, branched alkanes, aromatics, cycloalkanes). The molecular weight and carbon number of the species are also shown in the table.

Group	Molecular species	Carbon no.	Molecular weight [kg/kmol]	Density [kg/m3]	Speed of sound[m/s]
Normal alkanes	n-pentane	5	72.15	626.01*	1038*
	n-hexane	6	86.18	653.67	1066
	n-heptane	7	100.2	679.30	1144
	n-octane	8	114.2	698.24	1146
	n-nonane	9	128.2	713.33	1215
	n-decane	10	142.3	726.46	1250
	n-undecane	11	156.3	737.81	1256
	n-dodecane	12	170.3	761.96	1274
	n-tridecane	13	184.4	753.15	1295
	n-tetradecane	14	198.4	761.04	1312
	n-pentadecane	15	212.4	766.45**	1332**
	n-hexadecane	16	226.4	769.81	1338
Branched alkanes	iso-pentane(2-methylbutane)	5	72.15	618.15**	967.4**
	iso-hexane (2-methylpentane)	6	86.17	648.57	1053
	3-methylpentane	6	86.17	-	
	2,2-dimethylbutane	6	86.17	644.32	998.2
	iso-octane (2,2,4-trimethylpentane)	8	114.2	687.68	1082
	iso-cetane (2,2,4,4,6,8,8-heptamethylnonane)	16	226.4	781.10	1266
Aromatics	Benzene	6	78.11	873.89	1305
	Toluene	7	92.14	860.64	1328
	o-Xylene	8	106.2	875.91	1355
	m-Xylene	8	106.2	860.05	1328
	p-Xylene	8	106.2	856.63	1317
	Ethylbenzene	8	106.2	862.50	1319
	Mesitylene (1,3,5-trimethylbenzene)	9	120.2	861.15	1330
	Cumene (isopropyl benzene)	9	120.2	858.27	1308
Cycloalkanes	Cyclopentane	5	70.10	740.00	1204
	Cyclohexane	6	84.16	774.04	1255
	Methylcyclohexane	7	98.19	765.00	1215
	tr-decalin	10	138.3	865.81	1376

Table B.2 Density and speed of sound of the selected hydrocarbon molecular species at the standard state (298.15K, 0.1MPa) unless noted with superscript (*at 293.15K, **at 296.15K).

In Table B.3, the specific heat ratio, isothermal and isentropic bulk modulus, and the isochoric and isobaric molar heat capacity of the selected hydrocarbon molecular species are presented. The list of the species presented in Table B.3 are the same as that in Table B.2. The specific heat ratio of the species is calculated in two different ways in Table B.3: i) by using the ratio of the isentropic bulk modulus to the isothermal bulk modulus, and ii) by using the ratio of the isobaric molar heat capacity to the isochoric molar heat capacity. This was to ensure the consistency and reliability of the referenced data. The specific heat ratio values calculated in the two different ways agreed well with each other for all of the molecular species except for two molecular species (i.e., n-pentane and toluene). For n-pentane and toluene, the two calculated specific heat ratio values had considerable difference (i.e., $\geq$ 5%) raising the question to the consistency of the referenced data. Thus, the specific heat ratio of these two molecular species presented in Table B.3 should be considered as rough estimates.

Table B.3 confirms that the specific heat ratio of hydrocarbon species is very different from unity (i.e., "1") even in the liquid-phase. The species with the lowest specific heat ratio in Table B.3 is n-pentadecane with the γ value being 1.07, which is 7% higher than unity. For some species such as benzene, the value of γ is over 1.4, which is similar to the specific heat ratio of standard air. Thus, for hydrocarbon molecular species and mixtures, the difference between isentropic and isothermal bulk modulus should be accounted for in their liquid-phase.

Chemical group	Molecular species	B_s [MPa]	B_T [MPa]	γ= B_s/B_T	C_P [kJ/mol·K]	C_v [kJ/mol·K]	γ=C_P/C_v	Error between two γ values [%]
Normal alkanes	n-pentane	675.10^{*}	469.48^{*}	1.44^{*}	0.1677	0.1255	1.34	7.61
	n-hexane	743.14	597.37	1.24	0.1947	0.1510	1.29	3.51
	n-heptane	889.66	694.44	1.28	0.2252	0.1785	1.26	1.54
	n-octane	918.16	781.25	1.18	0.2551	0.2068	1.23	4.72
	n-nonane	1053.7	849.61	1.24	0.2840	0.2293	1.23	0.14
	n-decane	1135.9	914.07	1.24	$0.3256^{\dagger}$	$0.2656^{\dagger}$	$1.23^{\dagger}$	1.37
	n-undecane	1165.5	925.06	1.26	-			
	n-dodecane	1236.9	1012.1	1.22	0.3779	0.3105	1.22	0.41
	n-tridecane	1264.4	1054.8	1.20	$0.4039^{\dagger}$	$0.3407^{\dagger}$	$1.19^{\dagger}$	1.11
	n-tetradecane	1310.1	1096.4	1.19	-			
	n-pentadecane	1360.0^{**}	1265.8^{**}	1.07^{**}	-			
	n-hexadecane	1379.8	1162.7	1.19	-			
Branched alkanes	2-methylbutane	578.54^{**}	444.44^{**}	1.30^{**}	0.1648	0.1235	1.33	2.45
	2-methylpentane	719.51	544.66	1.32	$0.1919^{\dagger}$	$0.1537^{\dagger}$	$1.25^{\dagger}$	5.80
	3-methylpentane	757.17	581.73	1.30	-			
	2,2-dimethylbutane	642.10	504.54	1.27	-			
	iso-octane	806.12	661.37	1.22	-			
	iso-cetane	1253.7	1052.6	1.19	-			
Aromatics	Benzene	1489.4	1035.1	1.44	0.1332	0.0929	1.43	0.34
	Toluene	1518.2	1096.4	1.38	$0.1732^{\dagger}$	$0.1062^{\dagger}$	$1.63^{\dagger}$	15.09
	o-Xylene	1608.1	1233.0	1.30	-			
	m-Xylene	1516.7	1160.0	1.31	-			
	p-Xylene	1485.8	1164.1	1.28	-			
	Ethylbenzene	1500.5	1156.0	1.30	-			
	Mesitylene	1523.6	1265.8^{*}	-				
	Cumene	1469.0	1119.8	1.31	-			
Cyclo -alkanes	Cyclopentane	1072.7	736.37	1.46	-			
	Cyclohexane	1220.4	862.81	1.41	0.1537	0.1109	1.39	2.05
	Methylcyclohexane	1129.3	882.61	1.28	-			
	tr-decalin	1639.9	1317.5	1.24	-			

Table B.3 Isothermal (B_T) and isentropic bulk modulus (B_s) at 0.1MPa and 298.15K unless noted with superscript (*at 293.15K, **at 296.15K), isochoric (C_v) and isobaric molar heat capacity (C_P) at 0.1MPa, 300K unless noted with superscript (†at 298.15K), and the specific heat ratio (γ) of the selected hydrocarbon molecular species.

To show how the specific heat ratios of hydrocarbon species vary depending on their molecular structure and molecular weight, the values of the specific heat ratio listed in Table B.3 are presented in Figure B.1 as a function of carbon number for four different hydrocarbon groups (i.e., linear alkane, branched alkane, cycloalkane, aromatics). The specific heat ratio obtained from dividing C_p by C_v is primarily used in Figure B.1, but if the "C_p/C_v" was not available, γ value obtained from dividing B_s by B_T is presented in Figure B.1 instead. For the specific heat ratio of toluene, the specific heat ratio obtained from dividing B_s by B_T is exceptionally presented in Figure B.1 because the "C_p/C_v" had significant deviation from the general trend of the specific heat ratios of the other molecular species. Two main trends observed from Figure B.1 are as follows: i) specific heat ratio decreases with increasing carbon number for the molecular species with similar molecular structure; and ii) specific heat ratio of the cyclic hydrocarbons are greater than that of the acyclic hydrocarbons when compared at the same carbon number.

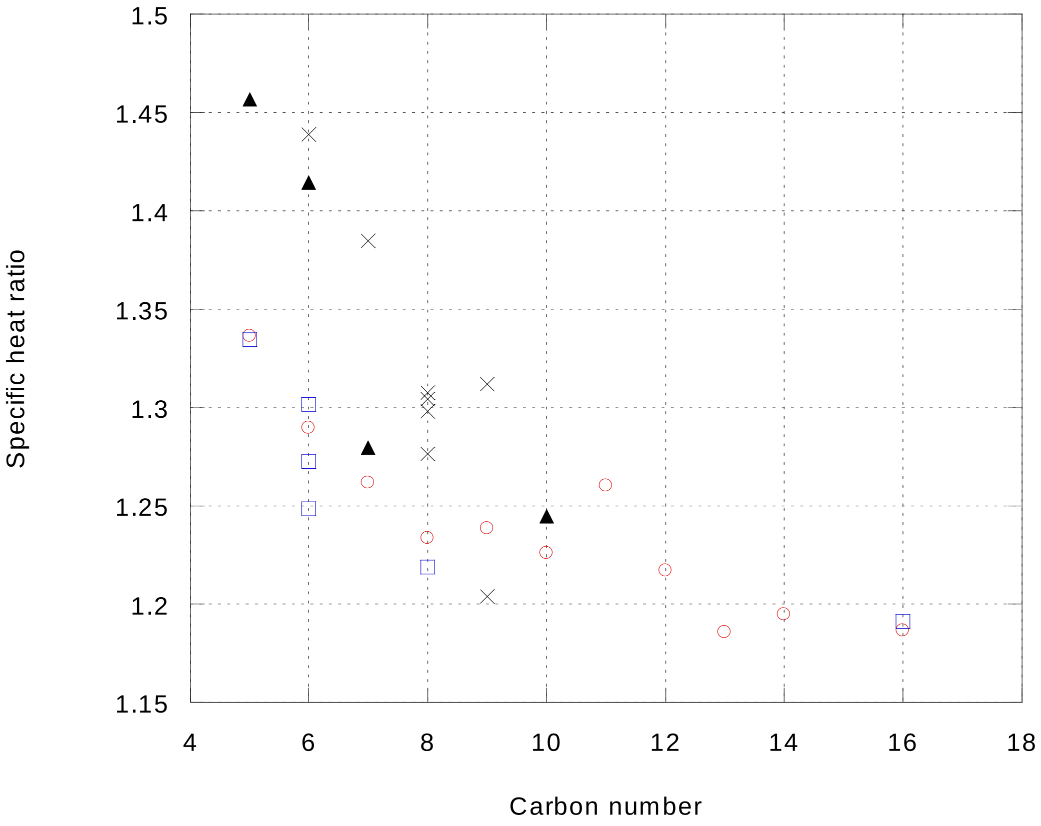

Figure B.1 Specific heat ratio of different hydrocarbon molecular species at the standard state (data from Table B.3) as a function of carbon number for (○) n-alkanes, (□) branched alkanes, (▲) cycloalkanes, and (×) aromatics.

B.3 Impact of Molecular Structure and Weight on Specific Heat Ratio of Hydrocarbons

To understand why the specific heat ratio of hydrocarbon molecular species is greater for the cyclic hydrocarbon species and for the species with lower carbon number, Equation B.1 is essential. In Equation B.1, α_p is isobaric thermal expansion coefficient, and V_m is molar volume.[20] Equation B.1 shows which macroscopic thermophysical properties are related to the degree of deviation of specific heat ratio from unity. The second term on the right-hand-side (RHS) (i.e., $\frac{T\alpha_p{}^2 V_m B_S}{C_P}$) in the equation is the degree of deviation of the specific heat ratio from unity. Therefore, we can explain the impact of molecular weight and structure on the specific heat ratio by explaining the impact of those (i.e., molecular weight and structure) on the 4 macroscopic thermophysical properties constituting this deviation term (i.e., α_p, V_m, B_s, C_P). Furthermore, when explaining the impact of molecular structure and weight on these 4 macroscopic thermophysical properties, the microscopic molecular theories governing intermolecular attraction and heat capacity can be used. In this section, the impact of molecular structure and weight on molar volume, isentropic bulk modulus, and isobaric thermal expansion coefficient will be first presented by using the microscopic molecular theory about "induced dipole – induced dipole" attraction (i.e., London dispersion force). Then, the impact of molecular structure and weight on isobaric heat capacity will be presented by using the statistical thermodynamics.

$$\gamma = \frac{B_S}{B_T} = 1 + \frac{T\alpha_p{}^2 V_m B_S}{C_P} \qquad \text{(Eq. B.1)}$$

B.3.1 Impact on Molar Volume, Isentropic Bulk Modulus and Isobaric Thermal Expansion Coefficient

When comparing the difference in intermolecular attraction in different molecular species, comparing the boiling points of the species can be a good "qualitative" method to see how molecular structure and weight affect the intermolecular attraction. The boiling point of different hydrocarbon species is referenced from DIPPR Project 801[24] and is compiled in Table B.4. In general, boiling point was higher for the molecular species with higher carbon number and ring structure. This suggests stronger intermolecular attraction for the species with higher carbon number and cyclic molecular structure, which is consistent with the findings in previous studies.[33]

	n-alkanes		cycloalkanes		aromatics	
Carbon no.	Molecular Species	Boiling Point [K]	Molecular Species	Boiling Point [K]	Molecular Species	Boiling Point [K]
5	n-pentane	309.22	cyclopentane	322.4	-	
6	n-hexane	341.88	cyclohexane	353.87	benzene	353.25
7	n-heptane	371.58	cycloheptane	391.94	-	
8	n-octane	398.83	cyclooctane	424.29	-	
9	n-nonane	423.97	-		-	
10	n-decane	447.31	tr-decalin	460.46	naphthalene	491.14
11	n-undecane	469.08	-		-	
12	n-dodecane	489.47	cyclododecane	517.15	-	
13	n-tridecane	508.62	-		-	
14	n-tetradecane	526.73	-		anthracene	615.18
15	n-pentadecane	543.84	-		-	
16	n-hexadecane	560.01	-		pyrene	667.95

Table B.4 Boiling point of the selected hydrocarbon species.

As a more explicit and quantitative way to compare the intermolecular attraction for different hydrocarbon molecular species, we can use London's equation for intermolecular attraction energy (i.e., Equation B.2). London established a simplified equation for the dispersion energy between two non-polar particles based on quantum mechanics.[34,35] Since the molecular species relevant to Chapter 5 only include non-polar hydrocarbons, the London dispersion energy (i.e., “induced dipole – induced dipole” attraction) is the only intermolecular attraction we need to account for. In Equation B.2, E_d is the magnitude of the dispersion attraction energy between two particles “*A*” and “*B*”, ε_o is the permittivity of vacuum, *I* is the first ionization energy, α is the polarizability, and *R* is the distance between the centers of the two particles *A* and *B*. Based on Equation B.2, the dispersion force is stronger for the molecular species with higher polarizability (α) and smaller mean distance (R). Thus, if we look at how polarizability and mean distance is determined by molecular structure and weight, we can infer the impact of molecular structure and weight on intermolecular attraction energy.

$$E_d = -\frac{3}{2(4\pi\varepsilon_o)^2}\frac{I_A I_B}{I_A+I_B}\frac{\alpha_A\alpha_B}{R^6} \qquad \text{(Eq. B.2)}$$

Polarizability is the tendency of a molecule to have instantaneous charge separation when electric field is applied to the molecule, and it increases as the total number of the electrons contained in a molecule increases and as the area over which electrons are spread is increased.[36] Thus, we can expect that the polarizability will increase for the species with higher carbon number, and will slightly decrease in the order of acyclic alkane, cycloalkane, and aromatics due to the decrease in the number of hydrogen atoms. Quantitatively, polarizability of a molecular species can be calculated using the “Clausius-Mossotti relation” as shown in Equation B.3, where ε_r is dielectric constant, *N* is number density, and ε_0 is permittivity of vacuum.[37]

To calculate the polarizability of different hydrocarbon species, the dielectric constants of the hydrocarbon species listed in Table B.4 are collected from DIPPR Project 801[24]. Then, Equation B.3 is used to calculate the polarizability. The polarizability of different hydrocarbon molecular species is presented in Figure B.2 as a function of carbon number for different hydrocarbon groups (i.e., linear alkanes, cycloalkanes, aromatics).

$$\frac{\varepsilon_r - 1}{\varepsilon_r + 2} = \frac{N\alpha}{3\varepsilon_0} \qquad \text{(Eq. B.3)}$$

For comparing the value of R (in Equation B.2) for different molecular species, Van der Waals volume is used. Van der Waals volume is the mean volume occupied by a molecule that causes repulsion when it is intervened by another molecule. So, it is generally accepted as a means to compare the value of R between different molecular species[38]. The Van der Waals volume of the hydrocarbon species listed in Table B.4 is referenced from DIPPR Project 801[24] and is presented in Figure B.3 as a function of carbon number for different hydrocarbon groups.

Figures B.2 and B.3 confirm the previously suggested impact of molecular structure and weight on the London dispersion force by using boiling point: the London dispersion force is stronger for the species with higher carbon number and ring structure. For the species with similar molecular structure (e.g., n-hexane compared to n-octane), the polarizability increases with increasing carbon number due to the increasing number of the electrons contained in a molecule (See Figure B.2). The increase in polarizability strengthens the intermolecular attraction, and this is macroscopically expressed as the increase in boiling point. Thus, the London dispersion force is stronger for the species with higher carbon number when the molecular structure is similar. For the molecular species with different molecular structure (but with the same carbon number), the Van der Waals volume is greater for the acyclic alkanes than for cyclic hydrocarbons (i.e., cycloalkanes and aromatics) (See Figure B.3). This indicates that the mean distance between nearest molecules is shorter for cyclic hydrocarbons than for acyclic counterparts. The smaller value of *R* in cyclic hydrocarbons overshadows its slightly smaller value of polarizability compared to the acyclic species, thus resulting in the stronger dispersion force.

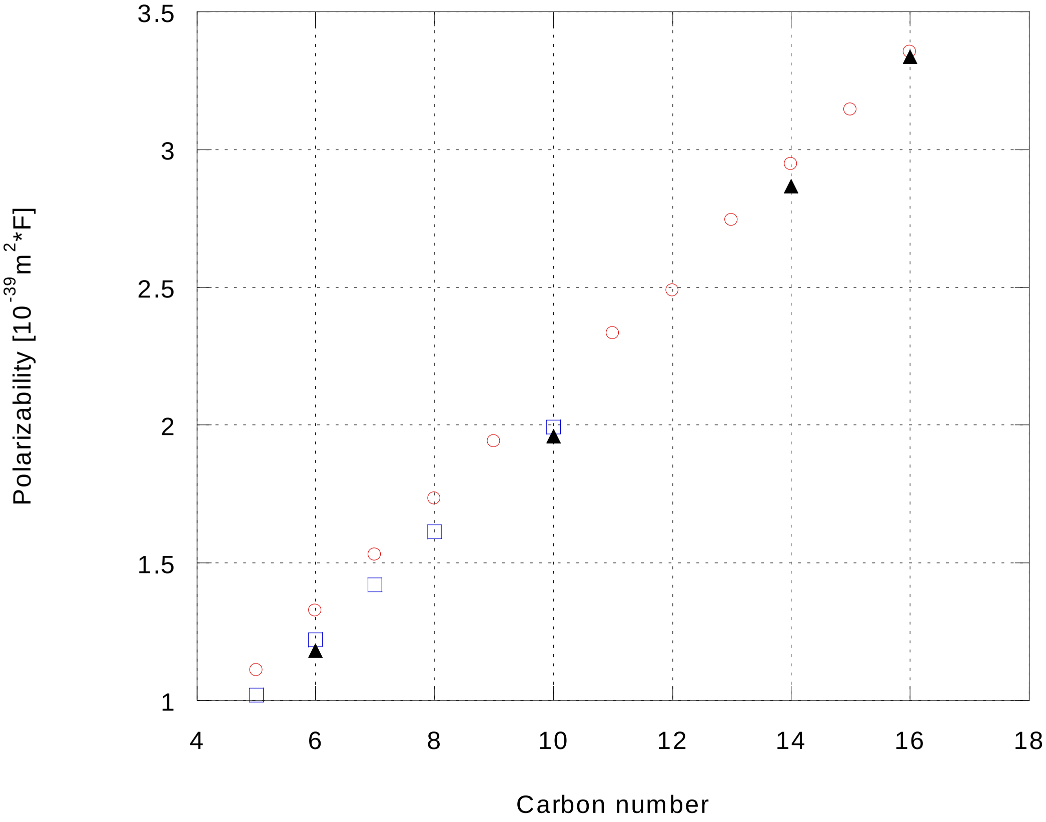

Figure B.2 Polarizability of the molecular species listed in Table B.4 as a function of carbon number for different hydrocarbon groups: (○) n-alkanes, (□) cycloalkanes, (▲) aromatics.

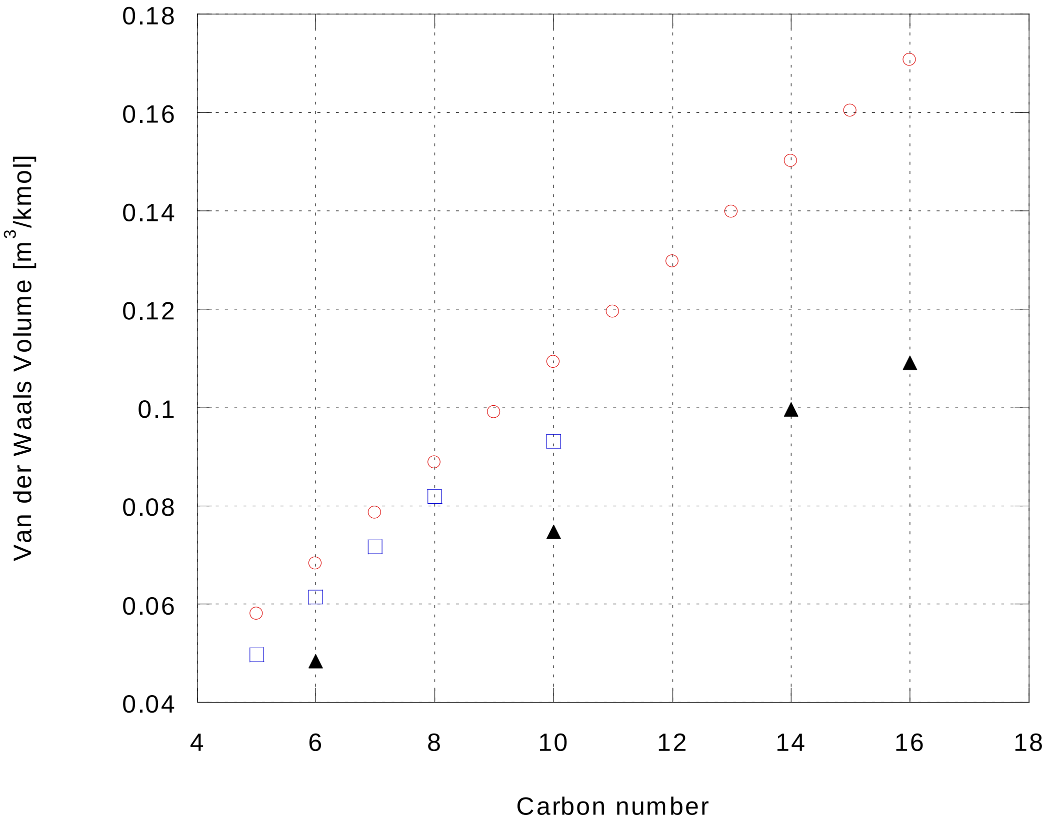

Figure B.3 Van der Waals volume of the molecular species listed in Table B.4 as a function of carbon number for different hydrocarbon groups: (○) n-alkanes, (□) cycloalkanes, (▲) aromatics.

The fact that the molecular species with higher carbon number and ring structure have stronger London dispersion force, in turn, explains how the molecular structure and molecular weight will influence the three macroscopic physical properties (i.e., V_m, α_p, B_s).

The impact of molecular structure and weight on the molar volume and isentropic bulk modulus will be first explained. The impact of molecular structure and molecular weight on the molar volume is shown in Figure B.4, and the impact of those on isentropic bulk modulus is presented in Figure B.5.

In Figure B.4, we can observe that the molar volume increases for the species with higher carbon number and acyclic molecular structure. In Figure B.5, we can observe that the isentropic bulk modulus increases for the species with higher carbon number and ring structure. Then, the combined observations from Figures B.4 and B.5 indicate that the cause for the increase in molar volume in two different comparison cases (i.e., comparison between the molecular species with different carbon number (n-hexane vs. n-octane) and comparison between the molecular species with different molecular structure (n-hexane vs. benzene)) can be different. For the first comparison case (i.e., n-hexane vs. n-octane), the species with greater molar volume (i.e., n-octane) also has greater isentropic bulk modulus while, for the second comparison case (i.e., n-hexane vs. benzene), the species with greater molar volume (i.e., n-hexane) has lower isentropic bulk modulus.

This is where the theory of intermolecular interaction comes into the play. It articulates how the molar volume increase in the two different comparison cases happens differently at microscopic scale. First, the reason why molar volume of acyclic species is greater than that of the cyclic counterpart (i.e., the species with the same carbon number) is because the void space between molecules is greater for acyclic species. The size of the molecule itself is not significantly different for acyclic and cyclic hydrocarbons if the carbon number is fixed. However, because London dispersion force is stronger for cyclic hydrocarbons than for acyclic species, the void space between molecules is smaller for cyclic hydrocarbons than for acyclic species. Since molar volume is the sum of “the volume directly occupied by the molecules” and “the void space between molecules”, the molar volume of the cyclic species becomes smaller than acyclic species due to the decrease in the void space. And since the void space is smaller for the cyclic species than for the acyclic counterparts, the cyclic species have stronger repulsion between molecules when pressure is applied. This results in the higher isentropic bulk modulus in cyclic species than in acyclic species.

However, the greater molar volume for the species with higher carbon number (when the molecular structure is similar) is not due to the increase in the void space. The void space is actually smaller for the species with higher carbon number because the London dispersion force is stronger for the species with higher carbon number. In this case, the greater molar volume is due to the increase in the volume directly occupied by the molecules. Thus, for the species with higher carbon number, the void space between molecules actually shrinks while the molar volume is increased. The decrease in the void space causes the stronger repulsion between molecules under pressure, which, in turn, results in the greater isentropic bulk modulus for the species with higher carbon number.

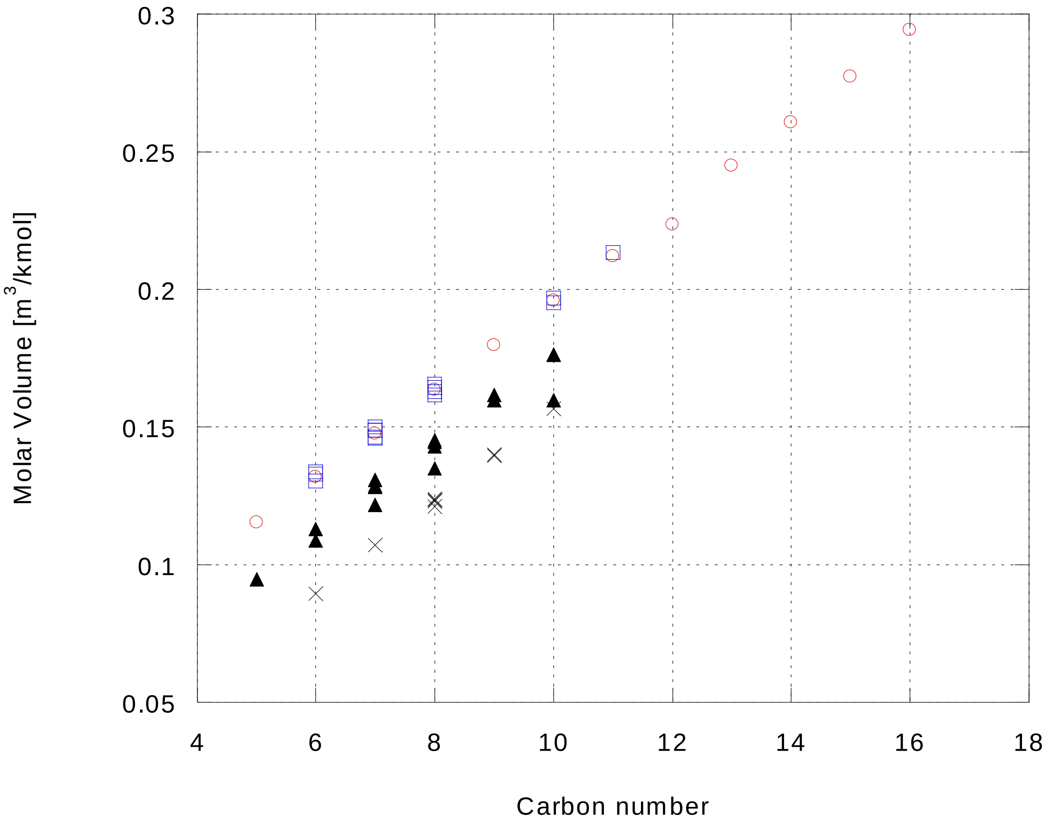

Figure B.4 Molar volume of different hydrocarbon species at standard state (298K, 0.1MPa) as a function of carbon number for different hydrocarbon groups: (○) n-alkanes, (□) br-alkanes, (▲) cycloalkanes, and (×) aromatics.

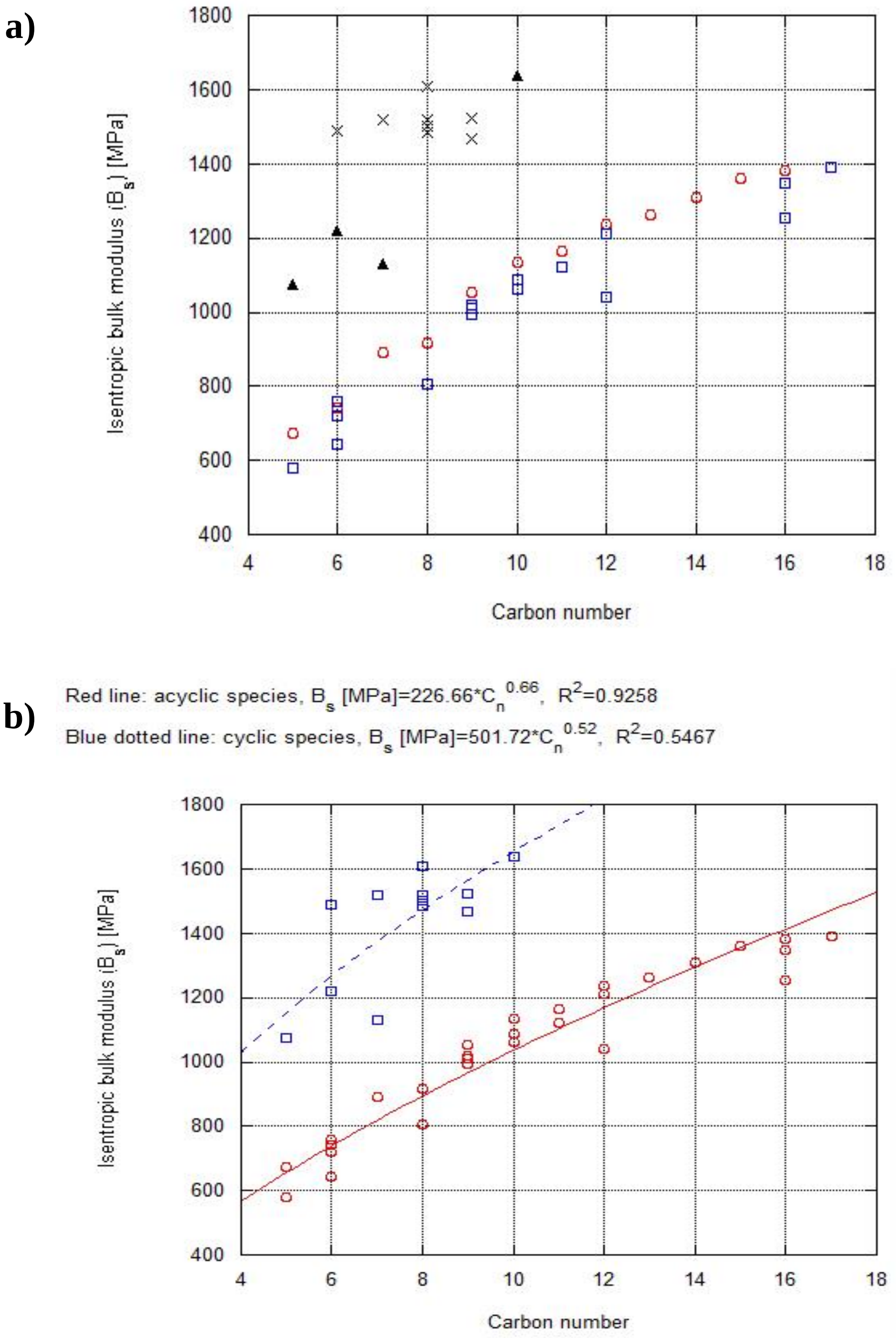

Figure B.5 Isentropic bulk modulus of different hydrocarbon molecular species at standard state (298K, 0.1MPa) as a function of carbon number **(a)** for (○) n-alkanes, (□) br-alkanes, (▲) cycloalkanes, (×) aromatics; **(b)** for (○) acyclic alkanes and (□) cyclic hydrocarbons. Least-square power law correlation between carbon number (C_n) and isentropic bulk modulus (B_s) is presented for acyclic alkanes (red solid line) and cyclic hydrocarbons (blue dotted line).

The variation of the isobaric thermal expansion coefficient by different molecular structure and molecular weight can be explained in a similar way. We calculated the isobaric thermal expansion coefficient of different hydrocarbon species from the referenced values of density over a wide range of temperature (at 0.1MPa) from DIPPR Project 801[24]. Figure B.6 shows the isobaric thermal expansion coefficient of different molecular species as a function of carbon number for different hydrocarbon groups. As expected, the thermal expansion coefficient decreases for the species with higher carbon number and ring structure. For the molecules with similar structure, the species with higher carbon number has greater London dispersion attraction, which results in the greater resistance against the thermal expansion of the void space between molecules, thus resulting in higher thermal expansion coefficient. For the species with the same carbon number but with different molecular structure, cyclic species have the greater London dispersion attraction than their acyclic counterparts to result in the greater resistance against the thermal expansion, which, in turn, results in higher thermal expansion coefficient.

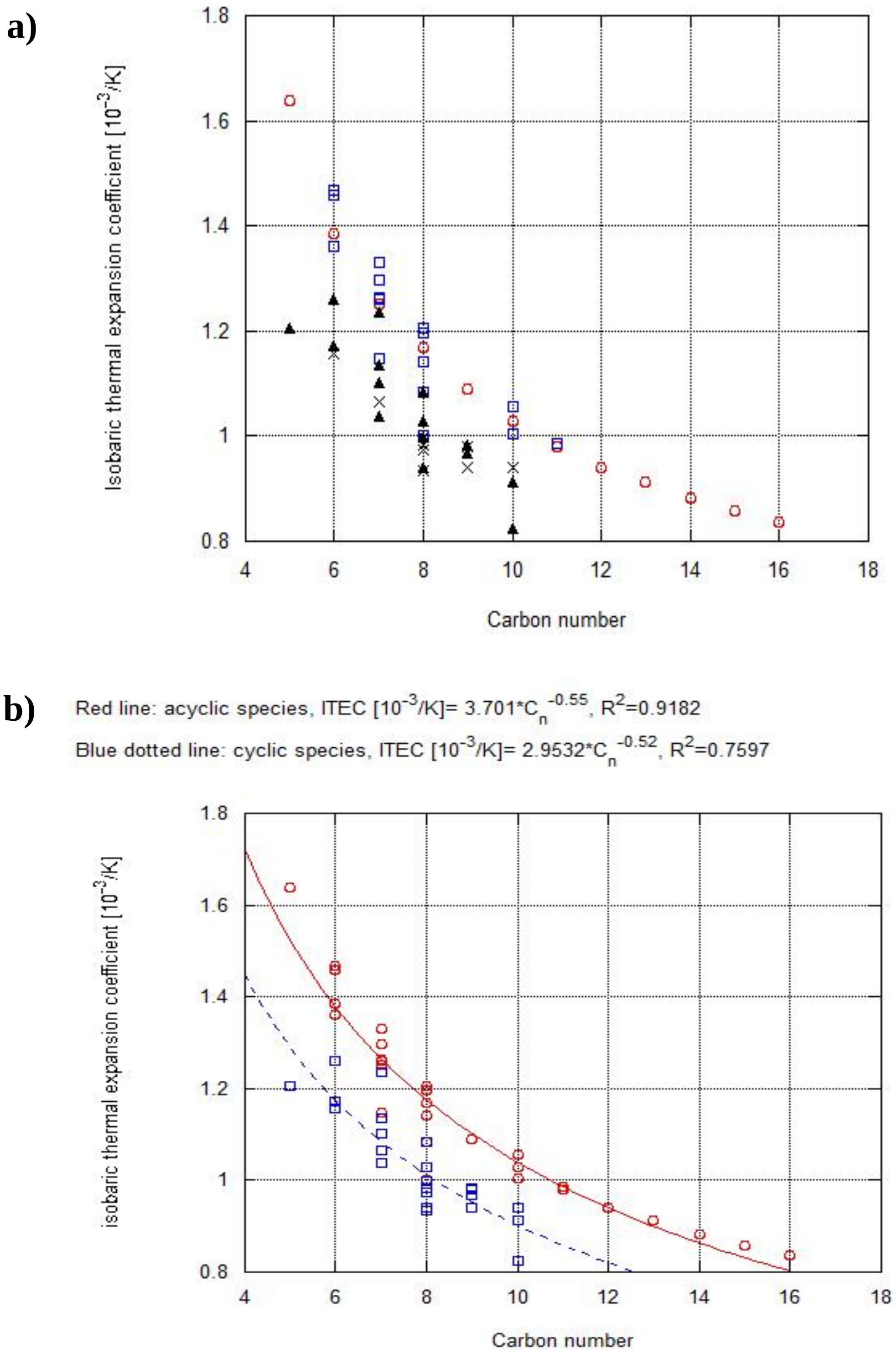

Figure B.6 Isobaric thermal expansion coefficient as a function of carbon number **(a)** for (○) n-alkanes, (□) br-alkanes, (▲) cycloalkanes, (×) aromatics, and **(b)** for (○) acyclic alkanes and (□) cyclic species. Least-square power law correlation between carbon number (C_n) and isobaric thermal expansion coefficient (ITEC) is presented for acyclic alkanes (red solid line) and cyclic hydrocarbons (blue dotted line).

B.3.2 Impact on Isobaric Heat Capacity

For the last macroscopic physical property contained in the deviation term (i.e., $\frac{T{\alpha_p}^2 V_m B_S}{C_P}$) in Equation B.1, or the molar heat capacity (C_p), the property should be revisited from a microscopic viewpoint to account for its variation depending on the molecular structure and molecular weight. Figure B.7 shows the molar heat capacity of different hydrocarbon species at standard state (i.e., 298K, 0.1MPa) as a function of carbon number for different hydrocarbon groups (i.e., linear alkanes, branched alkanes, aromatics, cycloalkanes). We can observe that molar heat capacity is greater for the species with higher carbon number and acyclic molecular structure.

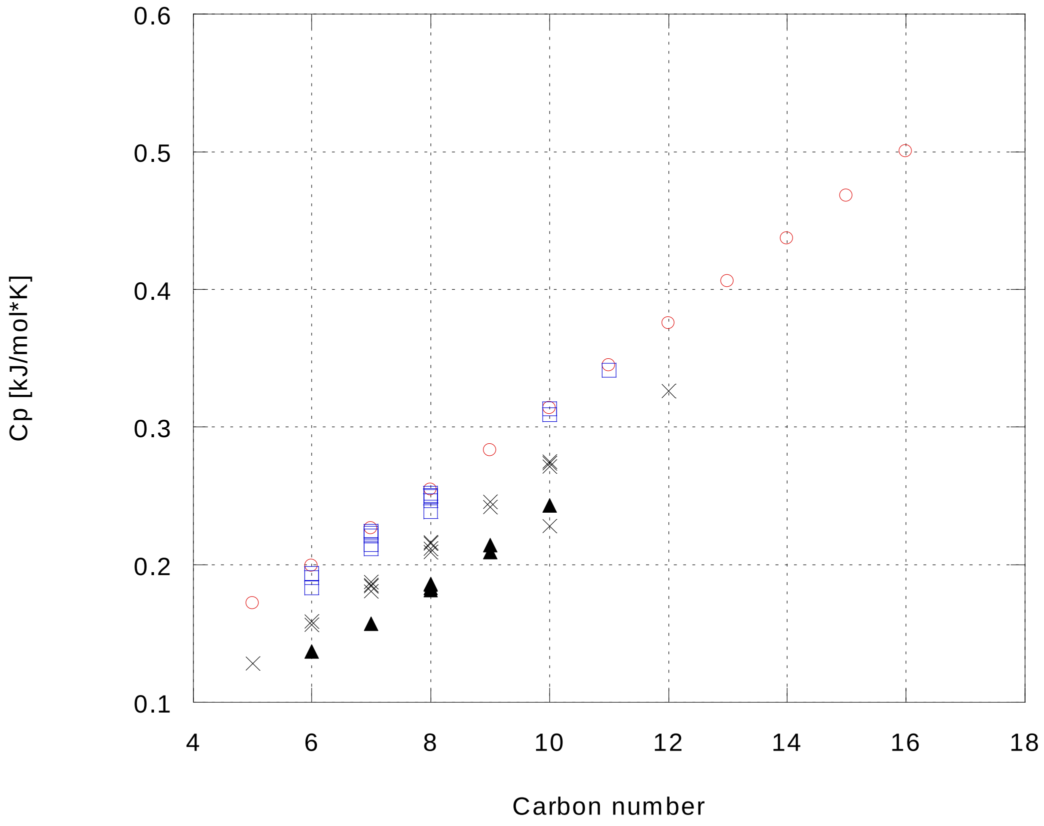

Figure B.7 Molar heat capacity of different hydrocarbon species at standard state (298K, 0.1MPa) as a function of carbon number for 4 different hydrocarbon groups: (○) n-alkanes, (□) branched alkanes, (▲) aromatics, (×) cycloalkanes.

From microscopic standpoint, molar heat capacity is the capacity of a molecule to store thermal energy in different energy modes available in a molecule (i.e., translational, rotational, vibrational, electrical, etc.).[39] The distribution of the thermal energy in different energy modes can be quantitatively expressed in the form of partition function. Equation B.4 is the mathematical definition of the partition function of a single molecule.[40] Here, q is the partition function of a single molecule, g is the degeneracy corresponding to each macrostate "j", β is the temperature parameter defined as "$\frac{1}{k_bT}$ " (k_b is Boltzmann constant), ε is the total internal energy. Subscript "*tot*" means that it encloses every energy mode available in a molecule, and subscript "i" denotes each microstate.

$$q_{tot} \equiv \sum g_j \exp(-\beta\varepsilon_j) = \sum_{i=1}^{n} e^{-\beta\varepsilon_i} \quad \text{(Eq. B.4)}$$

The total partition function of a molecule, "q_{tot}", can be divided into different types of partition function that corresponds to each division of the energy mode in a molecule. If each energy mode is independent to each other (i.e., $\varepsilon_{tot} = \sum \varepsilon_j$ and $g_{tot} = \prod g_j$), the total partition function can be written as the simple multiplication of the partition functions corresponding to each division of the energy mode as shown in Equation B.5.[41] In this study, this separation of the partition function is justified because our primary purpose is just to make a relative comparison between the partition functions of different molecular species. However, for the accurate calculation of the absolute value of the partition function of the molecular species in practice, the interaction between different divisions of the energy modes should be accounted for (e.g., the change in vibrational energy due to the rotation of the molecule).[42] In Equation B.5, the subscript "*tr*" means "translational", "*rot*" means "rotational","*vib*" means "vibrational", and "*elec*" means "electrical".

$$q_{tot} = q_{tr} \cdot q_{rot} \cdot q_{vib} \cdot q_{elec} \qquad \text{(Eq. B.5)}$$

For the temperature range relevant to Chapter 5 (i.e., 308K and 313K for bulk modulus measurement, and 318-338K for speed of sound measurement), it is reasonable to just account for three divisions of the energy modes (i.e., translational, rotational, and vibrational) because the electrical energy mode is only activated at very high temperature.[43] Thus, Equation B.5 can be simplified to Equation B.6.

$$q_{tot} = q_{tr} \cdot q_{rot} \cdot q_{vib} \qquad \text{(Eq. B.6)}$$

Furthermore, the three divisions of partition functions can be further divided into the partition functions corresponding to each degree of freedom as written in Equation B.7. Translational partition function is divided into three partition functions corresponding to each translational axis, and rotational partition function is divided into three partition functions corresponding to each axis of rotation. Vibrational partition function is divided into a set of partition functions each of which corresponds to the specific vibrational energy mode. Here, the subscript "s" denotes the total number of the vibrational degree of freedom of a molecule.

$$q_{tr} = q_{tr,x} \cdot q_{tr,y} \cdot q_{tr,z}$$

$$q_{rot} = q_{rot,x} \cdot q_{rot,y} \cdot q_{rot,z}$$

$$q_{vib} = q_{vib,1} \cdot q_{vib,2} \cdots q_{vib,s}$$

(Eq. B.7)

Then, Equations B.8 – B.10 provide how the translational, rotational, and vibrational partition functions of a polyatomic molecule are determined by the physical parameters of the molecule[44]. Equation B.8 corresponds to the translational partition function of a polyatomic molecule in a single direction. At a given temperature, the translational partition function ($q_{tr,x}$) is the function of the mass of a molecule (m) and the length scale of a box (a) in which the molecule is placed. Here, “h” is the planck constant. Equation B.9 corresponds to the average rotational partition function of a polyatomic molecule for a single rotational degree of freedom by assuming that the molecule is a rigid rotor. The rotational partition function ($q_{rot,1}$) depends on the moment of inertia in three different axes of rotation (I_A, I_B, I_C) and the symmetry factor (σ). Equation B.10 corresponds to the vibrational partition function of a polyatomic molecule with respect to a single vibrational degree of freedom by assuming that the vibrational unit is a harmonic oscillator. The vibrational partition function ($q_{vib,j}$) is the exponential function of the vibrational frequency (v), and it increases with lower vibrational frequency. In addition, the total vibrational partition function (q_{vib}) increases with increasing number of vibrational degree of freedom (s).

$$q_{tr,x} = \left(\frac{2\pi m k_b T}{h^2}\right)^{\frac{1}{2}} \cdot a \qquad \text{(Eq. B.8)}$$

$$q_{rot,1} = \sqrt[3]{\frac{8\pi^2 (8\pi^3 I_A I_B I_C)^{\frac{1}{2}} (k_b T)^{\frac{3}{2}}}{h^3 \sigma}} \qquad \text{(Eq. B.9)}$$

$$q_{vib,j} = \frac{1}{1 - e^{-\frac{h v_j}{k_b T}}} \qquad \text{(Eq. B.10)}$$

Then, based on Equations B.11 and B.12 which are the general thermodynamic relationships[45] to derive internal energy and heat capacity from the partition functions mentioned above, we can finally see how the physical parameters of a molecule affect its heat capacity.

$$< \varepsilon > = -\frac{\partial}{\partial \beta}(ln\, q) = k_b T^2 \frac{\partial}{\partial T}(ln\, q) \qquad \text{(Eq. B.11)}$$

$$c_v = \frac{\partial < \varepsilon >}{\partial T} \qquad \text{(Eq. B.12)}$$

If we plug Equations B.6 and B.7 into Equation B.11, we get Equation B.13. Then, we conduct the differentiation with respect to *T* in Equation B.13 to result in Equation B.14. Now, the expressions for each partition function (i.e., Equations B.8 – B.10) are plugged into Equation B.14 to result in Equation B.15.

$$k_b T^2 \frac{\partial}{\partial T}(ln\, q) = k_b T^2 \frac{\partial}{\partial T}(ln\, q_{tr} + ln\, q_{rot} + ln\, q_{vib})$$

$$= k_b T^2 \frac{\partial}{\partial T}\Big(\big(ln\, q_{tr,x} + \cdots + ln\, q_{tr,z}\big) + \big(ln\, {q_{rot,1}}^3\big) + \big(ln\, q_{vib,1} + \cdots ln\, q_{vib,s}\big)\Big) \quad \text{(Eq. B.13)}$$

$$< \varepsilon > = k_b T^2 \left\{ \begin{array}{c} \left(\frac{1}{q_{tr,x}}\frac{\partial q_{tr,x}}{\partial T} + \cdots + \frac{1}{q_{tr,z}}\frac{\partial q_{tr,z}}{\partial T}\right) \\ + \left(\frac{3}{q_{rot,1}}\frac{\partial q_{rot,1}}{\partial T}\right) + \left(\frac{1}{q_{vib,1}}\frac{\partial q_{vib,1}}{\partial T} + \cdots + \frac{1}{q_{vib,s}}\frac{\partial q_{vib,s}}{\partial T}\right) \end{array} \right\} \quad \text{(Eq. B.14)}$$

$$< \varepsilon > = k_b T^2 \left[\begin{array}{c} \left\{\frac{1}{T^{\frac{1}{2}}}\frac{\partial}{\partial T}\left(T^{\frac{1}{2}}\right) + \cdots\right\} + \frac{3}{T^{\frac{3}{2}}}\frac{\partial}{\partial T}\left(T^{\frac{3}{2}}\right) \\ + \left\{\left(1 - e^{-\frac{h\nu_1}{k_b T}}\right)\frac{\partial}{\partial T}\left(\frac{1}{1-e^{-\frac{h\nu_1}{k_b T}}}\right) + \cdots\right\} \end{array} \right] \quad \text{(Eq. B.15)}$$

For the vibrational contribution of the internal energy, or the last term of the RHS of Equation B.15 (i.e., $\left\{\left(1 - e^{-\frac{h\nu_1}{k_b T}}\right)\frac{\partial}{\partial T}\left(\frac{1}{1-e^{-\frac{h\nu_1}{k_b T}}}\right) + \cdots\right\}$), we conduct the differentiation with respect to *T* to result in Equation B.16.

$$< \varepsilon >_{vib} = \sum_{j=1}^{s} \left(\frac{h\nu_j\, e^{-\frac{h\nu_j}{k_b T}}}{\left(1-e^{-\frac{h\nu_j}{k_b T}}\right)} \right) \quad \text{(Eq. B.16)}$$

Then, from Equations B.15 and B.16, we can notice that the only temperature-independent parameters that affect total internal energy is the number of vibrational degree of freedom and vibrational frequency (i.e., *s, v*). Thus, at a fixed temperature, the total internal energy is the function of *s* and *v* as shown in Equation B.17.

$$< \varepsilon >|_T \sim < \varepsilon >_{vib}|_T \sim \sum_{j=1}^{s} \frac{v_j e^{-v_j}}{1-e^{-v_j}} \quad \text{(Eq. B.17)}$$

Since the derivative of the function "$\frac{xe^{-x}}{1-e^{-x}}$" is always negative, the total internal energy decreases with higher vibrational frequency (*v*). In addition, the total internal energy will increase with increasing number of the vibrational degree of freedom (*s*). This will directly guide us to understand how the heat capacity is determined by the physical parameters of a molecule. We take a derivative of the total internal energy with respect to *T* to obtain the expression for heat capacity. Since the total internal energy at a fixed temperature is only the function of the physical parameters related to the vibrational energy, we just take the derivative to Equation B.17 to result in Equation B.18. Then, at a fixed temperature, heat capacity becomes the function of only the vibrational frequency (*v*) and the number of vibrational degree of freedom (*s*) as shown in Equation B.19. The derivative of the function "$\frac{x^2e^{-x}}{(1-e^{-x})^2}$" is always negative, so, the heat capacity of a molecule increases with lower vibrational frequency. In addition, the heat capacity will also increase with increasing number of vibrational degree of freedom. Thus, the difference in the "number of vibrational degree of freedom" and "vibrational frequency" due to different molecular structure and molecular weight determines the heat capacity of a molecular species.

$$c_{v,vib} = \frac{\partial <\varepsilon>_{vib}}{\partial T} = \sum_{j=1}^{s} \left(\frac{\frac{(h\nu_j)^2}{k_b T^2} e^{-\frac{h\nu_j}{k_b T}}}{(1-e^{-\frac{h\nu_j}{k_b T}})^2} \right) \qquad \text{(Eq. B.18)}$$

$$c_v \,|_T \sim c_{v,vib}\big|_T \sim \sum_{j=1}^{s} \frac{{\nu_j}^2 e^{-\nu_j}}{(1-e^{-\nu_j})^2} \qquad \text{(Eq. B.19)}$$

If the number of atoms contained in a molecule is *x*, then, the total degree of freedom of a molecule is equal to "*3x"* (i.e., total degree of freedom of all the atoms contained in the molecule). A molecule has 3 translational degrees of freedom, and 3 (non-linear molecule) or 2 (linear molecule such as N_2 and CO_2) rotational degrees of freedom. Thus, the vibrational degrees of freedom are "*3x-6*" (non-linear molecule) or "*3x-5*" (linear molecule).[46] Thus, if the number of atoms contained in a molecule increases, the vibrational degrees of freedom increase. For hydrocarbons with similar molecular structure with different carbon number, the vibrational degrees of freedom increase with higher carbon number. For example, if we compare n-hexane to n-heptane, n-hexane has 3 less atoms (1 carbon and 2 hydrogens) than n-heptane, which results in 9 less vibrational degrees of freedom. Since "*s"* is decreased, the heat capacity of n-hexane is also smaller than that of n-heptane. The same logic applies for the comparison case between the acyclic hydrocarbons and cyclic hydrocarbons. If we compare n-hexane to cyclohexane or benzene, n-hexane has two more hydrogen atoms than cyclohexane, and 8 more hydrogen atoms than benzene, which results in 6 more vibrational degrees of freedom and 24 more vibrational degrees of freedom than cyclohexane and benzene, respectively. This is the major cause of the decrease in heat capacity in cyclic species compared to the acyclic species.

In addition, the "vibrational frequencies" are different for acyclic hydrocarbons and cyclic hydrocarbons. Equation B.20 is a simple harmonic oscillation model showing how vibrational frequency is determined by the physical parameters of the vibrational unit contained in a molecule.[47] The frequency increases with higher force constant (k) of the bond, and lower reduced mass (μ) of the vibration unit. The ring strain of the cyclic species increases the value of k in C-C bond (especially in aromatics because the bond order for aromatics is 1.5) to result in higher vibrational frequencies of some of the vibrational units in the molecule[48], which, in turn, contributes to the lower heat capacity of the cyclic species compared to acyclic species.

$$\nu = \frac{1}{2\pi}\sqrt{\frac{k}{\mu}} \qquad \text{(Eq. B.20)}$$

B.3.3. Conclusions

Based on the impact of molecular structure and weight on the 4 macroscopic physical properties (i.e., V_m, C_p, α_p, B_s) mentioned earlier, we can now fully understand how the specific heat ratio of a molecular species will differ by its molecular structure and molecular weight.

The molar volume increases for the species with higher carbon number and acyclic molecular structure. The isobaric molar heat capacity follows the same trend as the molar volume. In fact, the molar volume and heat capacity of hydrocarbon molecular species have very close linear relationship with each other. In Figure B.8, the isobaric molar heat capacity of 52 hydrocarbon species is plotted as a function of molar volume. The molecular species selected for Figure B.8 is the same as the species presented in Figures B.4 and B.6. We can observe a clear linear correlation between the molar volume and molar heat capacity. Thus, in the deviation term (i.e., $\frac{T\alpha_p{}^2V_mB_s}{C_P}$) in Equation B.1, the effect of molar volume is counterbalanced by the effect of molar heat capacity, thus leaving only two parameters (i.e., B_s, α_p) as the determinants of the value of specific heat ratio.

The isentropic bulk modulus is greater for the species with higher carbon number and ring structure while the isobaric thermal expansion coefficient has the totally opposite trend. Thus, we need to look at how the degree of the impact of the two physical properties are different for hydrocarbon species.

First, for the species with similar molecular structure, the degree of the decrease in the isobaric thermal expansion coefficient for higher carbon number species overshadows the degree of the increase in the isentropic bulk modulus. By using the power law correlation suggested in Figures B.5 and B.6, we can estimate how much increase in isentropic bulk modulus and how much decrease in isobaric thermal expansion coefficient will occur as the carbon number of the molecular species increases. For acyclic hydrocarbon species, the isentropic bulk modulus increases by 12.79% as the carbon number is increased from 5 to 6 while the isobaric thermal expansion coefficient decreases by 9.55%. The decrement of the isobaric thermal expansion coefficient is squared in the deviation term (i.e., $\frac{T\alpha_p{}^2 V_m B_s}{C_P}$) to result in 18.19%, which dominates the increment of the isentropic bulk modulus. As a result, the deviation term decreases about 8% as the carbon number is increased from 5 to 6 in acyclic hydrocarbon species, thus resulting in the decrease in specific heat ratio with higher carbon number.

Second, for the comparison between the acyclic species and cyclic species with the same carbon number, the degree of the increase in isentropic bulk modulus in cyclic species overwhelms the decrease in the isobaric thermal expansion coefficient. For example, if we compare the cyclic species with carbon number 6 to the acyclic counterpart, the isobaric thermal expansion coefficient of the species is 15.8% smaller than the acyclic counterpart. However, the isentropic bulk modulus of the cyclic species with carbon number 6 is 72.2% greater than the acyclic counterpart, which dominates the squared decrement (i.e., 29.1%) of the isobaric thermal expansion coefficient. As a result, the specific heat ratio of the cyclic species becomes much greater than the acyclic counterpart.

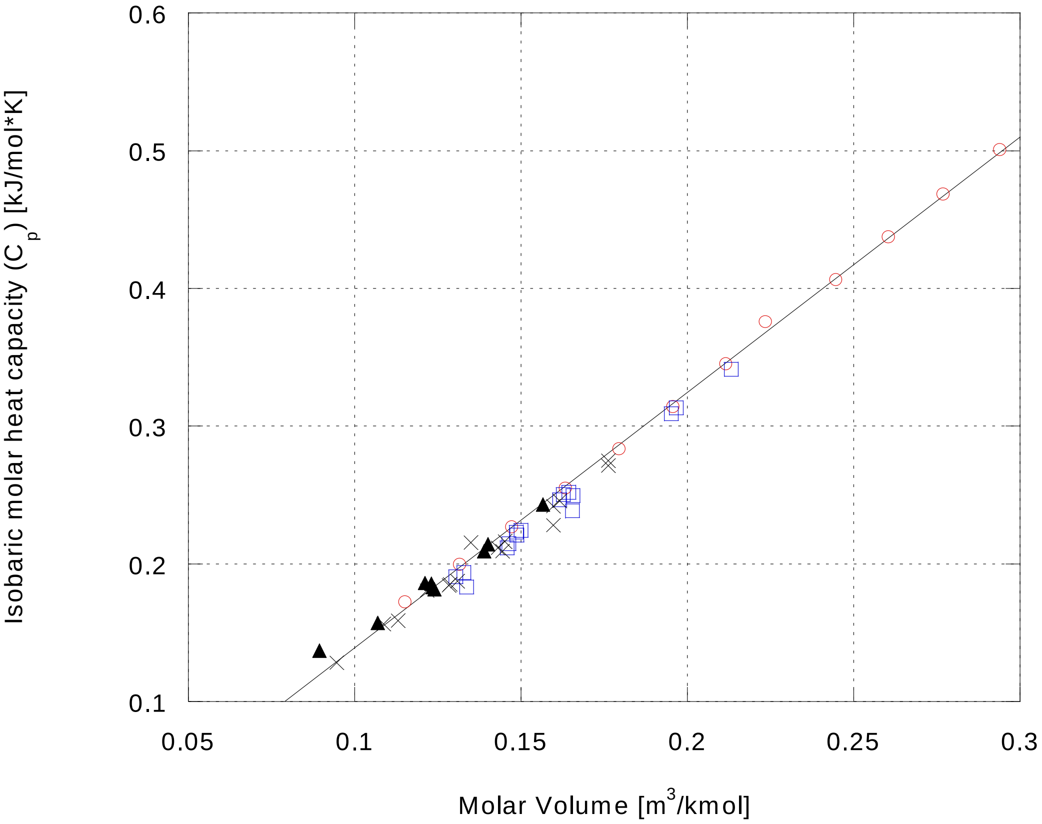

Figure B.8 Isobaric molar heat capacity as a function of molar volume. The line is the least-square linear regression for all of the 52 hydrocarbon species presented: $C_p[\frac{kJ}{(mol \cdot K)}] = 1.8409 V_m[\frac{m^3}{kmol}] - 0.0482$ with the R-squared value of 0.992. (○) n-alkanes, (□) branched alkanes, (▲) aromatics, (×) cycloalkanes.

B.4 References

[1] Poling, B.E.; Thomson, G.H.; Friend, D.G.; etc. Section 2-Physical and chemical data. *Perry's chemical engineers' handbook*, 8th ed.; McGraw-Hill: New York, 2008; pp. 2-229, 2-252, 2-254, 2-261, 2-274, 2-276, 2-300, 2-302, 2-316, 2-318, 2-324, 2-410.

[2] Giuliano Albo, P.A.; Lago, S.; Romeo, R.; Lorefice, S. High pressure density and speed-of-sound measurements in n-undecane and evidence of the effects of near-field diffraction, *J. Chem. Thermodyn.*, **2013**, 58, 95-100.

[3] Bessieres, D.; Plantier, F. Thermodynamic Consistency between Calorimetric Acoustic and Volumetric Measurements: Application to n-undecane, *J. Therm. Anal. Calorim*. **2007**, 89, 81-85.

[4] Khasanshin, T.S.; Shchamialiou, A.P.; Poddubskij, O.G. Thermodynamic properties of heavy n-alkanes in the liquid state: n-tridecane, *High Temperatures - High Pressures,* **2003/2004**, 35/36, 227-235.

[5] Daridon, J-L.; Lagourette, B. Ultrasonic velocity of liquid tridecane and tetradecane as a function of temperature and pressure, *High Temperatures - High Pressures*, **2000**, 32, 83-87.

[6] Bernardo, G.; Vesely, D. Solubility of Alkanes in a Polystyrene Matrix, *J. Appl. Polym. Sci.*, **2008,** 110, 2393-2398.

[7] Daridon, J.L.; Carrier, H.; Lagourette, B. Pressure Dependence of the Thermophysical Properties.

of n-Pentadecane and n-Heptadecane, *Int. J. Thermophys*., **2002**, 23, 697-708.

[8] Outcalt, S.; Laesecke, A.; Fortin, T.J. Density and speed of sound measurements of hexadecane, *J. Chem. Thermodyn*. **2010**, 42, 700-706.

[9] Brooks, D.B.; Howard, F.L.; Crafton.Jr, H.C. Physical properties of some purified aliphatic hydrocarbons, *J. Res. Natl. Bur. Stand.*, **1940,** 24, 33-45.

[10] Kumaran, M.K; Benson, G.C.; Halpin, C.J. Ultrasonic Speeds and Isentropic Compressibilities for Binary Mixtures of 1-hexanol with Hexane Isomers at 298.15 K, *J. Chem. Eng. Data*, **1983**, 28, 66-70.

[11] Moravkova, L.; Wagner, Z.; Sedlakova, Z.; Linek, J. Volumetric behaviour of binary and ternary liquid systems composed of ethanol, isooctane, and toluene at temperatures from (298.15 to 328.15) K. Experimental data and correlation, *J. Chem. Thermodyn*. **2011,** 43, 1906-1916.

[12] Luning Prak, D.J.; Alexandre, S.M.; Cowart, J.S.; Trulove, P.C. Density, Viscosity, Speed of Sound, Bulk Modulus, Surface Tension, and Flash Point of Binary Mixtures of n-Dodecane with 2,2,4,6,6-Pentamethylheptane or 2,2,4,4,6,8,8-Heptamethylnonane, *J. Chem. Eng. Data*, **2014,** 59, 1334-1346.

[13] Gahlyan, S.; Rani, M.; Maken, S. Ultrasonic speeds, viscosities, refractive indices and FT-IR spectroscopic studies of an oxygenate with aliphatic and aromatic hydrocarbons at 298.15 K and 308.15 K, *J. Mol. Liq.,* **2016**, 219, 1107-1123.

[14] Calvar, N.; Gonzalez, B.; Gomez, E.; Canosa, J. Density, Speed of Sound, and Refractive Index for Binary Mixtures Containing Cycloalkanes and Aromatic Compounds at T=313.15 K, *J. Chem. Eng. Data*, **2009,** 54, 1334-1339.

[15] Gonzalez, B.; Dominguez, I.; Gonzalez, E.J.; Dominguez, A. Density, Speed of Sound, and Refractive Index of the Binary Systems Cyclohexane (1) or Methylcyclohexane (1) or Cyclo-octane (1) with Benzene (2), Toluene (2), and Ethylbenzene (2) at Two Temperatures, *J. Chem. Eng. Data*, **2010,** 55, 1003-1011.

[16] Gonzalez-Olmos, R.; Iglesias, M.; Santos, B.M.R.P.; Mattedi, S.; Goenaga, J.M.; Resa, J.M. Influence of temperature on thermodynamic properties of substituted aromatic compounds, *Phys. Chem. Liq.*, **2010,** 48, 257-271.

[17] Dragoescu, D.; Sirbu, F.; Shchamialiou, A.; Khasanshin, T. Thermophysical properties of n-hexadecane + some alkylbenzenes binary mixtures at temperatures from 298.15 K to 318.15 K and atmospheric pressure, *J. Mol. Liq*., **2017,** 237, 208-215.

[18] Gonzalez, B.; Gonzalez, E.J.; Calvar, N.; Dominguez, I.; Canosa, J. Density, Speed of Sound, and Refractive Index for Binary Mixtures Containing Cycloalkanes with o-Xylene, m-Xylene, p-Xylene, and Mesitylene at T = (298.15 and 313.15) K, *J. Chem. Eng. Data*, **2010,** 55, 2294-2305.

[19] Miyake, Y.; Bessieres, D.; Plantier, F.; Ushiki, H.; Boned, C. The study of stereoisomerism influence on speed of sound, isentropic compressibility and heat capacity: application to cis-decalin and trans-decalin, *J. Therm. Anal. Calorim.*, **2008,** 91, 347-354.

[20] Marcus, Y.; Hefter, G.T. The Compressibility of Liquids at Ambient Temperature and Pressure, *J. Mol. Liq.,* **1997**, 73, 61-74.

[21] Tamura, K.; Kumaran, M.K.; Halpin, C.J.; Benson, G.C. Ultrasonic speeds and isentropic compressibilities of each of the mixtures: (Z-ethylbutan-l-01 + an isomer of hexane) at 298.15 K, *J. Chem. Thermodyn*., **1984**, 16, 145-152.

[22] Bessieres, D.; Pineiro, M.M.; De Ferron, G.; Plantier, F. Analysis of the orientational order effect on n-alkanes: Evidences on experimental response functions and description using Monte Carlo molecular simulation, *J. Chem. Phys*., **2010,** 133, 074507.

[23] Takagi, T.; Sakura, T. J.; Guedes, H.J.R. Speed of sound in liquid cyclic alkanes at temperatures between (283 and 343)K and pressures up to 20MPa, *J. Chem. Thermodyn*. **2002,** 34, 1943-1957.

[24] *DIPPR Project 801*; Design Institute for Physical Property Research, 2017. http://app.knovel.com/web/toc.v/cid:kpDIPPRPF7/viewerType:toc/root_slug:dippr-project-801-full/url_slug:dippr-project-801-full/?.

[25] Luning Prak, D.J.; Brown, E.K.; Trulove, P.C. Density, Viscosity, Speed of Sound, and Bulk Modulus of Methyl Alkanes, Dimethyl Alkanes, and Hydrotreated Renewable Fuels, *J. Chem. Eng. Data*, **2013,** 58, 2065-2075.

[26] Luning Prak, D.J.; Morris, R.E.; Cowart, J.S.; Hamilton, L.J.; Trulove, P.C. Density, Viscosity, Speed of Sound, Bulk Modulus, Surface Tension, and Flash Point of Direct Sugar to Hydrocarbon Diesel (DSH-76) and Binary Mixtures of N-Hexadecane and 2,2,4,6,6-Pentamethylheptane, *J. Chem. Eng. Data,* **2013**, 58, 3536-3544.

[27] Huang, D.; Simon, S.L.; McKenna, G.B. Chain length dependence of the thermodynamic properties of linear and cyclic alkanes and polymers, *J. Chem. Phys*., **2005,** 122, 084907.

[28] Domalski, E.S.; Hearing, E.D. Estimation of the Thermodynamic Properties of Hydrocarbons at 298.15 K, *J. Phys. Chem. Ref. Data***, 1988,** 17, 1637-1678.

[29] Ali, A.; Nain, A.K.; Chand, D.; Ahmad, R. Volumetric, ultrasonic, viscometric and refractive index behavior of binary mixtures of 2,2,4-trimethylpentane with aromatic hydrocarbons: An experimental and theoretical study, *Bull. Chem. Soc. Jpn.* **2006,** 79, 702-710.

[30] Sastry, N.V.; Patel, S.R.; Soni, S.S. Densities, Speeds of Sound, Excess Molar Volumes, and Excess Isentropic Compressibilities at T = (298.15 and 308.15) K for Methyl Methacrylate + 1-Alkanols (1-Butanol, 1-Pentanol, and 1-Heptanol) + Cyclohexane, + Benzene, + Toluene, + p-Xylene, and + Ethylbenzene, *J. Chem. Eng. Data*, **2011,** 56, 142-152.

[31] *National Institute of Standards and Technology (NIST) Chemistry WebBook, SRD 69*. http://webbook.nist.gov/cgi/cbook.cgi?ID=C98828&Mask=2#ref-4 (Accessed on February 12th, 2018).

[32] Miyake, Y.; Baylaucq, A.; Zeberg-Mikkelsen, C.K.; Galliero, G.; Ushiki, H.; Boned, C. Stereoisomeric effects on volumetric properties under pressure for the system cis- + trans-decalin, *Fluid Phase Equilib.*, **2007,** 252, 79-87.

[33] Dearden, J.C. Quantitative structure-property relationships for prediction of boiling point, vapor pressure, and melting point, *Environmental Toxicology and Chemistry*, **2003**, 22(8), 1696-1709.

[34] London, F. The general theory of molecular forces, *Trans. Faraday Soc.*, **1937**, 33, 8-26.

[35] Israelachvili, J.N. *Intermolecular and Surface Forces*, 3rd ed.; Academic Press: Burlington, MA., 2011; pp. 108-109.

[36] Anslyn, E.V.; Dougherty, D.A. *Modern physical organic chemistry*, 1st ed.; University Science Books: Sausalito, CA., 2006; pp.24-25.

[37] Van Rysselberghe, P. Remarks concerning the Clausius-Mossotti Law, *J. Phys. Chem.*, **1932**, 36, 1152-1155.

[38] Bondi, A. van der Waals Volumes and Radii, *J. Phys. Chem.*, **1964,** 68, 441-451.

[39] Laurendeau, N.M., *Statistical Thermodynamics: Fundamentals and applications,* 1st ed.; Cambridge university press: New York, 2005; pg. 167-168.

[40] Laurendeau, N.M. *Statistical Thermodynamics: Fundamentals and applications*, 1st ed.; Cambridge university press: New York, 2005; pg. 48.

[41] Laurendeau, N.M. *Statistical Thermodynamics: Fundamentals and applications*, 1st ed.; Cambridge university press: New York, 2005; pp. 161-162.

[42] Laurendeau, N.M. *Statistical Thermodynamics: Fundamentals and applications*, 1st ed.; Cambridge university press: New York, 2005; pg. 136.

[43] Laurendeau, N.M., *Statistical Thermodynamics: Fundamentals and applications,* 1st ed.; Cambridge university press: New York, 2005; pp.158-159.

[44] Laurendeau, N.M., *Statistical Thermodynamics: Fundamentals and applications,* 1st ed.; Cambridge university press: New York, 2005; pg. 192-198.

[45] Laurendeau, N.M., *Statistical Thermodynamics: Fundamentals and applications,* 1st ed.; Cambridge university press: New York, 2005; pg. 51-54.

[46] Segneanu, A.E.; Gozescu, I.; Dabici, A.; etc. Chapter 9 - Organic compounds FT-IR spectroscopy. In *Macro to nano spectroscopy*, 1st ed.; Uddin, J.; Intech: Rijeka, Croatia, 2012; pp.150-151.

[47] Segneanu, A.E.; Gozescu, I.; Dabici, A.; etc. Chapter 9 - Organic compounds FT-IR spectroscopy. In *Macro to nano spectroscopy*, 1st ed.; Uddin, J.; Intech: Rijeka, Croatia, 2012; pg.147.

[48] Segneanu, A.E.; Gozescu, I.; Dabici, A.; etc. Chapter 9 - Organic compounds FT-IR spectroscopy. In *Macro to nano spectroscopy*, 1st ed.; Uddin, J.; Intech: Rijeka, Croatia, 2012; pp.160-162.